EUROPEAN CONFERENCE ON INTEGRATED OPTICS

ECIO 2023

24th European Conference on Integrated Optics

x

19th April – 21th April

University of Twente
Enschede, Netherlands

UNIVERSITY OF TWENTE.

ECIO23

Steering Committee

Conference Chairs

Chairman: ***Sonia M. Garcia Blanco****, University of Twente*
Co-Chair: ***Lantian Chang****, University of Twente*

Scientific Committee Members

Mohand Achouche, 3-5 Labs, France
Imran Akca, Vrije Universiteit, Amsterdam, The Netherlands
Pavel Cheben, National Research Council, Canada
Qixiang Cheng, Cambridge University, United Kingdom
Daoxin Dai, Zhejiang University, China
Wolfgang Freude, Karlsrushe Institute of Technology, Germany
Dominic Gallagher, Photon Design, United Kingdom
Sonia Garcia Blanco, Twente University, The Netherlands
Kiichi Hamamoto, Kyushu University, Japan
David Marpaung, University of Twente
Di Liang, Hewlett Packard Labs, USA
Jelmer Renema, QuiX Quantum / University of Twente, The Netherlands
Pascual Muñoz, Universitat Politècnica de València, Spain
Richard Penty, Cambridge University, United Kingdom
Ryszard Piramidowicz, Warsaw University of Technology, Poland
Pepijn Pinkse, University of Twente, The Netherlands
Carlos Alonso Ramos, Paris Sud, France
Günther Roelkens, Ghent University, Belgium
Patrick Runge, Fraunhofer, HHI, Germany
Pablo Sanchis, Universitat Politècnica de València, Spain
Kevin Williams, Eindhoven University of Technology, The Netherlands
Hon Ki Tsang, Chinese University of Hong Kong
Gonzalo Wangüemert Pérez, University of Málaga, Spain
Francesco Morichetti, Politecnico di Milano
Lantian Chang, University of Twente

Local Organizing Committee

Sonia Garcia Blanco
Lantian Chang
Carlos Osornio Martinez
Soheila Mardani
Kai Wang
Dawson Bonneville
David Marpaung
Jelmer Renema

Pepijn Pinkse
Kaixuan Ye
Jose Nijhuis – Effing
Annerie Heesink
Karen Munnink
Nicole Meinster-Engbers
Jardi Timmerhuis

Program

Wednesday 19th April
Room WA-2

11:30-14:00	Registration (Bike hand out)
14:00-14:30	Opening ceremony
14:30-15:30	Plenary
15:30-16:30	Top scoring Session
16:30-17:15	Coffee break
17:15-18:30	Exhibition session
18:30-19:30	Panel discussion
19:30	Reception with dinner

Thursday 20th April

	Section 1: **Room WA-2**	Section 2: **Room WA-3**
8:45-9:30	Keynote 1 **Room WA-2**	
9:30-10:30	Tech and platforms	Devices
10:30-11:30	Coffee break & Poster	
11:30-12:30	Tech and platforms	Devices
12:30-13:30	Lunch & Exhibition	
13:30-14:15	Women in Photonics	
14:15-15:15	Tech and platforms	Applications
15:15-16:30	Coffee break & Poster	
16:30-17:45	Devices	Applications
19:00	Gala Dinner	

Program

	Friday 21th April	
	Section 1: **Room WA-1**	Section 2: **Room WA-3**
8:45-9:30	Keynote 2 **Room WA-1**	
9:30-10:30	Devices	Physical insights
10:30-11:30	Coffee break & Poster	
11:30-12:45	Devices	Tech and platforms
12:45-14:15	Lunch & Exhibition	
14:15-15:15	Devices	Applications
15:15-16:30	Coffee break & Poster	
16:30	Closing ceremony **Room WA-1**	

Physical insights: Novel physical insights and materials

Tech and platforms: Integrated photonic technologies and platforms

Devices: Devices and Integrated Circuits

Applications: Applications of PICs

Scientific Program
Wednesday 19th April 2023

11:30	**14:00**	**Registration** and Pick up bikes
14:00	**14:30**	**Opening ceremony (Room: WA-2).** **Chair: Prof. Dr. Sonia M. Garcia Blanco** Prof. Vinod Subramaniam, President, University of Twente Prof. Mike Wale, Photonics21
14:30	**15:30**	**Plenary (Room: WA-2). Chair: Prof. Dr. Sonia M. Garcia Blanco** **Progress in electronic-photonic integrated circuits and systems: platforms, devices and applications.** Professor Miloš Popović, Boston University.
15:30	**16:30**	**TOP SCORING SESSION (Room: WA-2)** **Chair: Prof. Dr. Wolfgang Freude** **Platforms.** Micro-transfer-printed O-band GaAs QD-on-Si DFB Laser on an advanced silicon photonics platform. Jing Zhang. **Devices.** Ultrafast frequency-agile narrow-linewidth lasers using lithium niobate integrated photonics. Viacheslav Snigirev. **Physical Insights.** Spectrally Programmable Individual Color Centers in Silicon Waveguides. Carlos Erando Herranz. **Applications:** Fully Integrated Quasi-Coherent Receiver Based on Co-hosted InP PIC and a SiGe ASIC. Francisco Rodrigues.
16:30	**17:15**	**COFFEE BREAK** *sponsored by* ***LioniX***
17:15	**18:30**	Opening of the exhibition session **(Room: WA-2)** **Chair: Prof. Dr. ir. Roel Baets**
18:30	**19:30**	Panel discussion **(Room: WA-2)** **Chair: Prof. Dr. Kevin Williams**
19:30		Reception with Dinner *Reception drinks sponsored by* ***PHIX, Synopsys, Luceda, and ePIXfab, VLC Photonics***

Scientific Program

Thursday 20th April 2023

08:45	**09:30**	**Keynote 1 (Room: WA-2)** **Visible light integrated photonics.** Joyce Poon.	
		Integrated photonic technologies and platforms (Room: WA-2) **Chair: Dr. Jonathan Bradley**	**Devices and Integrated Circuits (Room: WA-3)** **Chair: Prof. Dr. Carlos Alonso-Ramos**
09:30	**09:45**	Th1.1 **Invited**. **Waveguide amplifiers in Si3N4 platform**. Liu Yang.	Th2.1 **First experimental demonstration of a Generalized Mach-Zehnder Interferometer on Si3N4.** Stefanos Kovaios.
09:45	**10:00**		Th2.2 **Reverse Synthesis for the Configuration of Coupled Ring Resonators.** Xiangfeng Chen.
10:00	**10:15**	Th1.2 **Optical gain via multi-layer monolithic integration of Si3N4 with Al2O3:Er3+ waveguide amplifiers**. Carlos Osornio.	Th2.3. **Demonstration of nano-pixel 9:1 asymmetric power splitter.** Haisong Jiang
10:15	**10:30**	Th1.3 **Broadband and large mode-area on-chip amplifier**. Mahmoud Gaafar.	Th2.4 **Demonstrating Bidirectional Coupling Using a Monolithically Integrated Tunable Comb Source.** John McCarthy

		COFFEE BREAK (*sponsored by* *Chilas)* & POSTERS
		ID 124. **Third-Order Intermodulation Distortion Suppression Analysis for Dual-Parallel Mach-Zehnder Modulator Using Optical Carrier Band Processing.** Cristina Catalá-Lahoz.
		ID 132. **Loss engineering of a bimodal waveguide platform for biosensing.** Samuel M. Hörmann.
		ID 136. **Two-dimensional layered PtSe2 for High Speed Near-Infrared Electro-Optic Modulation.** Yi Wang.
		ID 138. **Generic Platform Integrated Frequency Shifter for Low Bandwidth Heterodyne Detection Systems.** Pablo López-Querol.
		ID 140. **Single-mode polymer ring resonator for sensor applications.** Lase Milgrave.
10:30	**11:30**	ID 141. **High Coupling Efficiency Waveguide Grating Couplers for Bound-states-in-the-Continuum waveguide on Lithium Niobate.** Hon Ki Tsang.
		ID 148. **Experimental demonstration of a low-loss broadband directional coupler based on subwavelength gratings metamaterials.** Jaime Vilas.
		ID 153. **Studying Open Scattering Channels in an Analog Physical Simulation**. Pepijn Pinkse.
		ID 157. **Integrated On-chip Light Control via Out-coupling Grating Structures for Quantum Applications.** Anastasiia Sorokina.
		ID 158. **Optical isolator element using nano-pixel for photonic integrated circuits.** Haisong Jiang.
		ID 162. **A Compact Apodized Grating Coupler for Perfectly Vertical Coupling.** Mingxiang Yang.

		Integrated photonic technologies and platforms (Room: WA-2) Chair: Prof. Dr. Pepijn Pinkse	**Devices and Integrated Circuits (Room: WA-3) Chair: Prof. Dr. Ing. Pascual Muñoz**
11:30	**11:45**	Th1.4 **Invited**. **Integration of quantum light sources, circuits and superconducting detectors on nanophotonic chips.** Carsten Schuck.	Th2.5. **Subwavelength metamaterial grating couplers on silicon nitride platform.** Daniel Benedikovic.
11:45	**12:00**		Th2.6. **Integrated four channel wavelength multiplexer in Thin Film Lithium Niobate for CWDM 400G/800G short reach communications.** Giuseppe Cusmai.
12:00	**12:15**	Th1.5. **Fiber-coupled plug-and-play heralded single photon source based on Ti:LiNbO3 and polymer technology**. Christian Kießler.	Th2.7. **Thermo-optically Tunable DBR Resonator with Ultra-broad Rejection Band for Silicon Photonic Applications.** Pratyasha Priyadarshini
12:15	**12:30**	Th1.6. **Programmable photorefractive optical synapses in integrated photonics for neuromorphic computing**. Elger A. Vlieg.	Th2.8. **Ultra-high resolution on-chip reconstructive spectrometer.** Chunhui Yao
12:30	**13:30**	**Lunch & Exhibition** *Lunch sponsored by* ***Aluvia***	
13:30	**14:15**	**Women in Photonics (Room: WA-2) Chair: Soheila Mardani Mehrabad**	

		Integrated photonic technologies and platforms (Room: WA-2) Chair: Dr. Dawson Bonneville	Applications of PICs (Room: WA-3) Chair: Carlos Osornio Martinez
14:15	**14:30**		Th2.9 **Soliton generation in a gallium phosphide photonic crystal cavity.** Alysa Davydova.
14:30	**14:45**	Th1.7. **Invited. Glass integrated photonics.** Jean-Emmanuel Broquin.	Th2.10. **Demonstration of low RMS differential phase noise across C-band for integrated, amplifying optical phased arrays.** Shiva Vikram Bhagavatula
14:45	**15:00**	Th1.8. **Damage Resistant Diced Waveguides in Ti-Indiffused Lithium Niobate for Second Harmonic Generation.** Michelle Kirsch.	Th2.11 **Sub-kHz linewidth, high power, frequency agile photonic integrated E-DBR laser.** Anat Siddharth
15:00	**15:15**	Th1.9. **Monolithic CMOS sample & hold circuit for sequential control of volatile actuators in Silicon Photonics.** Francesco Zanetto.	Th2.12 **Unconventional Optical Phased Array Antennas Integrated in a Programmable Photonic Integrated Circuit.** Nicola Anselmi.
15:15	**16:30**	**COFFEE BREAK (*sponsored by* Quix) & POSTERS**	
		ID 166. **Dual phase-amplitude silicon modulator driven by an ENZ transparent conducting oxide.** Juan Navarro-Arenas.	
		ID 169. **Coherency-broken cascaded SiN Bragg filters for attaining ultra-high rejection considering both TE/TM polarization.** David Enrique Medina Qurioz.	
		ID 173. **Design of a Broadband Polarization Controller Based on Silicon Nitride-Loaded Thin-Film Lithium Niobate.** Ivan Richter.	

COFFEE BREAK (*sponsored by* Quix) & POSTERS

15:15	**16:30**

ID 175. **Simulation study of propagation losses due to sidewall roughness of GaAs waveguides for single-photon sources in quantum applications.** Miloš Ljubotina.

ID 179. **Broadband, low-loss O-band Silicon Polarization Splitter-Rotator.** Theoni Prousalidi.

ID 180. **Towards Photonic Integrated Ion Traps for high-performance Quantum Computing and Atomic Clocks.** Carl-Frederik Grimpe.

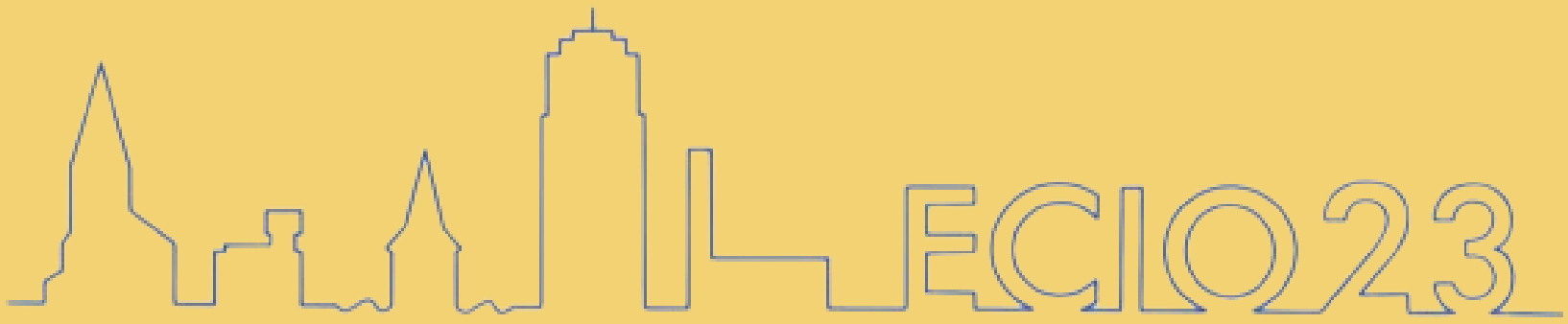
ID 182. **Fabrication tolerant directional coupler.** Yichen Liu.

ID 188. **Design of Mid-Infrared Supercontinuum Generation in a strip-loaded LNOI Waveguide through lateral leakage engineering.** Kokou Firmin Fiaboe.

ID 189. **Integration of superconducting nanowire single-photon detectors in subwavelength-grating-structured waveguides.** Alejandro Sánchez Postigo.

ID 190. **Polarization beam splitter in the silicon nitride platform for the 1 µm wavelength band.** Zindine MOKEDDEM.

ID 192. **Multiphysics simulation approach for polymer waveguide microring resonator based ultrasonic detectors.** Rainer Hainberger.



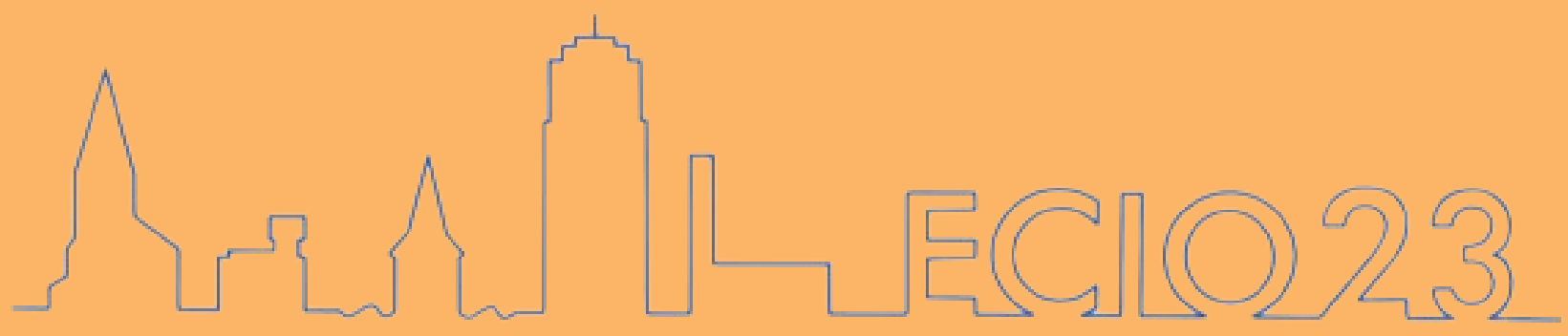
		Devices and Integrated Circuits (Room: WA-2) **Chair: Prof. Dr. Pablo Sanchis Kilders**	**Applications of PICs (Room: WA-3)** **Chair: Prof. Dr. Ir. David Marpaung**
16:30	**16:45**	Th1.10. **Suspended Gallium Arsenide Electro-Optic Racetrack Ring Modulator.** Haoyang Li.	Th2.13. **Invited. Astrocomb miniaturization.** Ewelina Obzrud
16:45	**17:00**	Th1.12. **Phase modulation in a Compact 8-channel Loop-back AWG based Integrated Comb Processor.** Louw Roel van der Zon.	
17:00	**17:15**	Th1.13. **1 GHz integrated electro-optical modulator in the 5.5-9 µm wavelength range.** Thi Hao Nhi Nguyen	Th2.14. **A Photonic Integrated High-power Soliton Microcomb Generator.** Xinru Li.
17:15	**17:30**	Th1.14 **Intra-Cavity Coherently Combining of DBR Lasers on an InP Generic Foundry Platform.** Rakesh Ranjan Kumar.	Th2.15. **Thermally controlled frequency comb generation in hybrid silicon quantum dot lasers.** Thibaut Renaud.
17:30	**17:45**		Th2.16. **Electro-Optic Packaging of Silicon Photonics-Based RF Multiplier for Clock Signal Generation in the Millimeter-Wave Band.** Claudio Porzi
19:00		**Gala Dinner** *sponsored by* **MESA+**	

Scientific Program

Friday 21th April 2023

08:45	**17:00**	**Return bikes at reception**		
08:45	**09:30**	**Keynote 2 (Room: WA-1)** **Chair: Dr. Jelmer Renema** **Integrated Photonics for Quantum and Artificial Neural Networks-based Signal Processing,** Roberto Morandotti		
		Devices and Integrated Circuits (Room: WA-1) **Chair: Prof. Andrea Melloni**		**Novel physical insights and materials (Room: WA-3)** **Prof. Dr. Wolfgang Freude**
09:30	**09:45**	F1.1 **Invited. 20-mode Quantum Photonic Processor as an industrial product.** Michiel de Goede.		F2.1 **Magneto-optical properties of e-beam evaporated EuS films for room temperature applications.** Frank Somhorst
09:45	**10:00**			F2.2. **Supersymmetric Compactification and Higher-Dimensional Rearrangement of Photonic Lattices.** Tom Wolterink
10:00	**10:15**	F1.2. **Fully On-chip Laser-integrated Entangled Photon Pair Source.** Michael Kues.		F2.3. **Investigations on Brillouin and Kerr properties of a low-index silicon oxynitride platform.** Kaixuan Ye
10:15	**10:30**	F1.3. **Frequency agile SiN-MEMS photonic integrated external cavity laser. Andrea Bancora.** Grigory Lihachev.		F2.4. **Enhanced Frequency Noise Discrimination Using Cavity-coupled Mach-Zehnder Interferometer.** Mohamad Hossein Idjadi

		COFFEE BREAK (*sponsored by **VLC Photonics*) & POSTERS**
10:30	**11:30**	ID 195. **High performance integrated silicon polarization beam splitter based on all-dielectric metamaterial cladding.** Andraž Debevc.
		ID 198. T**owards bimodal photonic sensing with coherent readout in silicon nitride.** Antonia Torres-Cubillo.
		ID 199. **Development of SiON-based photonic integrated circuits for the blue/near-UV wavelength range.** Ronan Kervazo.
		ID 201. **Parallel Sensing with Multiple Microrings on a single Bus Waveguide.** Lantian Chang.
		ID 203. **Taiji Resonators for Self-Referenced Exceptional Point Sensing.** Bjorn Jongebloed.
		ID 204. **High-frequency Scalable Modelling of 100 GHz Class Uni-Travelling Carrier Photodiodes.** Risab Gnanamani.
		ID 206. **Ultra-High-Extinction-Ratio Electro-Optic Switch Element.** Peng Bao.
		ID 208. **Narrow bandwidth tunable optical filter using apodized sampled gratings in InP-based generic integration platform.** Xiao Li.
		ID 209. **Design and optimization of graphene-on-silicon nitride integrated waveguide mode filters.** Fernando Martín-Romero.
		ID 213. **Free Spectral Range Sensing as a Novel Measurement Technique.** Gandolf Feigl.
		ID 215. **Tilted MMI based (de)multiplexer for monolithically integrated multichannel transmitters on InP platform.** Shirley Prado de la Cruz.
		ID 216. **Automated Model for Characterization of VCSEL Circuit-level Parameters Using Machine Learning.** Andrea Marchisio.

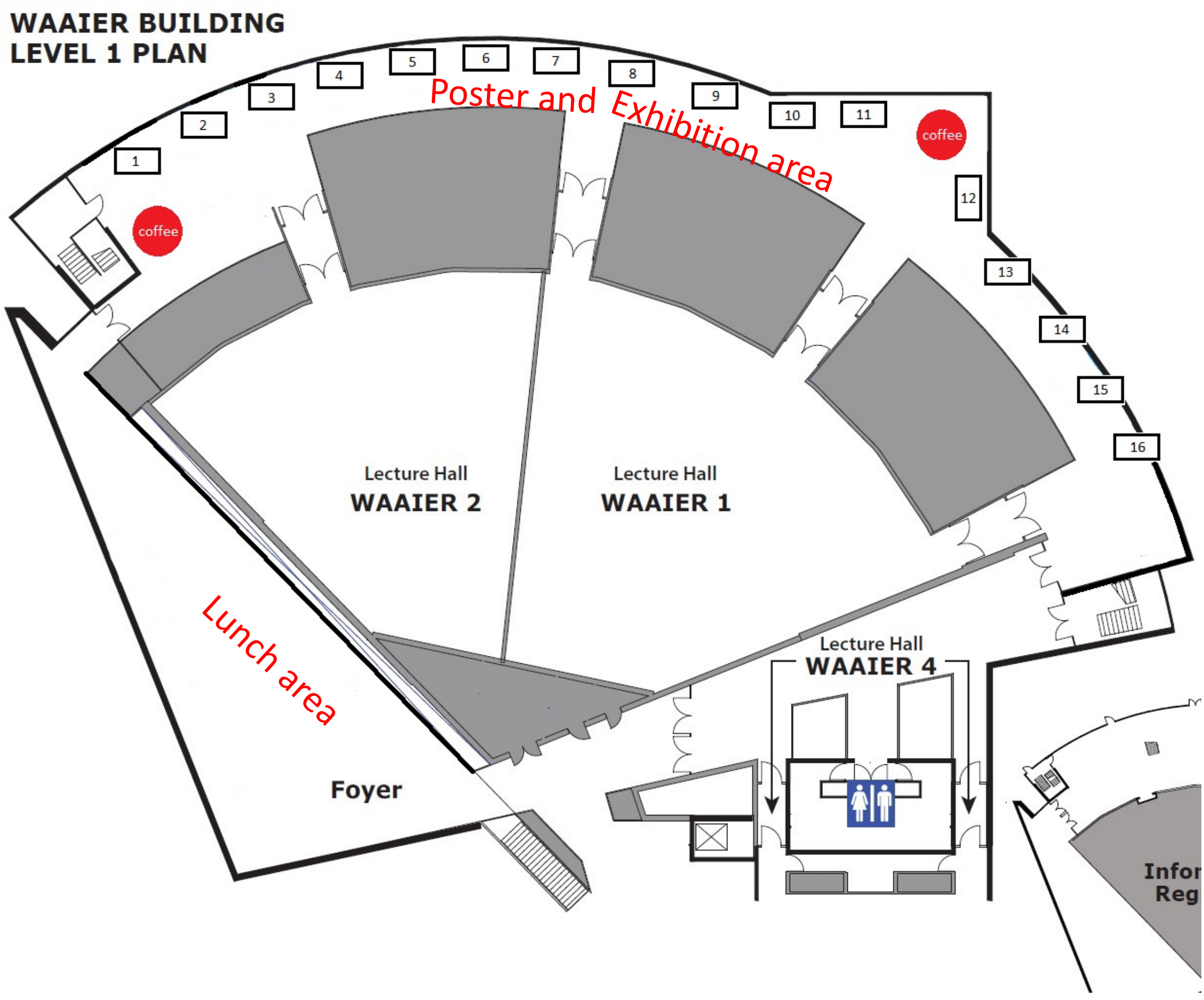


		Devices and Integrated Circuits (Room: WA-1) Chair: Dominic Ghallager	Integrated photonic technologies and platforms (Room: WA-3) Chair: Dr. Lantian Chang
11:30	**11:45**	F1.4. **Invited. programmable Integrated photonics.** Daniel Pérez López.	F2.5. **Development of an integrated optical sensor on chalcogenide glasses and on porous silicon for the mid-infrared spectroscopy.** Sofiane Meziani.
11:45	**12:00**		F2.6. **Integrated White-Light Interferometry for rapid dispersion and index measurements of InP waveguides.** Amer Bassal.
12:00	**12:15**	F1.5. **Photonic memory based on VO2/Si technology.** Juan Jose Seoane.	F2.7. **High-power CW >100 mW SOAs for active-passive integration.** Andrzej Jankowski.
12:15	**12:30**	F1.6. **A memristor-controlled multilevel non-volatile phase shifter for photonic integrated circuits.** Felix Hermann.	F2.8. **Temperature stabilization techniques for High Stability LO Generation using a Hybrid Integrated Dual InP-Si3N4 Laser Source.** Alberto Zarzuelo.
12:30	**12:45**	F1.7. **1x4 Vertical Power Splitter/Combiner: A Basic Building Block for Complex 3D Waveguide Routing Networks.** Madeleine Weigel.	F2.9 **Characterisation and mitigation of surface related optical loss in suspended GaAs photonic integrated circuits.** Robert Thomas.
12:45	**14:15**	**Lunch & Exhibition** *Lunch sponsored by **Photon Design** and **Yokogawa***	

		Devices and Integrated Circuits (Room: WA-1) Chair: Prof. Dr. Pepijn Pinkse	Applications of PICs (Room: WA-3) Chair: Dr. Dawson Bonneville
14:15	**14:30**	F1.8. **C-Band Apodized Chirped Gratings in Aluminum Oxide Strip Waveguides.** Milan Sinobad.	F2.10 **Integrated Photonic Processor Enabling Dynamic Mitigation of Turbulence-Induced Scintillation in an Optical Free Space Link.** Andres Martinez
14:30	**14:45**	F1.9 **Lasing in a Neodymium-doped Aluminium Oxide Taiji Resonator.** Dahnée Wojcik.	F2.11 **Miniature and non-contact photoacoustic system using silicon photonics-based Laser Doppler Vibrometer and compact excitation source.** Emiel Dieussaert
14:45	**15:00**	F1.10. **Accurate, high-speed tuning of an ultra-narrow linewidth external cavity laser.** Wilson Tsong	F2.12 **Integrated Microwave Photonic Receiver for Radar Applications.** Federico Camponeschi
15:00	**15:15**	F1.11 **A hybrid photonic integrated signal source with >1.5 THz continuous tunability and <0.25 GHz accuracy for mmW/THz applications.** Tianwen Qian.	F2.13 **Automatic mitigation of tilt and phase-front distortions in multichannel chip-to-chip free-space optical links.** SeyedMohammad SeyedinNavadeh
15:15	**16:30**	**COFFEE BREAK (*sponsored by* Jeppix) & POSTERS**	
		ID 220. **Investigation of periodic poling in LNOI.** Laura Bollmers.	
		ID 222. **Observation and enhancement of stimulated Brillouin scatering in tellurite covered silicon nitride waveguides** Roel Botter.	

		COFFEE BREAK (*sponsored by* Jeppix) & POSTERS
15:15	**16:30**	ID 229. **Lithium Niobate near IR waveguides for astrophotonic and spectrometry applications.** Noemie Mestre.
		ID 233. **Multiport interferometer from a multimode waveguide.** Mikhail Saygin.
		ID 235. **Modelling Brillouin activated microcombs in multi-layered silicon nitride waveguides.** Yvan Klaver.
		ID 238. **Multi-Mode Interference for Wavelength Demultiplexing.** Pedro Medeiros.
		ID 239. **Towards on-chip wavelength modulation spectroscopy at 1.5 µm via InP integrated photonics and low-cost driving hardware.** Stefano Tondini.
		ID 241. **Scalable Free-standing 3D Optical Circuit Design using Direct Laser Writing.** Pepijn Pinkse.
		ID 248. **Variable photonic integrated delay lines, a review.** Andrea Ivano Melloni.
		ID 251. **Towards Automatic Control of Two ORR-based TTD PIC Optical Beamforming using a Neural Network.** Bin Shi.
		Closing ceremony (Room: WA-1)
16:30	**17:00**	**Chair: Prof. Dr. Sonia Garcia Blanco**
		Poster price sponsored by: Journal of Nanophotonics
17:00		**Labs and company visits (optional)**

WAAIER layout



Sponsors

Lunch sponsored by: Aluvia (Aluvia Photonics), Photon Design (Photon Design - Your source of photonics CAD tools) and Yokogawa (Yokogawa Test & Measurement Corporation)

Coffee break sponsored by: LioniX (MEMS Foundry - LioniX International), Chilas (Chilas BV), Quix (QuiX Quantum), VLC Photonics (VLC Photonics . Engineering solutions for photonic integration) and Jeppix (Jeppix - Platform for photonic integrated components)

Drinks at reception sponsored by:
Reception dinner on Wednesday night sponsored by: PHIX (Home - PHIX Photonics Assembly), Synopsys (Synopsys | EDA Tools, Semiconductor IP and Application Security Solutions), Luceda (Luceda | Photonic IC Design Software (lucedaphotonics.com)), ePIXfab (ePIXfab-European Silicon Photonics Alliance) and VLC Photonics (VLC Photonics . Engineering solutions for photonic integration)

Gala dinner sponsored by: MESA+ (MESA+ Institute | University of Twente)

Poster price sponsored by: Journal of Nanophotonics (https://www.degruyter.com/journal/key/nanoph/html)

ECIO23

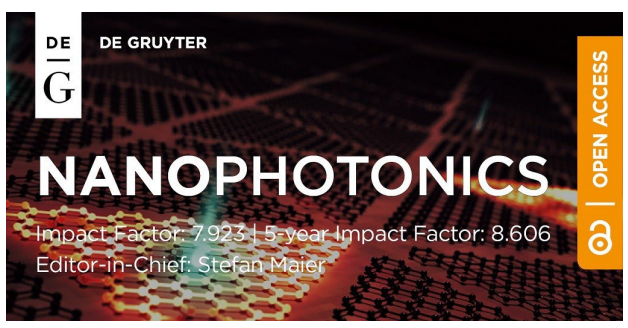
Sponsors

ALUVIA

chilas

ePIXfab

JePPIX
Platform for Photonic Integration



LIGENTEC

LIONIX INTERNATIONAL

LUCEDA PHOTONICS

LXT

UNIVERSITY OF TWENTE. | MESA+ INSTITUTE

Optiwave

YOKOGAWA

nanoscribe
A BICO COMPANY

SMART PHOTONICS
Independent InP Foundry

phix

Photon Design

QuiX
THE FASTEST WAY TO A QUANTUM FUTURE

RAITH

SYNOPSYS®
Silicon to Software™

THORLABS

VPIphotonics
DESIGN AUTOMATION

VLC PHOTONICS
A Hitachi Group Company

Micro-transfer-printed O-band GaAs QD-on-Si DFB Laser on an advanced silicon photonics platform

Jing Zhang[1,2*], Senbiao Qin[1,2], Laurens Bogaert[1,2], Igor Krestnikov[3], Konstantin Morozov[3], Johanna, Rimbock[4], Alex Farrell[5], Ruggero Loi[5], David Gomez[5], Peter Ossieur[6], Guy Lepage[7], Peter Verheyen[7], Joris Van Campenhout[7], Geert Morthier[1,2], and Gunther Roelkens[1,2]

[1]Photonics Research Group, INTEC, Ghent University - IMEC, Ghent, Belgium
[2]Center for Nano- and Biophotonics, Ghent University - IMEC, Ghent, Belgium
[3]Innolume GmbH, Konrad-Adenauer-Allee 11, 44263 Dortmund, Germany
[4] EV Group E.Thallner GmbH, DI Erich Thallner Str. 1, 4782 St. Florian am Inn, Austria
[5]X-Celeprint Ltd, Lee Maltings, Dyke Parade, Cork, Ireland
[6] IDLab, INTEC, Ghent University – IMEC, Ghent, Belgium
[7]IMEC, Kapeldreef 75, 3001 Heverlee, Belgium
[*] jingzhan.Zhang@ugent.be

We present wafer-scale micro-transfer printing of III-V devices on an advanced silicon photonics platform. Following this process flow, a GaAs QD-on-Si DFB laser is demonstrated. The resulting device exhibits single mode operation at 1300 nm with about 0.7 mW single-side waveguide-coupled output power and a side-mode-suppression-ratio of 44 dB at 40 °C.
Keywords**:** *Silicon Photonics, Micro-Transfer Printing, Distributed Feedback Laser*

INTRODUCTION

Silicon photonics (SiPh) attracted renewed interest in the past decades due to its great potential for the realization of powerful and energy-efficient photonic integrated circuits (PICs) with compact sizes. By taking the advantages of mature CMOS industry, complex silicon PICs can be manufactured on 200 mm or 300 mm wafers at low cost with guaranteed yield. However, the integration of low-cost integrated laser sources on Si wafers remains a challenge due to the poor light-emission properties of Si. III-V semiconductors are suitable for light emission in different wavelength ranges due to their direct and adjustable bandgaps. In recent years, III-V quantum dot lasers (QD lasers) have attracted extensive interest due to their superior characteristics, such as high temperature stability, low linewidth enhancement factor, high flexibility in gain bandwidth and emission wavelength engineering, etc. [1]. Different approaches have been developed to combine the best of III-V materials and Si. Multiple die-to-wafer bonding is one practical solution and has been commercialized for the manufacturing of optical transceivers in the past few years, but it requires significant modification to the established Si backend process flow. Hetero-epitaxial growth exhibits significant potential for the integration of III-V devices, especially III-V QD devices due to its lower sensitivity to defects, on SiPh wafers [1]. However, several challenges, such as the leveling between III-V and Si layers, imperfect material quality, etc. still remain to be addressed. In this work, we present the integration of III-V devices on advanced SiPh wafers using micro-transfer printing (µTP) [2]. Following this approach, an O-band GaAs QD DFB laser is integrated on the imec isipp50g platform [3]. The resulting device exhibits single mode operation around 1300 nm at 30 ℃. The maximum single-side waveguide-coupled power is measured to be over 0.7 mW.

MICRO-TRANSFER PRINTING

Micro-transfer printing became popular in both academia and industry in recent years. By using a Polydimethylsiloxane（PDMS) stamp, prefabricated device coupons released on the source substrate can be picked up and printed on to a SiPh target wafer one by one or in a massively parallel manner. This process can be fully automated, and the resulting alignment accuracy is up to (<1 µm @ 3σ) or even better depending on the size of the manipulated device arrays. A µTP experiment was first carried out on an industrial µTP tool, where an 8-inch SiPh wafer with pre-defined recesses and InP devices coupons (Fig. 1(a)) were used respectively as the target substrate and the source devices. The sizes of the recesses and the InP coupons are 100 µm X 1600 µm and 45 µm x 1400 µm, respectively. A set of fiducial markers are used to facilitate the automatic alignment by using a pattern recognition function integrated in the µTP tool. 160 coupons were printed one-by-one in an automatic manner. Fig. 1(b) shows an array of transfer-printed InP coupons on the target wafer. The fiducial markers and the recess are shown in Fig.1(c). As depicted in Fig. 1(d) and (e), less than 1 µm misalignment are achieved in both longitudinal and lateral directions for all printed coupons.

PROCESS FLOW OF THE MICRO-TRANSFER PRINTING OF GAAS QD DEVICES

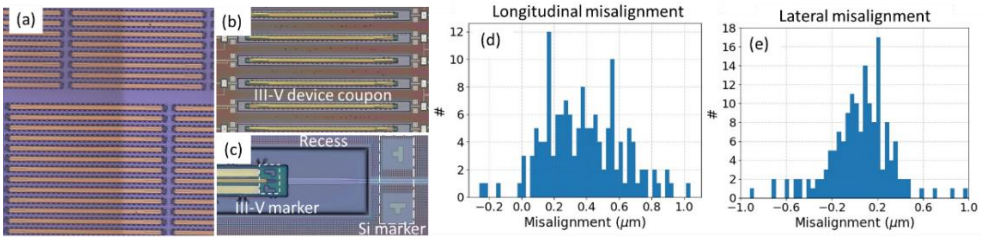


Fig. 1(a) Microscope image of the released InP SOA arrays on a source wafer, (b) An array of micro-transfer-printed InP SOAs on an 8-inch SiPh wafer, (c) Zoomed-in microscope image showing a transfer-printed InP OSA and the alignment makers.

Following the demonstration of micro-transfer-printed GaAs QD-on-Si DFB lasers in [4], an optimized process flow for the integration of GaAs QD lasers on advanced SiPh platforms is developed, as descripted in Fig. 2. The first few steps (Fig.2(a)-(c)) are the same as those explained in Ref. [4]. After the n-contact metal deposition the GaAs QD rib waveguide is passivated with a SiN layer (Fig.2(d)), which is also used as a hard mask to define the first coupon mesa by etching into the GaAs substrate. The coupon mesa is then encapsulated with a thick SiN and a thin SiOx layer (Fig.2(e)). After planarizing the III-V waveguide structures using a thick BCB layer and p-contact metal deposition, the second coupon mesa is defined by RIE etching to expose the SiN layer around the first coupon mesa (Fig.2(f)). After patterning the tether structures in the exposed SiN layer with a photoresist soft mask, the coupons are ready to release (Fig.2(g)). A 15 ℃ 1:1 37% HCl:DI solution is used in this work (Fig.2(h)). Fig. 2(i) shows the schematic of a SiPh substrate with pre-defined recesses. A spray coating process is applied to deposit about 60 nm DVS-BCB in the recess (Fig.2(j)). Prior to μTP process, the SiPh substrate is baked at 150 ℃ for 15 minutes. A PDMS stamp with a single post of 60 μm X 1800 μm is used to print the coupon (Fig.2(k,l)). The post-transfer printing processing includes photoresist encapsulation layer removal, BCB curing, and metal deposition (Fig.2(m)).

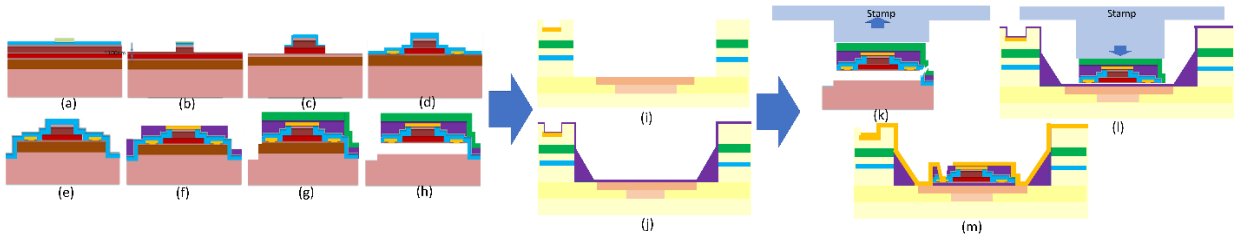


Fig. 2. Full process flow for the integration of GaAs QD devices on an advanced SiPh platform. (a-c) Rib waveguide definition, (d) n-contact metal deposition, (e) the first coupon mesa definition and SiN encapsulation, (f) the second coupon mesa definition, (g) tether definition, (h) release etch, (i) target SiPh wafer with pre-defined recesses, (j) DVS-BCB spray coating, (k) pick-up GaAs device using a PDMS stamp, (l) μTP GaAs SOA into the recess, (m) final metallization.

DESIGN AND FABRICATION OF GAAS QD-ON-SI DFB LASER

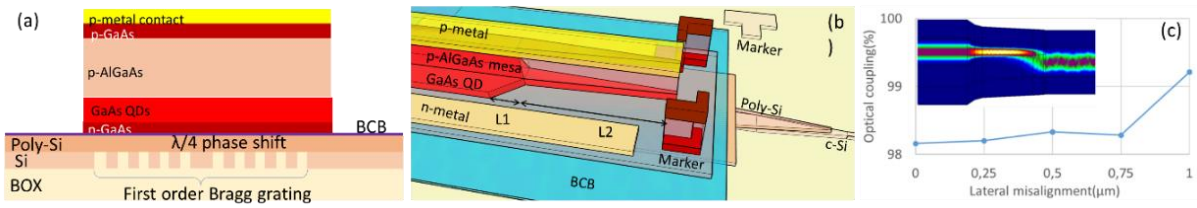


Fig. 3.(a) Schematic of the GaAs QD-on-Si DFB laser, (b) Schematic of the alignment-tolerant III-V/poly-Si/Si taper structure, (c)Simulated coupling efficiency as a function of lateral misalignment.

The Si waveguide circuits consists of a 220 nm thick crystalline Si device layer, a 160 nm thick polysilicon (poly-Si) overlay layer and a multiple-layer backend stack, which is opened locally over the DFB laser cavity to allow for close contact of the III-V layer to the exposed poly-Si layer. The GaAs QD/Si DFB laser cavity is schematically depicted in Fig. 3(a). The III-V/Si hybrid waveguide structure consisting of a GaAs QD rib waveguide and an underlying poly-Si/Si waveguide. The major design of the GaAs QD waveguide structure was kept the same as in Ref. [4], but a 1 μm thick p-$Al_{0.8}Ga_{0.2}As$ cladding and a 350 nm thick n-GaAs contact layer are used in this work. The Bragg grating is defined in a 9 μm wide crystalline Si layer with a 40 μm wide poly-Si layer on top. The length, period and duty cycle of the grating are 1 mm, 205 nm, and 50 %, respectively. A III-V/poly-Si/Si taper structure is used at each side of the laser cavity to couple the light to the underlying poly-Si/Si hybrid waveguides and then the Si wire waveguides, as shown in Fig.3 (b). With a 340 μm (L1=90, L2=250) long III-V/poly-Si/Si taper structure, efficient optical coupling with

excellent lateral alignment tolerance (>1 µm) can be achieved for the case of a 30 nm thick DVS-BCB bonding layer, as shown in Fig.3 (c).

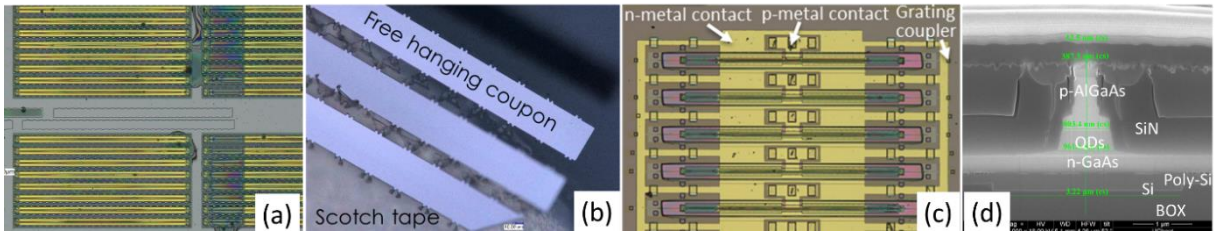


Fig. 4. (a) Microscope image of the released GaAs device coupons,(b) Bottom surface of the released coupons, (c) An array of DFB lasers with metal-contact pads,(d) Focused Ion Beam cross section at the taper section, showing a perfect alignment.

Fig. 4(a) shows a microscope image of a source wafer after release etching. The size of the coupons is 55 µm x 1700 µm. Smooth and defect-free bottom surface is observed under microscope, as shown in Fig. 4(b). The µTP process was carried out using an X-Celeprint µTP-100 lab-scale tool at room temperature in the cleanroom of Ghent university. Fig. 4(c) shows the resulting DFB lasers with metal contact pads. Fig. 4(d) shows a FIB cross section at the III-V/poly-Si/Si taper section. The thickness of the resulting DVS-BCB bonding layer is around 20 nm and the alignment is almost perfect.

CHARACTERIZATION

The resulting GaAs QD-on-Si DFB lasers were characterized on a vertical setup, which consists of a temperature-controlled stage, a pair of single mode fibre probes, a Keithley current source, a pair of DC probes, an HP power meter and an optical spectrum analyser. Fig. 5(a) shows the measured current-voltage curve, which shows a differential resistance of 4.6 Ω at 150 mA. Fig. 5(b) shows the recorded light-current curve, which reveals a threshold current of 65 mA and close to 0.7 mW single-side waveguide-coupled power. The abrupt fluctuation of the optical power indicates the existence of strong parasitic reflections. Fig. 5(c) shows a set of laser spectra at different bias levels. The measured device exhibits single mode operation around 1300 nm with 44 dB side-mode-suppression-ratio (SMSR). The sharp spurs shown in the DFB stopband also verifies the parasitic reflections to the laser cavity.

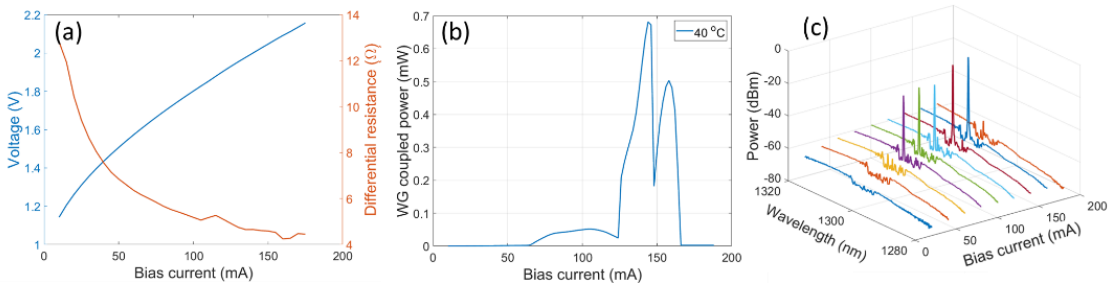


Fig. 5. Performance of a representative GaAs QD on Si DFB laser at 40 °C, (a) V-I curve and differential resistance, (b) P-I curve (c) Superposition of the output spectra with the increase of the applied bias current.

CONCLUSION

We demonstrated the µTP of 160 InP devices on an 8-inch SiPh wafer with <1 um alignment accuracy using an industrial µTP tool and developed a full process flow for the µTP of GaAs QD devices on advanced SiPh platforms. Following this process flow, a GaAs QD-on-Si DFB laser operating at 1300 nm with 44 dB SMSR is demonstrated. This work paves the way for the realization of III-V-on-Si devices/circuits on SiPh wafers using µTP.

Acknowledgements: This work was supported by the European Union's Horizon 2020 research and innovation programs under agreement 825453 (CALADAN),

References

[1] S. Pan et al. "Recent progress in epitaxial growth of III–V quantum-dot lasers on silicon substrate", J. Semicond., 40, 101302, 2019
[2] B. Corbett et al., "Transfer Printing for Silicon Photonics", Semicond. Semimet. , vol. 99, pp.43-70, 2018
[3] Europractice. Photonic integrated circuit prototyping and small volume production. https://www.imec-int.com/sites/default/files/imported/Photonic%2520integrated%2520circuit_EN_v4_MPW_yi_0.pdf
[4] J. Zhang, et al., "Micro-Transfer-Printed O-band GaAs QD III-V-on-Si DFB Laser", ECIO, Italy, p.paper W.P.13,2022

Ultrafast frequency-agile narrow-linewidth lasers using lithium niobate integrated photonics

(Student paper)

V. Snigirev[1,*], A. Riedhauser[2], G. Likhachev[1], J. Riemensberger[1], R. N. Wang[1], C. Moehl[2], M. Churaev[1], A. Siddharth[1], G. Huang[1], Y. Popoff[2,3], U. Drechsler[2], D. Caimi[2], S. Hoenl[2], J. Liu[1], P. Seidler[2], and T. J. Kippenberg[1]

[1] Institute of Physics, Swiss Federal Institute of Technology Lausanne (EPFL), CH-1015 Lausanne, Switzerland
[2] IBM Research Europe, Zurich, Säumerstrasse 4, CH-8803 Rüschlikon, Switzerland
[3] Integrated Systems Laboratory, Swiss Federal Institute of Technology Zurich (ETH Zürich), CH-8092 Zürich, Switzerland
[*] viacheslav.snigirev@epfl.ch

We present a narrow-linewidth frequency-agile integrated laser based on heterogeneously integrated thin-film lithium niobate on ultra-low-loss Damascene silicon nitride integrated photonic circuits. The platform features tapers with a transition loss of only 0.1 dB from a silicon nitride to a hybrid lithium niobate mode. Utilizing self-injection locking, we realize a tuneable laser with a tuning speed of 12 PHz/s. We also make a system-level demonstration by performing coherent frequency-modulated continuous-wave LiDAR ranging experiments.

Keywords: *thin-film lithium niobate, Damascene silicon nitride, heterogeneous integration, frequency-agile lasers, FMCW LiDAR*

INTRODUCTION

Recent progress in the field of thin-film lithium niobate integrated photonic circuits manifested itself in demonstrations of low-V_π electro-optic modulators [1, 2], generation of electro-optic frequency combs [3] and microwave-optical transduction [4]. Lithium-niobate-based circuitry can also be applied in the domain of integrated frequency-agile laser sources [5]. Ultra-low-noise lasers have been shown via self-injection locking of diode lasers to integrated [6] and whispering gallery modes [7] optical microresonators with high quality factors.

It has been recently shown that by using an optical microresonator with piezo-electrical actuation, one can endow such a laser with a MHz-wide tuning bandwidth and a GHz-wide frequency excursion range, as needed for coherent laser-based ranging [8]. Although both highly linear frequency modulation and high tuning efficiency were observed, the bandwidth of laser wavelength modulation is fundamentally limited by excitation of mechanical modes of the substrate by the actuator. Thus, phononic engineering is necessary to achieve high modulation frequencies (up to 10 MHz [8]). In contrast, electro-optic modulation does not excite mechanical modes of the chip, while supporting GHz bandwidths of modulation [1]. Therefore, we assembled an electro-optically tuneable laser comprising a heterogeneously integrated lithium-niobate-on-Damascene-silicon-nitride (LNOD) microresonator [9], combining the advantages of passive ultra-low-loss photonic circuits [10] with the electro-optic tunability. We demonstrate the potential for applications by performing frequency-modulated continuous-wave (FMCW) LiDAR experiments. The platform, *inter alia*, features a low-loss-taper transition of the silicon nitride integrated waveguide mode into a lithium niobate mode (see Fig. 1). It exhibits 0.1 dB loss per transition (versus 2 dB for the straight transition), and < 0.8 dB loss for ten cascaded transitions (see Fig. 1(d, f)). The taper is employed to enhance the back-reflection to the laser diode, thus, facilitating better locking conditions.

RESULTS

A conceptual representation of the tunable laser is given in Fig. 2(a). A distributed-feedback (DFB) indium phosphide laser is self-injection locked to an external LNOD microring resonator mode, and the output frequency is changed by applying voltage to electrodes placed along the resonator circumference. The structure of the LNOD waveguide (see Fig. 2(b)) leads to a hybrid optical mode that partially penetrates the layer of lithium niobate making possible electro-optic modulation. A high-quality factor for the LNOD mode is important for achieving a wide locking bandwidth and pronounced linewidth narrowing [11]. Because of the low-loss Damascene silicon nitride circuits underneath, the median intrinsic loss rate (see Fig. 2(c)) is $\kappa_0/(2\pi) = 100$ MHz, equivalent to a quality factor of 2×10^6. The self-injection-locked state of the laser is characterized by a locking bandwidth of 1.1 GHz, 30 dB suppression of the phase noise spectrum, and intrinsic frequency noise of 3 kHz (see Fig. 2(e)).

The frequency tuning potential of the laser can be inferred from Fig. 2(d), where the electro-optic response curve is measured by positioning a reference laser on the flank of a selected resonance and applying a voltage to the

electrodes with a vector network analyzer. The small-signal frequency response is flat, showing no degradation of modulation efficiency with the modulation frequency from 10 kHz to 100 MHz. For frequency-modulated continuous wave (FMCW) LiDAR [12], wavelength tuning with a linear ramp plays the central role. Thus, we characterize the tuning by applying a triangular voltage waveform to the microresonator electrodes (see Fig. 2(f)). Using a 10 MHz modulation frequency, we achieve a laser wavelength tuning rate of 12 PHz/s. The chirp nonlinearity at 100 kHz is $< 1\%$, and the tuning efficiency is 30 MHz/V. The tuning efficiency can be further improved by reducing the thickness of the silicon nitride waveguides and of the silicon oxide interlayer, thus, increasing the participation ratio of the optical mode in lithium niobate. Following this approach, efficiencies up to 300 MHz/V can be reached in a push-pull configuration, what has been experimentally verified.

As a proof-of-principle demonstration, we perform FMCW LiDAR measurements in a laboratory environment. For scene elements, we use a donut shape made of polystyrene and a plastic instrument box. The collected data, after processing, is presented as point clouds in Fig. 2(g) and (h). The evaluated resolution of these experiments is 15 cm.

DISCUSSION

By further increasing the quality factor of fabricated LNOD microresonators, it should be possible to increase the locking bandwidth and decrease the linewidth of the laser in the self-injection locked state. Thus, a finer resolution in FMCW ranging experiments would be expected. Also, introduction of loop-mirrors as a new circuitry element and use of racetrack resonators instead of microrings would further enhance back-reflection and tuning efficiency what eventually could lead to a coherent LiDAR engine at CMOS-compatible voltage levels.

Acknowledgements

This work was supported by Contract HR0011-20-2-0046 (NOVEL) from the Defense Advanced Research Projects Agency (DARPA), Microsystems Technology Office (MTO), and by funding from the European Union Horizon 2020 Research and Innovation Program under the Marie Sklodowska-Curie grant agreement No. 722923 (OMT) and No. 812818 (MICROCOMB), and under the FET-Proactive grant agreement No. 732894 (HOT). It was also supported by funding from the SNF under grant agreement No. 176563 (BRIDGE) and No. 186364 (QuantEOM).

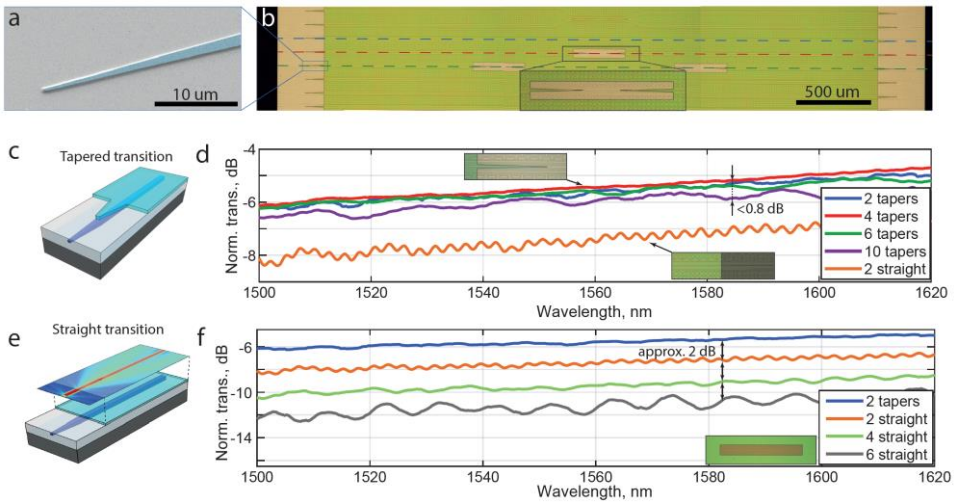


Fig. 1. ***Adiabatic mode transitions.*** *(a) False-colored SEM image of an LNOD taper. (b) Micrograph of a chip with tapers. (c) Illustration of a tapered transition. (d) Transmission spectra of breakout LNOD waveguides shown in (b) along with data for a straight transition as reference. (e) Illustration of a straight transition. (f) Transmission spectra of LNOD waveguides with straight transition breakouts.*

References

[1] C. Wang et al., Nature, **562**, 7725 (2018)
[2] M. Heet al., Nature Photonics, **13**, 5 (2019)
[3] M. Zhang et al., Nature, **568**, 7752 (2019)
[4] Y. Xu et al., Nature Communications, **12**, 4453 (2021)
[5] C. Op de Beeck et al., Optica, **8**, 10 (2021)
[6] W. Jin et al., Nature Photonics, **15**, 346 (2021)
[7] M. Soltani et al., Opt. Lett. **41**, 4375 (2016)
[8] G. Lihachev et al., arXiv: 2104.02990 (2021)
[9] M. Churaev et al., arXiv: 2112.02018 (2021)

[10] J. Liu et al., Nature Communications, **12**, 2236 (2021)
[11] N. M. Kondratiev et al., Optics Express, **25**, 23 (2017)
[12] D. Uttam et al., Journal of Lightwave Technology, **3**, 5 (1985)

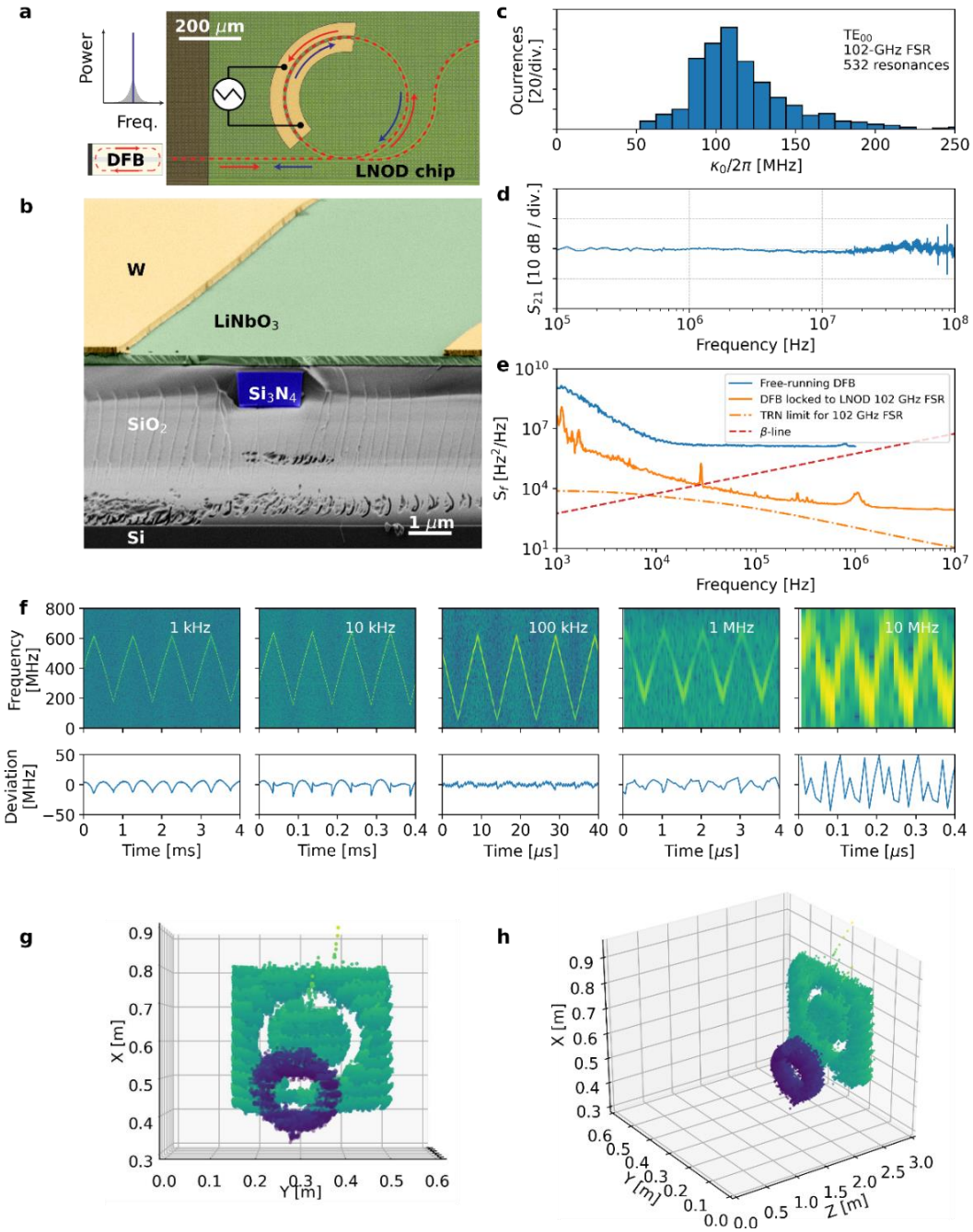


Fig. 2. ***SIL LNOD tunable laser.*** *(a) Schematic of the integrated tunable laser source. A DFB laser diode is self-injection locked to a high-Q optical mode of an LNOD microring resonator via butt coupling. Rayleigh scattering from inhomogeneities in the microring provide the feedback to the DFB. The laser frequency is modulated by applying a voltage from an arbitrary waveform generator to integrated tungsten electrodes. (b) False-colored scanning electron microscope image of a LNOD waveguide cross-section. (c) Histogram indicating intrinsic decay rate distribution of 532 resonances of a LNOD microring with a free spectral range (FSR) of 102 GHz. The median of the distribution is 100 MHz, corresponding to a quality factor of* 2×10^6*. (d) Frequency-dependent electro-optic modulation efficiency of the optical microresonator. (e) Laser frequency noise sprectra of the free-running DFB laser (blue line), of the DFB locked to a LNOD microring with 102-GHz FSR (solid orange line), its simulated thermorefractive noise limit (dash-dotted line), and* β*-line (dashed red line). (f) (Top row) Time-frequency analysis of triangular laser frequency chirps measured via the heterodyne beatnote between the tunable laser and a CW reference laser. (Bottom row) Deviation of measured laser frequency from an ideal triangular chirp. (g-h) Point clouds, representing a scene composed of a polystyrene donut shape and a plastic plane behind, obtained in FMCW LiDAR experiments with the tunable laser source.*

Spectrally Programmable Individual Color Centers in Silicon Waveguides

Carlos Errando-Herranz[1,2,3,†,*], Mihika Prabhu[1,†], Lorenzo De Santis[1,3], Ian Christen[1], Changchen Chen[1], Connor Gerlach[1], and Dirk Englund[1]

[1]Massachusetts Institute of Technology, 77 Massachusetts Av., Cambridge MA, 02139, USA
[2]University of Münster, Schlosspl. 2, Münster, 48149, Germany
[3]QuTech, Delft University of Technology, Lorentzweg 1, Delft, 2628 CJ, Netherlands
†Equal contribution
*carloseh@mit.edu

Color centers are leading qubit candidates for quantum information processing but are limited by their weak light-matter interactions and their operation wavelengths. Recently isolated color centers in silicon may, however, enable strong light-matter interactions at telecom wavelengths. We report on the integration of individual color centers in silicon photonic waveguides and their spectral programmability using optical tuning.
Keywords: *quantum photonics, color centers, single-photon emitters, silicon photonics*

INTRODUCTION

Color centers are leading candidates for quantum information processing due to their long spin coherence times and high-quality single-photon emission and spin-photon interfaces [1], [2]. Traditionally studied color centers are hosted in diamond and silicon carbide. However, these platforms face critical scaling challenges such as their lack of monolithic manufacturability and their visible or near-infrared operation wavelengths [3].

Recently, several color centers have been isolated in silicon [4]–[6], including the carbon-based G-center [7], [8]. Such color centers have shown single photon emission at telecom wavelengths, making them particularly attractive for quantum networking applications. A spin-photon interface based on silicon color centers could thus be seamlessly integrated into the world's most advanced microelectronic and photonic platforms.

We recently demonstrated the monolithic integration of single G-centers in silicon photonics and showed single photon emission in the telecommunications O-band with a narrow inhomogeneous linewidth into silicon waveguides [9]. However, their spectral programmability, key for achieving indistinguishable photons and required for all quantum communication and computing protocols, remains a challenge.

Here, we report on the first demonstration of spectral programmability of silicon color centers. We show optically-induced non-volatile spectral tuning up to 300 pm (55 GHz) in-situ in silicon photonic waveguides. The spectral shifts are comparable to the inhomogeneous distribution of 1.1 nm (200 GHz) and large enough to tune G-centers into standard 25-GHz telecom bands.

RESULTS

Our fabrication process proceeds as follows. To generate the G-centers, we start from a silicon-on-insulator (SOI) commercial wafer and implant it with carbon atoms, followed by a rapid thermal annealing process to heal the lattice. The cleaved chips were then patterned and etched down to the underlying silicon dioxide to make waveguides with single-mode operation in the O-band. The device under study consists of a looped-back waveguide (63.5 µm radius bend) and was cleaved on the edges for edge coupling to a fiber (Fig. 1a). A more detailed description of our sample and fabrication process can be found in Ref. [9].

Our measurement setup consists of a home-built confocal microscope designed for optical excitation of the device located inside a 6K cryogenic chamber. The collection consists of a lensed fiber (2.5 µm mode diameter) actively aligned to the waveguide facet. The collected color center emission is filtered via a free-space optical bandpass filter (1250 - 1550 nm) and detected via superconducting single-photon emitters or a spectrometer. More details on the measurement setup can be found in Ref. [9].

In our previous measurements with this sample, reported in Ref. [9], we observed diffraction-limited emission spots with a photoluminescence (PL) zero phonon line (ZPL) centered in 1278.7 ± 1.1 nm and two-level system saturation characteristics: lifetimes of 8.33 ± 0.68 ns fitting to a two-level system, and single-photon emission demonstrated via a through-waveguide second-order autocorrelation measurement $g^{(2)}(0) < 0.5$.

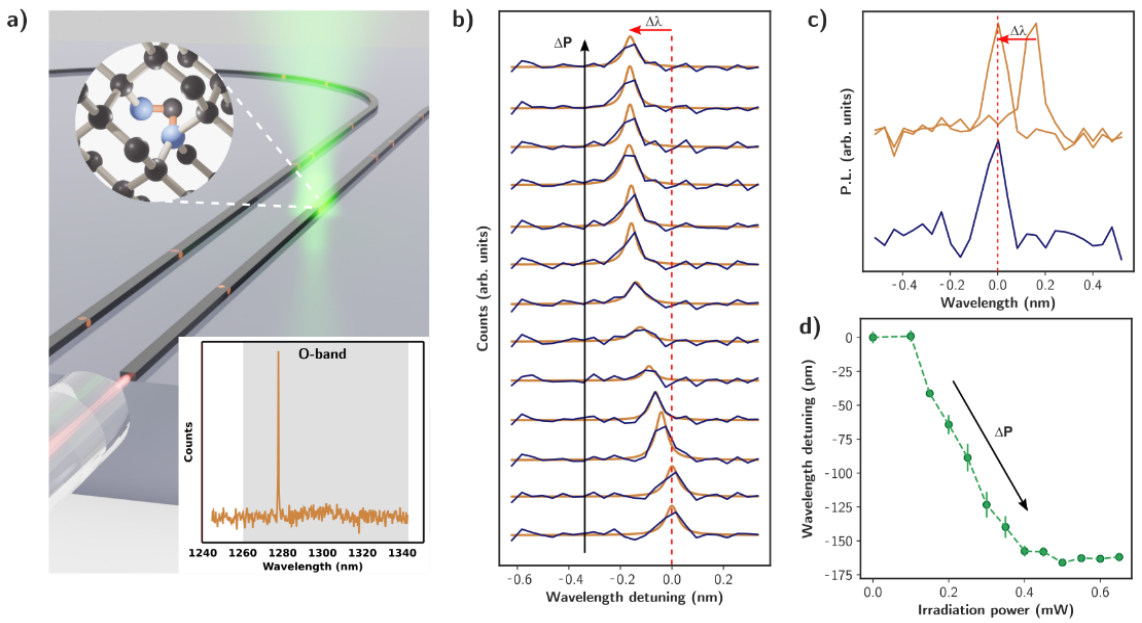


Fig. 1. a) Schematic of the device, showing the waveguide-coupled G-centers (zoom in showing the atomic configuration, with black = silicon and blue = carbon atoms), and a representative PL spectrum for a single emitter. b) By illuminating with increasing optical power, we observe non-volatile spectral detuning of the ZPL of a color center. c) This technique allows for spectral alignment of separate color centers in silicon. d) Fitted ZPL central wavelength versus increased optical tuning power for the device in b), showing controllable spectral shifts.

We demonstrate spectral programming and deactivation of single silicon color centers in this sample. To achieve these effects, we locally irradiate our G-centers with a 532 nm CW laser in-situ inside our 6 K cryostat.

We achieve spectral programming for the emitters under irradiation by illuminating with powers above 0.1 mW (estimated power density of 54.4 kWcm^{-2}) for 15 seconds, followed by probing PL measurements with excitation near the emitter saturation power. Under optical irradiation with powers above 0.1 mW, we consistently observe non-volatile ZPL spectral shifts for all but one of our 12 probed emitters. Example spectra of an emitter under increasing irradiation powers are shown in Fig. 1b. The average ZPL detuning for all sampled emitters is observed to be 150pm (27.5 GHz, see Fig. 1d), with a maximum detuning of 300pm (55GHz). The observed tuning range is large enough to match the 25 GHz telecommunication bands and to enable spectral alignment of separate emitters in the same waveguide (Fig. 1c).

For irradiation powers in the order of 1 mW (estimated power density of 544.3 kWcm^{-2}), we observe broadening and deactivation of the emitters. An example of this process can be found in Fig. 2. We observe that this effect is highly localized and leaves the waveguide and adjacent emitters unaffected (Fig. 2c).

In our experiments, the programming and deactivation effects are non-reversible.

Our thermal simulations rule out local annealing as the cause for the observed trimming and deactivation effects. Our hypothesis is that these effects are due to optically-induced variation of surface charge density leading to Stark tuning of the emitters, followed by ionization into a dark state for high irradiation powers.

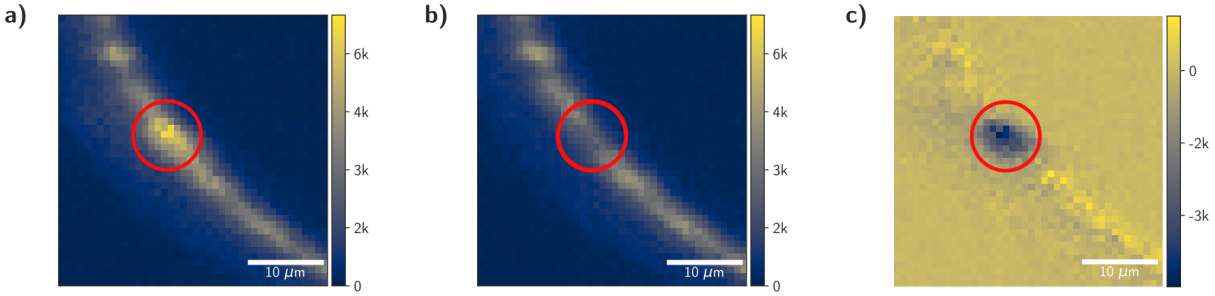


Fig. 2. a) Before and b) after PL maps of a section of a waveguide containing G-centers, showing the local deactivation of single color centers via high-power irradiation. Units are in counts per second. c) A subtracted image from a) and b), which highlights the locality of the effect. The red circle marks the irradiation location.

DISCUSSION

The demonstrated spectral programming provides a path towards in-situ fine-tuning of color center emission wavelength. The presented effect already enables the alignment of color center spectral lines into standard 25 GHz telecommunications bands, into cavities for enhanced light-matter interaction, or to other emitters and achieve quantum interference or cooperative emission. Moreover, the localized color center deactivation can be applied to trimming waveguides and cavities of interfering emitters. To reveal the physics explored in this work, further investigations are required. Examples may involve higher resolution spectroscopy, changing the geometry or crystal purity of samples, or experimenting with different optical tuning parameters.

In conclusion, we demonstrated for the first time the spectral programming and local deactivation of silicon color centers. We demonstrated significant non-volatile spectral tuning comparable to their inhomogeneous linewidth and showed spectral alignment between two separate color centers. Our results pave the way towards a silicon photonic color center platform for large-scale quantum information technologies.

Acknowledgements: C.E-H. and L.D. acknowledge funding from the European Union's Horizon 2020 research and innovation program under the Marie Sklodowska-Curie grant agreements No.896401 and 840393. M.P. acknowledges funding from the National Science Foundation (NSF) Convergence Accelerator Program under grant No.OIA-2040695 and Harvard MURI under grant No.W911NF-15-1-0548. I.C. acknowledges funding from the National Defense Science and Engineering Graduate (NDSEG) Fellowship Program and NSF award DMR-1747426. D.E. acknowledges support from the NSF RAISE TAQS program. This material is based on research sponsored by the Air Force Research Laboratory (AFRL), under agreement number FA8750-20-2-1007. The U.S. Government is authorized to reproduce and distribute reprints for Governmental purposes notwithstanding any copyright notation thereon. The views and conclusions contained herein are those of the authors and should not be interpreted as necessarily representing the official policies or endorsements, either expressed or implied, of the Air Force Research Laboratory (AFRL), or the U.S. Government.

References

[1] M. K. Bhaskar *et al.*, "Experimental demonstration of memory-enhanced quantum communication," *Nature*, vol. 580, no. 7801, pp. 60–64, Apr. 2020, doi: 10.1038/s41586-020-2103-5.

[2] G. Wolfowicz, C. P. Anderson, B. Diler, O. G. Poluektov, F. J. Heremans, and D. D. Awschalom, "Vanadium spin qubits as telecom quantum emitters in silicon carbide," *Science Advances*, May 2020, doi: 10.1126/sciadv.aaz1192.

[3] M. Ruf, N. H. Wan, H. Choi, D. Englund, and R. Hanson, "Quantum networks based on color centers in diamond," *Journal of Applied Physics*, vol. 130, no. 7, p. 070901, Aug. 2021, doi: 10.1063/5.0056534.

[4] Y. Baron *et al.*, "Detection of single W-centers in silicon," *arXiv:2108.04283 [physics, physics:quant-ph]*, Aug. 2021.

[5] L. Bergeron *et al.*, "Silicon-Integrated Telecommunications Photon-Spin Interface," *PRX Quantum*, vol. 1, no. 2, p. 020301, Oct. 2020, doi: 10.1103/PRXQuantum.1.020301.

[6] D. B. Higginbottom *et al.*, "Optical observation of single spins in silicon," *Nature*, vol. 607, no. 7918, Art. no. 7918, Jul. 2022, doi: 10.1038/s41586-022-04821-y.

[7] W. Redjem *et al.*, "Single artificial atoms in silicon emitting at telecom wavelengths," *Nat Electron*, vol. 3, no. 12, pp. 738–743, Dec. 2020, doi: 10.1038/s41928-020-00499-0.

[8] M. Hollenbach, Y. Berencén, U. Kentsch, M. Helm, and G. V. Astakhov, "Engineering telecom single-photon emitters in silicon for scalable quantum photonics," *Opt. Express, OE*, vol. 28, no. 18, pp. 26111–26121, Aug. 2020, doi: 10.1364/OE.397377.

[9] M. Prabhu, C. Errando-Herranz, L. De Santis, I. Christen, C. Chen, and D. R. Englund, "Individually Addressable Artificial Atoms in Silicon Photonics," *arXiv:2202.02342 [physics, physics:quant-ph]*, Feb. 2022, Accessed: May 04, 2022. [Online]. Available: http://arxiv.org/abs/2202.02342

Fully Integrated Quasi-Coherent Receiver Based on Co-hosted InP PIC and a SiGe ASIC

Francisco Rodrigues[1,2,3], João Santos[1,2,3], Carla Rodrigues[1], Angel Blanco Granja[1] and António Teixeira[2,3]

[1]PICadvanded, S.A., PCI-Creative Science Park Via do Conhecimento, Edifício Central, 3830-352 Ílhavo, Portugal
[2]Instituto de Telecomunicações (IT), University of aveiro, 3810-193 Aveiro, Portugal
[3]Department of Electronics, Telecommunications, and Informatics (DETI), University of Aveiro, 3810-193 Aveiro, Portugal
*francisco@picadvanced.com

A co-hosted quasi-coherent receiver involving a monolithic indium phosphide PIC and a fully integrated 30 GHz TIA and envelope detector ASIC is demonstrated and characterized for both C and L bands. Optical filterless channel selection is studied.
Keywords*: *PIC, ASIC, quasi-coherent,

INTRODUCTION

The ever-growing demand for bandwidth due to higher data center traffic requires improved networks that can grow organically with the needs. In today's network structure, the connection to the end user is typically in a point to multi-point manner through Passive Optical Networks (PON). PONs have evolved rapidly over the past few decades reaching mass deployment of 10 Gbit/s technologies and providing the first demonstration of 50 Gbit/s electro-optical implementation [1], [2]. This evolution has been achieved through the efforts of standardization bodies, maintaining basic principles such as coexistence, the use of intensity modulation (IM) or the maintenance of a high link budget, and in some cases the introduction of wavelength division multiplexing (WDM).

While network capabilities are improving, deployment costs are not expected to increase linearly with complexity, leading to a search for more powerful, albeit simpler, electro-optical hardware solutions. A winning path for such a search is the use of Photonic Integrated Circuits (PICs). Efforts to develop generic photonic integration processes have been developed globally, fostering the PIC ecosystem and increasing the maturity of the technology, and reducing the entry cost [3].

The use of a coherent receiver, i.e., a receiver architecture that is capable of recovering not only amplitude information but also its phase through the use of a local oscillator (LO) has been presented to achieve enhanced performance in future networks [4]. Coherent reception brings additional sensitivity i.e., extra power budget and higher bit rate while simultaneously using phase and amplitude schemes and channel tunability. These advantages arise from using the local oscillator which represents an attractive feature for WDM systems. Plenty of work has been carried out and reported to develop Application Specific Integrated Circuits (ASICs), co-packaged together with discrete optics when using IM alongside coherent detection. In this scenario, the receiver can reach demodulation bitrates up to 28 Gbit/s [5]. Along the same path of innovation, receivers for networks using IM based on PIC have also been proposed and reviewed [6], [7].

This paper presents the ultimate step towards the successful development of transceivers with quasi-coherent receivers that can be used in cost-sensitive networks, i.e., the fusion of a dedicated PIC and an ASIC in the same package. A quasi-coherent receiver leverages coherent detection, above mentioned, to detect only the amplitude while discarding the phase information of the received signal. The developed solution includes an electro-optical receiver based on a fully monolithic Indium Phosphide (InP) PIC co-hosted with a Silicon Germanium (SiGe) ASIC. It is designed to implement coherent detection for IM, which allows the receiver to act as a WDM filter while featuring polarization independence. The ASIC and PIC are co-packaged using a multi-pocket host of Silicon (Si) and the monolithic PIC was designed and fabricated to support both the C and L bands.

Co-hosted device and experimental setup

Fig 1 a) shows a detailed image of the co-hosted InP PIC + SiGe ASIC, through a proprietary Si multi-pocket which is thermally and mechanically connected to a custom Printed Circuit Board (PCB). The bottom layer of the device is a Thermoelectric Cooler (TEC) that is externally controlled to maintain the co-hosted device at the targeted temperature. The Si host contains slots for the ASIC and PIC and is geometrically designed to match the PIC and ASIC input/output interfaces and dimensions while minimizing the distance between their high-speed interfaces. The host also includes electrical traces and pads for the various interconnections required between the integrated

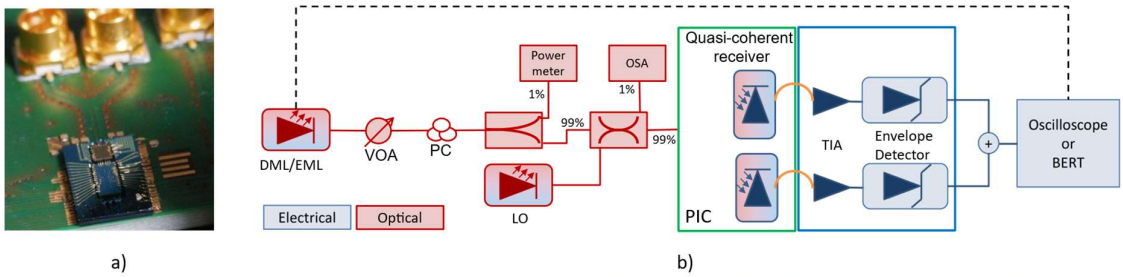


Fig. 1. a) Detailed image of the co-hosted InP PIC and SiGe ASIC. b) Block diagram of the device under test (DUT) and setup.

circuits and the PCB as well as V-grooves for fiber alignment. Wire bonds between the PIC and the ASIC connect the high-speed output of the PIN photodetectors to the input stage of the ASIC's transimpedance amplifier (TIA). The output of the ASIC is wire-bonded to the Si host RF lines designed and fabricated to provide a bandwidth of more than 30 GHz with an insertion loss of less than 1 dB. The host RF lines are then wire- bonded to the PCB RF lines.

The remaining DC electrical connections are made from the PIC /ASIC to the Si host through wire-bonding. The InP PIC was designed using the Fraunhofer Heinrich Hertz Institute (HHI) generic integration processes [8]. It features a simplified quasi-coherent architecture, capable of detecting the signal amplitude [9]. A LO used in heterodyne regime is mixed with the input signal and then split into two PIN receivers with equal amplitude and orthogonal components to achieve polarization independence. The electrical output signals from the coherent receiver feed the ASIC whose input stage is a high-speed linear TIA, followed by an envelope detector to downconvert the signals to baseband. The final stage comprises the electrical combination of the two components.

Fig. 1 b) shows the setup used to characterize the device. The green box represents the PIC which contains an LO and the quasi-coherent receiver with two PIN photodiodes and the blue box contains the ASIC, comprising the two TIAs and the necessary envelope detectors. The architecture also allows the use of an external LO. The input signal to the receiver is generated through a commercially available XFP and its evaluation board [9],[10], which is fed by a modulated signal generated with the Bit Error Rate Tester (BERT) ExoBERT2904 with 2^7 -1 Pseudo Random Sequences (PRBS) at 10 Gbit/s. The output signal from the transmitter goes through a polarization controller (PC) that locks the state of polarization through the measurements and feeds a 99%/1% 2x2 coupler used as a monitor. The remaining input of the 2x2 coupler is fed with an external tunable laser APEX AP3350A/3352A with wavelengths from 1526-1608 nm and ~300 kHz linewidth, this laser is used as external LO covering the bands under study on this paper. The optical interfacing is performed through a cleaved Standard Single Mode Fiber (SSMF) and a Spot Size Converter (SSC) at the PIC side. The differential electrical ASIC's output of the recovered signal is then connected to the Exo-BERT 2904 for real-time Bit Error Rate (BER) measurement or a digital scope TEKTRONIX DSA72004.

Experimental Results

The results shown in fig. 2, present the characterization of the implemented receiver in the context of WDM operation. The device working bandwidth was measured through the detection of a 10 Gbit/s signal, generated by commercial grade ONU (λ = 1532 nm DML) and OLT (λ = 1595 nm EML) NGPON-2 transceivers [10]. The eye diagrams from Fig.2 a) are shown for the optimal point of 10 Gbit/s operation. Starting from the ideal heterodyne frequency, ~22 GHz, the LO was swept so that we could access the optical power penalty for the BER of 10E-3, Fig 2b).

The measured device working bandwidth, indicated by the green arrows in Fig.2 b), is 9 GHz for C band (DML) and 13 GHz for L band (EML), showing the tolerance of the system to a lower cost commercial transceiver (DML), with the difference between each case being justified by the broader spectrum of the DML. Both cases are limited by the bandwidth of the ASIC (30 GHz). After testing the receiver's performance using one single wavelength channel, additional DML transmitters operating at other NGPON2 channels spaced according to the ITU-T grid were added to the setup shown in Fig. 1 to evaluate the performance and filter capabilities of the receiver when receiving multiple wavelength channels simultaneously. Fig. 2 c) compares, for a given measured BER value when transmitting CH1 (1532.68 nm, -10 dBm at the PIC input), the power penalty required to obtain the same BER value when simultaneously transmitting the desired IM signal through CH1 and another 10 Gbit/s IM signal in the adjacent channel CH2 (1533.47 nm) with different optical output powers of -5, 0 and +5 dBm. The observed power penalty is 1 dB when CH2 is emitting at -5 or 0 dBm and 1.5 dB when CH2 emits +5 dBm of optical power.

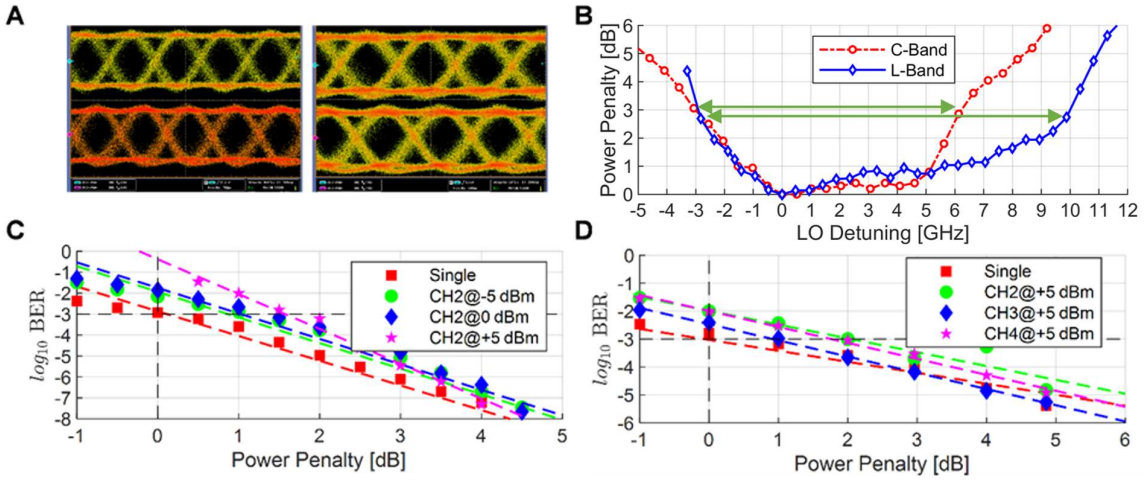


Fig. 2. a) Recovered eye diagrams for 10Gbps, b) Power penalty as a function of the LO frequency detuning for 10Gbps, c) Power penalty associated with different output powers, d) Power penalty associated with different propagating channels through 10km of SSMF

The same study was performed by including a 10 km optical fiber spool and adding other transmitters, CH3 (1534.25 nm) and CH4 (1535.04 nm). The results, depicted in Fig. 2 d) show that when CH2 or CH4 emit at the highest power (+5 dBm), there is 1 dB of power penalty between the CH1 (stated as Single) and CH4 and 2 dB between CH1 and CH2 which is the most adjacent channel, proving the filter and tuning capabilities of the quasi-coherent receiver presented in this paper.

Conclusion

A co-hosted InP Photonic Integrated Circuit, PIC, and SiGe ASIC receiver for quasi-coherent reception of IM modulated signals was demonstrated. The implemented system demonstrates its ability to demodulate 10 Gbit/s IM modulated signal at the specified NGPON2 channels. Using commercially available transmitters in the C (DML) and L (EML) bands, the device working bandwidth was measured by LO detuning. This test allowed to demonstrate the device capabilities of working with different types of transmitters and its wideband operation. It also demonstrated the filtering capabilities of the prototype when adjacent channels are simultaneously used, targeting WDM systems.

Acknowledgments: This work was funded by Fundo Europeu de Desenvolvimento Regional (FEDER), Projeto plugPON (Ref. POCI-01-0247-FEDER-047221).

References

[1] J. S. Wey, "The Outlook for PON Standardization: A Tutorial," *J. Light. Technol.*, vol. 38, no. 1, pp. 31–42, Jan. 2020, doi: 10.1109/JLT.2019.2950889.

[2] R. Rosales *et al.*, "First Demonstration of an E2 Class Downstream Link for 50Gb/s PON at 1342nm," in *2020 European Conference on Optical Communications (ECOC)*, Brussels, Belgium, Dec. 2020, pp. 1–4. doi: 10.1109/ECOC48923.2020.9333394.

[3] M. Smit, K. Williams, and J. van der Tol, "Past, present, and future of InP-based photonic integration," *APL Photonics*, vol. 4, no. 5, p. 050901, May 2019, doi: 10.1063/1.5087862.

[4] Y. Zhu *et al.*, "Comparative study of cost-effective coherent and direct detection schemes for 100 Gb/s/λ PON," *J. Opt. Commun. Netw.*, vol. 12, no. 9, p. D36, Sep. 2020, doi: 10.1364/JOCN.390911.

[5] G. Silva Valdecasa, O. G. Puertas, J. A. Altabas, M. Squartecchia, J. B. Jensen, and T. K. Johansen, "High-Speed SiGe BiCMOS Detector Enabling a 28 Gbps Quasi-Coherent Optical Receiver," *IEEE Trans. Circuits Syst. II Express Briefs*, vol. 69, no. 3, pp. 964–968, Mar. 2022, doi: 10.1109/TCSII.2021.3111451.

[6] A. Teixeira, "Photonic Integrated Circuits for NG-PON2 ONU Transceivers," in *2019 Optical Fiber Communications Conference and Exhibition (OFC)*, Mar. 2019, pp. 1–34.

[7] C. Pinho, F. Rodrigues, A. M. Tavares, C. Rodrigues, C. E. Rodrigues, and A. Teixeira, "Photonic Integrated Circuits for NGPON2 ONU Transceivers (Invited)," *Appl. Sci.*, vol. 10, no. 11, p. 4024, Jun. 2020, doi: 10.3390/app10114024.

[8] F. M. Soares *et al.*, "InP-Based Foundry PICs for Optical Interconnects," p. 16, 2019, doi: 10.3390/app9081588.

[9] B. Glance, "Polarization independent coherent optical receiver," *J. Light. Technol.*, vol. 5, no. 2, pp. 274–276, 1987, doi: 10.1109/JLT.1987.1075494.

[10] "Transceivers | PICadvanced | Aveiro," *PICadvanced Store*. https://www.picadvanced.store (accessed Jan. 20, 2023).

Optical gain via multi-layer monolithic integration of Si_3N_4 with $Al_2O_3:Er^{3+}$ waveguide amplifiers

(Student paper)

Carlos E. Osornio-Martinez[1*], Dawson B. Bonneville[1*], Meindert Dijkstra[1], and Sonia M. García-Blanco[1]

Integrated Optical Systems, MESA+ Institute for Nanotechnology, University of Twente, 7500 AE Enschede, The Netherlands.
d.b.bonneville@utwente.nl
*These authors both contributed equally to this work

In this work we report on the multi-layer integration of Si_3N_4 with $Al_2O_3:Er^{3+}$ waveguide amplifiers. Small signal internal gain of 2.5 dB is demonstrated at 1532 and 1550 nm as well as 2.1 dB at high signal powers, including powers up to 7.1 dBm launched at 1550 nm. Gain saturation was not demonstrated at high signal powers, which is promising for high power amplifiers for LIDAR sources. The result demonstrates the successful integration of an erbium doped gain medium on an established passive platform with insights towards maximizing the output power and the necessary material optimization steps.
Keywords**:** *Erbium doped waveguides, aluminium oxide, integrated amplifiers*

INTRODUCTION

Photonic integrated circuits (PICs) are a rapidly growing technology with applications in a variety of fields such as telecommunications, computing, healthcare, and sensing. To satisfy a large number of applications, it is becoming necessary to provide optical gain on-chip at a variety of wavelengths, on a variety of material platforms. Rare earth ions doped into various host materials are a promising optical gain media due to the available wavelengths, flexibility of processing techniques available and host insensitive properties. For this reason many of these devices have shown promise for integrated light sources that can be integrated into VLSI processes on silicon substrates [1,2]. Recently, industrially relevant gain levels were demonstrated in ion-implanted Si_3N_4 waveguides showing the promise of rare earth doped amplifiers in PICs with gain levels comparable to erbium doped fibres [3]. However, achieving scalable wafer processing of rare earth ion doped amplifiers that can be integrated onto a variety of underlying waveguide platforms, requires fabrication techniques that are more flexible and applicable to different material platforms [4]. In this work, we demonstrate the multi-layer integration of Si_3N_4 photonic circuits with $Al_2O_3:Er^{3+}$ waveguide amplifiers realized with reactive co-sputtering, electron beam lithography and reactive ion-etching. Gain is reported for low and high signal powers at wavelengths of 1532 and 1550 nm using bidirectional pumping at a wavelength of 1480 nm. Material optimization steps such as annealing and erbium concentration variation are discussed with the goal of maximizing the gain and increasing signal powers coming out of the chip.

RESULTS

Si_3N_4 waveguides were fabricated by LioniX International to achieve low-loss underlying circuits using a mature fabrication process. Devices on this passive layer were also used for characterizing waveguide and fiber-to-chip coupling losses via ring resonator measurements, 50/50 couplers for splitting light to a reference branch and taper structures for coupling the light from the underlying Si_3N_4 layer to the $Al_2O_3:Er^{3+}$ layer. A 200 nm buffer SiO_2 separates the Si_3N_4 from the Al_2O_3 waveguides. Reactive co-sputtering was used with purity controlled solid target precursors in oxygen ambient with a flow of 3.0 sccm following procedures outlined in [5]. A deposition rate of 4.5 nm/min was used to deposit a ~770 nm layer of $Al_2O_3:Er^{3+}$ with a dopant concentration of approximately 1.4×10^{20} ions/cm^3. Electron beam lithography was used to align to a revealed patterned Si_3N_4 feature to define the amplifiers on top of the vertical couplers using a dose of 1100 μC/cm^2. Reactive ion-etching (RIE) was performed to define the waveguides with 25 and 10 sccm of BCl_3 and HBr gas flows respectively at a chamber operating pressure of 3 mTorr and 25 W RF power. Plasma-enhanced chemical vapour deposition (PECVD) was used to deposit a SiO_2 cladding at a deposition rate of 37 nm/min using 200 and 710 sccm of SiH_4/N_2 and N_2O respectively, with a chamber pressure of 650 mTorr at 300 °C stage temperature and 60 W of power. Chips were diced and measured after annealing in a tube furnace in N_2 ambient at 600 °C.

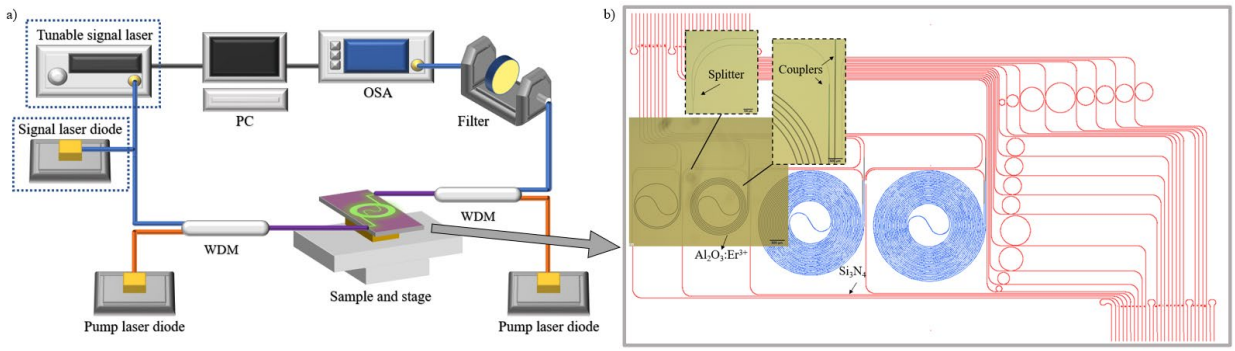


Fig. 1. a) Measurement setup used for characterization of amplifiers with a tunable and diode laser for low and high signal power outputs respectively. b) Layout of the multi-layer chips with Si_3N_4 circuits (red) patterned undeath $Al_2O_3:Er^{3+}$ (blue) amplifier sections of varying length. On-chip 50/50 splitters and multi-layer couplers shown for measurement of a reference branch and vertically coupling to the gain medium respectively.

Bidirectional pumping was achieved with the setup shown in Fig. 1a) with the use of two Anritsu 1480 nm diode pump lasers, each capable of reaching ~500 mW of incident power to the chip. Piezo controlled stages were used to couple PANDA single-mode polarization maintaining fibers to the chip where Si_3N_4 nanotapers were used to optimize modal overlap. A high-pass blocking filter cutting off wavelengths below 1500 nm was used to ensure additional spectral interference from the pumps and on-chip generated amplified spontaneous emission (ASE) or up-conversion did not reach the detector. Figure 1b) shows the layout of the chip used for gain measurements, which includes adiabatic transition tapers as vertical couplers from Si_3N_4 to the amplifier layer shown via optical microscope images. Passive ring resonator arrays can also be seen, which were included to estimate the coupling efficiency of the chip and passive waveguide loss, which corresponds to ~0.27 dB/cm at 1550 nm. Gain calculations were made assuming 3 dB of chip coupling losses, as well as 3 dB of splitting into and out of the passive coupler to the reference branch and amplifier section. Further measurements on these passive components are suggested to reduce uncertainty in the measured gain.

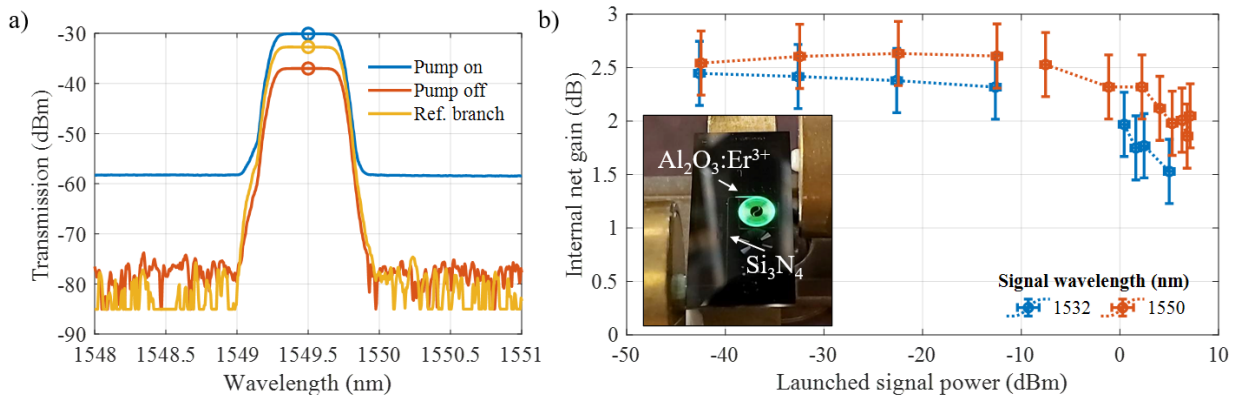


Fig. 2. a) Transmission data from the OSA showing a measurement of the Si_3N_4 reference branch and the amplifier with and without pumping. b) On-chip gain measured via Si_3N_4 waveguides with a 3.19 cm long $Al_2O_3:Er^{3+}$ waveguide amplifier for a variety of signal powers. Gain saturation shown not to occur at high signal powers up to 7.1 dBm for 1532 and 1550 nm for a launched pump power of ~150 mW. Sample shown during pumping of a ~17 cm $Al_2O_3:Er^{3+}$ waveguide amplifier (inset).

Figure 2 a) shows the measured transmission data used to extract the amplifier gain performance. The relation between the reference branch (i.e., in Si_3N_4) and the amplifier when the 1480 nm pumps are on and off. In this manner, the internal net gain of the amplifier (i.e., from Si_3N_4 to Si_3N_4) can be directly obtained by the ratio of the measured power at the output of the amplifier and reference branches [4]. The measured internal net gain at both 1532 and 1550 nm is shown in Figure 2 b), for a 3.19 cm long amplifier section, with a launched pump power of ~150 mW for launched signal powers up to 5.15 mW. Peak on-chip power is estimated to be 8.25 mW at 1550 nm. Shown in the inset is a ~17 cm chip during 1480 nm pumping where the transfer between layers can be seen visually by the up conversion in the $Al_2O_3:Er^{3+}$.

DISCUSSION

Gain demonstrated in the high-power regime shows a promising step towards high power amplifiers for LIDAR and other applications that require large amounts of off-chip power. Although the gain is low compared to other demonstrations [6-8], the presented results are preliminary. Many optimization steps can be taken, including the optimization of the amplifier length (i.e., in this work 3.19 cm), the annealing temperature, erbium concentration as well as features and alignment of the amplifier taper coupling sections. Scanning electron microscopy will be used to investigate any misalignment and further characterization can be done to ascertain the additional losses that may be impacting amplifier performance, such as losses at the signal wavelengths. Using the same processes in bulk Al_2O_3:Er^{3+} to define a single layer strip waveguide amplifier has lead to internal gain of up to ~20 dB in similar and higher concentrations (~3.0×10^{20} ions/cm^3) with identical annealing steps and process parameters [9]. There however, uncertainties such as the waveguide absorption and propagation losses are included in the measurement, as well as increased coupling losses to the chip. This discrepancy suggests further characterization of vertical multi-layer coupling losses should be investigated to validate results for the gain medium. It is also possible that higher concentrations could provide increased gain, which can be optimized for shorter or medium (1-10 cm) length amplifiers, whereas lower concentrations here will enable longer devices (20+ cm), which were unfortunately unavailable on the measured sample due to waveguide defects in the gain layer. Future work includes the further annealing and characterization of chips from this same wafer and amplifier sections of varying cross section and length.

Acknowledgements

The authors acknowledge the Grant Agreement 10107136 under the European Union and the partners in OPHELLIA - a collaborative research project funded by the European Union's Horizon 2020 research and innovation programme.

References

[1] W. A. P. M. Hendriks et al., *"Rare-earth ion doped Al_2O_3 for active integrated photonics,"* Advances in Physics X, vol. 6, no. 1, 2021.

[2] J. D. B. Bradley *et al.*, *"Monolithic erbium- and ytterbium-doped microring lasers on silicon chips,"* in *Optics Express,* vol. 22, no. 10, 2014.

[3] Y. Liu, et al., *"A photonic integrated circuit–based erbium-doped amplifier,"* Science, vol. 376, 2022.

[4] J. Mu, et al., *"High-gain waveguide amplifiers in Si_3N_4 technology via double-layer monolithic integration,"* Photonics Research, vol. 10, no. 8, 2020.

[5] C. I. Emmerik et al., *"Relative oxidation state of the target as guide line for depositing optical quality RF reactive magnetron sputtered Al2O3 layers,"* Optical Materials Express, vol. 10, no. 6, 2020.

[6] S. A. Vázquez-Córdova et al., *"Erbium-doped spiral amplifiers with 20 dB of net gain on silicon,"* Optics Express, vol. 22, no. 21, 2014.

[7] T. Chrysostomidis *et al.*, *"8×40 Gbps WDM Amplification in a Monolithically Integrated Al_2O_3:Er^{3+}-Si_3N_4 Waveguide Amplifier,"* in *IEEE Photonics Technology Letters*, vol. 33, no. 21, 2021.

[8] J. D. B. Bradley et al., *"Gain bandwidth of 80 nm and 2 dB/cm peak gain in Al_2O_3:Er^{3+} optical amplifiers on silicon,"* Journal of Optical Sciences America B, vol. 27, no. 2, 2010.

[9] D.B. Bonneville et al., *"Material optimization via optical and spectroscopic parameters of Al_2O_3:Er^{3+} for the development of amplifiers and lasers,"* in Proceedings of IEEE Benelux Photonics Chapter, 2022

Broadband and large mode-area on-chip amplifier

Mahmoud A. Gaafar[1], Kai Wang[2], Markus Ludwig[1], Thibault Wildi[1], Milan Sinobad[1], Jan Lorenzen[1], Henry Francis[3], Michael Gieselmann[3], Franz X Kärtner[1,4], Sonia M. Garcia-Blanco[2], Neetesh Singh[1], Tobias Herr[1,4,*]

[1]Center for Free-Electron Laser Science, Deutsches Elektron-Synchrotron, Notkestraße 85, Hamburg 22607, Germany
[2]Integrated Optical Systems, MESA+ Institute for Nanotechnology, University of Twente, 7500AE, Enschede, The Netherlands
[3]LIGENTEC SA, EPFL Innovation Par L, Chemin de la Dent-d'Oche 1B, Switzerland CH-1024 Ecublens, Switzerland
[4]Physics Department, Universität Hamburg, Luruper Chaussee 149, 22761 Hamburg, Germany
[*]tobias.herr@desy.de

Here, we present work towards a thulium-doped on-chip ultrafast amplifier, leveraging large mode-area gain waveguides with tailored group-velocity dispersion. We demonstrate 10 dB net gain for a broadband signal at 1820 nm inside a 5 cm-long waveguide.

INTRODUCTION

Amplification of ultrafast optical signals is key to a large number of applications in photonics. While ultrashort pulse amplification is well established in optical gain fibers, it is challenging to achieve in photonic-chip integrated waveguides. Recently, several integrated (quasi-)continuous-wave amplifiers have been demonstrated, based on rare-earth, heterogeneous semiconductor integration or nonlinear parametric gain [1-5]. On-chip amplification of ultrafast pulses, however, remains challenging due to the inherently small mode area and high optical nonlinearity in integrated waveguides. Here, we present our recent work towards an on-chip ultrafast amplifier, leveraging large mode-area gain waveguides with tailored group-velocity dispersion (GVD).

RESULTS

The amplifier structure combines silicon nitride (Si_3N_4) waveguides with a radio-frequency sputtered 1100 nm-thick thulium-doped alumina gain layer (Tm^{3+}: Al_2O_3), providing large gain bandwidth (1650nm-2000nm) and supporting sub-100 fs pulses. By designing the dimension of the Si_3N_4 waveguide, the waveguide's GVD, the mode confinement, and its overlap with the gain layer is tailored to achieve stable pulse propagation [6], low-loss waveguide bends and large optical gain (Fig. 1a-d) [7,8]. Fig. 1e shows amplified spontaneous emission (ASE) from a 5 cm-long amplifier characterized by a mode cross-section > 10 μm^2 in the gain section and an estimated Tm^{3+} concentration of $4.0 \times 10^{20} cm^{-3}$.

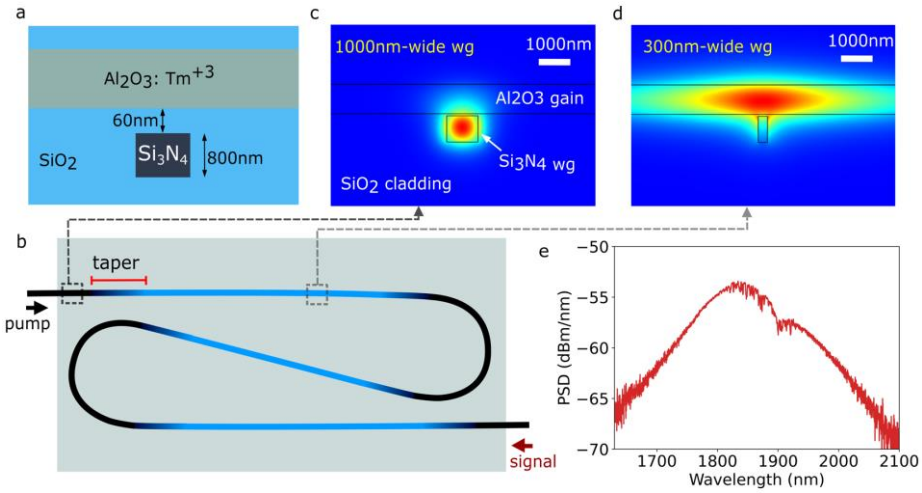


Fig. 1. (a) Schematic of amplifier waveguide cross-section with SiN height= 800 nm. The gain film (Al_2O_3 :Tm^{+3}) thickness= 1100 nm, above which a 1 µm silica layer is deposited for protection and dispersion management. (b) Schematic of spiral amplifier waveguide, black sections outline the wide Si_3N_4 waveguides (width 1000 nm) that confine the mode mostly to the waveguide core. Blue sections indicate narrow waveguide sections (width 300 nm) that will guide the mode with only weak confinement so that most of the optical power propagates in the doped Al_2O_3 cladding. Color gradient indicates the tapered waveguide

sections connecting the wide and narrow waveguides. The area where the doped Al_2O_3 cladding is deposited is highlighted by the green shaded-area. (c) and (d) TE mode profiles of signal at wavelength of 1830nm for both 1000nm and 300nm-wide waveguides, respectively. (e) Amplified spontaneous emission (ASE) from the amplifier waveguide.

Fig. 2a shows the on-chip output signal power as a function of input pump power for a pulsed input signal (1820 nm center wavelength, 0.1 mW). Broadband amplification with 10 dB net gain at pump power of 240mW (cf. circle in Fig. 2a) is presented in Fig. 2b.

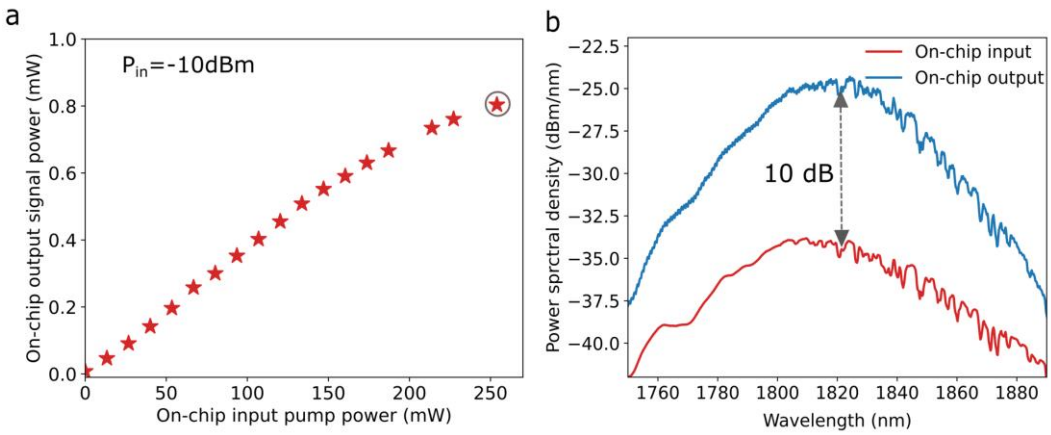


Fig. 2. (a) On-chip output signal pulse power. (b) Optical spectra of the input and output signals.

To summarize, the presented results open a pathway towards on-chip amplification of ultrashort pulses, with potential implications for spectroscopy, ranging or nonlinear mid-infrared light generation [9] in a chip-scale integrated photonic setting.

Funding: EU Horizon 2020 Research and Innovation Program (grant agreement 965124); Helmholtz Young Investigators Group VH-NG-1404.

References

[1] J. Mu et al., High-gain waveguide amplifiers in Si3N4 technology via double-layer monolithic integration, Photon. Res., vol. 8, pp. 1634, 2020
[2] Y. Liu et al., A photonic integrated circuit–basederbium-doped amplifier, Science, vol. 376, pp. 1309–1313, 2022
[3] Camiel Op de Beeck et al., Heterogeneous III-V on silicon nitride amplifiers and lasers via microtransfer printing, Optica, vol. 7, pp. 386, 2020
[4] J. Riemensberger et al., A photonic integrated continuous-travelling-wave parametric amplifier, Nature, vol. 612, pp. 56-61, 2022
[5] H. C. Frankis et al., Erbium-doped TeO_2-coated Si_3N_4 waveguide amplifiers with 5 dB net gain, Photon. Res., vol. 8, pp. 127-134, 2020
[6] J. M. Dudley et al., Self-similarity in ultrafast nonlinear optics, Nat. Phys., vol. 3, pp. 597, 2007
[7] N. Singh et al., Towards CW modelocked laser on chip – a large mode area and NLI for stretched pulse mode locking, Opt. Exp., vol. 28, pp. 22562, 2020
[8] Purnawirman et al., C- and L-band erbium-doped waveguide lasers with wafer-scale silicon nitride cavities, Opt. Lett., vol. 38, pp. 1760, 2013
[9] M. Tao et al., Super-flat supercontinuum generation from a Tm-doped fiber amplifier, Sci. Rep., vol. 6, pp. 23759, 2016

Integration of quantum light sources, circuits and superconducting detectors on nanophotonic chips.

Invited paper

Carsten Schuck

Department for Quantum Technology, University of Münster, Heisenbergstraße 11, 48149 Münster, Germany
Center for NanoTechnology (CeNTech), Heisenbergstr. 11, 48149 Münster, Germany
Center for Soft Nanoscience (SoN), Busso-Peus-Str. 10, 48149 Münster, Germany
* carsten.schuck@uni-muenster.de

Integrated optics holds great potential for overcoming scaling challenges and realizing complex functionalities in quantum technology. Here we show how large numbers of solid-state single photon sources and superconducting nanowire single-photon detectors can be integrated on nanophotonic chips. We further demonstrate a reinforcement learning-based inverse design method that allows for scaling down nanophotonic circuit components.

Keywords: *Single photon sources, SNSPD, inverse design, reinforcement learning*

INTRODUCTION

Quantum Technology promises tremendous advances in information processing, communication, and sensing, but many current implementations do not yet integrate all essential building blocks and neither scale to large system size. Here we focus on photonic approaches, which are a frontrunner for quantum communication applications but also hold promise for optical quantum computing, simulation, and remote sensing [1]. We identify quantum light sources, nanophotonic circuit components and single-photon detectors as essential building blocks and show how these can be replicated in large numbers on semiconductor chips by leveraging modern nanotechnology. Combining single photon sources and detectors with configurable optical, electrical and mechanical nanophotonic functionalities thus provides new means for realizing networks of quantum sensors, photonic information processors and quantum communication devices.

SINGEL PHOTON SOURCE INTEGRATION

Single-photon sources are of outstanding importance for a wide variety of tasks in quantum technology that employ photonic degrees of freedom for quantum information encoding. While several single-photon sources have shown excellent performance, they typically are individual single-emitter devices. Future quantum technology however will require large numbers of such quantum emitters that are integrated into a network architecture for sensing, computing, or communication tasks. This will be challenging to achieve with approaches relying on placing an individual emitter system under a high-numerical aperture objective for efficient fluorescence collection. Integrating single-photon emitters into nanophotonic circuits instead provides opportunities for scaling photonic quantum systems with multiple emitters to significantly smaller size, while maintaining functionality as a single-

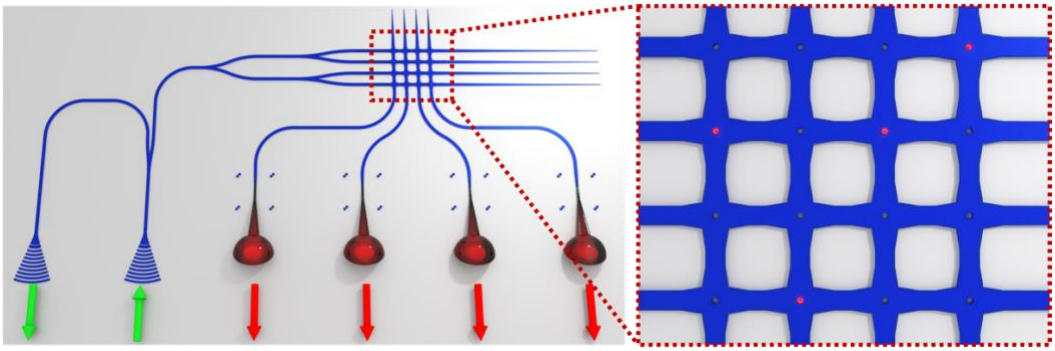


Fig. 1. Nanophotonic device that probabilistically integrates lithographically positioned colloidal quantum dots at the intersections of (horizontal) excitation and (vertical) collection waveguides. Electron beam and focused laser exposure allow for eliminating excess emitters. Upon optical excitation with 532 nm laser light, supplied from optical fibers via narrow bandwidth grating couplers (left), the quantum dots emit single photons into perpendicular collection waveguides that connect to optical fibers via efficient, broad bandwidth 3D polymer coupling interfaces (red).

photon source. Here we show how nanoscale solid-state quantum emitters, such as colloidal quantum dots, can be embedded into photonic integrated circuits [2]. Our approach allows for simultaneously addressing several emitter systems individually, but independently of one another from nanophotonic waveguides that connect to an optical fiber array via efficient and broadband coupling interfaces, as shown in Fig. 1. We increase integration yield of individual single-photon sources by processing colloidal quantum dots in solution, removing excess emitters via electron beam and focused laser exposure, and lithographic pattering for achieving high positioning accuracy. Our approach paves the way for integrating single photon sources at any desired position in a photonic integrated circuit where optical excitation and photon collection can be realized via independent waveguide-channels.

REINFORCEMENT LEARNING-BASED INVERSE DESIGN OF NANOPHOTONIC CIRCUIT COMPONENTS

As the complexity of photonic integrated circuits increases, scaling nanophotonic devices to smaller footprints becomes ever more important. Inverse design methods have shown to yield compact layouts for a wide variety of nanophotonic functionalities employing convex optimization techniques [3]. However, the topology of the solution space accessible with standard nanofabrication techniques is nonconvex, as evident from large numbers of local optima. Here we explore the possibility of interpreting nanophotonic black-box optimization problems as reinforcement learning (RL) tasks. We develop an algorithm, which shows stable and scalable learning behavior applicable to any pixel-discrete nanophotonic design problem that allows for assessing device performance via electromagnetic simulation to evaluate reward functions. Several interfaces to the data flow enable us to incorporate design constraints, for example to account for limitations of state-of-the-art nanofabrication capabilities. To demonstrate the universality of our approach we apply our RL-algorithm to a wide range of nanophotonic functionalities, such as mode converters and directional couplers, as shown in Fig. 2. 3D finite difference frequency domain simulations show that excellent device performance is achievable for extremely compact footprints. A silicon-on-insulator mode converter for transverse electric (TE) modes, shown in Fig. 2 a), achieves 95.3% conversion efficiency from the fundamental TE00 to the TE20 mode with minimal 0.1% crosstalk into the TE00 mode. If state-of-the-art nanofabrication constraints are taken into account by the algorithm the performance only decreases slightly to 93.7% TE00-to-TE20 conversion with 1.8% crosstalk to the fundamental mode, as shown in Fig. 2 b). In addition to functionality, the algorithm also allows for varying pixel size, material system, and operation wavelength, as shown for a 50:50 power splitter in tantalum pentoxide (Ta2O5) on insulator for 775 nm wavelength in Fig. 2c), achieving 84% transmission. If smaller pixels and nanofabrication constraints are considered the transmission improves to 91.4%, as shown in Fig. 2 d). While our RL-based inverse design algorithm already provides exciting prospects for dramatically increasing device density in photonic integrated circuits we anticipate that exploration mechanisms in delayed-reward environments, such as artificial curiosity, can lead to further improvements.

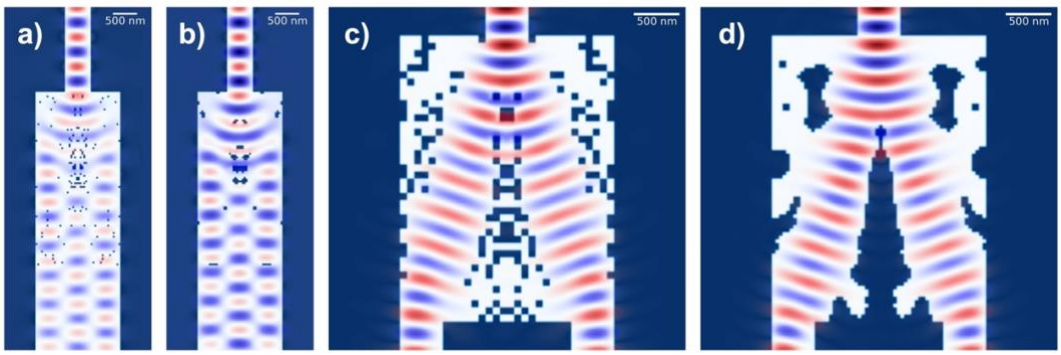


Fig. 2. a) Electrical field distribution in a TE00-TE20 mode converter in SOI for 1550 nm wavelength as calculated via reinforcement learning-based inverse design (top view). b) Same as in a) after incorporating realistic nanofabrication constraints into the inverse design algorithm. c) Electrical field distribution in a 50:50 power splitter in SOI for 1550 nm wavelength as calculated via reinforcement learning-based inverse design for 100 nm pixel size. d) Same as c) for a reduced pixel size of 50 nm and after incorporating realistic nanofabrication constraints into the inverse design algorithm

WAVEGUIDE-INTEGRATED SUPERCONDUCTING NANOWIRE SINGLE PHOTON DETECTORS

Chip-scale quantum photonic technology benefits strongly from integrating single-photon detectors into the nanophotonic circuitry, thus avoiding interface losses to separate stand-alone photon counting solutions. This is achievable by integrating superconducting nanowire single photon detectors on top of nanophotonic waveguides. Resulting devices have demonstrated >90% on-chip detection efficiency, dark count rates below 1 count per second and timing accuracies of a few 10 ps [4]. However, simultaneous operation of large numbers of independent devices on the same chip, efficient interfaces to fiber optic quantum communication channels and photon number resolving

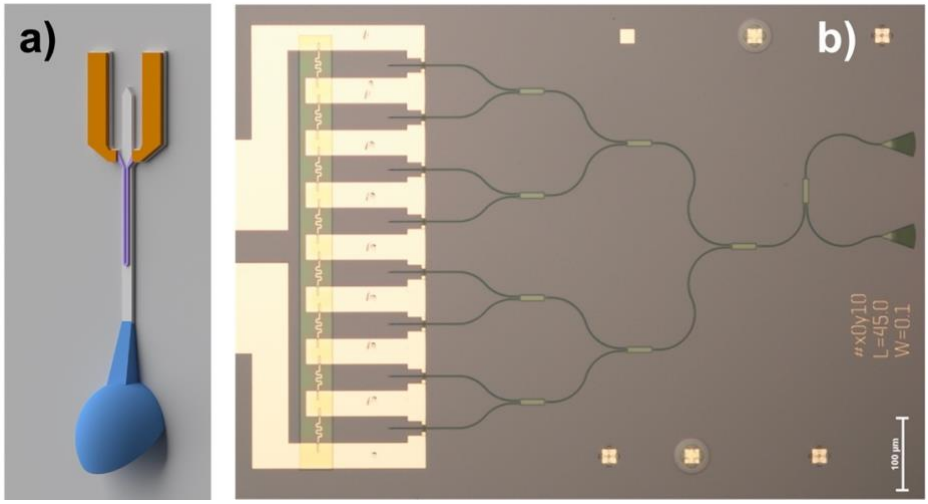


Fig. 3. a) Waveguide-integrated superconducting nanowire single photon detector (purple) with broad bandwidth 3D polymer coupling interface (blue). b) Photon number resolving superconducting nanowire detector architecture that translates optical input photon number into electrical output pulse height via parallel connected normal (Au) resistors.

capabilities have remained challenging. Here we show how direct laser writing allows for realizing 3D polymer coupling structures via two-photon polymerization to facilitate efficient fiber-chip interconnects, as shown in Fig. 3 a). We exploit these capabilities for enabling independent fiber access to up to 64 waveguide-integrated SNSPDs [5]. Simultaneous operation of these detectors has allowed us to perform quantum key distribution experiments that realize secret key rates of up to 3 Mbit/s on parallelizable channels [6]. We further configure SNSPDs and corresponding nanophotonic access to achieve quasi-photon number resolution. By connecting several nanowires in series with each individual nanowire connected to a parallel normal resistor, as shown in Fig. 3 d), it is possible to infer photon number in the input mode from the electrical output pulse height. We successfully realize these photon number resolving (PNR) capabilities for up to 16 nanowire elements. PNR-SNSPDs will be crucial for generating non-Gaussian states via photon number subtraction in fully integrated fashion and provide novel detector solutions to advanced quantum information processing and simulation tasks, such as Boson sampling.

CONCLUSION

We present progress towards realizing all essential ingredients for integrated quantum photonic technology, namely single photon sources, circuit components, and detectors, with compact form factor and individual addressability on integrated optical platforms. The favorable scaling properties of our approach have already enabled high rate quantum key distribution [6] and offer several exciting prospects for developing next generation quantum communication systems, sensors and information processing protocols.

ACKNOWLEDGMENTS

Acknowledgements: We acknowledge support from the Ministry for Culture and Science of North Rhine-Westphalia (421-8.03.03.02–130428), the German Research Foundation (DFG, CRC 1459), the Federal Ministry of Education and Research (BMBF, QuPAD Grant No. BMBF 13N14953) and the European Union's Horizon 2020 Research and Innovation Action under grant agreement no. 899824 (FET-OPEN, SURQUID) and the Münster Nanofabrication Facility (MNF).

References

[1] G. Moody, V. Sorger, D. J. Blumenthal, et al., *2022 Roadmap on integrated quantum photonics*, J. Phys. Photonics 4(1), 012501 (2022).

[2] A. Eich, T. C. Spiekermann, H. Gehring, et al., *Single-photon emission from individual nanophotonic integrated colloidal quantum dots*, ACS Photonics 9, 551 (2022).

[3] M. Butz, A. S. Abazi, R. Ross, B. Risse and C. Schuck, *Inverse Design of Nanophotonic Devices using Dynamic Binarization*, doi: 10.48550/arxiv.2211.10416 (2022), to appear in Optics Express.

[4] S. Ferrari, C. Schuck, W. H. P. Pernice, *Waveguide-integrated superconducting nanowire single-photon detectors*, Nanophotonics, 7(11), 1725 (2018).

[5] M. Häußler, R. Terhaar, M. A. Wolff, et al., *Scaling waveguide-integrated superconducting nanowire single-photon detector solutions to large numbers of independent optical channels*, Rev. Sci. Inst. 94(1), 013103 (2023).

[6] R. Terhaar, J. Rödiger, M. Häußler.,et al. , *Ultrafast quantum key distribution using fully parallelized quantum channels*, Opt. Express 31(2), 2675 (2023).

Fiber-coupled plug-and-play heralded single photon source based on Ti:LiNbO$_3$ and polymer technology

(student paper)

Christian Kießler[1,*], Hauke Conradi[2], Moritz Kleinert[2], Viktor Quiring[1], Harald Herrmann[1], Christine Silberhorn[1]

[1]Paderborn University, Integrated Quantum Optics, Institute for Photonic Quantum Systems (PhoQS), Warburger Str. 100, 33098 Paderborn,

[2]Fraunhofer HHI, Einsteinufer 37, 10587 Berlin

[*]christian.kiessler@uni-paderborn.de

We present the first chip-size fully integrated fiber-coupled Heralded Single Photon Source (HSPS) module based on a hybrid integration of a nonlinear lithium niobate waveguide into a polymer board. Photon pairs are generated via parametric down-conversion and then filtered and routed to two separate outputs. We measure a heralded second-order correlation function of $g_h^{(2)} = 0.05$ with a heralding efficiency of $\eta_h = 4.5\,\%$ at low pump powers.
Keywords: *heralded single photon source, hybrid integration, parametric down-conversion, lithium niobate*

INTRODUCTION

A reliable, but cost-effective generation of single-photon states is key for practical quantum communication systems. Different approaches are studied to build a practicable single photon source, such as quantum dots [1] or nonlinear photon-pair generation with heralding schemes [2]. A major challenge for these sources is an efficient coupling of the generated photons to optical fibers, which is necessary to use these sources practicably. First commercial HSPS are available as bench-top devices [3], but they are still far away from the ultimate goal of realizing a quantum- system-on-chip (QSoC) providing low cost, small size and robustness, which are the essential features for future commercial exploitation. Ultimately, in a fully integrated HSPS all different components for spontaneous parametric down conversion (SPDC), photon separation and pump filtering must be combined on one chip, which has not been demonstrated yet.

Here, we present a fully integrated chip-size, plug-and-play HSPS module based on lithium niobate and polymer technology. A polymer board (PolyBoard) is used as a chip platform, which enables the fabrication of waveguides and etched slots for the integration of different optical components [4]. Filters with various spectral and polarization characteristics can be glued into these etched slots, which open up the possibility for sufficient pump filtering and signal/idler separation. The PolyBoard is therefore a perfect platform for the integration of different optical components on chip. A SPDC process in a titanium-indiffused periodically poled z-cut lithium niobate waveguide (Ti:ppLN) is designed to generate photon pairs at $810\,\mathrm{nm}$ (signal) and $1550\,\mathrm{nm}$ (idler). The high second order nonlinearity of LiNbO$_3$ makes it a favorable choice for an efficient SPDC process [5]. The signal photons are used to herald the telecom photons. The Ti:ppLN waveguide is butt-coupled to the PolyBoard waveguide. The hybrid integration of a Ti:ppLN waveguide into the PolyBoard leads to a fully integrated module, which cannot be realized in one material alone. The signal wavelength of $810\,\mathrm{nm}$ enables the possibility for a future integration of silicon single-photon avalanche diodes (SPADs) to the module and therefore a possible commercially available device with small size, low cost, high robustness and reproducibility.

DESIGN AND COMPONENTS

We fabricated low loss waveguides in z-cut LiNbO$_3$ (typically $< 0.1\,\mathrm{dB/cm}$) by a titanium indiffusion. Periodic poling of the waveguides ensures the quasi-phase-matching condition for the designed type-0 phase-matched SPDC process with a pump wavelength at $532\,\mathrm{nm}$ and signal and idler at $810\,\mathrm{nm}$ and $1550\,\mathrm{nm}$, respectively. The Ti:ppLN crystal has a length of $15\,\mathrm{mm}$ and the endfacets are coated for high transmission efficiency within the module and suppression of pump light. A PM-fiber is glued to the input-facet of the Ti:ppLN waveguide and the output facet is coupled to a PolyBoard with integrated waveguides. A sketch of the module is shown in Figure 1a. An additional filter (LP) and dichroic mirror (DM) are integrated into etched slots in the PolyBoard for pump suppression and photon separation. SM-fibers are glued to the outputs and the whole module is mounted on top of a thermoelectric

cooler for temperature control. Figure 1b shows the assembled and packaged HSPS module with PM input-fiber (purple), two SM-output-fibers (yellow) and electrical contacts for temperature control.

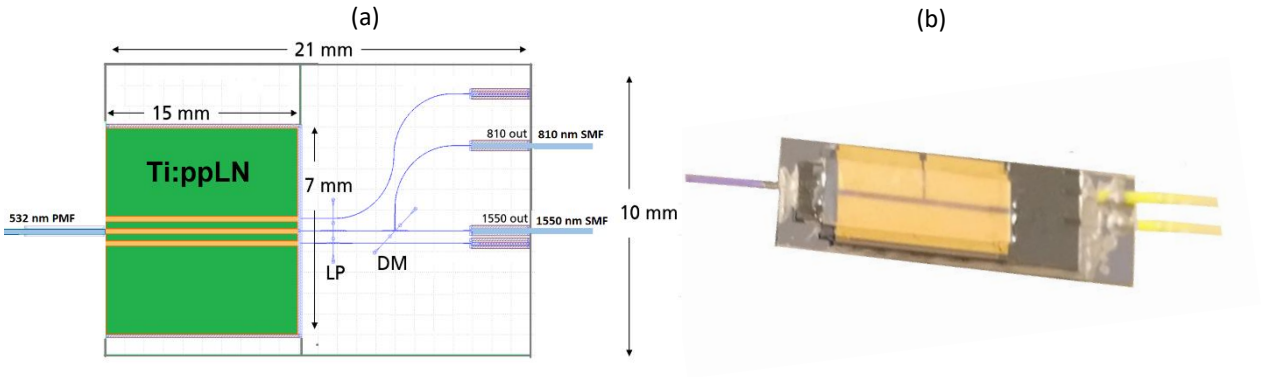


Fig 1. Design sketch of the HSPS module (a) and picture of the assembled module (b).

RESULTS

We performed a first characterization of the assembled module by pumping it with a cw-laser at $532\ \mathrm{nm}$ and analyzing the outputs with a spectrometer at visible wavelengths. Figure 2 shows the measured spectrum of the signal output port at three different temperatures measured with the integrated thermosensor. The intensity drop for high temperatures can be explained by a small misalignment in the module due to different expansions of the components. Peaks from higher-order modes and Cerenkov radiation are visible. We observe a perfect separation of signal and idler, since the spectrum of the idler output port shows no intensity counts at around $810\ \mathrm{nm}$ (see Figure 2, green).

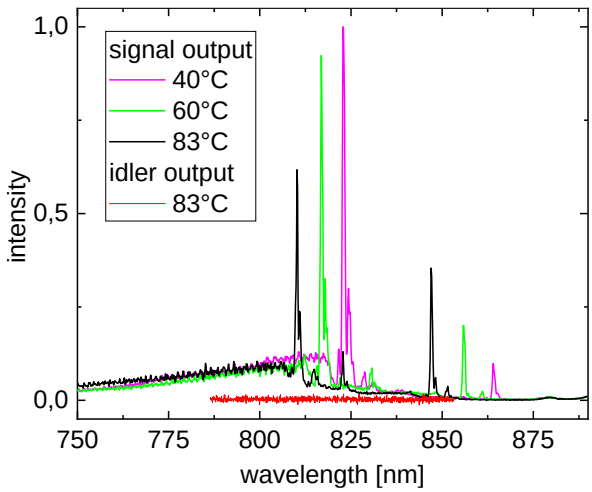


Fig 2. Measured HSPS module output spectra of the signal and idler photons at different temperatures.
No counts at around 810 nm in the idler output indicate a perfect separation of signal and idler photons.

We then investigated the single photon characteristics of the module by performing conditioned measurements with superconducting nanowire single-photon detectors. To determine the single photon and heralding performance of the module, we evaluated the heralding-efficiency η_h. The heralding-efficiency η_h describes the probability of a single photon in the idler output upon the detection event in the signal output. The power dependent heralding efficiency of the filtered module is shown in Figure 3a. For low pump powers $< 1\ \mu\mathrm{W}$, we can obtain a constant heralding efficiency of around $\eta_h = 3.5\ \%$. To evaluate the simultaneous generation of multiple photon pairs in the generated SPDC, we make use of the heralded second-order auto-correlation function $g_h^2(0)$. Figure 2b shows the measured $g_h^2(0)$ of the module for different pump powers. For low pump powers $< 1\ \mu\mathrm{W}$ the second-order autocorrelation function reaches values of $g_h^2(0) < 0.005$.

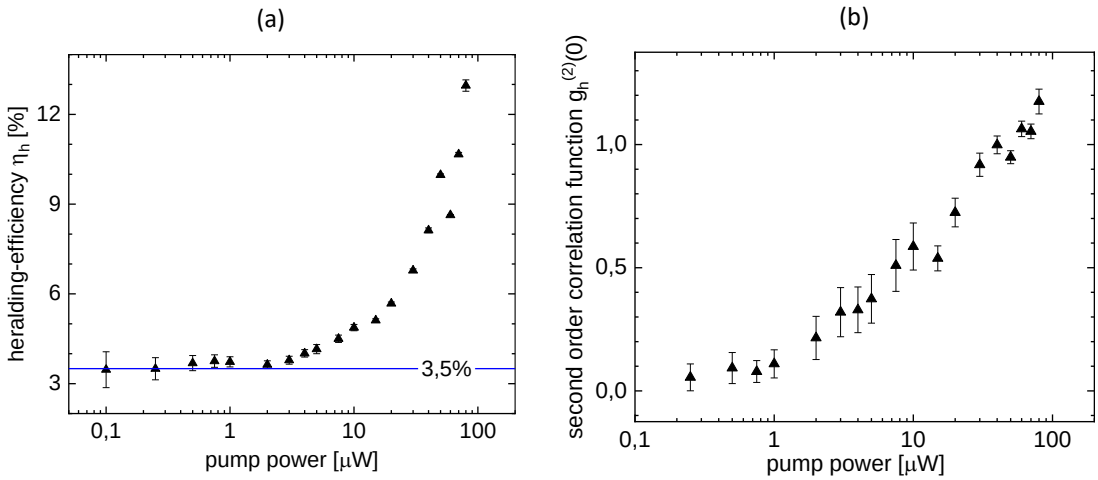


Fig 3. Heralding efficiency η_h vs. pump power of the filtered HSPS module (a). For low pump powers the heralding efficiency approaches a vlaue of $\eta_h = 3.5\%$. Heralded second-order auto-correlation function $g_h^2(0)$ vs. pump power (b). An increase for higher pump powers indicates the generation of higher-order photon components

DISCUSSION

We demonstrated the first chip-size ($(2 \times 1)\mathrm{cm}^2$) fully integrated fiber-coupled Heralded Single Photon Source module based on a hybrid integration of a Ti:ppLN waveguide into a polymer board with integrated optical components. For low pump powers, we can obtain a constant heralding efficiency of around ηh = 3.5%, which is low compared to other works [6]. It is important to mention that our module is a hybrid integration, which is not the case with the comparable sources. Non-optimal coupling between the two material systems leads to additional losses that reduce the heralding efficiency. We estimated the total losses within the assembled module by performing count rate measurements with different additional filter combinations to be $\eta_s = 1.5\ \%$ (18 dB losses) and $\eta_i = 5\ \%$ (13 dB losses) in the signal and the idler port, respectively. Significantly improving the coupling in the module could greatly lower losses, which should result in a higher heralding efficiency. For low pump powers the second-order autocorrelation function reaches values of $g_h^2(0) < 0.005$, which indicates an excellent single photon character and is comparable to a previous HSPS based on Ti:ppLN, developed and fabricated in our group [2].

The hybrid integration of Ti:ppLN into a PolyBoard opens up the opportunity for a future multi-channel source and a direct integration of silicon SPAD arrays for the detection of the signal photons on chip. The realization of a quantum system-on-chip (QSoC) providing low cost, small size and robustness is therefore conceivable with a hybrid integration approach.

ACKNOWLEDGEMENTS

This work was funded by the European Union's Horizon 2020 Research and Innovation Programme through Quantum-Flagship Project UNIQORN under Grant 820474.

References

[1] Y. Arakawa and M. J. Holmes, "Progress in quantum-dot single photon sources for quantum information technologies: A broad spectrum overview," Appl. Phys. Rev. 7, 2020.
[2] S. Krapick, H. Herrmann, V. Quiring, B. Brecht, H. Suche, and C. Silberhorn, "An efficient integrated two-color source for heralded single photons," New J. Phys. 15, 2013.
[3] Aurea Technology, "Twin Photon Source at telecom wavelengths," https://www.aureatechnology.com/en/products/twin-photons-source.html, 2023.
[4] N. Keil, C. Zawadzki, D. de Felipe, Z. Zhang, and N. Grote, "Polymer based platform for hybrid photonic integration," 2012.
[5] R. S. Weis and T. K. Gaylord, "Lithium niobate: Summary of physical properties and crystal structure," Appl. Phys. A 37, 191–203, 1985.
[6] S. Signorini and L. Pavesi, "On-chip heralded single photon sources," AVS Quantum Sci. 2, 2020.

Programmable photorefractive optical synapses in integrated photonics for neuromorphic computing

(Student paper)

Elger A. Vlieg[1*], Folkert Horst[1], Roger Dangel[1†] and Bert J. Offrein[1]

[1] IBM Research—Zurich, Säumerstrasse 4, Rüschlikon, 8803, Switzerland
[*]Corresponding author e-mail (vli@zurich.ibm.com)
[†]Previously employed at [1]

We experimentally demonstrate programmable optical synaptic connections for neuromorphic computing, based on the photorefractive effect, in an integrated photonic interconnect circuit. This provides the core components of an analog crossbar array for fast and efficient matrix-vector multiplications in artificial neural networks.
Keywords: *integrated optics, neuromorphic computing, synaptic connections, analog crossbar array, photorefractive effect, holography*

INTRODUCTION

For the past decade, the progress in artificial intelligence (AI) has been accompanied by an artificial neural network (ANN) size increase at an exponential rate close to 10x that of Moore's law [1]. This trend is unsustainable for general-purpose digital processors due to the increasing energy and hardware demands [1,2].

Analog neuromorphic computing is an emerging paradigm that aims to meet the processing requirements in AI [3,4]. A core building block of the neuromorphic computer is the synapse, which connects signal paths with a programmable coupling strength, and can be optimized by training for a desired AI task.

Analog synapses configured in a crossbar array network can accelerate matrix-vector multiplications (MVM) for the signal processing in ANNs (Fig. 1) [3-5]. Importantly, the signal propagation between densely connected layers yields a multiply-accumulate (MAC) workload that scales quadratically with network width, while the analog crossbar array can perform it with linear scaling on latency and energy [5]. Thus, the analog crossbar array is a promising architecture to enable ANNs with improved power-efficiency.

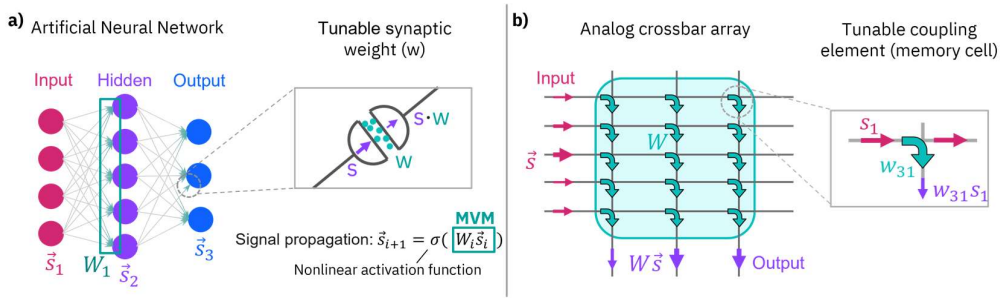


Fig. 1. ***a)*** *The signal transfer between fully-connected layers in artificial neural networks is given by the matrix-vector multiplication (MVM) of the synaptic weight matrix and the input neural signal vector.* ***b)*** *The analog crossbar array processor performs this synaptic signal transfer by physically implementing the synaptic connections.*

The optimal hardware implementation of the analog crossbar array is a topic of scientific investigation [3-5]. In this paper, we discuss the development of an integrated photonic implementation based on the photorefractive effect (Fig. 2) [5-7]. This architecture is particularly powerful since it supports all matrix operations for ANN backpropagation training by single-cycle execution steps [5]. The transposed matrix for back propagation is addressed by simply swapping the roles of the source and destination channels. The outer product for the synaptic weight update is enabled by a linear grating write response in both negative and positive directions (Fig 2. **b)**). Lastly, the photorefractive grating formation effectively occurs continuously, thereby offering a rich number of analog weight states required for training. On top of supporting efficient ANN training, this architecture helps to alleviate the scaling challenges in photonics by spatially superimposing the synaptic weights.

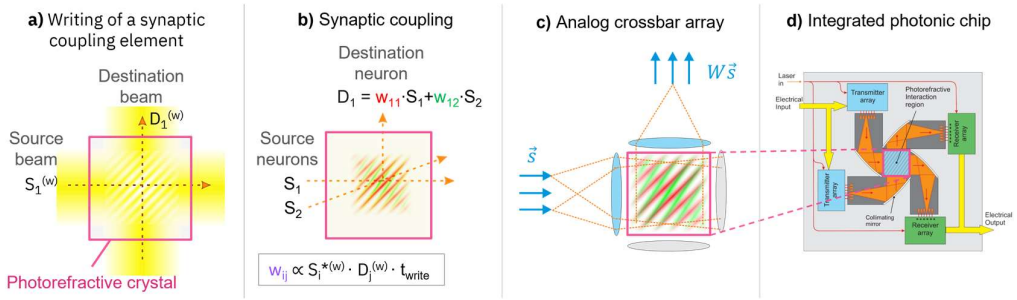


*Fig. 2. The proposed photorefractive crossbar array architecture in integrated photonics [5-7]. **a)** A source and destination laser beam yield a sinusoidal interference pattern, which is converted into a non-volatile refractive index grating by the photorefractive effect. **b)** The refractive index grating acts as a Bragg-mirror and thereby establishes a synaptic connection between the source and destination channel. Since Bragg-mirrors are angle-selective, synapses can be superimposed for angularly separated channels. **c)** Collimating optics are deployed to convert spatially separated I/O waveguides to the angular domain and back. **d)** All functional components are included on a single photonic integrated circuit.*

RESULTS

The realization of photorefractive photonic integrated circuits requires photorefractive thin-film substrates. These were achieved by thinning down photorefractive semi-insulating GaAs wafers, after wafer bonding them to Si substrates with a SiO_2 layer (Fig. 3).

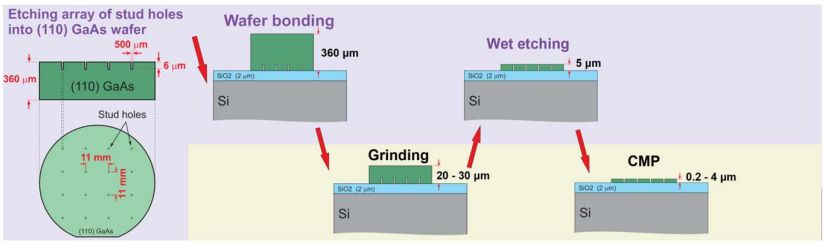


Fig. 3. Photorefractive GaAs wafers are thinned down to thicknesses suitable for photonic waveguides.

As a proof-of-concept, we first focused on demonstrating individual synapses in a prototype integrated crossbar circuit by photorefractive two-wave mixing (Fig. 4) [7]. A source and destination beam intersect inside the processor and form a photorefractive index grating. An electro-optic phase modulator (EOPM) is included on the source beam path to experimentally trigger grating write sequences by periodically shifting the phase of the optical interference pattern [5]. The EOPM is located off chip, and the source and destination signals are coupled into the photonic chip by a lensed fiber array.

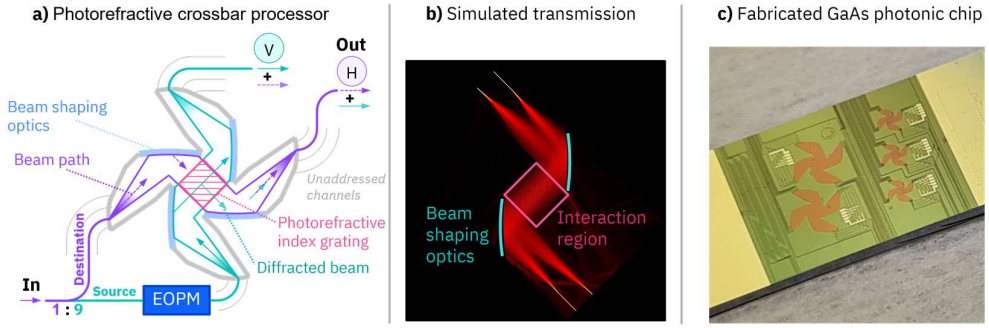


*Fig. 4. The experimental design for demonstrating photorefractive synapses by two-wave mixing [7]. **a)** A schematic of the prototype photonic crossbar circuit. **b)** The simulated transmission through the processor. **c)** The circuit realized in a photorefractive thin-film GaAs layer (Fig. 3).*

The results of the experiment in Fig. 4 are shown in Fig. 5. When the EOPM (gray) π phase-shifts the source beam, an intensity jump is visible due to the mirrored interference behavior between the output beams, followed by the rewriting of the synapse via an exponential saturation process. The analog formation of the coupling strength illustrates that the synaptic weight can in principle be programmed by write time (Fig. 2 **b)**).

Three different experiments were performed to confirm that the exponential trend corresponds to photorefractive two-wave mixing. Fig. 5 **a)** shows that based on the wavelength, the optical intensity either predominantly removes

or adds electrons in the GaAs deep charge traps underlying the photorefractive grating, yielding a π phase shift thereof [8]. Fig. 5 **b)** confirms that intensity is transferred between the horizontal and vertical processor branches (Fig 4. **a)**). Fig 5. **c)** demonstrates that the grating write speed is affected by the input optical power, as indicated by the initial slope steepness, corresponding to an accelerated charge excitation rate [7]. In Fig 5. **c)**, the 1.5mW trace has insufficient time to saturate the grating, yielding a near-linear write behavior at the expense of dynamic range.

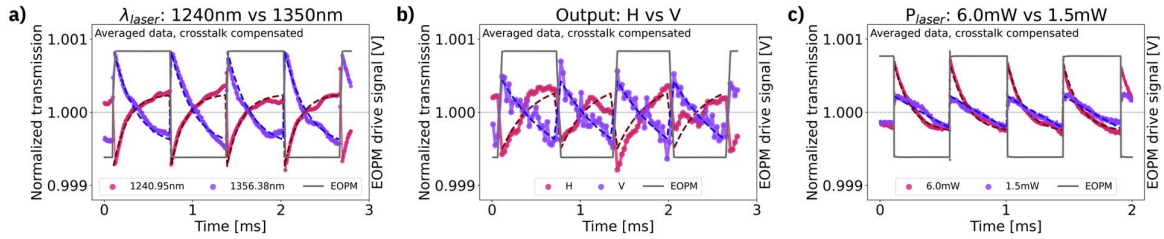


Fig. 5. The experimental periodic writing of photorefractive synapses with threefold verification. ***a)*** *A sign flip based on optical wavelength.* ***b)*** *A sign flip upon swapping the source and destination channels (Fig. 4* ***a)****).* ***c)*** *A response time modification based on optical power.*

As an extension to Fig. 5 **c)**, the fitted photorefractive response times for different laser powers are shown in Fig. 6. The datapoint at 6.0 mW is not captured by the fit. We expect that this is due to an overestimated effective optical power for all data points due to drifting lensed fibers yielding a reduced coupling efficiency. Importantly, the linear relationship in Fig 2. **b)** appears to hold.

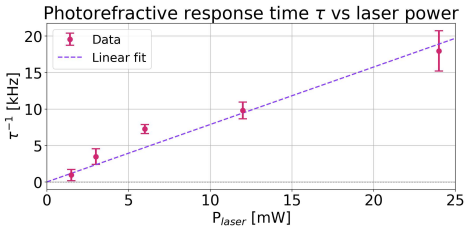


Fig. 6. The photorefractive response time τ for 5 different laser powers. The vertical error bars only indicate fit robustness, and exclude experimental reproducibility.

DISCUSSION

We report the realization of photorefractive optical synapses in integrated photonics, and thereby verified the basic operating principles of our crossbar array design. To extend this work to a fully functional crossbar array, programmable I/O circuitry needs to be included, so that multiple crossbar channels can be addressed in parallel and individually (Fig. 4 **a)**) [5]. Future work consists of fabricating a full crossbar array and demonstrating all relevant signal processing.

Acknowledgements: This project has received funding from the European Union's Horizon 2020 research and innovation program under grant agreement number 828841 (ChipAI) and 860360 (Post-Digital). We thank the Binnig and Rohrer Nanotechnology Center (BRNC).

References

[1] D. Narayanan et al., *Efficient Large-Scale Language Model Training on GPU Clusters Using Megatron-LM*, SC '21 58, pp. 1-15, 2021
[2] E. Strubell et al., *Energy and Policy Considerations for Modern Deep Learning Research*, AAAI 34(09), 13693-13696, 2020
[3] D. Marković et al., *Physics for neuromorphic computing*, Nat Rev Phys 2, pp. 499–510, 2020
[4] A. Sebastian et al., *Memory devices and applications for in-memory computing*, Nat. Nanotechnol. 15, pp. 529–544, 2020
[5] E. A. Vlieg et al., *An Integrated Photorefractive Analog Matrix-Vector Multiplier for Machine Learning*, Appl. Sci. 12(09), pp. 4226, 2022
[6] Y. Owechko, B.H. Soffer, *Holographic Neurocomputer Utilizing Laser Diode Light Source*, Proc. SPIE 2565, pp. 12–19, 1995
[7] P. Yeh, *Two-Wave Mixing in Nonlinear Media*, IEEE J. Quantum Electron. 25(3), pp. 484–519, 1989
[8] F. P. Strohkendl et al., *Hole–electron competition in photorefractive gratings*, Opt. Lett. 11, pp. 312-314, 1986

Damage Resistant Diced Waveguides in Ti-Indiffused Lithium Niobate for Second Harmonic Generation

(Student paper)

Michelle Kirsch[1*], Christian Kießler[1], Christof Eigner[1], Harald Herrmann[1] and Christine Silberhorn[1]

[1]Paderborn University, Integrated Quantum Optics, Institute for Photonic Quantum Systems (PhoQS), Warburger Str. 100, Paderborn, 33098, Germany
[*] michelle.kirsch@uni-paderborn.de

We demonstrate ridge waveguides fabricated by dicing in planarly titanium indiffused, periodically poled $LiNbO_3$ for second harmonic generation (SHG). They show width variations of ≤ 1 µm and losses of $\alpha_{TM} = 0.34 \frac{\mathrm{dB}}{\mathrm{cm}}$ ($\alpha_{TE} = 0.42 \frac{\mathrm{dB}}{\mathrm{cm}}$) for TM (TE) polarization. SHG with the fundamental wave around 1.55 µm could be demonstrated with an efficiency of $\eta = 9.44 \frac{\%}{\mathrm{W\,cm^2}}$ and a high photorefractive damage resistance of up to 500 mW pump power.

Keywords: *Lithium Niobate, Ridge Waveguide, Photorefraction, Second Harmonic Generation*

INTRODUCTION

Lithium niobate ($LiNbO_3$) is a widely used platform for integrated optic devices due to its wide transparency range and large $\chi^{(2)}$ nonlinear coefficient [1]. The internal polarisation allows for the fabrication of periodically poled structures and therefore quasi phase-matched processes for nonlinear frequency conversion. A well-established waveguide fabrication method in $LiNbO_3$ is the diffusion of Titanium (Ti) strips into the bulk crystal to increase the refractive index in the Ti-indiffused area. However, a common problem in Ti-indiffused strip waveguides is the low index contrast and the proneness to photorefractive damage, which prevents applications with high optical powers [2]. The photorefractive effect is intensity induced and alters the refractive index of the material and therefore disturbs nonlinear frequency conversion in periodically poled crystals.

A tighter light confinement in Ti-indiffused $LiNbO_3$ can be found in ridge structures, which are also less prone to the effect of photorefraction [2, 3]. Here, we demonstrate the fabrication of ridge waveguides by precision diamond dicing in planarly Ti-indiffused $LiNbO_3$. We optimized fabrication parameters to decrease propagation losses and investigated the effect of the waveguide geometry on second harmonic generation and photorefractive damage and achieve losses as low as $\alpha_{TE} = (0.42 \pm 0.02) \frac{\mathrm{dB}}{\mathrm{cm}}$ for TE and $\alpha_{TM} = (0.34 \pm 0.02) \frac{\mathrm{dB}}{\mathrm{cm}}$ for TM polarization, an efficiency of $\eta = 9.44 \frac{\%}{\mathrm{W\,cm^2}}$ and a high photorefractive damage resistance of up to 500 mW pump power.

FABRICATION

For the fabrication of ridge structures in LiNbO3 we use the precision dicing saw Disco DAD3430 with a diamond blade (RBT-9780 SD6000N100BR26). Before dicing, we deposited a planar Ti layer with a thickness of 60 nm on top of a z-cut $LiNbO_3$ sample and diffused it into the crystal in a diffusion oven at 1060 °C for 15.5 h. The prepared samples have a length of around 35 mm, a width of 12 mm and a thickness of 0.5 mm. To create waveguides for a type-0 phase-matched second harmonic conversion from 1550 nm to 775 nm, we periodically poled the Ti-indiffused sample with a poling period of $\Lambda = 17.51$ µm. After the diffusion and periodic poling, we cut trenches into a $LiNbO_3$ sample to create ridges and polish the facets by dicing as well. To evaluate the quality of our fabricated ridge waveguides we measured the geometric dimensions of single ridges and their variations along the structure. To analyze the overall shape of the ridge waveguides we took images with a scanning electron microscope (SEM). The facets of two diced ridges with different dimensions are presented in Fig. 1. The images reveal a smooth vertical profile with no chipping and sharp edges. We furthermore investigated the variation of the ridge width along the waveguide by measuring the top width at several points of a waveguide. The top width is measured with a laser confocal microscope revealing ridge width variations of $\Delta w_{ridge} = 1$ µm.

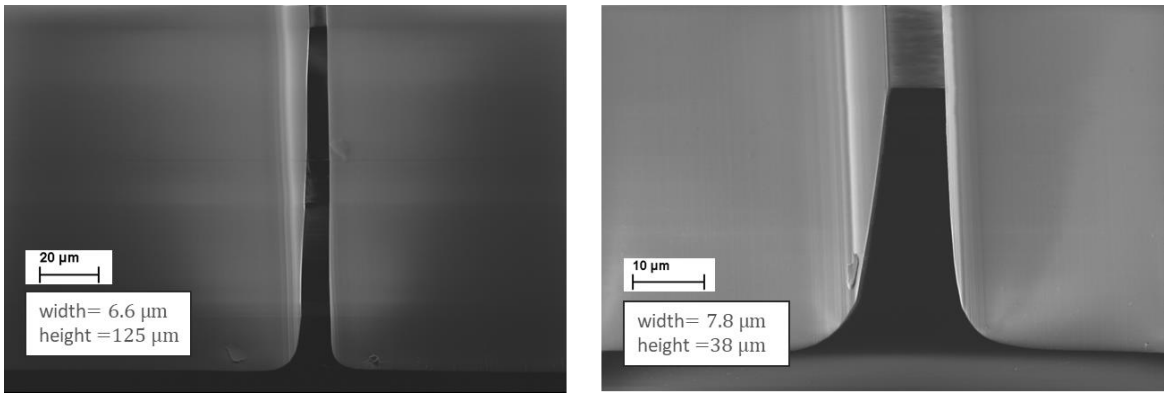


Fig. 1. SEM images of diced ridge waveguides in $LiNbO_3$ with different heights and top widths.

RESULTS

For measuring the waveguide propagation losses, we used the Fabry-Perot method [6]. We used a Tunics laser and scanned the wavelength around ~ 1550 nm to measure Fabry-Perot oscillations and calculate the propagation losses. We achieved losses as low as $\alpha_{TE} = (0.42 \pm 0.02)\,\frac{\mathrm{dB}}{\mathrm{cm}}$ for TE and $\alpha_{TM} = (0.34 \pm 0.02)\,\frac{\mathrm{dB}}{\mathrm{cm}}$ for TM polarization. These propagation losses are only an upper estimation, as the exact reflectivity of the diced end facets is not known and an ideal reflectivity was assumed in the calculation.

To characterize the SHG process, we measured the phase matching curve by tuning the fundamental wave (Tunics laser) and detecting the resulting second harmonic signal. An example of a measured phase matching curve of one ridge waveguide is presented in Fig.2. For different mode combinations, the phase matching condition is fulfilled at different pump wavelengths. The resulting intensity distribution of the second harmonic mode is displayed as insets presenting the fundamental mode in Fig. 2 (b) and a second order mode in Fig.2 (a). To determine the conversion efficiency, the power of the transmitted pump laser P_p and the power of the second harmonic signal P_{SH} is measured with a power meter for the excitation of the fundamental mode (Fig.2 (b)). We achieve a conversion efficiency of $\eta = 9.44\ \frac{\%}{\mathrm{W\ cm^2}}$.

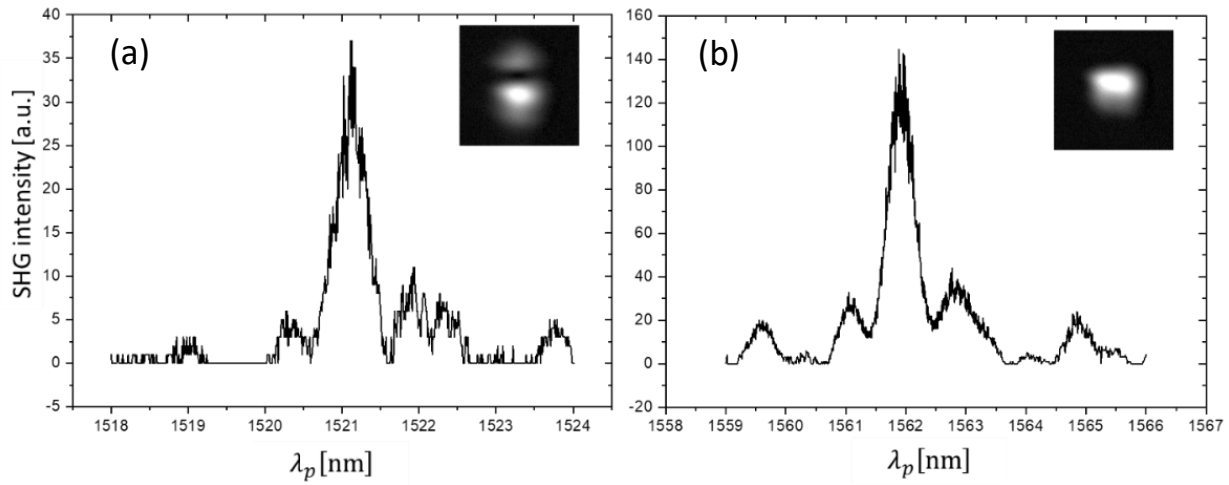


Fig. 2. Phase-matching curves of one waveguide for two different wavelength ranges. The wavelength of the pump laser λ_p is tuned and the intensity of the second harmonic generation (SHG) process measured. The associated second harmonic mode intensity distributions are presented in the insets as black and white images. The intensity distributions were measured with a CCD camera.

As conventional Ti-indiffused strip waveguides in $LiNbO_3$ are prone to photorefractive damage at high optical intensities, we investigated the optical power threshold at which the photorefractive effect occurs. We measured the power of the second harmonic signal P_{SH} in relation to the in-coupled pump power P_{coup}. These powers are

expected to have a quadratic dependency [1]. Strong photorefraction leads to stochastically fluctuating a refractive indices and, thus, prevent a homogeneous phase-matching along the interaction length. The measured second harmonic power in dependence of the in-coupled pump power is presented in Fig.3. The measurements were performed at room temperature without temperature stabilization of the sample. The quadratic dependency is visible up until a pump power of around 500 mW. This is where the photorefractive effect appears. In comparison, the photorefractive effect occurs already at a power of $P_p \approx 14$ mW in a Ti-indiffused $LiNbO_3$ strip waveguide [3].

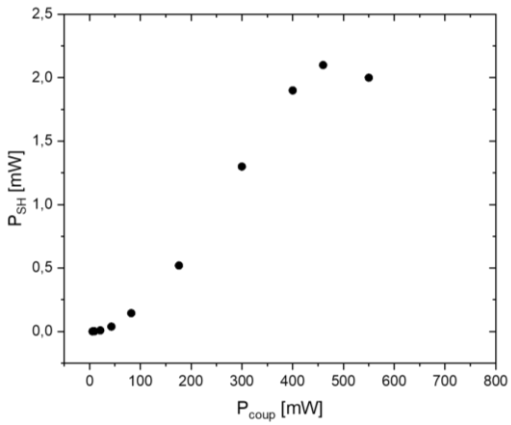


Fig. 3. Dependency of the coupled pump power P_{coup} and the resulting second harmonic power P_{SH} in the ridge waveguide measured with an optical power meter. The threshold at which the photorefractive effect occurs is at around 500 mW and indicates at the point where the quadratic dependency of the second harmonic and the pump power no longer holds.

DISCUSSION

This work presents the fabrication of ridge waveguides by precision dicing, which is a newly introduced method in our lab and had to be optimised beforehand. Considering the used fabrication method of dicing, the propagation losses of the waveguides are relatively small and comparable to similar work [4, 5]. The nonlinear characterization reveals good phase matching curves, regardless of geometry variation. For an ideal SHG process a sinc^2 shaped phase matching curve is expected. The measured phase matching curve does not correspond the ideal case but is very similar. The structural analysis of the ridge waveguide revealed a width variation of 1 µm along one ridge, which we expected to have a much greater effect on the shape of the curvature. This shows a high stability of the nonlinear interaction in this waveguide geometry. Furthermore, the waveguides have a high photorefractive damage resistance as a result of the ridge geometry. This could be due to the physical barrier of the ridge, restricting charge separation and reducing the amount of available charge carriers.

Acknowledgements: We acknowledge support by the German Federal Ministry of Education and Research (BMBF) through project QR.X (16KISQ012).

References

[1] R. W. Boyd, *Nonlinear optics,* Academic Press, London, 2020
[2] A. Hellwig, *Nonlinear Optical and Photorefractive Properties of Periodically Poled Channel Waveguides in Lithium Niobate*, Doctoral dissertation, Universitätsbibliothek Paderborn, Diss.,2011 (IST EINE DISS: WIE ZITIERE ICH DAS RICHTIG?)
[3] S. Pal, B. K. Das, and W. Sohler, *Photorefractive damage resistance in Ti: PPLN waveguides with ridge geometry*, Applied Physics B, 120, 4, pp. 737-749, 2015
[4] A. Gerthoffer, C. Guyot, W. Qiu, A. Ndao, M.-P. Bernal, and N. Courjal, *Strong reduction of propagation losses in LiNbO3 ridge waveguides*, Optical Materials, 38, pp.37-41, 2014
[5] S. Suntsov, C. E. Rüter, D. Brüske, and D. Kip, *Watt-level 775 nm SHG with 70% conversion efficiency and 97% pump depletion in annealed/reverse proton exchanged diced PPLN ridge waveguides*, Optics express, 29, 8, pp. 11386-11393, 2021
[6] R. Regener and W. Sohler, *Loss in Low-Finesse Ti:LiNbO$_3$ Optical Waveguide Resonators*, Applied Physics B, 36, 3, pp. 143-147, 1985

Monolithic CMOS sample & hold circuit for sequential control of volatile actuators in Silicon Photonics

Francesco Zanetto[1], Andres Martinez[1], Fabio Toso[1], Vittorio Grimaldi[1], Monica Crico[1], Francesco Morichetti[1], Andrea Melloni[1], Giorgio Ferrari[2], Marco Sampietro[1]

[1]Department of Electronics, Information and Bioengineering, Politecnico di Milano, p.za Leonardo da Vinci 32, Milano, Italy
[2]Department of Physics, Politecnico di Milano, p.za Leonardo da Vinci 32, Milano, Italy
* email: francesco.zanetto@polimi.it

This work presents a CMOS sample & hold circuit monolithically integrated into a Silicon Photonics chip to enable time-multiplexed control of volatile actuators. The device allows to drastically reduce the number of electrical connections needed to operate programmable photonic architectures, with no penalties in the optical performance. The approach was experimentally validated in a 10 Gbps routing scenario.

Keywords**:** *electronic-photonic co-integration, time-multiplexed control, sample & hold circuit*

INTRODUCTION

Large-scale programmable photonic circuits consist of integrated networks of elementary optical elements [1] whose working point needs to be configured and stabilized to program the overall photonic functionality. A real-time active control layer, currently implemented by electronic feedback loops through external circuitry connected to on-chip light sensors and actuators [2,3], is thus needed to ensure reliable optical operations. Although effective, the scaling of this approach is limited by the number of required electrical input/output (I/O) connections, that approaches a prohibitive level in large-scale architectures [4].

The use of time-multiplexed control signals is a promising solution to overcome the I/O bottleneck but it requires to integrate electronic functionalities on the photonic chip. To this aim, a monolithic multiplexer for sequential readout of light monitors has been already demonstrated, designed in a conventional 220 nm silicon photonics platform with no changes to the standard fabrication process [5]. However, to obtain a relevant reduction of the number of electrical I/Os, the approach needs to be extended also to the actuators. Here, we present on-chip integration of a CMOS sample & hold circuit enabling time-multiplexed operations of volatile actuators. The device is used to sequentially control the elementary building blocks of a programmable photonic circuit with no penalties in the optical performance, as demonstrated by error-free transmission of a 10-Gbps modulated signal.

SAMPLE & HOLD DESIGN AND INTEGRATION

The use of time-multiplexed signals to drive the actuators on a photonic chip is made difficult by the fact that the most common phase shifters, like heaters, MEMS or piezoelectric devices, are volatile, i.e. they require a continuous bias for their operation. A simple on-chip demultiplexer (DEMUX) is thus not enough to enable sequential control, since each actuator would be active only when specifically addressed. To keep the bias condition of the unselected devices stable, an electronic memory needs to be integrated on the photonic chip together with the DEMUX, effectively implementing a sample & hold (S&H) circuit.

We have integrated the S&H in a commercial Silicon Photonics foundry (AMF, Singapore), by employing non-standard transistors fabricated without changing the standard production process [5]. A schematic view of the MOSFET and its characteristic curve are reported in Figure 1a and 1b. The transistor is used to design both the S&H and the driver that provides the required current to the actuators (heaters in this demonstration) (Figure 1c). Considering that heaters require several mA of current to achieve a phase shift of more than 2π, the driver has been made by using 700 nMOSFETs in parallel, connected in source follower configuration to obtain a linear relation between gate voltage and current. The memory functionality is instead provided by the sample & hold (S&H) architecture connected to the driver gate. The S&H is made by exploiting the switches of a DEMUX and a bank of memory capacitors. When the switches are closed, the input charges the memory capacitors and defines the heaters current. When the switches are opened, the memory capacitors keep the gate voltages and thus the heaters current constant, maintaining the working conditions of the photonic devices. The maximum hold time, related to the leakage current of the switches and to the memory capacitance, is around one second in our prototype.

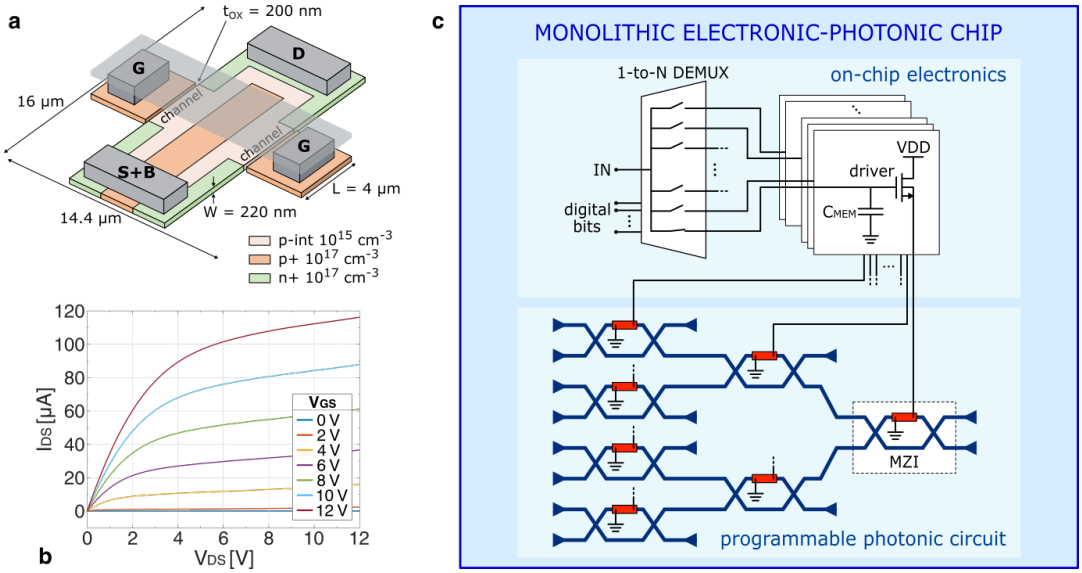


Fig. 1. a) 3D view and b) characteristic curve of the designed MOSFET in Silicon Photonics. c) Schematic view of the S&H circuit for time-multiplexed driving of integrated actuators.

ELECTRICAL AND OPTICAL CHARACTERIZATION

A top-view photograph of the fabricated circuit integrating a power MOSFET and a S&H is shown in Figure 2a. The integrated driver is used to control the phase shift in one arm of a balanced Mach-Zehnder interferometer (MZI), used as the elementary building block of a programmable photonic architecture (Figure 1c). Figure 2b shows that a current of up to 11 mA (blue curve) can be delivered by the driver when a supply of 12 V is used. This translates into a phase shift of around 3π in the thermally tuned waveguide, as confirmed by the voltage-dependent transmission of the MZI (red curve). Figure 2c shows the operation of the S&H circuit. The DEMUX bit command and the input voltage V_{IN} are controlled with two square waves at 10 kHz and 20 kHz, respectively. As expected, the input voltage causes variations of the heater current only when the S&H switch is closed (switch ON). Instead, when the switch is OFF, the current is kept constant by the memory capacitor and it is not affected by the input. The response time of the driver (around 300 ns) is much faster than the actuator thermal time constant (around 10 µs), confirming that the electronic circuit does not limit the functionality of the photonic device.

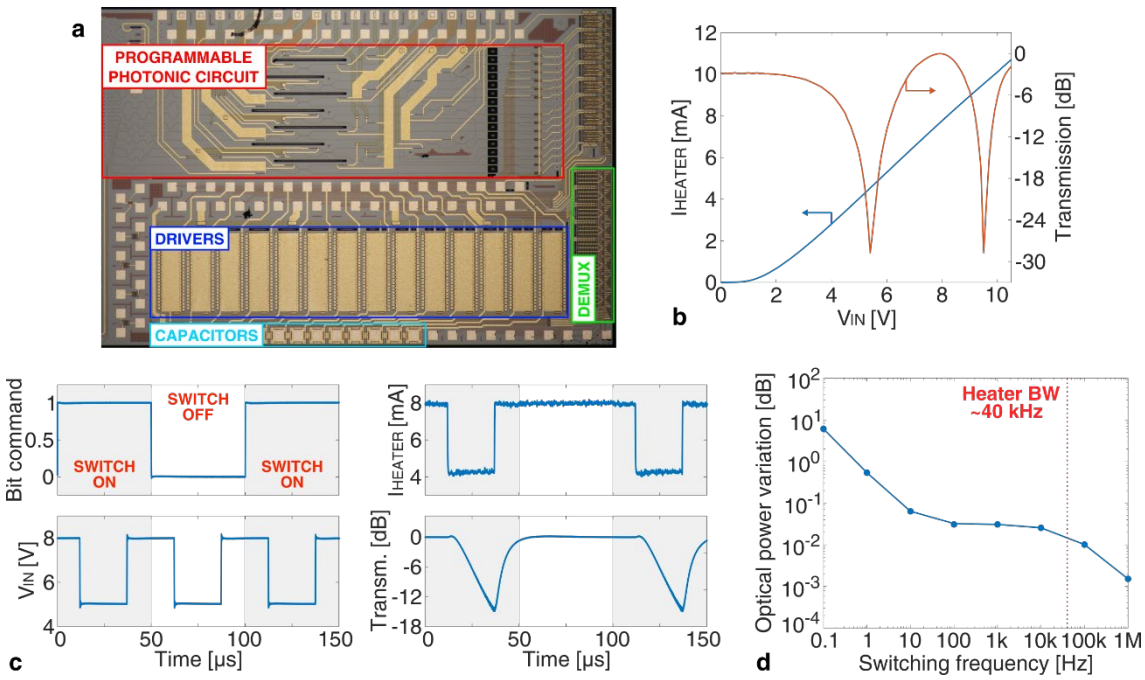


Fig. 2. a) Microscope photograph of the fabricated chip. b) Heater current and MZI transmission as a function of the S&H voltage. c) Measured heater current and MZI transmission as a function of the driver gate voltage and bit command. e) Variation of optical power at the output of a MZI operated in cross condition, as a function of the switching frequency.

The discharge time of the S&H has been investigated to verify the possibility of implementing an on-chip electronic memory for volatile thermal actuators. To this end, the driver voltage has been set to 5.5 V to bias the MZI at the minimum transmission point (-26 dB, Figure 2b) and the DEMUX bit command has been driven with a square wave of variable frequency. The change of optical power at the MZI output due to the S&H discharge is shown in Figure 2d. When the S&H is operated with a switching frequency above 100 Hz a negligible degradation of 0.03 dB is measured, demonstrating that the driver can maintain the heater current constant. The residual error is due to charge injection effects, that modify the stored voltage when the switch is opened. Since the DEMUX configuration can be updated in around 500 ns, it is possible to estimate that up to 20000 actuators can be time-multiplexed without penalties in the optical performance.

DEMONSTRATION OF 10G TRANSMISSION AND ROUTING

The impact of the discharge of the S&H driver on the quality of optical signals transmitted through MZI switches has also been investigated. To this aim, the portion of the photonic circuit shown in the inset of Figure 3a has been considered, where two optical signals modulated at 10 Gbps on-off keying (OOK) are injected at two input ports. The reference and the interference signals share the same wavelength of 1550 nm and have a power of -4 dBm and -8 dBm respectively. The impact of the interference signal is critically dependent on the working point of the first MZI, which is set and maintained by the S&H driver. Figure 3b shows the bit-error-rate (BER) measured at the reference signal output, for different values of the S&H switching frequency. The working point of the MZI is kept stable for refresh frequencies above few Hz, resulting in a BER that approaches the value of 10^{-11}, measured when the interference is switched off. A degradation of the BER instead occurs at low frequency because the S&H discharge induces a drift of the MZI bias point and a consequent lower suppression of the interference signal. Figura 3c shows the eye diagrams that are observed when the suppression of interference signal is minimum (max interference) and where the S&H switching frequency is set to 0.1 Hz and 10 Hz respectively, the latter providing a suppression of more than 20 dB (see Figure 2d).

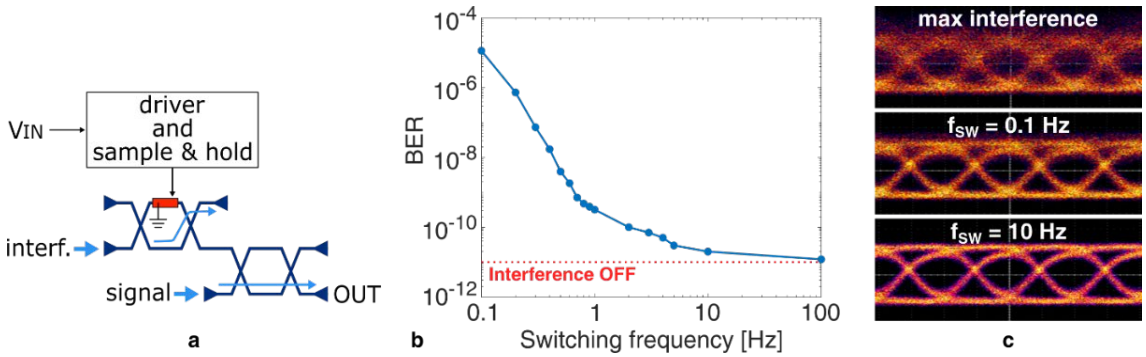


Fig. 3. a) Schematic view of the optical structure controlled with the S&H. b) BER measurement as a function of the switching frequency and c) output eye diagrams, certifying no optical penalties when S&H is operated at a refresh rate above 10 Hz.

CONCLUSIONS

We demonstrated the possibility of controlling silicon photonic circuits by time-multiplexing the electrical signals needed to drive the integrated actuators. Thanks to the integration of a CMOS S&H circuit, the working point of multiple thermal actuators can be sequentially set and hold, allowing a drastic reduction of the number of electrical I/Os. Notably, this functionality can be straightforwardly applied to generic volatile actuators, including electrooptic, ferroelectric, piezoelectric or liquid crystal phase shifters integrated in silicon waveguides.

Acknowledgements: part of the work was done at PoliFab, the nanofabrication facility of Politecnico di Milano.

References

[1] W. Bogaerts et al., *Programmable photonic circuits*, Nature, vol. 586, no. 7828, pp. 207-216, 2020.
[2] K. Padmaraju et al., *Resolving the thermal challenges for silicon microring resonator devices*, Nanophotonics, vol. 3, no. 4-5, pp. 269-281, 2014
[3] M. Milanizadeh et al., *Control and Calibration Recipes for Photonic Integrated Circuits*, IEEE Journal of Selected Topics in Quantum Electronics, vol. 26, no. 5, pp. 1-10, 2020.
[4] A. Ribeiro et al., *Column-row addressing of thermo-optic phase shifters for controlling large silicon photonic circuits*, IEEE Journal of Selected Topics in Quantum Electronics, vol. 26, no. 5, pp. 1-8, 2020.
[5] F. Zanetto et al., *Zero-Change Monolithic Integration of CMOS Electronics in Silicon Photonics*, preprint available at Research Square, doi: https://doi.org/10.21203/rs.3.rs-1451155/v1, 2022.

Suspended Gallium Arsenide Electro-Optic Racetrack Ring Modulator

Student paper

Haoyang Li, Robert Thomas and Krishna Coimbatore Balram*

Quantum Engineering Technology Labs and Department of Electrical and Electronic Engineering, University of Bristol, Woodland Road, Bristol BS8 1UB, United Kingdom
*krishna.coimbatorebalram@bristol.ac.uk

We present the design, fabrication and characterization of electro-optic racetrack ring modulator on suspended gallium-arsenide (GaAs) platform. This is the first demonstration of active devices fabricated on suspended thin-film GaAs with multi-layer metallization while exhibiting desirable electro-optic performances. This work opens up the route towards dense passive and active device monolithic integration achieving optimal system performance.

Keywords**:** *Racetrack ring resonator, electro-optic modulator, gallium arsenide optoelectronics*

INTRODUCTION

For the past decade, the silicon photonic integrated circuits (PICs) have revolutionized the scale, complexity and performance of photonic devices and optical communication. Nevertheless, due to the lack of desirable optical properties, silicon photonics proves a severe limitation to achieving system performance. These limitations include an absence of direct bandgap and $\chi^{(2)}$ nonlinearity to build fast optoelectronic devices, and the lack of zero piezoelectric response to build acousto-optic devices.[1] This forces silicon photonics to resort with other traditional optical material like III-V and ferroelectric materials, and will suffer coupling loss during the energy transfer between different material systems.

While efforts have been made on bringing III-V materials to silicon photonics by hybrid integration, there has been relatively little effort on improving the existing III-V PIC platform by applying ideas from silicon photonics manufacturing. In particular, gallium arsenide has always been the material of choice for high-speed devices for its high electron mobility and the availability of low-loss semi-insulating substrate.[2] GaAs possesses all the desirable optical properties that silicon lacks: a direct bandgap, a $\chi^{(2)}$ nonlinearity, and a piezoelectric coefficient which activates mutual links among microwave, acoustic and optical domain. The refractive index of GaAs is close to silicon at λ = 1.55μm, making it easy to transfer a variety of optimised photonic designs and fabrication process flows between the platforms. In contrast to other electro-optic materials like lithium niobate, it has a high refractive index allowing compact component design at small footprint to achieving system performance. GaAs also provides a natural route towards incorporating active gain media like quantum dots and wells in favour of monolithic integration in both classical and quantum photonics. Traditionally integrated photonics in GaAs suffers from the low index contrast achievable between GaAs and the AlGaAs buffers which serve as waveguide cladding layers. The low index contrast leads to large mode sizes and bend radii which make photonic integration challenging.[3]

In this work, we bring the idea from silicon photonics and silicon microelectromechanical systems (MEMS) foundry to build high-performance electrical-optic modulators (EOM) on the suspended GaAs platform. This platform, by releasing the thin-film GaAs on low-index media of air, generates a large index contrast to tightly confine optical mode in waveguides. The reduced optical mode size enables us to build compact structures without incurring extra scattering losses. Our suspended EOM demonstrates that active devices requiring multi-layer metallization can be built on suspended GaAs platform. Exhibiting desirable electro-optic performance, the racetrack ring EOM from high yield (>90%) cleanroom fabrication has shown as a strong proof of principle. The tight optical confinement also enables a reduced electrode separation and higher effective electric fields resulting in a lower half-wave (V_π) voltage (required for achieving π phase shifts). This work opens up route towards dense monolithic integration up to wafer scale, and underpins a variety of III-V experiments ranging from quantum photonics to cryogenic photonics for satellite communication.

RESULTS

The racetrack design for EOM is chosen mainly for the ease proof of principle, since the resonator is environment-sensitive, and is susceptible to change induced by EO modulation. The geometry of the suspended GaAs racetrack ring EOM is shown as Fig. 1(a) in an angled view (silicon dioxide cladding unshown). The modulator consists of a pair of surface grating couplers (blue) as optical input and output, a 385-um-long optical racetrack resonator with point coupling design to bus waveguide (pink), and microwave electrodes (gold) to deliver electrical signals. The device has three electrical connections for a ground-signal-ground (GSG) configuration, with two ground electrodes seated on the n-doped substrate and a signal electrode above the racetrack expect for coupler region. A not-to-scale view of

waveguide cross section in Fig. 1(b) shows the relative position of electrodes to the waveguides. When a voltage is applied across the signal and ground electrodes, a vertical electric field (black arrow) is induced predominantly in the vertical direction overlapping with the TE polarized optical mode (color scale) due to the Pockels effect. When the ring is near resonance and the coupled portion of light oscillates inside the cavity, this overlap transforms the optical phase (frequency) of propagating light and change into intensity modulation that can be detected from the output.

The fabrication of the suspended EOM begins with a 340-nm (001)-oriented GaAs epitaxial layer. Fig. 1(c) shows the optical micrograph of a fabricated suspended racetrack EOM. The devices are fabricated first by structuring optical components and tethers by Electron-Beam Lithography. All structures are then suspended by surrounding tethers and a selective wet etch through etch holes to remove the underlying $Al_{0.65}Ga_{0.35}As$ layer. A 2.6-um-thick silicon dioxide (SiO_2) cladding is then deposited over the device to separate the electrode from the waveguide to reduce metal absorption losses. In addition, SiO_2 improves the rigidity of the suspended structures by pinning them at the corners of the etch holes. This has been proven to survive even in high-power ultrasonic bath, thus the suspended structure can bear the load of heavy electrodes. To make sure a sufficient delivery of electrical signal, we use wire-bonding to connect the devices with outer signal source, as shown in the camera view in Fig. 1(d).

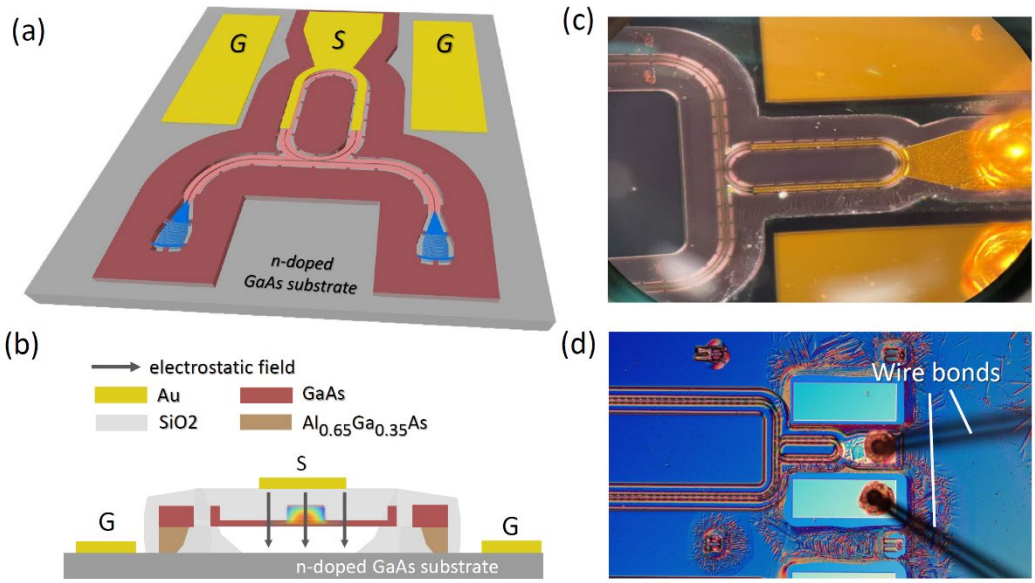


Fig. 1 Device geometry of suspended GaAs electro-optic modulator in (a) angled 3D view and (b) cross-sectional view. (c) The device dark-field images and (d) the top-camera view showing devices driven via wire bonds

Fig. 2(a) shows the optical spectrum and its Lorentzian fit of one resonant mode around 1550nm. The loaded quality factor (Q) of the resonator is 98,000 and the extinction ratio is 3dB. It is determined that the resonator works at the under-coupled regime (where intrinsic propagation attenuation is greater than coupling coefficient). The obtained intrinsic Q is 113,000 corresponding to a linear propagation loss of ~6dB/cm, which is still far from the optimal loss in thin-film GaAs waveguide (~1dB/cm), but can be further reduced by improving fabrication quality.

To determine the EO performance of the modulator, an RF signal with peak-to-peak voltage ($V_{P\text{-}P}$) of 5V is used to drive the modulator. The intensity-modulated output is detected by high-speed photodetector (PD) and then fed to the lock-in amplifier as measured modulation amplitude. The pump laser is scanned across the optical resonance and the EO modulation is measured as a function of wavelength, as shown in Fig. 2(a) (dark blue). We can extract the modulation index, β, the relative phase shift induced by EO modulation, which is defined as:

$$\beta = \frac{1}{2}\frac{\Delta\lambda}{FWHM} \tag{1}$$

where $\Delta\lambda$ is the full wavelength swing under the applied signal amplitude and FWHM is the linewidth of the optical resonance. The theoretical small-signal analysis model [5-6] gives us the fit of $\beta \approx 0.07$ at 2MHz. Backed out from β, a modulator V_π of ~ 70V is obtained, which indicates a relatively small modulation efficiency for our first EO devices. Nevertheless, V_π can be further improved by reducing the gap between the electrode and the waveguides. The large index contrast of waveguide provides the feasibility to make the devices on a more compact level while preserving a low optical loss. Besides, improving the SiO_2 deposition quality also a larger portion of effective electric field overlapping with optical waveguide. Besides, V_π can be reduced by pulling the design near to the critical coupling regime to achieve as high Q as possible. Taken all into account, the V_π can be optimized down to sub-10V at our current device dimension of sub-millimeter.

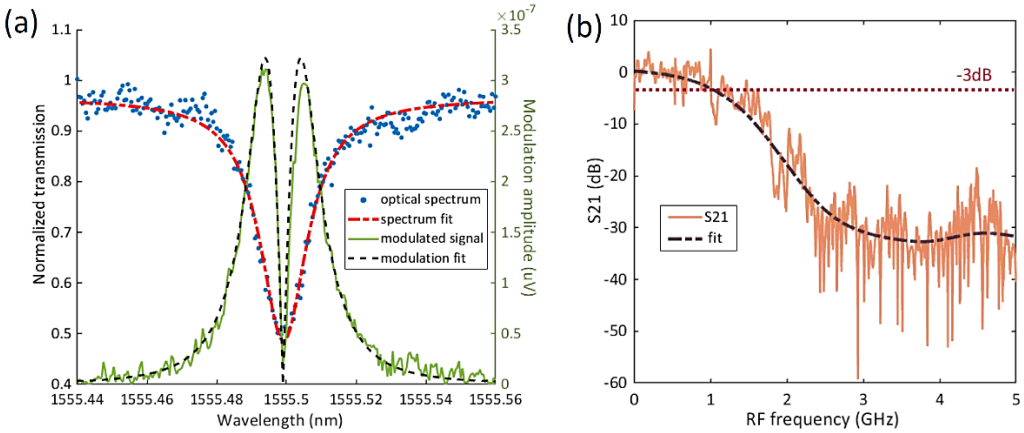


Fig. 2 (a) Experimental data and theoretical fit for optical spectrum, and EO modulation as a function of wavelength. (b) EO bandwidth of the modulator working at linear point (maximum EO modulation point)

The modulation bandwidth is measured by setting the pump wavelength at the maximum slope point, or linear point, of the optical resonance, where the maximum EO modulation is achieved. The modulator is driven at 0V DC bias with a small signal from vector network analyzer (VNA) swept from 1MHz to 6GHz, which shows a 3dB bandwidth of 1GHz. (Fig. 2(b)) One key limiting factor of the measured bandwidth is the wire bonds that used for source connection. The actual EO bandwidth can be out by de-embedding the peripherals. On the other hand, trade-off between optical quality factor and RF bandwidth exists. A low Q leads to a high bandwidth but a poor modulation efficiency.[7] The device design needs to be tailored to balance the typical trade-off relation between modulation efficiency and bandwidth and keep both at desirable levels for various application scenarios.

DISCUSSION

We've demonstrated the device geometry and fabrication process of suspended GaAs electro-optic racetrack ring modulators, which possesses high yield and desirable EO performances. The rigidity of the suspended platform provides feasibility for fabricating electro-optic devices with multi-layer metallization. In the recent future, the high index suspended platform enables a more compact device design and the V_π of the EOM will be significantly reduced to sub-10V with small footprints. Furthermore, we will extend this platform towards monolithic integration incorporating active gain media for making laser and photodetector. This will be revolutionary for device applications in wide-ranging areas from cryogenic photonics and quantum computing to satellite communication.

Acknowledgements: We would like to acknowledge funding support from the Engineering and Physical Sciences Research Council (EP/V052179/1).

References

[1] P. Jiang and K. C. Balram, *Suspended gallium arsenide platform for building large scale photonic integrated circuits: passive devices,* Opt. Express, vol. 28, no. 8, p. 12262, 2020.

[2] A. Chen, E. J. Murphy, and N. Hy, *BROADBAND OPTICAL MODULATORS: Science, Technology, and Applications*, CRC Press, Boca Raton, 2012.

[3] C. P. Dietrich et al., *GaAs integrated quantum photonics: Towards compact and multi-functional quantum photonic integrated circuits*, Laser Photon Rev, vol. 10, no. 6, pp. 870–894, 2016

[4] A. Khurana, P. Jiang, and K. C. Balram, *Piezo-Optomechanical Signal Transduction Using Lamb-Wave Supermodes in a Suspended Gallium Arsenide Photonic-Integrated-Circuit Platform*, Phys. Rev. Appl., vol. 18, no. 5, p. 054030, 2022.

[5] B. Pile et al., *Small-signal analysis of microring resonator modulators*, Opt. Express, vol. 22, no. 12, p. 14913, 2014.

[6] S. Valle and K. C. Balram, *High-frequency, resonant acousto-optic modulators fabricated in a MEMS foundry platform*, Opt. Lett., vol. 44, no. 15, p. 3777, 2019.

[7] Y. Hao et al., *Trade-off between optical modulation amplitude and modulation bandwidth of silicon micro-ring modulators*, Opt. Express, vol. 22, no. 12, pp. 15178–15189, 2014.

Phase modulation in a Compact 8-channel Loop-back AWG based Integrated Comb Processor

Student paper

Louw Roel van der Zon[1*], Luis A. Bru[1], Pascual Muñoz[1], Daniel Pastor[1]

[1]Universitat Politècnica de València, Cami Vera s/n, València, 46022, Spain
[*] roel.vanderzon@upv.es

For the realization of integrated microcomb-based systems, integrated photonic interposers that connect, operate, and process the optical signals that transit between the many photonic components are needed. In this work, the phase modulation characteristics of an 8-channel integrated comb source spectral processor based on an arrayed-waveguide grating are presented. The phase response of the device is characterized using optical frequency domain interferometry.

***Keywords*:** Microresonator frequency comb, comb processor, silicon nitride, phase modulation, optical frequency domain interferometry

INTRODUCTION

Optical microcombs, generated in micro and nanophotonic resonators, have substantially broadened the reach of applications of optical frequency combs [1]. A variety of applications have been shown to benefit from the use of microcombs [2],[3]. Integrated microcomb-based systems need optical interposer that connect, operate, and process the optical signals [4]. Soliton microcombs can be used in radio frequency (RF) arbitrary waveform generation, which has an ultrahigh analog bandwidth as major advantage. Such a system can be implemented as a photonic integrated circuit [5], where an integrated optical waveshaper, or spectral processor, is used to modulate the amplitude and phase of a soliton microcomb.

In this work, an optical interposer as a spectral processor is presented: an 8-channel loop-back AWG based integrated comb processor (ICP), designed to modulate both amplitude and phase of separated comb lines. The device was introduced in [6], where its amplitude modulation was shown. Here, we present a characterization of the phase modulation of the device using optical frequency domain interferometry (OFDI). Different strategies to characterize the phase response of the ICP may be adopted: firstly, an interferometer with the device under test (DUT) and a delay line can be analyzed using a broadband source and an optical spectral analyzer (OSA). Here, the OSA resolution is a limiting factor and the path length difference (PLD) should be chosen accordingly. On chip a balanced Mach-Zehnder interferometer (MZI) could be created. The balanced MZI can then be used to characterize the ICP phase response by analyzing the amplitude response of this MZI. OFDI, a swept-wavelength technique, allows for the characterization of photonic devices with very high resolution, which makes it suitable for integrated devices. The optical amplitude and phase response of the DUT can be assessed in both the time and the spectral domains [8]. Therefore, as demonstrated in [7] and [8], the technique can be adapted to retrieve the phase characteristics of the ICP.

DESIGN AND MEASUREMENTS

The ICP consists of a 9-channel AWG in loop-back configuration, in 8 the arms of the loop-back symmetrical MZIs are placed, which leaves the 9th channel for the in- and output of the signal. The floorplan of the ICP is shown in Fig. 1 (b). The first sidelobe of the AWG's channels are suppressed 22 dB. Each channel can be modulated in both amplitude and phase employing thermal phase shifters on both MZI arms. The MZIs, tested separately, show a 37 dB extinction ratio when a 37 mA current is applied to one of the heaters, this results in a spectral processor with an amplitude modulation reaching a suppression ratio of up to 22 dB. The chip is characterized by vertically coupling light using grating couplers. The design and amplitude modulation has been demonstrated in [6]. The graph in Fig. 1 (a) shows the transmission of the spectral processor, the peak around 1553 nm is the input channel, which is not controllable in the loop-back. Left to this peak there are 8 channels, controllable in amplitude and phase. The response of the AWG isn't flat and the loop-back configuration doubles that. The response is also slanted due to using the side input of the AWG. The device has been fabricated in a Si_3N_4 platform with SiO_2 substrate and SiO_2 cladding at Myfab Chalmers. The substrate is thermally oxidized silicon. The thermal oxide thickness is 3 µm with a refractive index of 1.4431 at 1550nm, the LPCVD Si_3N_4 is 200nm thick and has a refractive index of 1.99. The top cladding is fabricated as first a layer of 1 µm of LPCVD SiO_2 with a refractive index of 1.4439. On top is a 2 µm of

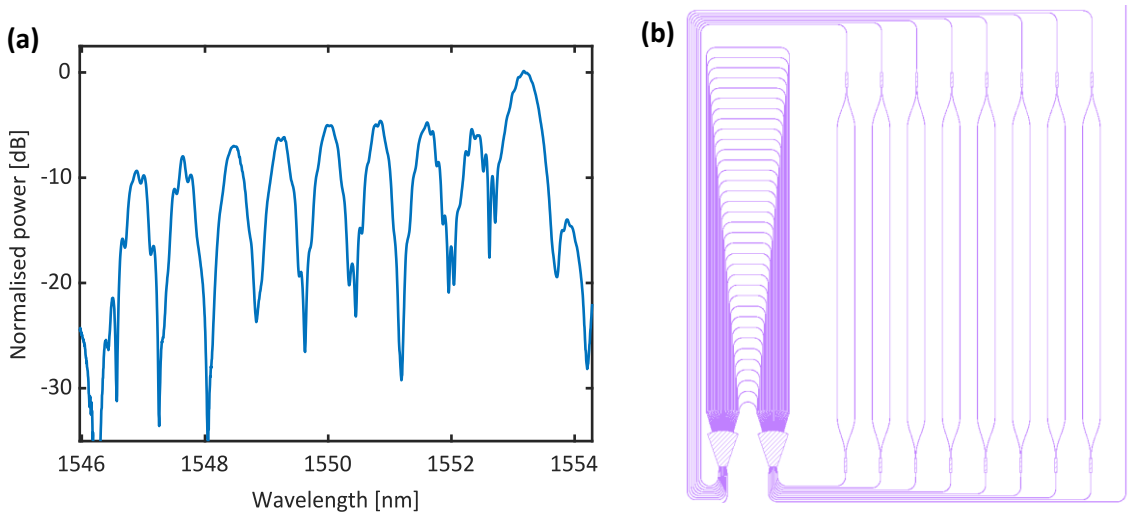


Fig. 1. (a) The transmission response of the spectral processor, the response of the grating coupler has been substracted to show the response of only the processor. From left to right the 8 controllable channels are visible, the highest, 9th peak is the AWG channel used for guiding the light in and out of the loop-back onfiguration. (b) The floorplan of the spectral processor. The total device measures 2.4 mm by 2.7 mm.

PECVD SiO_2 with refractive index 1.4595. The structures are defined via electron-beam lithography using a 500 x 500 µm2 square writing field and are deep etched [6]. The fabrication of the Si_3N_4 structures follows the procedure described in [9].

For modulating the phase in one of the ICP channels, an equal current is applied to the heaters on both arms of the MZIs that are implemented in the loop-back layout. This will induce an equal phase shift in both arms so that after combining the two signals the amplitude remains unchanged. The heaters have a resistivity of 215 Ω each, the amplitude response of the MZI shows the phase tuners reach a π phase shift when a 37 mA current is applied, resulting in a 294 mW power consumption per for a π phase shift.

Although the measured crosstalk in amplitude for the MZIs is negligible, any temperature difference can cause a phase error in the loop-back channels or AWG. For this reason, the phase modulation tests are set up in a way that the same total power is applied to the chip. While in succeeding tests the applied current in one channel is rising till 37 mA, the other channels applied current is lowered in value. In these conditions, two different experiments, A and B, are carried out, by doing increasing / decreasing phase modulation on channels 1 and 4 in case A, and 4 and 8, in B, respectively. Each experiment is divided into 4 tuning steps or iterations, where measurements are performed, sweeping values in the {0,37} mA range. The chip is wirebonded on a PCB, which is placed on a heatsink that is temperature controlled by a Peltier.

In the OFDI setup, the DUT is placed in an optical fiber MZI with a given PLD. A tunable laser wavelength sweep of 100 nm span around $\lambda = 1550$ nm is performed, giving an interference pattern that is photodetected and transformed to digital data. The resulting DUT interferogram is properly linearized in frequency by using a secondary MZI with higher PLD, a common strategy in OFDI.

RESULTS

In Fig. 2 (a), it is shown the obtained interferogram for the first iteration of experiment A. The interferogram is pass filtered to a single central band (shown in blue), where the ICP channels are found. Then, inverse fast Fourier transform (FFT) is applied to obtain the time domain response. The resulting trace in amplitude is shown below, zoomed to the region of interest. The broadened peak at the left corresponds to the remaining direct AWG contribution, while the ICP channels contributions, each of them convolved with the AWG response correspondingly, are superimposed in the second (highlighted in orange) group at the right, where their center positions are indicated with dashed lines. The next processing step consists of applying a window filter to isolate the ICP contributions, and then conduct a trace crop to re-center the trace, individually, to the positions of the channel centers. Under these conditions, ideally, the corresponding spectral phase response plateaus along the corresponding frequency region of the channel. Hence, we proceed accordingly and, once the re-centered traces are available for each of the 8 channels, FFT algorithm is systematically applied to reconstruct the corresponding spectra, obtaining amplitude and phase traces as shown in Fig. 2 (a) for channel 4. As expected, the phase curve, although somewhat affected by adjacent channels, is fairly steady in the region of the channel band. The spectral

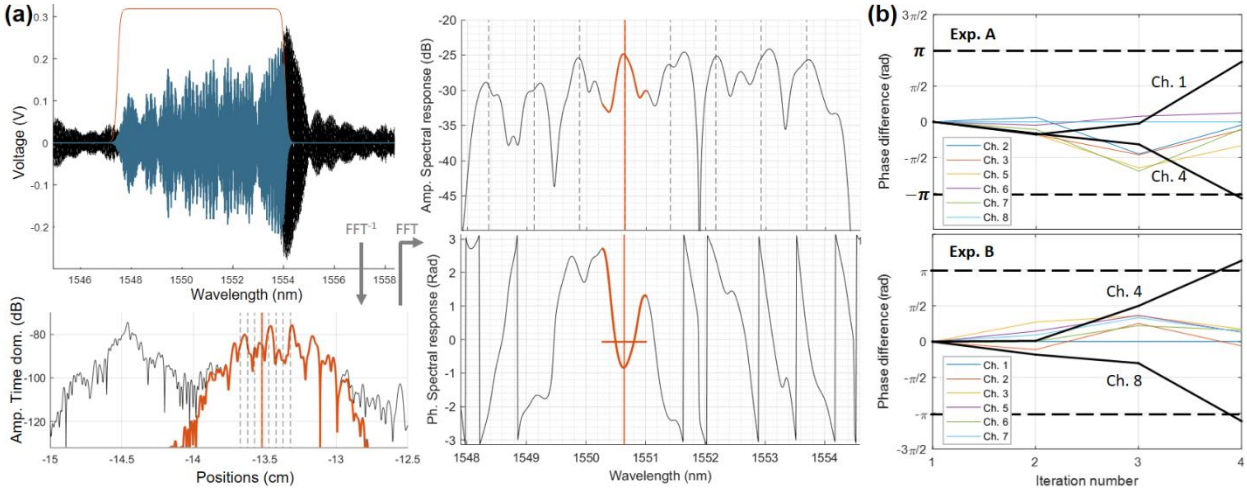


Fig. 2. (a) OFDI processing including DUT interferogram, time domain response, and amplitud and phase spectral response reconstructed from individual channel re-centering process. (b) Phase differences for the two performed experiments.

amplitude is also shown above, where just the 8 ICP channels are visible, having disappeared the direct AWG contribution after its complete removal in the time domain picture. Phase is then assessed in the region of the channel for each case. While these values lack of physical meaning separately, and vary from one measurement take to another in OFDI [8], it does a relative evaluation of them and, accordingly, we calculate the phase differences between each channel and the outer channel, i.e. channel 8 and 1 for experiments A and B, respectively. Since iteration 1 corresponds to the origin of heater tuning, we set this phase difference to zero, as reference, and compute the evolution of this quantity along the electrical tuning iterations. The results for both experiments are shown in Fig. 2 (b) where, as expected, the corresponding traces for the tuned channels (in bold black curves) evolve from 0 to, roughly but clearly, $\pm\pi$, while the unperturbed channels (shown in different colors) maintain a steadier evolution, not exempt from a certain degree of variation.

DISCUSSION

The comb processor presented in [6] has been characterized for its phase modulation capabilities using the OFDI technique as described in [8]. The experimental results show the phase modulation evolution along the tuning in both experiments, and demonstrates the correct functioning of the ICP device. However, some thermal crosstalk between the arms of the loop-back structure, together with channel optical crosstalk originated in the AWG, leads to the slight variation of phase observed for the unperturbed channels. Therefore, the device performance may be improved in future designs by adopting thermal crosstalk reduction strategies, e.g. air trenches to thermally isolate tuner regions, reducing the length of the arms, and also by refinements in the design of the AWG. The ICP could be used as an optical interposer and opens a viable path for on chip RF arbitrary waveform generation. A common Si_3N_4 thickness for broadband comb sources is 790nm, for comb generation and modulation on the same chip, this difference in thickness can be overcome with use of photonic interposers [4].

References

[1] Cundiff, S. T. & Ye, J. Colloquium: femtosecond optical frequency combs. Rev. Mod. Phys. 75, 325–342 (2003).

[2] Kippenberg, T. J. et al. *Dissipative Kerr solitons in optical microresonators*. Science 361, eaan8083 (2018).

[3] Gaeta, A. L., Lipson, M. & Kippenberg, T. J. *Photonic-chip-based frequency combs.* Nat. Photonics 13, 158–169 (2019).

[4] A. Rao, G. Moille, X Lu, Daron A. Westly, Davi de Sacchett, Michael Geiselmann, Michael Zervas, Scott B. Papp, John Bowers, and Kartik Srinivasan.,*Towards integrated photonic interposers for processing octavespanning microresonator frequency combs.* Light Sci Appl 10 109 (2021).

[5] Beichen Wang, Zijiao Yang, Shuman Sun, and Xu Yi, *Radio-frequency line-by-line Fourier synthesis based on optical soliton microcombs*, Photon. Res. 10, 932-938 (2022)

[6] L.R. van der Zon, P. Muñoz, D. Pastor, M. Girardi, V. Torres-Company, *Compact 8-channel Loop-back AWG based Integrated Comb Processor,* in Proceedings of the Conference 2021 IEEE 17th International Conference on Group IV Photonics (GFP), 2021.

[7] K. Twayana, Z. Ye, Ó. B. Helgason, K. Vijayan, M. Karlsson, V. Torres-Company, *Frequency-comb-calibrated swept-wavelength interferometry,* Optics Express, Vol. 29, 15/19 July 2021.

[8] L.A. Bru, *Optical Frequency Domain Interferometry for the characterization and development of complex and tunable photonic integrated circuits*, PhD thesis, Universitat Politècnica de València, 2022.

[9] Xiaonan Hu, Marcello Girardi, Zhichao Ye, Pascual Muñoz, Anders Larsson, and Victor Torres-Company, *"Si_3N_4 photonic integration platform at 1 μm for optical interconnects,"* Opt. Express 28, 13019-13031 (2020)

1 GHz integrated electro-optical modulator in the 5.5-9 µm wavelength range

Student paper

Thi Hao Nhi Nguyen[1], Natnicha Koompai[1], Victor Turpaud[1], Miguel Montesinos-Ballester[1,3], Jonathan Peltier[1], Jacopo Frigerio[2], Andrea Ballabio[2], Jean-René Coudevylle[1], Cédric Villebasse[1], David Bouville[1], Carlos Alonso-Ramos[1], Laurent Vivien[1], Giovanni Isella[2], and Delphine Marris-Morini[1]

[1] Centre de Nanosciences et de Nanotechnologies, Université Paris-Saclay, CNRS, 91120 Palaiseau, France
[2] L-NESS, Dipartimento di Fisica, Politecnico di Milano, Polo di Como, Via Anzani 42, 22100 Como, Italy
[3] Current affilliation: Institute for Quantum Electronics, ETH Zurich, 8093 Zurich, Switzerland
*Author: thi-hao-nhi.nguyen@universite-paris-saclay.fr;

Abstract: An integrated mid-infrared (MIR) electro-optical modulator (EOM) is a critical device, either to improve the signal to noise ratio of the detection by synchronous detection, or for advanced sensing systems exploiting dual comb spectroscopy. In this work, the free carrier plasma dispersion effect has been exploited in a Schottky diode embedded in a graded Silicon Germanium (SiGe) photonic waveguide to demonstrate a broadband integrated modulator. The RF response of the device has been optimized to achieve high-speed operation. An integrated EOM operates at RF frequency up to 1 GHz, from 5 to 9 µm wavelengths is demonstrated. © 2023
Keywords**:** *Electro-optical modulator, silicon photonics, silicon, germanium, mid-IR wavelength,*

INTRODUCTION

Mid-infrared (mid-IR) spectroscopy is of a great importance to detect the traces related to environmental and toxic vapors. The on-chip integration of spectroscopic system is promising for the development of compact and efficient sensors. [1-3]. Integrated electro-optical modulator (EOM) operating in this wavelength range is interesting for many applications, such as sensitivity enhancement via on-chip synchronous detection or dual comb spectroscopy. Preliminary demonstration on an integrated modulator based on a silicon germanium (SiGe) graded-index platform operating in the mid-IR range was reported previously [4]. This modulator exploited free carrier concentration variations in a Schottky diode to obtain absorption coefficient variations. Here we report the optimization of the RF behavior of the device, with high speed operation demonstrated now up to 1 GHz in a broadband range of wavelengths from 5 to 9 µm [5].

RESULTS

a. Experimental results

The schematic view of the electro-optical modulator embedded in integrated-waveguide SiGe graded platform is depicted in Fig. 1a. The refractive index is linearly tuning from pure Si to pure Ge along 6 µm thick graded layer which is epitaxially grown on a highly n-doped Silicon substrate with doping concentration of 2 x 10^{19} cm^{-3}. This graded epi layer is non-intentionally doped, with a residual n-doped concentration estimated to be in the order of 10^{15}-10^{16} cm^{-3}. To achieve high speed operation, a careful design of the electrical access and of the RF electrodes is required, in order to (i) ensure that the equivalent RC product is compatible with high-speed operation, (ii) achieve impedance matching with the equipment used for the electro-optical characterization (50 ohms) to avoid high RF signal reflection and (iii) reduce the speed difference between electrical and optical signals propagating along the modulator. Grounded coplanar waveguide (CPWG) electrodes have been exploited with the width of signal line path (S) and the gap between these metallic electrodes of 4 µm and 10 µm, respectively. The waveguide width and etching depth are 6 µm and 5.5 µm, respectively. The electric field profile of the TE mode with 300 nm thin Gold layer (Au) at the wavelength of 6.4 µm is shown in Fig. 1b, showing a light confinement at the top of the waveguide. The metallic layers are deposited on backside and on the top of the waveguide, which enables to form vertically the Schottky diode. When the reversed bias voltage applied to the device, the enlargement of depletion region allows for variation of the absorption coefficient of the guided mode, and for modulation of the optical transmission. Fig. 1c shows a SEM image of the fabricated sample with grounded coplanar structure of the top electrodes.

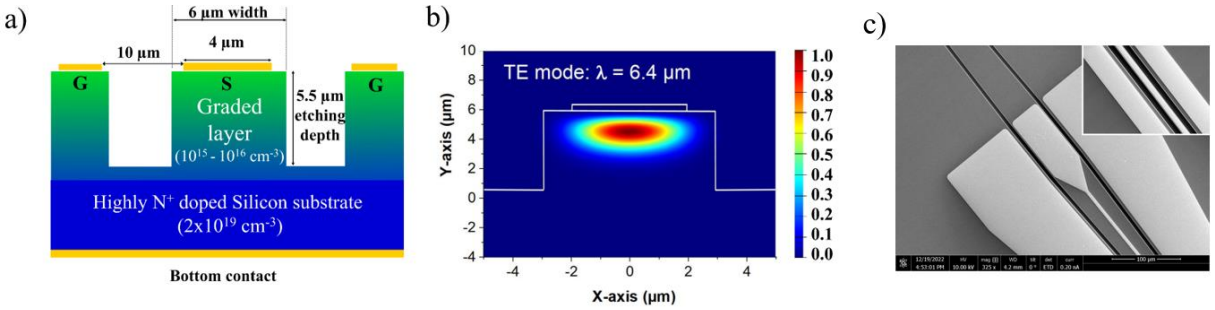


Fig. 1. (a) Schematic view of the modulator. (b) Electric field profile of the TE mode at 6.4 µm wavelength. (c) SEM picture of the fabricated device. The grounded coplanar waveguide Ground-Signal-Ground electrodes (GSG) can be seen.

Current-voltage (I-V) characterization of the modulator is reported in Fig. 2a. A good rectifying behavior is obtained, which confirms that a depletion region is formed at the top of the waveguide. From this measurement, a Schottky barrier of 0.58 eV can be extracted. On the other hand, capacitance-voltage (C-V) characterizations have been performed to investigate the evolution of the depleted region below the top contact when the reverse voltage is increased. The C-V measurement has been done on different specific square-shaped mesa fabricated on the same photonic circuit. A linear variation of the diode capacitance with respect to the device areas can be seen in Fig. 2b. As expected, the capacitance decreases when the amplitude of the reverse voltage increases which means that the depleted region is enlarged (shown in Fig. 2c).

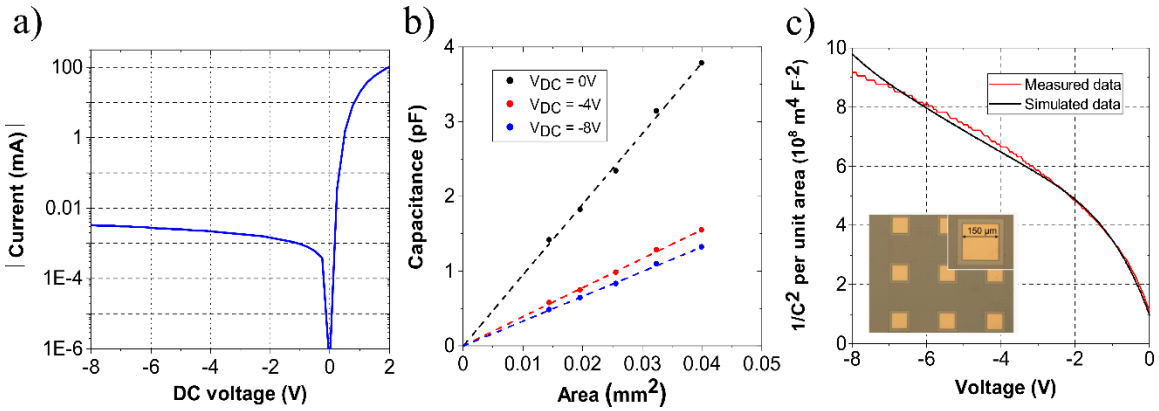


Fig. 2. Electrical characterizations of EOM device. a) IV measurement of the integrated modulator. b) Capacitance/voltage characteristics as a function of device areas with different bias applied voltages. c) Comparison between measured and the simulated results of $1/C^2$ as a function of reverse bias voltages. Inset: Microscopy image of the fabricated mesa structure.

The modulation efficiency is then characterized. The relative optical transmission which is normalized with optical transmission at zero bias applied is shown in Fig. 3a as a function of reversed bias voltages at different mid-IR wavelengths. When the reversed bias voltage increases, the overlap between the space charge region and the optical mode is higher, thus the absorption of the optical mode due to free carrier concentration decreases, which leads to a larger optical transmission. Extinction ratio higher than 1dB is obtained the wavelength of 9 µm.

Dynamic characterization has also been performed to characterize the speed of the device. To this end, the light coming out from the output of the device is sent to a fast mid-IR detector operating up to 600 MHz. An electrical spectrum analyzer is used to measure the photodetected signal as a function of the RF frequency that is applied on the electrodes. Fig. 3b shows the photodetected signal as a function of the RF frequency in depletion schemes. Optical modulation can be measured up to 1 GHz RF frequency, where a signal to noise ratio larger than 10 dB is still obtained. No sharp drop is seen even at this frequency which indicates that the modulator can probably operates at higher frequencies. However, higher frequencies are currently limited by the experimental set-up.

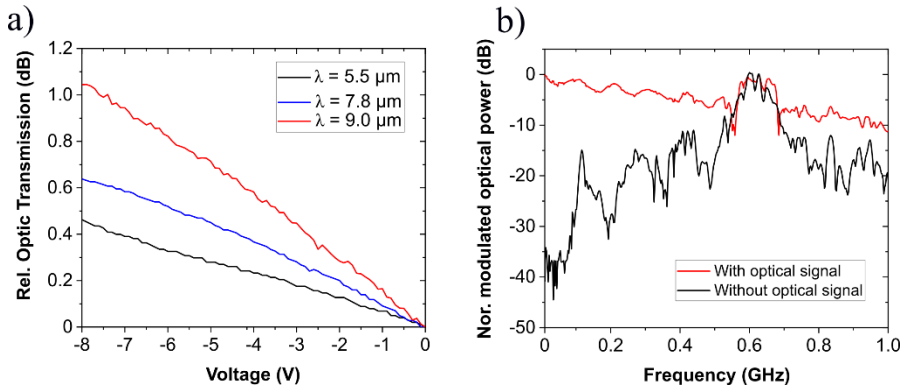


Fig. 3. Electro-optical modulator characterization (a) in DC regime: variation of the optical transmission as a function of the applied voltage. (b) in the dynamic regime: amplitude of the photodetected signal as a function of the applied voltage RF frequency.

CONCLUSION

This work focuses on an integrated electro-optical modulator based on a Schottky diode embedded in a graded SiGe optical waveguide. This modulator can operate in a wide wavelength range of the mid-IR spectrum (5 - 9 µm wavelength). Extinction ratio up to 1dB is reported, at the wavelength of 9µm. Coplanar waveguide has been optimized for high speed operation. Interestingly, the integrated electro-optical modulator shows operation up to 1GHz.

Acknowledgements

This work was supported by Light-up Project (ANR-19-CE24-0002-01). This work was partly supported by the French RENATECH network.

References

[1] G. Z. Mashanovich *et al.*, " Group IV mid-infrared photonics ", Opt. Mater.Express 8, p. 2276 (2018).
[2] H. Lin *et al.*, " Mid-infrared integrated photonics on silicon: a perspective ", Nanophotonics 7, p. 393 (2018).
[3] D. Marris-Morini *et al.*, " Germanium-based integrated photonics from near- to mid-infrared applications ", Nanophotonics 7, (2018).
[4] M. Montesinos-Ballester *et al.*, "Ge-rich graded SiGe waveguides and interferometers from 5 to 11 µm wavelength", Opt. Express 28 (9), p. 12771 (2020).

Intra-Cavity Coherently Combining of DBR Lasers on an InP Generic Foundry Platform

Rakesh Ranjan Kumar[1], Lars Nielsen[1], Nicolas Volet[1], and Martijn J. R. Heck[1,2]

[1]Department of Electrical and Computer Engineering, Aarhus University, 8200, Aarhus N, Denmark
[2]Eindhoven Hendrik Casimir Institute, Eindhoven University of Technology, 5600 MB, Eindhoven, the Netherlands
* Corresponding email: rakesh@ece.au.dk

We report an intra-cavity coherent combining of two DBR lasers with on-chip power of ~9.5 mW at the injection current of 42 mA in both gain sections simultaneously. The combined DBR laser operates in a single mode regime with a side-mode suppression ratio of 36 dB on an InP generic foundry platform.

Keywords**:** *Integrated optics, Integrated lasers, Indium Phosphide*

INTRODUCTION

Integrated semiconductor lasers are an essential component to miniaturize or scale photonic technologies [1, 2]. The maximum power of a single DBR laser is limited due to heating of the active gain region with increasing current density. Therefore, coherent beam combination (CBC) of integrated DBR lasers diodes can overcome these limitations by distributing the power across a larger active area, and thus provides a path for scaling the optical power. CBC laser systems have traditionally been made from bulky optical components such as optical fibers, lenses, external cavities, and diffraction gratings on a free-space optical bench [3,4]. These components do not provide a scalable and cost-effective solution. In contrast, integration of such components on a chip would provide a scalable, miniaturized, and cost-effective solution. A chip-based CBC laser system has been demonstrated using a hybrid InP-Si_3N_4 technology [5]. However, this demonstration requires hybrid integration of two different dies, which adds to the fabrication, and packaging complexity. Thus, it does not provide a cost-effective solution. In this work, we report for the first time a monolithically integrated intracavity CBC based on two DBR lasers on an InP generic foundry platform.

DEVICE DESIGN AND EXPERIMENTAL RESULTS

We employ CBC of two DBR lasers by adding a common intra-cavity 50:50 MMI splitter as sketched in Fig.1. The DBR lasers are combined in a way that feedback is equally distributed over both arms from the DBR1 mirror. Furthermore, both DBR lasers are coherently combined when the constructive interference occurs at the output port that is in the lower arm of the MMI ports. Consequently, the upper arm of MMI ports goes into destructive interference of two laser beams and it can be monitored by an incorporated photodiode. The InP circuit was fabricated via a multi-project wafer (MPW) run at SMART Photonics with components that are part of the default process design kit (PDK). The upper and the lower arms of the laser cavity consist of DBR mirrors, SOAs, and phase-shifters. The lengths of DBR1, PhS1, SOA1, and DBR3 are 100 µm, 400 µm, 500 µm, and 300 µm respectively and total cavity length in upper/lower arm is about 2.3 mm. The other components in the lower arm are identical compared to the upper arm. More details about the waveguide cross-section and SOA component are provided in the Ref [2]. The coupling coefficient of the DBR grating is fixed to 50 cm^{-1}. All active components (DBRs, SOAs, PhS, and PD) can be electrically driven through a common cathode ground at the n-substrate at the backside of the chip.

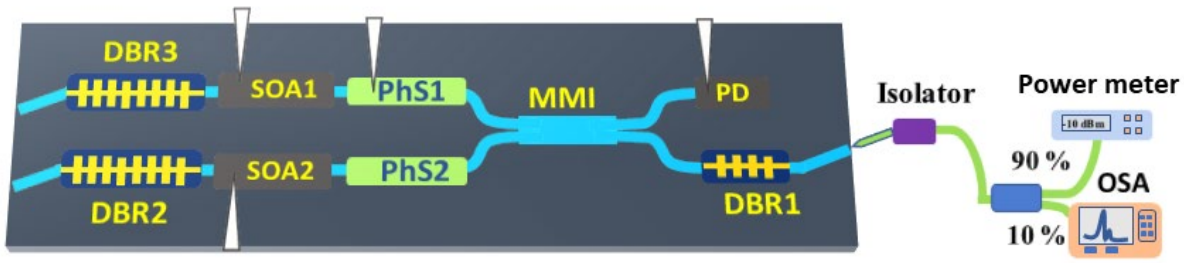


Fig. 1. Schematic of the chip and experimental set-up. SOA: semiconductor optical amplifier, DBR: distributed Bragg reflector, PhS: phase shifter, PD: photodiode, OSA: optical spectrum analyzer.

The output of the waveguide facet of the laser is angled at 7° and anti-refection coated to minimize back reflection. The chip is mounted on a temperature-controlled stage. The laser output is collected by a lensed fiber with coupling loss of ~4.5 dB. The L-I curves and photocurrent response of individual and combined DBR lasers are plotted in Fig. 2(a-d) and output power is corrected for the fiber-to-chip insertion loss. The threshold current of individual and combined DBR lasers are observed to be 30 mA and 20 mA, respectively.

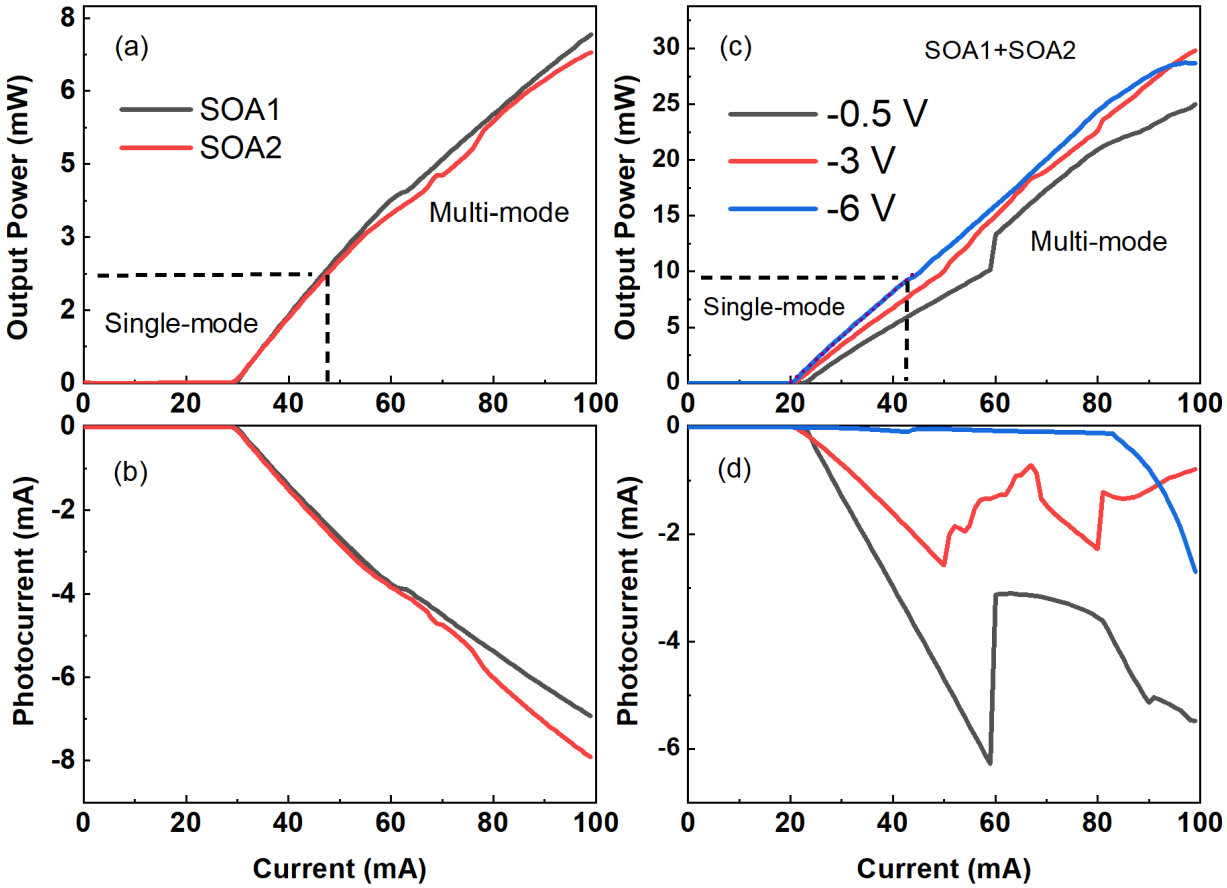


Fig. 2(a-b) L-I curve and photocurrent response of the individual DBR laser with only one SOA driven at a time. (c-d) L-I curves and photocurrent response with both SOA1 and SOA2 driven simultaneously with a pre-selected voltage on one of the phase shifters, which shows the increase in output power and decrease in photocurrent because of constructive and destructive interference in the corresponding MMI ports.

To coherently combine the DBR lasers using an intra-cavity MMI splitter, the voltage of one of the phase shifters was tuned at three different values which increases the output power as shown in Fig. 2(c). This plot is obtained by varying the currents of SOA1 and SOA2 simultaneously with pre-selected voltages on one of the phase-shifters. The maximum output power is observed when the constructive interference occurs at -6V on the phase-shifter and the modes of the two parallel laser cavities are aligned. Consequently, photocurrent is reduced because of destructive interference in the corresponding MMI port as plotted in Fig. 2(d). Hence, both cavities are aligned with an MMI port connected to the feedback mirror DBR1 and all power exits at the same MMI port. Thus, the threshold current of the combined DBR lasers is reduced due to lower internal loss inside the cavity. Moreover, the photocurrent increases with the SOA current in the individual operation of the DBR laser in Fig. 2(b) as expected without any combining effect where the equal power simply splits in both arms of the MMI ports. The individual DBR lasers account for at least ~6 dB extra internal loss for one round-trip. Hence, the output power of the combined laser is expected to be 4 times higher than that of an individual DBR laser operation. We also reported the slope efficiency which is inversely proportional to the internal cavity losses [6]. Hence, we obtained the slope efficiencies from the L-I curves in the individual and combined DBR lasers which are 122 mW/A and 410 mW/A, respectively. Therefore, we report a combining efficiency of ~ 84 % at 42 mA in both SOA on an integrated chip.

We have also reported the optical spectra of combined case of the DBR lasers in the regime where single mode operation in Fig. 3(a) changes to multimode regime in Fig. 3(b). Fig. 3(a) shows that the side-mode suppression ratio (SMSR) of 36 dB at 42 mA current in both SOA simultaneously. The multimode regime in the Fig. 3(b) is observed due to the amplification of the side longitudinal modes at the higher current ~ 45 mA in both SOA.

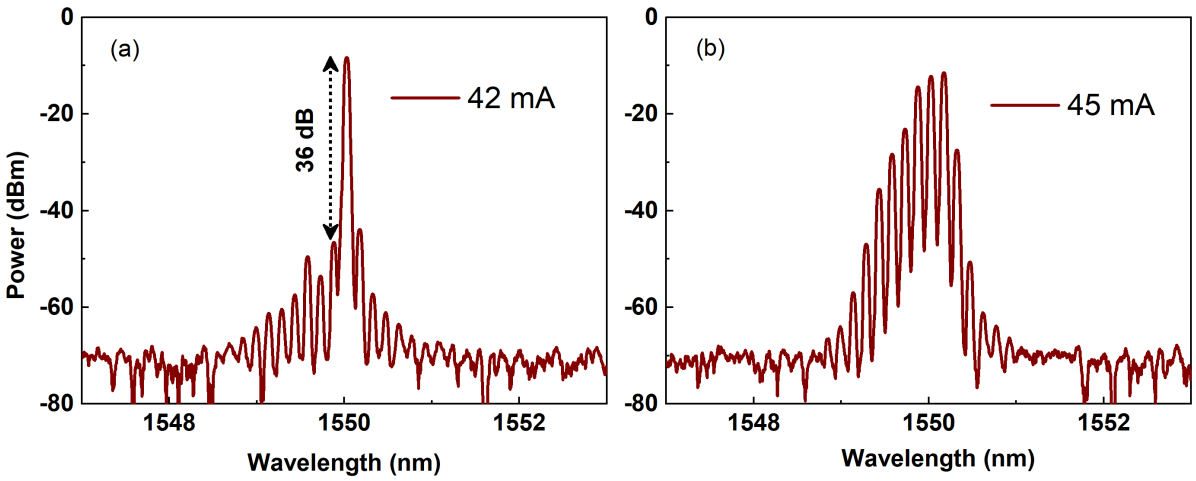


Fig. 3 Optical spectra in combining case at -6V on one of the phase shifters. (a) single mode regime with side-mode suppression ratio of 36 dB (b) multimode regime is observed due to amplification of side longitudnal modes. The current values were denoted in both SOA at the same time.

DISCUSSION

We noticed that the passband of the DBR grating mirror is much wider than the free-spectral range of the laser cavities. Therefore, many side modes get amplified as injection current increases. The measured output power in the single-mode regime is limited in this paper but shows the potential to obtain a higher power up to 28 mW on a single chip. However, this limitation can be further improved by designing narrower grating mirrors which can suppress the side modes amplification at the higher injection current. Besides, one can implement an imbalance length of two DBR lasers to circumvent such multimode behavior at the higher current [7]. Moreover, the combining efficiency of ~ 84 % in this work is limited by the differences in total cavity losses in the lower and upper arm of the MMI ports. In addition, we notice that the combining efficiency is reduced over time. Thus, output power is reduced due to the phase error that may be caused by spontaneous emission or environmental temperature variation. Therefore, a feedback control circuit is required to maintain the output power using an on-chip photocurrent electrical signal to correct the phase-error to maintain the output power at a desired value.

CONCLUSION

We demonstrated the intra-cavity CBC of the DBR lasers which emits an on-chip power of ~9.5 mW (~ 3.35 mW in the fiber) at 42 mA in both SOAs with SMSR of 36 dB. This is based on fully monolithic approach and can be further scaled to more DBR lasers which increases the output power linearly with the number of arms coherently combined. This work will pave the way for higher power lasers by circuit design techniques, using generic integration platforms, which can e.g., improve the bit error rate in optical communications.

Acknowledgements: This work was supported by the funding agency Innovation Fund Denmark through CRYPTO-Q and INCOM project.

References

[1] L. Chang, S. Liu, and J. E. Bowers, “Integrated optical frequency comb technologies,” Nature Photonics, vol. 16, pp. 95-108, 2022.

[2] R. R. Kumar, A. Hansel, M. Far Brusatori, L. Nielsen, L. M. Augustin, N. Volet, and M. J. R. Heck, “A 10-kHz intrinsic linewidth coupled extended cavity DBR laser monolithically integrated on an InP platform,” Optics Letters, vol. 47. pp. 2346-2349, 2022.

[3] O. Andrusyak, V. Smirnov, G. Venus, V. Rotar, and L. Glebov, “Spectral combining and coherent coupling of lasers by volume Bragg gratings,” IEEE Journal of Selected Topics in Quantum Electronics, vol. 15, pp. 344-353, 2009.

[4] M. Fridman, “Efficient coherent addition of fiber lasers in free space,” Optics Letters, vol. 32, pp. 790-792, 2007.

[5] Y. Zhu, Y. Zhao, and L. Zhu, “Loss induced coherent combining in InP-Si_3N_4 hybrid platform,” Scientific Reports, vol.8, no.878, 2018.

[6] Larry A. Coldren, Scott W. Corzine, and Milan L. Masanovic, “Diode lasers and photonic integrated circuits,” 2nd edition, Wiley, p. 62, 2012.

[7] D. Sabourdy, V. Kermene, A. Desfarges-Berthelemot, M. Vampouille, A. Bathelemy, “Coherent combining of two Nd-YAG lasers in a Vernier-Michelson-type cavity,” Applied Physics B, vol. 75, pp. 503-507, 2002.

First experimental demonstration of a Generalized Mach-Zehnder Interferometer on Si_3N_4

(Student paper)

Stefanos Kovaios[1,2*], Apostolos Tsakyridis[1,2], George Giamougiannis[1,2], Konstantinos Fotiadis[1,2], Davide Sacchetto[3], Michael Zervas[3], Miltiadis Moralis-Pegios[1,2] and Nikos Pleros[1,2]

[1]School Of Informatics, Aristotle University of Thessaloniki, Thessaloniki, 54124, Greece
[2]Center of Interdisciplinary Research & Innovation, Balkan Center, Thessaloniki, 57001, Greece
[3]Ligentec SA, Chemin de la Dent-d'Oche 1B, 1024 Ecublens, Switzerland

[*] sdkovaios@csd.auth.gr

We experimentally demonstrate the first Si_3N_4 4×4 Generalized Mach-Zehnder Interferometer, capable of operating both as an optical switch and as a variable power splitter, exhibiting an average loss of 2.4 dB and maximum crosstalk of -10.2 dB.
Keywords: *photonic integrated circuits, optical computing, variable power splitter, linear optics*

INTRODUCTION

Linear optics has been established as a primary field of research in integrated photonics, with several implementations of photonic circuitries being theoretically and experimentally demonstrated in applications such as neuromorphic optical computing [1,2], unitary and universal linear processors [3], and high-performance optical switches [2]. At the core of these schemes, lies the 2×2 Mach Zehnder Interferometer (MZI), characterized by its reliable performance in several photonic integration platforms. Despite its unquestionable merits, the performance of large-scale photonic architectures based on the 2×2 MZI could be degraded, due to differential path losses rising either from the component's internal losses or from the inevitable introduction of waveguide crossings in the complete layouts. An approach towards overcoming these drawbacks would be to scale the elementary block itself, and expand the 2×2 MZI into an N×N generalized structure (GMZI) [4,5]. Since their original proposal [6,7], GMZIs were successfully deployed in switching [7] and variable power splitting applications in several photonic integration platforms [8-10], whereas recent theoretical findings have revealed the prospect of realizing fidelity restorable universal processors through GMZI based meshes [4,5]. Provided that N×N GMZIs could be fabricated as a reliable and low loss device, they could serve as a fundamental building block for compact and high-performance photonic architectures.

In this paper, we present a low-loss 4×4 GMZI fabricated for the first time on the Si_3N_4 platform and demonstrate experimentally its performance as a variable power splitter and a 1×4 switch. The passive characterization of the structure reveals low insertion losses of 2.4±0.4 dB across all port combinations in the C-band. Its experimental validation as a variable 1:4 power splitter indicates that the power levels obtained at each of its output can cover the entire range between 0 to 100%, while its successful operation as a 1×4 switch has been also experimentally evaluated revealing a maximum crosstalk of -10.2 dB.

EXPERIMENTAL SETUP

The 4×4 GMZI fabricated in Si_3N_4 along with the setup utilized for its experimental study are illustrated in Fig. 1(a), whereas the characteristic schematic of the device is presented in Fig. 1(b). The 4×4 GMZI is constructed by connecting two 4×4 MMIs with an array of 4 waveguides of arbitrary length, each equipped with an independent phase shifter. In our design, the lengths of the interconnecting waveguides were set to $L_{1,4}$ ~ 1.9 mm and $L_{2,3}$ ~ 1.3 mm, while each waveguide was equipped with an integrated thermo-optical phase shifter, capable of providing π-shift when driven with 300 mW of applied electrical power.

A tunable laser, operating in the C-band, was used for generating the optical inputs, denoted as X_i. The optical signal was injected through integrated spot size converters into one of the input ports of the structure, with the optical outputs' power Y_{ij} captured by a multichannel power meter. The phase shifters were accessed through a DC probe and driven by a multi-channel digital to analog converter (DAC)

EXPERIMENTAL RESULTS

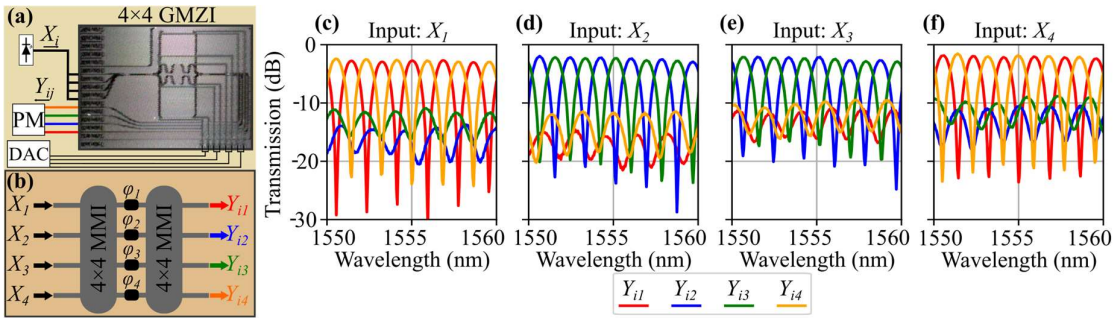


Fig. 1. (a) The experimental setup for the study of the 4×4 GMZI, fabricated in the Si_3N_4 platform, consisting of a single CW laser source and a multichannel powermeter, in addition to an electrical DAC allowing the control of the thermooptical phase shifters. (b) Schematic of the 4×4 GMZI, for operation under single optical inputs. (c)-(d) Passive characterization of the 4×4 GMZI, where the normalized output power spectra for all single inputs X_1-X_4 are presented

The normalized output power spectra or all four output ports of the 4×4 GMZI are presented Fig. 1(c)-(f) respectively. Our measurements reveal an average insertion loss of approximately 2.4 dB and distinct characteristics for each acquired spectra. Firstly, the appearance of a characteristic free spectral range (FSR), equal to approximately 1.8 nm, is evident in all outputs, and originates from the symmetric length difference of the interleaved waveguides introduced in our design. Moreover, the output ports present similar behavior in pairs, identified as Y_{j1}-Y_{j4} and Y_{j2}-Y_{j3}. The existence of these pairs is in accordance with the theoretical analysis of the ideal 4×4 GMZI [7], where the device behavior was projected to resemble pairs of ideal 1:2 splitters: Inputs $X_{1,4}$ are equally split into outputs Y_{j1}, Y_{j4}, whereas inputs $X_{2,3}$ split into outputs Y_{j2}, Y_{j3} , forming a primary pair with characteristic resonances and significant extinction ratio (ER) originating from the introduced arm length difference. This trend is also persistent in our measurements, with the non-primary outputs having non-zero power due to structural variations in the fabricated waveguides, and deviations in the MMI outputs' phase and power splitting ratios with respect to the ideally expected values.

Followingly, we performed a series of active measurements by introducing several combinations of phase shifts to our device, through applying electrical power to the underlying phase shifters in the range of 0-390 mW. We define each set of applied electrical power values (P_1,P_2,P_3,P_4) as a GMZI configuration, equivalent to a set of optical phase shifts. We performed single wavelength measurements at 1555 nm and recorded the optical power outputs for a series of 2352 GMZI configurations, corresponding to different settings of pairs of phase shifters. A DC voltage, corresponding to electrical powers in the range of 0-390 mW, is applied to each phase shifter.

The results validating the performance of the 4×4 GMZI as a switch are presented in Fig. 2, using indicatively the input X_2. In order to identify a switch state from our measurements, we follow an iterative procedure: The switch state for output Y_{ij} corresponds to a specific GMZI configuration at which: a) additional losses to Y_{ij} do not exceed 7 dB, b) the maximum crosstalk to the remaining ports is -10 dB. If no switch states are identified, the crosstalk threshold has been reduced in steps of 0.5 dB, until a switch state is recognized. If multiple switch states arise, the state exhibiting the minimum additional loss is selected. As shown in Fig. 2(a)-(d), the GMZI operates adequately as a switch, where crosstalk levels less than -10 dB are observed for all outputs. The GMZI switch configurations for the outputs Y_{21}–Y_{24} were: (295,0,196,0), (0,247,252,0), (0,39,0,0) and (278,174,0,0) mW respectively. The

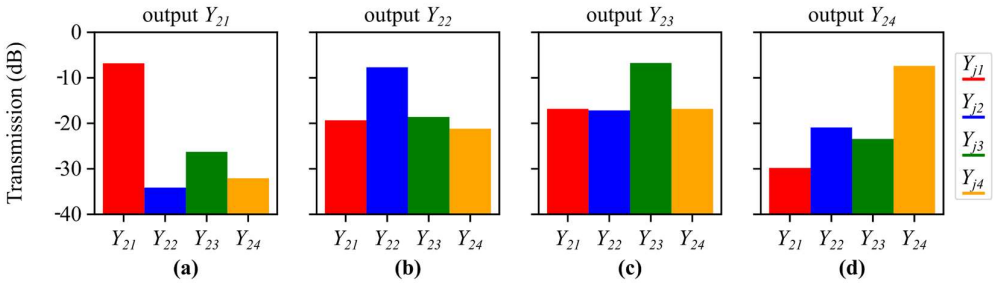


Fig. 2.: Operation of the 4×4 GMZI as a switch for different single inputs. Indicatively, the results corresponding to the outputs Y_{21}-Y_{24} are presented in (a)-(d) respectively.

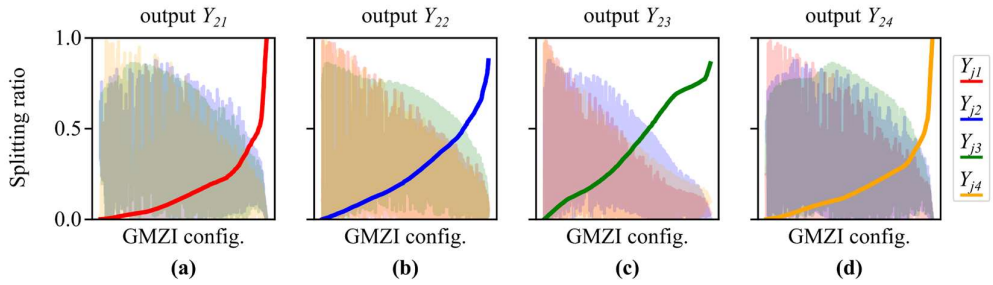


Fig. 3: Output power splitting ratio recorded for different GMZI configurations Indicatively, the results corresponding to the outputs Y_{21}-Y_{24} are presented in (a)-(d) respectively.

performance of the 4x4 GMZI could be further improved, by varying more than two phase shifters simultaneously, which could also lead to reduced crosstalk values.

Finally, we focused on the performance of the 4×4 GMZI when it was enforced to operate as a variable power splitter - with the target being that the splitting ratio level at a certain output port can take any value between 0 to 100%. The power splitting limits of the GMZI are extracted from the relevant power splitting ratios of the outputs, which are presented in Fig. 3(a)-(d), indicatively for the case of the single input X_2. The splitting ratio of each output at a specific GMZI configuration was calculated by dividing the output power by the total output power captured from the device. As depicted in our results, the 4×4 GMZI exhibited a great tunability range, extending from 0 up to (0.98, 0.88, 0.99,0.84) for outputs Y_{21}-Y_{24} respectively. The splitting ratio range for output ports Y_{22} and Y_{24} can be in principle boosted if more than two phase shifters could be simultaneously tuned.

Acknowledgements: The work was in part funded by the EU-projects SIPHO-G (101017194) and OCTAPUS (101070009)) and by the Hellenic Foundation for Research and Innovation (H.F.R.I.) under the “First Call for H.F.R.I. Research Projects to support Faculty members and Researchers and the procurement of high-cost research equipment grant” (Project number 4233, DeepLight).

References

[1] G. Dabos, et al., "*Neuromorphic photonic technologies and architectures: scaling opportunities and performance frontiers [Invited]*", Opt. Mater. Express 12, 2343-2367, 2022
[2] M. Moralis-Pegios, et al., "*Neuromorphic Silicon Photonics and Hardware-Aware Deep Learning for High-Speed Inference*", Journal of Lightwave Technology, vol. 40, no. 10, pp. 3243-3254, DOI: 10.1109/JLT.2022.3171831, 2022
[3] W.A. Clements, et al., "*Optimal design for universal multiport interferometers*", Optica 3, 1460-1465, 2016
[4] G. Giamougiannis, et al., "*Universal Linear Optics Revisited: New Perspectives for Neuromorphic Computing with Silicon Photonics*", Journal of Selected Topics in Quantum Electronics, vol. 29, no. 2: Optical Computing, pp. 1-16, DOI:10.1109/JSTQE.2022.3228318, 2023
[5] Tsakyridis, A., et al., "*Fidelity Restorable Universal Linear Optics*", Adv. Photonics Res., 3: 2200001, DOI: 10.1002/adpr.202200001, 2022
[6] G. Weihs, et.al, "*All-fiber three-path Mach–Zehnder interferometer*", Opt. Lett. 21, 302-304, 1996
[7] R. M. Jenkins, et al., “*Novel 1×N and N×N integrated optical switches using self-imaging multimode GaAs/AlGaAs waveguides*”, Appl. Phys. Lett., vol. 64, pp. 684–686, 1994
[8] N. S. Lagali, et al., "*Analysis of generalized Mach-Zehnder interferometers for variable-ratio power splitting and optimized switching*", Journal of Lightwave Technology, vol. 17, no. 12, pp. 2542-2550, 1999
[9] R. Tang, et al., "*Reconfigurable all-optical on-chip MIMO three-mode demultiplexing based on multi-plane light conversion*", Opt. Lett. 43, 1798-1801, 2018
[10] R. Tanomura, et al., "*Monolithic InP optical unitary converter based on multi-plane light conversion*", Opt. Express 28, 25392-25399, 2020

Reverse Synthesis for the Configuration of Coupled Ring Resonators

(Student paper)

Xiangfeng Chen[1,2], Muhammad Umar Khan [1,2] and Wim Bogaerts[1,2]

[1] Ghent University - IMEC, Photonic Research Group, Department of Information Technology, Gent, Belgium.
[2]Center of Nano and Biophotonics, Ghent University, Belgium
*xiangfeng.chen@ugent.be

We report a generic programmable waveguide mesh with tungsten heaters as tunable elements on the IMEC iSiPP50G PSV+ Platform. The thermal calibration procedure is illustrated, and the thermal coupling relationship is fitted. Overcompensation is observed using such fitting Reverse Synthesis is proposed for the configuration of coupled ring structures. Steps and target responses are reported in detail for the 3-ring synthesis example.
Keywords: *Programmable Photonics, CROW Synthesis, Thermal Eigenmode Decomposition*

Introduction

We are developing generic programmable meshes that consist of tuneable Mach-Zehnder interferometers (MZIs), which can be reconfigured to different complex functions without redesigning the chip [1]. However, the close integration of multiple heaters generates thermal crosstalk, complicating the control. The strategy based on thermal eigenmode decomposition requires a very accurate abstraction of thermal coupling from the system [2], and we observe overcompensation in our system. The reverse synthesis method is proposed to split up the configuration procedure, leveraging analytical guidance on each response of the ring within the chain of rings.

Thermal Crosstalk Compensation

This silicon photonics chip is based on the IMEC iSiPP50G PSV+ platform, which supports passive waveguides with overhead tungsten heaters. Also, an additional etch of the back-end-of-line (BEOL) stack (The “EXPO” layer) is used as an additional thermal insulation around the Tungsten heaters, as shown in Fig1. (a). We use a fiber array to characterize the circuits, stabilizing it using a reference waveguide. The tunable MZIs in the mesh are wire-bonded to a multi-channel voltage source through a simple printed circuit board. We manually adjust the power delivered on the tungsten heaters “dc7”, “dc2” and “dc4” sequentially so that the circuit gives a single ring resonance. The "ring1" building blocks are highlighted in green in the schematic view of the mesh in Fig1(b). The measured spectrum is plotted in blue in Fig2.(a). The cross-correlation is utilized to calibrate the phase shift while we change the driving power of the phase-shifter inside of the ring, namely”ps1”. We cross-correlate the blue spectrum with the orange spectrum yielding one data point with phase change(π) of the ring vs the driving power of the "ps1" as in Fig.2(b). All other heaters in the mesh are calibrated the same way from 0 to 71.6mW. We use phase change(π) vs delivered power(mW) to represent the thermal coefficient caused by on-chip crosstalk: Every heater except those highlighted in green is calibrated with this thermal crosstalk term and normalized by the thermal coefficient of the “ps1”. All phase shifters in this mesh have identical designs, but their thermal surroundings can differ due to metal wiring. The resulting thermal coupling coefficients are plotted in Fig.2(c) and fitted with the power law (Ax^{-k}).

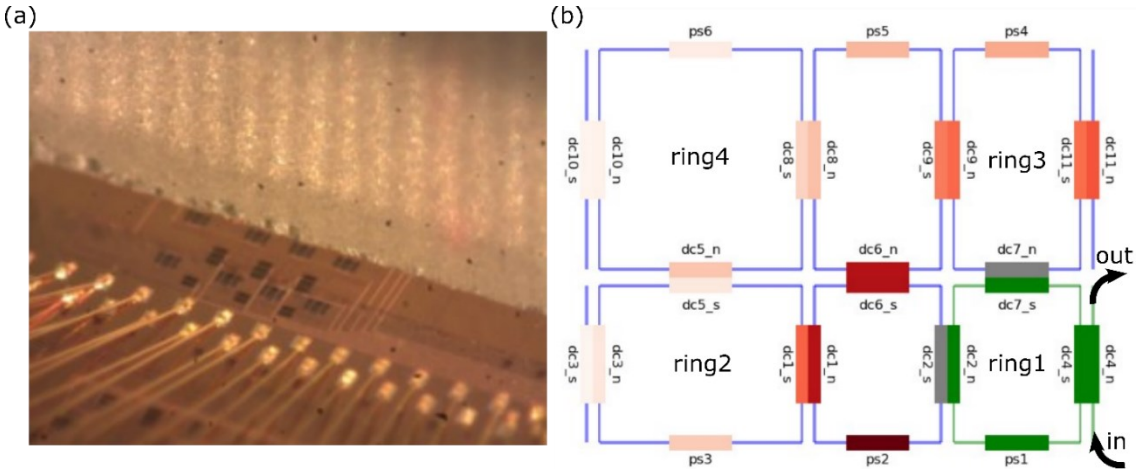


Fig.1.(a) Wire-bonded programmable mesh is aligned with fiber arrays for optical measurements; (b)Relative phase shift(π) difference caused by on-chip thermal crosstalk is illustrated in terms of heatmap with schematics of the mesh.

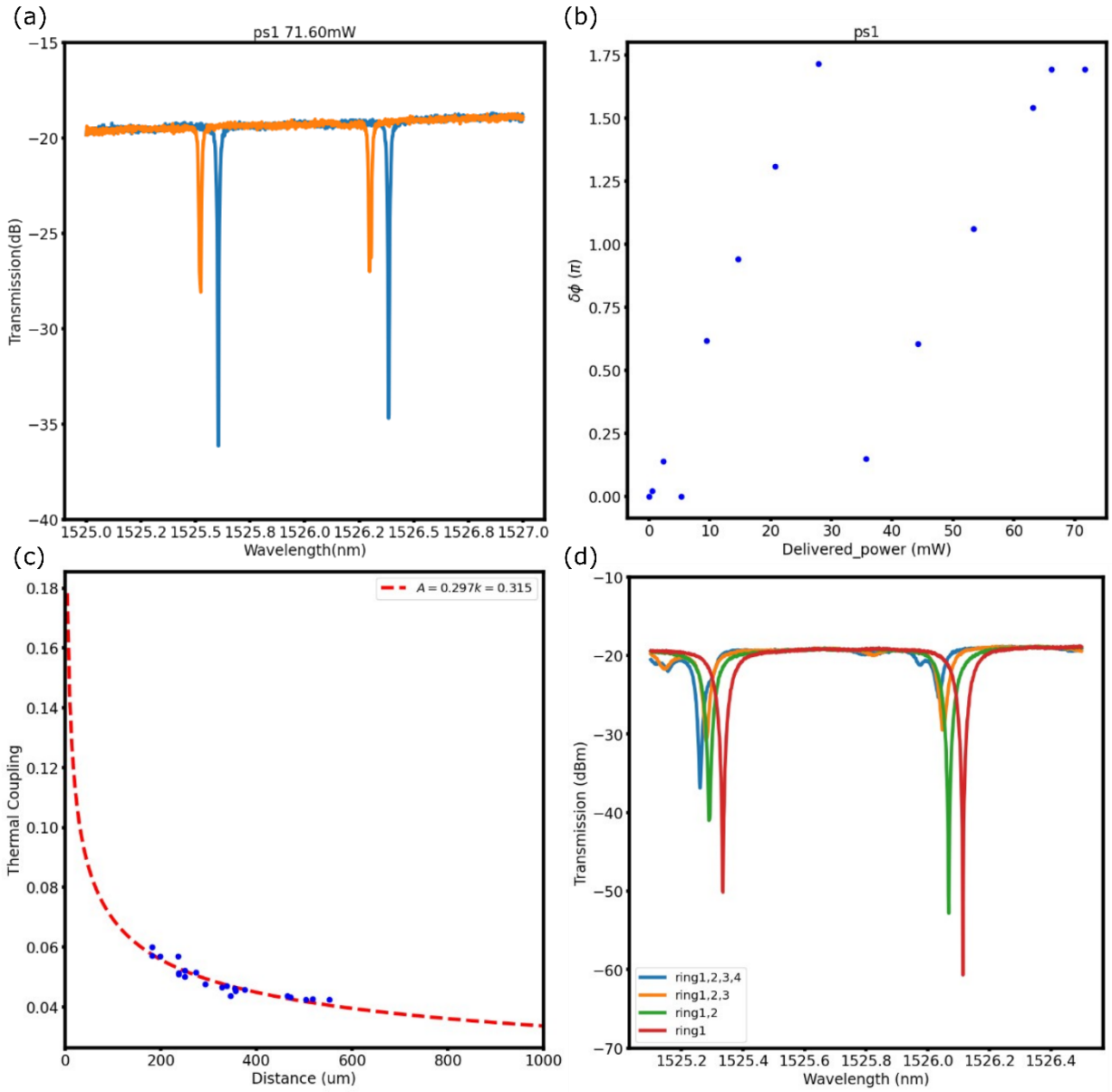


Fig. 2. (a) the spectrum of the ring1 before(blue) and after(orange) setting the power of" ps1" to 71.60mW;(b) Phase shift changes while tuning the power of "ps1" inside the ring1; (c)the normalized thermal coupling coefficient is fitted with the power law (Ax^{-k}).;(d) the spectrum of the ring1 while we accumulatively add more configurations of rings to the mesh.

From this fitting, we derive the thermal coupling matrix for every heater in this circuit for the configuration based on thermal eigenmode decomposition [2]. The same thermal coupling matrix as derived from Fig. 2(c) is used in the thermal compensation and further tested with all four cases in Fig. 2(d): we keep adding one ring in the mesh configuration and keep the power of heaters at the same value as those in the previous configuration. It demonstrates that our fitted matrix overcompensates the thermal crosstalk effect in the mesh in Fig 2(d). As we configure more heaters for complex functions, for instance, the coupled ring optical waveguides (CROW) inside the mesh, configuration even with thermal compensation accumulatively brings the desired coupling and phase outside of the region where local optimization of the tunable components could restore.

Reverse Synthesis Method

We report the overcompensation of the thermal coupling relationship fitted by the power law: we configure a ring within the mesh and use it as the temperature sensor to calibrate the thermal coupling matrix for the thermal eigenmode decomposition. We have two main ideas to improve the way of configuration: One, we could improve the thermal coupling matrix calibration by using more localized temperature sensors projecting more accurate heat distribution of the circuit; Two, we could subset the eigenmode decomposition routines into iterative thermal compensation with local optimization for each ring within the complex filter functions.

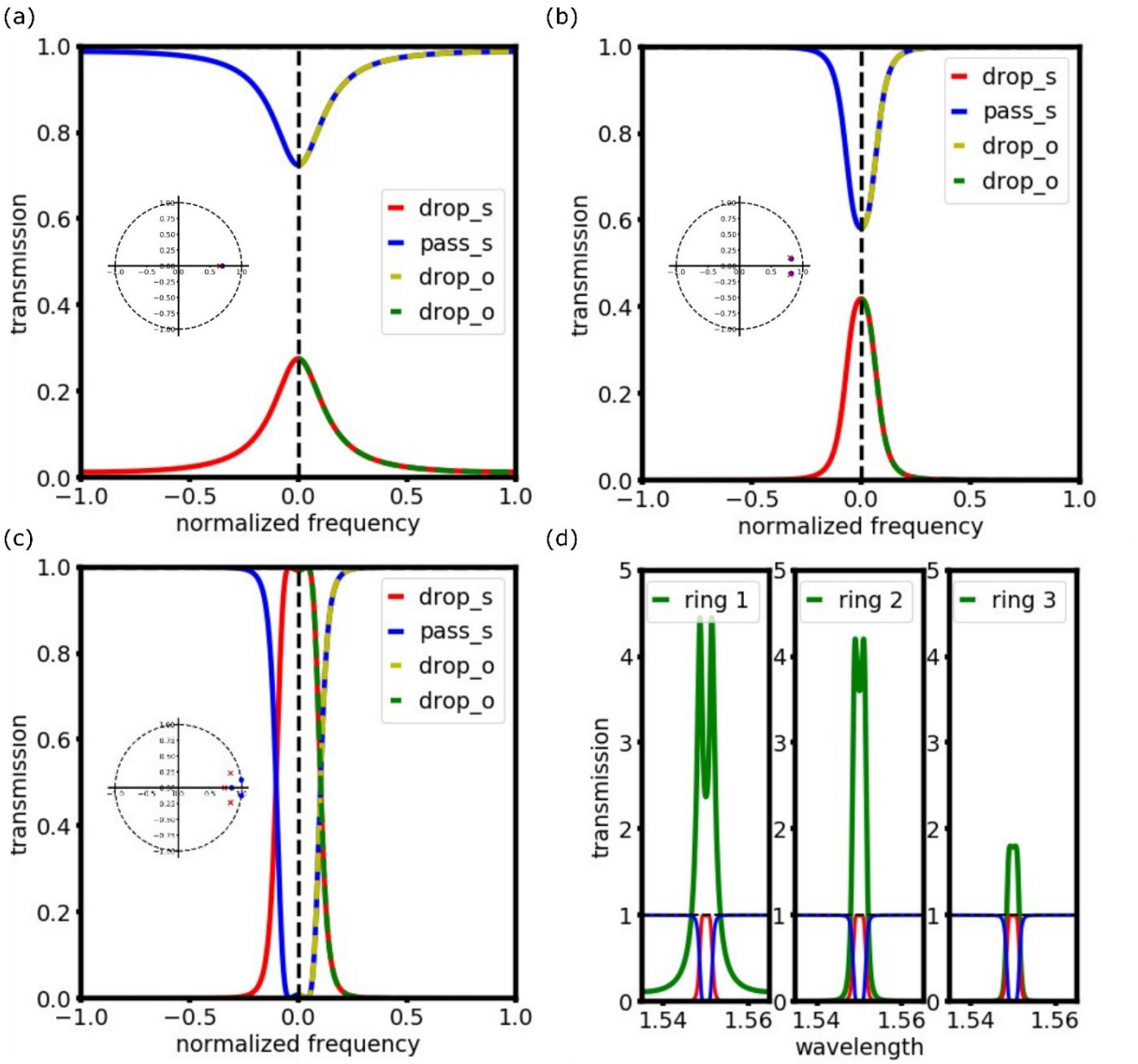


Fig.3. (a-c) Transmission vs normalized frequency with pole zero diagram for reverse synthesis;(d) Spectrum inside of rings.

The synthesis algorithms described by Madsen and Zhao [3] provide a solid basis for the application-specific wavelength filter design based on CROW. We further develop the algorithm since we replace the directional couplers with tuneable MZIs and replace the passive ring waveguides with tuneable phase shifters to achieve re-configuration [4]. The backbone of these algorithms is a recursive step-down function where we start from the user-specific all-pole target polynomials and iteratively synthesize the phase shift of waveguides and coupling coefficients from the last ring to the first ring. The spectral factorization is used to match the pairs of poles (A_N) and zeros (B_N) in each iteration. The process is like opening a chain of rings one by one. The poles (A_N) determine the drop port response ($\frac{\Gamma}{A_N}$). Zeros (B_N) together with poles (A_N) determine the through port response ($\frac{B_N}{A_N}$). If we use the process in reverse for the CROW configuration, the process is like attaching the chain of rings one by one with local optimization and thermal compensation. For example, the process is illustrated in Fig. 3 for the case of 3-ring CROW: we sequentially stabilize the response of 1 ring (as in Fig.3a)), 2 rings (as in Fig. 3(b)), and 3 rings (as in Fig. 3(c)). As in Fig. 3(d), it can also work with technologies where power monitors are inside the rings.

References

[1] D. Pérez, A. López, P. Dasmahapatra and J. Capmany, "Multipurpose self-configuration of programmable photonic circuits," Nature communications, vol. 11, no. 1, pp. 1–11, 2020.

[2] M. Milanizadeh, D. Aguiar, A. Melloni, and F. Morichetti."Canceling thermal cross-talk effects in photonic integrated circuits. Journal of Lightwave Technology", 37(4), 1325-1332,2019.

[3] C. K. Madsen and J. H. Zhao, "Optical filter design and analysis". Wiley New York, 1999.

[4] X. Chen, W. Bogaerts, "An Algorithm for Reconfigurable Coupled Resonator Optical Waveguides", IEEE Photonics Society Summer Topicals, p.WB1.4, 2022

Demonstration of nano-pixel 9:1 asymmetric power splitter

(Student paper)

Yuta Shimamura, Haisong Jiang, Kensei Yamauchi, Ryota Kuwahata, Ryoma Matsuo, and Kiichi Hamamoto

Kyushu University, 6-1 Kasuga-koen, Kashuga, Fukuoka 816-8580, Japan
* shimamura.yuta.455@s.kyushu-u.ac.jp

Asymmetric power splitter was realized using nano-pixel configuration. The implemented device was realized in an area of 3.2 µm × 3.4 µm. It demonstrated asymmetric splitting ratio of 9:1 with excess loss of 4 dB at 1550 nm.
Keywords: *Power splitter, Nano-pixel*

INTRODUCTION

Power-splitter is one of the fundamental optical devices. Especially waveguide-based power-splitter is attractive as it offers several applications including: 1) Mach-Zhender interferometer, 2) output power monitor, and others. As to our purpose, we have been researching and developing an optical integrated circuit to realize a compact breath sensing system (see Fig. 1). As is shown in the figure, power-splitter is, anyway, one of the key-elements [1]. In this case most of the light power must be returned back into the loop whereas slight portion must be monitored apart from the loop. This requirement arises "asymmetric" power-splitter. This is because the monitored power may be sufficient with relatively low power, on the other hand, most of the propagating light must be returned back into the loop to achiever high sensitivity. As to the power splitter, Y-junction and MMI (multi-mode-interference) have been widely used; however; there is insufficient design theory to realize asymmetric splitting [2]. Directional coupler has a potential of asymmetric splitting; however; the length of the device is relatively long (close to around mm) and relatively less robust in general [3]. In this paper, we demonstrate a new potential of using nano-pixel [4-9] for asymmetric splitting. The implemented device was realized in an area of 3.2 µm × 3.4 µm. It demonstrated highly asymmetric splitting of 9:1 with propagation loss of 4 dB at 1550 nm.

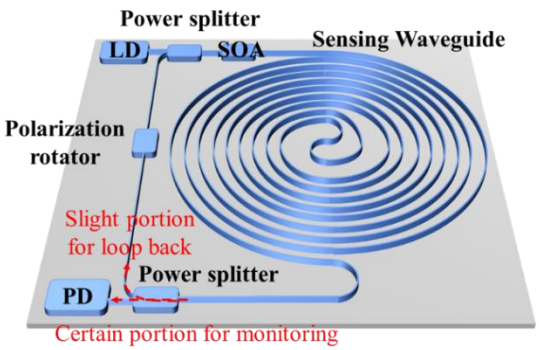


Fig. 1. Photonic integrates circuit for breath sensing

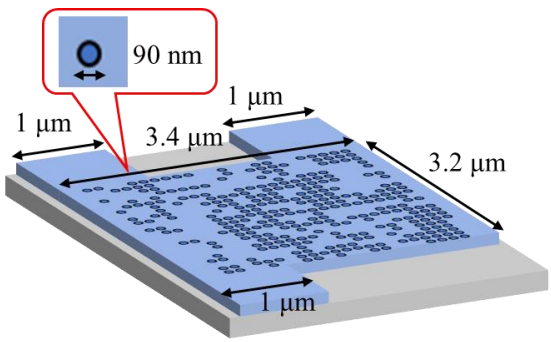
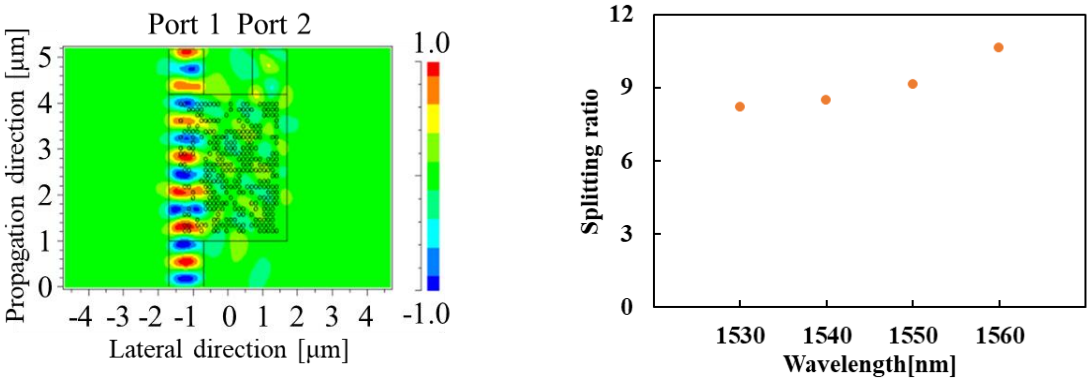


Fig. 2. 9:1 power splitter using nano-pixel

Device Design

Asymmetric splitting device was designed using 3.2 µm × 3.4 µm pixel waveguide (see Fig. 2). The layer structure consists of 100 nm Si- core on top of 1 µm SiO_2 cladding. Each pixel in the nano-pixel waveguide was in a size of 120 nm ×120 nm square. In some pixels, 90 nm radius circular-void are arranged so as to realize the desired 9:1 splitting. The layout of the pixel-pattern was arranged using machine-learning including deep-learning and direct binary search (DBS) [10-11]. There are two issues when highly asymmetric splitting is designed. One is the way to find the initial pattern before starting DBS, and the other is as to criteria setting in DBS. As to the initial pattern finding, we exploited machine-learning. As to the criteria setting, we introduced vector criteria including excess loss and splitting ratio and carried DBS in forward direction. Normally in DBS process, inverse design is used as this scheme leads simple criteria. It becomes sufficient to monitor only the excess loss at the input in this case. In case of designing highly asymmetric splitting, however, this process seems not appropriate even in case of perfect 9:1 combined light power injection is used from two output waveguides simultaneously (and the excess loss is

monitored at the input in this case.). We noticed that the power balance of 9:1 was not completely secured and was sacrificed rather than the total excess loss when we verified the splitting performance after the regular DBS design process. To overcome this issue, we relied on DBS in forward direction with vector criteria in this work. As a result, relatively ideal performance was confirmed in FDTD (finite-difference time-domain) simulation. Figure 3 shows the results. As Fig. 3 (a) shows clearly, most of the light propagated toward main output (port 1), whereas slight portion of the injected light comes out from monitor-port (port 2). Figure 3 (b) shows the splitting ratio as a function of wavelength. 9:1 splitting was secured at entire C-band.



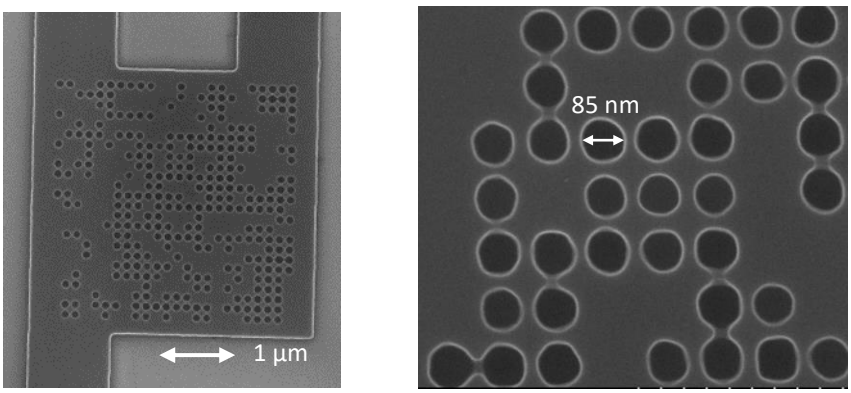
(a) *(b)*

Fig. 3. FDTD simulation result

(a)Counter map, (b) Wavelength dependency of splitting ratio

RESULTS AND DISCUSSION

We fabricated the asymmetric power splitter using SOI wafer. EB-lithography was used for air-hole patterns as well as side-wall formation mask, and ICP (inductively coupled plasma) dry-etching was used for the nano-pixel and the waveguide implementation. Figure 4 shows the top view of the fabricated device. The realized air-hole diameter is estimated to be around 85 nm which is slightly narrower, but not too small, rather than the design. To help the characterization especially asymmetric splitting, S-bend waveguides were integrated at both sides of the device. 1550 nm light was used and coupled through the cleaved facet using hemi-spherical lensed fibre. The light output from the device was measured using IR (infra-red) camera. Figure 5 shows NFP (near-field-pattern) of the device. As shown clearly in the figure, asymmetric power splitting was confirmed successfully. To make the precise splitting ration estimation, we verified the power portion monitored in NFP. Figure 6 shows the results. As shown in the figure, a splitting ratio of 9:1 was confirmed successfully at 1550 nm. In addition, we also verified the wavelength dependency at entire C-band. As is also shown, the ratio was kept almost similar along entire C-band (except 1530 nm case) that mostly agrees with the simulated results. The evaluated propagation loss was estimated to be 4 dB including S-bending waveguide loss.



(a) *(b)*

Fig. 4. Fabricated device

(a) 9:1 power splitter, (b) Nano-pixel region

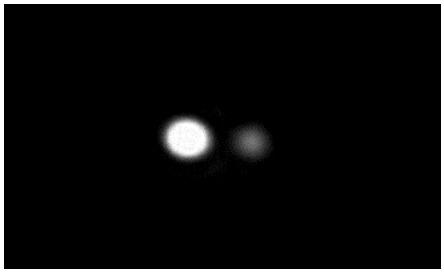


Fig. 5. Near field pattern

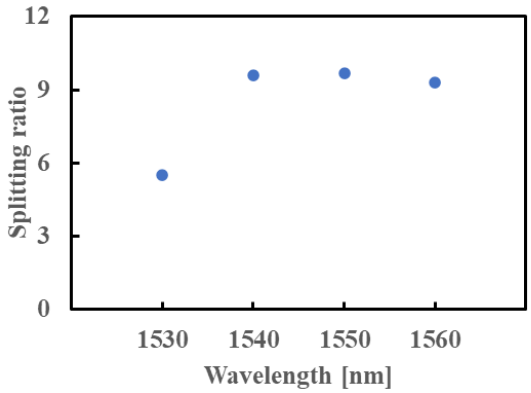


Fig. 6 Wavelength dependency of splitting ratio

Conclusion

We demonstrated nano-pixel asymmetric power splitter with the area of 3.2 µm × 3.4 µm. It demonstrated asymmetric splitting ratio of 9:1 successfully with propagation loss of 4 dB at 1550 nm. We believe that we can realize fully integrated breath-sensing circuit with this asymmetric power splitter soon in the future.

Acknowledgments

This work has been supported financially by SECOM Science and Technology Foundation. A part of this work was supported by "Nanotechnology Platform Japan" of the Ministry of Education, Culture, Sports, Science and Technology (MEXT), and fabrication was conducted in Takeda Cleanroom with help of Nanofabrication Platform Center of School of Engineering, the University of Tokyo, Japan.

References

[1] Y. Shimamura, et.al., "First Implementation of Asymmetric Power Splitter by using Nano-Pixel Integrated with Sensing High-Mesa Waveguide", Proc. MOC, 2022, #1049
[2] W. M. Henry et.al., "Asymmetric multimode Y-junction splitters", Opt. Quantum Electron. **29**, 379–392, 1997.
[3] Q. Li, Y. Song, et.al., "Asymmetric plasmonic-dielectric coupler with short coupling length, high extinction ratio, and low insertion loss", Opt. Lett. **35**, 3153–3155, 2010.
[4] Z. Li, et.al., "Ultra-compact high efficiency and low crosstalk optical interconnection structures based on inverse designed nanophotonic elements", Sci. Rep., **10**, 11993, 2020
[5] M. H. Tahersima, et.al., "Deep Neural Network Inverse Design of Integrated Photonic Power Splitters", Sci. Rep., **9**, 2019
[6] H. Ma, et.al., "Inverse-designed arbitrary-input and ultra-compact 1 × N power splitters based on high symmetric structure", Sci. Rep., **10**, 2020
[7] A. Y. Piggot, et.al., "Inverse design and demonstration of a compact and broadband on-chip wavelength demultiplexer", Nat. Photon., **9**, 374-378, 2015.
[8] K. Shoda, et.al., "Equal input, compact optical power coupler based on a nano-pixel structure designed with machine learning", Jpn. J. Appl. Phys., **61**, SK1017, 2022
[9] Y. Wang, et.al., "Space-mode compressor by using nano-pixel", Jpn. J. Appl. Phys., **61**, SK1022, 2022
[10] B. Shen, et.al., "An integrated-nanophotonics polarization beamsplitter with 2.4×2.4 µm2 footprint", Nat. Photon., **9**, 378-382, 2015
[11] T. Fujisawa et.al., "Bayesian direct-binary-search algorithm for the efficient design of mosaic-based power splitters", OSA Contin. **4**, 1258-1270, 2021

Demonstrating Bidirectional Coupling Using a Monolithically Integrated Tunable Comb Source

(Student paper)

John McCarthy[1,2], Diarmuid O'Sullivan[2], Maryam Shayesteh[3], Mohamad Dernaika[1] , Bryan Kelleher[1,2] and Frank Peters[1,2]

[1]Tyndall National Institute, Lee Maltings, Cork City, Ireland
[2]Physics Department, University College Cork, College Road, Cork City, Ireland
[3]University of Southampton, Southampton, Hampshire, UK
* john.mccarthy@tyndall.ie

A bidirectionally coupled comb is demonstrated using a monolithically integrated Photonic Integrated Circuit (PIC). The tunable comb source is created by gain switching a slave Fabry-Pérot laser that is injection locked to a master slotted Fabry-Pérot laser. The master section of the PIC produces a single mode spectrum with a tunable range of 1557nm – 1573nm. Bidirectional coupling is observed as the comb is detected through the facet of the gain switched slave laser as well as through the facet of the single mode master laser.
Keywords: *Frequency comb generation, gain switching, bidirectional coupling*

INTRODUCTION

Optical frequency comb sources (OFCS) show significant promise in many modern day applications such as spectroscopy [1], space based instruments [2] and high speed telecommunications [3]. OFCS generate equally spaced spectral carriers with a known phase and relation between adjacent carriers. Due to their precise and stable frequency and relative phases, they can be used in wavelength division multiplexing (WDM) communications to create coherent optical superchannels, where guard bands between neighbouring WDM signals are no longer required [4]. One method of generating optical frequency combs in a PIC (which is the method described in this paper) is by injection locking a slave laser with a single mode master laser and gain switching the slave laser by applying a high power radio frequency (RF) signal.

The comb source itself is demonstrated by injection locking a gain switched slave laser to a single mode master laser. Injection locking using an external master laser has previously been demonstrated to reduce phase noise and linewidth in gain switched lasers [5]. In this work, these two lasers are integrated in a strongly coupled master slave configuration [6], whereby the slave laser is optically phase locked to that of the master. The single mode characteristics of the slave laser has been known to improve by on-chip optical phase locking, particularly with increasing the side mode suppression ratio (SMSR) of the slave [7]. The master laser is more heavily biased than the slave, and so the two sections are operating in an asymmetric bias regime. So while no isolator exists between the two lasers, the asymmetry of the operation has been known to allow for injection locking [8]. The slave laser is then gain switched by a high power RF signal to generate the optical combs.

In this paper, we focus on an on-chip phenomena whereby the generated comb is measured through both the end facet of the master and end facet of the slave laser where it is generated. This is a demonstration of bidirectional coupling due to the relative short lifetime of the generated photons. This is an advantage for future PIC designs as it allows for a comb to be propagated along different outputs without requiring a more complicated design.

DEVICE DESIGN

The device was fabricated with commercially available material designed for the emission at 1550 nm, purchased from IQE. The lasing material consists of 5 compressively strained 6 nm wide AlGaInAs quantum wells on an n-doped InP substrate. The upper p-doped cladding consists of a 0.2 µm InGaAs cap layer, which is followed by a 0.05 µm of InGaAsP, lattice matched to 1.62 µm of InP. The ridge and slot features are defined by standard lithographic techniques, with a ridge width of 2.5 µm and a height of 1.7 µm, and a slot width of 1 µm, with the ridge etch stopping above the quantum wells [9]. The slots were used for both optical reflection, as well as electrical isolation between the different sections of the PIC. A ground-signal-ground (GSG) contact was added to the slave section to allow for the high-frequency gain switching of the device.

The master section of the device is made up of a gain section, 600 µm in length, and a mirror section. The mirror section is made up of 8 slots with an interslot separation of 108 µm. These slots act as reflective defects along the

ridge by creating regions of lower effective refractive index, effectively creating a master laser that is both single mode and tunable [5,10]. This master laser couples through a deep etched isolation slot and is integrated with a 1100 µm deep etched waveguide. This waveguide is in turn integrated with a 410 µm slave laser via another deep etched facet.

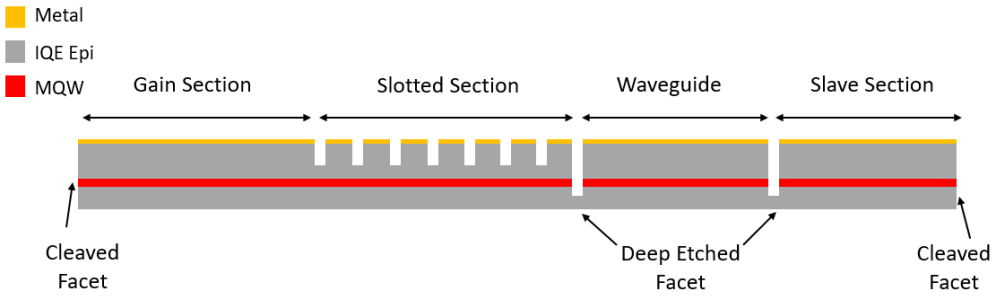


Fig. 1. Side view of PIC design.

RESULTS

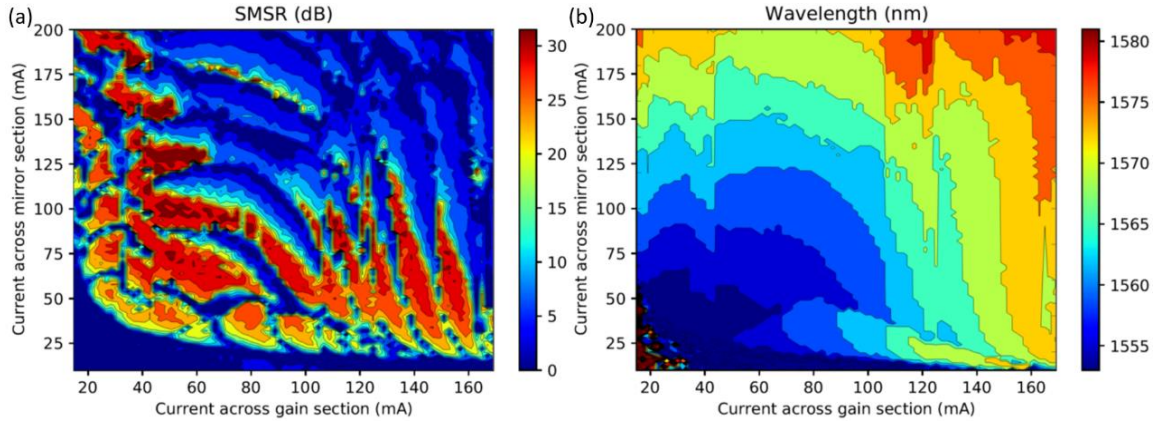


Fig. 2. (a) SMSR and (b) lasing wavelength of the master laser.

The master laser was initially characterized by biasing the gain and mirror sections of the device independently, sweeping the current through both sections and measuring the spectra through the cleaved facet of the master laser at each interval. The SMSR and lasing wavelength were recorded and plotted as shown in Fig. 2.

When the single mode nature of the master laser was determined, the deep etched waveguide was biased enough to make the waveguide passive, The slave laser was also biased just above threshold current and the spectra of the slave laser was optically phased locked to that of the master. A strong RF signal was applied to the slave laser to allow for gain switching to occur and a comb to be generated.

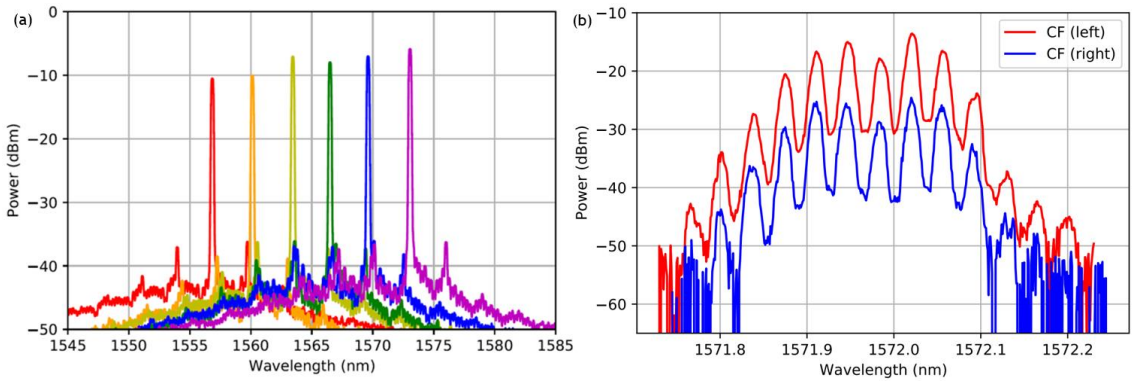


Fig. 3. (a) Single mode spectra determined by the master laser (b) Generated combs measured through the left and right facets.

Once the generated comb was detected through the slave laser facet (the right facet in Fig. 1), the comb was also detected through the master laser facet (the left facet). This is demonstrated in Fig.3(b).

This phenomenon is an example of bidirectional coupling which occurs between the single mode and gain switched lasers, and using the delayed differential equation model, simulations support these results (Fig. 4). The delay in the injection from the physical space between the lasers is also taken into account. The delay is normalized to the photon lifetime and this value is adjusted to determine the effect of the delay, and by doing so, the effect of the size of the device. As demonstrated in Fig. 4, the bidirectional model works best at producing combs at small delays. This is consistent with the experimental results as it is an on-chip device.

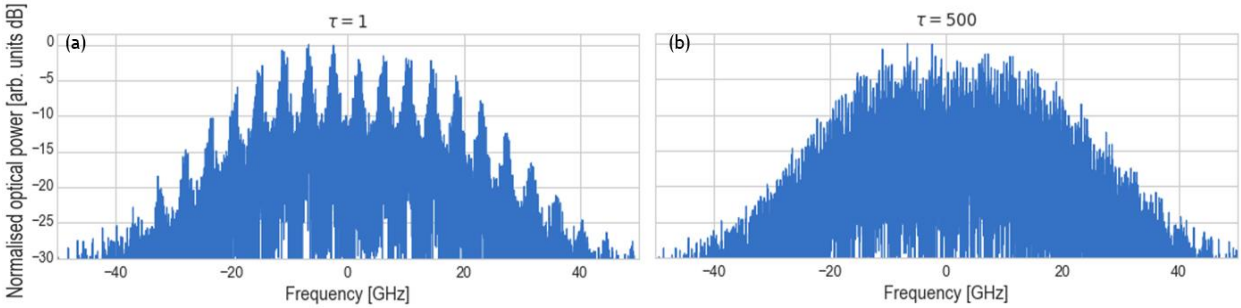


Fig. 4. Simulation of a bidirectional comb with a photonic lifetime of (a) 10 ps and (b) 5 ns.

CONCLUSION

This PIC demonstrates how a bidirectional coupled comb can be attained with an on-chip device. An optical frequency comb was obtained from the PIC by gain switching a slave laser that has been injection locked to a single mode master laser. Due to the reflective defects caused by the slots used in the mirror of the master, the master laser was shown to have a single mode and tunable wavelength. The short photon lifetime of the on-chip device allows for the bidirectional coupling to occur, as the comb generated by the gain switched slave laser is also detectable through the master laser. This is an advantage for future PIC designs as it allows for a comb to be propagated along different outputs without requiring a more complicated design.

ACKNOWLEDGMENTS

This work was supported by Science Foundation Ireland under grants 12/RC/2276 (IPIC), and SFI/13/IA/1960.

References

[1] I. Coddington, W. Swann, and N. Newbury, “Coherent multiheterodyne spectroscopy using stabilized optical frequency combs,”

[2] X. Wang, S. Takahashi, K. Takamasu, and H. Matsumoto, “Space position measurement using long-path heterodyne interferometer with optical frequency comb,” Opt. Express 20(3), 2725-2732 (2012).D. Jones, *Title of publication*, Journal name, vol. 1, no. 2, pp. 121-127, 2012

[3] A. Ellis and F. Gunning, “Spectral density enhancement using coherent WDM,” IEEE Photon. Technol. Lett. 17(2), 504-506 (2005).

[4] R. Zhou, P. M. Anandarajah, D. G. Pascual, J. O’Carroll, R. Phelan, B. Kelly, and L. P. Barry, “Monolithically integrated 2-section lasers for injection locked gain switched comb generation,” Optical Fiber Communications Conference and Exhibition (2014).

[5] L .Barry, P. Anandarajah, and A. Kaszubowska, “Optical pulse generation at frequencies up to “0 GHz using external-injection seeding of a gain switched commercial fabry-perot laser,” IEEE Photonics Technol. Lett. 13, 1014-1016 (2001).

[6] J. K. Alexander, P. E. Morrissey, H. Yang, P.J. Marraccini, B. Corbett, and F. H. Peters, “Monolithically integrated low linewidth comb source using gain switched slotted fabry-perot lasers,” Opt. Express 24, 7960-7965 (2016).

[7] A. Tauke-Pedretti, G. A. Vawter, E. J. Skogen, G. Peake, M. Overberg, C. Alford, W. W. Chow, Z. S. Yang, D. Torres, and F.Cajas, “Mutual injection locking of monolithically integrated coupled-cavity DBR lasers,” IEEE Photonics Technol. Lett. 23, 908-910 (2011).

[8] A. H. Perrott, L. Caro, M. Dernaika, and F.H. Peters, “A comparison between off and on-chip injection locking in a photonic integrated circuit,” Photonics 6 (2019).

[9] Zhengkai Jia, Hua Yang, Alison H. Perrott, Hui Wang, and Frank H. Peters, "Study on the proximity of QWI in InP-based AlGaInAs MQWs using the IFVD method and its application in single frequency teardrop laser diodes," Opt. Express 28, 31904-31913 (2020)

[10] Q. Y. Lu, W. H. Guo, R. Phelan, D. Byrne, J. F. Donegan, P. Lambkin, and B. Corbett, “Analysis of slot characteristics in slotted singlemode semiconductor lasers using the 2-D scattering matrix method,” IEEE Photonics Technol. Lett. 18, 2605-2607 (2006).

Subwavelength metamaterial grating couplers on silicon nitride platform

Student paper

Radovan Korcek[1], William Fraser[2], Daniel Benedikovic[1,2,3,*], Carlos Alonso-Ramos[4], Laurent Vivien[4], Pavel Cheben[5], Jens H. Schmid[5], Maziyar Milanizadeh[5], and Winnie N. Ye[2]

[1]Dept. Multimedia and Information-Communication Technologies, University of Zilina, 010 26 Zilina, Slovakia
[2]Dept. Electronics, Carleton University, ON K1S5B6 Ottawa, Canada
[3]University Science Park, University of Zilina, 010 26 Zilina, Slovakia
[4]Centre de Nanosciences et de Nanotechnologies, CNRS, Universite Paris-Saclay, 91120 Palaiseau, France
[5]National Research Council Canada, ON K1A 0R6 Ottawa, Canada
[*]daniel.benedikovic@uniza.sk

We present design and experimental results of single-etch silicon nitride grating couplers engineered with sub-wavelength grating metamaterials. For fabricated devices, we measured coupling loss of -3.9 dB and -4.4 dB at *C*-band wavelength range. Moreover, by judiciously designing the apodized-imaging grating coupler topology, fibre-to-chip coupling loss of -1.6 dB loss is predicted by finite difference time domain simulations.

Keywords: *Surface grating couplers, Subwavelength metamaterials, Silicon Nitride platform*

INTRODUCTION

Near-infrared (NIR) wavebands, ranging from 1260 nm to 1675 nm, are particularly interesting for communication applications, including short-reach data communications and long-distance telecommunications. Such applications call upon integrated platforms for developing low-cost and high-yield systems on a photonic chip. Among others, silicon nitride (SiN) is a compelling platform for photonic integration due to its wide transparency, low waveguide losses, and compatibility with complementary metal-oxide-semiconductor (CMOS) fabrication processes [1]. Waveguide dimensions in high-index contrast integrated photonics are typically in the sub-micrometric range, making the interconnection between the chip and external ports particularly challenging. Even though compared to silicon-on-insulator (SOI) waveguides [2], the index contrast (of about1 to 0.5) between the SiN waveguide core and its air/silicon dioxide (SiO_2) cladding is more moderate, it is still challenging to obtain low coupling loss, when the integrated SiN chips are interfaced with standard optical fibres [1,2]. Surface grating couplers are an attractive solution for coupling light in and out from photonic waveguides. Grating couplers are compliant with planar manufacturing and wafer-level testing, allow flexible placement on a chip surface, and have comparatively large alignment tolerances to fibre attachments. However, SiN waveguide couplers have higher losses due to the reduced the grating strength. To date, a number of approaches have been explored [3-8], with a steady progress in increasing the coupling efficiency. This includes SiN couplers with Bragg and metal mirror underneath [3,4], stair-like gratings [5], bi-layer topologies [6] and top overlays [7], or SiN-on-SOI platforms [8]. However, such approaches are comparatively complex to fabricate and require dedicated processing steps, which indeed comes with additional expenses. To keep the process cost low, single-etch grating couplers appear as optimal choice. Nevertheless, the limited degree of design freedom in single-etch devices has so far been the limiting factor to boost their coupling performances.

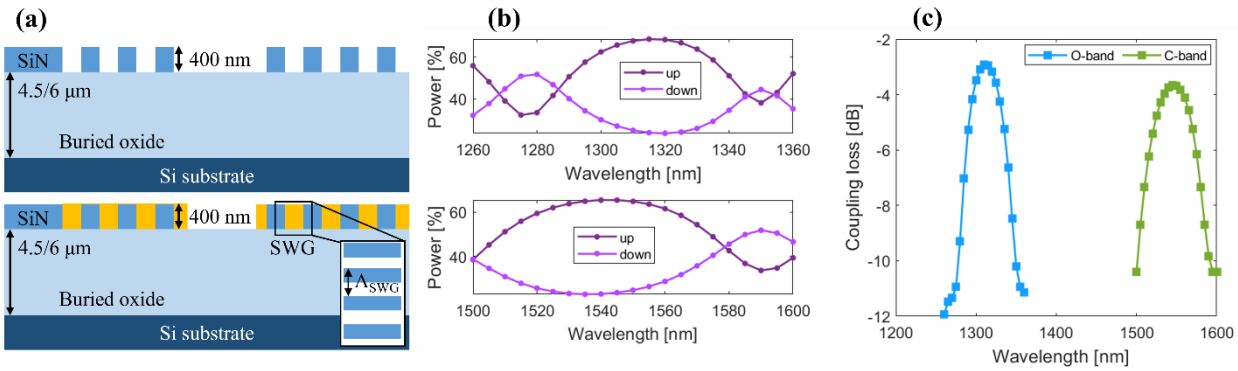


Fig. 1: (a) Vertical schematics of the single-etch grating couplers, without and with SWG-index-engineered grooves. (b) Power radiated upwards and downwards and (c) coupling loss as a function of wavelength for O- and C-band device designs.

In this work, we report on design and experiments of single-etch-step surface grating couplers realized on the SiN photonic platform, with and without a subwavelength grating (SWG) engineered medium. Since their first demonstration in silicon photonics [10,11], SWG metamaterials [12-14] have been used as a powerful engineering tool for overcoming performance limitations of conventional silicon photonic devices. Grating couplers are designed for central wavelengths of 1.31 µm (*O*-band) and 1.55 µm (*C*-band), respectively, both harnessed by mainstream fibre-optic communication systems.

UNIFORM GRATING COUPLERS

Figure 1(a) shows a side view schematics of the single-etch SiN surface grating couplers, without and with SWG-engineered grooves. Couplers are made in a 400 nm SiN platform, with either 4.5 µm or 6 µm thick buried oxides (BOX). The air serves as upper cladding. The light from standard optical fibers, with mode field diameters (MFDs) of 9.2 µm (at 1.31 µm) and 10.4 µm (at 1.55 µm), is coupled into a SiN chip to the in-plane transverse electric (TE) fundamental mode of the waveguide. Grating couplers were designed and analyzed by using Lumerical finite difference time (FDTD) tool from the Ansys, Inc [9].

Figures 1(b) shows the powers radiated towards an optical fiber and a bottom Si substrate as a function of the wavelength for *O*-band and *C*-band couplers, respectively. In both coupler designs, the power up and the power down reach their maxima and minima of about 68% and 23%, respectively, yielding a peak grating directionality up to 70%. The directionality of the coupler is governed by the effect of thin-film interference at the substrate-to-BOX interface. The maximum directionality can be obtained by optimizing the BOX thickness or by judiciously adjusting the grating radiation angle [15-17]. With designed coupling angles of -36° and 4.5 µm BOX (*O*-band) and -15° and 6 µm BOX (*C*-band), the peak coupling losses of -2.8 dB and -3.7 dB are predicted by FDTD calculations. In both designs, negative coupling angles are chosen to favor single-beam operation, while avoiding higher-order radiation. Figure 1(c) shows the spectral performance of designed *O*-band and *C*-band fiber-chip grating couplers. The 1-dB coupler bandwidths are 33 nm and 41 nm, respectively.

Grating couplers were fabricated on a SiN platform with 400 nm core and 6 µm BOX and connected in a back-to-back configuration using adiabatic tapers and interconnection single-mode strip waveguides. The couplers and interconnecting waveguides were defined in the same step by electron beam lithography. The device patterns were transferred into the SiN waveguide layer by reactive ion etching. Figure 2(a) show a fiber-chip coupling loss as a function of the wavelength for a uniform *C*-band-operated grating couplers, with air and SWG fully etched grooves. The back-to-back tested peak coupling losses are -3.9 dB and -4.4 dB, respectively.

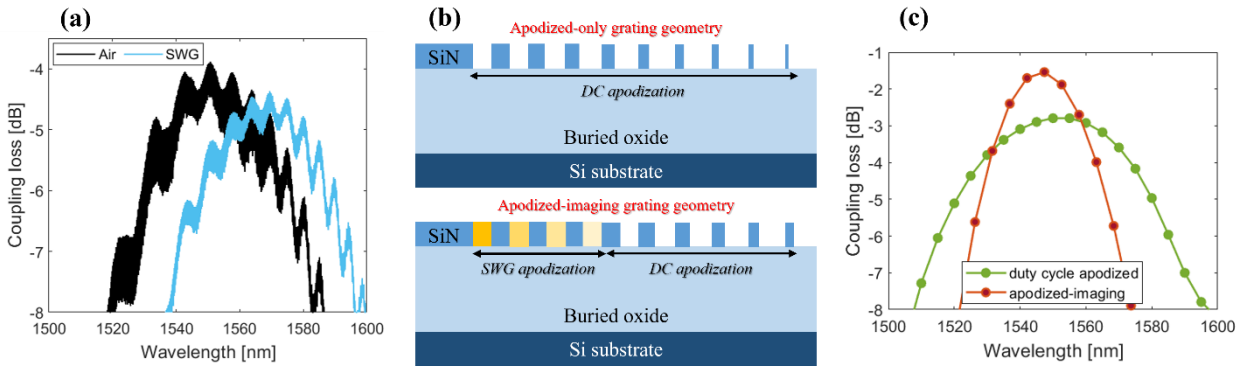


Fig. 2: (a) Measured coupling loss as a function of wavelength for fabricated SiN surface grating couplers. (b) Vertical schematics and (c) calculated coupling loss of the apodized and apodized-imaging surface grating couplers.

APODIZED GRATING COUPLERS

Due to the lower index contrast in SiN waveguides, grating couplers are too weak, which makes it difficult to design gratings that radiate all the power within a length that matches the MFD of conventional optical fibers. Further improvement of grating coupler performance was obtained through grating apodization.

Here, grating couplers were apodized by exploiting two apodization schemes: (i.) single duty cycle apodization and (ii.) combined apodization via duty cycle and SWG refractive index engineering, while leveraging a self-imaging effect. In both schemes, the grating strength is varied along the direction of mode propagation by either changing the duty cycle or by changing the duty cycle and synthesizing different SWG metamaterials in fully etched grating grooves. Both apodization approaches are schematically shown in Fig. 2(b). In the first case, the grating radiation angle is kept constant for all grating radiation units and the grating period was appropriately chirped , thus satisfying the phase matching condition. In the second case, besides the grating strength adjustment, the coupling angle and the period are not constant, yet they are allowed to vary along the mode propagation to facilitate the imaging effect

Figure 2(c) shows the coupling loss as a function of the wavelength for grating coupler designs at telecom spectral range, with duty cycle and self-imaging-assisted apodizations. The peak coupling loss for a duty cycle apodized design was estimated to be -2.9 dB, while apodized-imaging design improved the fiber-chip coupling loss up to -1.6 dB. Compared to the uniform grating coupler, the enhancement in coupling loss is directly linked to the improved modal overlaps between the profile of the out-radiated grating mode and Gaussian-like optical fiber mode.

CONCLUSION

In this work, we reported on low-loss surface grating couplers with engineered SWG metamaterials on a SiN waveguide platform and single-etch step fabrication. Measured devices yielded coupling loss of -3.9 dB and -4.4 dB near 1.55 µm wavelength range. Furthermore, optimized fiber-chip couplers with apodized-imaging grating geometry yielded coupling loss of -1.6 dB. These results are promising for the development of low-cost and efficient fiber-coupled surface grating interfaces as required by SiN-founded applications, including interconnects, communications, and quantum science.

Acknowledgements

This work was supported by the Slovak Research and Development Agency under the project APVV-21-0217, Slovak Research Agency VEGA 1/0113/22, and Grant System of University of Zilina No. 1/2022 (17335).

References

[1] C. Xiang, W. Jin, and J. E. Bowers, *Silicon nitride passive and active photonic integrated circuits: trends and prospects*, Photonics Research, vol. 10, no 6, pp. A82-A96, 2022

[2] Roel Baets, et al., *Silicon Photonics: silicon nitride versus silicon-on-insulator*, In Proc. of Optical Fiber Communication Conference, pp. Th3J.1, 2016

[3] S. Nambiar, A. Chatterjee, and S. K. Selvaraja, *Comprehensive grating enabled silicon nitride fiber-chip couplers in the SNIR wavelength band*, Optics Express, vol. 30, no. 3, pp. 4327-4341, 2022

[4] S. Romero-García, F. Merget, F. Zhong, H. Finkelstein, and J. Witzens, *Visible wavelength silicon nitride focusing grating coupler with AlCu/TiN reflector*, Optics Letters, vol. 38, no 14, pp. 2521-2523, 2013

[5] Y. Chen, T. Domínguez Bucio, A. Z. Khokhar, M. Banakar, K. Grabska, F. Y. Gardes, R. Halir, Í. Molina-Fernández, P. Cheben, and J.-J. He, *Experimental demonstration of an apodized-imaging chip-fiber grating coupler for Si3N4 waveguides*, Optics Letters, vol. 42, no. 18, pp. 3566-3569, 2017

[6] E. W. Ong, N. M. Fahrenkopf, and D. D. Coolbaugh, *SiNx bilayer grating coupler for photonic systems*, OSA Continuum, vol. 1, no. 1, pp. 13-25, 2018

[7] B. Chmielak, S. Suckow, J. Parra, V. C. Duarte, T. Mengual, M. A. Piqueras, A. L. Giesecke, M. C. Lemme, and P. Sanchis, *High-efficiency grating coupler for an ultralow-loss Si3N4-based platform*, Optics Letters, vol. 47, no. 10, pp. 2498-2501, 2022

[8] S. Guerber, C. Alonso-Ramos, D. Benedikovic, D. Pérez-Galacho, X. Le Roux, N. Vulliet, S. Crémer, L. Babaud, J. Planchot, D. Benoit, P. Chantraine, F. Leverd, D. Ristoiu, P. Grosse, D. Marris-Morini, L. Vivien, C. Baudot, and F. Boeuf, *Integrated SiN on SOI dual photonic devices for advanced datacom solutions*, In Proc. SPIE Photonics Europe, pp. 106860W, 2018

[9] Ansys Lumerical FDTD. Available: http://ansys.com

[10] P. Cheben, D-X. Xu, S. Janz, and A. Densmore, *Subwavelength waveguide grating for mode conversion and light coupling in integrated optics*, Optics Express, vol. 14, no. 11, pp. 4695-4702, 2006.

[11] P. Cheben, P. J. Bock, J. H. Schmid, J. Lapointe, S. Janz, D.-X. Xu, A. Densmore, A. Delâge, B. Lamontagne, and T. J. Hall, *Refractive index engineering with subwavelength gratings for efficient microphotonic couplers and planar waveguide multiplexers*, Optics Letters, vol. 35, no 15, pp. 2526-2528, 2010

[12] P. Cheben, R. Halir, J. Schmid, H. Atwater, D. Smith, *Subwavelength integrated photonics*, Nature, vol. 560, no. 7720, pp. 565-572, 2018

[13] R. Halir, A. Ortega-Moñux, D. Benedikovic, G. Z. Mashanovich, J. G. Wangüemert-Pérez, J. H. Schmid, Í. Molina-Fernández, and P. Cheben, *Subwavelength-Grating Metamaterial Structures for Silicon Photonic Devices*, Proceedings of the IEEE, vol. 106, no. 12, pp. 2144-2157, 2018

[14] J. M. Luque-González, A. Sánchez-Postigo, A. Hadij-ElHouati, A. Ortega-Moñux, J. G. Wangüemert-Pérez, J. H. Schmid, P. Cheben, Í. Molina-Fernández, and R. Halir, *A review of silicon subwavelength gratings: building break-through devices with anisotropic metamaterials*, Nanophotonics, vol. 10, no.11, pp. 2765-2797, 2021

[15] D. Benedikovic, P. Cheben, J. H. Schmid, D.-X. Xu, J. Lapointe, S. Wang, R. Halir, A. Ortega-Moñux, S. Janz, and M. Dado, *High-efficiency single etch step apodized surface grating coupler using subwavelength structure*, Laser and Photonics Reviews, vol. 8, no. 6, pp. 93-97, 2014

[16] D. Benedikovic, P. Cheben, J. H. Schmid, D.-X. Xu, B. Lamontagne, S. Wang, J. Lapointe, R. Halir, A. Ortega-Moñux, S. Janz, and M. Dado, *Subwavelength index engineered surface grating coupler with sub-decibel efficiency for 220-nm silicon-on-insulator waveguides*, Optics Express, vol. 23, no. 17, pp. 22628-22635, 2015

[17] D. Benedikovic, C. Alonso-Ramos, P. Cheben, J. H. Schmid, S. Wang, R. Halir, A. Ortega-Moñux, D.-X. Xu, L. Vivien, J. Lapointe, S. Janz, and M. Dado, *Single-etch subwavelength engineered fiber-chip grating couplers for 1.3 µm datacom wavelength band*, Optics Express, vol. 24, no. 12, pp. 12893-12904, 2016

Integrated four channel wavelength multiplexer in Thin Film Lithium Niobate for CWDM 400G/800G short reach communications

Giuseppe Cusmai[1], Riccardo Marchetti[1], Piero Orlandi[1], Andrea Martellosio[1] and Roberto Longone[1]

[1] Advanced Fiber Resourced – San Donato Milanese, 20097 Italy
* giuseppe.cusmai@fiber-resources.com

A four-channel multiplexer operating in the O-band for 400GBASE-FR4 and 800G-2xFR4 applications is demonstrated on Thin Film Lithium Niobate. Critical phase error arising from fabrication process is analysed. Design improvements are discussed to increase multiplexer tolerance to phase error.
Keywords: *LNOI, multiplexer, lithium niobate, optical waveguides*

INTRODUCTION

Over the last few years Thin Film Lithium Niobate (TFLN) arose as a very promising technological platform for several applications. The possibility for new generation devices, complex architectures with small footprints and low losses have made TFLN attractive in different fields such as telecommunication and datacom, quantum photonics and sensing. This is due, from one side, to the excellent properties of LiNbO3 (electro-optic, nonlinear-optic, acousto-optic, piezoelectric and pyroelectric) and from the other side to the high integration potential enabled by the high index contrast. Datacom applications are of particular interest since costs, footprint, bandwidth and losses are critical requirements. These requirements can be met only by a technological platform able to integrate various functionality on a single chip as, for example, wavelength management in case of CWDM communication protocols. Key CWDM-based protocols for the development of short reach intra-datacenter communications (from 500 m up to 2 Km) are the 400GBASE-FR4 and the 800G-2xFR4. The first, addressing 400 Gigabit ethernet links through a 4 channels CWDM system, the latter addressing 800 Gigabit ethernet links through a system based on two parallel 4 channels CWDM lanes. Both operating in the O-band. Fundamental building blocks for these applications are wavelength multiplexer (MUXes) and de-multiplexers (DE-MUXes). Different solutions providing wavelength multiplexing have been proposed in many integrated photonics platforms [1-3] but the most performing in terms of insertion loss and crosstalk are based on interferometric filters, enabling very high flat top optical responses [4]. On the other hand, a severe drawback for these architectures is the high sensitivity to interferometric paths phase errors which are linked to technological limits in controlling optical waveguides characteristics (i.e., side-wall roughness, etch depth, film thickness and refractive index uniformity) [3]. On more mature platforms this issue has been reasonably solved [3], while recent TFLN platforms are still struggling to achieve a process control in waveguide definition enabling acceptable phase errors for passive interferometric structures designs.

In this work we present a passive MUX fabricated on 4” TFLN X-Cut wafers for transmitters targeting FR4 and 2xFR4 applications. The architecture is based on well-known cascaded Mach Zehnder Interferometers (MZIs) lattice filters [6]. A statistical analysis of the results obtained on several realizations of the device is presented. Then, through a comparison between statistical experimental data and theory the process phase error has been quantified. Finally, some considerations on possible design improvements to increase tolerance to process fluctuations are presented.

DESIGN AN MODELING

X-Cut TFLN wafers are considered for the design and realization of the device. The simulated waveguide cross section is reported in Fig.1(a).

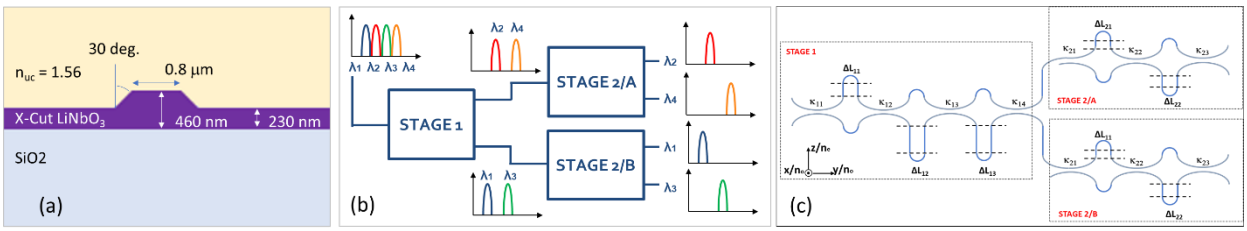


Fig. 1. (a) Waveguide cross section. (b) Block diagram schematics of the multiplexer. (c) Schematics of the multiplexer stages.

A LiNbO3 film thickness of 460 nm and an etch depth of 230 nm has been set to minimize polarization rotation effects that might occur due to TE and TM modes hybridization [7,8]. A 0.8 μm waveguide width ensures single mode operation in the O-band. A waveguide sidewall angle of 30° is then considered as representative of the final waveguide shape due to the etching process. An upper cladding with refractive index n_{uc}=1.56 at 1310 nm is taken into account. Under these conditions the quasi-TE fundamental mode effective index and group index are n_{effY}=1.900, n_{gY}=2.206 along crystal Y-axis propagation direction (Y-prop) and n_{effZ}=1.967, n_{gZ}=2.354 along crystal Z-axis propagation direction (Z-prop).

The proposed 4-channels CWDM MUX is based on a double stage cascaded MZIs lattice filters according to [4,5] and schematically reported in Fig.1(b) and Fig.1(c). Stage1 combines odd and even channels couples with a free spectral range (FSR) equal to 20 nm. Stage2/A and Stage2/B combine respectively even and odd channels with FSR = 40nm. Channels central wavelengths are λ_1=1271 nm, λ_2=1291 nm, λ_3=1311 nm and λ_4=1331 nm. In-band channel spectral response flat top shape is increased as the number of MZIs is increased within each stage. For Stage1 the choice has been to use 3 lattices cascaded MZIs, while only 2 are used in Stage2/A and Stage2/B. Coupling coefficients κ_{ij} and geometrical length imbalance ΔL_{ij} (where i refers to the stage number and j to the device number within the stage) are set to: κ_{11}=0.5, κ_{12}=0.2, κ_{13}=0.2, κ_{14}=0.04, $\Delta L_{11}=\Delta L$, $\Delta L_{12}=2*\Delta L$, $\Delta L_{13}=2*\Delta L+\Delta L_\pi$ for Stage1 and κ_{21}=0.5, κ_{22}=0.29, κ_{23}=0.08, $\Delta L_{21}=\Delta L/2$, $\Delta L_{22}=\Delta L$ for Stage2, where ΔL=36.45 μm and ΔL_π=0.33 μm for Stage1, ΔL=18.5 μm for Stage2/A and ΔL=18.22 μm for Stage2/B. The complete device ends up having a total of 14 interferometric paths (3 in Stage1 = 6 arms, 2 in Stage2/A = 4 arms, 2 in Stage2/B = 4 arms).

To minimize phase error effects due to mode conversion, length imbalances are designed in Z-prop exploiting the higher birefringence between the first quasi-TE and first quasi-TM mode. Bend waveguides with bending radius equal to 100 μm have been used to ensure negligible radiation losses. Given this, the simulated ideal transfer functions are reported in Fig.2(a) as dashed black lines.

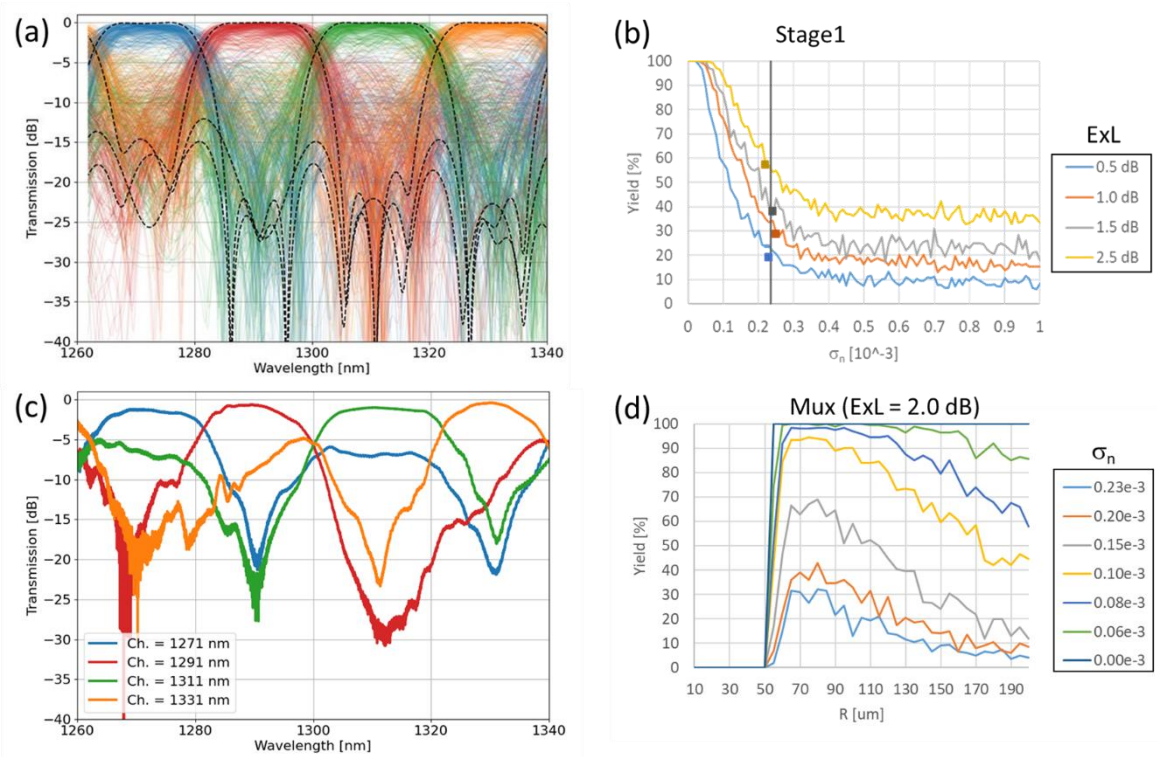


Fig.2. (a) Simulated ideal transfer functions (dashed) of the MUX and effects of random phased errors on the MZIs arms. (b) Stage1 simulated and experimental (squares) yield as a function of σ_n and pass/fail threshold ExL. (c) Measured performance of a fabricated MUX having ExL=2.0 dB. (d) MUX yield as a function of bending radius R and σ_n for ExL = 2.0 dB.

To model the impact of phase error on device performances, we have added a random phase to each optical path of the interferometers $\Delta\phi_v = (2\pi/\lambda)nL_v$ (v=1 to 14) where n is a gaussian stochastic variable with mean equal to 0 and standard deviation equal to σ_n, L_v is the geometrical length of the considered path. In Fig.2(a) as transparent lines are reported the simulated transfer functions obtained in case of 100 realizations with σ_n=0.1e-3. The larger σ_n the greater is the detrimental effect. To quantify the detrimental effect as a function of σ_n we have set the quality parameter as the maximum loss among the channels central wavelengths (MaxLoss) and defined a yield as the ratio between pass and overall realizations where pass are the realizations respecting MaxLoss < ExL being ExL the

threshold value for the pass/fail criteria. Simulated results limited to Stage1 only are reported in Fig.2(b) as solid lines in case of 100 realizations for each value of σ_n and ExL. With the considered conditions, a σ_n <= 0.1e-3 should be attained to provide high yield.

EXPERIMENTAL RESULTS AND ANALYSIS

800G-2xFR4 transmitters have been fabricated using commercially available 4'' LNOI X-Cut wafers. Low-loss waveguides (<0.25 dB/cm), electro-optic modulators, grating couplers (for testing and monitoring Photodiodes), Spot Size Converters (SSC) edge couplers (<1.5 dB/interface) and the 2 multiplexers have been defined with ICP process. To analyze the impact of the phase errors on the MUX, a stand-alone MUX as well as a Stage1-only interleaver structure have been fabricated. An example of a fabricated MUX with ExL=2.0dB is reported in Fig.2(c).

By comparing model predictions and experimental yield of Stage1 fabrications (over 60) as a function of ExL, we have estimated σ_n as reported in Fig.2(b) (square symbols). By setting ExL to 0.5dB, 1.0dB, 1.5dB and 2.5dB we have obtained yields of 19%, 28.6%, 38.1% and 57.1% respectively. The four experimental points match the theoretical curves if σ_n=0.23e-3.

To improve tolerance, we have simulated yield of the MUX as a function of σ_n and a design radius of curvature including radiation and propagation losses in the model. Results are reported in Fig.2(d). Maximum yields are achieved for bending radius equal to 80 μm which turns out to be the best compromise between radiation, propagation losses and device footprint. With σ_n =0.23e-3 a maximum yield of 30% is foreseen. With process improvement enabling σ_n =0.1e-3 a yield above 90% can be reached.

DISCUSSION

Experimental data of the designed multiplexer structures fabricated on a 4" X-Cut TFLN wafers have been analyzed to gather yield statistics based on a variable value of pass/fail criteria (maximum channel insertion loss).

By comparing the experimental and theoretical yield as a function of pass/fail loss threshold, we have determined process phase error standard deviation to be σ_n=0.23e-3.

Our model prediction is that tolerance to process phase errors can be improved by reducing building blocks footprint acting for instance on the choice of maximum bending radius which should be the best tradeoff between radiation, propagation losses and device footprint. Optimum radius of curvature turns out to be 80 μm. Moreover, process improvements decreasing σ_n to 0.1e-3 would enable multiplexer yields up to 90%. Future designs will be aimed to confirm this theoretical prediction.

References

[1] Y. Hu et al., *MMI for wavelength filtering and WDM on the SOI platform*, in Proceedings of IEEE Photonic Society 24th Annual Meeting, pp. 615-616, 2011

[2] W. Shi et al., *Ultra-compact, flat-top demultiplexer using anti-reflection contra-directional couplers for CWDM networks on silicon*, Optics express, vol. 21, no. 6, pp. 6733-6738, 2013

[3] Gengxin Chen et al., *Four-channel CWDM device on a thin-film lithium niobate platform using an angled multimode interferometer structure*, Photonics Research vol. 10, no. 1, pp. 8-13, 2022

[4] S. S. Cheung and M. R. T. Tan, *Silicon nitride (Si_3N_4) (De-)multiplexers for 1-μm CWDM optical interconnects*, Journal of Lightwave Technology, vol. 38, no. 13, pp. 3404-3413, 2020

[5] S. Dwivedi et. al, *Coarse wavelength division multiplexer on silicon-on-insulator for 100 GbE*, in IEEE 12th International Conference on Group IV Photonics (GFP), pp. 9-10, 2015

[6] F. Horst et al., *Cascaded Mach-Zehnder wavelength filters in silicon photonics for low loss and flat pass-band WDM (de-) multiplexing*, Optics express, vol. 21, no. 10, pp. 11652-11658, 2013

[7] C. K. Madsen, J. H. Zhao, *Optical filter design and analysis*, Wiley, New York, 1999.

[8] G. Cavicchioli et al., *Mitigating Polarization Rotation Effects in Thin-Film Lithium Niobate Waveguides*, in Proceedings of 23rd European Conference on Integrated Optics, pp. 45-47, 2022

[9] A. Pan et al., *Fundamental mode hybridization in a thin film lithium niobate ridge waveguide*, Optics Express, vol. 27, no. 24, 2019.

Thermo-optically Tunable DBR Resonator with Ultra-broad Rejection Band for Silicon Photonic Applications

Student paper

Pratyasha Priyadarshini*, Arnab Goswami, Ashitosh Velamuri and Bijoy Krishna Das

Centre for Programmable Photonic Integrated Circuits and Systems
Department of Electrical Engineering, IIT Madras, Chennai – 600036, India
* priyadarshinipratyasha@gmail.com

A design of compact DBR resonators (~ 40 µm-long) integrated in SOI rib waveguide structure has been demonstrated, exhibiting a resonance bandwidth as low as 40 pm (λ_r ~ 1550 nm) with an extinction of ~ 35 dB over a rejection band of ~ 60 nm. The resonance peak has been thermo-optically tuned over a wide range of wavelength at a rate of ~ 95 pm/mW. The device is shown to be effective in ASE noise suppression of an amplified pump laser.
Keywords: *Silicon Photonics, DBR Resonators, Tunable Filters, Noise Suppression*

INTRODUCTION

Resonator devices find many applications in photonic integrated circuits (PICs). For example, microring resonators (MRRs) in all-pass and add-drop configurations are widely used in CMOS compatible silicon photonics technologies for filtering, switching, modulation, sensing and nonlinear signal processing [1]. Distributed Bragg reflector (DBR) based resonators can be a good alternative to overcome certain limitations of an MRR. To be specific, a DBR resonator can be designed to oscillate in a single longitudinal mode. Moreover, a suitably designed DBR resonator can potentially offer a broad sideband rejection, enabling noise suppression around the resonant wavelength of interest and it can be widely tuned via thermo-optic effect and plasma dispersion effect. Recently, some DBR based resonators have been demonstrated for various applications such as sensing, wavelength add-drop multiplexing, modulation and microwave signal processing [2] as well as quantum photonic applications [3]. The rejection bandwidth around the resonance wavelength of a singly resonant DBR has been reported to be ~ 15 nm for a device length of > 150 µm [4]. In this paper, we demonstrate a compact design of DBR cavity (device length of ~ 40 µm), resonating around λ ~ 1550 nm within an ultra-broad rejection band (~ 60 nm). We have also shown experimentally the thermo-optic detuning characteristics of resonance wavelength with a slab-integrated metal microheater and suppression of ASE noise associated with an amplified pump laser which is tuned to operate at resonance.

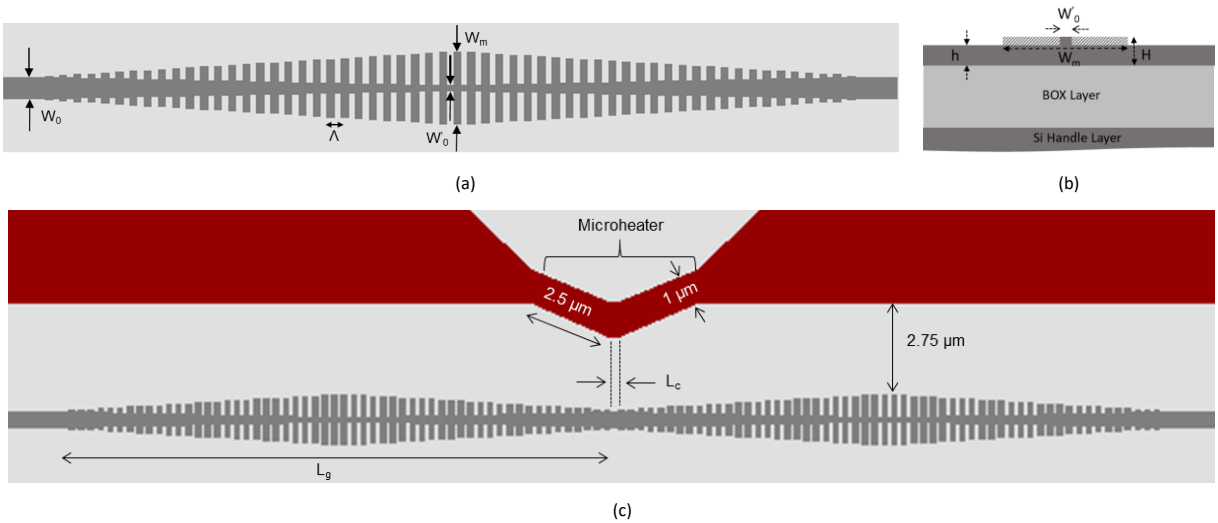


Fig. 1. Schematics of the proposed DBR resonator along with design variables and parameters: (a) top-view of DBR structure integrated into a single-mode rib waveguide used as cavity mirrors, (b) cross-section view of the DBR at the center, and (c) top-view of the proposed device integrated with Ti microheater. H - device layer thickness (220 nm), h - rib height (150 nm), W_0 - input/output waveguide width for fundamental TE mode guidance (~ 500 nm), W_m - maximum width of the DBR, W'_0 - minimum width of the tapered waveguide, Λ - grating period, L_g - length of the DBR mirror, L_c - length of the cavity.

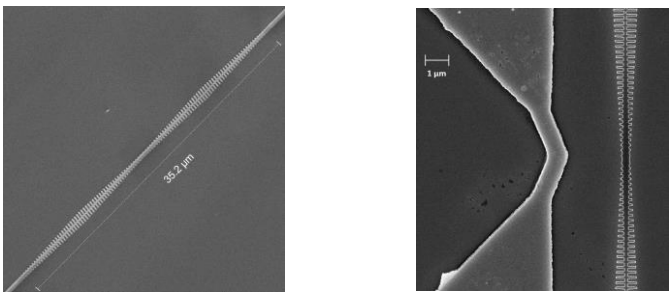
DESIGN AND FABRICATION

Based on our earlier reported experimental results and theoretical simulations, a compact design of single-stage DBR cavity has been optimized. The design scheme of the device has been shown in Fig. 1 along with design variables and parameters. The parameter values of the DBR structure have been optimized following the design rule in Ref. [5]. The values of L_g, W_m, W'_0 and the grating periodicity Λ (50 % duty cycle) are carefully chosen to obtain high reflectivity over a broad wavelength range around a Bragg wavelength of $\lambda_B \sim 1550$ nm. Higher reflectivity of the DBRs results into higher Q of the cavity, but at the cost of transmission loss at the resonance. Thus, for given values of W_m, W'_0 and Λ, we can simply control the L_g for a desired reflectivity and L_c for desired number of resonances within the stopband. For experimental demonstration, we have fabricated six different devices (D1 – D6) using two different DBR mirror lengths and three different cavity lengths as given in Table 1. Other design parameters were kept common for all the devices (W_m= 1.5 µm, W'_0 = 100 nm and Λ = 292 nm).

Table 1. Values of L_g and L_c used for device fabrication

Device	D1	D2	D3	D4	D5	D6
L_g (µm)	17.5	20.5	17.5	20.5	17.5	20.5
L_c (µm)	8		6		0.146	
Calculated no. of resonances	3		2		1	

A Ti-microheater (see Fig. 1) was integrated at the center of the DBR cavity for thermo-optic tuning of the resonances. The input/output waveguides were designed to support only the fundamental TE-mode (H = 220 nm, h = 150 nm and W_0= 450 nm). For characterization, the input/output waveguides were terminated with standard grating couplers. The length between input/output grating couplers has been set to ~ 3 mm for all the devices. To obtain normalized transmission characteristics, a reference waveguide (same as input/output waveguide parameters) was also fabricated with a same length of ~ 3 mm. The devices were fabricated using our in-house fabrication facilities and the details can be found elsewhere [6]. Fig. 2 shows the SEM images of a fabricated device of cavity length 0.146 µm (D5) and slab-integrated microheater.



(a) (b)

Fig. 2. SEM images of a fabricated device (D5): (a) single mode DBR resonator with waveguide DBR mirrors of cavity length 146 nm (45° tilted) and (b) zoomed cavity region with slab-integrated metal microheater.

EXPERIMENTAL RESULTS

The fabricated devices were characterized using a high resolution (0.8 pm) and high sensitivity (-75 dBm) optical source spectrum analyzer (APEX 2043B). The thermo-optic tuning of the cavity was achieved by biasing the microheaters using a Keithley source meter (model no. 2420). The normalized transmission characteristics of the devices with cavity lengths 8 µm (D1 and D2), 6 µm (D3 and D4) and 0.146 µm (D5 and D6) are given in Fig. 3(a), 3(b) and 3(c), respectively. As predicted, they are found to be triply-, doubly- and singly-resonant, respectively. It is observed from the transmission characteristics that the rejection bandwidth and extinction are found to be DBR length independent for a given cavity length. However, the Q values (transmission peaks) of the resonances are observed to be higher (lower) for the longer DBRs, which is in accordance with our theoretical prediction. The DBR rejection bandwidth is measured to be about ~ 60 nm for all the fabricated devices (D1-D6) i.e., nearly same for both the DBR lengths as predicted by the simulation results. The number of resonances are found to be 3, 2 and 1 for cavity lengths of 8 µm, 6 µm and 0.146 µm which are also consistent with the theory. In case of multimode resonators, the free spectral range (FSR) between resonances for longer DBRs is found to be slightly lower than that of shorter DBRs. This is attributed to the longer effective cavity length for the longer DBRs: the coupling strength between forward and backward propagating waves expected to be lower in case of longer DBR (as the values of both W_m and W'_0 are same for both the DBR lengths). The Q value of a singly resonant cavity with L_g = 17.5 µm (20.5 µm) is found to be ~ 39,000 (17,000) and corresponding out-of-band rejection is ~ 35 dB (~ 40 dB).

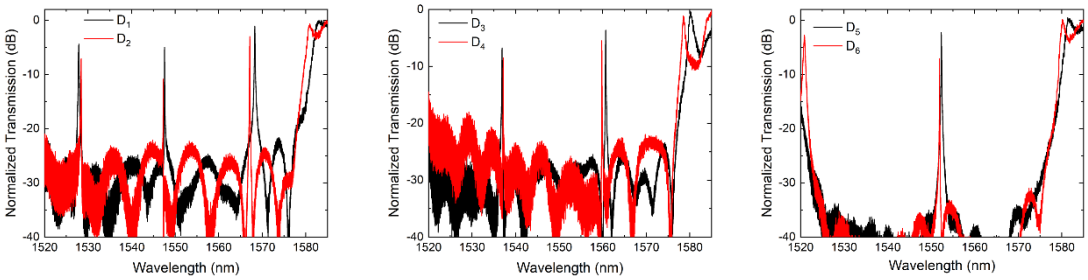


Fig. 3. Transmission spectra of fabricated devices normalized with respect to the reference waveguides. DBR resonators with cavity length of (a) 8 µm, (b) 6 µm and (c) 0.146 µm (inset the zoomed resonance peak of D5).

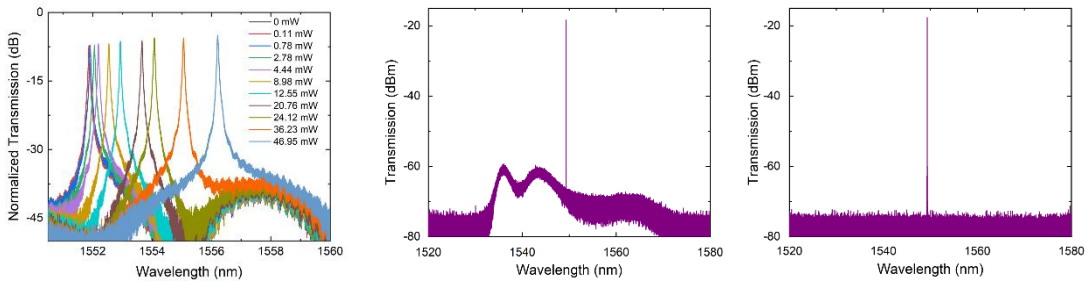


Fig. 4. Application use cases for a singly resonant DBR cavity (D6): Thermo-optic detuning of resonant wavelength for different heater powers (a), transmission of a pre-amplified pump laser through a reference waveguide (b) and ASE noise suppressed pump laser through the DBR cavity (c).

Fig. 4 shows experimental demonstrations of two application use cases of a singly resonant DBR cavity (D6). The first application is the wide range tuning of resonant wavelength using a microheater as shown in Fig. 4 (a). The tuning slope is obtained as ~ 95 pm/mW, which could be improved by introducing trenches through slab as well as BOX layer. However, the slab integrated microheater design (without trenches) can facilitate a faster switching response as reported in Ref. [6]. We also observed that the switching response for our fabricated devices is relatively faster (< 3 µs). We have also shown experimentally that the fabricated singly resonant devices are efficient to filter noisy pump laser source, which is essential for quantum photonic applications. Fig. 4(b) shows a pump laser associated with ASE noise transmitted through a reference waveguide, whereas Fig. 4(c) shows the filtered pump laser (with noise suppressed to the detection limit of the optical spectrum analyzer) when passed through the device.

CONCLUSION

In summary, we have reported the design and demonstration of a compact DBR cavity which can be potentially useful for various silicon photonic applications such as tunable narrow bandpass filters, faster thermo-optic switching and high-speed electro-optic modulators (by integrating pn-junction across the cavity). The experimentally obtained figure-of-merits can be improved further by reducing waveguide losses and by integrating efficient active elements.

Acknowledgements: The authors gratefully acknowledge MeitY, Govt. of India for sponsoring to establish CoE-CPPICS and CNNP at IIT Madras.

References

[1] Wim Bogaerts et al. "*Silicon microring resonators*", Laser & Photonics Reviews, vol. 6, no 1, pp. 47-73, 2012
[2] W. Zhang et al., *"A fully reconfigurable waveguide Bragg grating for programmable photonic signal processing*," Nature communications, vol. 9, no. 1, pp. 1-9, April 2018
[3] Shengjie Xie et al., *"On-chip Fabry–Perot Bragg grating cavity enhanced four-wave mixing*," ACS Photonics, vol. 7, no. 4, pp. 1009-1015, March 2020
[4] Fabio Falconi et al., "*Widely tunable silicon photonics narrow-linewidth passband filter based on phase-shifted waveguide Bragg grating*", 2018 International Topical Meeting on Microwave Photonics (MWP), IEEE, pp. 1-4, 2018
[5] Sumi R et al., *"Integrated optical linear edge filters using apodized sub-wavelength grating waveguides in SOI*," IEEE Photonics Technology Letters, vol. 31, no. 17, pp. 1449-1452, September 2019
[6] Ramesh K. Gupta et al., "*Performance analysis of metal-microheater integrated silicon waveguide phase-shifters*," OSA Continuum, vol.1, no. 2, pp. 703-714, 2018

Ultra-high resolution on-chip reconstructive spectrometer

(Student paper)

Chunhui Yao, Minjia Chen, Qixiang Cheng* and Richard V. Penty

Centre for Photonic Systems, Electrical Engineering Division, Department of Engineering, University of Cambridge, 9 JJ Thomson Avenue, Cambridge, CB3 0FA, U.K.
* qc223@cam.ac.uk

We present a novel design of on-chip reconstructive spectrometer with ultra-high resolution and broad bandwidth. Based on a multi-stage reconfigurable network, our method permits a scalable number of sampling channels that avoids passive splitting loss. Distinct micro-ring resonators are distributed over the network to enable diverse channel spectral responses with high sampling efficiency. Using the silicon nitride photonic integration platform, we experimentally demonstrate a 50 pm resolution over a 120 nm bandwidth with 128 sampling channels.

Keywords: *On-chip spectrometer, reconfigurable, ultra-high resolution, broadband, SiN platform*

Introduction

The past decades have seen miniaturized optical spectrometers addressing numerous applications, such as in situ chemical detection, astronomical sensing, wearable biological monitoring, and etc[1,2]. Nevertheless, the size reduction of spectrometers inevitably brings strong trade-off between the resolution and bandwidth. For example, some demonstrations based on narrowband filters or spatial heterodyne Fourier-transform can achieve high resolutions but suffer from limited bandwidths since the scales of their filter or interferometer arrays are physically restricted by the passive power splitting scheme and the footprint[3,4]. A clear technical bottleneck can be observed that none of the miniaturized spectrometers so far demonstrated can simultaneously achieve < 0.1 nm resolution and > 100 nm bandwidth, which are often required for biomedical sensing, industrial chemical monitoring scenarios[5,6].

In recent years, the reconstructive spectrometer (RS) has drawn extensive attention from the community. Via a number of sampling channels with distinct spectral responses, RSs can convert an arbitrary incident spectrum into a set of aggregated optical power intensities, allowing the recovery of the incident spectrum by solving linear equations. With proper engineering of the channel spectral responses, RSs can resolve a large number of spectral pixels with a moderate number of sampling channels. Nevertheless, the reported miniaturized RSs typically rely on lumped passive spectral filter designs which bonds the number of sampling channels [7]. Here, we present the design of an on-chip reconstructive spectrometer that achieves both ultra-high resolution and broad bandwidth. The passive power fan-out in conventional RS designs is replaced by a reconfigurable optical network which allows the incident light to be actively routed into different sampling channels without sacrificing the power intensity. Over-coupled micro-ring resonators (MRRs) with varying spectral properties are distributed over the network, and act as broadband spectral filters to create distinctive spectral responses for each channel. Based on a commercial silicon nitride (SiN) photonic integration platform, we experimentally demonstrate a ~50 pm resolution over a 120 nm bandwidth using 128 sampling channels.

Design and principle

Figure 1(a) shows the system schematic of our reconstructive spectrometer based on a multi-stage reconfigurable network and distributed MRR filters. Each stage (except for the fan-out) consists of two vertically arranged 2×2 MZIs followed by a waveguide crossing that interconnects the upper and lower MZIs between adjacent stages. MRRs are distributed after the output ports of each MZI, and serve as broadband spectral filters. Thereby, an incident signal can be actively routed through different optical paths (i.e., by reconfiguring the cross/bar state of the MZIs). As each MZI cell is set in a binary fashion, the number of total sampling channels grows exponentially with the increase of stage number, as:

$$\begin{cases} N_{channel} = 2^{N+1} \\ N_{MZI} = 2N + 1 \end{cases} \quad (1)$$

where $N_{channel}$, N_{MZI}, and N are the channel number, number of MZIs, and stage number respectively. Following this topology, a high number of sampling channels (with no splitting loss) can be readily created. A successful RS also requires proper tailoring of the channel spectral responses. Detailed mathematical elaboration of the

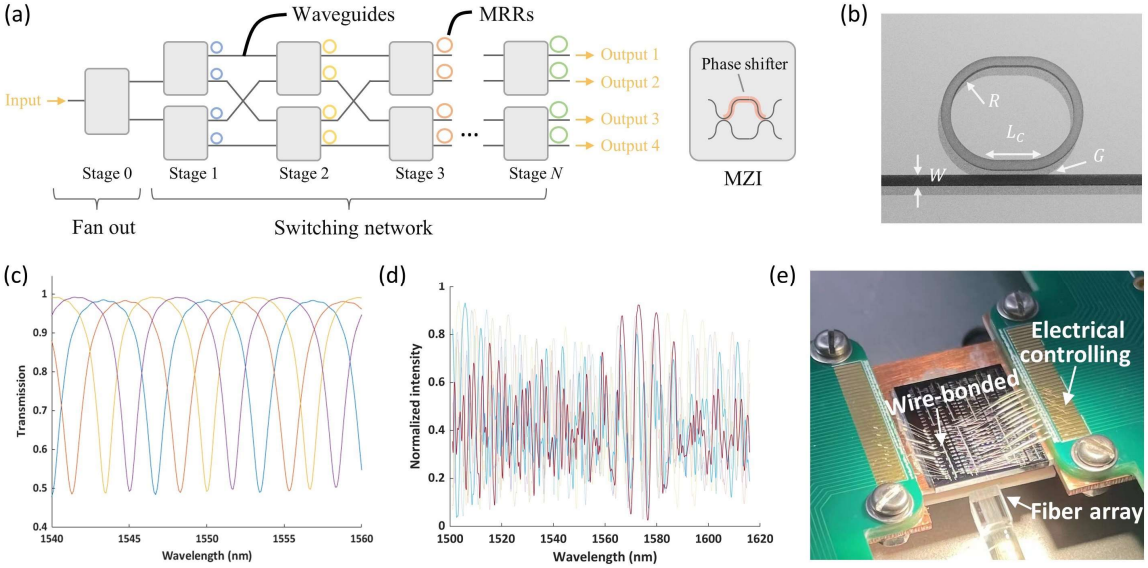


Fig. 1. (a) System schematic of the proposed reconstructive spectrometer. (b) Schematic of the racetrack MRR. (c)Simulated transmission spectra of the four MRRs at a certain stage. (d) Simulated spectral responses of a few sampling channels. (e) Photograph of our packaged on-chip reconstructive spectrometer

computational spectrum reconstruction can be found in ref[1,2]. In general, there are two key requirements for the channel spectral responses of RSs: 1) small self-correlation length, i.e., rapid fluctuations in the wavelength domain to enable high sampling efficiency; 2) high orthogonality between channels. To fulfill these two targets, we develop a distributed spectral filtering method with over-coupled racetrack MRRs. By adjusting the geometry, Fig. 1(b), of each MRR, its spectral response, including the FSR, finesse, and resonance wavelength can be fully manipulated. Here we set the FSR of the MRRs for the different stages to increase from ~4 nm to ~8 nm and maintain their finesse at ~7 to enable rapid spectral fluctuations (resulting in high sampling efficiency). The resonant wavelength of each MRR is also fine adjusted to differ from all the other, as shown by Fig. 1(c). Since different sampling channel passes through different combinations of MRRs, the cascaded spectral responses can therefore be highly distinctive. Figure 1(d) shows several examples of the channel spectral responses. It can be clearly seen that the abovementioned two requirements have been successfully achieved. Based on such design scheme, we implemented a 6-stage reconstructive spectrometer (i.e., 128 sampling channels) on a SiN platform, as shown by Fig 1(e). A microcontroller unit with customized driving broads is developed for the electrical control of the reconfigurable system. An ultra-high NA fiber array with a mode diameter of about 3.5 µm is used to match the edge couplers for the optical IO, which achieves an about 3 dB loss per facet. The measured total on-chip loss is around 5 dB at 1550 nm.

Experimental results

To test the performance of our fabricated spectrometer, we first calibrate the spectral responses of all 128 sampling channels by launching an ASE broadband light source through the chip and measuring the transmission spectra with a benchtop spectrum analyzer, as shown by Fig 2(a). The calculated spectral self-correlation is about 0.57 nm (see ref[8]), indicating a high sampling resolution. We then apply DFB lasers (with linewidths < 10 MHz, i.e., spectral widths < ~1 pm) at different wavelengths as narrowband inputs and use an optical power meter to detect the aggregated power intensities at the output ports. The sampling spectral window is set between 1500 nm to 1620 nm (i.e., a bandwidth of 120 nm). Based on the pre-calibrated channel spectral responses (also referred as the transmission matrix) and the vector of detected power intensities, we use a nonlinear optimization algorithm, namely the CVX algorithm[9], to reconstruct the incident laser signals. Figure 2(c-e) shows the reconstructed spectra (references obtained using a benchtop spectrum analyzer). The FWHM of the resolved peaks is maintained at ~50 pm for the different wavelength inputs, illustrating that our spectrometer can detect narrow spectral components with an ultra-high resolution down to 50 pm. The slight reconstruction errors can be attributed to the measurement inconsistencies between the calibration and testing.

The reconfigurable optical network of our device also permits a user-definable resolution by differently grouping sampling channels, allowing a programmable performance to balance the computational complexity, measurement time, and resource consumption. Thus, in experiment, we investigate the relationship between the resolution and channel number by applying different numbers of sampling channels to reconstruct the narrowband inputs and resolve the resolutions. As shown by Fig. 2(e), a clear downward trend can be observed that the spectrometer

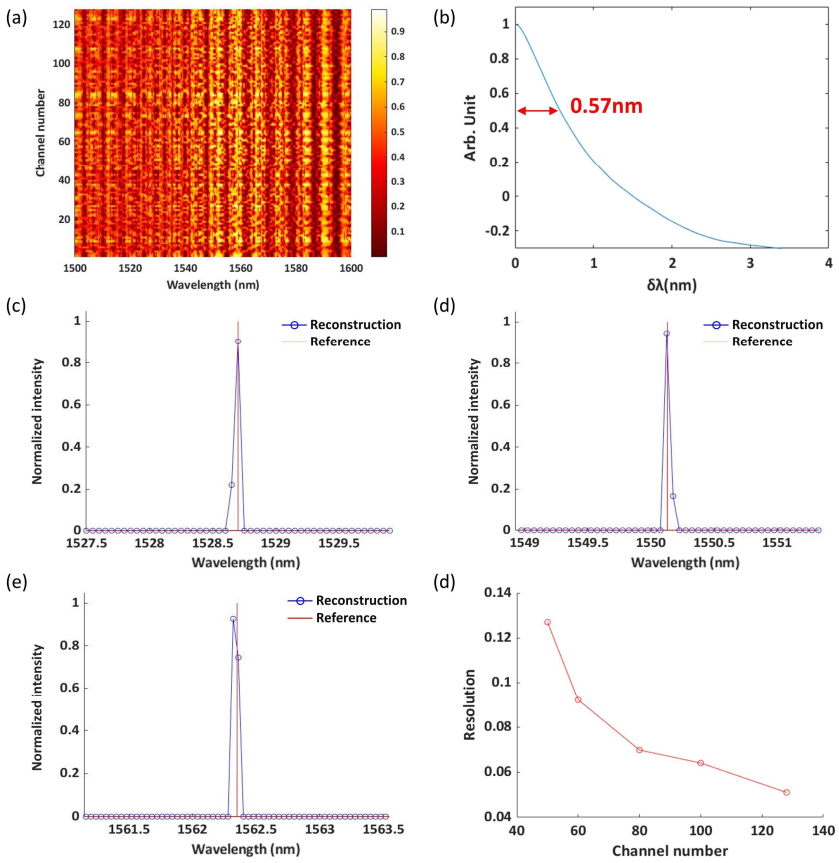


Fig. 2. (a) 2D map of the measured spectral responses of the 128 sampling channels. The scale bar represents the normalized transmission intensity. (b) Calculated spectral self-correlation function C(Δλ) (c-e) Reconstruction results of the narrowband incident signals at different wavelengths, respectively. (f) Spectrometer resolution vs. channel number

resolution continuously improves as the sampling channel increases. Accordingly, we foresee that the resolution of our design can be further extended by scaling up the network with more sampling channels.

Conclusion

In this paper, we present a novel design of on-chip reconstructive spectrometer with ultra-high resolution and broad bandwidth. The passive splitting-to-detection schemes is replaced by a reconfigurable network to create a scalable number of sampling channels. We also develop a distributed spectral filtering method using various MRRs to generate diverse channel spectral responses with high sampling efficiency. Experimentally, we demonstrate a 128-channel spectrometer on a SiN platform and realize an ultra-high resolution of ~50 pm resolution with 120 nm bandwidth.

References

1. *Yang, Z., et al. Miniaturization of optical spectrometers. Science 371, eabe0722 (2021).*
2. *Li, A., et al. Advances in cost-effective integrated spectrometers. Light Sci Appl 11, 174 (2022).*
3. *Paudel, U. & Rose, T. Ultra-high resolution and broadband chip-scale speckle enhanced Fourier-transform spectrometer. Opt. Express 28, 16469 (2020).*
4. *Zhang, L. et al. Ultrahigh-resolution on-chip spectrometer with silicon photonic resonators. OEA 5, 210100–9 (2022).*
5. *Ramasahayam, S., et al. Noninvasive Estimation of Blood Glucose Concentration Using Near Infrared Optodes. in Sensing Technology: Current Status and Future Trends IV. doi:10.1007/978-3-319-12898-6_4.*
6. *Cossel, K. C. et al. Open-path dual-comb spectroscopy to an airborne retroreflector. OPTICA 4, 724–728 (2017).*
7. *Redding, B., et al. Compact spectrometer based on a disordered photonic chip. Nature Photon 7, 746–751 (2013).*
8. *Wan, Y., Fan, X. & He, Z. Review on Speckle-Based Spectrum Analyzer. Photonic Sens 11, 187–202 (2021).*
9. *Michael, G. & Stephen, B. CVX: Matlab software for disciplined convex programming, version 2.0 beta.*

Soliton generation in a gallium phosphide photonic crystal cavity

Alisa Davydova[1,*], Alberto Nardi[2], Nikolai Kuznetsov[1], Charles Möhl[2], Miles H. Anderson[1], Johann Riemensberger[1], Tobias J. Kippenberg[1] and Paul Seidler[2]

[1]Institute of Physics, Swiss Federal Institute of Technology Lausanne (EPFL), CH-1015 Lausanne, Switzerland
[2] IBM Research Europe, Zurich, Säumerstrasse 4, CH-8803 Rüschlikon, Switzerland
[*] alisa.davydova@epfl.ch

Ring resonators are widely used for soliton generation, however the possibilities for dispersion engineering are limited. Here we overcome this challenge by employing photonic crystal reflectors providing anomalous dispersion in a Fabry-Pérot resonator based on gallium phosphide. With subharmonic pulsed pumping, we generate stable dissipative Kerr soliton frequency combs.

Keywords: dissipative Kerr solitons, gallium phosphide, photonic crystals, dispersion engineering

INTRODUCTION

Dissipative Kerr solitons (DKSs) have been extensively studied during the past decades and their relevance to many applications demonstrated. Among several material platforms for DKS formation [1], silicon nitride (Si_3N_4) ring microresonators have become most common. However, ring resonators do not offer many design degrees of freedom; usually only waveguide thickness and width can be varied. Photonic-crystal Fabry-Pérot (PC-FP) resonators have gained attention because of the flexibility in dispersion engineering provided by multiple geometric degrees of freedom in the design of the photonic crystal reflectors (PCR) [2]. In principle, almost any dispersion profile can be achieved over the optical transparency range of the material system.

Recently, frequency comb generation has been demonstrated with a photonic crystal cavity made of silicon nitride [3], but the low index contrast of the system prevents formation of broad soliton combs. Narrow solitons with a bandwidth of about 50 nm were reported. In addition, a large number of periods (~100) were required in the non-chirped PCRs to reach high reflectivity and a create a cavity with a high quality factor. A dual-pump approach was utilized to balance the thermorefractive effect [4].

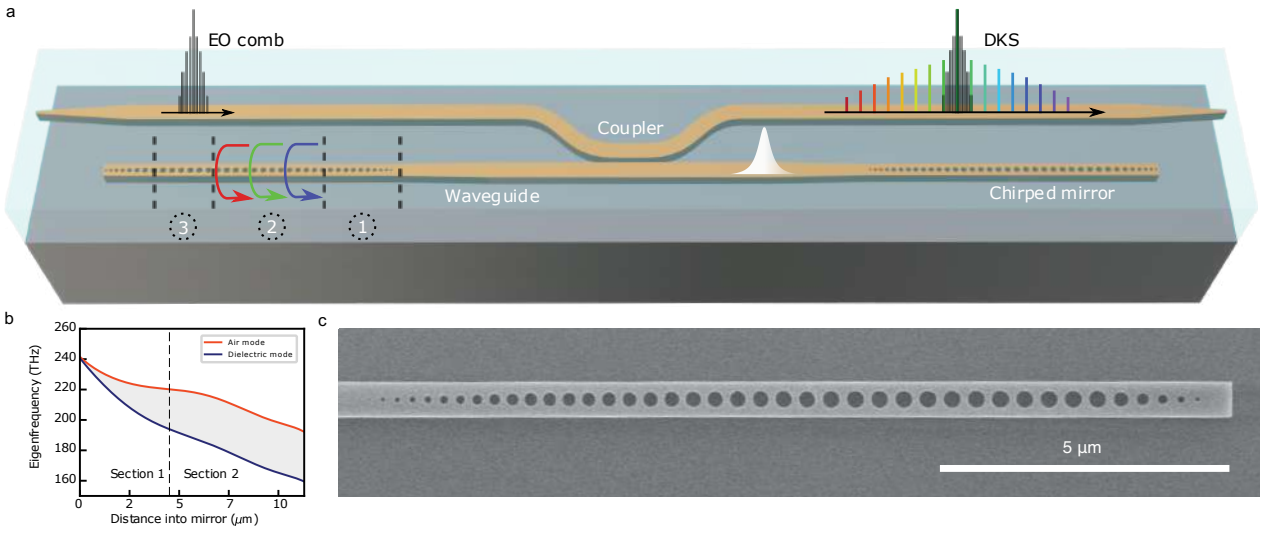


Fig. 1 *Photonic-crystal Fabry-Pérot resonator.* ***(a)*** *Schematic of a PC-FP resonator made of GaP comprising a straight waveguide with normal dispersion terminated with PCRs that contribute anomalous dispersion. Section 1 of the chirped mirrors ensures an adiabatic transition from the waveguide to the mirror. In section 2, lower frequencies are reflected deeper in the PCR (anomalous dispersion). Section 3 is composed of holes with fixed dimensions to enhance the reflectivity of the PCR at low frequencies.* ***(b)*** *Evolution of the transverse electric (TE) bandgap as a function of depth in the mirror.* ***(c)*** *Scanning electron microscopy image of a fabricated PCR.*

Gallium phosphide (GaP) offers several attractive properties for integrated nonlinear optics: a high refractive index ($n_0 \approx 3$), high third-order nonlinearity (200 times larger than that of silicon nitride), non-zero second-order nonlinearity due to its non-centrosymmetric crystal structure, negligible two-photon absorption for wavelengths above 1.1 µm, and a recently developed nanofabrication process. These characteristics make GaP a promising candidate for realizing PC-FP resonators with high-reflectivity chirped PCRs for broad DKS generation. Note that frequency comb formation has been observed in GaP ring resonators, but coherent DKS combs have never been generated. One issue is the high thermorefractive coefficient of III-V materials, which can prevent DKS generation at room temperature [5]. To overcome this problem, one can use optical pulses to pump the devices, enhancing the nonlinear frequency conversion while avoiding significant heating.

In this work, we present DKS generation in a PC-FP resonator made of GaP driven by optical pulses from an electro-optic (EO) frequency comb. For soliton formation, the repetition frequency of the EO comb is finely tuned to match a sub-harmonic of the free spectral range (FSR) of the resonator. We show that properly designed non-periodic PCRs can be used to create monolithic high-finesse microcavities that overcome the dispersion limitations of the ring resonator geometry without affecting the optical quality factor. We achieve record-low losses and even higher quality factors than those of GaP ring resonators [6].

DEVICE DESIGN AND CHARACTERIZATION

The resonator design is shown in Fig. 1a. The central straight waveguide portion has normal dispersion. The PCRs at the two ends consisting of a waveguide patterned with holes provide anomalous dispersion and form a monolithic Fabry-Pérot cavity. Initial sections of the mirrors where the hole radius is gradually increased (Fig. 1 c) create a smooth transition between the central waveguide and the two PCRs. Linear variation of the PCR dimensions over 15 more periods leads to a chirp in the center frequency of the photonic bandgap (see Fig. 1 b). Light is coupled in and out of the device via a directional coupler to a bus waveguide with inverse tapers at the edge of the chip for coupling to fibers. The entire structure is cladded with silicon dioxide.

Fig. 2d displays the measured and simulated integrated dispersion

$$D_{int} = \omega_\mu - \omega_0 - \mu D_1 = \frac{\mu^2 D_2}{2!} + \frac{\mu^3 D_3}{3!} + \cdots$$

of the PC-FP resonator used in this work for soliton generation, where μ is the mode index, the D_i are the dispersion parameters, and ω_0 is the pump frequency. The microresonator is characterized by a free spectral range FSR =55.9 GHz and mean intrinsic loss $\kappa_0/(2\pi) \approx 333$ MHz (see Fig. 2b). The anomalous dispersion is described in terms of the parameter $D_2/2\pi = -c/n_g D_1^2 \beta_2 = 3.0$ MHz.

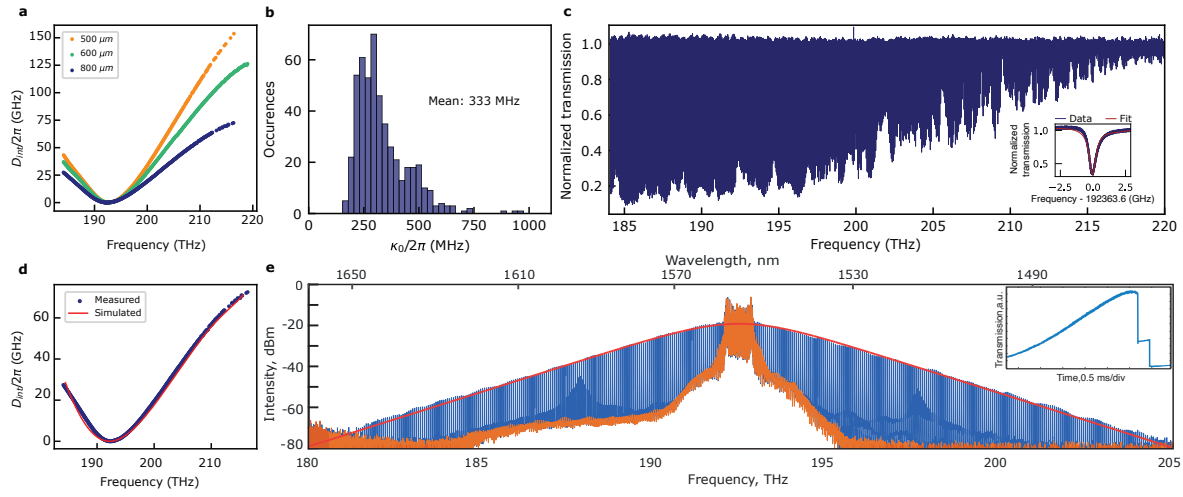


Fig. 2 *Resonator characterization and soliton generation in a PC-FP resonator with a FSR of 55.9 GHz.* ***(a)*** *Dispersion plots of devices with various waveguide lengths (i.e., 500 µm, 600 µm and 800 µm), and a width of 900 µm. The waveguide contributes to the normal dispersion, resulting in less total anomalous dispersion with longer waveguide sections.* ***(b)*** *Distribution of intrinsic loss rates of the individual resonances .* ***(c)*** *Normalized transmission spectrum of a PC-FP resonator. Inset: Data and fit of the central resonance pumped in this work for DKS generation. $\kappa_0/(2\pi)$ is 366 MHz and $\kappa_{ex}/(2\pi)$ is 132 MHz.* ***(d)*** *Mesured and simulated integrated dispersion of the same device.* ***(e)*** *Reflected spectra of the soliton state (blue) and off resonance (orange), with the latter corresponding to the spectrum of the EO-comb. The inset shows the evolution of the generated light from the microresonator as the pump is tuned towards lower frequencies.*

Note that a unit cell of the PCR has many degrees of freedom to engineer the photonic bandgap: waveguide width and thickness, hole pitch, hole radius, and even the shape of the holes (e.g., circular, elliptical, or rectangular). Depending on the targeted FSR, PCRs with different dispersion profiles can also be combined, such that the waveguide length between them can be independently chosen to achieve a specific roundtrip time.

The reproducibility of device fabrication has been confirmed through spectroscopic measurements of many devices. By increasing the waveguide length between the PCRs (i.e., normal dispersion contribution), we find that the overall net dispersion becomes less anomalous, as expected (see Fig. 2a). In Fig. 2c, we report the transmission spectrum

between 184 THz and 220 THz for the device used for DKS generation. Consistent with the chirped photonic bandgap, we also see that the PCRs exhibit lower reflectivity above 200 THz. Intrinsic quality factors are as high as $Q_0 = 1.2 \times 10^6$, a record value for GaP integrated microresonators.

SOLITON GENERATION

For soliton formation, the input optical pulses were generated by an EO comb created by employing a combination of amplitude and phase modulators as well as dispersion compensation [7]. The output of the device is measured in both reflection and transmission with an optical spectrum analyzer, and a photodiode reads the trace of the signal during the laser scan to track the resonance shape. To match the cavity FSR, the EO-comb repetition rate is set to FSR/4 = 55.916 GHz/4 = 13.979 GHz. We recorded soliton generation with on-chip input average power as low as 50 mW. However, we use 200 - 250 mW to study the soliton characteristics, as that power level is high enough to generate long-lived solitons but low enough to avoid the irreversible damage observed with continuous-wave pumping. The reflected spectrum of the soliton is displayed in Fig. 2e. The orange spectrum is collected with the pump off resonance and corresponds to the spectrum of the pump pulse. The detected soliton spectrum spans over 200 nm or 25 THz and includes 450 lines covering the reflection bandwidth of the PCRs. From a fit of the soliton spectrum to a hyperbolic secant-squared profile, we infer a full width at half maximum of 3 THz, corresponding to a soliton duration of 100 fs.

DISCUSSION

With appropriate design geometries for targeted photonic bandgaps, PC-FP resonators enable operation at wavelength ranges that are inaccessible in ring resonators, as the latter are often constrained by the limited geometric degrees of freedom and the normal dispersion of the materials used. In addition to versatile dispersion engineering, the form factor of integrated PC-FP resonators offers the possibility of large-scale integration. In our case, more than 200 devices fit on a chip with dimensions of 3×7 mm^2.

For soliton generation, improvement in the soliton bandwidth should be possible by extending the working range of the PCRs. To generate octave spanning solitons, the dispersion of the PCRs must of course be carefully designed to balance the contribution of the waveguide dispersion at all frequencies of interest.

Acknowledgements: This work was supported by funding from the European Union Horizon 2020 Programme for Research and Innovation under grant agreement No. 812818 (Marie Curie ETN MICROCOMB). J. R. acknowledges funding from the SNF Ambizione grant No. 201923. All samples were fabricated at the Binnig and Rohrer Nanotechnology Center (BRNC) at IBM Research Europe, Zurich.

References

[1] T. J. Kippenberg, A. L. Gaeta, et al. Dissipative Kerr solitons in optical microresonators, Science, vol. 361, eaan8083, 2018.
[2] S-P. Yu, H. Jung, T. C. Briles, K. Srinivasan and S. B. Papp, "Photonic-Crystal-Reflector Nanoresonators for Kerr-Frequency Combs", ACS Photonics, vol. 6, pp.2083-2089, 2019.
[3] T. Wildi, M. A. Gaafar, T. Voumard, M. Ludwig and Tobias Herr, "Soliton Pulses in Photonic Crystal Fabry-Perot Microresonators", unpublished, arXiv:2206.10410, 2022.
[4] S. Zhang, J. M. Silver, et al., Sub-milliwatt-level microresonator solitons with extended access range using an auxiliary laser, Optica 6, 206, 2019.
[5] G. Moille et al., "Dissipative Kerr Solitons in a III-V Microresonator", Laser & Photonics Reviews, vol. 14, 200002, 2020.
[6] D. J. Wilson, K. Schneider, et al.,"Integrated gallium phosphide nonlinear photonics",Nat. Photonics,vol.14, pp.57–62, 2020.
[7] E. Obrzud, S. Lecomte, et al., Temporal solitons in microresonators driven by optical pulses, Nat. Phtotnics, 11, 600, 2017.

Demonstration of low RMS differential phase noise across C-band for integrated, amplifying optical phased arrays

B.S. Vikram[1], M. Gagino[1] , A. Millan-Mejia[2] , L. Augustin[2], K.A. Williams[1],

V. Dolores Calzadilla[1,3]

[1]Department of Electrical Engineering and the Eindhoven Hendrik Casimir Institute, Eindhoven University of Technology, Groene Loper 19, 5612 AP Eindhoven, The Netherlands
[2]SMART Photonics, High Tech Campus 29, AE Eindhoven, The Netherlands
[3]Photonic Integration Technology Center, Groene Loper 19, 5612 AP Eindhoven, The Netherlands
s.v.bhagavatula@tue.nl, v.calzadilla@tue.nl

We experimentally demonstrate low RMS differential phase noise (<10mrad) across C-band in optical phased array channels integrated with in-line semiconductor optical amplifiers using a generic InP photonic integrated platform without active phase locking.
Keywords: *differential phase noise, optical phased array, InP, semiconductor optical amplifier*

INTRODUCTION

Optical phased arrays (OPAs) enable agile solid-state beam steering for free-space optical communications (FSO), light detection and ranging (LiDAR), and beam-combining systems. The amplitude and phase tuning provided by OPA elements with optical amplifiers and phase modulators allows superior tailoring of the far-field in comparison to OPAs with only phase control elements. This allows adaptive ranging in LiDAR applications. However, amplifier noise and path length fluctuation induced phase noise temporally decorrelates the signals in the arms of the OPA, degrading the side lobe suppression ratio and pointing accuracy of the beam. Optical phase-locked loops (OPLLs) can be used to mitigate the relative phase fluctuations between signal sources [1], [2]. Multilevel OPLLs are proposed for locking the array elements with individual fiber amplifiers in a coherent beam combining system [3], significantly increasing the complexity and limiting the scalability of the number of elements in the OPA: N-1 OPLLs are needed for an N-element OPA with one element as a reference. The miniaturization offered by integrated photonic OPAs would reduce the path length fluctuations over the fiber-based OPAs. OPAs have been demonstrated in various integrated platforms such as silicon (Si) [4], indium phosphide (InP) [5], and silicon nitride (SiN) [6]. InP provides an established fabrication platform for implementing active OPAs with the building blocks such as integrated semiconductor optical amplifiers (SOAs) and phase modulators [7]. Phase noise (temporal phase fluctuations) induced through carrier density fluctuations and amplified spontaneous emission (ASE) from the SOAs along with minor path length fluctuations will determine the extent of phase correlation among the OPA channels.

In this work, we propose the first measurements (to the best of our knowledge) of differential phase noise (DPN) between two channels in a photonic integrated circuit (PIC) based amplifying OPA monolithically integrated with an MMI-based interferometer and a photodetector. These C-band measurements show that the InP OPA provides low RMS DPN (also referred to as RMS phase error) (<10 mrad in 100 Hz to 1 MHz frequency offset without any PLLs) and does not need active phase locking between the array elements. In comparison, for conventional fiber based systems [8],[9], active phase locking with OPLLs is required to reduce the RMS DPN to a few milliradians (8.2 mrad in 0.1 Hz to 6 kHz frequency offset with PLLs in [8], 314.2 mrad with PLL in [9]).

EXPERIMENTAL SETUP

Fig.1(a) shows the setup schematic showing sections of the InP PIC (integrated test system for OPAs) fabricated in the foundry platform of SMART photonics. An external laser with narrow linewidth (+14 dBm, 100 kHz, Keysight 81960A) acts as the source laser for the OPA operated at 18 ^{0}C. The TE polarized signal is amplified by a booster SOA (Keithley 2602B, current density ($J_{booster}$) of 5 kA/cm^2) and is split by a star coupler to feed the individual OPA channels, each controlled by a phase modulator and a channel SOA (Thorlabs LDC 8005, operated at J_{SOA} of 5 kA/cm^2). Characterizing the DPN between OPA elements allows the use of analytic equations [10] to evaluate the influence on the far-field pattern and beam-pointing error under the assumption of uncorrelated phase errors between array elements. To perform the measurement, a fraction of the output power from each adjacent OPA element is mixed through multimode interference couplers (MMI couplers), and their beat is detected with an on-chip photodetector. An external bias tee biases the photodiode (-2V), and extracts the RF beat to be processed by an electronic spectrum analyzer (Agilent E4448A). A frequency shift of 3 MHz is synthesized by modulating one of the phase modulators (the other is unbiased) for measuring the heterodyne beat signal.

Fig.1 (b) shows an N- channel optical phased array with the field in each arm given by $E_{i,N} = A_N \exp(j(\omega t + \phi_1 - (N-1)\Delta\phi))$, where A_N is the amplitude of the Nth channel, ω is the angular frequency, t is the time, ϕ_1 is the common phase, and $\Delta\phi$ is the differential phase. The beat signal between the two OPA elements ($\propto |(E1\ E2^*)|^2$) extracts the influence of the DPN (channel SOA noise and path length fluctuations) while cancelling out the common phase noise sourced from the laser and the booster SOA.

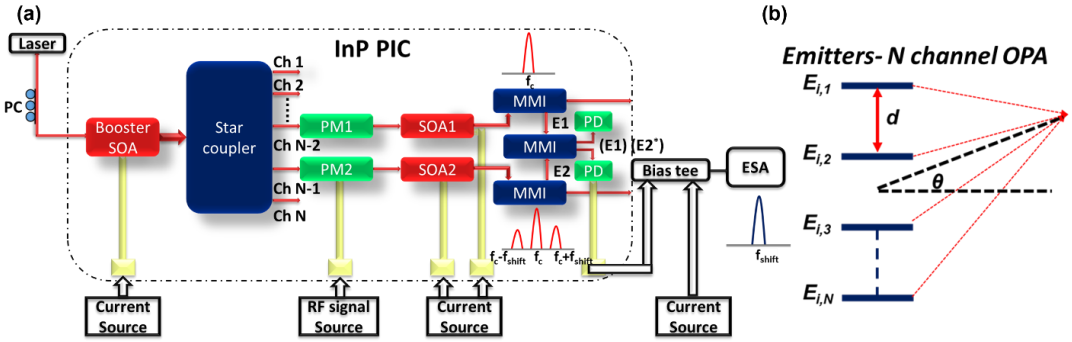


Fig. 1. (a) Schematic of the setup showing the sections of chip utilized for differential phase noise measurements. SOA- semiconductor optical amplifier, MMI-multimode interference coupler, PM-phase modulator, ESA- electrical spectrum analyzer, PD-photodiode, PC- polarization controller, (b) Optical phased array with N-emitters, pitch d, steering angle θ, and fields $E_{i,N}$.

RESULTS

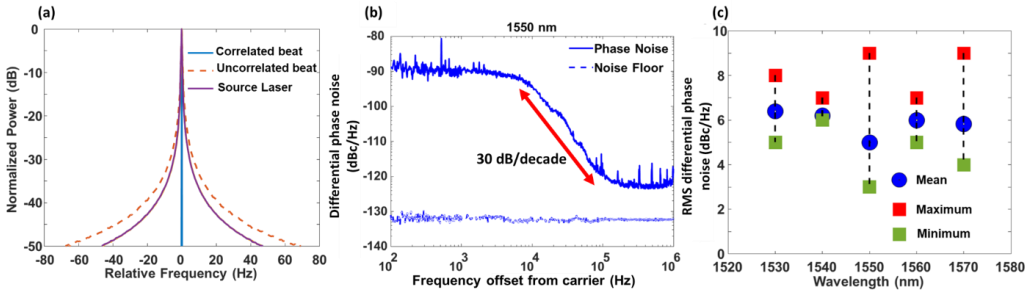


Figure 2 (a) The beat signal when the two lasers with identical line shapes (only one shown) have completely correlated (blue solid line) and uncorrelated (red dashed line) temporal phase fluctuations, (b) Measured differential phase noise spectrum with the source laser at 1550 nm along with measurement noise floor, and (c)Measured RMS differential phase noise in the C-band.

Fig.2 (a) shows the proof of principle simulations elucidating the influence of electric field correlation between the two paths sourced by the same laser. When the temporal phase fluctuations are identical (correlated), the beat signal collapses to the resolution limit of the measurement system. In contrast, the linewidth of the beat signal increases for the uncorrelated case. The measured DPN spectrum is shown in Fig. 2(b) with the source laser operating at 1550 nm. From 100 kHz to 10 kHz, the DPN climbs at a rate of 30 dB/decade similar to the case where the temporal phase fluctuations of the lasers are weakly correlated. Below 10 kHz, the growth of the differential phase noise is arrested to 2 dB/decade, similar to the case where the temporal phase fluctuations are strongly correlated. The measured DPN spectrum also presents similarities to the phase noise of lasers locked by an OPLL [2]. Even without an OPLL, the measured DPN is akin to the case where an OPLL with a loop bandwidth of nearly 10 kHz is implemented. Fig. 2(c) shows the RMS differential phase noise (integrating the DPN plot from 100 Hz to 1 MHz) which is less than 10 mrad across the C-band, corresponding to stability better than λ/600. The impact of the DPN on the far-field beam pattern and the pointing error is evaluated through closed-form analytic equations for the case of emitters with uncorrelated phase errors between the elements [10] using equations (1-3).

$$I_G^{unpert} = \frac{\sin^2(\pi N\theta d/\lambda)}{\sin^2(\pi\theta d/\lambda)} \quad (1)$$

$$I_G^{uncorr} = \exp\left(-\sigma_\phi^2\right) I_G^{unpert} + N\left(1 - \exp\left(-\sigma_\phi^2\right)\right) \quad (2)$$

$$\theta_{pointingRMS} = \frac{1}{2\pi}\sqrt{\frac{12\sigma_\phi^2}{N(N^2-1)d^2}} \quad (3)$$

Here, N is the number of channels in the array, θ is the angular position, d is the channel spacing, λ is the wavelength, σ_φ is the standard deviation of the phase error between two elements(RMS DPN), I_G^{unpert} is the unperturbed (ideal) far-field intensity, I_G^{uncorr} is the far-field intensity with uncorrelated phase errors, and $\theta_{pointing\ RMS}$ is the RMS pointing error. Fig. 3(a) shows the influence of RMS DPN on the far-field intensity (100 element OPA, 2.2 µm channel spacing). When the RMS DPN is less than 100 mrad, the side-lobe suppression ratio is 13.2 dB which deteriorates to 12 dB at an RMS phase noise of 1000 mrad. Fig. 3(b) shows the calculated pointing error [9] as a function of the number of array elements. In the present case (<10 mrad), the pointing error is less than 100 µrad enabling LiDAR and FSO [11].

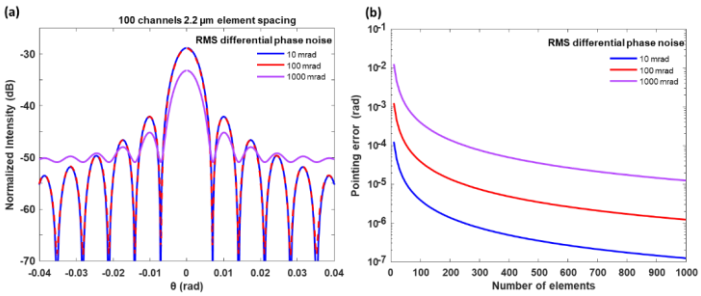


Figure 3 Impact of differential phase noise on (a) far-field beam pattern for a 100-channel OPA with 2.2 µm spacing and (b) Pointing error dependence on the number of elements and RMS differential phase noise.

CONCLUSIONS

Low RMS differential phase noise (<10 mrad) is measured across the C-band between the InP OPA channels enabling their utilization for LiDAR and short-range FSO without the need for implementing OPLLs. The results are promising for reducing the complexity of optical phased arrays with amplitude control while maintaining low pointing error and minimally distorting the far-field pattern.

Acknowledgment: The authors would like to acknowledge Gilles Feugnet and Jerome Bourderionnet from Thales Research and Technology, for insightful technical discussions. This work has received funding support from the European Union Horizon 2020 program through the NewControl project under grant no 826653.

References

[1] Sasa Ristic, Ashish Bhardwaj, Mark J. Rodwell, Larry A. Coldren, and Leif A. Johansson, "An optical phase-locked loop photonic integrated circuit," Journal of Lightwave Technology, vol. 28, no. 4, pp. 526–538, 2009.

[2] K. Balakier, M. J. Fice, L. Ponnampalam, A. J. Seeds, and C. C. Renaud, "Monolithically Integrated Optical Phase Lock Loop for Microwave Photonics," Journal of Lightwave Technology, vol. 32, no. 20, pp. 3893–3900, Oct. 2014, doi: 10.1109/JLT.2014.2317941.

[3] A. Yariv et al., "Coherent beam combining with multilevel optical phase-locked loops," JOSA B, Vol. 24, Issue 12, pp. 2930-2939, vol. 24, no. 12, pp. 2930–2939, Dec. 2007, doi: 10.1364/JOSAB.24.002930.

[4] K. van Acoleyen, W. Bogaerts, and R. Baets, "Two-dimensional dispersive off-chip beam scanner fabricated on silicon-on-insulator," IEEE Photonics Technology Letters, vol. 23, no. 17, pp. 1270–1272, 2011, doi: 10.1109/LPT.2011.2159785.

[5] M. Gagino, M. B. J. van Rijn, E. A. J. M. Bente, M. K. Smit, and V. Dolores-Calzadilla, "Broadband Operation of an InP Optical Phased Array," IEEE Photonics Technology Letters, vol. 34, no. 10, pp. 541–544, May 2022, doi: 10.1109/LPT.2022.3171979.

[6] B. Szelag et al., "SiN integrated optical phased arrays for two-dimensional beam steering at a single near-infrared wavelength," Optics Express, Vol. 27, Issue 4, pp. 5851-5858, vol. 27, no. 4, pp. 5851–5858, Feb. 2019, doi: 10.1364/OE.27.005851.

[7] L. M. Augustin et al., "InP-Based Generic Foundry Platform for Photonic Integrated Circuits," IEEE Journal of Selected Topics in Quantum Electronics, vol. 24, no. 1, Jan. 2018, doi: 10.1109/JSTQE.2017.2720967.

[8] D. R. Gozzard, L. E. Roberts, J. T. Spollard, P. G. Sibley, and D. A. Shaddock, "Fast beam steering with an optical phased array," Opt Lett, vol. 45, no. 13, p. 3793, Jul. 2020, doi: 10.1364/OL.393007.

[9] K. Yang et al., "Coherent Polarization Beam Combination by Microcontroller-Based Phase-Locking Method," in IEEE Photonics Technology Letters, vol. 28, no. 20, pp. 2129-2132, 15 Oct.15, 2016, doi: 10.1109/LPT.2016.2582500.

[10] C. D. Nabors, "Effects of phase errors on coherent emitter arrays," Applied Optics, Vol. 33, Issue 12, pp. 2284-2289, vol. 33, no. 12, pp. 2284–2289, Apr. 1994, doi: 10.1364/AO.33.002284.

[11] T. Song, Q. Wang, M.-W. Wu, T. Ohtsuki, M. Gurusamy, and P.-Y. Kam, "Impact of Pointing Errors on the Error Performance of Intersatellite Laser Communications," Journal of Lightwave Technology, vol. 35, no. 14, pp. 3082–3091, Jul. 2017, doi: 10.1109/JLT.2017.2705132.

Sub-kHz linewidth, high power, frequency agile photonic integrated E-DBR laser

(Student paper)

Anat Siddharth, Grigory Lihachev, Rui Ning Wang, Xinru Ji, Zheru Qiu, Johann Riemensberger, and Tobias J. Kippenberg

Institute of Physics, Swiss Federal Institute of Technology Lausanne (EPFL), CH-1015 Lausanne, Switzerland
* anat.siddharth@epfl.ch

We demonstrate a novel class of lasers, based on hybrid integration of an RSOA with an extended-distributed Bragg reflector (E-DBR) laser cavity implemented on a Si_3N_4 chip with microheaters. This enables us to reach sub-kHz laser linewidth with more than 30 mW output power and mode-hop free tuning range upto 62.4 GHz.
Keywords: *Integrated Photonics, Lasers, frequency-agile tuning*

INTRODUCTION

Silicon Nitride (Si_3N_4) waveguides with ultralow propagation loss [1] provides an ideal platform to develop high performance lasers exhibiting high output power and low phase noise. Such lasers are key components in wide-range of applications such as coherent communication systems [2], ultraprecise timing [3], spectroscopy [4], LiDAR [5], etc. Lasers require minimal optical loss since it directly correlates to performance, including lasing threshold, output power, and wall-plug efficiency. In addition, employing an ultra-low-loss waveguide for the laser cavity enables us to increase the effective cavity length while maintaining high-power operation and thereby significantly lowering the laser linewidth. An extended laser cavity is significant because it increases the photon lifetime in the laser cavity, which increases the coherence of a narrow linewidth laser.

An extended Bragg grating with a narrow bandwidth and high side-lobe suppression is an excellent option among external cavity designs. The narrow mode spacing of the extended cavity can be effectively counteracted by the narrower bandwidth of the extended Bragg grating resulting in an extended-distributed Bragg reflector (E-DBR) laser [6]. The narrow-band feedback of the E-DBR laser helps in reducing the white frequency noise as compared to that of solitary gain section lasers such as monolithic III-V DFB lasers.

Integration of microheaters enables tuning of Bragg wavelength via thermo-optic effect and hence leading to mode-hop free tuning of the E-DBR laser. E-DBR laser requires no specific tuning of its laser cavity, effectively making it a turn-key laser system for on-field applications.

RESULTS

Figure 1a depicts the schematic of the E-DBR laser based on hybrid integration of a Reflective Semiconductor Optical Amplifier (RSOA) and Si_3N_4 photonic chip. The RSOA with 90% back facet reflection is edge-coupled to the Si_3N_4 photonic chip using angled tapered Si_3N_4 waveguide optimized for efficient coupling of light. The RSOA is mounted on a thermo-electric cooler for stabilizing its temperature and is operated at 25 degrees Celsius. The Si_3N_4 waveguides are fabricated using a subtractive process and have a uniform height and width of 200 nm and 2.5 μm, respectively. Stochiometric Si_3N_4 thin films are grown with low-pressure chemical vapour deposition (LPCVD) and etched in a Flourine chemistry. The waveguides are fully buried in SiO_2 cladding where the bottom cladding is made of 10 μm thick thermal oxide whereas, the top cladding is composed of TEOS and low-temperature oxide of 3 μm thickness. The entire device sits on a 230 μm -thick Si substrate. Ti/Pt heaters are fabricated atop SiO_2 cladding, with a 2.5 μm offset from the waveguide. The Si_3N_4 waveguide exhibits linear losses less than 1 dBm^{-1}.

Figure 1b presents a False-colored scanning electron microscope (SEM) image showing the Si_3N_4 waveguide with post gratings. The posts provide a weak perturbation of the effective refractive index of the low-confined fundamental TE mode at the Bragg wavelength, and constructively adds up the desired optical reflection at this wavelength. A second-order grating of 8 mm length was chosen for fabrication ease yielding the grating period as 997.1 nm for 1550 nm Bragg wavelength. The grating post-size is 350 nm and the gap of the posts from the waveguide was varied to sweep the coupling constant κ from 0.2 cm^{-1} to 2 cm^{-1}.

Figure 1c shows the single-sided power spectral density (PSD) of the laser frequency noise. This measurement was done by heterodyne beatnote spectroscopy by beating a reference external cavity diode laser (free running Toptica CTL) with the E-DBR laser. The recorded data for the in-phase and quadrature components of the beatnote were processed by Welch's method [7] to retrieve the single sided phase noise power spectral density $S_{\phi\phi}$ that was converted to frequency noise S_{ff}. The frequency noise of the E-DBR laser is limited by the reference laser below 2 kHz. The laser frequency noise reaches a value (white noise floor) of 305 Hz^2/Hz at a 4 MHz offset, corresponding to the intrinsic laser linewidth of 957 Hz.

Figure 1d shows the optical spectrum of the E-DBR laser at different applied heater powers. The laser can be tuned mode-hop free over a tuning range of 62.4 GHz with more than 30 mW output power in lensed fiber and side mode suppression ratio (SMSR) greater than 60 dB. The heaters' efficiency can be improved by appropriately positioning the metal over the optical waveguide and optimizing the cladding thickness.

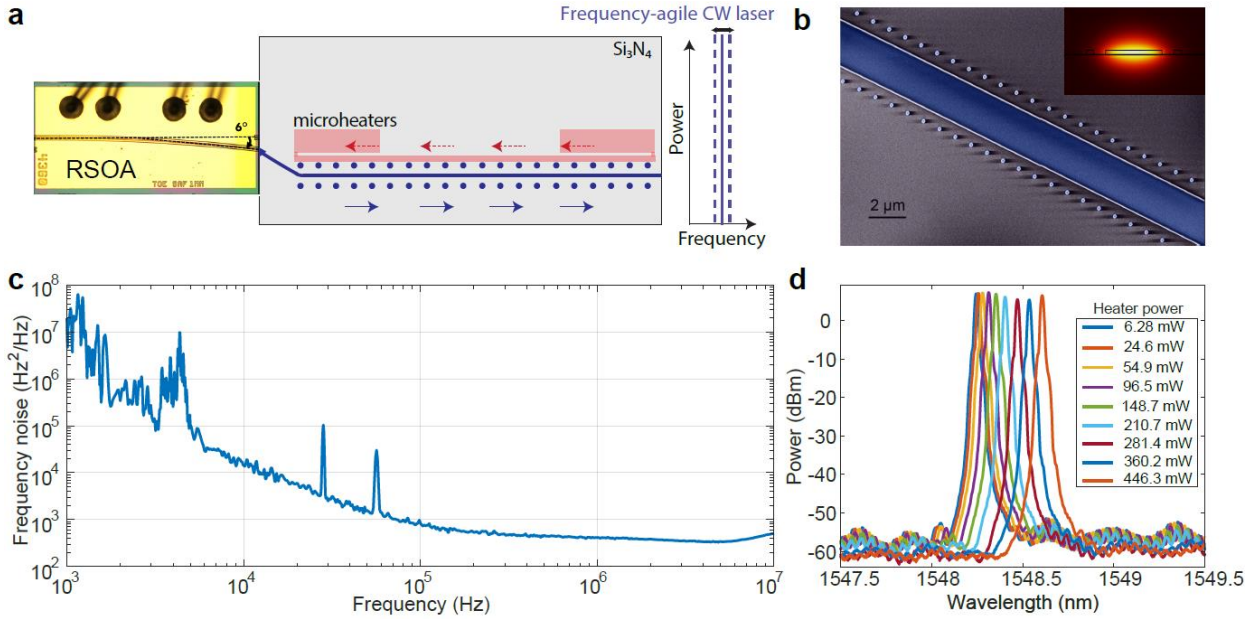


Fig. 1. (a) Schematic of the E-DBR laser based on hybrid integration of an RSOA and Si_3N_4 photonic chip. The integrated microheaters are used to tune the lasing wavelength. (b) False-colored scanning electron microscope (SEM) image showing the Si_3N_4 waveguide with post gratings. The inset shows the FEM simulation of the fundamental optical mode at the wavelength of 1550 nm. (c) Frequency noise spectra of the E-DBR laser system at the wavelength of 1548.5 nm. (d) Optical spectra of the E-DBR laser at different wavelengths by applying different electrical power on the integrated microheater.

DISCUSSION

The performance of the E-DBR laser can be further enhanced by increasing the length of the grating and reducing the coupling constant κ. This would increase the reflectivity at the Bragg wavelength and reduce the grating bandwidth. For further noise suppression, the E-DBR laser can be edge-coupled and self-injection locked to a high-Q Si_3N_4 spiral resonator on a separate chip [8]. Also, hybrid packaging is a robust method to improve long-term laser stability and reduce laser frequency noise below 1 kHz offsets by eliminating acoustic instabilities inherent to the unpackaged optical setup.

In summary, we demonstrate a E-DBR laser using RSOA and Si_3N_4 photonic chip with integrated heaters allowing mode-hop free tuning upto 62.4 GHz. The laser exhibits sub-kHz linewidth and output power more than 30 mW and it can be endowed with high-speed frequency-agility using piezoelectric material such as Lead Zirconate Titanate (PZT) or Aluminum Nitride (AlN). Such photonic integrated lasers can provide superior attributes in compactness, phase-noise, and power as compared to external cavity lasers while maintaining turn-key operability. The demonstrated approach is based on foundry-ready processes for large-volume photonic integrated circuits.

Acknowledgements: This publication was supported by Contract W911NF2120248 (NINJA) from the Defense Advanced Research Projects Agency (DARPA), Microsystems Technology Office (MTO) A.S. acknowledges the support from the European Space Technology Centre with ESA Contract No. 4000135357/21/NL/GLC/my. J.R. acknowledges support from the Swiss National Science Foundation under Grant No. 201923 (Ambizione).

References

[1] J. Liu et al., “High-yield, wafer-scale fabrication of ultralow-loss, dispersion-engineered silicon nitride photonic circuits”, Nature Photonics 12, 1 (2021).
[2] Olsson et al., “Probabilistically shaped PDM 4096-QAM transmission over up to 200 km of fiber using standard intradyne detection,” Optics express 26, 4 (2018).
[3] Newman et al., “Architecture for the photonic integration of an optical atomic clock,” Optica 6, 680-685 (2019).
[4] Millot et al., “Frequency-agile dual-comb spectroscopy,” Nature Photonics 10, 1 (2016).
[5] Lihachev et al., “Low-noise frequency-agile photonic integrated lasers for coherent ranging,” Nature communications 13, 1 (2022).
[6] Xiang et al., “Ultra-narrow linewidth laser based on a semiconductor gain chip and extended Si 3 N 4 Bragg grating”, Optics letters 44, 15 (2019).
[7] P.Welch, “The use of fast fourier transform for the estimation of power spectra: A method based on time averaging over short, modified periodograms”, IEEE Trans. on Audio Electroacoustics, 15, 70-73 (1967).
[8] Guo et al., “Chip-Based Laser with 1 Hertz Integrated Linewidth”, Science Advances 8, 43 (2022).

Unconventional Optical Phased Array Antennas Integrated in a Programmable Photonic Integrated Circuit

(Student paper)

Nicola Anselmi[2], Seyedmohammad Seyedinnavadeh[1], Paolo Rocca[2,3], Andrea Massa[2,4,5], Maziyar Milanizadeh[1,6], Francesco Morichetti[1] and Andrea Melloni[1]

[1]Dipartimento di Elettronica, Informazione e Bioingegneria, Politecnico di Milano, Milan, Italy,
[2]ELEDIA Research Center (ELEDIA@UniTN - University of Trento), DICAM, Trento, Italy
[3]ELEDIA Research Center (ELEDIA@XIDIAN - Xidian University), Xi'an, Shaanxi Province, China
[4]ELEDIA Research Center (ELEDIA@UESTC - UESTC), Chengdu, China
[5]ELEDIA Research Center (ELEDIA@TSINGHUA - Tsinghua University), Beijing, China
[6]now with National Research Council, Ottawa, Canada
* corresponding author e-mail: nicola.anselmi.1@unitn.it

We report on the design and experimental validation of an unconventional optical phased array architecture integrated with a silicon photonic programmable processor. A 16-elements thinned array layout is optimized by using a multi-objective approach, providing the best trade-off between array complexity and radiation pattern performance.

***Keywords*:** Optical Phased Array, Grating Coupler, Free Space Optics, Beam forming

INTRODUCTION

On-chip manipulation of free-space optical (FSO) beams is attracting increasing interest for wide range of applications, such as localization, positioning and ranging (LiDAR), advanced metrology, FSO communication, and imaging [1]. Optical phased arrays (OPAs) enable efficient shaping and steering of the waveform beam by controlling the relative phase and amplitude of the light radiated by each antenna element [2]. However, 2D OPAs with uniformly spaced antennas, suffer from scalability limits due to relatively large size of the optical antennas and also spacing between them for routing of the optical systems, which are both larger than several wavelengths [3]. These constraints lead to the presence of multiple closely spaced grating lobes, an issue that is well known in the context of radio frequency (RF) phased array design [4]-[6]. This issue can be mitigated by designing unconventional OPA architectures, such as thinned array architectures [5] and sparse arrays [6], where the elements are irregularly positioned within the array aperture.

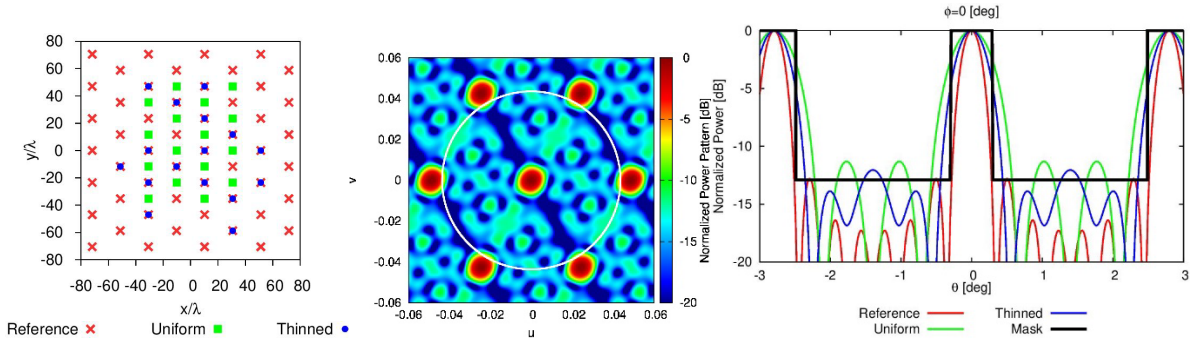
In this work, we propose and experimentally validate the design of an unconventional array architecture integrated with a silicon photonic programmable processor. OPAs thinned architectures are optimized through a multi-objective optimization, minimizing both the number of array elements and the deviation from desired beam pattern performances. The proposed nonuniform OPA configuration enables a significant reduction of the number of antennas, with advantages in the footprint and control complexity of the photonic processor.

NONUNIFORM ARRAY DESIGN

The proposed nonuniform OPA design method aims to meet a set of requirements on the radiation pattern of the array, while simplifying its architecture complexity by reducing the number of radiating elements. Towards this end, let us consider a reference array of N optical antennas positioned over a triangular grid on the (x,y)-plane. By considering identical ideal isotropic radiating elements, the far-field power pattern is expressed as [4]

$$P(\theta,\phi) = \left|\sum_{n=1}^{N} a_n \; e^{j\frac{2\pi}{\lambda}(x_n \sin\theta\cos\phi + y_n \sin\theta\sin\phi)}\right|^2 \quad (1)$$

where λ is the wavelength, (x_n, y_n) are the elements positions, and a_n, n = 1,…,N, are the amplitude coefficients. Figure 1(a) reports an example of a N = 56 elements reference array (red crosses), with spacing $d_x = 20.5\lambda$ and $d_y = 23.5\lambda$ along the *x* and *y* axes, respectively. The power pattern of the array, uniformly illuminated (i.e., $a_n = 1.0$, n = 1,…,N), satisfies an upper bound mask requiring a beamwidth (BW) narrower than 0.6 [deg] (10 mrad) and a side-lobe level (SLL) equal to -13 [dB] for $\theta < 2.5$ [deg]. Figure 1(c) shows the comparison of the reference array pattern with the mask along the $\phi = 0$ [deg] cut. To reduce the number of elements, the array is thinned by retaining only a subset of the reference array antennas, while all others are removed [5]. Towards this end, the thinning sequence is represented as a binary vector, and a multi-objective Genetic-Algorithm optimization is used to search for the optimal thinning configuration that (i) minimize the number of the thinned array elements, and (ii) minimize the mismatch between the power pattern and the reference mask.



(a) (b) (c)

Fig. 1. (a) The reference, uniform and "thinned" nonuniform array layouts, (b) 2D color-map of the normalized power pattern in (u,v) plane, *and (c) 1D cut of the radiation pattern along* $\phi = 0$ [deg].

Figure 1(a) reports the configuration of the optimized nonuniform thinned array of 16 elements (blue circles), whose 2D radiation pattern is shown in Fig. 2(b). Fig. 1(c) shows the 1D pattern along the $\phi = 0$ [deg] cut and over the (u,v)-plane, being $u = sin\theta\, cos\phi$ and $\theta \leq 2.4$ [deg] angular range (i.e., until the first grating lobe), and a BW < 0.49 [deg], despite a reduction of 71% in the number of elements. The optimized thinned array is then compared with the uniform array having the same number of elements and characterized by a uniform spacing between the elements (green squares in Fig. 1a). As can be noticed from Fig. 1(c), the designed thinned array shows a narrower BW with respect to the uniform one, moreover, thanks to the optimized layout, the nonuniform thinned array allows to limit the sidelobes close to the main lobe region.

PHOTONIC CHIP DESIGN AND EXPERIMENTAL RESULTS

The proposed OPA structure was integrated in a photonic integrated circuit that can be operated as an adaptive transmitter (or receiver) for FSO beams. Figure 2(a) shows a micrograph of the photonic chip fabricated in a standard Si-photonics platform using 220-nm wide waveguides WG (AMF foundry), which is designed to work around wavelength of $\lambda = 1.55\ \mu\text{m}$. The antenna array elements are realized via vertically emitting grating couplers that are placed according to the configuration of Fig. 1(a). The simulated far-field beam of the grating coupler (with $\Lambda = 630\ \text{nm}$ pitch) is shown in Fig. 2(b) which has a beamwidth of $9° \times 5°$ and a tilt angle of $10°$. Each element of the array is routed and connected to one of the 16 waveguides of a programmable photonic processor (Fig. 2a). The photonic processor consists of a 16x1 binary tree mesh of beam combiners/splitters, which are realized by using thermally tuneable Mach-Zehnder Interferometers (MZI). If used as a transmitter (1 input WG, 16 output antennas), the light at the input waveguide of the mesh is routed across the binary tree architecture, which can provide arbitrary amplitude and phase to each individual element of the OPA; if used as a receiver (16 input antennas, 1 output WG), the photonic processor can coherently combine the received beams impinging on its antenna array to the output waveguide.

To perform experimental characterization of the OPA assisted by the photonic processor, the photonic chip is mounted on a printed circuit board which is connected to a custom-designed electronic board consisting of a microprocessor and several channels both for actuation and reading out. The circuit board is mounted in a free-space optical setup (Fig. 2c), which is shown schematically in Fig. 2(d). A biconvex lens ($f = 100\ \text{mm}$) is placed in Fourier transforming configuration for focusing/collimation and a tilted mirror is aligned to deflect the vertically emitting beam of the array to horizontal direction. At the other end of the setup, a fiber collimator package with beam waist diameter of $w_0 = 1.12\ \text{mm}$ is placed at back focal plane of the lens as transmitter/receiver of the beams. The configuration of the photonic processor is performed by using the circuit as a receiver; the light is injected from fiber collimator to the OPA and the photonic processor is tuned in order to coherently combine at the output WG the power coupled by the array. The algorithm used for self-calibration and configuration of MZIs of the mesh is based on maximization of the output power by using separate dithering frequency demodulation for different actuating channels [7].

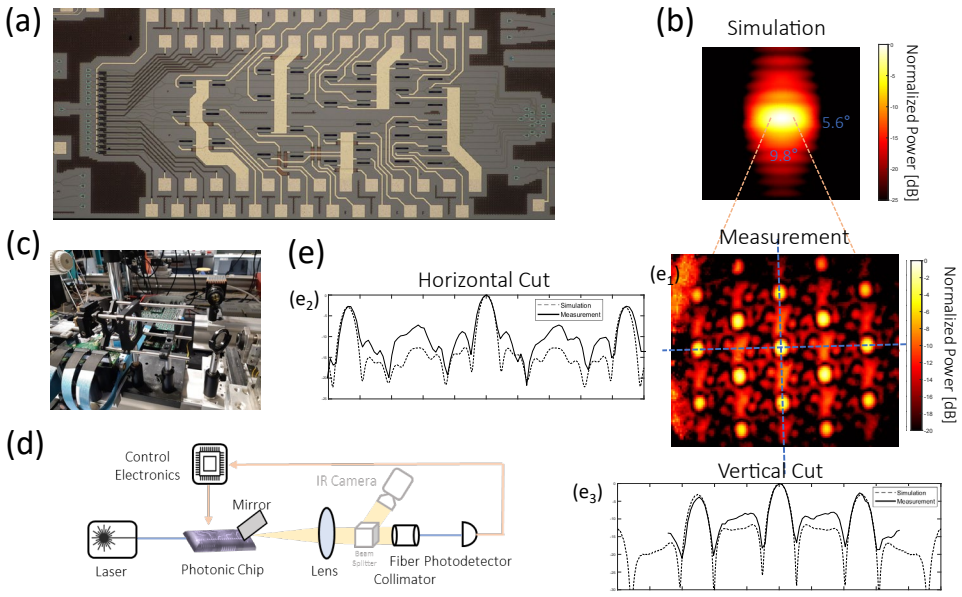


Fig. 2. (a) Top-view microphotograph of the silicon photonic chip integrating the MZI-based photonic processor and the proposed nonuniform OPA; (b) simulated radiation diagram of the single antenna element (grating coupler) of the OPA; (c) photograph and (d) schematic of the experimental setup; (e) camera view measurement of the 2D (e_1) radiation diagram of the nonuniform OPA in broad side configuration and 1D cut along (e_2) horizontal and (e_3) vertical directions.

After configuration of the processor, the direction of propagation is reversed in order to capture the far field emitted by the array when the processor is kept on the tuned configuration. To this aim, a beam splitter and IR camera is used (Fig. 2d). The far field captured is shown in Fig. 2(e_1), along with the horizontal and vertical cuts in Figs. 2(e_2) and 2(e_3), respectively (note that the fabricated array is rotated by 30° with respect to the proposed design in Fig. 1a). As it can be noticed, it has a good agreement with the simulated far field. A more precise characterization of individual MZIs will lead to more uniform excitation of the array, and thus lower side lobe levels in the pattern; however, exploiting self-configuring binary tree architecture in the processor, the photonic circuit can be used to automatically shape and steer the transmitting beam to an FSO receiver, or vice versa, can adapt to arbitrary transmitted FSO beams impinging on the array as a receiver.

CONCLUSION

We reported on the design of a thinned OPA architecture integrated in a silicon photonic platform that enables a significant reduction of the number of antennas with respect to a uniform OPA. The effectiveness of the proposed structure is validated experimentally by directly observing the radiation pattern generated by the OPA when the beam is pointed towards the broadside direction through active control of a photonic integrated processor. Future work is oriented to the use of fabricated circuit as an integrated transmitter/receiver in FSO communication links [8], as well as in the optimization of the OPAs layout when scanning the beam within the field of view.

References

[1] B. Schwarz, "Mapping the world in 3D", Nature Photon., vol. 4, pp. 429-430, Jul. 2010.
[2] Sun, J., Timurdogan, E., Yaacobi, A. et al. “Large-scale nanophotonic phased array,” Nature 493, 195–199 (2013). https://doi.org/10.1038/nature11727
[3] R. Fatemi, A. Khachaturian and A. Hajimiri, "A Nonuniform Sparse 2-D Large-FOV Optical Phased Array with a Low-Power PWM Drive," IEEE Journal of Solid-State Circuits, vol. 54, no. 5, pp. 1200-1215, May 2019.
[4] P. Rocca et al., “Unconventional phased array architectures and design methodologies—A review,” Proc. IEEE, vol. 104, no. 3, pp. 544–560, Mar. 2016.
[5] M. Salucci, G. Gottardi, N. Anselmi, and G. Oliveri, "Planar thinned array design by hybrid analytical-stochastic optimization," IET Microw. Antennas Propag., vol. 11, no. 13, pp. 1841-1845, Oct. 2017
[6] G. Oliveri and A. Massa, “Bayesian compressive sampling for pattern synthesis with maximally sparse non-uniform linear arrays,” IEEE Trans. Antennas Propag., vol. 59, no. 2, pp. 467-481, Feb. 2011.
[7] F. Zanetto,et al. “Dithering-based real-time control of cascaded silicon photonic devices by means of non-invasive detectors,” IET Optoelectron. 15, 111–120 (2021).
[8] Milanizadeh, M., SeyedinNavadeh, S., Zanetto, F. et al. Separating arbitrary free-space beams with an integrated photonic processor. Light Sci Appl 11, 197 (2022).

Astrocomb Miniaturization

(Invited paper)

Ewelina Obrzud[1]

[1]Swiss Center for Electronics and Microtechnology (CSEM), Jaquet Droz 1, Neuchâtel, Switzerland
* ewelina.obrzud@csem.ch

Searches for extrasolar planets, their characterisation, and measurements of fundamental constants' variability are key applications of extreme-precision astronomical spectroscopy. Laser frequency combs (LFCs) are recognised as a valuable tool for precise and accurate spectrograph calibration. This talk presents how exploiting new technologies and progress in nonlinear optics can provide miniaturized LFCs in the visible and near-infrared.
Keywords: *laser frequency comb, photonic integrated circuit, lithium niobate on insulator, nonlinear waveguides, astronomical spectroscopy*

INTRODUCTION

Laser frequency combs (LFCs) provide spectra composed of a large set of laser lines equally spaced in optical frequency, with each comb line frequency known with great precision and accuracy. LFC permit linking the optical fequencies to the SI time standard and provide absolute accuracy. Thanks to these characteristics, astrocombs (LFCs designed for use in astronomy) have been recognised as an invaluable tool in astronomy, namely in astronomical spectrograph calibration. Precise and accurate spectrograph calibration is crucial in exoplanet detection and characterisation, and determination of the fundamental physical constant variability. However, due to the specificity of astronomical spectrographs – their broad wavelength coverage (from IR to Vis/UV) and frequency resolution (>10 GHz) - generation of astrocombs suitable for spectrograph calibration still faces several challenges. Despite their complexity, they have already allowed to reach measurement precision not achievable with other calibration techniques[1-3].

RESULTS

Most of the astrocombs currently in use are based on optically filtered mode-locked lasers[3-5]. In recent years other technologies were proposed to address shortcomings of the existing systems. One of such technologies is based on resonantly enhanced nonlinear optical frequency conversion in optical microresonators[6] that has been proposed as way to miniaturize and simplify astrocombs. Microresonators, optical cavities of mm-scale, are able to generate low-noise frequency combs with comb line spacing from 10s of GHz up to THz. These optical pulse sources can be integrated on chip on various platforms enabling operation in different wavelength ranges. Microresontaor-based astrocombs have already been demonstrated as a potential future astronomical spectrograph calibrator with notable demonstrations on the NIRSPEC and GIANO-B spectrographs[7, 8].

Another platform suitable for astrocomb generation is based on electro-optic modulation (EOM) of a continuous wave laser. This technology is currently based on off the shelf EOM from the telecom industry, and it has already been proven to satisfy the requirements of the astronomical community. Several systems have already been tested[9, 10] and deployed[11, 12] in astronomical observatories. The on-chip integration of electro-optic frequency combs is the following step of the development of this technology, which will address the need of efficiency, scalability, and flexibility of the EOM. Impressive results have already been published[13, 14].

Regardless of the laser source, the development of nonlinear media for efficient spectral broadening is ongoing with photonic integrated circuit (PIC) - based nonlinear waveguides offering improved optical characteristics over standard highly nonlinear silica fibres and photonic crystal fibres. Exploiting high $\chi^{(3)}$ nonlinearities in materials such as silicon nitride[15, 16], tantalum pentoxide[17, 18] or aluminium nitride[19, 20] and in lithium niobate[21, 22] , where high $\chi^{(2)}$ nonlinearity is also present, provides an opportunity for ultra-broadband spectral coverage with relatively low optical pulse energies (< 100pJ), which is especially important for high repetition rate LFCs where pulse energies are limited, particularly for optical fibre-based setups. Of high relevance for astrocomb generation is reaching the blue/near UV band, which can be attained by exploiting frequency up-conversion mechanisms such as second harmonic generation (SHG) or sum-frequency generation (SFG) in, for example, periodically poled lithium niobate on insulator (PPLNOI).

CSEM participates in all of these efforts related to the development of astrocombs and has been developing astrocomb systems based on both the electro-optic modulation and microresonator technologies[7,10] (Figure 1c) as well as has been participating in the investigations related to nonlinear frequency conversion in

photonic integrated waveguides[23] (Figure 1f, g, h). Currently CSEM is engaged in providing an astrocomb based on EOM technology for the NIRPS spectrograph. Also, CSEM is actively pursuing the miniaturization of such systems in different research projects and with various academic partners. An active line of CSEM's research is the development of chip-scale and efficient frequency transfer to the blue/near UV (Figure 1 i, j) and on-chip EOM LFCs. Crucial to such activities are the collaboration with DESY in Germany and EPFL in Switzerland, together with CSEM's own microfabrication facilities. In particular, CSEM is developing a LNOI platform[24] which can provide low-loss waveguides (<10 dB/m), periodic poling, two photonic layers for optimized single mode guidance both at telecom and NIR/VIS, and metal deposition for high bandwidth on-chip EO driving. Examples of LNOI structures are shown in Figure 1 a,b,d and e.

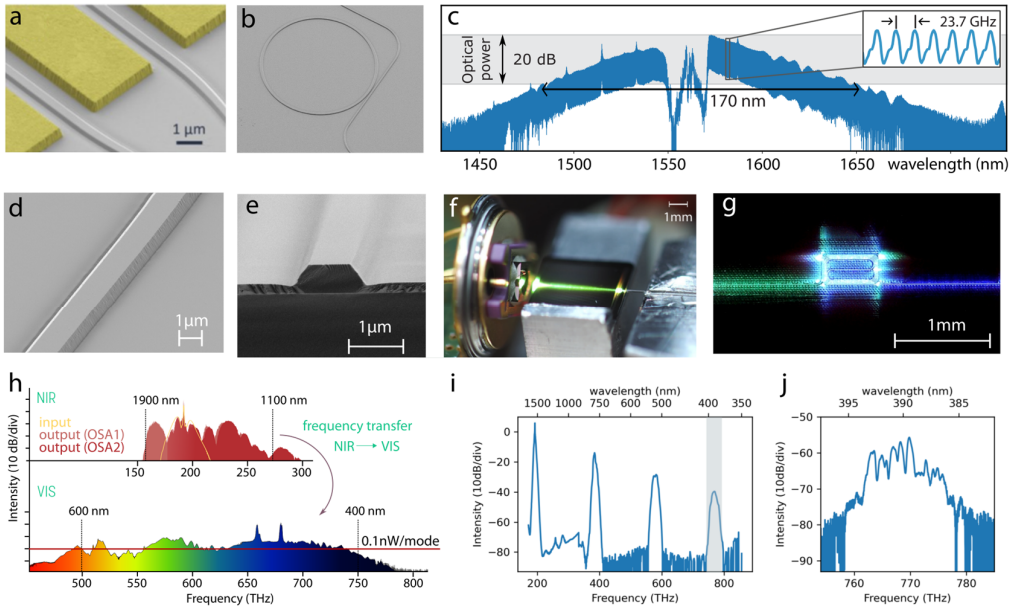


Fig. 1. a), b) SEM images of an intensity modulator and microresonator on LNOI fabricated at CSEM, respectively. c) optical spectrum obtained with a pulse-pumped optical microresonator[7]. d), e) SEM images of a LNOI nonlinear waveguide fabricated at CSEM. f) Setup for a direct on-chip self-referencing of a laser using a LNOI nonlinear waveguide[25]. g), h) Silicon nitride spiral waveguide in operation and the resulting NIR and VIS optical spectra obtained after injecting sub-100fs, 1550nm, 10GHz optical pulses obtained from an electro-optic pulse source[23]. i), j) Optical spectrum obtained when pumping a LNOI waveguide with 1550nm, 18 GHz optical pulses obtained from an electro-optic pulse source and the inset into the 4th harmonic, respectivel[26].

DISCUSSION

Overall, all this research can help achieve improved spectral coverage, efficiency, and miniaturization of LFCs that will benefit astronomical spectroscopy.

References

[1] Probst et al. A crucial test for astronomical spectrograph calibration with frequency combs. Nat. Astronomy, Vol. 4, p.603-608 (2020)
[2] Fredrick et al. A 30 GHz laser frequency comb for high-precision radial velocity calibration and exoplanet searches. APS April Meeting 2019, abstract id.X08.006 (2019)
[3] Li et al. *A laser frequency comb that enables radial velocity measurements with a precision of 1cms-1.* Nature, 452:610–612,(2008)
[4] Wilken *High-precision calibration of spectrographs*. Monthly Notices of the Royal Astronomical Society, 405(1): L16–L20 (2010)
[5] Steinmetz et al., *Laser Frequency Combs for Astronomical Observations*. Science, 321:1335 (2008)
[6] Kippenberg, Gaeta, Lipson, Gorodetsky *Dissipative Kerr solitons in optical microresonators*. Science, Vol. 361, 6402 (2018).
[7] Obrzud et al., *A microphotonic astrocomb*. Nature Photonics 13, 31–35 (2019)
[8] Suh et al. *Searching for exoplanets using a microresonator astrocomb*. Nature Photonics 13, 25–30 (2019).
[9] Yi et al., *Demonstration of a near-IR line-referenced electro-optical laser frequency comb for precision radial velocity measurements in astronomy. Nature Communications*, *7*, 1–9 (2016)

[10] Obrzud et al., "*Broadband near-infrared astronomical spectrometer calibration and on-sky validation with an electro-optic laser frequency comb*," Opt. Express 26, 34830-34841 (2018)
[11] Metcalf et al., *Stellar spectroscopy in the near-infrared with a laser frequency comb. Optica*, *6*(2), 233, (2019)
[12] Serizawa et al., *"Laser frequency comb system for the infrared Doppler spectrograph on the Subaru Telescope,*" Proc. SPIE 12188, Advances in Optical and Mechanical Technologies for Telescopes and Instrumentation V, 121885J (2022)
[13] Zhang et al., *Broadband electro-optic frequency comb generation in a lithium niobate microring resonator*. Nature 568, 373–377 (2019).
[14] Yu et al., Integrated femtosecond pulse generator on thin-film lithium niobate. Nature Vol. 612, 252–258 (2022)
[15] Porcel *et al. Two-octave spanning supercontinuum generation in stoichiometric silicon nitride waveguides pumped at telecom wavelengths.* Opt. Express, OE 25, 1542–1554 (2017).
[16] Carlson et al. *Self-referenced frequency combs using high-efficiency silicon-nitride waveguides.* Opt. Lett., OL 42, 2314–2317 (2017).
[17] Lamee at al., *Nanophotonic tantala waveguides for supercontinuum generation pumped at 1560 nm*. Opt. Lett., OL *45, 4192–4195 (2020).*
[18] Woods et al., *Supercontinuum generation in tantalum pentoxide waveguides for pump wavelengths in the 900 nm to 1500 nm spectral region*, Opt. Express 28, 32173-32184 (2020).
[19] Hickstein *et al. Ultrabroadband Supercontinuum Generation and Frequency-Comb Stabilization Using On-Chip Waveguides with Both Cubic and Quadratic Nonlinearities.* Physical Review Applied 8, (2017).
[20] *Lu et al. Ultraviolet to mid-infrared supercontinuum generation in single-crystalline aluminum nitride waveguides.* Opt.Lett., OL 45, 4499–4502 (2020).
[21] Lu et al., *Octave-spanning supercontinuum generation in nanoscale lithium niobate waveguides*. Opt. Lett. Vol. 44, 1492-1495 (2019)
[22] Reig Escalé et al., *Generation of 280 THz-spanning near-ultraviolet light in lithium niobate-on-insulator waveguides with sub-100 pJ pulses* APL Photonics 5, 121301 (2020).
[23] Obrzud et al. *Visible blue-to-red 10 GHz frequency comb via on-chip triple-sum-frequency generation*. Opt. Lett. 44, 5290 (2019).
[24] Jacopo et al. "*Wafer-scale fabrication of low-loss waveguides in lithium niobate on insulator (LNOI) integrated photonics platform*." European Conference and Exhibition on Optical Communication. Optica Publishing Group, 2022.
[25] Obrzud et al., *Stable and compact RF-to-optical link using lithium niobate on insulator waveguides*, APL Photonics 6, 121303 (2021)
[26] Ludwig et al., *in preparation*.

A Photonic Integrated High-power Soliton Microcomb Generator

(Student paper)

Xinru Ji[1,2], Yang Liu[1,2], Zheru Qiu[1,2], Rui Ning Wang[1,2],

Johann Riemensberger[1,2], Andrey Voloshin[1,2], and Tobias J. Kippenberg[1,2]

[1]Institute of Physics, Swiss Federal Institute of Technology Lausanne (EPFL), CH-1015 Lausanne, Switzerland
[2]Center for Quantum Science and Engineering, Swiss Federal Institute of Technology Lausanne (EPFL), CH-1015 Lausanne, Switzerland

*yang.lau@epfl.ch

We demonstrate a compact soliton microcomb light source. The soliton is generated from a Kerr microresonator and amplified by an erbium-implanted gain section integrated on the same photonic chip. We achieved an output power of 7.9 mW at a compact device footprint of 12.5 mm².

Keywords: *soliton, Kerr microresonator, erbium ion implantation*

INTRODUCTION

Soliton microcombs in photonic integrated Kerr microresonators are enabling unprecedented measurement precision and novel applications in a variety of fields [1]. The generation of soliton microcombs typically exhibits a low conversion (~1-4 %) efficiency [2], and post-amplification is required in practically all applications [3]. Therefore, large-scale, bench-top, fiber-based amplifiers are usually needed, which however, increases power consumption and impedes the ultimate system miniaturization demanded by emerging applications.

The on-chip amplification of soliton microcombs has been made possible until recently by the demonstration of a high-power, broadband, integrated erbium-implanted Si_3N_4 optical amplifier (EDWA) that can produce 30 dB on-chip net gain with an output power exceeding 100 mW [4]. This EDWA was applied to amplify a 20 GHz free spectral range (FSR) soliton microcomb [5], and performance comparable to commercial erbium-doped fiber amplifiers was achieved.

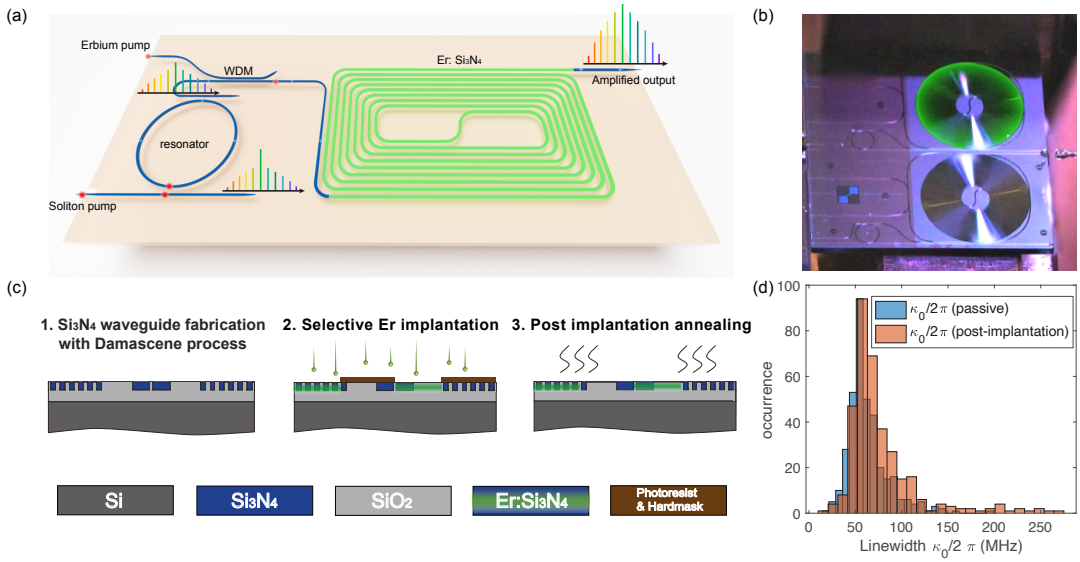


Fig. 1. Integrated high-power soliton microcomb generator. (a) A schematic design of the high-power soliton generator. Soliton is generated in a Kerr microresonator and extracted with a waveguide at the drop port for amplification. The erbium ions are optically excited by a 1480-nm pump laser via an integrated dichroic mirror. (b) A photo of the fabricated device. The dimension of the photonic chip is 5×5 mm², with two devices integrated. The footprint of one device is 12.5 mm². (c) A simplified process flow for device fabrication. Steps 1 represents the device fabricated with the photonic Damascene process, including DUV stepper lithography, LPCVD Si_3N_4 deposition, high-temperature annealing and top surface planarization. Steps 2-3 depict the selective implantation of erbium ions into the Si_3N_4 waveguide. (d) Histogram of intrinsic linewidth $\kappa_0/2\pi$ of the masked microresonator before and after ion implantation.

Nevertheless, such a demonstration was based on two separate Si_3N_4 chips, which introduced unwanted coupling losses that can degrade the signal-to-noise ratio, and increase the system complexity and required pump power.

RESULTS

Here, we demonstrate a compact high-power soliton generator, by integrating both Kerr microresonators and erbium-implanted gain sections on the same photonic chip, since the passive and active devices inherently share the same Si_3N_4 material and waveguide layers. This allows for advantages such as compactness, reduced insertion loss, cost, power consumption, and optical SNR, as well as low system complexity. The schematic of a photonic integrated high-power soliton generator is depicted in Figure 1(a). The generated soliton is extracted from a drop waveguide coupled to the Kerr resonator for amplification, where a microcomb with a lower carrier-to-sideband ratio is obtained to avoid gain saturation by the excess residual pump carrier.

The passive Si_3N_4 devices were fabricated using the photonic Damascene process [6]. The simplified fabrication process flow is depicted in Figure 1(c). The gain section was realized with three consecutive erbium ion implantations with a beam energy up to 2 MeV, to achieve a large overlap factor between the erbium ions and the waveguide optical mode. The microresonator was selectively masked with photoresist during implantation to preserve its properties such as optical loss and dispersion. The erbium ion concentration for doping the gain spiral is 1.68×10^{20} cm^3. The waveguide dimension is 2.1 µm×0.7 µm, featuring anomalous dispersion and an estimated overlapping factor of 0.5. The fabricated device is shown in Figure 1(b). The microresonator is characterized with scanning laser spectroscopy from 1350 to 1630 nm. From the fitted resonance linewidth, the intrinsic loss rate $\kappa_0/2\pi$ can be extracted. We characterize the microresonator by the most probable value of $\kappa_0/2\pi$ = 50 MHz, corresponding to a quality factor of 3.88×10^6. Figure 1(d) presents the histogram of the intrinsic loss rate distribution before and after erbium ion implantation, from which we confirm that the low loss property of the passive Kerr microresonator was conserved.

We then performed on-chip soliton amplification using the experimental setup shown in Figure 2(a). With an on-chip continuous-wave (CW) pump power of 380 mW at 1556.5 nm, a single soliton of 100 GHz FSR was generated. The loaded resonance linewidth $\kappa/2\pi$ is 60 MHz and the output power was measured as 0.031 mW. Next, we optically pumped the erbium ions using 1480 nm laser diodes in both forward and backward directions. The amplified soliton at the output, along with the input soliton power level, are depicted in Figure 2(c). We achieved an on-chip amplified soliton output power of 7.9 mW, corresponding to a power gain of ~24 dB. The demonstrated output power was limited by the small microcomb power as the amplifier input, stemming from the low external coupling rate $\kappa_{ex}/2\pi$ between the microresonator and the drop waveguide (~10 MHz). When the on-chip gain reached 24 dB, we observed parasitic lasing at unwanted wavelengths that can saturate the gain and power for microcomb amplification. Polishing the chip facet with an angle and utilizing UHNA fibers with matching cleaved facets will further minimize the parasitic lasing and enhance the amplified soliton power.

In conclusion, we demonstrated a compact soliton microcomb generator with an output power of 7.9 mW using on-chip amplification of soliton microcomb. This device will be suitable for applications such as LiDAR, photonic generation of microwaves, and high-power multi-wavelength coherent transceivers for high-speed coherent optical communications.

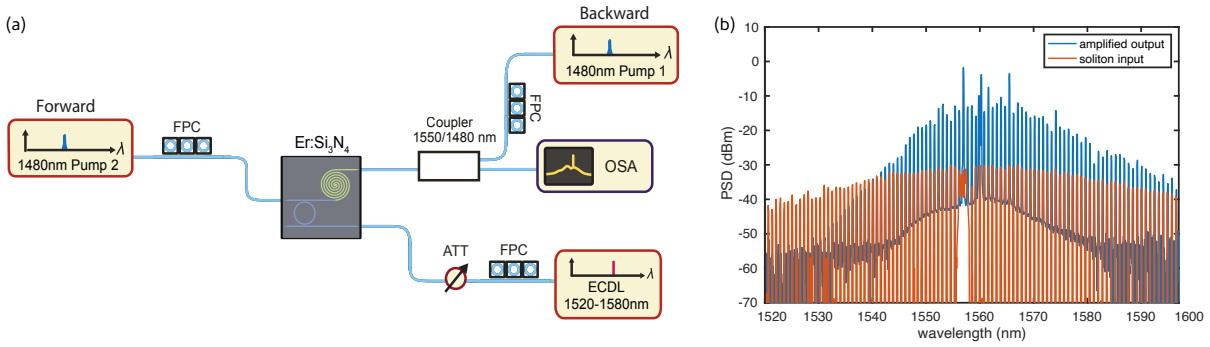


Fig. 2. Experimental results for on-chip soliton amplification. (a) Experimental setup for soliton generation and amplification. ECDL: external cavity diode laser; ATT, tunable optical attenuator; FPC, fiber polarization controller; OSA, optical spectrum analyzer. (b) Amplified soliton spectrum at the output (in blue). The red spectrum plots the generated soliton extracted at the microresonator drop port.

Acknowledgements: This work was supported by the Air Force Office of Scientific Research (AFOSR) under Award No. FA9550-19-1-0250, by the EU H2020 research and innovation program under grant No. 965124 (FEMTOCHIP), and by Marie Sklodowska-Curie IF grant No. 898594 (CompADC). This was further supported by the Swiss National Science Foundation under grant agreement No. 192293. J.R. acknowledges support from an SNSF Ambizione Fellowship (201923). The Si_3N_4 chips were fabricated in the EPFL center of MicroNanoTechnology (CMi) and are implanted in the Ion Beam Centre at the University of Surrey.

References

[1] T. Kippenberg et al., *Microresonator-Based Optical Frequency Combs*, Science 332, 555-559 (2011)
[2] C. Bao et al., *Nonlinear conversion efficiency in Kerr frequency comb generation*, Opt. Lett. 39, 6126-6129 (2014)
[3] H. Shu et al., *Microcomb-driven silicon photonic systems*, Nature 605.7910, 457-463 (2022)
[4] Y. Liu, et al., *A photonic integrated circuit-based erbium-doped amplifier*, Science 376, 1309-1313 (2022)
[5] X. Ji et al., *Compact, spatial-mode-interaction-free, ultralow-loss, nonlinear photonic integrated circuits*, Communication Physics 5.1, 1-9 (2022)
[6] J. Liu et al., *High-yield, wafer-scale fabrication of ultralow-loss, dispersion-engineered silicon nitride photonic circuits*, Nature Communications 12, 2236 (2021)

Thermally controlled frequency comb generation in hybrid silicon quantum dot lasers

(Student paper)

Thibaut Renaud[1]*, Heming Huang[1], Geza Kurczveil[2], Di Liang[2], R.G. Beausoleil[2] and Frédéric Grillot[1,3]

[1]LTCI, Télécom Paris, Institut Polytechnique de Paris, 19 place Marguerite Perey, 91120 Palaiseau, France
[2]Large-Scale Integrated Photonics Lab, Hewlett Packard Labs, Hewlett Packard Enterprise, Milpitas, CA 95035, USA
[3]Center for High Technology Materials, University of New-Mexico, 1313 Goddard SE, Albuquerque, USA
*correspondence to: thibaut.renaud@telecom-paris.fr

This work investigates the spectral properties of a hybrid silicon InAs/GaAs quantum dot comb laser. Experiments show that the comb bandwidth can be nicely improved through a proper thermal-control. They also unveil the possibility to achieve comb operation without pulses as a direct consequence of the background dispersion. As discussed hereinafter, these effects result from different contributions of both materials and device parameters of the quantum dot laser. Overall, these results provide novel findings for the conception of next-generation multi-channel optical transceivers for short-reach inter-chip communications.
***Keywords*: Quantum dots, frequency combs, optical interconnects, silicon photonics**

INTRODUCTION

Over the past two decades, high performance computing (HPC) has been deeply incorporated in the network infrastructure as the global Internet usage is ramping up[1]. Nowadays, hyperscale data centers and supercomputers are installed around the world to share the extensive loads of demands on intense computing power and high-volume transmission. However, current Von Neumann architecture of modern computers requires frequent exchanges between computing and storage units and is becoming an explicit limiting factor of the performance of the global network[2], as off-chip communications are commonly established over electric wires/cables, where the transmission capacity per link is dependent on data rate and distance, and the general energy efficiency is less than ideal. Moreover, when considering distributed systems, intensive inter-server and inter-rack hardware resource sharing can further exacerbate the bandwidth bottleneck problem[3]. One viable solution to overcome such obstacle, is to replace inter-chip, inter-server, and inter-rack electric wires and cables with high-performance optical interlinks, that are considerably more energy-efficient and rather independent on reach. To fully leverage the transmission capacity of optical carrier, photonic integration technology enabled integrated Dense Wavelength Division Multiplexing (DWDM) system has been proposed, allowing to lay out data line array through a single optical waveguide/fiber, and reducing circuit complexity by removing redundant footprints. Thanks to the major breakthroughs in silicon-based photonic integrated circuits (PICs) over recent years, compact optical transmitters that incorporate DWDM functionalities can be envisioned in the near future[4]. On this stage, it is preferable to use one single optical frequency comb (OFC) laser as light source instead of multiple single-mode lasers to keep the chip design simple, however, manipulating the OFC to provide required number of channels is a rather challenging task. To this end, semiconductor lasers made with quantum dots (QD) as an active gain media are considered as an attractive candidate, hence providing high optical gain with a low threshold current density, which are all desired properties for achieving high performance integrated sources. Moreover, owing to the dot size dispersion, QD lasers often exhibit a wide gain spectrum, ideal for OFC generation[5]. In this work, we investigate the comb properties of a hybrid silicon InAs/GaAs QD comb laser. By varying the temperature from 20°C to 50°C, the comb width is found to increase with respectively 20, 22, 30 and 40 lines above floor level. We believe that this thermally controlled frequency comb generation is achieved from the linewidth enhancement factor (α_H) and the homogenous broadening which are both temperature-dependent. On another hand, our beat note measurements point out the possible to achieve frequency comb enhancement without pulses in the time domain. This phenomenon is explained through the group velocity dispersion (GVD) which is not fully compensated by the optical nonlinearities of the saturable absorber. Overall, these results bring new insights on QD comb lasers and can therefore be utilized for the conception of future DWDM optical transceivers for short-reach optical interlinks.

LASER STRUCTURE

The studied laser has a multi-section cavity design, schematically represented in Figure 1(a). Two mirrors with 50% and 100% reflectivity define the 2.6-mm-long laser cavity. The 1.4-mm-long active region includes a semiconductor

optical amplifier (SOA) with a 176-µm-long saturable absorber (SA) placed in a middle, in a colliding pulse configuration. Such SA placement allows to take advantage of the second harmonic, providing richer channel spacing at high bit-rate[6]. The epitaxial structure consists in 8 layers of InAs QDs in GaAs, integrated on silicon. The optical mode transfer between the III-V and Si waveguides is realized by modes converters at the edge of the active region. A grating coupler (GC) couples the light out of the chip, to be collected in a micro-lensed optical fiber.

The epitaxial structure is obtained by taking an unpatterned wafer of InAs/GaAs QDs and wafer-bonding it to a Silicon-on-Insulator (SOI) wafer with already patterned Si passive devices. Standard III-V processing techniques are then used to etch the QD material and deposit the p- and n-contacts. A more detailed explanation of the epitaxial processes and laser structure can be found elsewhere[4,6].

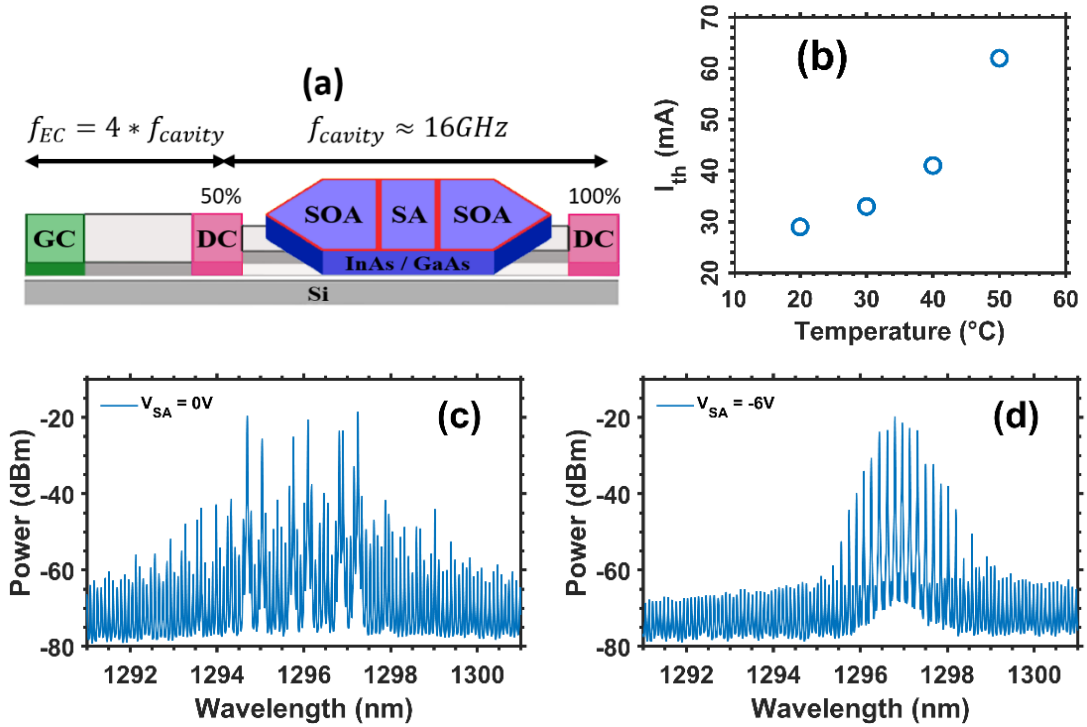


Fig. 1. (a) Schematics of the laser design. SOA: semiconductor optical amplifier; SA: saturable absorber; GC: Grating Coupler; DC: directional coupler. (b) Thermal dependence of the threshold current of the laser at V_{SA} = -6V. (c)(d) Optical spectra of the laser at 2×I_{th} and 20°C.

Figure 1(b) shows the variation of the threshold current I_{th} with the temperature, at an applied voltage of V_{SA} = -6V. The I_{th} increases from 23 mA to 28 mA when the SA voltage goes from 0V to -6V at room temperature, and then to 32 mA, 40 mA and 61 mA when the temperature is raised respectively to 30°C, 40°C and 50°C. The increase of internal loss coefficient in the SA results in a higher threshold at higher SA voltages. The relatively important increase of the threshold with temperature compared to other QD devices might be explained by the change in the refractive index of the external cavity resulting in increased losses. The optical spectra depicted in Figure 1(c) and (d) show the evolution of the frequency comb at room temperature (20°C) and $2 \times I_{th}$, with respect to the applied reverse voltage. Under these conditions, the emission wavelength is centered around 1296 nm and 1297 nm, respectively. At -6V, the comb spectrum takes place with 20 lines above the noise floor, and with 6 lines within the -10 dB bandwidth.

RESULTS AND DISCUSSION

Figure 2(a) shows the optical spectra of the laser under increasing temperatures of 20°C, 30°C, 40°C and 50°C, for bias conditions of $I = 2 \times I_{th}$ and V_{SA} = -6V. The emission wavelength of the different spectra is respectively centered around 1297 nm, 1299 nm, 1303 nm and 1305 nm, which is attributed to the thermal redshift of the gain envelope. The comb width appears to increase with the temperature, with respectively 20, 22, 30 and 40 lines above floor level, and 6, 8, 11 and 12 lines within a -10 dB power variation from the highest power mode of each spectrum, as delimited by the arrows in figure 2(a). While the reason for this temperature-dependence comb spectrum is not fully understood yet, we believe that both the α_H and the homogeneous broadening play a determinant role in this behavior. These two parameters are indeed temperature dependent[7]. Assuming a QD as a two-level atomic system and that the entire gain media of the QD laser is composed of uniform nanostructures, we demonstrated in a prior work[8] that the comb bandwidth $\Delta\upsilon \propto \Gamma \times \alpha_H$ with Γ being the homogeneous broadening

of the QD transition and the α_H calculated on the entire comb spectrum. In the laser under study, the α_H is found to increase with temperature from about 1 to 6 (not shown here) whereas the increase of the homogenous broadening with temperature makes the coupling among the dots much stronger.

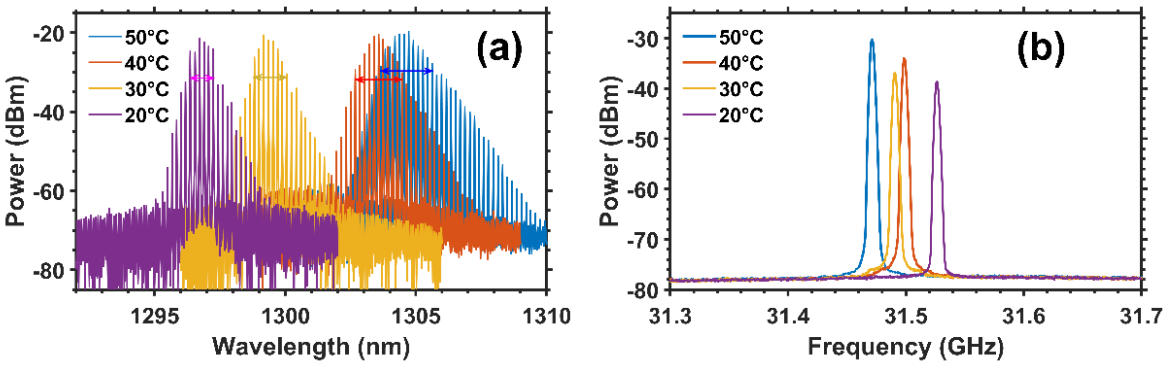


Fig. 2. Thermal dependence of (a) the optical spectrum and (b) the RF beatnote of the laser ***at*** $\boldsymbol{I = 2 \times I_{th}}$ *and* V_{SA} *= -6V.*

Since lasing photons can therefore be emitted not only from energetically resonant dots but also from other non-resonant ones, these effects can result in a dependence of the comb properties with temperature. The strengthening of the comb properties is also further highlighted by Figure 2(b), which displays the corresponding intermode beat note along with the peak power at different temperatures. The beat note frequency of 31.5 GHz is found at twice the free-spectral range of the cavity, which is coherent with the optical comb spectrum where alternates between lasing and suppressed comb lines are observed. Such second-harmonic generation directly results from the colliding pulse configuration of the laser cavity[9]. Finally, although the beat note appears quite stable over temperature, the linewidth of 3MHz results in an incomplete mode-locking. We checked the corresponding temporal dynamics and no pulses were clearly observed whatever the operating conditions (not shown here). This effect directly results from the GVD that is not compensated by the optical nonlinearities in the cavity, hence preventing phase-locking of the modes. Indeed, in order for the beatnotes to lock, some optical nonlinearity coming from saturable absorption or from four-wave mixing within the gain medium is necessary to overcome the dispersion.[10]

CONCLUSION

This work investigates the influence of external conditions on a multi-section hybrid silicon InAs/GaAs QD comb laser. Particularly, we found that the comb properties are thermally-controlled at high reverse bias, that can be translated into a wider comb. These results also unveil the possibility to achieve comb operation without pulses as a direct consequence of the background dispersion which is useful for future DWDM optical transceiver in short-reach inter-chip communications. Further work will concentrate on the modelling our QD comb laser taking into account the GVD. We will also measure how the GVD behaves with temperature.

Acknowledgements: This work is supported by Hewlett Packard Enterprise (HPE).

References

[1] Verified Market Research, *High-Performance Computing (HPC) Market Size, Share & Forecast*, 2022.
[2] *Beyond von Neumann*, Nat. Nanotechnol. **15**, 507, 2020.
[3] Y. Shen et al., *Silicon Photonics for Extreme Scale Systems*, J. Light. Technol. **37**(2), 245-259, 2019.
[4] G. Kurczveil et al., *Innovative DWDM Silicon Photonics for High- Performance Computing*, in M. Nikdast et al., *Silicon Photonics For High-Performance Computing And Beyond* (pp. 191-221), CRC Press, 2022.
[5] K. Nishi et al., *Development of Quantum Dot Lasers for Data-Com and Silicon Photonics Applications*, IEEE J. Sel. Top. Quantum Electron. **23**(6), pp. 1-7, 2017.
[6] G. Kurczveil, D. Liang, M. Fiorentino, and R. G. Beausoleil, *Robust hybrid quantum dot laser for integrated silicon photonics*, Opt. Express **24**, pp. 16167–16174, 2016.
[7] L. Besombes, K. Kheng, L. Marsal, and H. Mariette, *Acoustic phonon broadening mechanism in single quantum dot emission*, Phys. Rev. B **63**, 155307, 2001.
[8] B. Dong et al., *Frequency comb dynamics of a 1.3μm hybrid-silicon quantum dot semiconductor laser with optical injection*, Opt. Lett. **44**, 5755–5758, 2019.
[9] G. Liu, P. J. Poole, Z. Lu, J. Liu, Y. Mao, M. Vachon, and P. Barrios, *InAs/InP quantum dot mode-locked laser with an aggregate 12.544 Tbit/s transmission capacity*, Opt. Express **30**, 3205-3214, 2022.
[10] J. Duan, H. Huang, B. Dong, J.C. Norman, Z. Zhang, J.E. Bowers, and F. Grillot, *Dynamic and nonlinear properties of epitaxial quantum dot lasers on silicon for isolator-free integration*, Photon. Res. **7**, 1222-1228, 2019.

Electro-Optic Packaging of Silicon Photonics-Based RF Multiplier for Clock Signal Generation in the Millimeter-Wave Band

Antonio Malacarne[1], Luca Roselli[2], Marco Chiesa[3], Alessandra Bigongiari[4], Manuel Reza[5], Antonio D'Errico[4], Antonella Bogoni[1,5], Claudio Porzi[5]*

[1] Photonic Networks & Technologies National Laboratory, CNIT, Pisa, Italy.
[2]Department of Engineering, University of Perugia, Perugia, Italy
[3]CamGraPhIC srl, Pisa, Italy
[4]Ericsson Research, Pisa, Italy
[5]TeCIP Institute, Scuola Superiore Sant'Anna, Pisa, Italy
[*]claudio.porzi@santannapisa.it

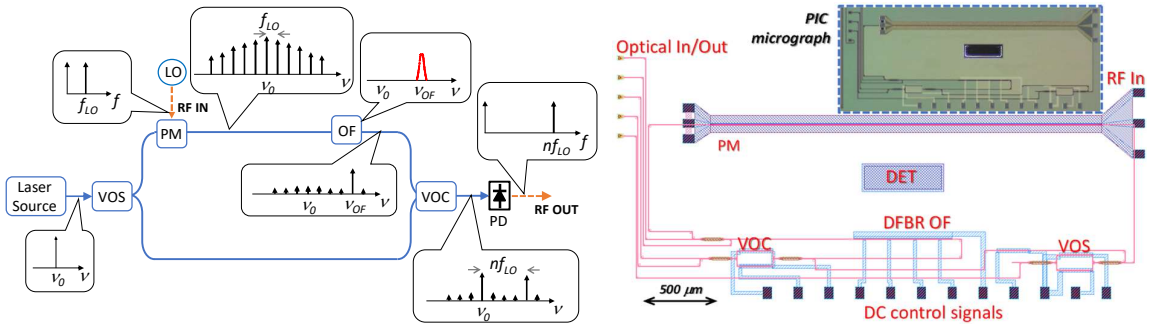
The design stages of a packaged silicon photonics RF processor for mm-wave reference clock distribution in 5G/6G radio access networks are presented. A wideband interconnection board including high-power handling bias tee is designed and implemented. Preliminary on-chip validation confirms spectrally pure 100 GHz signal generation from a 20 GHz input tone.
Keywords: *Integrated microwave photonics, silicon photonics, opto-electronic packaging*

INTRODUCTION

In 5G/6G mobile networks, operations such as ultra-low latency communications or wireless backhauling can be supported through high-capacity wireless links in the millimeter (mm)-wave band, where large bandwidth is available [1]. The quality of the radio signal would benefit from distributing a reference clock from a centralized base station toward network's peripherals using radio-over-fiber (RoF) approaches. By overcoming the impairments associated with recovering local clocks from jittered data samples, a common time reference enforces coordinated operations such as carrier aggregation or joint MIMO transmission techniques [2]. Additionally, costly RF oscillators at the antenna sites can be avoided, which is an appealing feature in the dense-cell architecture of 5G/6G networks. A further reduction of the system costs can be introduced by developing suitable photonic-integrated RF frequency synthetisers, and we recently demonstrated on-chip sixfold frequency multiplication of a microwave source up to 110 GHz with negligeable excess phase noise (PN) in a photonic integrated circuit (PIC) realized in silicon-on-insulator (SOI) technology [3]. Careful interfacing with the driving electronics and compact electro-optic packaging is however required for evaluating the circuit performance in field trials and its subsequent deployment in practical application scenarios. The design strategy for a miniaturized functionally packaged silicon photonics (SiP)-based programmable RF frequency multiplier is here reported. A matching network for the RF signal feeding the PIC is designed for operating over a wide frequency range of ~ 8 GHz centered around 20 GHz, and subsequently implemented on a printed circuit board (PCB). The design also aims at providing large tolerance to load conditions for the on-chip SiP electro-optic modulator as well as to the variations in the length of the wedge-bonds required for board-to-PIC connection. Preliminary on-chip characterization of the circuit operation is reported.

CIRCUIT OPERATION AND IMPLEMENTATION

The operation of the photonic-integrated RF synthesizer is illustrated in Fig. 1(a), where the RF/optical signals spectra along the circuit are also schematized in the insets. An external laser source (LS) delivers an optical carrier at the optical frequency ν_0 to the PIC. The circuit then relies on optical frequency comb (OFC) generation in a carrier-depletion-based SiP phase modulator (PM) driven by a local oscillator (LO) signal at f_{LO} followed by a highly selective bandpass optical filter (OF) that isolates a single tone out of the comb and suppresses all the other spectral components. The output of the filter is then recoupled with the input laser carrier portion that is obtained by splitting the PIC input signal. The circuit output thus consists of an optical carrier and a single high-order harmonic sideband spaced by nf_{LO} from ν_0, being n the selected harmonic order. This signal is thus suitable for being transmitted over a RoF link without suffering from the RF power fading effect associated with the interplay of fiber chromatic dispersion and symmetric spectrum of standard dual-sideband modulation. The on-chip input variable optical splitter (VOS) and output variable optical coupler (VOC) allow the relative carrier-to-sideband amplitude levels to be precisely controlled at the PIC output for optimizing the RF output power generated by a high-speed photodiode (PD) after a fiber link. The mask layout used for circuit realization through a standard multi-process wafer service in SOI technology [4] is then shown in Fig. 1(b), along with a micrograph of the fabricated device. The



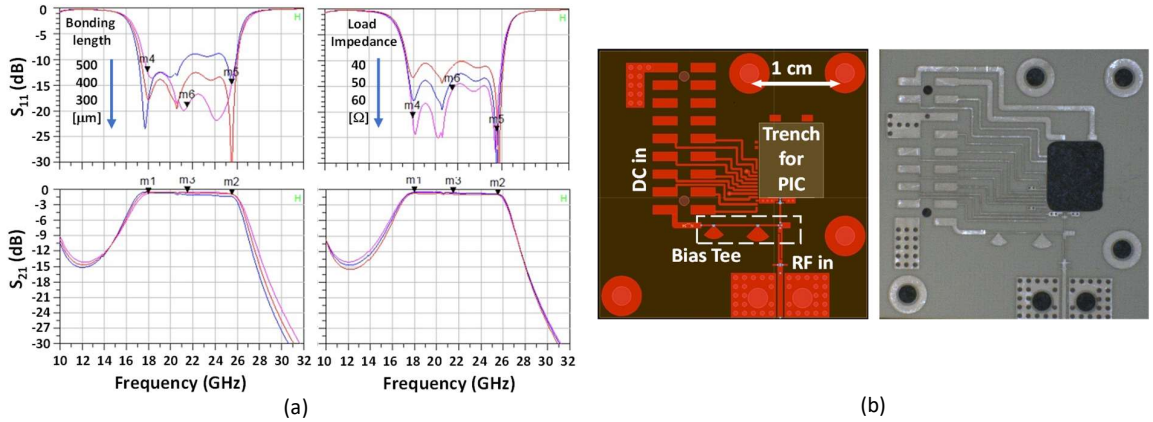
(a) (b)

Fig. 1. (a) Operation scheme; (b) Mask layout for circuit implementation in SOI technology (inset: micrograph of fabricated PIC).

integrated OF is implemented with a compact 4th-order distributed feedback resonator (DFBR) architecture, realized in a silicon strip waveguide Bragg grating (BG). The filter can be continuously tuned by controlling through local micro-heaters the optical path of four coupled cavities embedded within five BG mirrors [4], and thermally controlled Mach-Zehnder interferometers realizes the VOS/VOC structures. An air-filled deep etch trench (DET) through the full stack and down 60 μm into the silicon substrate is placed within the layout to improve the thermal isolation of the integrated OF and mitigate its wavelength drift as the RF/bias driving conditions of the PM-based OFC source are adjusted.

MATCHING NETWORK DESIGN AND PCB REALIZATION

Parallel to PIC fabrication, a PCB to be wedge-bonded to the PIC, carrying both the input LO reference for OFC generation and the control signals for the different on-chip actuators, has been developed. Coupling of the microwave signal with the DC reverse bias of the SiP modulator pn-junction is performed through an on-board bias tee. Since the comb source benefits from driving the SiP PM with large voltage values and considering power dissipation due to RF and DC bias signals at the termination load of the traveling-wave line realized above the modulator, a custom design for the bias tee able to support power levels of up to about 1.5 W has been adopted. The matching network is designed to operate in proximity of the SiP modulator cut-off frequency, which is about 20 GHz at the typical operating reverse-bias voltage levels of ~4 V. This allows attaining the mm-wave band with a relatively low multiplication factor of the input LO frequency, which helps in keeping the optical power of the selected OFC tone sufficiently large. A relatively broad range of about 8 GHz around this value has been also pursued for the operating frequencies, which can be advantageous for flexible selection of f_{LO} or in presence of wideband modulated RF driving signals [6]. The effect of wedge-bonds has been included in the model according to [7]. The results of the first guess design simulations of the interconnection including bias-tee are reported in Fig. 2(a), where the S_{11} and S_{21} parameters under variations around nominal values of the wedge-bond lengths as well as of the load impedance for the traveling-wave circuit carrying the modulator driving signal, are reported. A return loss below about 10 dB over a 18-26 GHz range is provided by simulations under the different load and wedge-bond length conditions. The PCB layout and a picture of the fabricated structure are also shown in Fig. 2(b). Contact pads are realized at the RF port for mounting a K-type connector to input the LO signal and the relevant transition between circuit microstrip and coplanar lines has been optimized too.



(a) (b)

Fig. 2. (a) Simulated S_{11} and S_{22} parameters of the on-board interconnection including bias tee under different (right) wire-bond lengths and (left) PM load impedance; (b) Layout of the designed PCB and micrograph of fabricated sample.

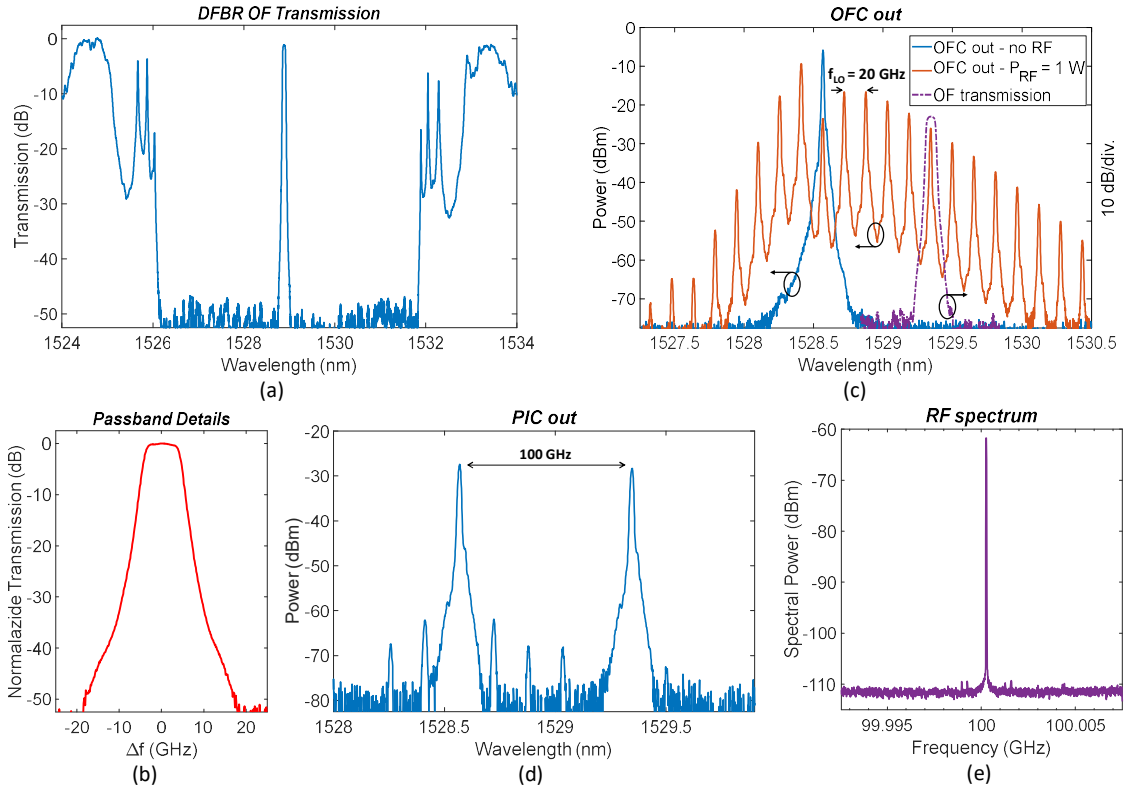


Fig. 3. (a) Full-span DFBR OF transmission; (b) Details of passband peak versus normalized frequency; (c) OFC source output spectra; (d) Optical spectrum at PIC output; (e) RF spectrum of generated 100 GHz clock.

PIC CHARACTERIZATION RESULTS

Preliminary on-chip testing of the circuit components and full-scheme operation is then performed. The measured transmission of the DFBR OF over a wide wavelength span, and the details of the transmission window in the center of the 6 nm-wide filter stopband are reported in Fig. 3(a) and (b), respectively. The passband peak exhibits a small insertion loss of ~1 dB, with a −3 dB width of about 8.5 GHz, and a rejection as large as 50 dB at 20 GHz from the central frequency. The spectrum at the output of the PM-based OFC generator is then shown in Fig. 3(b), when f_{LO} is 20 GHz and the driving power delivered to the RF probes contacting the modulator electrodes is ~ 30 dBm. The output carrier without applied RF signal is also shown, as well as the shape of the OF tuned in correspondence of the 5th-order longer-wavelength modulator sideband, spaced by 100 GHz from the input laser carrier. The optical spectrum of the composite signal (i.e., selected sideband and re-inserted carrier) at the PIC output is then shown in Fig. 3(d), illustrating a large minimum suppression of the spurious harmonics of about 34 dB. The corresponding RF spectrum of the synthetized 100 GHz continuous-wave signal, obtained through heterodyne detection with harmonic mixers in a signal spectrum analyzer is also reported in the figure.

Acknowledgements: This work has been supported by the project COSMOS within the FISR funding scheme of the Italian Ministry of University and Research (grant number FISR2019_03476).

References

[1] S. Tripathi, N. V. Sabu, A. K. Gupta, and H. S. Dhillon, “Millimeter wave and terahertz spectrum for 6G wireless,” in 6G Mobile Wireless Networks. Springer, 2021, pp. 83–121.

[2] D. P. Venmani, Y. Lagadec, O. Lemoult and F. Deletre, "Phase and time synchronization for 5G C-RAN: Requirements design challenges and recent advances in standardization", EAI Endorsed Trans. Ind. Netw. Intell. Syst., vol. 5, no. 15, pp. 1-7, 2018.

[3] A. Malacarne, A. Bigongiari, A. D'Errico, A. Bogoni and C. Porzi, "Reconfigurable Low Phase Noise RF Carrier Generation up to W-Band in Silicon Photonics Technology," J. Lightw. Technol., vol. 40, no. 20, pp. 6891-6900, 2022.

[4] https://europractice-ic.com/mpw-prototyping/siphotonics/imec/.

[5] C. Porzi, G. J. Sharp, M. Sorel, and A. Bogoni, “Silicon photonics high-order distributed feedback resonators filters,” IEEE J. Quantum Electron., vol. 56, no. 1, pp. 1–9, 2020.

[6] C. Porzi, F. Falconi, M. Sorel and A. Bogoni, "Broadband and High-Capacity Silicon Photonics Single-Sideband Modulator," in Journal of Lightwave Technology, vol. 40, no. 2, pp. 538-546, 2022.

[7] F. Alimenti, P. Mezzanotte, L. Roselli, and R. Sorrentino, “Modeling and characterization of the bonding-wire interconnection,” IEEE Trans. Microw. Theory Tech., vol. 49, no. 1, pp. 142–150, 2001.

Integrated Photonics for Quantum and Artificial Neural Networks-based Signal Processing

(Invited paper)

Luigi Di Lauro[1], Stefania Sciara[1], Abdul Rahim Aadhi[1], Nicola Montaut[1], Imtiaz Alamgir[1], Bennet Fischer[1], Hao Yu[1,2], Celine Mazoukh[1], Mario Chemnitz[1], Brent E. Little[3], Sai T. Chu[4], David J. Moss[5], Zhiming Wang[2] and Roberto Morandotti[1,2]*

[1]Institut national de la recherche scientifique (INRS-EMT), Varennes J3X 1S2, Canada
[2]Institute of Fundamental and Frontier Sciences, University of Electronic Science and Technology of China, China
[3]QXP Technology, Inc, China
[4]City University of Hong Kong, China
[5]Optical Sciences Centre, Swinburne University of Technology, Australia
* Roberto.Morandotti@inrs.ca

Integrated photonics is contributing to new emerging technologies for information processing based on machine learning and quantum science. On-chip devices offer viable solutions to perform simultaneous operations at high speeds, reduced power consumption, and on small footprints. In this work, we use integrated photonics to demonstrate highly efficient, intelligent, and secure classical and quantum communication at telecom regimes.

***Keywords*:** *Integrated photonics, machine learning, artificial neural networks, entangled photon states, quantum key distribution, telecom networks*

INTRODUCTION

Integrated photonics is raising considerable interest in the advancement of several emerging smart technologies, including artificial neural networks, machine learning (ML) [1], and quantum information processing [2]. In this context, on-chip photonic circuits, which can perform multiple simultaneous operations at high speeds, offer unique platforms to implement these technologies while using established fabrication techniques and exploiting conventional fiber telecom networks [3].

ML and integrated photonics have been used to implement all-optical neural networks (ONNs) for the optimization of telecom data transmission [4] and analog signal processing, as well as for language translation, cancer diagnosis, and image processing [5]. However, current implementations of ONNs are still characterized by high latency and low processing speeds, which make them inefficient to process large data sets. In quantum science, integrated photonic platforms and systems have been used to implement quantum communication in both free space [6] and fiber [7] infrastructures to guarantee unbreakable security of transmitted data throughout propagation channels. However, quantum secure communications over fiber networks still suffer from limited propagation distances and low transmission speeds, mainly due to scattering and losses affecting photons in fiber channels [8].

In this work, we explore and exploit integrated photonics to develop reconfigurable ONNs applied for processing and reconstruction of nonlinearly distorted telecom signals at ultrafast speeds. In parallel, we utilize on-chip photonics for quantum-enabled secure data transmission, where we tackle the generation and processing of complex entangled photon states to be used for high-speed quantum key distribution (QKD). We tackle these two implementations by making use of a single all-integrated photonic platform, which comprises a silicon-based nonlinear source (spiral waveguide [9] or microring resonator [10-12]) and an on-chip programmable interferometry system [13,14].

RESULTS

Our research strategy relies on a photonic platform, which is compatible with complementary metal–oxide–semiconductor (CMOS) fabrication techniques [10], as well as with optical fiber networks that are used for standard telecommunications [11,12]. Such a platform consists of two main components. The first component is an integrated silicon-based nonlinear source, i.e., a spiral waveguide or a microring resonator. These are used for i) the generation of either classical or quantum light over a broad spectrum of integrated frequency combs (a set of multiple, equally spaced colors forming the frequency lines) [11,15] and ii) to realize the nodes (i.e., the artificial

neurons) of our ONNs. The second component is a cascade of on-chip programmable interferometers [13,14], which are used for preparing the pulses that are thereafter injected into the spiral waveguide to generate entangled photons, as well as for quantum state processing.

The connections among the nodes of our proposed ONNs, i.e., the network topology, consisting of either a feed-forward [4,5] or a recurrent configuration [5]. The former architecture features unidirectional connections for 'static' data processing, such as images. The latter architecture features feedback connections among the nodes for 'dynamic' data processing. The density of the encoded information in our ONNs can be further increased via the use of integrated frequency combs [15] generated by a microring resonator and manipulated by means of multiplexing techniques. We optimize and benchmark our ONNs with ML supervising learning algorithms, which make use of the Ridge regression method for training [8]. We implemented different standardized benchmarking tests, e.g., the Mackey-Glass chaotic time series prediction and the classification of bits in n-parity operations (e.g., the n-bits XOR task [16]). We apply our ONNs for nonlinear telecom channel regeneration with the aim of restoring the initial temporal waveform of a transmitted signal, which undergoes distortion and nonlinear effects while propagating in optical fibers. This task generally requires extensive knowledge of the transmission system, such as fiber dispersion, absorption, and nonlinearity of the medium. The goal is to provide well-performing ONN-based platforms, highly versatile and integrable to optically process telecom signals at an ultra-high speed and reduced latency. From preliminary results, we estimate that our tunable ONN devices can process and accurately reconstruct nonlinearly distorted telecom waveforms achieving speeds above GHz/s at nanosecond latencies.

The spiral waveguide and the cascade of on-chip interferometers can also be exploited for the generation of high-dimensional (qudit) time-entangled photon states at telecom wavelengths. The interferometers are programmed in such a way as to split an input laser pulse into a coherent train of *d* pulses with equal amplitudes and discrete tunable spacing. The burst is then launched into the spiral waveguide to induce spontaneous four-wave mixing and thus generate time-entangled photon pairs centered at 1,550 nm. The time dimensionality of the photon pairs, i.e., the number of time modes per photon, is given by the number of *d* pulses exciting the spiral. The programmable interferometers, combined with external fiber-based GHz speed phase modulation, are used for quantum state processing, that is, for quantum interference and quantum state tomography measurements. We explore the applicability of our quantum photonic platform (spiral waveguide and on-chip interferometers) for telecom-compatible quantum secure communications. To this end, we aim for the implementation of proof-of-concept QKD based on time-entangled photonic qudits. The use of entangled photons provides robustness against eavesdropping attacks, as they allow the exchange of a device-independent secret key. The use of qudits guarantees an increase in the secret key rate, noise resilience, and information capacity. From preliminary tests, we estimate a record high secret key rate of a few hundred kbit/second, as well as a quantum bit error rate below 12%. These results show the high robustness of the cryptography key generated via our photonic qudits against eavesdropping attacks.

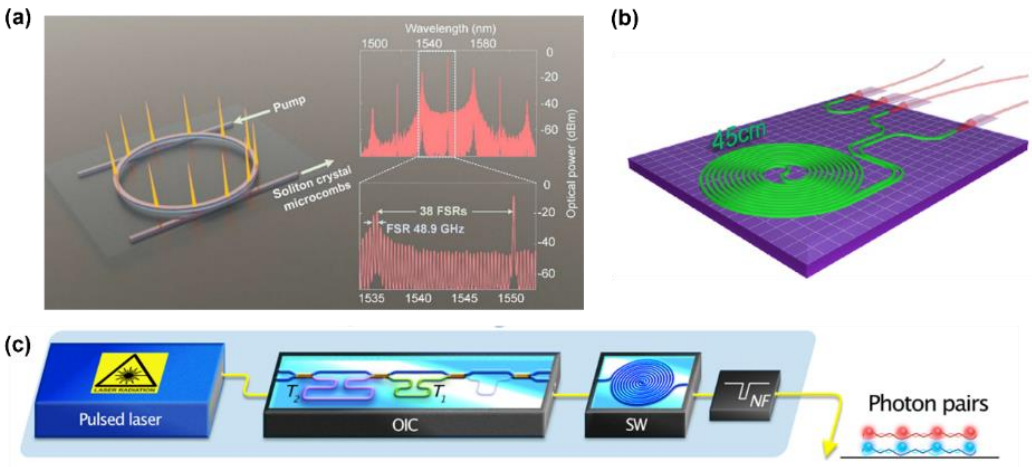


Fig. 1. (a) Schematic representation of an integrated microring resonator with a free spectral range (FSR) of 48.9 GHz employed for the generation of a comb spectrum centered at 1,550 nm arising from soliton crystals. Adapted from [17]. (b) Schematic representation of a 45 cm-long spiral waveguide (green) connected with circuit terminals (red lines). Adapted from [9]. (c) Schematic representation of the scheme used for photon state generation. OIC: on-chip interferometer cascade; T_1, T_2: transmission ratios of the interferometers; SW: spiral waveguide; NF: notch filter.

DISCUSSION

The use of on-chip photonic devices to develop ONNs will contribute to the advancement of the current state of the art in photonic machine learning and artificial neural networks for the advent of emerging smart technologies, such as the Internet of Things. This is unattainable with current electronic-based artificial neural networks as well as software-based ML solutions that still make use of the von-Neumann computer architecture, both increasingly suffering from several bottlenecks [5]. Microring resonators and spiral waveguides are compact and robust devices that are compatible with CMOS fabrication techniques and allow for high nonlinearity at low power, which is a feature required to establish an ONN. Microring resonators also offer dramatic information content scaling by either time or frequency multiplexing/demultiplexing, which makes them useful for many telecom applications. In this regard, time multiplexing techniques can be used to extend our QKD tests to multiple users covering different channels of the telecom C band. Increasing the complexity of our photonic qudits by, e.g., increasing the single-state dimensionality or the number of photons, will further bring enhancement of the secret key rate, as well as of the security of QKD protocols.

The compatibility with CMOS fabrication techniques and fiber telecom infrastructures, combined with the small footprint (μm-nm), power (milliwatts), and low heat consumption profiles of our platform, will position our research in line with the needs for energy efficiency required by current, as well as next-generation telecom technologies. Finally, our research can pave the way toward the advancement of current digital signal processing methods and encoding techniques for ultra-dense data transmission protocols, compatible with 5G and upcoming 6G networks. Our approaches will also yield unprecedented results in terms of quantum state processing and data transmission speeds, as well as in the security of quantum optical signals over fiber telecom networks.

References

[1] M. Nikdast, S. Pasricha, G. Nicolescu, A. Seyedi, D. Liang (Eds.), *Silicon photonics for high-performance computing and beyond*, CRC Press, Boca Raton, 2021

[2] F. Flamini, N. Spagnolo, F. Sciarrino, *Photonic quantum information processing: a review*, Reports on Progress in Physics, vol. 82, no. 1, 016001, pp. 1-32, 2019

[3] W. Bogaerts, D. Pérez, J. Capmany, D.A.B. Miller, J. Poon, D. Englund, F. Morichetti, A. Melloni, Programmable photonic circuits, Nature, vol. 586, pp. 207-216, 2020

[4] X. Xu, M. Tan, B. Corcoran, J. Wu, A. Boes, T.G. Nguyen, S.T. Chu, B.E. Little, D.G. Hicks, R. Morandotti, A. Mitchell, D.J. Moss, *11 TOPS photonic convolutional accelarator for optical neural networks*, Nature, vol. 589, pp. 44-51, 2021

[5] B.J. Shastri, A.N. Tait, T. Ferreira de Lima, W.H.P. Pernice, H. Bhaskaran, C.D. Wright, P.R. Prucnal, *Photonics for artificial intelligence and neuromorphic computing*, Nature Photonics, vol. 15, pp. 102-114, 2021

[6] S. Mishra, A. Biswas, S. Patil, P. Chandravanshi, V. Mongia, T. Sharma, A. Rani, S. Prabhakar, S. Ramachandran, R.P. Singh, *BBM92 quantum key distribution over a free space dusty channel of 200 meters*", Journal of Optics, vol. 24, n. 074002, 2022

[7] W. Wen, Z. Chen, L. Lu, W. Yan, W. Xue, P. Zhang, Y. Lu, S. Zhu, X. Ma, *Realizing an entanglement-based multiuser quantum network with integrated photonics*, Physical Review Applied, vol. 18, n. 024059, 2022

[8] N.T. Islam, C. Cahall, A. Aragoneses, A. Lezama, J. Kim, and D.J. Gauthier, *Robust and stable delay interferometers with application to d -dimensional time-frequency quantum key distribution*, Physical Review Applied, vol. 7, n. 044010, 2017

[9] D. Duchesne, M. Peccianti, M.R.E. Lamont, M. Ferrera, L. Razzari, F. Légaré, R. Morandotti, S.T. Chu, B.E. Little, D.J. Moss, *Supercontinuum generation in a high index doped silica glass spiral waveguide*, Optics Express, vol. 18, pp. 923-930, 2010

[10] D.J. Moss, R. Morandotti, A.L. Gaeta, M. Lipson, *New CMOS-compatible platforms based on silicon nitride and Hydex for nonlinear optics*, Nature Photonics, vol. 7, pp. 597-607, 2013

[11] M. Kues, C. Reimer, P. Roztocki, L. Romero Cortés, S. Sciara, B. Wetzel, Y. Zhang, A. Cino, S.T. Chu, B.E. Little, D.J. Moss, L. Caspani, J. Azaña, R. Morandotti, *On-chip generation of high-dimensional entangled quantum states and their coherent control*, Nature, vol. 546, pp. 622-626, 2017

[12] C. Reimer, S. Sciara, P. Roztocki, M. Islam, L. Romero Cortes, Y. Zhang, B. Fischer, S. Loranger, R. Kashyap, A. Cino, S.T. Chu, B.E. Little, D.J. Moss, L. Caspani, W. Munro, J. Azaña, M. Kues, R. Morandotti, *High-dimensional one-way quantum processing implemented on d-level cluster states*, Nature Physics, vol. 15, pp. 148-151, 2018

[13] B. Wetzel, M. Kues, P. Roztocki, C. Reimer, P.L. Godin, M. Rowley, B.E. Little, S.T. Chu, E. Viktorov, D. Moss, A. Pasquazii, M. Peccianti, R. Morandotti, *Customizing supercontinuum generation via on-chip adaptive temporal pulse-splitting*, Nature Communications, vol. 9, n. 4884, 2018

[14] Fischer, M. Chemnitz, B. MacLellan, P. Roztocki, R. Helsten, B. Wetzel, B.E. Little, S.T. Chu, D.J. Moss, J. Azaña, R. Morandotti, *Autonomous on-chip interferometry for reconfigurable optical waveform generation*, Optica, vol. 8, pp. 1268-1276, 2021

[15] C. Reimer, M. Kues, P. Roztocki, B. Wetzel, F. Grazioso, B.E. Little, S.T. Chu, T. Johnston, Y. Bromberg, L. Caspani, D.J. Moss, R. Morandotti, *Generation of multiphoton entangled quantum states by means of integrated frequency combs*, Science, vol. 351, n. 6278, pp. 1176-1180, 2016

[16] A. Lugnan, A. Katumba, F. Laporte, M. Freiberger, S. Sackesyn, C. Ma, E. Gooskens, J. Dambre, P. Bienstman, *Photonic neuromorphic information processing and reservoir computing*, APL Photonics, vol. 5, n. 020901, 2020.

[17] X. Xu, M. Tan, B. Corcoran, J. Wu, T.G. Nguyen, A. Boes, S.T. Chu, B.E. Little, R. Morandotti, A. Mitchell, D.G. Hicks, D.J. Moss, *Photonic perceptron based on a Kerr microcomb for high-speed, scalable, optical neural networks*, Laser & Photonics Reviews, vol. 14, n. 2000070, 2020

Fully On-chip Laser-integrated Entangled Photon Pair Source

(Student paper) / (Invited paper)

Raktim Haldar[1,2,3,*], Hatam Mahmudlu[1,2,3], Robert Johanning[1,2], Anahita Khodadad Kashi[1,2,3], Albert van Rees[4], Jörn P. Epping[5], Klaus-J. Boller[4], and Michael Kues[1,2,3,†]

[1]Institute of Photonics, Leibniz University Hannover, Nienburger Straße 17, D-30167, Hannover, Germany
[2]Hannover Centre for Optical Technologies, Leibniz University Hannover, Nienburger Straße 17, D-30167, Hannover, Germany
[3]Cluster of Excellence PhoenixD, Leibniz University Hannover, Hannover, Germany
[4]University of Twente, PO Box 217, Enschede, 7500 AL, The Netherlands
[5]QuiX, Enschede, The Netherlands
[*]raktim.haldar@iop.uni-hannover.de, [†]michael.kues@iop.uni-hannover.de

We demonstrate the first electrically-pumped laser-integrated quantum light source of entangled photons. The hybrid InP-SiN source emits frequency-bin entangled two- and high-dimensional states in the telecommunications band. It is fully integrated, compact, and field-deployable, bringing the required scalability to photonic quantum information processing.
Keywords: *quantum light sources, integration, entangled photon pairs, hybrid systems*

INTRODUCTION

Integrated photonic platforms can realize and process optical entangled quantum states in highly compact, robust, and scalable chips, enabling the implementation of long-distance quantum-secured communication, quantum-accelerated information processing, and non-classical metrology [1]. Notably, all previous on-chip entangled quantum photonic sources and the pioneering on-chip demonstrations of nonclassical functionalities were dependent on external excitation lasers, thereby making these systems overall non-reproducible, bulky, impractical, and thus precluding out-of-lab use as well as production at large scale [2].

To address this drawback, it is critical to realize a fully integrated quantum light source of entangled photons, where the laser is integrated. Such a system will allow all stages of quantum information processing to be on a single chip, bringing ultimately the required stability and scalability.

However, to date, the major technical challenge inhibiting a fully on-chip quantum light system was to integrate a stable and tunable laser together with a high rejection filter that eliminates laser sideband noise [3, 4], and a nonlinear parametric source of entangled photons. The absence of a unique material platform that is superior in all quantum photonic functionalities (i.e., low-loss guiding, filtering, efficient parametric generation of entangled

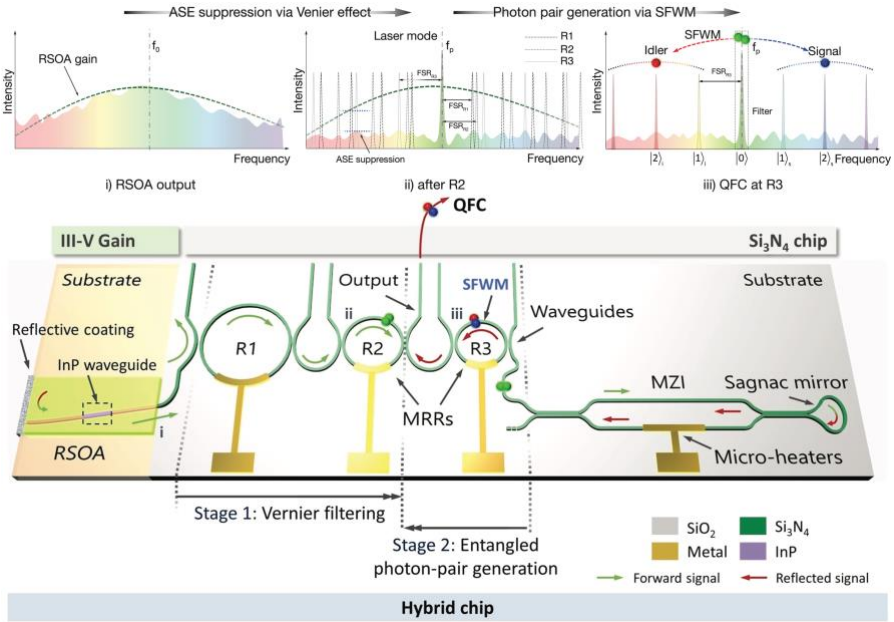


Figure 1 Laser-integrated photonic quantum light source of frequency-bin entangled photon pairs: An electrically pumped InP gain-section, i.e. a reflective semiconductor optical amplifier (RSOA) providing optical gain is coupled to a Si_3N_4 chip containing a three microring resonator (R1, R2, and R3) Vernier filter and a Mach-Zehnder interferometer (MZI) with a Sagnac loop mirror.

photons pairs, and their active manipulation) while providing at the same time optical gain, mainly impedes monolithic integration.

Here, we demonstrate for the first time a fully laser-integrated quantum light source that is capable of addressing these challenges by using an elaborated chip design and exploiting hybrid integration technologies [5]. The source directly generates frequency-bin entangled photons, i.e., high-dimensional quantum frequency comb (QFC).

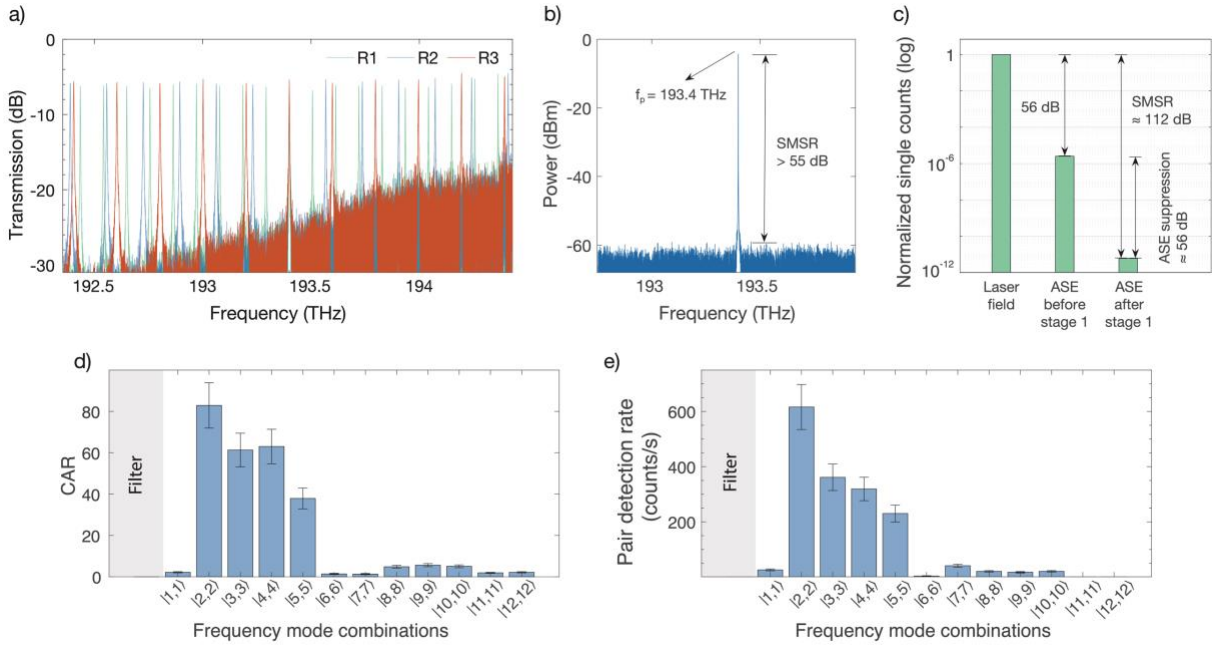


Figure 2 a) Measured transmission spectra of Si_3N_4 microrings R1, R2, and R3. b) Classical output spectrum showing the laser line at a frequency of 193.4 THz with a side-mode suppression ratio (SMSR) of >55 dB (Measurement limited by the dynamic range of the OSA). c) Measurements utilizing single photon detectors allowed to determine an SMSR ≈ 112dB, and an amplified spontaneous emission (ASE) suppression of ≈ 56 dB. d) Coincidence-to-accidental ratio (CAR) for respective frequency pairs for a detected excitation power of 3.9mW. e) Detection rate, i.e., the number of the coincidence counts per second, for the respective frequency pairs.

RESULTS

The hybrid quantum source, as shown in Fig. 1a, comprises an electrically-pumped InP gain section and a Si_3N_4 low-loss microring filter. It has a size comparable to a one-euro coin [5]. The three rings, i.e. R1, R2, and R3 form a Vernier filtering stage, which is further connected to an MZI and a Sagnac loop. The Sagnac loop mirror together with the reflecting coating at the RSOA forms a lasing cavity. Resonances of R1, R2, and R3 are aligned at f_p = 193.4 THz through the microheaters (see Fig. 2a).

Providing optical gain, the system starts lasing on this frequency mode (see Fig. 2b). The backward propagating laser field from the loop mirror acts as the excitation signal for a spontaneous four-wave mixing process within the third ring R3 producing signal/idler photons on the resonances and thus a quantum frequency comb. The Venier filter stage is central to this design as it was not only used to define the laser mode but more importantly to suppress amplified spontaneous emission (ASE) emerging from the gain medium. The ASE would otherwise introduce noise on the frequency components the photon pair signal is generated, which decrease the signal to noise ratio usually to a level where the photon correlations are not detectable. An ASE suppression of 56dB was demonstrated via single photon level leasurements, leading to a laser's side-mode suppression ratio (SMSR) of 122dB (see Fig 2c).

This highly efficient noise suppression Vernier filtering stage facilitated high-performance parameters such as a high coincidence-to-accidental ratio (CAR) of ~80 with a remarkable pair detection rate of ~620 Hz and a pair emission bandwidth of ~1 THz over four resonant modes in the telecom band (see Fig. 2d,e). We performed quantum interference measurement and quantum state tomography (QST) on frequency modes 2-3, 3-4, and 2-3-4 to verify the direct creation of two- and high-dimensional frequency-bin entangled quantum states (qubits/qudits) (see Fig. 3). Quantum interference measurements with visibilities > 96%, and QST with fidelities from 0.99 to 0.85 for two and three-dimensional Bell states, respectively, affirmed the generation of excellent-quality entangled photon states from this nonclassical light source.

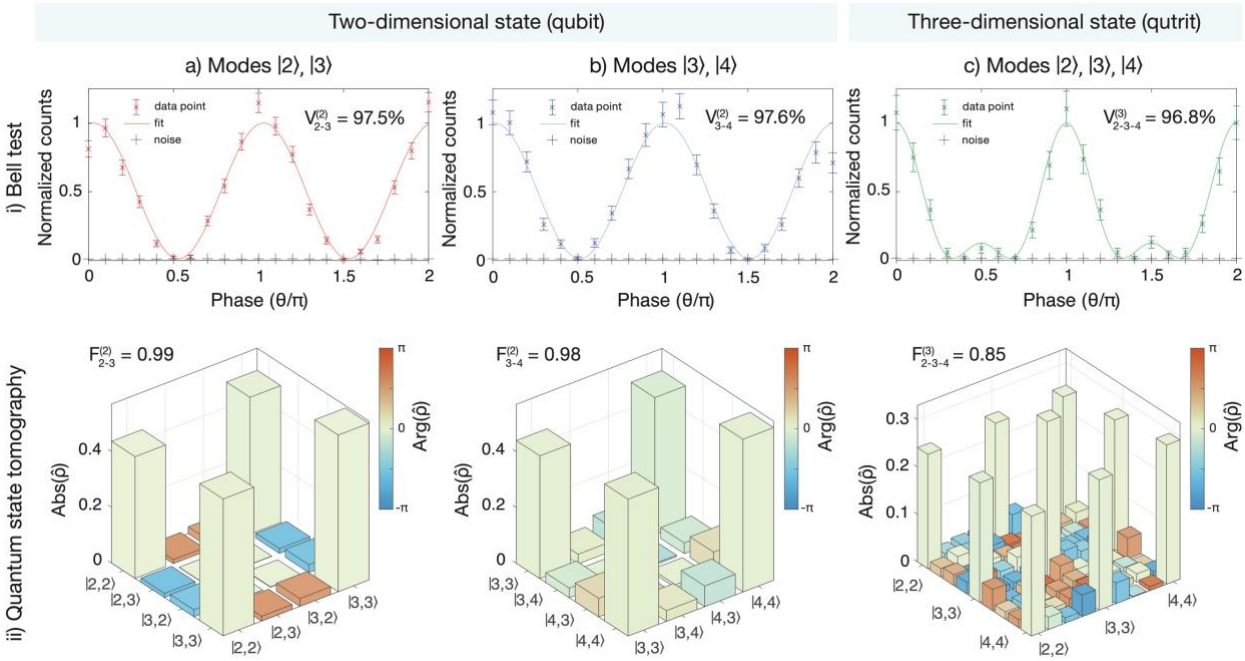


Figure 3 Performance of the quantum photonic source. Bell inequality violation and quantum state tomography of frequency-entangled qubit and qutrit states. First line (i), Bell test characterization of qubit and qutrit states. The error bars show the root of the absolute count numbers; the error of the noise background is smaller than the marker size. Second line (ii), quantum state tomography for qubit and qutrit QFC states. First column a), two-qubit state (composed of 2nd and 3rd resonances). Second column b), two-qubit state (composed of 3rd and 4th resonances). Third column c), bi-photon qutrit state (composed of 2nd, 3rd and 4th resonances).

DISCUSSION

In conclusion, our work is the first demonstration of an on-chip, scalable, light-weight, and readily deployable quantum light source. The novel architecture of this chip, i.e., the integration of a laser-cavity that includes a tunable Vernier filter, allows the required suppression of amplified spontaneous emission and thus furnishes high-quality entangled photons. This work facilitates necessary technological advancements for building quantum processors, quantum internet devices, and quantum satellite systems in a fully-integrated, stable, and field-deployable format meeting industrial requirements.

Acknowledgements

The project was funded by the German federal ministry of education and research, Quantum Futur Program (PQuMAL), and the European Research Council (ERC) under the European Union's Horizon 2020 research and innovation programme under grant agreement No. 947603 (QFreC project), and the Deutsche Forschungs-gemeinschaft (DFG, German Research Foundation) under Germany's Excellence Strategy within the Cluster of Excellence PhoenixD (EXC 2122, Project ID 390833453). R. H. acknowledges the financial support provided by the Alexander von Humboldt Stiftung to conduct the research. A.V.R., J. E., and K.-J. B. acknowledge funding from the EU within the project 3PEAT.

References

[1] J. Wang et al., *Integrated photonic quantum technologies*, Nat. Photonics 14, 273-284 (2020).
[2] E. Pelucchi et al., *The potential and global outlook of integrated photonics for quantum technologies*, Nat. Rev. Phys. 4, 194-208 (2022).
[3] A. W. Elshaari et al., *Hybrid integrated quantum photonic circuits*, Nat. Photonics 14, 285-298 (2020).
[4] M. Kues et al., *On-chip generation of high-dimensional entangled quantum states and their coherent control*, Nature 546, 622-626 (2017).
[5] Y. Fan et al., *Hybrid integrated InP-Si3N4 diode laser with a 40-Hz intrinsic linewidth*, Opt. Express 28, 21713-21728 (2020).

Frequency agile Si_3N_4-MEMS photonic integrated external cavity laser

Student paper

Andrea Bancora[1], Grigory Lihachev[1], Viacheslav Snigirev[1], Hao Tian[2], Johann Riemensberger[1], Vladimir Shadymov[1], Anat Siddharth[1], Alaina Attanasio[2], Rui Ning Wang[1], Diego Visani[1], Andrey Voloshin[1], Sunil A. Bhave[2] and Tobias J. Kippenberg[1,*]

[1]Institute of Physics, Swiss Federal Institute of Technology Lausanne (EPFL), CH-1015 Lausanne, Switzerland
[2]OxideMEMS Lab, Purdue University, 47907 West Lafayette, IN, USA
[*]tobias.kippenberg@epfl.ch

We demonstrate a Vernier ring laser at 1550 nm with 6 mW output power, 400 GHz intrinsic laser linewidth, linear frequency tuning of 1.5 GHz at 100 kHz chirp rate and wavelength switching with 7 ns rise time and 75 nW power consumption using silicon nitride photonic chip with integrated PZT actuators. We perform FMCW LiDAR for a target scene 10 m away with a 8.5 cm distance resolution.
Keywords**:** *FMCW LiDAR, hybrid integrated laser, silicon nitride, Vernier laser*

INTRODUCTION

External cavity lasers (ECL) with feedback circuits implemented in photonic integrated circuits demonstrated significant progress in recent years[1]. Frequency selective reflection can be achieved with Vernier filters in an integrated photonic circuit. Vernier filter based lasers have significantly matured with the realization of filters in silicon[2], silicon nitride[3] or other material platforms[4] and reached sub-kHz intrinsic laser linewidths[5]. High frequency modulation speed (exahertz/s) and switching speed of up to 50 MHz have only been demonstrated recently in Vernier based intgerated lasers based on lithium niobate[6]. Several application areas would benefit from such low noise, frequency agile and RSOA based external cavity integrated laser. Examples are fast wavelength switching for data centers, which has been studied in digital supermode distributed Bragg reflector (DS-DBR), Vernier-tuned distributed Bragg reflector (VT-DBR) and DFB configurations with mode-hop-free wavelength tuning and wavelength switching[7] demonstrated using integrated heaters with speeds up to 10 kHz. Another application is FMCW LiDAR, where high laser frequency tuning linearity and low frequency noise of the laser are crucial to measuring distance and velocity at mid to long ranges[8]. Despite significant progress, the fast and linearly tunable integrated laser requires either a DFB laser with e-beam lithography fabrication steps or MEMS-VCSELs with additional linearization.

Here, we report a hybrid integrated ECL based on RSOA and Vernier filters in low loss Si_3N_4 PIC enhanced with integrated piezoelectric actuator, which constitute a low cost solution, alleviating the use of DFB, while enabling high coherence and fast (MHz bandwidth), linear and low power frequency tuning.

RESULTS

Fig. 1(a) shows the schematic of the laser. An InP reflective semiconductor optical amplifier (RSOA) with 90% back facet reflectivity is edge coupled to the SiN PIC with a directional coupler and two cascaded microrings in a Vernier filter configuration. The SiN microrings R1 and R2 with FSR_1=96.7 GHz, FSR_2=97.9 GHz have intrinsic linewidths of 43.5 MHz and 64.4 MHz with symmetric input/drop-port coupling of 96.0 MHz correspondingly. The laser frequency in our device is controlled with a structure fabricated on top of SiN chip, which comprises a PZT actuator for fast actuation and microheaters for Vernier filter alignment. Figure 1(b) presents a laser frequency tuning scheme. First, we align a resonance pair of the two rings to achieve CW lasing by applying DC voltage to the microheater. Then, a triangular voltage signal applied simultaneously to both piezoactuators, resulting in a linear laser frequency sweep. Applying a square signal to a single piezoactuator allows for fast wavelength switching. Frequency noise measurements of the hybrid packaged laser by heterodyne beatnote spectroscopy show that the laser frequency noise reaches a value (white noise floor) of 127 Hz^2/Hz at a 6 MHz offset, corresponding to an intrinsic laser linewidth of 400 Hz. We next characterize the frequency agility of the laser (Fig. 1(c,e,g). We apply a triangular signal with 11 V_{PP} amplitude from an arbitrary frequency generator simultaneously to both PZT actuators at a frequency of 100 kHz. The laser output frequency is measured by a heterodyne beatnote with a reference ECDL on a fast photodetector. Figure 1(c,e,g) present the processed laser frequency spectrograms with the corresponding nonlinearities at 100 kHz ramping frequency. Frequency excursion of 1516 MHz with 1% nonlinearity at 100 kHz is observed using the PZT actuators without any additional linearization (the maximum tuning range of the laser in a single mode regime is limited by 3 GHz). To reach lower tuning nonlinearities we implemented a predistortion

compensation routine. After 10 iterations, at 100 kHz modulation frequency, the achieved RMS nonlinearity reaches as low as 3.85 MHz (0.25%). Results on the fast wavelength switching are presented in Fig. 1(d,f,k). To switch the wavelength of the laser we align the Vernier filter with a microheater and then actuate only one ring with the PZT actuator, applying a square signal from 0 V to 8 V at a 100 kHz rate. Fig. 1(d) depicts the transmission power in both channels, showing wavelength switching of 97 GHz at 100 kHz rate. To determine switching speed we fit the rise and fall transmission curves with hyperbolic tangent function. Fitting yields 10–90% rise time of 7 ns and fall time of 6 ns (see Fig. 1(f,k)). Such fast wavelength switching and low measured actuator power consumption per switching of only 75 nW demonstrate an advantage of Vernier ring lasers with integrated PZT actuators over microheaters with typical switching times of hundreds of nanoseconds.

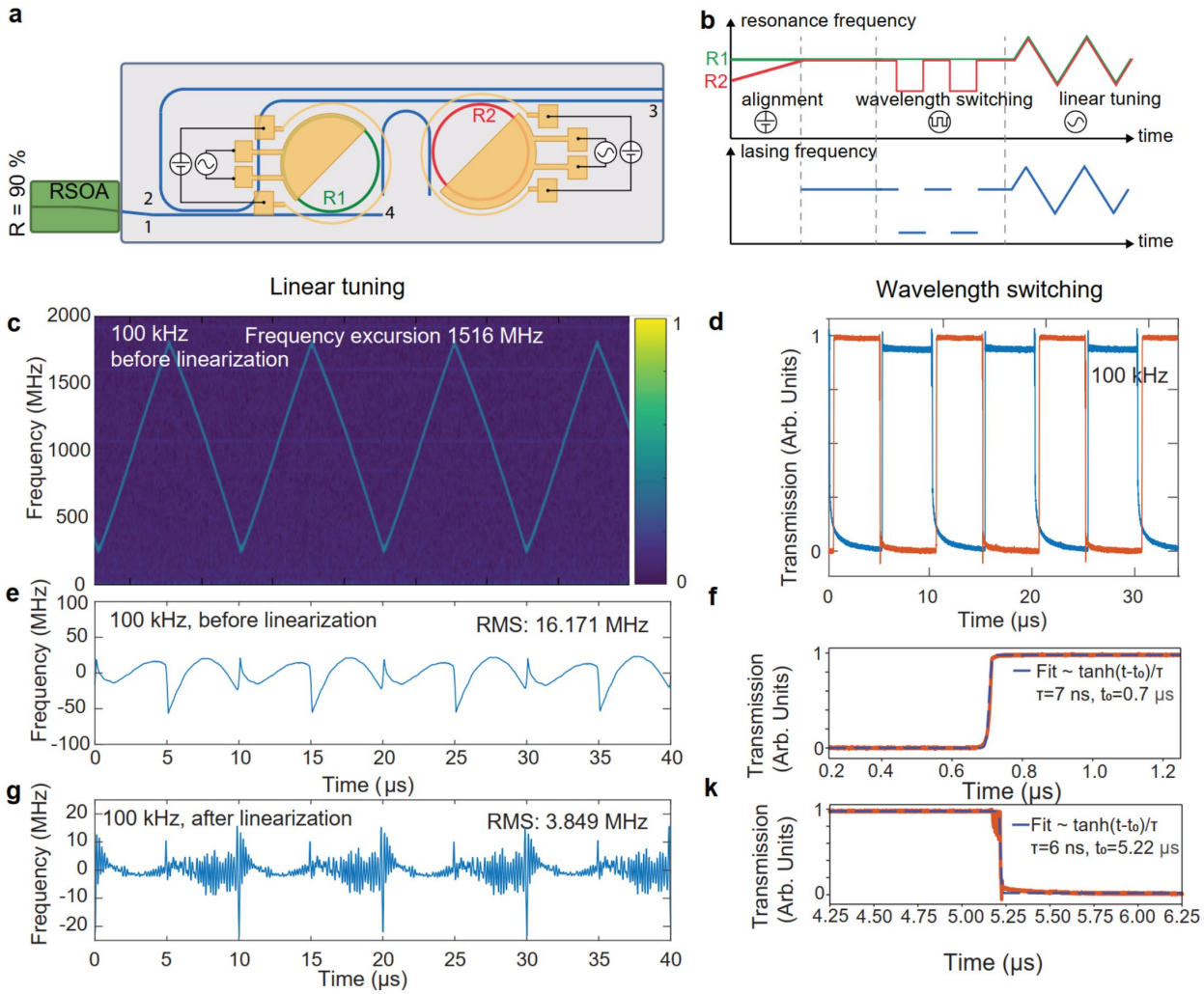


Fig. 1. Integrated external cavity laser. (a) Schematics of the laser. (b) Laser frequency tuning schematic. Coarse alignment of resonances of 2 microrings to observe lasing is done with integrated microheaters. Triangular voltage signal applied simultaneously to both piezoactuators results in linear laser frequency sweep. Applying square signal to a single piezoactuator allows to perform fast wavelength switching. (c) Laser frequency spectrogram with the corresponding nonlinearities (e,g) at 100 kHz chirp frequency upon applying 11 Vpp non-corrected ramp signal (e) and after 10 iterations of predistortion compensation (g). (d) Measured transmission at 2 different wavelength channels, demonstrating wavelength switching at 100 kHz rate. (e,f) Transmission curve (red) and its fit (blue) reveal the rise time of 7 ns and the fall time of 6 ns.

Acknowledgements: This publication was supported by Contract NINJA LASER (W911NF2120248) from the Defense Advanced Research Projects Agency (DARPA), Microsystems Technology Office (MTO). J.R. acknowledges funding from the SNSF via an Ambizione Fellowship (No. 201923). A.S. acknowledges support from the European Space Technology Centre with ESA Contract No. 4000135357/21/NL/GLC/my. The samples were fabricated in the EPFL center of MicroNanoTechnology (CMi).

References

1. Tran, M. A., Huang, D. & Bowers, J. E. Tutorial on narrow linewidth tunable semiconductor lasers using Si/III-V heterogeneous integration. *APL Photonics* **4**, 111101 (2019).
2. Tran, M. A. *et al.* Ring-Resonator Based Widely-Tunable Narrow-Linewidth Si/InP Integrated Lasers. *IEEE J. Sel. Top. Quantum Electron.* **26**, 1–14 (2020).
3. Boller, K.-J. *et al.* Hybrid Integrated Semiconductor Lasers with Silicon Nitride Feedback Circuits. *Photonics* **7**, 4 (2020).
4. Radosavljevic, S. *et al.* Mid-infrared Vernier racetrack resonator tunable filter implemented on a germanium on SOI waveguide platform [Invited]. *Opt. Mater. Express* **8**, 824–835 (2018).
5. Fan, Y. *et al.* Hybrid integrated InP-Si_3N_4 diode laser with a 40-Hz intrinsic linewidth. *Opt. Express* **28**, 21713 (2020).
6. Integrated Pockels laser | Nature Communications. https://www.nature.com/articles/s41467-022-33101-6.
7. Srinivasan, S. *et al.* Coupled-Ring-Resonator-Mirror-Based Heterogeneous III–V Silicon Tunable Laser. *IEEE Photonics J.* **7**, 1–8 (2015).
8. Behroozpour, B. *et al.* Electronic-Photonic Integrated Circuit for 3D Microimaging. *IEEE J. Solid-State Circuits* **52**, 161–172 (2017).

Photonic memory based on VO_2/Si technology

Jorge Parra[1], Juan Jose Seoane[1], Juan Navarro-Arenas[1,2], Maria Recaman[3], Jean-Pierre Locquet[3], and Pablo Sanchis[1,*]

[1]Nanophotonics Technology Center, Universitat Politècnica de València, Camino de Vera s/n, 46022 Valencia, Spain
[2]Institute of Materials Science (ICMUV), Universitat de València, Carrer del Catedràtic José Beltran Martinez, 2, 46980, Valencia, Spain
[3]Department of Physics and Astronomy, KU Leuven, Celestijnenlaan 200D, 3001 Leuven, Belgium
[*] pabsanki@ntc.upv.es

In this work, we report a photonic memory in silicon photonics by exploiting the insulator-metal hysteresis of vanadium dioxide (VO_2). Our photonic memory based on a 5-µm-long VO_2/Si waveguide is maintained using ~150 µW of optical power, and can be on-chip written/erased using standard silicon building blocks.
Keywords: *photonic memory, vanadium dioxide, silicon photonics*

INTRODUCTION

Optical data storage in integrated optics has become an intense research topic in recent years, motivated by the possibility of achieving parallel operation with ultralow latency using light [1]. Such features are required to overcome one of the bottlenecks that limit classical von Neumann computation architectures using electronic circuitry, i.e., the interconnection between the processor and memory. However, light-based interconnections between the processor and memory require optical/electrical conversion. Hence, photonic memories are highly appealing to remove such a limitation. Additionally, the emergence of integrated photonic artificial intelligence relying on non-von Neumann architectures [2] directly benefits from photonic memories due to the possibility of performing in-memory computing, i.e., running calculations in the memory element [3].

Integrating chalcogenide-based phase-change materials (PCMs), such as GST, is currently the most established way to enable memory functionalities in silicon photonic devices [4]. These compounds exhibit an inherited non-volatile response when they are changed between the amorphous and crystalline states. However, the phase change requires a high-temperature increase (~600 °C) followed by fast cooling (> 10 °C/ns) in the amorphization process [5]. In this context, an alternative PCM compound such as vanadium dioxide (VO_2) can overcome those challenging temperature requirements by offering a phase transition temperature near room temperature (~68 °C) [6], [7]. Although VO_2 is a volatile PCM, the memory effect can be achieved by harnessing their hysteretic insulator-metal transition (IMT), as recently demonstrated in hybrid VO_2/Si waveguides by electronic biasing the IMT [8]. On the other hand, VO_2 provides a unitary contrast in the complex refractive index in the near-infrared similar to GST [10].

In this work, we propose a photonic memory based on an ultra-compact VO_2/Si waveguide. In comparison with previous work [8], our approach is all-photonic since the memory state is changed and maintained using light and standard integrated photonic building blocks, surpassing the need to include specific electronic circuitry in the VO_2 to keep the memory state.

RESULTS

The concept and working principle of the proposed integrated photonic memory is depicted in Fig. 1(a). The memory is based on a 500 nm x 220 nm silicon (Si) waveguide with a 40-nm-thick VO_2 patch on top. The length of the hybrid waveguide is 5 µm and is covered with SiO_2. The memory is optimized for the transverse-magnetic (TM) polarization to maximize the light-matter interaction between the evanescent field and VO_2. Memory effect is achieved by leveraging the photoinduced hysteretic IMT of the VO_2 (see inset of Fig. 1(a)). Hence, the memory is written/erased by modulating a continuous-wave signal (optical bias) with a certain optical power that is adjusted within the hysteresis response of the VO_2. When a writing pulse is delivered to the hybrid waveguide, the VO_2 changes from the low-loss insulating state to the high-loss metallic state. Once the pulse is removed, the VO_2 remains metallic due to the optical bias (written memory state). To recover the insulating state (erase the memory), the optical signal must be reduced below the bias threshold using a low power-erasing pulse.

Fig. 1(b) shows the experimental transmission response of the hybrid VO_2/Si waveguide (see inset of Fig. 1(b)) as a function of the optical power using a continuous-wave signal at 1550 nm. The IMT of the VO_2 was photothermally triggered. The injected optical power was controlled with an off-chip erbium-doped optical amplifier. The insulator-metal transition starts around 450 µW, whereas the insulating state is recovered when the optical signal is removed.

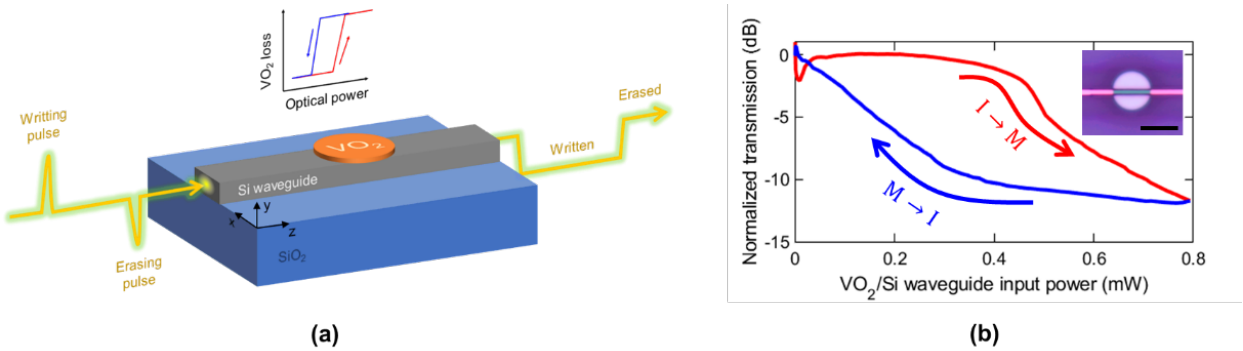


Fig. 1. (a) Illustration and working principle of the proposed memory based on a hybrid VO_2/Si technology. (b) Transmission of the 5-µm-long VO_2/Si waveguide as a function of the optical power using a CW signal at 1550 nm. The hysteresis is obtained by sweeping back and forth the input power. The temperature of the chip was set at 20 °C. The inset shows a micrograph of the characterized hybrid waveguide. The scale bar is 5 µm.

To demonstrate on-chip memory operation, we placed an asymmetric Mach-Zehnder interferometer (MZI) before the hybrid VO_2/Si waveguide. In this regard, writing (erasing) pulses could be achieved by changing the effective refractive index of the long (short) MZI arm. Fig. 2(a) shows an optical micrograph of the fabricated memory device comprising the MZI and the hybrid VO_2/Si waveguide before depositing the metallic heaters on top. The structures were patterned using e-beam lithography, and the VO_2 layer was deposited using molecular beam epitaxy. The chip was covered with a 1.4-µm-thick SiO_2 cladding. Then, 100-nm-thick titanium heaters and electrodes were fabricated by evaporation. The length of the microheaters was 80 µm.

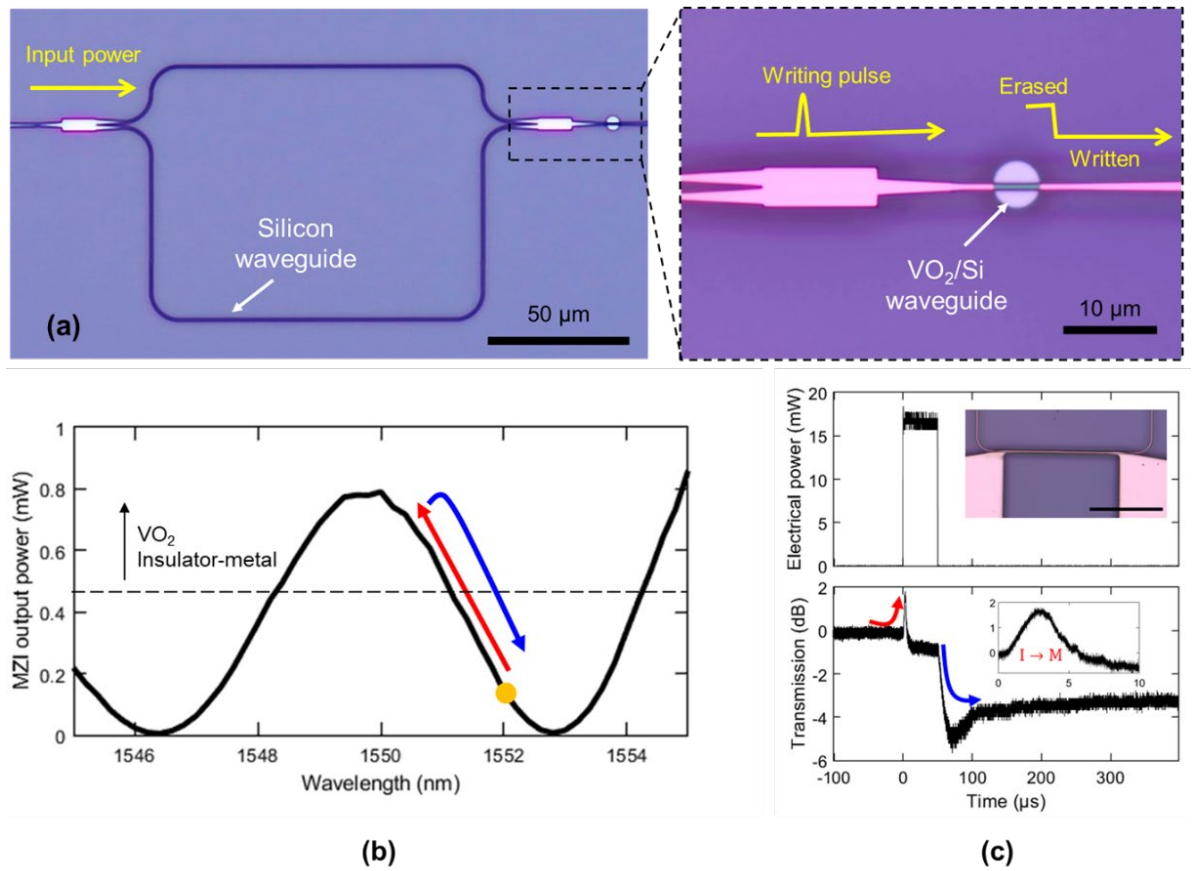


Fig. 2. (a) Optical micrograph of the fabricated VO_2/Si memory using a MZI to on-chip write/erase the memory. A continuous wave signal with a certain bias, in both optical power and wavelength, is injected in the MZI to generate the writing pulse by heating the long arm and afterward keeping the memory written. (b) MZI spectral response when 1.6 mW optical signal is injected into the MZI. The dot stands for the operating wavelength utilized to write the memory. (d) Applied electrical pulse to the heater of the long arm (top inset, the scale bar is 50 µm) and normalized optical transmission of the memory when injecting 1.6 mW optical signal at 1552 nm.

To demonstrate the memory function, the optical signal was set at 1552 nm (see Fig. 2(b)). For this value, the memory is in the erased state as we estimate around 150 μW of optical power delivered to the VO_2/Si waveguide in order to be within the hysteresis loop of the VO_2 (see Fig. 1(b)). The memory is written by applying an electrical pulse to the heater on the long arm of the MZI. In this manner, the optical response of the MZI is redshifted toward a maximum, and thereby the delivered power to the hybrid waveguide increases (inducing the insulator-metal transition) and changes the memory to the written state. The written memory state is maintained when the electrical pulse is removed due to the VO_2 hysteresis and the optical bias set by the selected wavelength and optical power of the input signal.

The temporal dynamics of a writing process are shown in Fig. 2(c) when a 50-μs-long pulse is applied to the heater of the MZI long arm (see Fig. 2(c) top inset). The electrical power of the pulse was ~17 mW (~4.5 V) in order to shift the MZI response toward one of its maximums. The normalized transmission of the memory can be seen in the lower graph of Fig. 2(d). Before applying the electrical pulse, the memory is erased with the VO_2 in the insulating state. Once the electrical pulse is applied, the transmission of the memory increases due to the redshift of the MZI until the VO_2 absorbs sufficient optical power to trigger its insulator-metal transition (see Fig. 2(c) bottom inset). Then, the optical transmission suffers a decrease caused by the optical losses induced by the metallic state of the VO_2. Upon the electrical pulse being removed, the transmission drops and is maintained (written state) because the MZI response returns to the original position (see Fig. 2(b)) while VO_2 remains in the metallic state.

DISCUSSION

In summary, we have proposed a photonic memory based on an ultra-compact hybrid VO_2/Si waveguide of just 5 μm length. The memory exploits the IMT hysteresis to provide a bistable response. Although the memory is volatile, the holding power required to maintain the memory written can be as low as 150 μW. On the other hand, the writing/erasing process could be achieved on-chip using standard silicon photonic building blocks such as thermo-optical controlled MZI. Such a memory device may be useful in photonic applications benefiting from in-memory computing neural networks or tensor cores.

Acknowledgments: Funding from the European Union's Horizon Europe by the granting Authority "HADEA (European Health and Digital Executive Agency) under Grant Agreement No 101070690 (PHOENIX). Grant PID2019-111460GB-I00 funded by MCIN/AEI/10.13039/501100011033, by "ERDF A way of making Europe". Grants 2-PAID-10-22 and 2-PAID-01-22 funded by Universitat Politècncia de València. Grant MS21-037 funded by European Union Next-Generation EU.

References

[1] C. Lian, C. Vagionas, T. Alexoudi, N. Pleros, N. Youngblood, and C. Ríos, 'Photonic (computational) memories: tunable nanophotonics for data storage and computing', *Nanophotonics*, vol. 11, no. 17, pp. 3823–3854, Aug. 2022, doi: 10.1515/nanoph-2022-0089.

[2] B. J. Shastri *et al.*, 'Photonics for artificial intelligence and neuromorphic computing', *Nat Photonics*, vol. 15, no. 2, pp. 102–114, Feb. 2021, doi: 10.1038/s41566-020-00754-y.

[3] A. Sebastian, M. le Gallo, R. Khaddam-Aljameh, and E. Eleftheriou, 'Memory devices and applications for in-memory computing', *Nat Nanotechnol*, vol. 15, no. 7, pp. 529–544, Jul. 2020, doi: 10.1038/s41565-020-0655-z.

[4] J. Parra, I. Olivares, A. Brimont, and P. Sanchis, 'Toward Non-volatile Switching in Silicon Photonic Devices', *Laser Photon Rev*, vol. 15, no. 6, p. 2000501, Jun. 2021, doi: 10.1002/lpor.202000501.

[5] A. Redaelli, A. Pirovano, A. Benvenuti, and A. L. Lacaita, 'Threshold switching and phase transition numerical models for phase change memory simulations', *J Appl Phys*, vol. 103, no. 11, p. 111101, Jun. 2008, doi: 10.1063/1.2931951.

[6] A. Joushaghani, J. Jeong, S. Paradis, D. Alain, J. Stewart Aitchison, and J. K. S. Poon, 'Wavelength-size hybrid Si-VO_2 waveguide electroabsorption optical switches and photodetectors', *Opt Express*, vol. 23, no. 3, p. 3657, Feb. 2015, doi: 10.1364/OE.23.003657.

[7] S. Cueff *et al.*, 'VO_2 nanophotonics', *APL Photonics*, vol. 5, no. 11, p. 110901, Nov. 2020, doi: 10.1063/5.0028093.

[8] Y. Jung, H. Han, A. Sharma, J. Jeong, S. S. P. Parkin, and J. K. S. Poon, 'Integrated Hybrid VO_2 –Silicon Optical Memory', *ACS Photonics*, vol. 9, no. 1, pp. 217–223, Jan. 2022, doi: 10.1021/acsphotonics.1c01410.

A memristor-controlled multilevel non-volatile phase shifter for photonic integrated circuits

Student paper

Ludovico Carraria Martinotti[1], Felix Hermann[1*], Tommaso Stecconi, Antonio La Porta, Folkert Horst, Valeria Bragaglia, and Bert Jan Offrein

IBM Research Europe - Zurich, Säumerstrasse 4, Rüschlikon, 8803, Switzerland
[1] Equally contributing authors
[*]eli@zurich.ibm.com

Programmable Photonic Integrated Circuits (PIC) are a rapidly growing field promising energy-efficient high-speed signal processing. To connect various information processing elements and perform operations, an efficient, reprogrammable non-volatile optical phase shifting element with high retention is needed. In this work, we demonstrate a Mach-Zehnder Interferometer (MZI) controlled by a non-volatile, multi-level memristor.
Keywords: *PIC, Memristor, Non-volatile, Integrated optics, Phase Shifter*

INTRODUCTION

Field-Programmable Gate Arrays (FPGAs) have revolutionized the semiconductor industry, allowing for reconfigurable and multi-purpose hardware. Another implementation, Application Specific Integrated Circuits (ASICs), offer better performance overall, at the cost of design and fabrication overhead due to their limited purpose [1]. Current integrated photonics solutions are ASIC-like, missing their programmable counterpart.

With the refinement of the design, manufacturing and testing processes of silicon integrated photonics, new implementations based on an increasing number of optical components are emerging, ranging between multipurpose photonic signal processors ([2], [3]), optical quantum computers ([4]) and machine learning accelerators ([5]). A key component shared between all PICs are optical phase shifters. Non-volatile phase shifters could prove to be beneficial for the upscaling and efficiency of reprogrammable integrated photonic circuits [6], simplifying the electro-optical control of photonic circuits.

In this work, an implementation of a basic building block for programmable photonic integrated circuits is demonstrated. Previous works have shown the exploitation of ferroelectric material to achieve multi-level, non-volatile phase shifters [7]. Here, we demonstrate a multi-level optical phase shifting element utilizing the non-volatility of filamentary metal-oxide based memristors. By combining a memristor-controlled voltage divider, an amplification stage and a thermo-optic phase shifter, we show that this implementation allows to obtain many non-volatile optical transmission states of an integrated photonic Mach-Zehnder Interferometer (MZI).

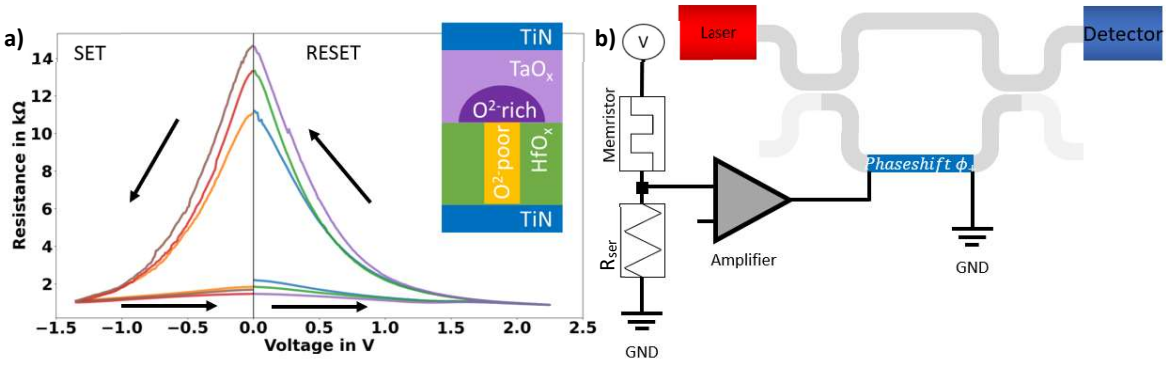


Fig. 1. a) *Memristor resistance versus the applied voltage. Multiple curves are shown, with different maximum voltage V_{Max}. The inset in the top right schematically shows the material stack of the memristive device [8].* ***b)*** *Schematic of the experimental setup linking the memristor to the optical phase shifter. The memristor is integrated in a voltage divider configuration as depicted on the left. The ratio of the two resistors defines the output voltage of the divider and so controls the output signal of the amplifier, driving the thermo-optic phase shifter. Continuous wave laser light is used to read out the phase shift via an integrated photonic MZI.*

EXPERIMENT

The filamentary memristor stack exploited in this work consists of 25nm TiN/ 20nm TaO_x/5.7nm HfO_2/25nm TiN (inset fig. 1a) fabricated on a Si++ doped substrate (bottom electrode BE), with an additional W plug as top contact (top electrode TE). The conductive filament is formed in previously pristine devices by applying a positive voltage sweep up to 5.5 V between TE (V+) and BE (ground). When reaching the breakdown voltage, a conductive filament forms in the HfO_2. TaO_x is substoichiometric, therefore it can oxidize through the electrically induced O^{2-} ions from the HfO_2 filament (see [8, 9]).

A negative voltage induces an electric field across the memristor, pushing the oxygen ions back into the HfO_2 layer, causing a reduction of the resistance, whereas a positive voltage drives the ions into the TaO_x layer, thus increasing the resistance. A fine tuning of the maximum applied voltage enables a gradual transition between Highest Resistive State (HRS) and Lowest Resistive State (LRS) (fig. 1a).

The measurement setup is shown in fig. (1b). The memristor and a fixed 4.7 kΩ resistor R_{ser} placed in series act as a voltage divider. The memristive state is read out at a constant bias of 0.4 V. The low voltage guarantees long resistive retention, as it is well-below the switching threshold of the device. The output signal of the voltage divider depends on the ratio of the two resistors. To allow high voltage applications, we link the voltage divider with an amplifier (A=10x) to the thermo-optical phase shifter (fig. 1b). The discrete elements and memristors are mounted on a Printed Circuit Board (PCB). Individual memristive devices are connected via wire bonds. The supply voltage of the amplification stage is set to 12 V.

The symmetric MZI is processed on an SOI-Wafer. Tungsten lines on top of the patterned Si-waveguides are utilized as joule heaters. Grating couplers are used to in- and output laser light from a tunable laser at 1550nm wavelength. The transmission of a MZI driven by a thermal phase shifter is given in Eq 1 ([13]),

$$T = a \cdot \cos\left(\frac{1}{t} \cdot P + \phi_0\right) + O \qquad \text{(Eq 1)}$$

where a is the amplitude, O is a constant offset, t is the power for a 2π phase shift, P is the power applied and ϕ_0 the phase shift at 0V.

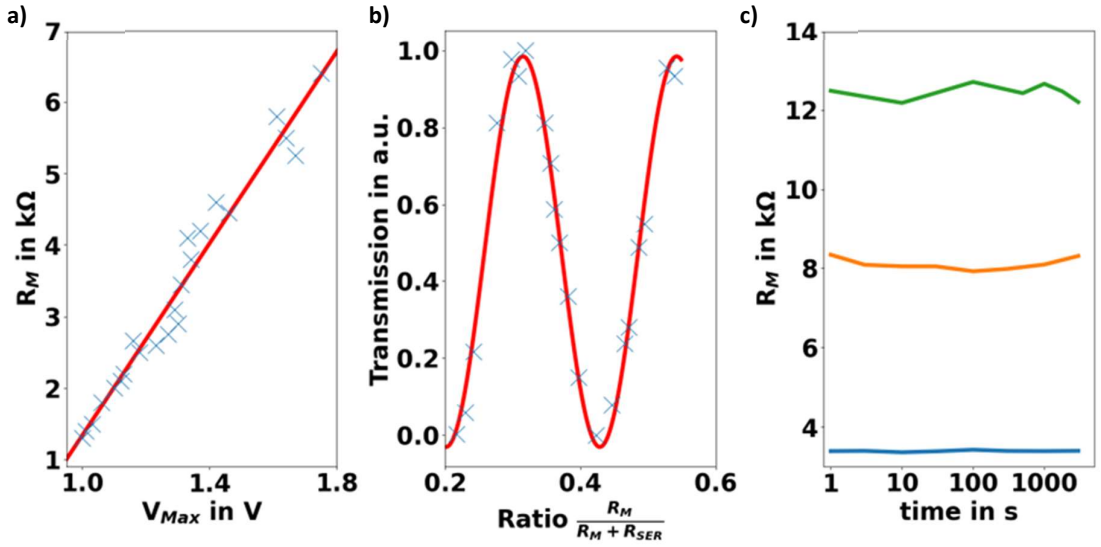


Fig. 2 a) *The resistive state of the memristor R_M as a function of the maximum voltage V_{Max}. The resistive values are represented by blue crosses, a linear regression is plotted by a solid red line.* ***b)*** *MZI-Output plotted against the divider's resistance ratio.* ***c)*** *Memristor retention for three resistance values.*

RESULTS & DISCUSSION

Fig. 2a depicts the relation between the memristive state and the maximum applied voltage V_{max}. By tuning V_{max}, up to 23 resistive states are demonstrated in this example. Thereby, R_M can be adjusted between 1.3 and 6.4 $k\Omega$, an On/Off ratio of 4.9. With a serial resistance of 4.7 kΩ, the voltage divider delivers an output signal between 0.16 and 0.32 V, which is then amplified to 1.6 - 3.2 V on the phase shifter. The output range can be adapted by changing the serial resistance as well as the amplification. Fig. 2b shows the corresponding optical transmission of the MZI The resistance-phase shift relation is computed using the sinusoidal fit of the transmission data using Eq. 1. With an applied signal of only 0.4V at the voltage divider, a 3π optical phase shift is achieved. For the use as non-volatile optical phase shifter, retention is an important figure of merit. In fig. 2c, typical retention of three states of memristive devices measured for up to 3000s are shown.

By increasing the memristor resistivity, as demonstrated in [8], 10x lower power consumption of the voltage divider can be achieved. The here shown combination of the memristor-based voltage divider and the amplifier allows for 23 optical phase states distributed across a range from 3π. Using voltage pulses for programming the memristor, as in [8], is a power-efficient way to set the desired state. This concept of realizing non-volatile optical phase shifters is compatible with back-end of the line processes and can be integrated on most photonic platforms.

CONCLUSION

In this work, we presented a multi-level, non-volatile, photonic phase shifter, utilizing a memristor element in combination with an integrated photonic MZI. We have demonstrated up to 23 reconfigurable states with measured retention up to 3000s. Filamentary memristors are a promising technology for electrically tunable, non-volatile, large scale integration voltage dividers. The application is not limited to MZIs and phase shifters, but can also be used to control other photonic integrated components such as laser sources, amplifiers or electro-absorption elements. This basic building block enables fast and reliable operation of next generation programmable PICs, hardware accelerators for optical neural networks, inference deep neural networks as well as integrated photonic quantum computing [10-13].

ACKNOWLEDGEMENTS

The authors acknowledge the Binnig and Rohrer Nanotechnology Center (BRNC) at IBM Research Europe - Zürich. This work was funded by the European Union within the “NEoteRIC” (grant ID: 871330), “NEBULA” (grant ID: 871658) and “PlasmoniAC” (grant ID: 871391) projects.

References

[1] Trimberger, S. M. Three ages of FPGAs: a retrospective on the first thirty years of FPGA technology. In Proc. IEEE Vol. 103, 318–331 (IEEE, 2015).
[2] Liu, W. et al. A fully reconfigurable photonic integrated signal processor. Nat. Photon. 10, 190–195 (2016).
[3] Pérez-López, D., López, A., DasMahapatra, P. & Capmany, J. Multipurpose self-configuration of programmable photonic circuits. Nat. Commun. 11, 1–11 (2020).
[4] Wang, J., Sciarrino, F., Laing, A. & Thompson, M. G. Integrated photonic quantum technologies. Nat. Photon. 14, 273–284 (2020).
[5] Feldmann, J., Youngblood, N., Wright, C. D., Bhaskaran, H. & Pernice, W. H. P. All-optical spiking neurosynaptic networks with self-learning capabilities. Nature 569, 208–214 (2019).
[6] Parra, J., Olivares, I., Brimont, A. & Sanchis, P. Toward nonvolatile switching in silicon photonic devices. Laser Photon. Rev. 15, 1–18 (2021).
[7] Geler-Kremer, Jacqueline, et al. "A ferroelectric multilevel non-volatile photonic phase shifter." Nature Photonics 16.7 (2022): 491-497.
[8] Stecconi, Tommaso, et al. “Filamentary TaOx/HfO2 ReRAM Devices for Neural Networks Training with Analog In-Memory Computing.” Advanced Electronic Materials 8.10 (2022): 2200448.
[9] Stecconi, T., et al. “Role of Conductive-Metal-Oxide to HfO x, Interfacial Layer on the Switching Properties of Bilayer TaO x/HfO x ReRAM.” ESSDERC 2022-IEEE 52nd European Solid-State Device Research Conference (ESSDERC). IEEE, 2022.
[10] Feldmann, J. et al. Parallel convolutional processing using an integrated photonic tensor core. Nature 589, 52–58 (2021).
[11] Shen, Y. et al. Deep learning with coherent nanophotonic circuits. Nat. Photon. 11, 441–446 (2017).
[12] Arrazola, J. M. et al. Quantum circuits with many photons on a programmable nanophotonic chip. Nature 591, 54–60 (2021).
[13] Saghaei, Hamed, Payam Elyasi, and Rouhollah Karimzadeh. "Design, fabrication, and characterization of Mach–Zehnder interferometers." Photonics and Nanostructures-Fundamentals and Applications 37 (2019): 100733.

1x4 Vertical Power Splitter/Combiner: A Basic Building Block for Complex 3D Waveguide Routing Networks

(Student paper)

Madeleine Weigel[1*], Jan H. Bach[1], Martin Kresse[1], Klara Mihov[1], Crispin Zawadzki[1], Moritz Kleinert[1], Philipp Winklhofer[1], Tianwen Qian[1], Jakob Reck[1], David de Felipe[1], Norbert Keil[1] and Martin Schell[1]

[1]Fraunhofer Heinrich Hertz Institute, Einsteinufer 37, Berlin, 10587, Germany
[*] madeleine.weigel@hhi.fraunhofer.de

A novel polymer-based 1x4 vertical multimode interference (MMI) coupler for 3D photonics is presented. It connects four vertically stacked waveguide layers with a spacing of 21.6 µm (center-to-center). The functionality is demonstrated on a fabricated device.
Keywords: *3D photonic integration, polymer-based platform, multi-mode interference coupler*

INTRODUCTION

Introducing a new level of design freedom through 3D integration in photonic integrated circuits (PICs) requires the development of new 3D basic building blocks. Application areas for 3D PICs are large-scale optical switching matrices and optical beam forming networks for 2D beam steering in LIDAR and wireless optical communication. These applications benefit from crossing-free waveguide routing, thus reduced crosstalk, and significantly increased design flexibility through 3D photonics. In this work, a new basic building block, a 1x4 3D MMI (Fig. 1), is presented for the first time. The starting point for the development of the 1x4 3D MMI is the well-known planar 1x4 MMI [1]. In addition, 3D waveguide networks have already been successfully demonstrated in the hybrid integration platform PolyBoard [2, 3] and first vertical 3D MMIs have been realized on this platform as well [4]. So far, this has been limited to direct connections between two vertical stacked waveguide layers. A component frequently used for this purpose is the 1x1 3D MMI, which was also used to connect four waveguide layers in cascaded form [5]. The novel 3D MMI coupler proposed in this work directly connects four vertically stacked waveguide layers for the first time and allows to fabricate switching matrices with a small footprint and to realize 3D optical phased arrays with four vertically stacked waveguide layers showing the necessary uniformly distributed light intensity.

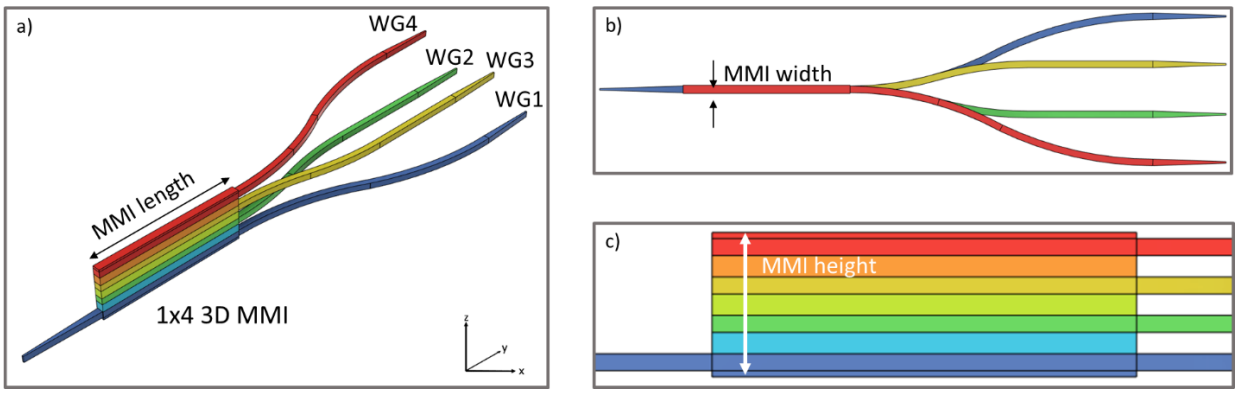


Fig. 1: Design of the 1x4 3D MMI to connect four vertically stacked waveguide layers. The 3D illustration a) includes the nomenclature of the output waveguides. The 1x4 3D MMI is shown schematically in (b) top view and in (c) side view with visualization of the layered structure.

DESIGN AND SIMULATION

The structure of the vertical 1x4 3D MMI is shown in Fig. 1. The light is guided from the blue single-mode input waveguide on the left side to the MMI section. Single-mode operation at a wavelength of 1550 nm is ensured by choosing a rectangular waveguide with a cross-section of 3.2 µm x 3.2 µm with a refractive index contrast of 0.03 between cladding and core. In the vertical MMI area of the 1x4 3D MMI (Fig. 1 c), a multi-mode field is generated by self-interference of the single-mode input. According to the self-imaging theory [1, 6] and by suitable choice and combination of the parameters MMI length, MMI width and MMI height, four images of the input field distribution with equally distributed intensities and phases are created at the end facet of the MMI, which can be coupled into the four single-mode output waveguides WG1 to WG4. In order to optimize the dimensions of the 1x4 MMI with respect to low losses, low imbalance, and a large offset-tolerance, the layout of the 1x4 3D MMI (Fig. 1) was

implemented and simulated in FIMMWAVE. Based on the self-imaging theory [1, 6] all three parameters are correlated with each other and had to be considered simultaneously in the simulation to find the best trade-off. The challenge is to optimally meet the requirements of the 1x4 3D MMI design with respect to these three performance parameters while ensuring a certain tolerance for technological imperfections.

The MMI height is determined by both the height of the waveguide layers and the desired vertical spacing between the waveguide layers of 4.0 µm (Fig. 1). This vertical spacing was chosen to avoid evanescent coupling between the waveguide layers. The MMI has a height of 21.6 µm (center-to-center). In a first variation of the MMI width and length, an optimal point with an imbalance of 0.1 dB and an excess loss of 1.5 dB per optical path plus 6 dB inherent 1x4 MMI loss was determined for a wavelength of 1550 nm. These data were determined for an MMI width of 4.1 µm. To further reduce losses, the simulation was adjusted to add an additional layer below the lowest and above the top waveguide layer (Fig. 1 c). This increase in overall MMI height results in a broadening of the MMI region as a function of MMI length, and for a fixed MMI width, a combination of height and length can be found for which MMI losses are minimal. These additional layers are used for the first time in the PolyBoard 3D PICs.

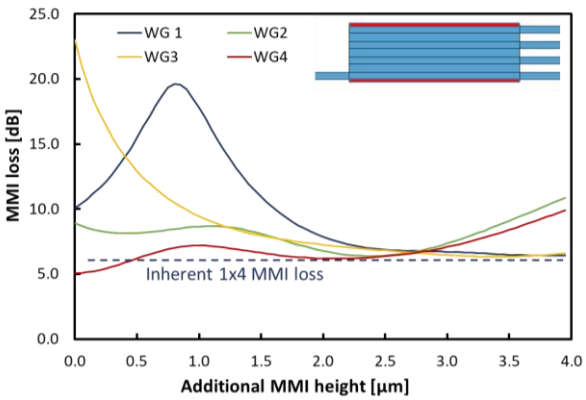


Fig. 2: Simulation of the MMI loss as a function of the additional MMI height at fixed MMI length of 809 µm and MMI width of 4.1 µm per output waveguide at a wavelength of 1550 nm.

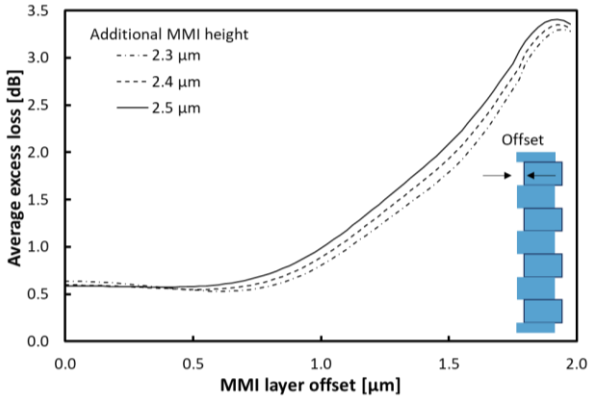


Fig. 3: Simulated average excess loss for all outputs as a function of the variation of the 1x4 3D MMI offset for three different additional MMI heights. To simplify the simulation, the offset was inserted at the four waveguide layers. Here, the offset is the same for all layers and in the same direction.

In the simulation of the additional layers, their influence on the losses and imbalance was considered for different MMI lengths. In Fig. 2, the losses per output waveguide are plotted as a function of the additional height for an MMI length of 809 µm. For an additional MMI height of 2.5 µm, the MMI excess losses are on average 0.6 dB lower (excl. the 6 dB inherent 1x4 MMI losses). In comparison, the imbalance has increased slightly by 0.5 dB.

In the final step, the technology-induced misalignment between the waveguide layers and its effects are investigated to obtain a functional MMI design with large on-wafer yield. The 1x4 3D MMI is fabricated with a total of nine waveguide and intermediate layers (Fig. 1). The offset between these nine layers is created by aligning the mask layers during UV lithography. The 1x4 3D MMI design is expected to have sufficient tolerance to this unavoidable misalignment. To simplify the simulation, it was assumed that the layers have an offset from each other that alternates but always points in the same direction and with the same value to each other. This type of offset represents a worst possible case, since the overlapping contact area of the layers is significantly reduced, drastically affecting the effective width of the MMI. In Fig. 3, the offset was varied for three different additional heights, with the MMI length of 809 µm and the MMI width of 4.1 µm fixed. The figure shows that the additional layers have little effect on the losses due to the offset. However, the design shows sharply increasing losses at an offset > 1 µm. Within the manufacturing accuracy of the layer thicknesses, an additional MMI height of 2.4 µm is targeted.

CHARACTERIZATION

The design from the previous section was fabricated on wafer scale [4]. Fig. 4 shows a top view of a 3D PIC with an initial 1x4 3D MMI (length: 809 µm). The chip was spectrally characterized in a fiber-chip-fiber arrangement. The wavelength dependent losses for all four output waveguides are shown in Fig. 5. The 1x4 3D MMI works in all input-output waveguide combinations. Nevertheless, the significantly increased losses compared to the simulation should be noted. For reference, the losses in the best-case scenario are composed of twice the fiber-chip coupling and propagation losses, which are 1 dB, and the inherent 1x4 MMI losses of 6 dB per path. At a wavelength of 1550 nm, the 1x4 3D MMI coupler has an additional loss of 2.6 dB at best and 6.5 dB at worst case. The MMI losses of about 0.6 dB, which are given by design, are also included here.

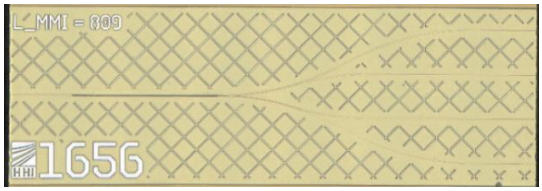


Fig. 4: Microscope image of a fabricated polymer-based 3D PIC with a 1x4 3D MMI (compare Fig. 1b).

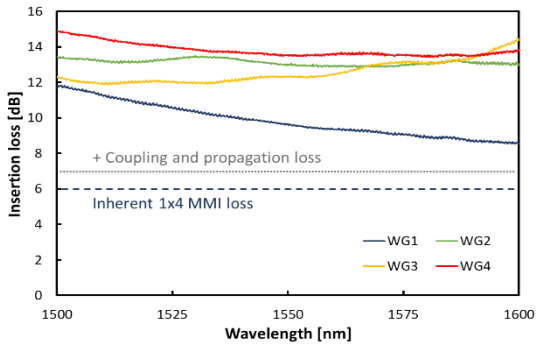


Fig. 5: Measurement results for a 1x4 3D MMI with the parameters: MMI length = 809 µm, MMI width 4.1 µm and additional height 2.4 µm. The insertion loss was measured as a function of wavelength for each output waveguide.

A cross section of the MMI region revealed that the offsets between the layers are much more complex than considered in the simulation, because the waveguides are shifted non-uniformly and in different directions to each other. Table 1 shows the measured offset data, the measured MMI losses at a wavelength of 1550 nm, and the simulation data per waveguide. When the offset was measured, the deviation of the waveguide and intermediate layers from the next deeper layer was determined. To check the influence of the measured offset, the 1x4 3D MMI was fitted with these data. The obtained simulation results are listed in the last column and show that the losses increase significantly for three of the four waveguides due to the offset. Noticeable is the significant deviation from the measured data of waveguide WG3. A possible explanation is a deviation of the actually achieved layer heights from the nominal values. To reduce losses, a reduction of the offset is necessary. This goal can be achieved by introducing a new tool for UV lithography which facilitates the alignment of the layers during the process step and thus increases the accuracy.

Table 1: Comparison of measurement results of the four output waveguides with simulation results

Waveguide No.	Measurement: Offset [µm]	Measurement: Excess loss [dB]	Simulation: Excess loss without offset [dB]	Simulation: Excess loss with measured offset [dB]
WG1	0.0 ± 0.3	2.6	1.1	2.7
WG2	0.0 ± 0.3	6.0	0.4	4.1
WG3	- 1.9 ± 0.3	5.3	1.0	0
WG4	0.3 ± 0.3	6.5	0.2	3.0

CONCLUSION

The designed, fabricated and characterized 1x4 vertical MMI connecting four vertically stacked waveguide layers is the first device of its kind. To implement the 1x4 3D MMI, a design was created using a parameter set for height, length and width with low excess losses of 0.7 dB and an imbalance of 0.9 dB. Principle functionality was demonstrated despite higher losses. Reducing the offset between the waveguide layers has a major impact on reducing excess losses from average of 5.1 dB to 0.7 dB and the imbalance by 3.5 dB. Especially in the lithography process, there are further possibilities, such as picture grabbing, to reduce this offset. In addition, the device presented here opens up new possibilities for implementing crossing-free optical switching matrices, small-footprint 3D optical phased arrays, and beam forming networks in 3D photonic integrated circuits.

Acknowledgment: This work was partially funded by the European Commission through the project ICT-3PEAT [contract number 780502] and partially funded by European Regional Development Fund (EFRE) and Berlin thought the project “Transferzentrum 5G Technologien - Leistungszentrum Digitale Vernetzung Phase III”.

References

[1] L.B. Soldano et al., *Optical Multi-Mode Interference Devices Based on Self-Imaging: Principles and Applications*, J. of Lightwave Technology, Vol. 13, no. 4, p. 615, 1995.
[2] M. Kleinert et al., *Photonic integrated devices and functions on hybrid polymer platform,* Photonics West, 10098-45, 2017.
[3] D. de Felipe et al., *Recent Developments in Polymer-Based Photonic Components for Disruptive Capacity Upgrade in Data Centers,* J. of Lightwave Technology, Vol. 35, no. 4, p. 683, 2017.
[4] M. Nuck, et al., *Low-loss Vertical MMI Coupler for 3D Photonic Integration,* ECOC, Tu3.C4, 2018.
[5] M. Weigel, et al., *3D Photonic Integration: Cascaded 1x1 3D Multi-Mode Interference Couplers for Vertical Multi-layer Connections,* ECIO, Session 11, 2020.
[6] J. Zhao et al., *Optimal design of multimode interference couplers using an improved self-imaging theory,* Optics Communications, Vol. 281, p. 1576, 2008.

C-Band Apodized Chirped Gratings in Aluminum Oxide Strip Waveguides

Milan Sinobad[1,*], Jan Lorenzen[1], Kai Wang[2], Meindert Dijkstra[2], Mahmoud A. Gaafar[1], Tobias Herr[1,3], Sonia M. Garcia-Blanco[2], Neetesh Singh[1,*], Franz X. Kärtner[1,3]

[*] corresponding author e-mail: milan.sinobad@desy.de, neetesh.singh@desy.de

[1]Center for Free-Electron Laser Science, Deutsches Elektronen-Synchrotron, Notkestraße 85, Hamburg 22607, Germany
[2]Integrated Optical Systems, MESA+ Institute for Nanotechnology, University of Twente, 7500AE, Enschede, The Netherlands
[3] Physics Department, Universität Hamburg, Luruper Chaussee 149, 22761 Hamburg, Germany

We report on apodized chirped Bragg gratings in aluminum oxide strip waveguides. Applications for this device include nonlinear photonics, specifically dispersion compensation in mode-locked lasers operating in the telecom C-band.
Keywords: *Apodized chirped Bragg gratings, aluminum oxide strip waveguides*

INTRODUCTION

Apodized chirped Bragg gratings (ACGs) are widely used in ultrafast laser systems to compensate for the dispersive effects that can cause degradation of the laser pulse. The advancements in ultrafast lasers on a silicon chip in recent years [1-3], have attracted the increasing interest of researchers in dispersion control using ACGs for ultrashort pulse generation [4]. ACGs are being studied in silicon-on-insulator [5-7] and more recently, in silicon nitride-on-insulator [8, 9] platforms. In this work, we report the design, fabrication, and characterization of ACGs in aluminum oxide strip waveguides at telecom wavelengths.

Aluminum oxide (Al_2O_3) waveguides are an ideal gain host material for ultrafast lasers on a silicon chip as it offers several advantages, such as broadband low-loss operation from ultraviolet to mid-infrared, multi-layer integration with CMOS platforms, and high rare earth ion solubility [10]. A moderate refractive index in aluminum oxide (1.72 at 1550 nm) makes ACGs manufactured in Al_2O_3-on-insulator less sensitive to fabrication variations than ACGs in silicon and silicon nitride-on-insulator platforms.

RESULTS

We designed the Al_2O_3-in-SiO_2 ACG to have a flat group delay dispersion around 1560 nm in TE polarization. We used uniform-period Bragg gratings (Λ = 516 nm) with corrugated side waveguide walls and applied squared-cosine apodization. The linear chirp of the Bragg wavelength (λ_B) is achieved by increasing the effective mode index (n_{eff}) along the grating using relation $\lambda_B(z) = 2\, n_{eff}(z)\, \Lambda$ (see *Figure 1* a). The average waveguide widths are w_{in} = 578 nm at the input, w = 1100 nm in the middle, and w_{out} = 2422 nm at the output of the 516 µm long grating. The corrugation depth Δw in the middle of the ACG is 500 nm. ACGs were fabricated in several steps. The 550 nm thick aluminum oxide layer has been deposited by reactive sputtering on the top of a thermally oxidized silicon wafer. The ACGs were patterned using electron beam lithography and etched by reactive ion etching. The resulting alumina oxide strip waveguides with a sidewall angle of around 80 degrees were protected with PECVD silica cladding. *Figure 1* (b) shows the cross-section of the fabricated waveguide.

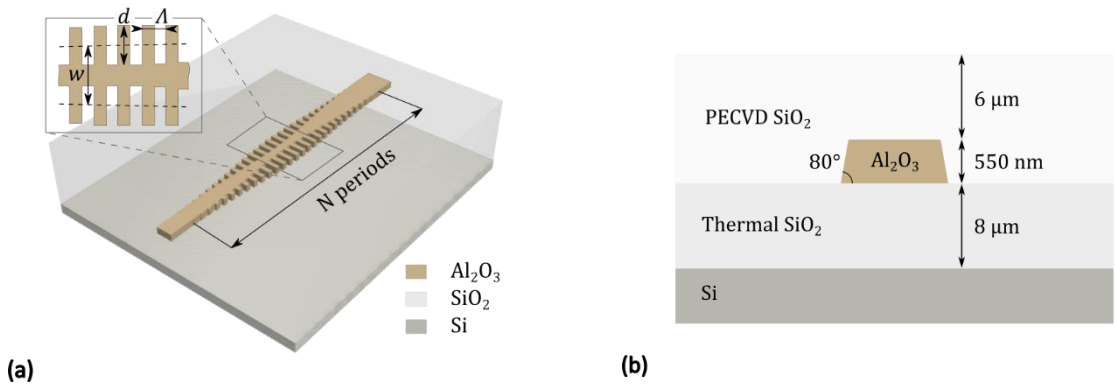


Figure 1 (a) schematics of aluminum oxide apodized chirped grating buried in silica cladding. The inset of the figure shows the parameters of the ACG and the tapered average width profile with dashed lines, (b) Cross-section of the 550 nm thick aluminum oxide strip waveguide

We performed transmission measurements by coupling supercontinuum light in TE polarization into the waveguide and measuring the transmitted power spectrum using an optical spectrum analyzer. *Figure 2* (a) shows the measured power spectrum of the transmitted light through the waveguide with the ACG (black curve) and a straight 1.6 µm wide reference waveguide (red curve). Dispersion measurements are performed with a home-built white-light interferometry setup [11]. We obtained information about the dispersion of the gratings from the Fourier transform of the measured interferogram.

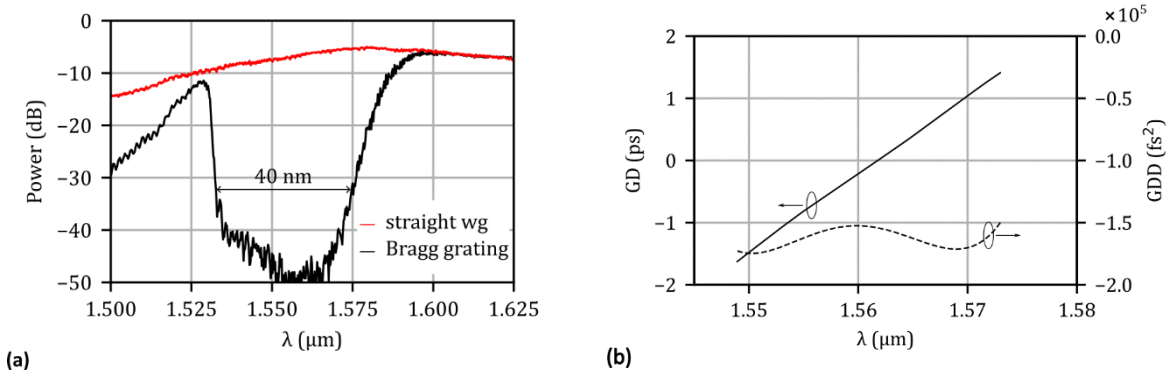


Figure 2 (a) the measured transmitted power spectrum from the ACG and reference straight waveguide. (b) The extracted group delay (GD) is on the left axis and group delay dispersion (GDD) is on the right axis.

The measured transmission spectrum from the ACG shows a strong drop in the transmission to less than 1% (-20 dB) around over a 40 nm bandwidth in comparison to the transmitted signal through the reference waveguide (see *Figure 2* (a). In a wavelength range between 1550 nm and 1573 nm, we measured the phase of the interfering reflected signals from the ACG and reference mirror with a standard deviation of σ = 0.013 π rad from the fitted curve. A group delay (GD) and group delay dispersion (GDD) were extracted from the measured phase as the first and second derivatives of the 9th-order polynomial fit (see *Figure 2* b). This results in flat dispersion of -163270 fs^2 (0.1280 ps/nm) and a deviation of 7520 fs^2 from 1550 nm to 1573 nm with a corresponding GD of 3.03 ps. Flat and smooth GDD over 23 nm bandwidth can enable dispersion compensation for 150 fs pulses in on-chip mode-locked lasers.

CONCLUSION

What reported the design, manufacturing, and characterization of the Al_2O_3-in-SiO_2 ACG working around 1560 nm wavelength. The ACG provides a strong reflection over around a 40 nm bandwidth and smooth and flat dispersion over a 23 nm bandwidth. Our ACG can be readily applied for intracavity dispersion compensation of 150 fs pulses in the C-band for applications such as in integrated femtosecond lasers.

Acknowledgments: Authors acknowledge support by Eu Horizon 2020 Framework Programme (Grant Agreement No.: 965124 Femtochip).

References

[1] K. Shtyrkova et al., Optics Express, vol. 27, no. 3, pp. 3542-3556, 2019.
[2] N. Singh, E. Ippen, and F. X. Kärtner, Optics Express, vol. 28, no. 15, pp. 22562-22579, 2020.
[3] A. Hermans et al., APL Photonics, vol. 6, no. 9, p. 096102, 2021.
[4] F. X. Kärtner et al., Optics Letters, vol. 22, no. 11, pp. 831-833, 1997.
[5] D. T. H. Tanet al., Optics Letters, vol. 33, no. 24, pp. 3013-3015, 2008.
[6] A. D. Simard, Y. Painchaud, and S. LaRochelle, Optics Express, vol. 21, no. 7, pp. 8953-8963,2013.
[7] M. Ma et al., IEEE Photonics Technology Letters, vol. 30, no. 1, pp. 111-114, 2018.
[8] P. T. Callahan et al., Conference on Lasers and Electro-Optics (CLEO), 2016.
[9] Z. Du et al., APL Photonics, vol. 5, no. 10, p. 101302, 2020.
[10] W. A. P. M. Hendriks et al., Advances in Physics: X, vol. 6, no. 1, p. 1833753, 2021.
[11] S. Diddams and J.-C. Diels, Journal of the Optical Society of America B, vol. 13, no. 6, pp. 1120-1129, 1996.

Lasing in a Neodymium-doped Aluminium Oxide Taiji Resonator

Student paper

Dahnée Wojcik*, Bjorn Jongebloed, Carlos Osornio-Martínez, Sonia M. García-Blanco

Integrated Optical Systems, MESA+ Institute for Nanotechnology, University of Twente, 7500 AE Enschede, The Netherlands.
* d.j.m.wojcik@student.utwente.nl

In many applications in integrated optics, high output power and mode stability are required for an on-chip laser. This could be achieved by using unidirectional lasing. However, on-chip lasers with a microring cavity are either not stable or prone to spontaneous switching. In this contribution, a low-cost design for stable unidirectional lasing is proposed: a Nd^{3+}-doped Al_2O_3 Taiji resonator. Moreover, lasing is experimentally shown.
Keywords: *Laser, Taiji resonator, neodymium, Aluminium Oxide*

INTRODUCTION

Unidirectional lasing leads to higher output power, increased mode stability and a single frequency spectrum [1] in comparison with a simple microring resonator (MRR) laser. Moreover, it obviously has the advantage of one stable direction of laser light. These advantages are necessities for many applications in integrated optics, like for instance optical isolators based on four-wave mixing [2], coherent (on-chip) communication and sensing [3].

It has been attempted to create unidirectional lasers with simple MRRs. However, these MRR lasers have stability issues and are prone to spontaneous switching between clockwise and counterclockwise modes, due to backscattering effects. Stable unidirectional lasing has been shown in photonic integrated circuits (PICs), by using an MRR with an S-shaped bus waveguide in its cavity connected with a Y-junction to the ring [4]–[6]. The designs were, however, electrically pumped and had to be either pumped with a relative high current or were very sensitive to the pump current. Furthermore, unidirectional lasing can be achieved by breaking chiral symmetry in the context of sensing [7].

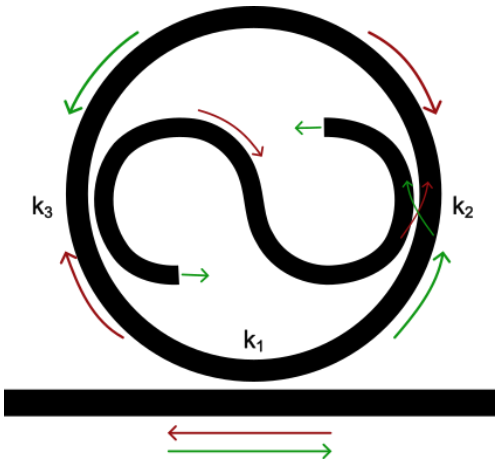


Fig. 1. The design for the Taiji resonator. The clockwise (CW) mode is indicated with red and the counterclockwise (CCW) mode with green. The ends of the S-waveguide are tapered with a skewed end facet.

In this work, a Taiji resonator (TJR) is studied. While the TJR is interesting for sensing applications, due to its predicted exceptional point sensitivity [8], when the waveguide material is doped with rare-earth ions, the TJR also allows for unidirectional lasing [1]. The TJR is formed by embedding an S-shaped waveguide inside the cavity of an MRR. In that regard, it is a simple device structure. Fig. 1 shows the schematic design of the TJR. Here, the clockwise (CW) mode can couple to the counterclockwise (CCW) mode, but not the other way around. This leads to a preferred mode with a lower laser threshold.

A theoretical investigation has been done, which states that stable unidirectional lasing occurs for a certain coupling to the S-waveguide [1]. There should be enough coupling compared to the inherent loss in the ring to create enough back-reflection. This creates a non-chirality with a preferred lasing mode. However, coupling of the CW mode to the CCW mode will also lead to a loss of the CCW, such that the laser threshold can become too high.

Neodymium has a broad emission cross-section at 1064 nm wavelength when pumped at 800 nm. Moreover, it has

no reabsorption, and it constitutes a four-level system gain medium [9]. Since light with a 1064 nm wavelength is not absorbed by water, a 1064 nm laser in integrated optics is relevant. Therefore, there are various biological imaging applications, applications for sensing and for fluid dynamic visualisation [10].

Aluminium oxide is the base core material. It has a very wide transparency window (from UV to IR), which makes it interesting in many integrated optic applications. Furthermore, Al_2O_3 has a high solubility for rare-earth ions and it has a high refractive index, which leads to more compact designs in PICs.

METHODS

We deposit a Nd^{3+}:Al_2O_3 layer on a silicon wafer covered by an 8 µm thick thermal oxide layer, with RF reactive co-sputtering (AJA ATC 1500) from metallic targets in oxygen atmosphere. The oxygen flow was kept constant. The power on the neodymium target was 14 W. In this way, a Nd^{3+}:Al_2O_3 layer with a thickness of 390 nm is deposited. The Nd^{3+}:Al_2O_3 is covered with a negative resist (ARN7520.18) and conductive coating (AR-PC 5090.02) by spin-coating, after which the resist is patterned with E-beam lithography (RAITH EBPG5150). After development, the Nd^{3+}:Al_2O_3 is etched using reactive ion etching (Oxford PlasmaPro 100 Cobra). Then, residual photoresist is removed and a SiO_2 cladding is deposited (Oxford PECVD 80).

The lasing spectra of the TJR is measured. The setup depicted in Fig. 2 allows for pumping the TJR and observing the lasing modes. The pump laser is a Ti:Sapphire laser, that can be tuned to emit light at 800 nm. This is a suitable wavelength to excite the gain medium. An optical spectrum analyser (Hewlett Packard 70950B) is used as spectrometer to measure the light emitted by the TJR laser with a resolution of 0.1 nm. The CW lasing mode is observed by optically pumping the TJR from the right (as indicated in Fig. 1), while the CCW mode is observed when the TJR is pumped from the left. The pump light is butt-coupled with a polarization-maintaining (PM) fibre into our waveguides.

To promote stable lasing, the chip will be placed on a temperature-controlled stage. By keeping the temperature constant, the resonance wavelengths of the TJR are more constant. The stable resonance wavelengths, then, support in stable lasing.

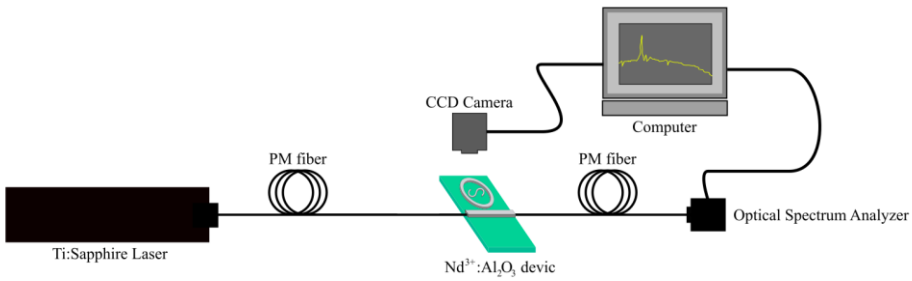


Fig. 2. Schematic overview of the set-up for measuring the transmission spectrum of a resonator in a PIC.

RESULTS

The lasing spectra from the CW mode and CCW mode of the TJR is shown in Fig. 3, for an incident pump power of approximately 25.3 mW. The TJR shows multimode lasing near 1076 nm which corresponds to the emission peak of Nd^{3+} that is centred around 1064 nm. In Fig. 3c, a black-and-white picture can be seen of the TJR, during the experiment. The white pixels indicate the signal wavelength.

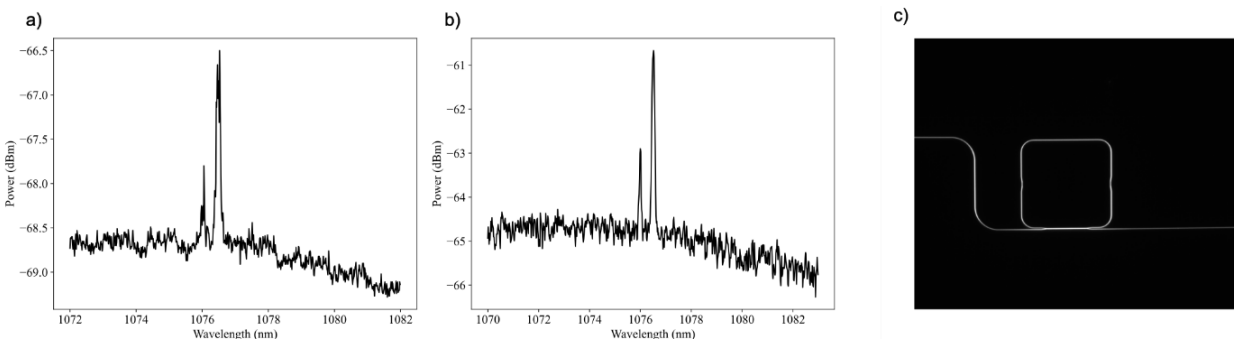


Fig. 3. The laser spectra of the CW mode (a) and the CCW mode (b) of the TJR near the 1064 nm gain peak. A black-white picture was made (c) while the Taiji was pumped from the left. The white pixels indicate scattered light of the signal intensity. The pump wavelength is filtered by cut-on filters from 900 nm, 850 nm and 800 nm.

The power of the lasing peak as seen in Fig. 3, was measured for multiple pump powers for both the CW and CCW modes. The resulting measurements and linear fit can be seen in Fig. 4. It should be noted that the slope efficiency of the CW mode is an order of magnitude higher than the slope efficiency of the CCW mode.

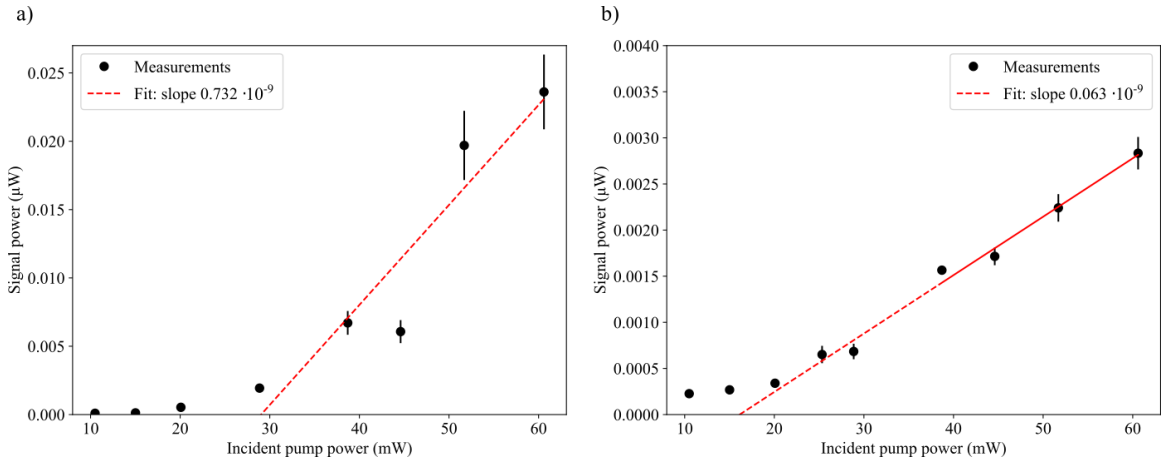


Fig. 4. The signal power measured for different incident pump powers, when the TJR was pumped from the right (a) and from the left (b), measuring the CW mode and CCW mode, respectively.

DISCUSSION AND CONCLUSION

The multimode lasing is mainly due to the combination of a small free spectral range (FSR) and a high pump power. In future design iterations, the FSR can be increased by reducing the circumference of the ring.

The slope efficiency of the CW mode is an order of magnitude larger than the CCW mode slope efficiency, as can be seen in Fig. 4. This indicates a weak directional-dependent emission. However, the CCW mode is expected to be the preferred lasing mode. The difference is therefore attributed to more scatter points in the bus waveguide to the right.

The observation of lasing modes in a Nd^{3+}: Al_2O_3 TJR is a promising result in the search for on-chip unidirectional lasing. To show that the TJR clearly exhibits unidirectional lasing, more investigation is necessary. The first step is to increase the coupling from the laser cavity to the S-waveguide. More coupling from the ring to the S-waveguide should increase the non-chirality of the TJR and, therefore, the TJR prefers one mode more strongly above the other.

References

[1] A. Muñoz de las Heras and I. Carusotto, “Unidirectional lasing in nonlinear Taiji microring resonators,” Phys Rev A (Coll Park), vol. 104, no. 4, p. 043501, Oct. 2021, doi: https://doi.org/10.1103/PhysRevA.104.043501.
[2] A. Muñoz de las Heras and I. Carusotto, “Optical isolators based on nonreciprocal four-wave mixing,” Phys Rev A (Coll Park), vol. 106, no. 6, p. 063523, Dec. 2022, doi: 10.1103/PhysRevA.106.063523.
[3] J. Lin et al., “Electro-optic tuning of a single-frequency ultranarrow linewidth microdisk laser,” Advanced Photonics, vol. 4, no. 3, May 2022, doi: 10.1117/1.AP.4.3.036001.
[4] J. P. Hohimer, G. A. Vawter, and D. C. Craft, “Unidirectional operation in a semiconductor ring diode laser,” Appl. Phys. Lett, vol. 62, p. 1185, 1993, doi: 10.1063/1.108728.
[5] J. P. Hohimer and G. A. Vawter, “Unidirectional semiconductor ring lasers with racetrack cavities,” Appl. Phys. Lett, vol. 63, p. 2459, 1993, doi: 10.1063/1.110474.
[6] W. D. Sacher, M. L. Davenport, M. J. R Heck, J. C. Mikkelsen, J. K. S Poon, and J. E. Bowers, “Unidirectional hybrid silicon ring laserwith an intracavity S-bend,” Laser Photon. Rev, vol. 6, pp. 511–517, 2012, doi: 10.1364/OE.23.026369.
[7] B. Peng et al., “Chiral modes and directional lasing at exceptional points,” Proc Natl Acad Sci U S A, vol. 113, no. 25, pp. 6845–6850, Jun. 2016, doi: 10.1073/PNAS.1603318113/SUPPL_FILE/PNAS.1603318113.SAPP.PDF.
[8] R. Franchi, S. Biasi, F. Mione, and L. Pavesi, “On the response of the Taiji microresonator against small perturbation of the counter propagating mode,” p. 13, Mar. 2022, doi: 10.1117/12.2608157.
[9] J. Yang, “Neodymium-doped Waveguide Amplifiers and Lasers for Integrated Optical Applications,” University of Twente, Enschede, 2010.
[10] G. N. Palafox, R. B. Wicker, and C. J. Elkins, “Rapid In-Vitro Physiologic Flow Experimentation Using Rapid Prototyping And Particle Image Velocimetry,” 2003, pp. 0419–0420. Accessed: Feb. 03, 2023. [Online]. Available: https://www2.tulane.edu/~sbc2003/pdfdocs/0419.PDF

Accurate, high-speed tuning of an ultra-narrow linewidth external cavity laser

Wilson Tsong[1], Ian van den Vlekkert[1], Sami Musa[1], Rustem Agaoglu[2], Ibrahim Olcer[2], Oxan N. van Leeuwen[3], Willy Bergsma[3], Edwin J. Klein[3], Dimitri Geskus[1]

[1]Chilas B.V., luchthavenweg 1, 5657 EB Eindhoven, The Netherlands
[2]Insigma Engineering, 19 Mayıs Mah. Sümer Sk. Sümko Sitesi K-2 Blok D2 Kadıköy 34736 İstanbul, Turkiye
[3]LioniX International B.V., Hengelosestraat 500, 7521 AN Enschede, The Netherlands

We demonstrate wavelength tuning of a compact external cavity semiconductor laser formed by hybrid integration InP and Si_3N_4 chips. We achieved a scan range covering the C-band with scan resolution of 5 pm providing <13 dBm of output power. Via fast acquisition we demonstrate fast scanning of the wavelength reaching 5 nm within 200 ms.
Keywords: *Tunable laser, External cavity laser, Ultra narrow linewidth, Hybrid integration, Vernier filter, Photonic integration.*

INTRODUCTION

In this work we present the last advancements on tuning external cavity lasers (ECLs) based on a vernier micro ring resonators (MRR). The wavelength of the presented laser can be freely tuned over 100 nm wavelength range, well beyond the C-telecom bandwidth, and similar designs prove to scan at much broader wavelength ranges, yet providing tens of mW of output power [1, 2]. The lasers show great potential in in many applications [3-5]. These MMR Vernier based ECL laser sources are relatively new, and the way of tuning the wavelength is differs significantly from other types of tunable lasers such as well-established laser types like VECSELs, DFB lasers, Littman-Littrow based tunable lasers. Where the wavelength of most of the tunable lasers can be tuned using only 1 or 2 Actuators, exhibiting an almost linear actuation throughout the full wavelength tuning range. The here presented Vernier based actuators (at least 3 actuators) have to cycle through 2π phase shifts between 50 and few hundred times to span the full wavelength range. Therefore tuning of the Vernier based ECLs require high resolution mapping, for high resolution wavelength tuning. In addition the actuator elements have to be fast, in order to scan the wavelength of high speed, full range applications such as Optical Coherence Tomography (OCT).

In this paper we show the obtained results of mapping the laser's characteristics, resulting in a lookup table (LUT). In the second part we push the actuation of the laser to its maximum speed, where we tune the laser over 5 nm range at high speed using a dense LUT, and where we optimize the performance of the laser by a dynamical update of the LUT while scanning the laser. These preliminary results show the potential of the scan speed of the Chilas laser and all MMR based ECLs.

DESIGN

The external cavity laser consists of hybrid integrated indium phosphate (InP) reflective semiconductor optical amplifier (RSOA) and TriPleX silicon nitride (Si_3N_4) external cavity. Here, the RSOA act as gain medium, and feedback is provided by a wavelength selective mirror in the Si_3N_4 photonic integrated circuit (PIC). Wavelength selection is achieved by a vernier filter consisting 2 MRRs. The optical output is interfaced to a polarization maintaining fiber using end face coupling. This commercially available laser source is packaged in a 14-pins butterfly package. The schematic of the laser and its design are shown in Fig. 1.

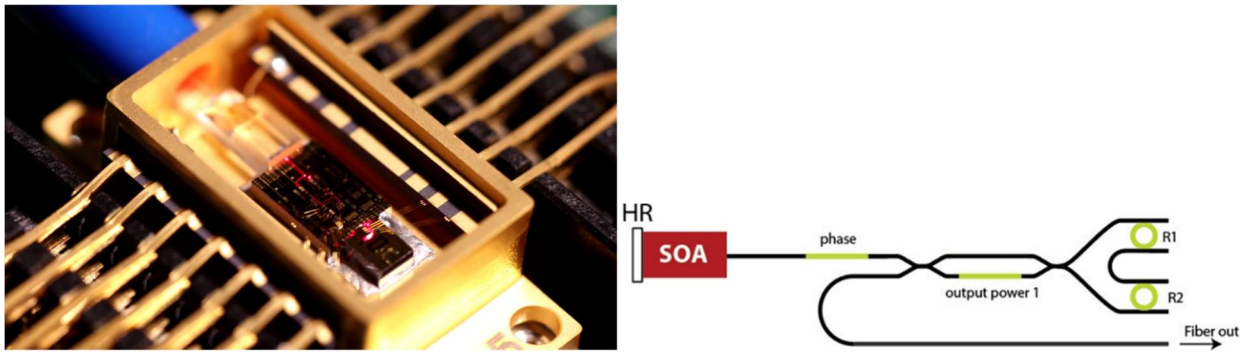


Fig. 1. Photograph and schematic of the Chilas CT3 PIC based external cavity laser module.

The gain section is a reflective semiconductor optical amplifier (RSOA). The RSOA gain section is pumped using an externally driven current. The externally pumped current causes stimulated emission and therefore a high output power of light. The gain section, which has a broad emission band, is coupled to a photonic integrated circuit in the silicon nitride Si_3N_4 realized using TriPleX waveguide technology. TriPleX waveguide technology has the advantage of having extremely low waveguide losses, of ≤ 0.07 dB / cm. The light from the gain section is guided in the Si_3N_4 external cavity through a symmetric Mach-Zehnder interferometer (MZI), and afterwards towards two micro-ring resonators (MRRs) with near-identical but varying circumference length around 1 mm.

Platinum resistive heaters elements are placed onto the waveguides. These heaters can be controlled to support high, single-mode output power the tuning of the output wavelength by changing the refractive index of the underlying waveguide with a thermo-optic effect. Two heaters are placed onto the two rings for wavelength tuning, one heater at one arm of the MZI, and a fourth heater is equipped on a bus waveguide inside the cavity to change its phase. To obtain a 2π phase shift tuning at either of the MRR, a voltage close to 14 V is needed. For the other heaters, this value is close to 8 V.

THEORY

The tuning principle is fully derived from the waveguide structure containing the double MRRs and the MZI. The two rings form a Vernier filter with a combined free spectral range (FSR of 100 nm), here the smaller ring has a designed FSR of 1.73 nm and the larger ring a FSR of 1.70 nm. The two MRRs in the structure act as a Vernier filter. Broadband light travelling through the two resonators will emit a single-mode light output. In Fig. 2 the principle of the wavelength tuning of the laser is demonstrated. Fig. 2a depicts an example of ring responses of the two MRRs of a laser. The broadband light coming from the gain section will enter the first ring resonator, ring 1. The wavelength spectrum of light leaving a micro ring resonator is depicted in Fig. 2a. Due to interference between the light in the ring with itself, only wavelengths at the peaks of the spectrum can exit. With two rings, this process is repeated. Due to the small circumference length difference, the spectrum has a small FSR difference, thus the peaks are slightly mismatched. So, the peaks do not match within a certain range and are able to tune to any wavelength within that range, which is called the span. In order to obtain single-mode lasing , the peaks of both rings ought to be moved to the target wavelength, shown in Fig. 2a. Increasing the heat across the waveguide by applying a higher voltage through the leads of the heater will cause a phase shift of the spectrum shown in Fig. 2a, it will shift towards higher wavelengths. Thus, to obtain a lasing peak at the target wavelength, the heaters have to be tuned for a phase shift of ϕ_1 and ϕ_2 for ring 1 and ring 2 respectively. The Vernier response in that situation is given by Fig. 2b, which is the result of a multiplication of the two ring spectra. Here, the side modes are suppressed due to destructive interference within the ring and will die out as they do not reach lasing threshold. Only one wavelength will remain. Part of the light will be guided back to the gain section for feedback to amplify light at that wavelength, and the other part will be coupled outwards to the fiber output.

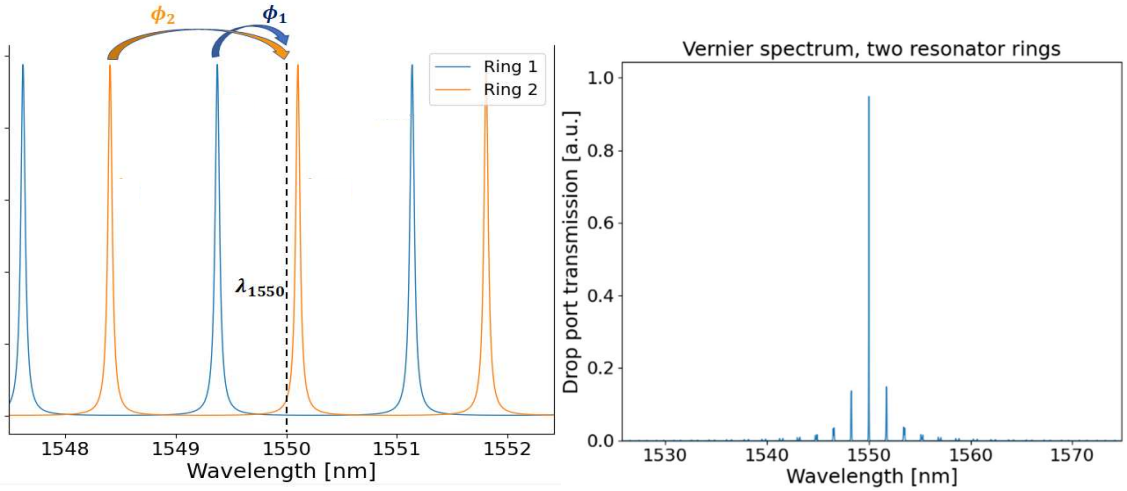


Figure 2. (a): Example demonstrating the ring response and principle of wavelength tuning. The x-axis denotes the output wavelength, and y-axis the transmission. To tune to a specific wavelength (here: 1550 nm), ring 1 and ring 2 needs to be tuned by a phase of ϕ_1 and ϕ_2 specifically. (b): Example of the resulting Vernier response when the rings are aligned at one wavelength (here: 1550 nm).

MAKING THE LOOKUP TABLE (LUT)

The laser system is located inside a 14-pin golden butterfly package and is installed inside the tunable laser controller (TLC). The TLC contains all the necessary hardware to switch on the laser and control the heaters. The optical fiber output of the laser is connected with a 50/50 splitter to measure the output power and the emission spectrum simultaneously. Using a routine a measured dataset is generated, cleaning of the dataset and removal of erroneous data points is done using curve fitting algorithms. This results in a LUT addressing a wavelength range between 1528 nm and 1569 nm, with a resolution of 5 pm. A measurement is performed using another "set-get" routine checking the performance of the LUT systematically Fig. 3a.

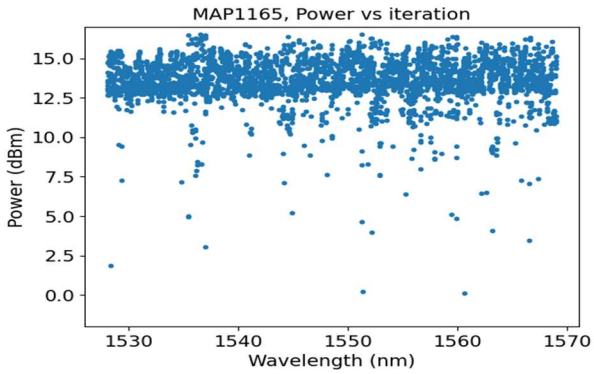


Fig. 3, Graph of power as a function of wavelength for more than 3700 points with a single-mode wavelength output between 1528 and 1569 nm. In this example we obtain an wavelength accuracy of ~ 90% (90% is both single mode, inside the same ring resonance, and above 10 dBm), The majority of the solutions provide a output power between 13 and 16 dBm.

FAST WAVELENGTH TUNING OF THE EXTERNAL CAVITY LASER.

In order to achieve fast tuning a part of the LUT is loaded into a small EEPROM memory cell inside the tunable laser controller (TLC) avoiding any PC to TLC communication related timing issues. The LUT elements are send to the heater drivers of the laser using a local running routine with an interval time of 200 us per element. In this way the system cycles through the full set of 1000 preloaded laser configurations within a total cycle time of 200 ms, while covering 5 nm wavelength range. To measure the emission wavelength of the laser a tunable filter is used for fast acquisition of the wavelength. This tunable filter provides both power as wavelength information at a very high sampling speed. Both the tuning of the laser, and the tunable filter are synchronized to each other. The software interface has a sampling is well below the 200 us interval time, and therefore allows updating of individual heater settings in the LUT while continuously running the scanning laser routine. This dynamical updating of heater settings allows maximization of the output power for each individual entry of the LUT. This results in a fairly flat output power of the laser while scanning as presented in Fig. 4.

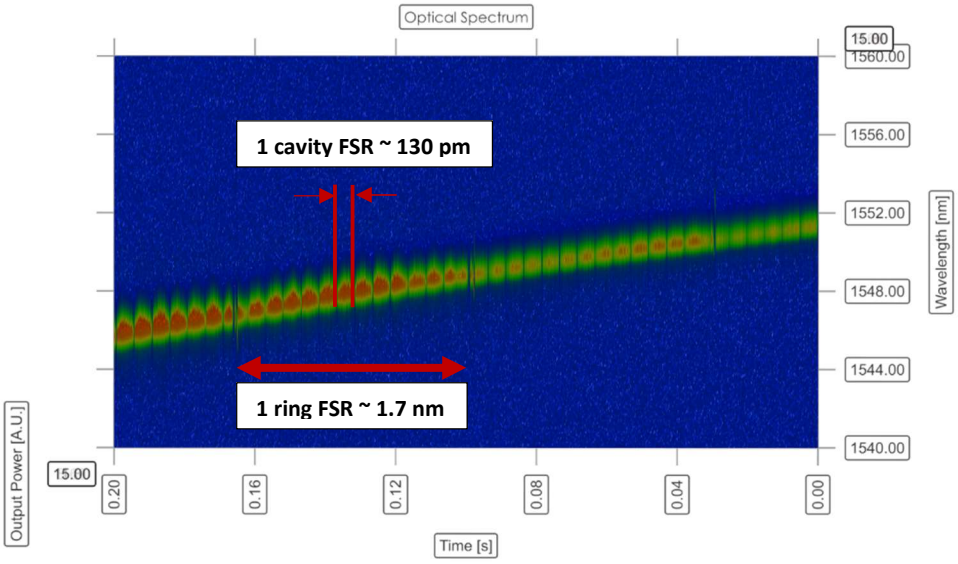


Figure 4, Output power as function of wavelength.

When looking at the results of fast scanning, we can indicate clear patterns, the fine patterns originate from the laser scanning through the cavity FSR with an interval of ~130 pm, we assume this scan is modehop-free. The larger patterns correspond to the FSRs of the rings, being ~1.7 nm. Here the “dark” spots originate from the 2π phase jumps the laser has to make, and therefore is not optimally tuned during a few milliseconds. Ongoing efforts are made to improve the tuning algorithms, and improve the acquisition speeds.

CONCLUSIONS

We have demonstrated high accurate wavelength setting of an vernier based ECL, providing a LUT of 50 nm and a resolution of 5 pm. Measurements show <90% setting accuracy within 10 pm resolution, and power levels between 13 and 16 dBm. Using the combination of fast scanning and fast spectral acquisition of the laser we demonstrate 5 nm wavelength tuning of the laser within 200 ms. Based on these results we anticipate to scan the full telecom C-band within 1 second using our off the shelf tunable laser source.

References

[1] Yuyao Guo, Xinhang Li, Minhui Jin, Liangjun Lu, Jingya Xie, Jianping Chen, and Linjie Zhou , "Hybrid integrated external cavity laser with a 172-nm tuning range", APL Photonics 7, 066101 (2022).

[2] Wilson Tsong, Ian van den Vlekkert, Sami Musa, Raimond N. Frentrop, Noor A. Schilder, Marcel Hoekman, Arjan Meijerink, Edwin J. Klein, Dimitri Geskus, “139 nm tuning range, high speed wavelength modulation, and high output power up to 60 mW from a single gain, two-ring vernier external cavity laser”, SPIE Photonics West 12424-26, (2023).

[3] H. Mahmudlu, R. Johanning, A. K. Kashi, A. van Rees, J. P. Epping, R. Haldar, K.-J. Boller, and M. Kues, “Fully on-chip photonic turnkey quantum source for entangled qubit/qudit state generation,” arXiv, 2206.08715, (2022).

[4] Z. L. Newman, V. Maurice, T. Drake, J. R. Stone, T. C. Briles, D. T. Spencer, C. Fredrick, Q. Li, D. Westly, B. R. Ilic, B. Shen, M.-G. Suh, K. Y. Yang, C. Johnson, D. M. S. Johnson, L. Hollberg, K. J. Vahala, K. Srinivasan, S. A. Diddams, J. Kitching, S. B. Papp, and M. T. Hummon, “Architecture for the photonic integration of an optical atomic clock,” Optica, vol. 6, no. 5, pp. 680–685 (2019).

[5] K. Zou, Z. Zhang, P. Liao, H. Wang, Y. Cao, A. Almaiman, A. Fallahpour, F. Alishahi, N. Satyan, G. Rakuljic, M. Tur, A. Yariv, and A. E. Willner, “Higher-order QAM data transmission using a high-coherence hybrid Si/III–V semiconductor laser,” Optics Letters, vol. 45, no. 6, pp. 1499–1502 (2020).

A hybrid photonic integrated signal source with >1.5 THz continuous tunability and <0.25 GHz accuracy for mmW/THz applications

(Student paper)

Tianwen Qian, Peer Liebermann, Martin Kresse, Klara Mihov, Jakob Reck, Madeleine Weigel, Moritz Kleinert, Crispin Zawadzki, David de Felipe, Norbert Keil and Martin Schell

Fraunhofer Institute for Telecommunications, Heinrich Hertz Institute, HHI, 10587 Berlin, Germany
tianwen.qian@hhi.fraunhofer.de

We present a hybrid photonic integrated mmW/THz signal source, which comprises two tunable lasers and on-chip wavelength meters. The continuous wavelength tunability of a single laser is over 12 nm (1.5 THz), and the wavelength meter accuracy is below 0.002 nm (0.25 GHz) over the entire C-band.
Keywords: *hybrid integration, tunable laser, continuous tuning, continuous wave terahertz*

INTRODUCTION

Using the optical heterodyning technique to generate continuous wave (CW) electrical signals with frequencies ranging from the millimeter range (from 67 GHz to 300 GHz) to the terahertz range (above 300 GHz) is a simple and straightforward method enabling the mmW/THz applications [1–3]. With two optical wavelengths that are mixed on a photodiode, the electrical beat signal generated at the output is only limited by the bandwidth of the photodetector. Besides, in order to control the generated mmW/THz frequency, it is mandatory to know the absolute value of the two wavelengths and achieve mode-hope-free tuning within the target frequency range.

In this paper, we present an mmW/THz signal source based on a hybrid photonic integrated circuit (PIC), which comprises two hybrid tunable DBR lasers for the generation of optical signals. These signals are used for the photonic generation of the mmW/THz signals. The tunable laser provides continuous tuning over 12 nm in the C-band. Additionally, on-chip wavelength meters are implemented on the PIC using thin-film filters (TFF), etalons, and PDs allowing for on-chip read-out of the laser wavelength.

DESIGN AND THEORY

Fig. 1 shows the design of such a signal source, as well as the fabricated and assembled PIC based on Fraunhofer HHI's hybrid photonic integration platform PolyBoard [4, 5]. Starting from the left-hand side, an InP chip with two active sections bonded on an AlN submount is butt-coupled to the polymer chip. After each active section, the PolyBoard chip comprises thermo-optically tunable phase shifters and Bragg gratings to implement two tunable distributed Bragg reflector (DBR) lasers. In the central part of the PIC, thermo-optically tunable phase shifters allow for phase tuning of the generated optical signals. Additionally, variable optical attenuators (VOAs) have been included in order to allow for equalization of the amplitude of the two signals generated by the tunable lasers. On the right-hand side of the chip, U-grooves are placed to connect the fibers directly. Finally, the upper and lower parts of the PIC feature power-monitor photodiodes (PD-MO) and wavelength meters. The wavelength meter comprises a pre-etched slot for the insertion of a TFF which shows a monotonic frequency dependence, and U-grooves with different lengths to insert coated GRIN lenses for the implementation of the two etalons.

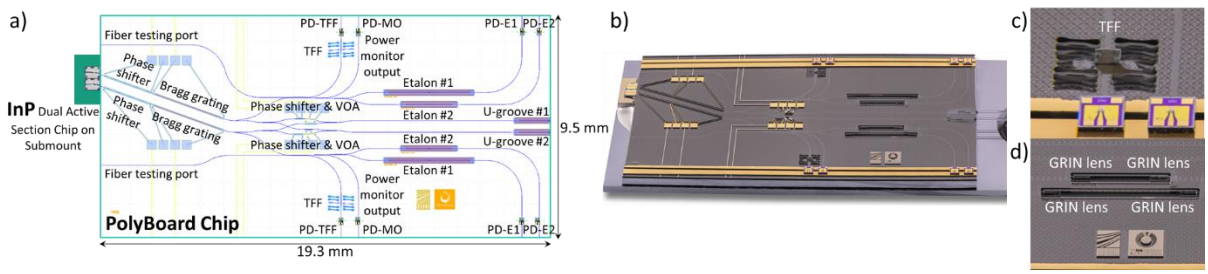


Fig. 1. Fiber-coupled THz signal source containing assembled PDs, TFFs, etalons, and butt-coupled with InP dual active section chip. a) GDS design of such PIC. b) Assembled PIC coupled with fibers fixed on Si-carrier. c) TFF inserted in the pre-etched slot and PDs mounted on the top surface of the PolyBoard. d) Coated GRIN lenses form two etalon structures inserted in the U-grooves.

A key requirement in the design is that the tunable lasers allow for continuous tuning. By scanning through the grating and phase section heating currents, Fig. 2 a) shows the wavelength mapping of such a laser. The solid lines show the mode-hop boundaries between adjacent modes, and the dashed line marks a trajectory possible for continuous

tuning. In this work, the target frequency sweep amounts to 3 THz, which is equivalent to a wavelength range of 24 nm in the C-band. This implies that, if each tunable laser is tuned counter-directionally in order to achieve a difference in the wavelengths of up to 24 nm, each of them has to be tuned 12 nm continuously. In order to allow for continuous tuning, the use of long phase shifters is necessary to avoid mode-hops [6]. In Fig. 2 b), the calculated tuning range with varying lengths of the phase shifter is shown. As can be seen, for a phase section length of 2 mm, 12 nm continuous tuning can be achieved. The Bragg gratings have been designed to ensure single mode operation in the resulting cavity length.

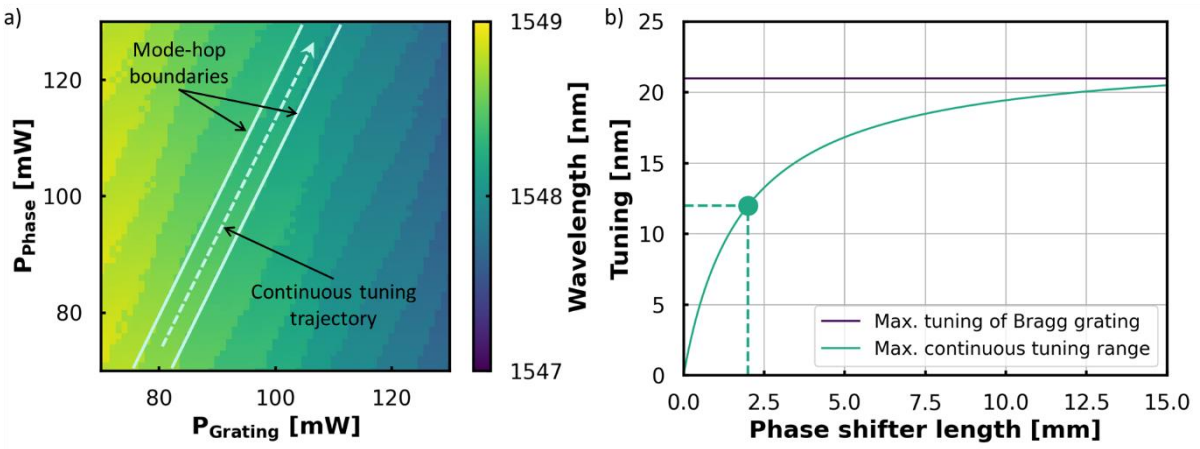


Fig. 2. a) Wavelength mapping retrieved by scanning the grating and phase section heating currents of the tunable laser. The solid lines show the mode-hop boundaries, and the dashed line marks a possible trajectory for continuous tuning. b) Calculated tuning range with varying phase shifter length. The marked green dot indicates the target 12 nm tuning range resulting in a 2 mm phase section length.

The working principle of the on-chip wavelength meter has been reported in [7]. In this design, two etalon structures with different free spectral ranges (FSR) have been implemented to allow exploring the Vernier effect and ensure a higher resolution of the wavelength determination. As can be seen in the exemplary plot in Fig. 3, firstly, the wavelength is roughly determined through the edge filter, which indicates two other photocurrents on the corresponding curves of the two etalon structures. Secondly, by comparing the slopes of these two etalon curves, the one with a steeper slope is used to determine the wavelength, since the steeper rising or falling slope enhances the accuracy of the wavelength determination.

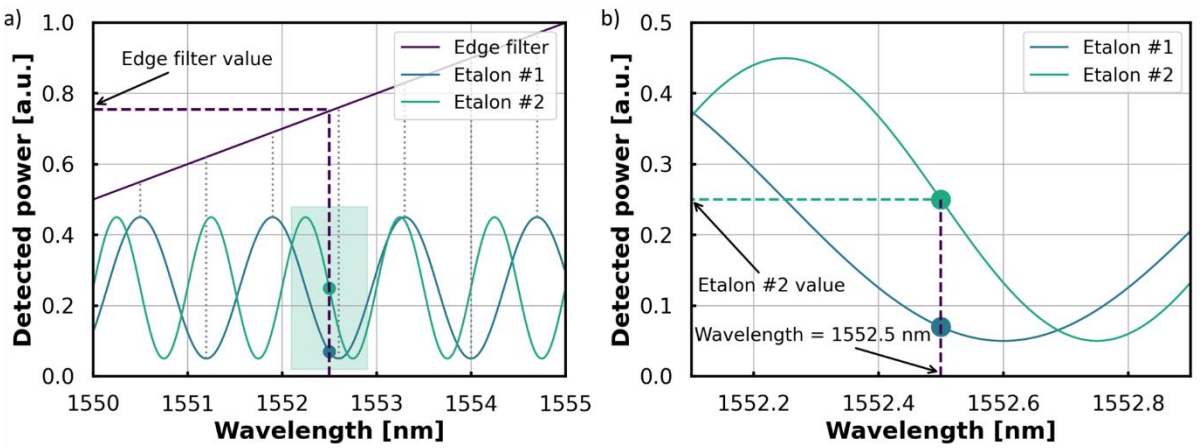


Fig. 3. Exemplary detected power versus wavelength after the edge filter and two etalons. a) The edge filter is used for coarse wavelength determination, which indicates two other values on the corresponding etalon curves. b) The one with a steeper slope is used to determine the wavelength by evaluating the two etalon curves.

RESULTS

The continuous tuning test and wavelength meter test have been conducted individually. Continuous tuning algorithms following the trajectory between mode-hop boundaries have been developed. The test is done on the single tunable laser test structure, which has the same parameter as on the PIC and is fabricated on the same wafer. By simultaneously driving the Bragg grating and the phase shifter, Fig. 4 a) shows the retrieved wavelength with increasing driving steps. As can be seen, a continuous wavelength tuning range of 14.3 nm has been achieved. With each one of the two lasers of the PIC being tuned over the 12 nm (1.5 THz) range, targeted 3 THz frequency sweeps

could be achieved. Moreover, the wavelength read-out algorithms for determining the slope of the etalon curves were developed, and wavelength read-out tests were performed. For these tests, an optical signal of 0 dBm from an external tunable laser source was coupled into the fiber testing port, followed by a wavelength meter consisting of an edge filter and two etalons with slightly varied FSR (Etalon #1: 51.37 GHz, Etalon #2: 50.85 GHz). In Fig. 4 b), the measured wavelength on the on-chip wavelength meter versus the set wavelength on the external tunable laser is plotted, showing that a good agreement has been reached between the retrieved and the target wavelength. Fig. 4 b) also shows the read-out deviations from the target wavelength. Over 99% of the measurement points show a deviation lower than 0.05 nm, which corresponds to an average deviation less than 0.002 nm, in the C-band corresponds to an error in the frequency read-out lower than 0.25 GHz.

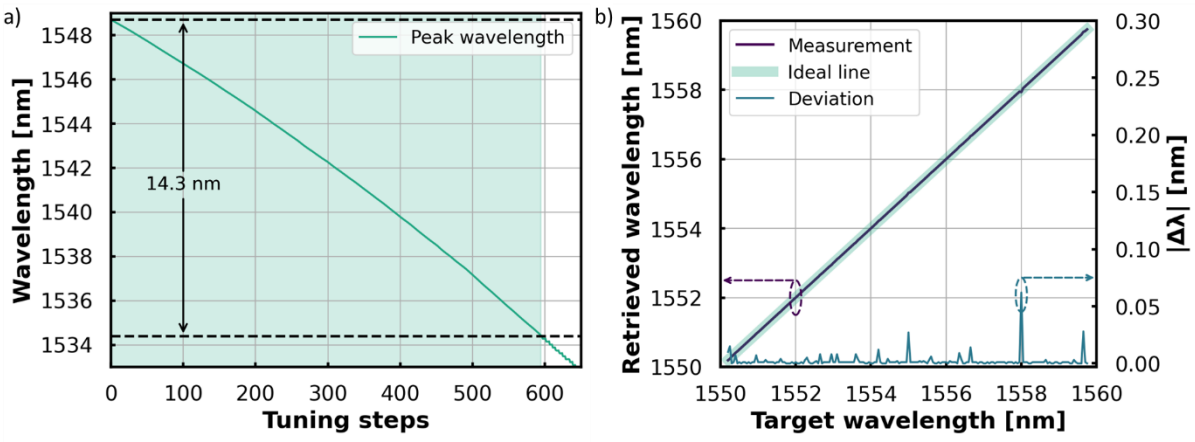


Fig. 4. a) Continuous tuning of 14.3 nm is achieved by driving the Bragg grating and phase shifter simultaneously, following a trajectory between the mode-hop boundaries. b) Wavelength meter test with two etalon structures shows the enhanced resolution with an average deviation below 0.002 nm, which corresponds to 0.25 GHz in C-band.

CONCLUSION

We successfully demonstrated a fiber-coupled photonic hybrid integrated mmW/THz signal source, which comprises two hybrid continuous tunable DBR lasers and on-chip wavelength meters. The continuous tunability of the laser is over 12 nm (1.5 THz), by combining both lasers, a 3 THz continuous tuning range could be achieved. Additionally, the on-chip wavelength meters implement two etalon structures and the enhanced accuracy reaches below 0.002 nm (0.25 GHz) over the entire C-band. The above-demonstrated work paves the way for future mmW/THz applications.

Acknowledgments: This work was partly financed by the European Union's Horizon 2020 Research and Innovation Programme, in the framework of the TERAmeasure project (Grant agreement ID: 862788).

References

[1] T. Nagatsuma, G. Ducournau, C. C Renaud, *Advances in terahertz communications accelerated by photonics,* Nat. Photon., vol. 10, no. 6, pp. 371-9, 2016.

[2] G. Carpintero, S. Hisatake, D. de Felipe, R. Guzman, T. Nagatsuma, N. Keil, *Wireless Data Transmission at Terahertz Carrier Waves Generated from a Hybrid InP-Polymer Dual Tunable DBR Laser Photonic Integrated Circuit,* Sci. Rep., vol. 8, no. 1, pp. 1-7, 2018.

[3] T. Qian, M. Deumer, Y. D Gupta, S. Nellen, B. Schuler, H. Conradi, M. Kresse, J. Reck, K. Mihov, M. Kleinert, M. Weigel, C. Zawadzki, D. de Felipe, B. Globisch, M. Baier, N. Keil, M. Schell, *Hybrid Polymer THz Receiver PIC with Waveguide Integrated Photoconductive Antenna: Concept and 1st Characterization Results*, in Proceedings of the Optical Fiber Communication Conference (OFC) 2022, pp. W3D.6, 2022.

[4] D. de Felipe, M. Kleinert, C. Zawadzki, A. Polatynski, G. Irmscher, W. Brinker, M. Moehrle, H.-G. Bach, N. Keil, M. Schell, *Recent Developments in Polymer-Based Photonic Components for Disruptive Capacity Upgrade in Data Centers,* J. Lightwave Technol., vol. 35, no. 4, pp. 683-9, 2017.

[5] M. Kleinert, M. Nuck, H. Conradi, D. de Felipe, M. Kresse, W. Brinker, C. Zawadzki, N. Keil, M. Schell, *A platform approach towards hybrid photonic integration and assembly for communications, sensing, and quantum technologies based on a polymer waveguide technology*, in Proceedings of the 2019 IEEE CPMT Symposium Japan (ICSJ), pp. 25-30, 2019.

[6] D. de Felipe, M. Happach, S. Nellen, W. Brinker, M. Kleinert, C. Zawadzki, M. Möhrle, N. Keil, T. Göbel, K. Petermann, M. Schell, *Hybrid polymer/InP dual DBR laser for 1.5 µm continuous-wave terahertz systems*, in Proceedings of the SPIE OPTO, pp. 195-201, 2016.

[7] A. Schoenau, T. Qian, P. Liebermann, C. Kastner, H. Conradi, M. Kresse, D. de Felipe, M. Baier, N. Keil, M. Schell, *Hybridly Integrated Photonic Integrated Circuit for Wavelength and Polarization Determination*, in Proceedings of the 2022 European Conference on Integrated Optics (ECIO), pp. W.B.3, 2022.

Magneto-optical properties of e-beam evaporated EuS films for room temperature applications

(Student paper)

F.H.B. Somhorst[1,†*], M.L. Meretska[1], M. Ossiander[1], Y. Hou[2], J. Moodera[2,3], and F. Capasso[1]

[1]Harvard John A. Paulson School of Engineering and Applied Sciences, Harvard University, 9 Oxford Street, Cambridge, MA 02134, USA
[2]Francis Bitter Magnet Laboratory and Plasma Science and Fusion Center, Massachusetts Institute of Technology, 150 Albany Street, Cambridge, MA 02139, USA
[3]Physics Department, Massachusetts Institute of Technology, 77 Mass Avenue, Cambridge, MA 02142, USA
†Present address: MESA+ Institute for Nanotechnology, University of Twente, P.O. box 217, Enschede, 7500 AE, The Netherlands
* f.h.b.somhorst@utwente.nl

Traditionally, magneto-optical effects enable non-reciprocal optical response engineering in devices such as optical isolators. Unfortunately, conventionally used materials are bulky and hard to pattern, making scaling to integrated optics difficult. Here, we report on the Verdet-constant measurements between 600 – 800 nm at room temperature of e-beam evaporated EuS, which appears to be an order of magnitude higher than conventional TGG.
Keywords: *Farady effect, Magneto-optics, Light-matter interaction, Verdet constant, Room temperature, Polarization, Optical isolator, Nanofabrication, Europium Sulfide, Thin film, Refractive index*

INTRODUCTION

Light-matter interaction subjected to a magnetic field leads to a plethora of important physical effects that affect light polarization, including the Faraday effect [1]. The Faraday effect is exhibited as a rotation of the (linear) polarization vector when light propagates through a magneto-optical material parallel to the applied magnetic field. The rotation θ is proportional to the applied magnetic field strength B and the propagation distance travelled through the magneto-optical material L. Below the saturation magnetic field strength, the rotation can be well described by

$$\theta = VBL, \tag{1}$$

where the proportionally constant V is known as the Verdet constant. For paramagnetic materials, such as EuS at room temperature, the wavelength dispersion within the tail of a resonance is usually modelled as [2]

$$V = \frac{E}{\lambda^2 - \lambda_0^2}, \tag{2}$$

where the proportionality constant E is dependent on the paramagnetic ion volume concentration, temperature, transition probability and Landé splitting factor, λ is the wavelength of interest, and λ_0 is the resonance transition wavelength of the paramagnetic ions.

Magneto-optical effects differ from the asymmetric power transmission associated with chiral media, because the orientation of the magnetic field determines the rotation direction of the polarization vector. Unlike approaches relying on nonlinear effects or time modulation, magneto-optical effects break the Lorentz reciprocity in a passive system [3]. Many optical devices have been realized using these effects, including magneto-optical modulators [4], circulators [5], and isolators [6]. One of the most widely used magneto-optical materials, terbium gallium garnet (TGG) crystal, has a moderate Verdet constant of ~10^3 deg T^{-1} m^{-1} for 600 – 800 nm wavelength [7]. Accordingly, a 45 deg rotation at 1 T field strength requires roughly a material length of several cm. Given a certain material, Eq. 1 suggests that scaling down to smaller lengths requires an increase in magnetic field strength. However, this requires strong magnetics and at some point the magnetic field will be saturated.

Therefore, a next step is to investigate materials with a higher Verdet constant and accompanied by fabrication simplicity that pave the way for the engineering of nanophotonic structures that enhance magneto-optical effects. Eu-chalcogenides such as EuS are known to have a remarkably high Verdet constant at cryogenic temperatures [8], but unlike other Eu-chalcogenides, the Verdet constant of EuS at room temperature has long been overlooked [9].

Recently, we published the first measurements of the magneto-optical properties of thin-film EuS at room temperature [10].

RESULTS

In this study, we measured the Verdet dispersion between 600 – 800 nm wavelength. Additionally, we measured the refractive index and extinction coefficient of EuS using ellipsometry. All EuS films used in this study are deposited by electron-beam evaporation, where the substrate was kept at room temperature. The base vacuum of the system was ~6 x 10^{-8} Torr whereas during electron-beam evaporation of EuS it was at ~2 x 10^{-6} Torr.

For the refractive index measurements, we prepared a half-inch silicon square substrate with a 100 nm thick film of EuS. We used a spectroscopic ellipsometer (J.A. Woollam V-VASE32) to measure the real and imaginary part of the refractive index of the EuS film inside and outside the visible spectral range. The ellipsometry fits for 400 – 1000 nm wavelength are presented in Fig. 1(a). In addition, we applied the Sellmeier model to the refractive index data between 650 – 800 nm. The Sellmeier model used is given by

$$n^2(\lambda) = 1 + \frac{A_1\lambda^2}{\lambda^2 - {B_1}^2}, \tag{3}$$

for which we found fitting parameters A_1 = 3.0117 and B_1 = 0.2527 um. The resulting fit is presented in Fig. 1(b).

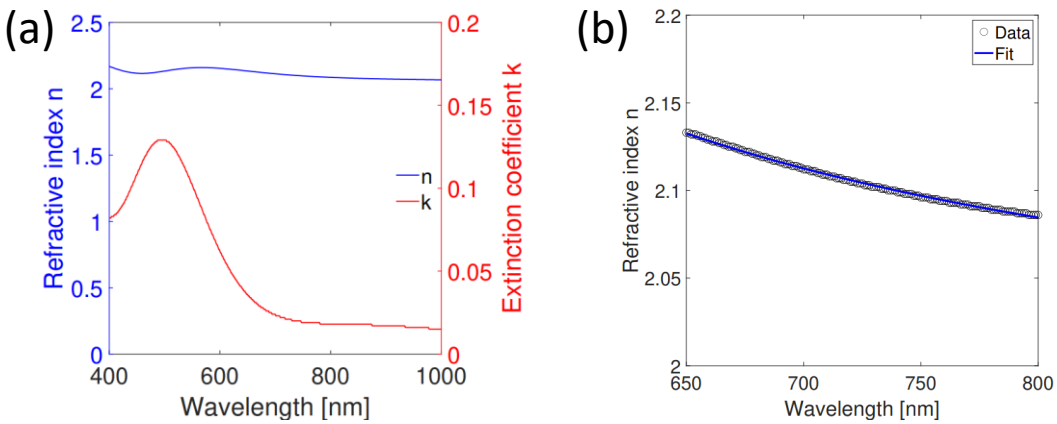


Fig. 1. Optical characterization of EuS. (a) The real (blue) and imaginary (red) part of the refractive index of EuS are extracted from ellipsometry measurements. (b) Sellmeier fit (Eq. 3) to the EuS refractive index data between 650 – 800 nm.

For the Verdet constant measurements, we prepared a 1 um thick EuS film on a 0.5 mm thick glass substrate. Our experimental setup is described in Ref. [10]. We used a home-built magnetic assembly that oscillated at 1 Hz and generated more than 1 T of magnetic field strength at the sample position. Our results are corrected for the Faraday rotation contribution of the glass substrate. The results of the Verdet constant measurements are presented in Fig. 2(a). The original Verdet constant measurements at 8 K temperature are presented in Fig. 2(b) [8].

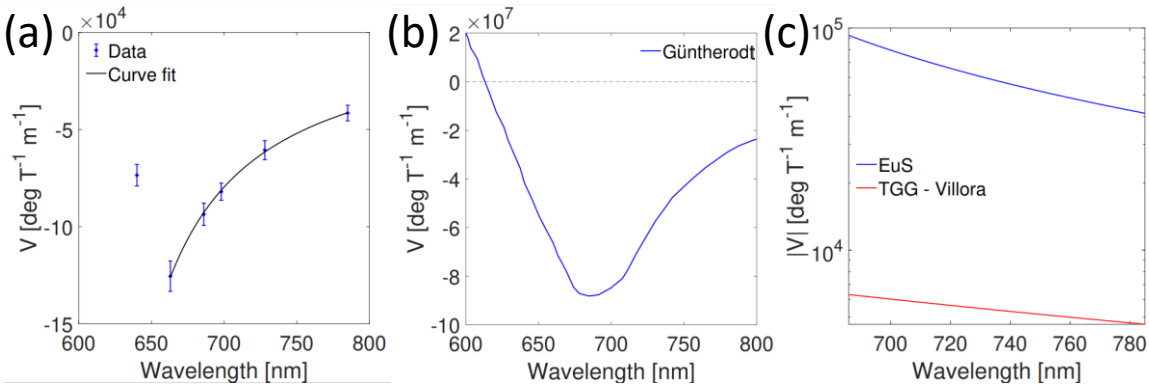


Fig. 2. Dispersion of the EuS Verdet constant. (a) Measured Verdet constant at room temperature and the fit to the data according Eq. 2. Error bars represent 95% confidence interval. (b) Verdet constant at 6 K [8]. Zero is indicated by the dashed line. Note the qualitative similar features of the resonance dip present in both graphs. (c) Verdet constant magnitude of EuS (blue) and TGG (red) [7] at room temperature. Note the order of magnitude difference.

We observe a similar qualitative behavior, therefore we omit the datapoint at 640 nm wavelength to fit the data with the model of Eq. 2. The extracted parameters are E = -10872 deg um^2 T^{-1} m^{-1} and λ_0 = 0.5944 um. The results for EuS are compared with the results of commonly used TGG in Fig. 2(c) [7]. We observe an order of magnitude higher Verdet constant for EuS.

DISCUSSION

We presented room temperature measurements of the Verdet constant, refractive index and extinction coefficient of thin-film EuS in the 600-800 nm wavelength range. In addition, we provided fitting parameters to commonly used dispersion models for the Verdet constant and refractive index. In recent years, nanophotonic devices have been proposed to enhance the magneto-optical response per unit length. Often these devices rely on patterning or depositing magneto-optical materials, making fabrication simplicity an important aspect. EuS can be easily deposited on top of patterned structures without losing its magneto-optical properties, making it an exciting material despite its moderate extinction coefficient. The fabrication simplicity of EuS thin films could potentially drive the realization of magneto-optical devices in integrated optics.

Acknowledgements: This work was supported by the Air Force Office of Scientific Research under Award No. FA9550-19-1-0352. M. Ossiander is supported by a Feodor-Lynen Fellowship from the Alexander von Humboldt Foundation. The work at MIT was supported by the Army Research Office (No. ARO W911NF-20-2-0061), the National Science Foundation (No. NSF-DMR 1700137), the Office of Naval Research (No. N00014-20-1-2306), and the Center for Integrated Quantum Materials (No. NSF-DMR 1231319). This work was performed in part at the Harvard University Center for Nanoscale Systems (CNS); a member of the National Nanotechnology Coordinated Infrastructure Network (NNCI), which is supported by the National Science Foundation under NSF Award No. ECCS-2025158.

References

[1] E. Hecht, *Optics*, Pearson, 2012
[2] J.Y. Jo, Y. Kim, C.K. Hwangbo et al, *Sensitive measurement of the magneto-optic effect in the near infrared wavelength region with weak alternating magnetic fields,* Opt. Mater. Express, vol. 8, no. 9, pp. 2636-2642, 2018
[3] D. Floess and H. Giessen, *Nonreciprocal hybrid magnetoplasmonics,* Rep. Prog. Phys., vol. 81, no. 11, pp. 116401, 2018
[4] B. Sepúlveda, G. Armelles, and L. M. Lechuga, *Magneto-optical phase modulation in integrated Mach-Zehnder interferometric sensors,* Sens. Actuators, vol. 134, no. 2, pp. 339-347, 2007
[5] D. Huang, P. Pintus, C. Zhang et al, *Dynamically reconfigurable integrated optical circulators,* Optica, vol. 4, no. 1, pp. 23-30, 2017
[6] Q. Du, C. Wang, Y. Zhang et al, *Monolithic on-chip magneto-optical isolator with 3 dB insertion loss and 40 dB isolation ratio,* ACS Photonics, vol. 5, no. 12, pp. 5010-5016, 2018
[7] E.G. Villora, P. Molina, M. Nakamura et al, *Faraday rotator properties {Tb_3}{$Sc_{1.95}Lu_{0.05}$}(Al_3)O_{12}, a highly transparent terbium-garnet for visible infrared optical isolators,* Appl. Phys. Lett., vol. 99, no. 1, pp. 011111, 2011
[8] G. Güntherodt, J. Schoenes, and P. Wachter, *Optical constants of the Eu chalcogenides above and below the magnetic ordering temperatures,* J. Appl. Phys., vol. 41, no. 3, pp. 1083-1084, 1970
[9] J. O. Dimmock, *Magneto-optical properties of the Eu-chalcogendes* in *The Physics of Opto-Electronic Materials,* Springer, pp. 255-271, 1971
[10] M.L. Meretska, F.H.B. Somhorst, M. Ossiander et al, *Measurements of the magneto-optical properties of thin-film EuS at room temperature in the visible spectrum,* Appl. Phys. Lett., vol. 120, no. 25, pp. 251103, 2022

Supersymmetric Compactification and Higher-Dimensional Rearrangement of Photonic Lattices

Tom A. W. Wolterink*, Matthias Heinrich, and Alexander Szameit

Institute for Physics, University of Rostock, Albert-Einstein-Straße 23, 18059 Rostock, Germany
* tom.wolterink@uni-rostock.de

Self-imaging photonic lattices enable perfect transfer of quantum and classical states, yet are challenging to implement at scale. We harness supersymmetry to engineer compacted two-dimensional systems exhibiting equivalent characteristics and experimentally investigate their dynamics.

Keywords: *supersymmetric optics, photonic lattices, self-imaging, state transfer, fs-laser writing*

INTRODUCTION

The evolution dynamics of wave-mechanical systems are governed by the full set of their modes and their respective eigenvalues. The key task of transferring arbitrary excitation patterns between two specific planes can therefore be accomplished by an appropriate structure of the eigenvalue spectrum. Along these lines, self-imaging is particularly effective if the spectrum is equidistantly spaced, similar to that of the harmonic oscillator. In finite-size discrete systems, the so-called J_x lattice fulfils this condition and has been employed for the perfect coherent transfer of quantum and classical states alike [1–3]. Yet, implementing large-scale J_x arrays remains experimentally challenging, as this class of systems relies on a precise realization of a large number of different yet finely tuned nearest-neighbor interaction strengths spanning a substantial dynamic range.

To overcome these limitations, we leverage the concept of supersymmetric (SUSY) photonics [4,5] and present a method to design families of compact two-dimensional equivalent systems that inherit the spectral and key dynamic features of one-dimensional J_x arrays while requiring dramatically fewer distinct coupling values [6].

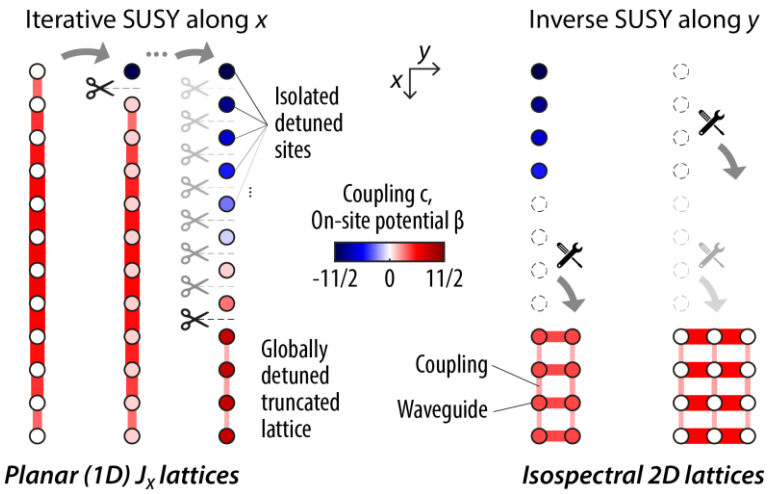


Fig. 1. Transforming a one-dimensional J_x array of twelve sites into a two-dimensional array through subsequent supersymmetry transformations. Color/linewidth indicates the relative strength of the coupling and detuning between sites.

TRANSFORMATION METHOD

Our approach relies on applying a sequence of discrete SUSY transformations to the original tridiagonal Hamiltonian of a planar J_x array to transform it into one that represents isospectral two-dimensional lattices. As example, we here consider a 12-site J_x array in Fig. 1. Applying a discrete SUSY transformation results in its first-order unbroken

superpartner, a globally detuned 11-site J_x array, which retains the spectrum of the original array with the exception of a single removed eigenvalue whose eigenstate resides on an isolated site. Iteratively repeating this procedure results in a sequence of higher-order superpartners and isolated sites. Next, we reattach these sites in a series of inverse SUSY transformation steps in the orthogonal direction, thereby constructing two-dimensional arrays. The final array of 4 × 3 sites is a two-dimensional J_x array where coupling in *y* direction is increased compared to the *x* direction. This two-dimensional structure and its original one-dimensional counterpart share all their eigenvalues and will therefore exhibit similar characteristics.

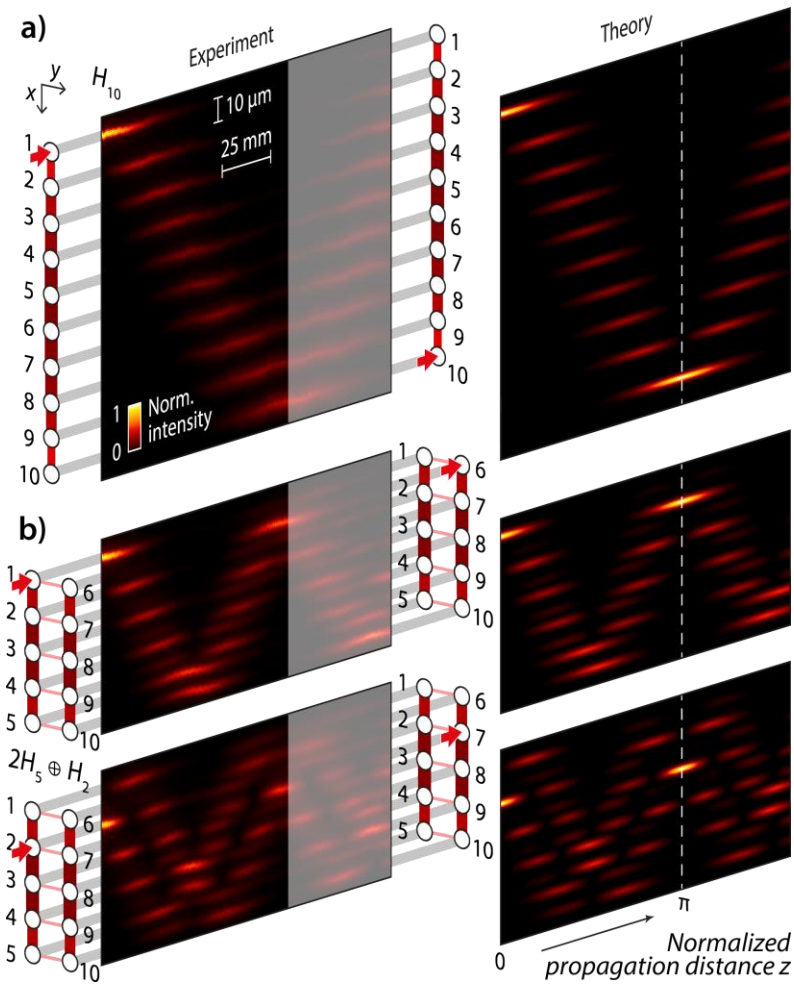


Fig. 2. Measured (left) and calculated (right) evolution dynamics of light in a) a ten-waveguide J_x array and b) its two-dimensional superpartner. In each panel, the initially excited and imaging target waveguides are marked by arrows. The imaging distance z = π is indicated by semitransparent overlay (experiments) and dashed lines (simulations), respectively.

RESULTS

We experimentally realize these systems in arrays of evanescently coupled waveguides fabricated by femtosecond-laser direct writing [7] and investigate their imaging properties by recording the intensity dynamics of guided light through fluorescence microscopy [8]. We implement a conventional ten-waveguide J_x array and its two-dimensional superpartner of 5 × 2 sites. Figure 2 shows the observed light evolution for distinct input waveguides in each of these systems. We find that, while exhibiting systematically different dynamics in these two systems, light coalesces to the single target waveguide at the same imaging distance, demonstrating the desired perfect state transfer enabled by their identical spectra.

In conclusion, our method readily allows for the design of compact self-imaging architectures with a minimum of structural parameters. By enabling increased robustness to perturbations and fabrication inaccuracies, it provides an avenue for high-fidelity coherence-maintaining state transfer in larger-scale photonic circuits.

References

[1] M. Christandl, N. Datta, A. Ekert, and A. J. Landahl, *Perfect State Transfer in Quantum Spin Networks*, Phys. Rev. Lett., vol. 92, no. 18, pp. 187902, 2004.

[2] A. Perez-Leija, R. Keil, A. Kay, H. Moya-Cessa, S. Nolte, L.-C. Kwek, B. M. Rodríguez-Lara, A. Szameit, and D. N. Christodoulides, *Coherent quantum transport in photonic lattices*, Phys. Rev. A, vol. 87, no. 1, pp. 012309, 2013.

[3] A. Perez-Leija, R. Keil, H. Moya-Cessa, A. Szameit, and D. N. Christodoulides, *Perfect transfer of path-entangled photons in J_x photonic lattices*, Phys. Rev. A, vol. 87, no. 2, pp. 022303, 2013.

[4] M.-A. Miri, M. Heinrich, R. El-Ganainy, and D. N. Christodoulides, *Supersymmetric optical structures*, Phys. Rev. Lett., vol. 110, no. 23, pp. 233902, 2013.

[5] M. Heinrich, M.-A. Miri, S. Stützer, R. El-Ganainy, S. Nolte, A. Szameit, and D. N. Christodoulides, *Supersymmetric mode converters*, Nat. Commun. , vol. 5, no. 1, pp. 3698, 2014.

[6] T.A.W. Wolterink, M. Heinrich, and A. Szameit, *Supersymmetric reshaping and higher-dimensional rearrangement of photonic lattices*, arXiv:2209.12847, 2022.

[7] A. Szameit and S. Nolte, *Discrete optics in femtosecond-laser-written photonic structures*, J. Phys. B, vol. 43, no. 16, pp. 163001, 2010.

[8] A. Szameit, F. Dreisow, H. Hartung, S. Nolte, A. Tünnermann, and F. Lederer, *Quasi-incoherent propagation in waveguide arrays*, Appl. Phys. Lett. , vol. 90, no. 24, pp. 241113, 2007.

Investigations on Brillouin and Kerr properties of a low-index silicon oxynitride platform

(Student paper)

Kaixuan Ye[1], Yvan Klaver[1], Oscar A Jimenez Gordillo[2], Roel Botter[1], Okky Daulay[1], Francesco Morichetti[2], Andrea Melloni[2], and David Marpaung[1,*]

[1] Nonlinear Nanophotonics, MESA+ Institute of Nanotechnology, Department for Science and Technology, Applied Nanophotonics, University of Twente, 7522 NB Enschede, The Netherlands
[2] Dipartimento di Elettronica, Informazione e Bioingegneria (DEIB), Politecnico di Milano, 20133, Italy
[*] david.marpaung@utwente.nl

We investigate the Brillouin and Kerr properties of a low-index (n=1.513 @ 1550 nm) silicon oxynitride (SiON) platform. We observed, for the first time, the backward SBS in SiON waveguides. The measured Brillouin gain coefficient is around 0.3 m-1W-1. We also characterized its nonlinear parameter γ, which is around 0.02 m-1W-1. This work presents a low-index photonic integrated platform that is both Brillouin and Kerr active.

Keywords: *Stimulated Brillouin scattering, four-wave mixing, silicon oxynitride*

INTRODUCTION

Stimulated Brillouin scattering (SBS), which is an interaction between optical and acoustic waves, is currently revolutionizing the photonic integrated circuit designs. Featuring a narrow-band (tens of MHz) gain resonance shifted around tens of GHz away from the pump light, the on-chip SBS plays a significant role in microwave photonics, narrow-linewidth integrated lasers, and on-chip nonreciprocal light propagation [1]. Efficient on-chip SBS process requires a relatively large photoelastic coefficient p12 and simultaneously guiding of both the optical and gigahertz acoustic waves in a waveguide, making it difficult to be realized in most integrated platforms.

Silicon oxynitride (SiON) is a highly-developed integrated platform that has appealing properties including low propagation loss, wide transparency window, lack of multi-photon absorption effects, and stress-free fabrication [2]. The mainstream SiON platforms usually have a relatively high refractive index that is close to Si3N4 [2,3]. The high refractive index induces a high nonlinear index and makes it useful for the Kerr-based nonlinear optic applications. Nevertheless, those SiON waveguides have a meager photoelastic coefficient p12. Moreover, the acoustic velocity in those SiON waveguides is also higher than in the cladding, leading to a poor guidance of the acoustic wave. Plagued by these two problems, the SBS effect is too weak and has never been detected in SiON waveguides before.

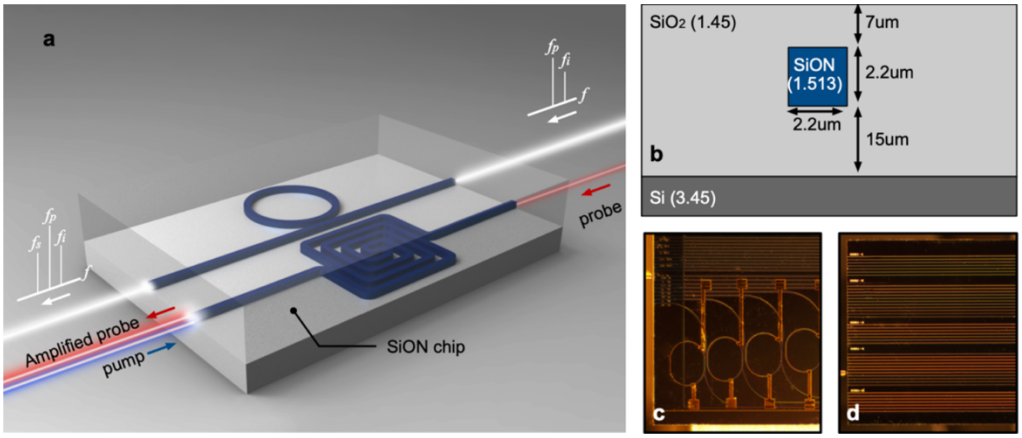


Fig. 1. (a) Artistic representation of the SiON waveguides, showing the four-wave mixing (FWM) process in an all-pass microring resonator and the backward stimulated Brillouin scattering (SBS) in a spiral waveguide. (b) The cross section of the SiON platform in our work. (c) The chip photograph of the SiON microring resonators with a FSR of 50 GHz. (d) The chip photograph of the 5-cm SiON straight waveguide.

In this work, we investigate the Brillouin and Kerr properties of a SiON integrated platform with a relatively lower refractive index (n=1.513 @ 1550 nm). Contrasting to SiON platforms mentioned above, the SiON platform

investigated here has a larger photoelastic coefficient p12, lower acoustic velocity, and a larger cross section, all of which contribute to an enhanced SBS effect. We observed, for the first time, the backward SBS in the SiON waveguide. We also characterized the Brillouin gain coefficient gb of the SiON waveguides with different widths. Furthermore, we measured the nonlinear parameter γ and nonlinear index n2 of this SiON platform with four wave mixing experiments in a ring resonator. This platform is both Brillouin and Kerr active and opens the way to explore the interplay between the SBS and Kerr effect and even build unique applications like Brillouin-assisted Kerr frequency comb in an integrated platform.

RESULTS

We performed the backward SBS and four-wave mixing experiments in single-pass (spiral or straight) waveguides and microring resonators respectively, as shown in Fig.1(a). The cross section of this platform is shown in Fig.1(b) [4]. The 2.2 µm-thick SiON layer has a refractive index n of 1.513 at 1550 nm. It is on top of a 15 µm SiO2 layer and is covered by a 7 µm-thick SiO2 upper cladding. The refractive index contrast Δn between the core and the cladding is 4.4%, guaranteeing a bending radius of 600 µm with negligible radiation losses. Fig.1(c) shows the photograph of the microring resonators in this platform with a free spectral range (FSR) of 50 GHz and coupling coefficients varying from 0.05 to 0.8. Fig.1(d) shows the photograph of several groups of 5-cm straight waveguides with different widths. The measured propagation loss of those straight waveguide is around 0.25 dB/cm with coupling loss of round 3 dB/facet.

We first built a finite element model in COMSOL to estimate the SBS response of the SiON waveguides in this work. The simulated optical field and the corresponding acoustic response of the 2.2 µm-wide SiON waveguide are shown in Fig.2 (a) and (b), respectively. The optical field is well confined around the SiON core area because of the total internal reflection (TIR). However, the TIR condition does not hold for the acoustic response because the acoustic velocity of the SiON (~ 6.2 km/s) is higher than that of the SiO2 (~5.9 km/s). As a result, part of the acoustic field would scatter into the cladding as shown in Fig.2(b). Nevertheless, most of the acoustic field still remains inside the SiON core because of the relatively large cross section area. This results in a large overlap between the optical and acoustic fields, and consequently, contribute to a relatively large Brillouin gain coefficient.

To verify the simulation results, we characterized the SBS responses of the SiON waveguides with a pump-probe experimental apparatus [5]. The pump and probe light are intensity-modulated at slightly different frequencies and coupled into the opposite facets of the waveguide. We keep the pump frequency fixed at around 192 THz (around 1561 nm) while sweeping the probe at frequencies down shifted from the pump by about 15 GHz. When the frequency difference between the pump and the probe is close to the Brillouin frequency shift of the SiON waveguide, the probe will experience the SBS gain and a peak will be detected at the lock-in amplifier.

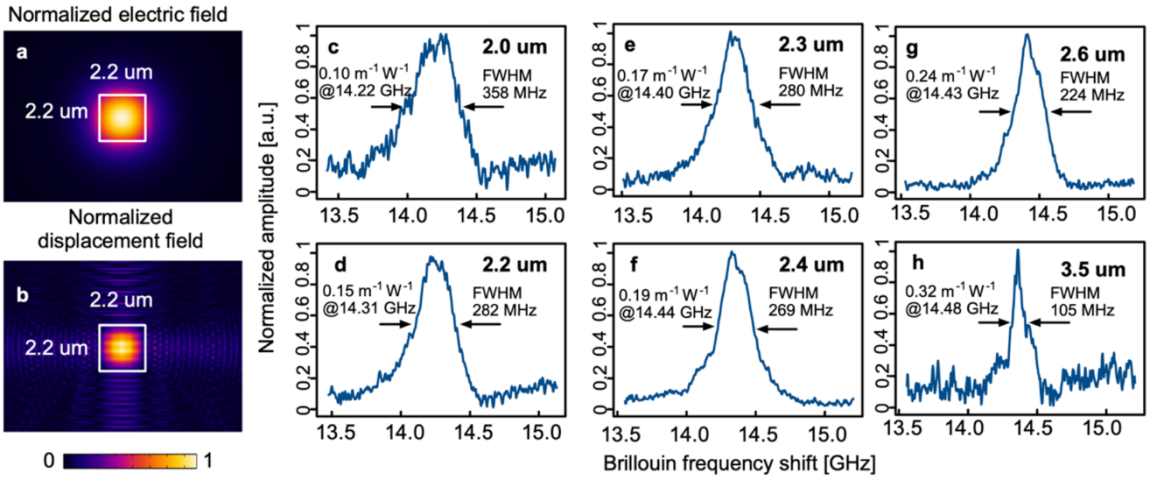


Fig. 2. (a) Simulated optical mode of the SiON waveguide. (b) Simulated acoustic response of the SiON waveguide. (c)-(h) Measured SBS gain spectra of the 2.0 µm, 2.2 µm, 2.3 µm, 2.4 µm, 2.6 µm, and 3.5 µm-wide SiON waveguides, respectively.

Several 5 cm-long SiON waveguides are characterized to investigate the influence of waveguide width on the Brillouin gain spectra, and the measured SBS responses of the 2.0 µm, 2.2 µm, 2.3 µm, 2.4 µm, 2.6 µm, and 3.5 µm-wide waveguides are shown in Fig.2(c) to (h), respectively. All waveguides show a clear peak well above the noise floor with the Brillouin frequency shift increases from 14.22 GHz for the 2.0 µm waveguide to 14.48 GHz for the 3.5 µm waveguide. The Brillouin gain coefficient gb increases from 0.1 m-1W-1 to around 0.32 m-1W-1 when the

waveguide width increases from 2.0 µm to 3.5 µm. In the meantime, the linewidth of the SBS peak reduces from 358 MHz to around 105 MHz. The increasing Brillouin gain coefficient and the narrowing SBS linewidth indicates better acoustic confinement when the SiON waveguides become wider.

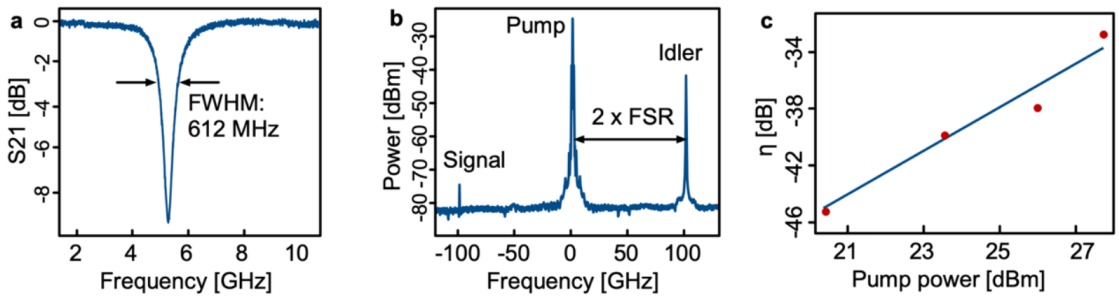


Fig. 3. (a) Measured resonance response of the SiON ring resonator. (b) Measured four-wave mixing response of the SiON ring resonator. (c) Conversion efficiency of the four-wave mixing at different pump power.

We further investigated the Kerr properties of this SiON platform. Previous SiON platforms are widely used for Kerr-based nonlinear optics applications because of the large nonlinear parameter γ. However, the nonlinear parameter γ are highly dependent on the refractive index and the geometry of the waveguide. The SiON waveguide in this work has relatively lower refractive index and a larger cross section compared with other SiON platforms [2,3], and the nonlinear parameter γ of the SiON waveguide in this platform has never been characterized before. We devised a four-wave mixing (FWM) experiment for the nonlinear index characterization. The all-pass ring resonator is used to enhance the FWM in the SiON waveguide so that the contribution from fibers in the setup can be ignored.

To calculate the field enhancement factor of the FWM process in the ring resonator, we first characterized the resonance response of the ring resonator, as shown in Fig.3 (a). The ring resonator applied in our experiment is made of the 2.2 µm-wide SiON waveguide and it has a FSR of 50 GHz and a power coupling coefficient of 0.05. The measured FWHM is around 612 MHz with an extinction ratio of 8.9 dB, corresponding to a Q factor of 330 k and a propagation loss of 0.27 dB/cm. Fig. 3 (b) shows the measured FWM response of the 50 GHz SiON ring resonator. A clear peak is shown at 2 FSR down shifted from the pump frequency, which is the signal generated from the FWM process between the pump and idler in the ring resonator. The nonlinear index n2 and nonlinear parameter γ of the SiON waveguide in this platform can be calculated from the conversion efficiency between the idler and the signal. Fig. 3 (c) shows the conversion efficiency of the FWM process at different pump power. The calculated γ and n2 of the 2.2 µm-wide SiON waveguide is around 0.024 m-1W-1 and 4.16 m2/W, respectively.

DISCUSSION

In this work, we investigated the Brillouin and Kerr properties of a SiON integrated platform with a relatively low refractive index. We observed, for the first time, the backward SBS response of those SiON waveguides. We also measured its nonlinear index n2 and nonlinear parameter γ. These SiON waveguides can be fabricated in a versatile and low-loss integrated platform and can potentially lead to a plethora of Brillouin/Kerr-based applications, including narrow-bandwidth microwave photonic filter, and narrow-linewidth lasers, and optical frequency combs.

REFERENCES

[1] B. J. Eggleton, C. G. Poulton, P. T. Rakich, M. J. Steel, and G. Bahl, Brillouin integrated photonics, Nat. Photonics, vol. 13, pp. 664-677, 2019.

[2] D. J. Moss, R. Morandotti, A. L. Gaeta, and M. Lipson, New CMOS-compatible platforms based on silicon nitride and hydex for nonlinear optics, Nat. Photonics vol. 7, pp. 597–607, 2013.

[3] G. Piccoli, M. Sanna, M. Borghi, L. Pavesi, and M. Ghulinyan, Silicon oxynitride platform for linear and nonlinear photonics at NIR wavelengths, Opt. Mater. Express vol. 12, 2022.

[4] F. Morichetti, S. Grillanda, S. Manandhar, V. Shutthanandan, L. Kimerling, A. Melloni, and A. M. Agarwal, Alpha radiation effects on silicon oxynitride waveguides, ACS Photonics, vol. 3, pp. 1569–1574, 2016.

[5] R. Botter, K. Ye, Y. Klaver, R. Suryadharma, O. Daulay, G. Liu, J. van den Hoogen, L. Kanger, P. van der Slot, E. Klein, M. Hoekman, C. Roeloffzen, Y. Liu, and D. Marpaung, Guided-acoustic stimulated Brillouin scattering in silicon nitride photonic circuits, Sci. Adv., vol. 8, pp. 2196, 2022.

Enhanced Frequency Noise Discrimination Using Cavity-coupled Mach-Zehnder Interferometer

Mohamad Hossein Idjadi[1,*] and Andrea Blanco-Redondo[1]

[1]Bell Laboratories, Nokia, 600 Mountain Avenue, Murray Hill, New Jersey 07974, USA
[*] corresponding author: mohamad.idjadi@nokia-bell-labs.com

Here, an enhanced frequency noise discriminator is proposed using a cavity-coupled Mach-Zehnder interferometer and demonstrated on a general-purpose programmable integrated photonics platform. The frequency noise measurement sensitivity is similar to the well-known Pound-Drever-Hall architecture but owns a passive, simpler, and more compact design. The proposed structure can be utilized in integrated laser frequency stabilization architectures.
Keywords: *Frequency discriminator, Laser stabilization, Programmable photonics, Laser frequency noise, Pound-Drever-Hall (PDH)*

INTRODUCTION

Frequency noise discriminators play an essential role in laser frequency noise characterization and frequency/phase stabilization. Different frequency noise discriminator architectures have been proposed, including a Fabry-Perot cavity in a Pound-Drever-Hall (PDH) laser frequency-locking architecture [1] and an unbalanced Mach-Zehnder interferometer (MZI) [2-6]. The PDH control loop, despite its excellent performance, requires fast optical phase modulation that leaves residual amplitude noise and ultimately degrades the laser noise performance [7,8]. On the other hand, an unbalanced MZI can be used to detect laser frequency noise without a need for phase modulation. However, the unbalanced MZIs proposed to date require large space on-chip for similar discrimination sensitivity. The cavity-coupled MZI structure with a large number of cascaded ring resonators in the arms of the MZI has been proposed as an optical filter to improve the linearity of frequency discrimination in broad-band microwave-photonic links [6]. Here, we propose, analyze, and demonstrate the use of a cavity-coupled MZI as a laser frequency noise discriminator that offers high sensitivity in noise measurement while can potentially occupy a fraction of the photonic chip area compared to its counterparts, thanks to the resonance effect. The proposed architecture provides sensitive frequency noise measurement capability that can be utilized in an integrated electro-optic feedback loop to detect laser frequency fluctuations, process the error signal in the electrical domain, and feed it back to the laser to suppress its frequency noise.

PRINCIPLE OF OPERATION

Figure 1(a) shows a generalized block diagram of a frequency discriminator where it receives an incoming electric field oscillating at the optical frequency (ω_0), compares its frequency fluctuations with a frequency reference (ω_{ref}), and generates a proportional electronic signal. This electrical signal, *i.e.,* the error signal, can be used to either characterize the frequency noise of a laser (Fig. 1(b)) or to stabilize its frequency when used in a feedback control loop (Fig. 1(c)) [4]. It is worth mentioning that the performance of a frequency discriminator can be quantified as its sensitivity to frequency fluctuations (*i.e.,* the slope of the current-frequency curve). Figure 2 shows three examples of frequency discriminator architectures with optical input and electrical output ports: the PDH loop, an MZI with true-time delay, and the proposed cavity-coupled MZI. In Fig. 2(b) and (c), the error signal (I_{out}) at the output of the balanced photodetectors can be written as

$$I_{out}(\omega) = RP_0|T(\omega)|\sin(\measuredangle T(\omega) - \phi), \quad (1)$$

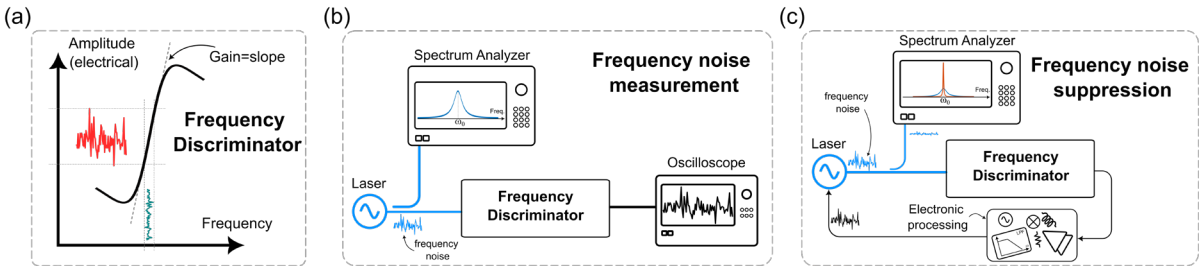


Fig. 1. (a) The frequency noise discriminator. Potential applications of a frequency noise discriminator in (b) laser frequency noise measurement (b) and laser frequency noise suppression using an electro-optic feedback loop.

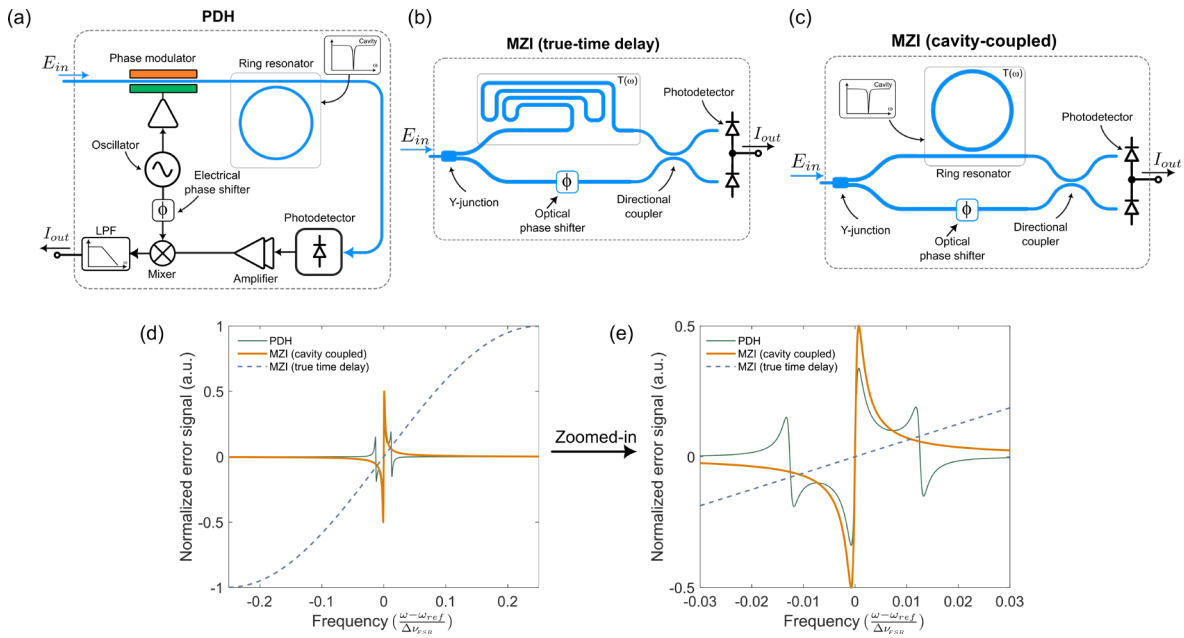


Fig. 2. (a) The PDH frequency discriminator. A laser is phase modulated using a local oscillator (LO) and is filtered by a ring resonator. The ring resonator acts as a frequency reference. The output of the ring resonator is photo-detected, amplified, down-converted with the same LO frequency, and finally, low-pass filtered. (b) A conventional MZI with a true-time delay in one arm. An optical phase shifter is used to adjust the phase of the two arms of the MZI. The MZI is terminated with balanced photodetectors. (c) The cavity-coupled MZI. In this architecture, a ring resonator is used as a phase and frequency reference, and its output is coherently detected using balanced photodetectors. (d, e) Simulation of the normalized error signals.

where $R, P_0, |T(\omega)|, \measuredangle T(\omega), \omega$, and ϕ are photodetector responsivity, laser power, amplitude, and phase of the reference transfer function, laser instantaneous frequency, and the static bias phase on the other arm of the MZI, respectively. Without loss of generality, we can consider a high quality-factor (Q-factor) ring resonator or a low loss waveguide as the frequency reference and the error signal (I_{out}) can be calculated numerically using Eq. (1). For the numerical calculation, the waveguide loss is assumed 0.2 dB/cm and the ring circumference in the case of PDH loop and the cavity-coupled MZI are identical and equal to the length difference in an unbalanced conventional MZI architecture in Fig. 2(b) (L= 1 mm). This corresponds to a Q-factor of about 1.6 million for the ring resonator at the resonance wavelength of 1550 nm. Also, the local oscillator frequency in PDH architecture is 1 GHz, and the optical and electrical phase shifters are optimized accordingly. Figure 2(d) shows the comparison between the normalized error signal for these three cases. As shown in Fig. 2(d), all three error signals are asymmetric around the reference frequency (ω_{ref}), which is the resonance frequency of the ring resonator and the quadrature point of the MZI with true-time delay. This asymmetric response is essential for the laser frequency control loop to distinguish the frequency compensation direction required for frequency locking. As shown in Fig. 2(e), it is clear that given the same waveguide length and electronics gain, the PDH and the cavity-coupled MZI (Figs. 2(a) and 2(c)) have considerably higher frequency detection gain (*i.e.,* the slope at $\omega = \omega_{ref}$) compared to a conventional MZI (Fig. 2(b)). The frequency discrimination gain for PDH, MZI with true-time delay, and cavity-coupled MZI are 1.14×10^{-8} [Hz^{-1}], 8×10^{-11} [Hz^{-1}], and 1.7×10^{-8} [Hz^{-1}], respectively. In general, the higher the Q-factor of the ring, the higher the noise discrimination sensitivity. Thanks to the resonance effect in the cavity-couple MZI, the frequency discrimination sensitivity is more than two orders of magnitude higher than a conventional MZI but unlike the PDH architecture, no phase modulation and complex electronics are required.

EXPERIMENTAL DEMONSTRATION

Figure 3 shows the proof-of-concept experimental demonstration of the proposed cavity-coupled MZI frequency noise discriminator. We implemented the proposed photonic integrated circuit (PIC) on a general-purpose programmable photonics platform consisting of a programmable mesh of integrated 2x2 directional couplers and phase shifters (iPronics SmartLight Processor) [9]. Figure 3(a) shows the implemented PIC in which different photonic functionalities (e.g. power splitter, ring resonator, and MZI) can be implemented by adjusting the coupling ratio of each programmable unit cell (PUCs), *i.e.,* tuneable couplers. Figure 3(b) shows the equivalent schematic for the implemented PIC where the input light (E_{in}) is coupled to the structure and the ring resonator output (E_{out0}) and the MZI outputs ($E_{out1(+)}, E_{out1(-)}$) are coupled out using optical fibers. The phase of the MZI is adjusted using

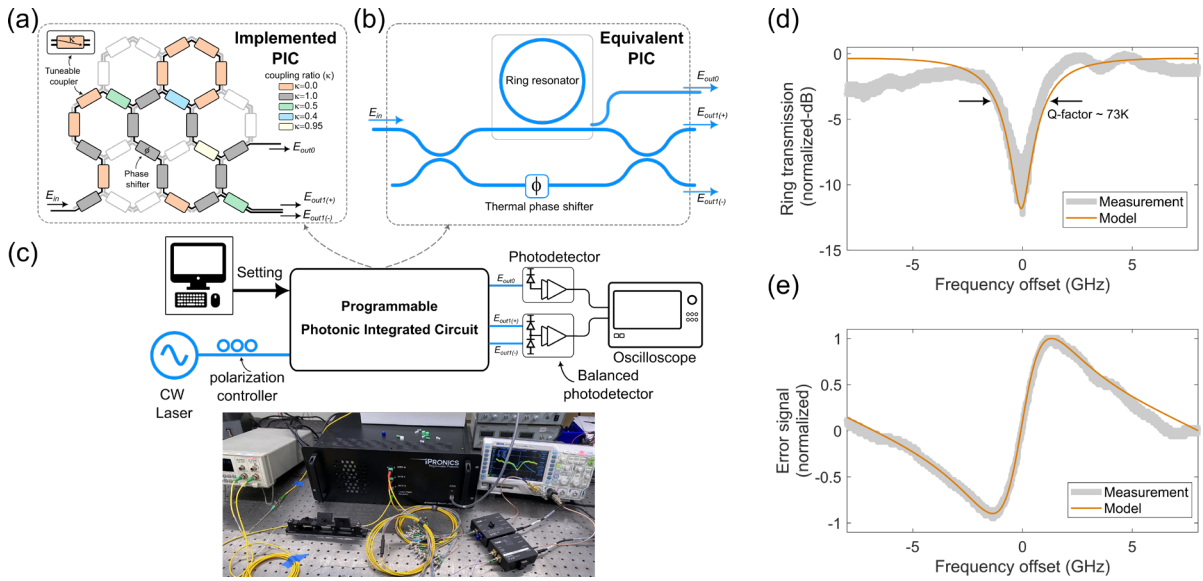


Fig. 3. Experimental demonstration of the proposed cavity-coupled MZI acting as a frequency noise discriminator. (a) The implemented PIC is based on a programmable mesh of integrated directional couplers. (b) The equivalent schematic of the implemented PIC. (c) the measurement setup. (d) The normalized ring resonator response, and (e) the measured error signal. The frequency offset is defined relative to the ring resonance frequency.

thermal phase shifters. Figure 3(c) shows the measurement setup. A tuneable 10 mW continuous wave laser is coupled into the programmable PIC and its wavelength is swept from 1549 nm to 1551 nm with 1 pm resolution. The PUC settings are uploaded by a computer and the output electric fields, $E_{out1(+)}$, $E_{out1(-)}$, and E_{out0}, are photo-detected using Thorlabs PDB470C and PDB450C photodetectors and monitored on an oscilloscope. Figure 3(d) shows the normalized resonance response of the ring resonator coupled to the MZI. Given the loss of each PUC (~0.48 dB), the measured ring resonator Q-factor and the extinction ratio are about 73K and 12 dB, respectively. The PUC basic unit length is 811.41 μm which sets the ring FSR to about 15 GHz. Figure 3(e) shows the measured error signal which agrees well with the mathematical model. As shown in Fig. 3(e), the error signal is asymmetric around the reference ring resonance frequency with the normalized frequency noise discriminator gain of about 10^{-9} [Hz^{-1}]. This gain is limited by the PUC's insertion losses and consequently the limited ring resonator Q-factor.

DISCUSSION

Here we propose, analyze, and experimentally demonstrate the use of a cavity-coupled MZI as an enhanced frequency noise discriminator. The proposed architecture leverages the resonance effect of the cavity and coherent detection in an MZI architecture. The frequency noise detection sensitivity of the proposed architecture is similar to the well-known PDH architecture while it owns a less complex design, lower power consumption control electronics, and does not require phase modulation which would, inevitably, introduce residual amplitude modulation. Finally, as a proof of concept, we implemented this architecture on an integrated programmable photonic platform. The limitations of the programmable photonic platform can be solved by implementing the PIC on an application-specific tape-out process. The enhanced frequency noise discrimination can be utilized in a variety of applications such as laser frequency noise suppression to achieve compact low-cost narrow linewidth lasers.

References

[1] R. W. P. Drever, et al., *Laser phase and frequency stabilization using an optical resonator,* Appl. Phys. B, vol. 31, no.2, pp. 97-105, 1983.
[2] W. V. Sorin, et al., *Frequency domain analysis of an optical FM discriminator*, J. Light. Technol., vol. 10, no .6, pp. 787-793, 1992.
[3] M.H. Idjadi, et al., *Integrated Pound– Drever– Hall laser stabilization system in silicon*, Nat. Commun., vol. 8, no.1, pp. 1-9, 2017.
[4] M.H. Idjadi, et al., *Nanophotonic phase noise filter in silicon*, Nat. Photon., vo. 14, no. 4, pp. 234-239, 2020.
[5] F. Aflatouni, et al. Wideband tunable laser phase noise reduction using single sideband modulation in an electro-optical feed-forward scheme, Optics letters vol. 37, no .2, pp. 196-198, 2012.
[6] X. Xiaobo, et al., *Ring-assisted frequency discriminator with improved linearity*, IEEE Photonics Technology Letters, vol. 14, no. 8, pp. 1136-1138, 2002
[7] X. Shi, et al., *Suppression of residual amplitude modulation effects in Pound–Drever–Hall locking*, Appl. Phys. B, vol. 124, no.8, pp. 1-7, 2018.
[8] H. Shen, et al., *Systematic and quantitative analysis of residual amplitude modulation in Pound-Drever-Hall frequency stabilization*, Phys. Rev. A, vol. 92, no.6, pp. 063809, 2015.
[9] W. Bogaerts, et al., *Programmable photonic circuits*, Nature, vol. 586, no. 7828, pp. 207-216, 2020.

Development of an integrated optical sensor on chalcogenide glasses and on porous silicon for the mid-infrared spectroscopy

(Student paper)

S. Meziani[1], A. Jaafar[1] L. Bodiou[1], N. Lorrain[1], , P. Pirasteh[1], A. Bénardais[2], A. Hammouti[1], R. Courson[3], J.Rouxel[3], J. Lemaitre[1], C. Boussard-Pledel[2], M. Guendouz[1], V. Nazabal[2] et J. Charrier[1]

[1]Univ Rennes, CNRS, Institut Foton-UMR 6082, 22305 Lannion, France
[2]CNRS UMR 6226 ISCR, Université de Rennes 1, 22302 Rennes, France
[3]Ifremer, Laboratoire Détection Capteurs et Mesures, F-29280 Plouzané, France

sofiane.meziani@univ-rennes1.fr

This work presents the development of photonic integrated circuits based on chalcogenide glasses and porous silicon materials dedicated to mid-infrared (mid-IR) sensing. Optical losses of the different platforms are measured for a wavelength range spanning from 4.0 to 4.44 µm and 6.9 to 8.8 µm. At 4.28 µm, corresponding to carbon dioxide maximum absorption, propagation losses of 6.00 ± 0.46 dB/cm and 11.76 ± 0.2 dB/cm are demonstrated using, respectively, chalcogenide and porous silicon platforms. Based on these losses and interaction schemes between optical field and target molecules, either evanescent or volume detection, the expected sensitivity and limit of detection of both platforms are discussed. Experimental demonstration of $C0_2$ sensing in the mid-IR using both chalcogenide and porous silicon platforms is also provided.

Keywords: *Integrated Optics; Chalcogenide Glasses; Pourous Silicon; Optical Bench; Mid-Infrared; Sensing; Spectroscopy.*

1. INTRODUCTION

In recent years, there has been a growing scientific interest for the development of mid-infrared (mid-IR) photonic circuits dedicated to optical sensing applications [1] thanks to the remarkable progress in development of optical sources such as QCL and supercontinuum sources [2,3]. The presence, in this wavelength range, of the absorption bands displayed by several toxic and polluting molecules makes mid-IR sensor well placed to respond to a diverse range of users, in-situ and sometimes harsh environment applications. This level of performance has created an innovative need for materials and guiding structures. The use of integrated optical circuits as sensors has various advantages such as manufacturing cost and compactness of the packages. However, these circuits must be fabricated from mid-IR transparent materials. Chalcogenide glasses (ChG) and porous silicon (PSi) have a great potential for the design of such circuits. ChG glasses display extended transparency ranging from near infrared to 20 µm depending on their composition [4] whereas porous silicon is transparent from 1 to 8 µm [5]. ChG can be used for evanescent field spectroscopy sensing but interaction with targeted molecules can be further enhanced using PSi as the open pores enable volume detection. In this paper, we propose a suitable mid-IR optical bench setup developed to characterise the transmission of PSi ridge waveguides in the wavelength ranges of 4.0 - 4.44 µm and of ChG ridge waveguides in the wavelength ranges of 6.9 - 8.8 µm.

FABRICATION OF INTEGRATED OPTICAL CIRCUITS

Prior the fabrication step, the ridge waveguide structures were designed using a commercial software (FIMMWAVE, Photon Design) to obtain the geometrical dimensions, width (w) and height (h), ensuring single-mode propagation while maximizing, for evanescent wave detection, the evanescent power factor in the superstrate.

Platform based on Chalcogenide glasses

A 5 µm confinement layer of $Ge_{28.1}Sb_{6.3}Se_{65.6}$ was grown an n-type Si (001) substrate by RF magnetron sputtering. This layer was covered by a guiding layer of composition $Ge_{12.5}Sb_{25}Se_{62.5}$. Single mode ridge waveguides (w=6 µm) widths were then fabricated using a classical i-line photolithographic process followed by a dry etching procedure at low pressure combining reactive ion etching (RIE) and inductively coupled plasma (ICP) etching (5 sccm CHF_3, 5

mTorr, 75 W ICP, 25 W RF). The waveguides obtained at the end of the process had a guiding layer thickness of 1.9 µm and a width of 6 µm (Fig.1-a) with corresponding refractive index values are equal to 2.69 and 2.49 at 4.28 µm for the guiding and confinement layers respectively.

Platform based on Porous silicon

PSi guiding and confinement layers were prepared by electrochemical anodization of a heavily doped P (100) silicon substrate with a 5 mΩ.cm resistivity and using applied current densities of 50 and 100 mA/cm^2, respectively, for specific times. The electrolyte was formed by combining hydrofluoric acid (50 %) with ethanol and deionized water in the ratio of 2-2-1. Refractive index is tuned by changing the porosity that depends on applied current density. In this way, two layers were fabricated: a 2.3 µm guiding layer with a porosity of 60% and a 5µm confinement layer with a porosity of 73% with corresponding refractive indices equal to 1.83 and 1.47 at 4.28 µm respectively. As showed on Figure 1-b, single mode ridge waveguides of 6-µm width were then fabricated using photolithography and dry etching techniques [6].

A PDMS fluidic cell was used for the detection of CO_2 with different sensing interaction lengths for the two platforms (Figure1-c).

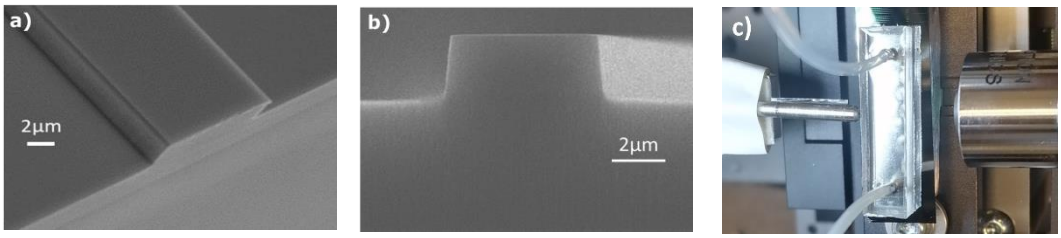


Fig. 1 . SEM Image of fabricated ridge waveguides (a) Chalcogenide glasses (b)Porous silicon. (c) Picture of the PDMS cell on a sample used for CO_2 sensing.

2. Optical bench and characterisation of guiding structures

Optical characterizations were performed by coupling the output of four tunable QCL emitting from λ=3.9 to 4.6 µm and from λ= 6.9 to 11 µm (MIRCAT from Daylight Solutions) into the ridge waveguides by using chalcogenide glass fiber. The output signal from the waveguide was collimated on a detector using a mid-IR objective lens. To improve signal to noise ratio, lock-in technique was used. The photolithography mask used consists of several sets of waveguides of different lengths. This configuration allows propagation loss measurements using a non-destructive cut-back method. Using mid-IR optical characterizations bench, PSi and ChG waveguides transmission was measured for wavelengths ranging from 4 µm to 4.44 µm. The same measurements were performed between

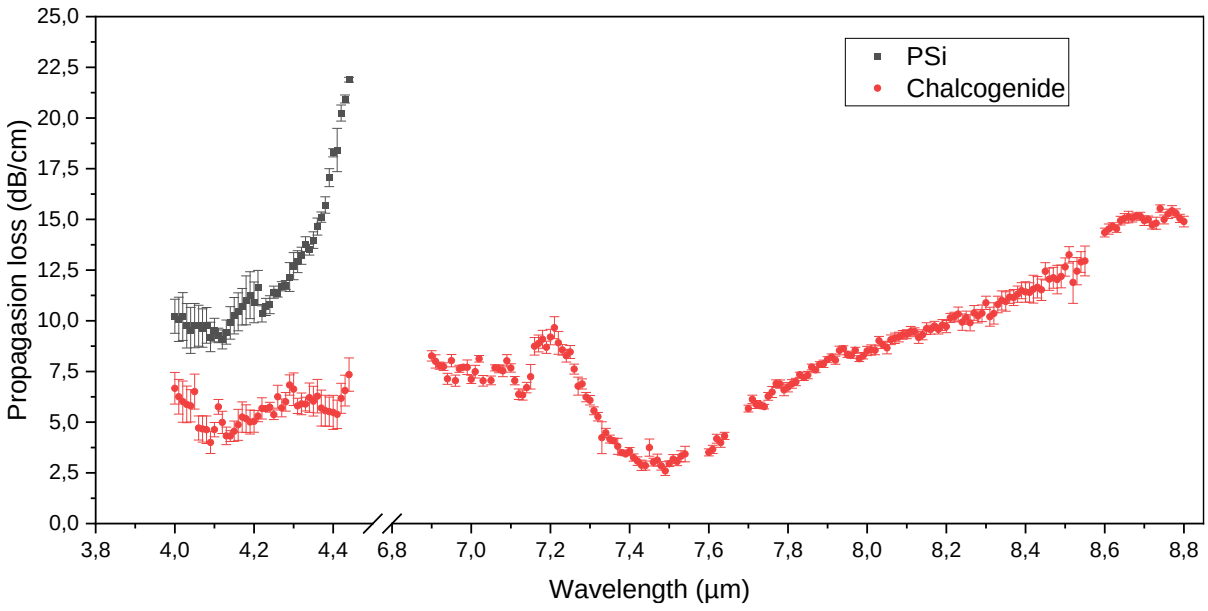


Fig. 2: Propagation losses as a function of the wavelength for porous silicon and chalcogenide glasses single mode waveguides. The laser does not cover the wavelength range between 4.6 and 6.9µm.

6.9 µm and 8.8 µm, only for ChG waveguides thanks to their extended materials transparency. To measure the propagation loss, a decreasing exponential function fit was applied to the measured signals for all waveguide lengths (from 8 to 13 mm with 0.5 mm step increment) and for each wavelength. The evolution of these losses in the two wavelength ranges [4.0 - 4.44 µm] for PSi and ChG waveguides and [6.9 - 8.8] µm for ChG waveguides is displayed in Figure 2. Higher propagation losses are expected from PSi due to volume diffusion but also due to the adsorption of different molecules present in ambient air inside the pores. The latter cause of losses are not expected in ChG, however additional propagation losses can results from the presence of a layer of a few nanometers of fluoropolymer [7] that is absorbent for this wavelength range. This layer is formed on the waveguide surface during the fluorine chemistry-based RIE etching.

Sensing demonstration

Transduction tests are carried out for CO_2 sensing. Figure 3-b shows the transduction results obtained from PSi waveguides. Using a PDMS cell (Figure 1-c) to make CO_2 – N_2 gas mixture in contact with the waveguide. CO_2 concentration up to 4970 ppm was detected around the two tabulated absorption lines of CO_2 around 4.23 µm and 4.28 µm [8]. The regeneration of the sensor application is demonstrated in figure 3-c by increasing and decreasing gradually the CO_2 concentration starting and finishing by a N_2 purge with a fixed laser wavelength emission at 4.26 µm.

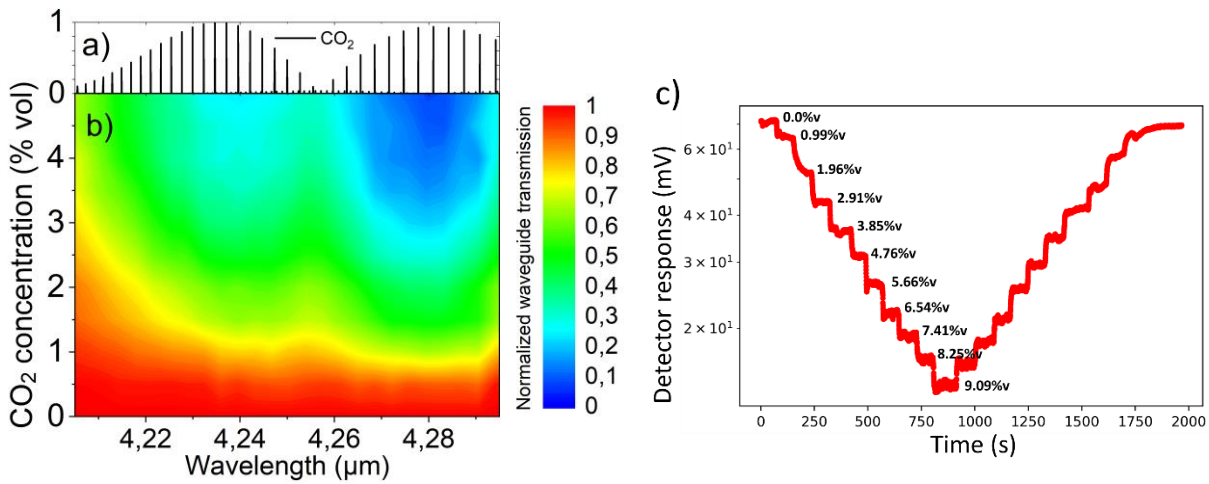


Fig. 3: (a) Normalized CO_2 absorption [8]. (b) Normalized waveguide transmission as a function of the wavelength for different CO_2 concentration. (c) Intensity evolution at λ=4.26µm for different CO_2 concentration.

Conclusion

The optical properties of chalcogenides glasses and porous silicon are promising for the development of an integrated optical platform for volume or evanescent wave sensing applications. Propagation losses are measured in the mid-IR from 4.0 to 4.44µm and from 6.9 to 8.8µm. Carbon dioxide sensing is demonstrated using porous silicon ridge waveguide on CO_2 absorption peak at 4.28µm. Technological processing optimization is actually performed for both sensing platforms to further reduce their respective limit of detection but also to achieve detection of higher CO2 concentrations using either evanescent wave and volume detection.

References

[1] H. Lin et al., Nanophotonics, vol. 7, no 2, p. 393-420, févr. 2018
[2] M. Razeghi, W. Zhou, S. Slivken, Q.-Y. Lu, D. Wu, et R. McClintock, Appl. Opt., AO, vol. 56, no 31, p. H30-H44, nov. 2017
[3] F. Cheng et al., Opt. Express, OE, vol. 28, no 24, p. 36497-36504, nov. 2020, doi: 10.1364/OE.405528.
[4] B. J. Eggleton, B. Luther-Davies, et K. Richardson, Nature Photon, vol. 5, no 3, p. 141-148, mars 2011
[5] G. J. Hawkins, PhD thesis - The University of Reading, Department of Cybernetics, 1998
[6] M. Duris et al., Opt. Mater. Express, OME, vol. 10, no 8, p. 1921-1930, août 2020
[7] M. Baillieul et al., ACS Omega, vol. 7, no 51, p. 47840-47850, déc. 2022
[8] I. E. Gordon et al., Journal of Quantitative Spectroscopy and Radiative Transfer, vol. 203, p. 3-69, déc. 2017

Integrated White-Light Interferometry for rapid dispersion and index measurements of InP waveguides

(Student paper)

Amer Bassal, Oliver Abdeen, Martin Schell

Fraunhofer-Institut für Nachrichtentechnik, Heinrich-Hertz-Institut, 10587 Berlin, Germany
amer.bassal@hhi.fraunhofer.de

Using spontaneous emissions of an integrated optical amplifier and a Mach-Zehnder interferometer, the index and dispersion of InP waveguides are rapidly measured with an optical spectrum analyser via a single fiber coupling.
Keywords: *Mach-Zehnder interferometers, spontaneous emissions, group index, dispersion*

INTRODUCTION

Photonic integrated circuit (PIC) production in InP is a complex process with many fabrication steps and parameters that can cause a lot of statistical variations in the performance of the produced chips. Therefore there is a need to measure the performance of each produced wafer at multiple positions. And for large batches of wafers, there is a demand for fast and yet accurate measurements. This means a low number of fiber couplings and a high tolerance to fiber misalignments, coupling and system losses. One important parameter is the group index of passive waveguides (WGs) since this parameter affects all passive building blocks (BB) as well as active BBs and composite structures like Mach-Zehnder modulators, mode-locked lasers, ring laser and all integrated lasers in general.

One of the simplest and reliable methods of measuring the group index, thus the dispersion, of waveguides and optical fibres is using a Mach-Zehnder interferometer (MZI). The method uses a broad-band light source to obtain the interferogram from which the free spectral range (FSR), the spectral distance between peaks, and in turn the group index are obtained. The light source can be a tuneable laser which sweeps through the required wavelength range and in this case the detector is a p.i.n photodiode as done for integrated photonics in a previous paper [1]. The other light source option is a broad-band, or white light, light emitting diode (LED) and in this case an optical spectrum analyser (OSA) on the other end captures the interferogram. This MZI technique was used to measure the dispersion of fibers compared to air [2] and was also done for holey fibers [3]. The technique was also used to measure silicon-on-insulator waveguides [4] and photonic crystal waveguides [5]. In all of the measurements an external white light source is used, however, the spontaneous emissions from quantum well lasers can also be used to obtain their own index [6]. Therefore it is possible to use an integrated MZI with a semiconductor optical amplifier (SOA) as a white light LED for index measurements.

In this paper, we propose a MZI based method, requiring only a single fiber coupling, to obtain the group index and chromatic dispersion of 600 nm deep WGs in Indium Phosphide (InP) PICs. The integrated MZI structure has an arm length difference of 500 µm are fed with spontaneous emissions from the monolithically integrated SOA, which eliminates the need for an external tuneable wide-band laser source. The fiber alignment to the chip facet is much more tolerable and much faster to perform in the case of a white light source. This because there is no need couple light in and the index measurements only require the peaks to be detected, rather than the power values. Moreover, since the SOA quantum wells emit light in the transverse electric (TE) mode, there is no need for a polarization calibration of the setup. This allows for a much more rapid, stable and lower cost measurements.

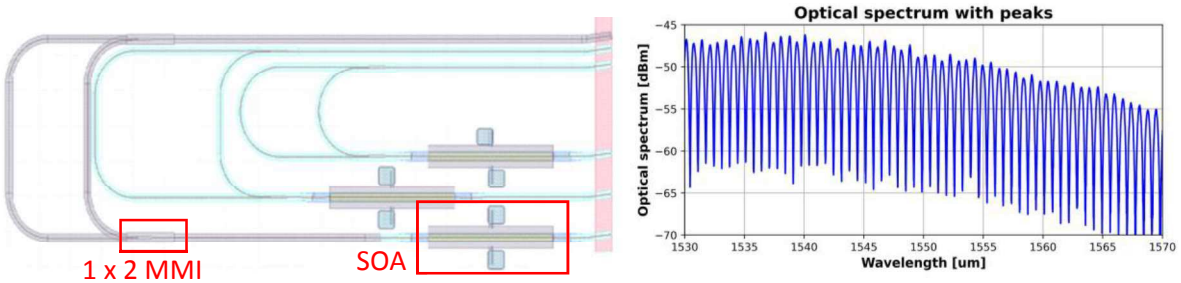


Fig. 1. (a) The layout of the MZI structure, and (b) the optical spectrum.

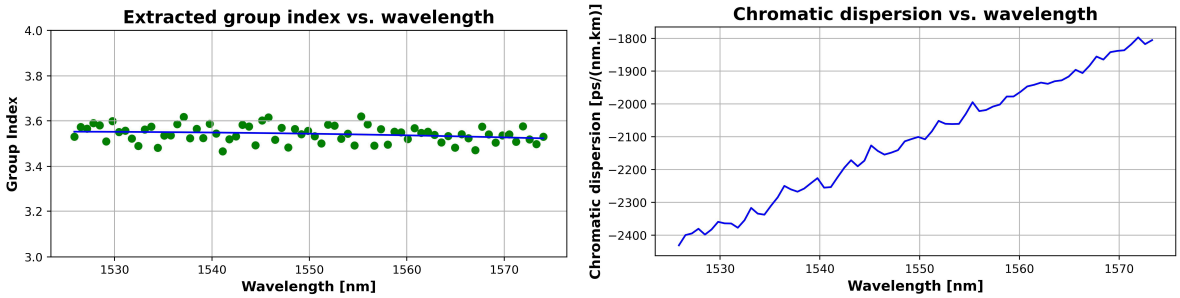


Fig. 2. (a) The extracted group index with a second order fit and (b) the chromatic dispersion.

THEORY AND METHODOLOGY

Fig. 1(a) shows the layout of the integrated MZI structures. The SOAs emit wide-band spontaneous emissions which are split using 1x2 multi-mode interference couplers (MMIs) into the two WG arms of the MZI which are combined again with another 1x2 MMI, then the light is coupled out with a single mode fiber though the cleaved facet. The MZI structure has an arm length difference ΔL = 500 µm. The output light coupled in the fiber is fed into an optical spectrum analyzer which records the interferogram with a spectral resolution of 0.07 nm. The different wavelengths emitted by the SOAs interfere with each other as can be described by the following equation,

$$I_{out}(\lambda) = I_{in}(\lambda)e^{-\alpha L}\left[e^{-2\alpha\Delta L}S_1^2 + S_2^2 + 2e^{-\alpha\Delta L}S_1S_2\cos\left(\frac{2\pi n_e(\lambda)}{\lambda}\Delta L\right)\right] \quad (1)$$

where I_{in} is the SOA intensity as a function of wavelength, α is the propagation loss, S_1 and S_2 are the MMI intensity splitting ratios, and $n_e(\lambda)$ is the waveguide effective index. The $Iout$ spectrum shows fringes due to the interference as expected from the cosine argument.

Given ΔL, at each wavelength the group index is obtained from the FSR as detailed in the next section. The FSR is expressed as $\Delta\lambda=\lambda^2/n_g\Delta L$ from which the group index is obtained, and in turn, the chromatic dispersion which is obtained as $D(\lambda) = dn_g(\lambda)/cd\lambda$, where c is the speed of light.

RESULTS AND ANALYSIS

The SOAs where first powered and the output light was coupled to a fiber and aligned for the maximum power coupling into the OSA. The bias current of the SOA is then adjusted to obtain the cleanest interferogram, clear of any other parasitic interferences. The optimal bias current is 50 mA. The interferogram is then captured on the OSA with a resolution of 0.07 nm as shown in Fig. 1. (b). The FSR was then obtained by fitting a parabola around each peak yielding the group index spectrum in Fig. 2 (a). Around 1550 nm, a group index of 3.53 and a chromatic dispersion of D = -2100 ps/(nm.km) can be observed for the WG under test, which has an Fe doped InGaAsP core. The figure also includes a second order fit, from which the maximum deviation is estimated to be roughly 2.5%. Similar group index and dispersion values have been previously reported around 1550 nm, such as ng = 3.49 for InGaAsP WGs [7] and D = -1700 ps/(nm.km) calculated from [8] for a pure InP sample. For an InGaAsP SOA, the waveguide dispersion is found to be -540 ps/(nm.km), and about 30000 ps/(nm.km) including

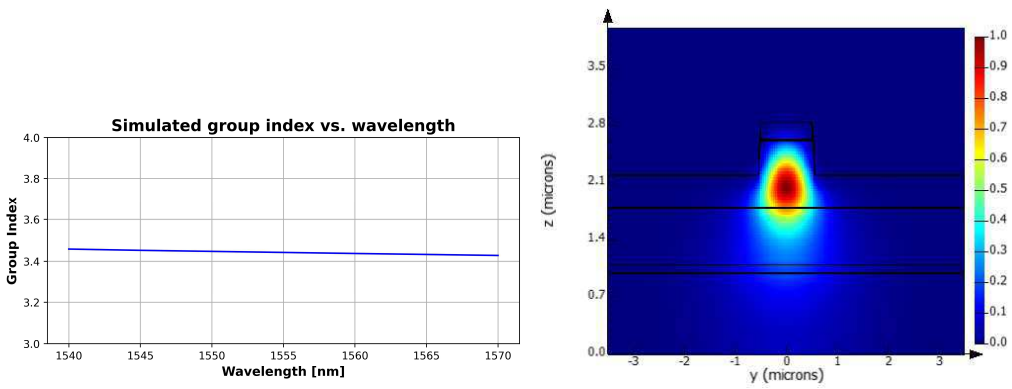


Fig. 3. (a) The simulated group index and (b) the electric field intensity of the TE mode in the WG cross section.

the material dispersion [9]. The large increase of the dispersion due to the material is attributed to the band-gap of the SOA which is 1540 nm [9], compared to that of the passive waveguides measured in this paper, about 1050 nm, which is far from the measurement wavelength of 1550 nm.

The WG was also simulated using an eigenmode solver to obtain the same values. The resulting electric field intensity of the WG cross section is shown is Fig. 3. (b). The simulated group index is shown in Fig. 3. (a) which is close to the measured values with and error of about 2.8% at 1550nm. This could be explained by the change in the etch depth of the WGs and by the material modeling as well as the epitaxial growth. The material in this simulation was modeled using the Sellmeier coefficients fitted for fabricated InP and InGaAsP materials [10].

References

[1] A. Bassal, G. Binet, W. Diels, A. Schönau, O. Abdeen, M. Baier, M. Schell, *Practical characterization of InP Waveguides and MMI couplers using Mach-Zehnder interferometers*, 23rd European Conference on Integrated Optics (ECIO), Milan, Italy, 2022

[2] J. Y. Lee and D. Y. Kim, *Versatile chromatic dispersion measurement of a single mode fiber using spectral white light interferometry*, Vol. 14, Issue 24, pp. 11608-11615, 2006

[3] P. Hlubina, D. Ciprian, R. Chlebus, *Group index dispersion of holey fibres measured by a white-light spectral interferometric technique*, Optics Communications, Vol. 281, Issues 15–16, pp. 4008-4013, 2008

[4] F. Leo, U. Dave, S. Keyvaninia, B. Kuyken, and G. Roelkens, *Measurement and tuning of the chromatic dispersion of a silicon photonic wire around the half band gap spectral region*, Vol. 39, Issue 3, pp. 711-714, 2014

[5] D. Kim, S. Kim, S. Lee, K. Kim, J. Lee, and E. Lee, *A New Method of Measuring Localized Chromatic Dispersion of Structured Nanowaveguide Devices Using White-Light Interferometry*, Journal of Lightwave Technology Vol. 30, Issue 1, pp. 43-48, 2012

[6] C. Chang, S. Chuang, J. R. Minch, W. Fang, Y. K. Chen and T. Tanbun-Ek, *Amplified spontaneous emission spectroscopy in strained quantum-well lasers*, IEEE Journal of Selected Topics in Quantum Electronics, Vol. 1, Issue. 4, pp. 1100-1107, 1995

[7] D. Rabus, M. Hamacher, *MMI-coupled ring resonators in GaInAsP-InP*, IEEE Photonics Technology Letters, Vol. 13, Issue 8, pp. 812-814, 2001

[8] G. Pettit, W. Turner, *Refractive Index of InP,* Journal of Applied Physics, Vol. 36, pp. 2081-2081, 1965

[9] P. Runge, R. Elschner and K. Petermann, *Chromatic Dispersion in InGaAsP Semiconductor Optical Amplifiers*, in IEEE Journal of Quantum Electronics, Vol. 46, Issue. 5, pp. 644-649, 2010

[10] B. Broberg and S. Lindgren, *Refractive index of In1−xGaxAsyP1−y layers and InP in the transparent wavelength region*, Journal of Applied Physics Vol. 55, Issue 9, p. 3376, 1984

High-power CW >100 mW SOAs for active-passive integration

Student paper

Andrzej Jankowski[1], Stefanos Andreou [1], Steven Kleijn[1], Alonso Millan-Mejia[1], Pim Voorthuijzen[1], Thijs Buckers[1] and Luc Augustin[1]

[1]SMART Photonics, High Tech Campus 29, 5656 AE Eindhoven, The Netherlands
* luc.augustin@smartphotonics.nl

We report the first experimental results on our high-power continuous-wave (CW) multi-quantum-well amplifiers operating in 1550 nm range over a wide temperature span. Devices are compatible with active passive integration on an InP foundry platform. CW total output power of 100 mW at room temperature is recorded.

Keywords: *Ridge, high-power, SOA, amplifiers*

INTRODUCTION

Photonic integrated circuits' rapid market growth requires mature and reliable components fabricated with standardized industrial integration processes [1][2]. High-power devices at 1550 nm are the key components that find application in various modern systems, including lidar, telecommunication, and spectroscopy [3][4]. In this paper we present preliminary measurements and optical simulations of multi-quantum-well semiconductor optical amplifiers (SOA's) processed within SMART Photonics' InP foundry technology platform. The devices are designed for active-passive integration with other building blocks that are available within existing process design kits (PDKs).

DEVICE FABRICATION AND DESIGN

A general overview of the layer stack is presented in Fig. 1a. The designed layer stack is grown by metalorganic chemical vapor deposition (MOCVD) epitaxy. The stack is grown on an n-type InP substrate with a Q1.25 guiding layer positioned below an n-InP spacer layer, graded index separate confinement InGaAsP layers, and the quantum-well layer stack. The active region of the device is composed of compressively strained quantum wells that are separated with tensile strained barriers, followed by P-InP cladding and a P-InGaAs contact layer. A ridge structure is defined by lithography, followed by dry and wet etching. After wafer-thinning to 150 µm, devices are cleaved.

Offset quantum wells are utilized in the device design to lower the confinement factor and consequently increase the saturation output power of the semiconductor optical amplifier [5]. In Fig. 1b optical simulations of confinement factor (Γ) vs. thickness of the n-InP spacer layer results are presented. In the layer stack design, 100 nm of InP is chosen corresponding to ~1.8% of Γ in the active device region. Optical simulations of the ridge etch depth and width were performed to assure single-mode operation.

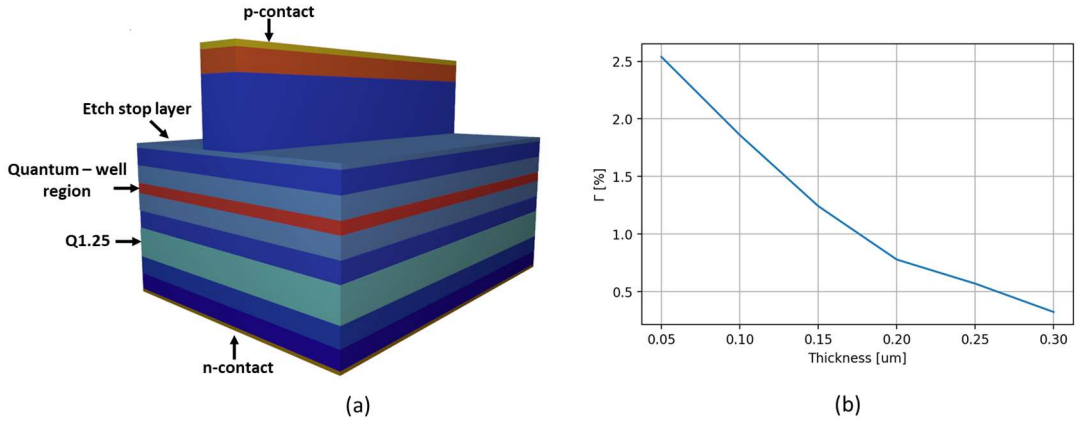


Fig. 1. Schematic overview of the layer stack (a) and (b) simulated optical confinement factor vs thickness of InP layer above optical waveguide core Q1.25.

RESULTS AND DISCUSSION

Firstly, Fabry Pérot (FP) lasers are characterised. Investigated devices were measured under continuous-wave (CW) and pulsed-mode operation. Cleaved and uncoated bars were directly placed in vacuum contact with the n-contact side on a copper mount, which was temperature-controlled by a thermoelectric cooler on top of a water-cooled

heat sink. The output power is measured by collecting the output light an integrating sphere. The optical spectrum is measured using a cleaved single mode fiber and an optical spectrum analyser (OSA). Light-current and voltage-current measurements were performed as a function of temperature varying from 20 °C up to 50°C as long-wavelength InGaAsP devices are known to be strongly temperature-dependent [6].

The output power characteristics are presented in Fig. 2a, recorded under CW (solid-lines) and pulsed-mode (dashed-lines) operation, respectively. The maximum CW total output power (of both facets) of 100 mW is recorded for a device length of 2000 µm and ridge width of 4 µm at room temperature, with 86 mA of threshold current (I_{th}). Based on measured output power levels, the saturation power of an SOA should be higher due to higher facet reflectivity. The thermal roll-off of the output power is clearly visible. Additional power loss due to heat under CW operation shows at least 15% lower output powers at the same temperature point in comparison to pulsed-mode operation. Threshold current and threshold current density (J_{the}) increase over temperatures is depicted in Fig. 2b. The value of transparency threshold current density derived from linear fit of J_{th} and inverse cavity length is estimated to be 716 A/cm^2.

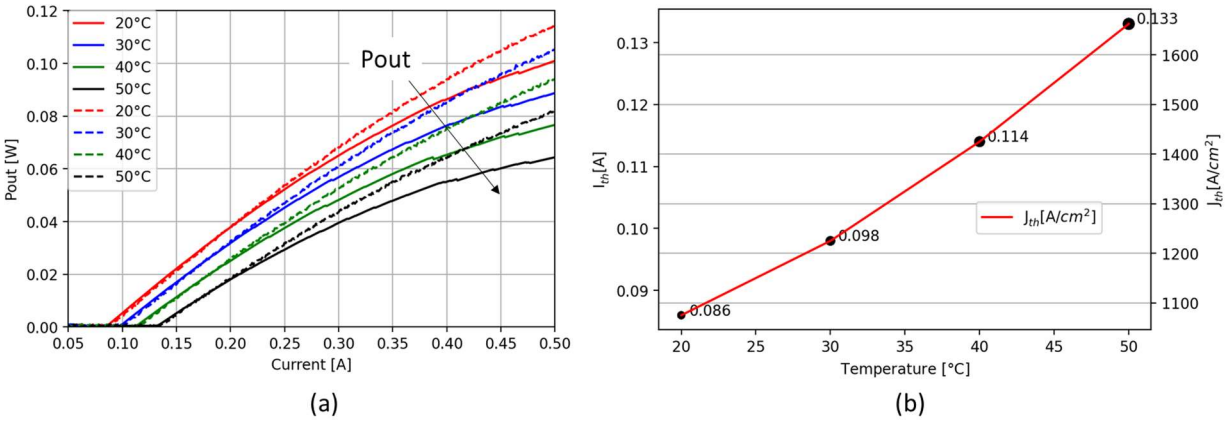


Fig. 2. (a) Measured light-current characteristics over temperature range between 20°C and 50°C, under CW operation (solid lines), pulsed-mode operation (dashed-lines) for the device length = 2000 µm and ridge width = 4 µm. (b) Recorded threshold current (I_{th}, left axis) and threshold current densities (J_{th}, right axis) vs. temperature.

Characteristic temperature measurements are presented in Fig. 3a and corresponding wall-plug efficiency in Fig. 3b. Recorded T_0 value of 68.5 K corresponds well with reported values in the literature [6], but it also suggests further improvements in thermal management are required.

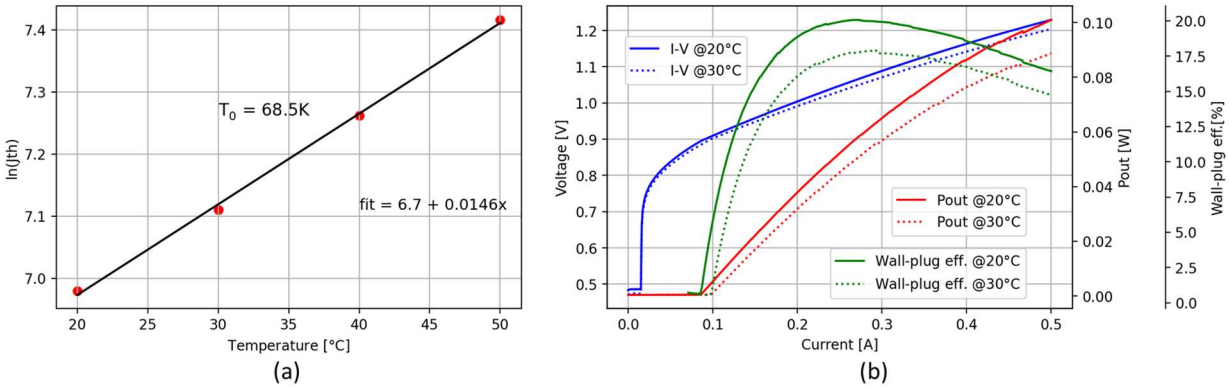


Fig. 3. (a) Characteristic temperature (T0) measurements and (b) measured characteristics of I-V, LI-V, and wall-plug efficiency at 20 °C and 30 °C. Device length = 2000 µm and ridge width = 4 µm.

We used an optical spectrum analyzer (OSA) to record the optical emission spectra operating around 1550nm. In Fig. 4, the optical spectra of the device are presented measured at 20 °C and 30 °C. The thermal red-shift of the wavelength emission is about 0.5 nm/K.

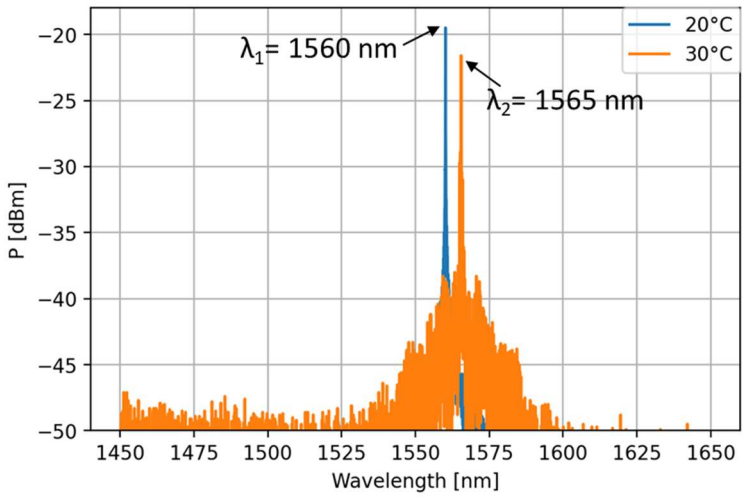


Fig. 4. Recorded optical spectrum at 20 °C for the device length of 2000 µm and 4 µm of ridge width.

SUMMARY

We have presented experimental measurement results of FP lasers fabricated on our InP foundry platform compatible with active-passive integration. Proposed devices show capability of >100 mW of total output power under CW operation and integration of SOAs with saturation powers at higher power levels due to higher facet reflectivity. Further analysis of SOAs using anti-reflective coated devices is planned.

As expected, strong temperature-dependent effects reducing the performance are observed. These influences are also confirmed in T_0 measurements, which suggest further improvements in thermal optimization are required to lower the thermal sensitivity of the devices. Introduction of Al-based Quantum wells will further improve the temperature behaviour.

References

[1] M. Smit, K. Williams, *Past, Present, and Future of InP-Based Photonic Integration* in APL Photonics 4, no. 5, 2019
[2] L. M. Augustin, R. Santos, *InP-Based Generic Foundry Platform for Photonic Integrated Circuits,* in IEEE Journal of Selected Topics in Quantum Electronics 24, no. 1, 2018
[3] D. Marpaung, J. Yao, *Integrated Microwave Photonics*, Nature Photonics 13, no. 2, 2019
[4] LiDAR application note, *Photonic integrated circuits for LiDAR*, SMART Photonics, 2021 (https://smartphotonics.hubspotpagebuilder.com/lidar)
[5] L. Nielsen, M. J. R. Heck, *Boosting the Output Power and Wall-Plug Efficiency of Lasers on a Generic InP Platform* in Integrated Optics: Devices, Materials, and Technologies XXV, SPIE, 2021
[6] J. Piprek, P. Abraham, *Self-Consistent Analysis of High-Temperature Effects on Strained-Layer Multiquantum-Well InGaAsP-InP Lasers* in IEEE Journal of Quantum Electronics 36, no. 3, 2000

Temperature stabilization techniques for High Stability LO Generation using a Hybrid Integrated Dual InP-Si_3N_4 Laser Source

(Student paper)

Alberto Zarzuelo[1*], Jessica César[1], Robinson Guzmán[1], Luis Gonzalez[1], Charoula Mitsolidou[2], Roelof Bernardus Timens[2], Chris Roeloffzen[2] and Guillermo Carpintero[1]

[1]Universidad Carlos III de Madrid, Av. De la Universidad 30, Leganés, 28911, Spain
[2]LioniX International BV, Hengelosestraat 500, Enschede, 7521 AN, The Netherlands
[*] azarzuel@pa.uc3m.es

We propose a study of temperature stabilization techniques for a hybrid integrated InP-Si_3N_4 laser under free running condition for microwave generation based on optical heterodyning. Long-term drift exhibited by the device over certain time is performed as key parameter. Free-running drift reduction is one of the goals of this experiment which has been measured along different scenarios. Optical drift has been improved from up to 500 MHz, in the worst case, to around 100 MHz measured over 6 hours on a thermal controlled environment.

Keywords: *microwave photonics, integrated optics*

INTRODUCTION

To the date, a wide range of applications field has RF frequency generation as its core function. As the requirements are becoming more demanding, especially in terms of increase the data capacity. There is an interest of improving this capacity and the flexibility [1]. All this driven by the need to work in higher frequency bands to enable large bandwidth availability. Although conventional RF based-on device are capable to reach high frequencies up to millimeter-Waves, high-end microwave electronic mixers and circuitry are bulky, heavy, expensive and sensitive to electromagnetic interference (EMI). Applications relying on the interfacing between radiofrequency (RF) signals and optical fiber network segments, call for flexible, agile and compact devices. Such as global wireless fifth generation (5G) communications [2], radar based civil surveillance [3], fast analog-to-digital converters [4] and clock recovery systems [5]. Moreover, RF systems with increased complexity, large frequency tuning range and broad bandwidth are urgent for signal generation and processing areas.

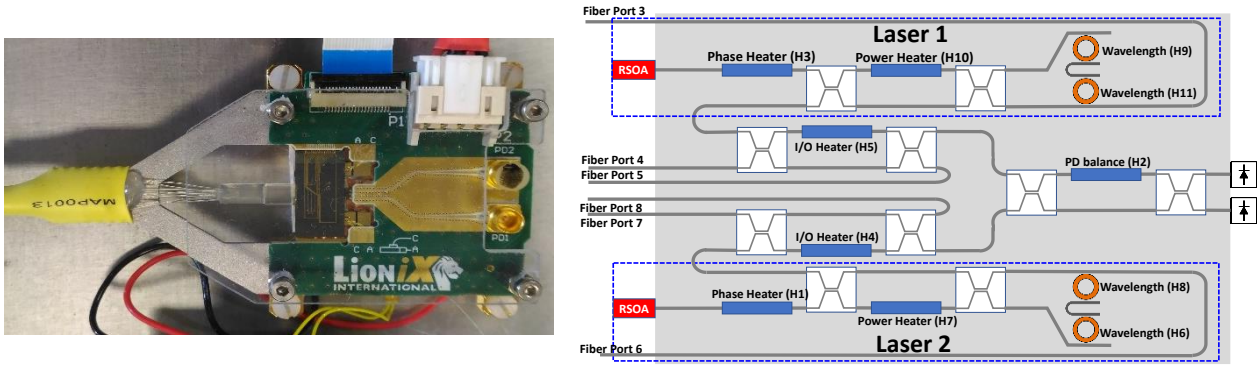
Microwave Photonics (MWP) emerges to be a promising and low-cost alternative. In this case, the local oscillator RF signals can be distributed using optical fiber instead of electrical connections, bringing important advantages in terms of mass, power and volume. These advantages fueled the development of MWP technology, mainly based on discrete components interconnected through optical fibre. This approach has been shown to limit energy-efficiency and scalability, and, as a result, high volume application. In addition, optical fibre interconnections, sensitive to thermal fluctuations, introduce optical path length variations that affect the quality of the generated signals [6]. Photonic integration has been identified as a technology that can significantly reduce this dependence, since all components in the system and their interconnections are fabricated in a single chip, a Photonic Integrated Circuit (PIC). The use of photonic integration technology for microwave photonic applications has recently coined the term of integrated MWP (iMWP).

Microwave photonic frequency generation can range from few MHz up to THz range facing the conventional RF LO generators. However, despite of integrating the two lasers on the same chip, the fact that these are two free-running lasers usually results in a large phase noise of the beat note and long-term drift of the frequency [7]. While the two lasers can have very low intrinsic linewidth (less than 1 kHz), the RF beat-note still exhibits a long-term drift due to electrical, thermal & noise instabilities. This issue is not acceptable specially if this drift reaches the range of the RF signal channelizing producing an overlap between different channels. Even if a stabilization technique is used to control the lasers, such as optical phase locked loop or injection locking, the amount of drift could be problematic. Specially, if lasers go out of range of the control system used. In this paper, we present a thermal study of a hybrid integrated dual laser using different approaches in order to reduce the amount of drift and improve the performance of the RF generated LO.

DEVICE DESCRIPTION

An InP/Si3N4 hybrid integrated dual laser module will be used in this work. The device is shown schematically in **Fig. 1 (b)**. As can be observed, it includes two identical laser structures, which are outlined on the figure using blue dashed boxes labeled Laser1 and Laser2 respectively. Each laser cavity is formed through hybrid integration of an

InP Quantum-Well (QW) gain chip (red boxes) and a Si3N4 (proprietary Si3N4 waveguide technology from LioniX International) chip (grey shaded area) using butt-coupling. The InP gain chip is double-pass reflective semiconductor optical amplifier (RSOA) through high-reflective (HR) coating on the leftmost edge, which forms one of the cavity mirrors. The other mirror is an integrated mirror structure in the Si3N4 substrate, based on a pair of micro ring resonators (MRR-A and MRR-B) which provide a wavelength tunable optical feedback. The two MRRs have Free Spectral Range (FSR) around 1.6 nm (200 GHz), with slightly different radiuses to enable wavelength tuning through the Vernier effect. In between the two mirrors, the lasers include a thermally adjustable Phase Tuning Section (PTS) that allows fine tuning of the cavity length for output power maximization and a 2x2 symmetric Mach-Zehnder Interferometer based Thermo-Optic Power Coupler (MZI-TOPC) [8] which allows control of the amount of light fed back to the laser cavity. A photograph of the InP/Si3N4 hybrid integrated dual laser module is shown in Fig. 1 (a).

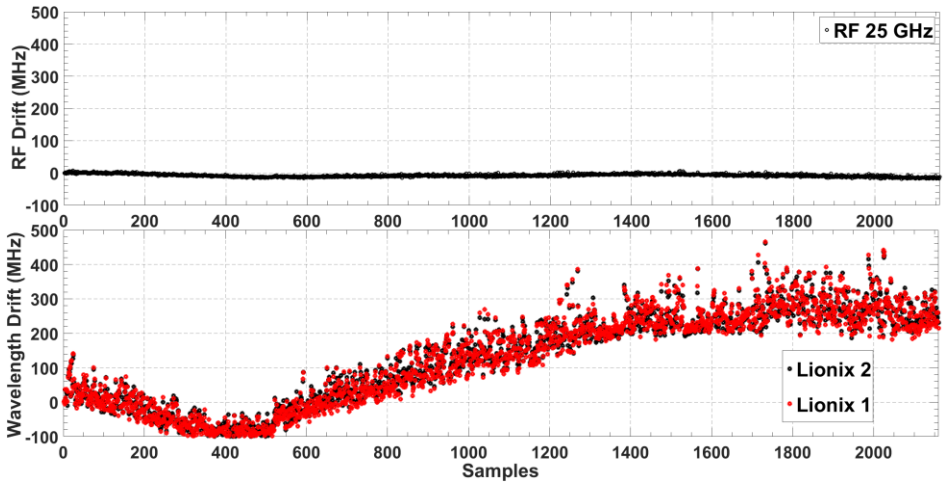


(a) *(b)*

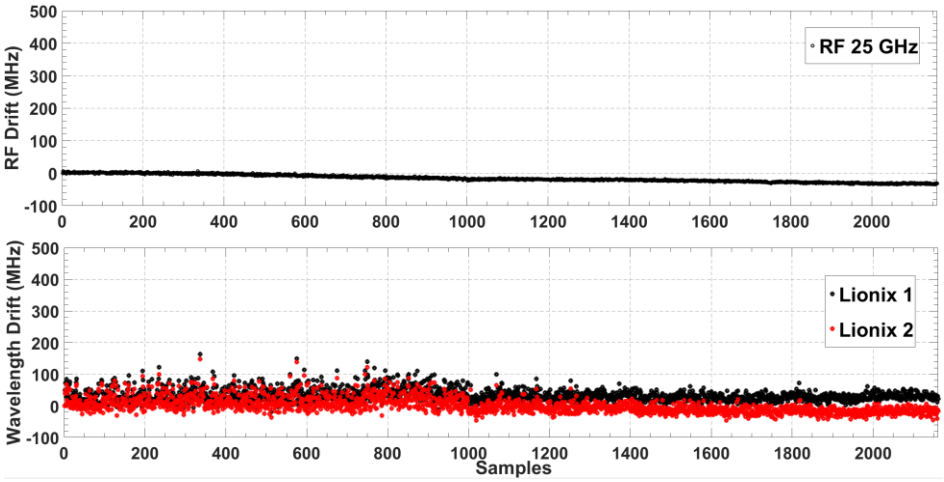
Fig. 1. (a) InP-Si3N4 hybrid integrated dual laser module is assembled on a thermally controlled base. (b) Schematic representation of the device.

RESULTS

The emission wavelength of the lasers during this experiment is around 1550 nm. The current injected into the gain section of each independent laser is 40mA, while the H5 and H4 heaters used to control the external coupling ratio on both lasers are biased at 13.632 V and 13.55 V, respectively. Tuning the biasing point of these heaters we can maximize the optical power at each laser output. The heaters that control the wavelength setting H9/H11 and H8/H6 are biased with a voltage of 0 volts and 11,159 volts, respectively for Laser 1 and Laser 2, so that an optical frequency difference between both lasers is established at 25 GHz. Fig. 2 shows the long-term drift of electrical beat-note RF signal (upper) and optical drift (lower) measured over 6 hours. Two different approaches have been measured. In Fig. 2(a) the measurement was taken with a standard optical breadboard while Fig. 2(b) was measured using a water-cooled breadboard where the temperature of the heat-sink mass was fully controlled by a Chiller. As it can be notice, the first approach the optical drift goes up to 500 MHz while with the second approach the drift keeps around 100 MHz exhibiting a one fifth improvement with respect the first approach.



(a)



(b)

Fig. 2. Temporal evolution of the drift of the InP/Si3N4 hybrid integrated dual laser module measured over a period of 12 hours. Optical drift of each laser of the dual module (below). Electrical drift of the generated RF frequency (above). (a) Using standard-optical breadboard. (b) Using water-cooled breadboard with chiller

Fig. 2 (a) and (b), upper, shows the electrical drift of the generated RF tone for each approach. We can see that the two approaches are quite similar. Despite the fact that both lasers are independent, they are close to each other (mm distance). They share same thermal control. The thermal fluctuations produce similar the optical drift on each laser. The electrical beat note is generated as product of the wavelength difference between Laser 1 and Laser 2, so if the displacement produced by thermal drift of each laser is synchronized, the drift on the RF beat-note reduced. As shown in Fig. 2 (a) and (b), they have similar behaviour that ranges from -42 MHz to +18 MHz with respect to the starting RF frequency.

CONCLUSSIONS

We have presented temperature stabilization study of an InP/Si3N4 hybrid integrated dual laser. Two different approaches have been compared in order to reduce drift of the lasers. We demonstrated a one-fifth reduction of the optical drift using a fully temperature-controlled environment keeping both lasers around 100 MHz drift, what is more suitable for a potential stabilization system. The wavelength drifts produced by thermal fluctuations when lasers are under the same control are correlated. This results on a reduction of the electrical drift of the generated RF frequency. We have measured an electrical drift that ranges between -18 MHz to 48 MHz with respect to the initial frequency measured over 6 hours under free running condition in both approaches.

References

[1] S. Roux et al., *"Advanced photonic payloads for broadband telecom satellites: Integration and tests of a representative repeater demonstrator"*, Proc. SPIE 11180, International Conference on Space Optics ICSO, 2018

[2] M. H. Alsharif and R. Nordin, *"Evolution towards fifth generation (5G) wireless networks: Current trends and challenges in the deployment of millimeter wave, massive MIMO, and small cells"*, Telecomm. Syst. 64(4), 617–637, 2017

[3] P. Ghelfi et al., *"A fully photonics-based coherent radar system"*, Nature 507(7492), 341–345, 2014

[4] L. Yu et al., *"Electro-optical switching based demultiplexing in high-speed photonic analog-to-digital converter based on actively mode-lock laser"*, International Topical Meeting on Microwave Photonics, 2017

[5] X. Li and J. Yu, "*Generation and heterodyne detection of >100-Gb/s Q-band PDM-64QAM mm-wave signal*", IEEE Photonics Technol. Lett. 29(1), 27–30, 2017.

[6] Nagatsuma, T., H. Ito and Iwatsuki K., *"Generation of Low-phase Noise and Frequency-tunable Millimeter-/terahertz-waves Using Optical Heterodyning Techniques with Uni-traveling Carrier Photodiodes"* European Microwave Conference, 2006

[7] L. Gonzalez-Guerrero et al., *"InP-Si3N4 Hybrid Integrated Optical Source for High-purity Mm-wave Communications"*, Optical Fiber Communications Conference and Exhibition (OFC), pp. 1-3, 2022

[8] *C. G. H. Roeloffzen et al., "Silicon nitride microwave photonic circuits", Opt. Express 21, 22937-22961, 2013*

Characterisation and mitigation of surface related optical loss in suspended GaAs photonic integrated circuits

Robert Thomas[1,*], Haoyang Li[1], Jude Laverock[2] and Krishna C. Balram[1]

[1] Quantum Engineering Technology Labs and Department of Electrical and Electronic Engineering, University of Bristol, Woodland Road, Bristol, BS8 1QU, UK
[2] School of Chemistry, University of Bristol, Cantocks Close, Bristol BS8 1TS, UK
[*] eu21581@bristol.ac.uk

Suspended GaAs photonic integrated circuits (PIC) offer a potential route towards monolithic integration of active and passive device functionality for improved efficiency and component density. Thus far, however, progress has been limited by excessive optical losses that occur at the surface of GaAs waveguides. In this work, we quantify the optical propagation loss due to surface absorption in a suspended GaAs PIC platform, probe its origins using X-ray photoemission spectroscopy (XPS), and show that it can be mitigated by surface passivation using an atomic layer deposition (ALD) of alumina. ***Keywords***: *Photonic integrated circuit, Gallium Arsenide, optical loss, surface state absorption, ring resonators, rib waveguides*

INTRODUCTION

No one PIC platform possesses all the optical, mechanical, and electronic properties that would enable arbitrary scale, complexity, and functionality of monolithically integrated devices. That said, of all the materials commonly used in integrated optics, III-Vs like gallium arsenide and indium phosphide, perhaps, come closest in this regard. III-V direct band gap materials enable efficient on-chip light emission and detection and with non-linear electro-optic and piezo-electric coefficients can enable other active functionalities; fast modulation; routing and signal processing. Of the available III-V materials, however, GaAs offers the key advantage of 8" fab, developed for electronics, but, with the potential for higher performance photonics. Nevertheless, when implemented within a GaAs/AlGaAs waveguide, poor optical confinement (due to the low index contrast between GaAs and AlGaAs) leads to large mode sizes, and bend radii, which make photonic integration challenging. A solution to the issue of mode confinement is to remove GaAs waveguides and other photonic structures from their underlying substrate to increase the index contrast between the GaAs waveguide core and the surrounding material [1]. In previous work [2], we reported a robust fabrication technique for a suspended GaAs PIC platform that enables strong mode confinement through the release of photonic structures by wet etch removal of an intermediate sacrificial layer of AlGaAs and demonstrated standard passive PIC components: grating couplers, waveguides, ring-resonators and waveguide splitters. Whilst overcoming the mode confinement issue, propagation losses in these 220 nm thick suspended GaAs waveguides were excessive, 10.7 dB/cm, when compared to equivalent 220 nm and 340 nm silicon on insulator (SOI) offerings (propagation loss ≈ 1dB/cm). We attribute this excessive loss to photon absorption by mid-band gap trap states at the surface of the GaAs waveguides. While there has been some recent work to address this issue of surface passivation of these trap states in III-Vs [3-5], building on work in GaAs electronics, a systematic exploration of the origin of surface loss, its quantification and mitigation by surface passivation techniques is critical to advancing research on III-V PICs.

In this work, we use micro-ring resonators (MRR), fabricated in our suspended GaAs platform, to quantify surface absorption and passivation. The MRR devices are fabricated from 370/1000 nm GaAs/$Al_{0.6}Ga_{0.4}As$ layers epitaxially grown on an undoped GaAs substrate. To differentiate losses occurring at the surface of the waveguides from those in their bulk, we compare the intrinsic quality factor, Q_i values (extracted from measurements of the loaded Q [6]) of devices measured with and without an (8 ± 2) nm thick conformal surface coating of alumina (deposited via ALD). By altering the chemistry of the GaAs surface reconstruction layer, the differential loss measured for treated and untreated devices is directly attributable to mechanisms that occur at the surface of the waveguides alone. The Q_i factors of the of the treated and untreated devices are calculated by numerically fitting a skewed Lorentzian function [7] to resonances recorded in the transmission spectra of the MRRs with the experimental set up illustrated in Figure 1. The wavelength response of the device is measured by sweeping the output wavelength of a tunable laser source in 0.5 pm increments (from short to long wavelength) and recording the transmitted power at each step. For both the ALD treated and untreated samples three different MRR devices were tested with between 2 - 4 resonances recorded for each device.

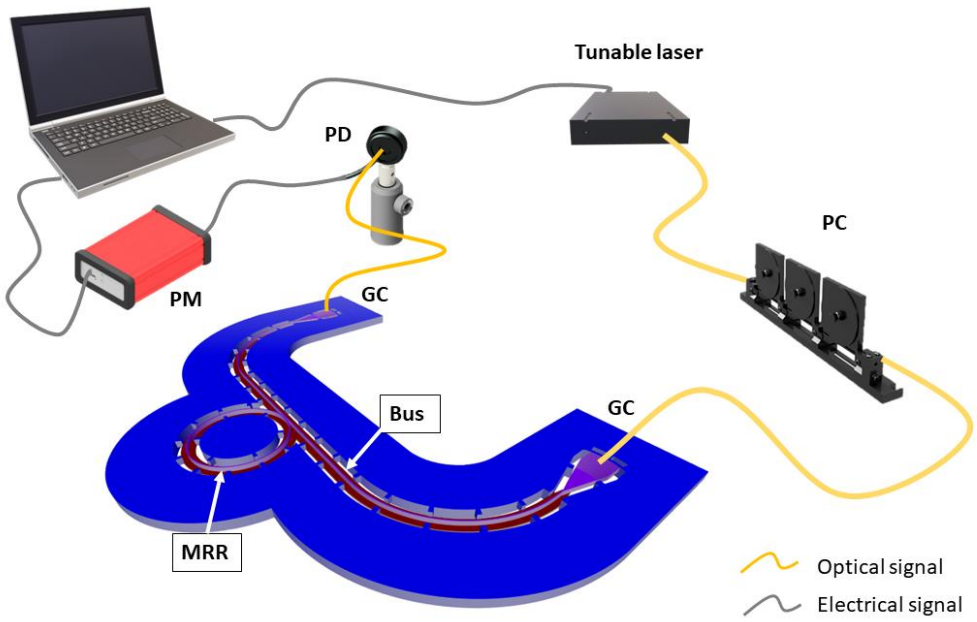
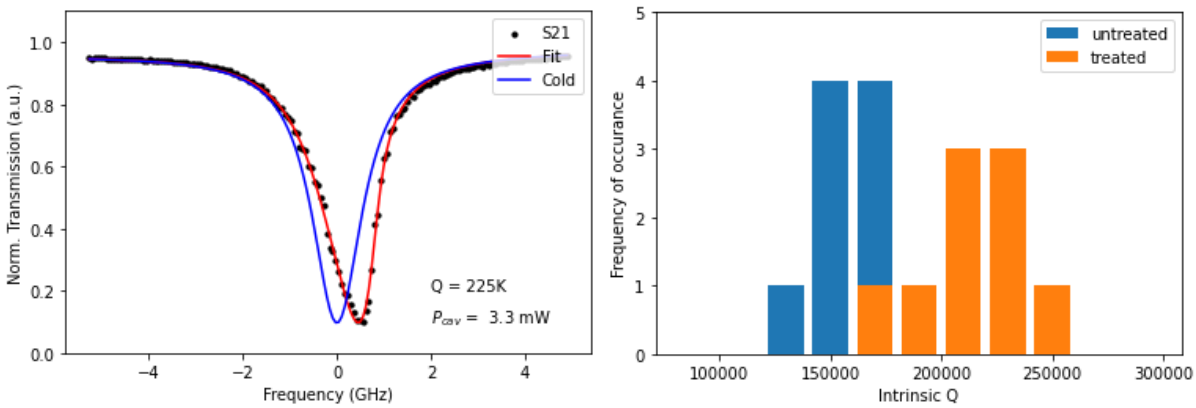


Fig. 1a. Illustration of the experimental set up for measuring MRR transmission spectra. light from a tunable laser passes through a polarization controller (PC), for TE polarized light only, and is inserted into the device via one a pair of tapered grating couplers (GC) situated at either end of the bus waveguide that couples at its mid-point to a 50 µm diameter MRR. The transmitted light from the second GC is fiber coupled to photodetector (PD) and the signal measured with a power meter (PM).

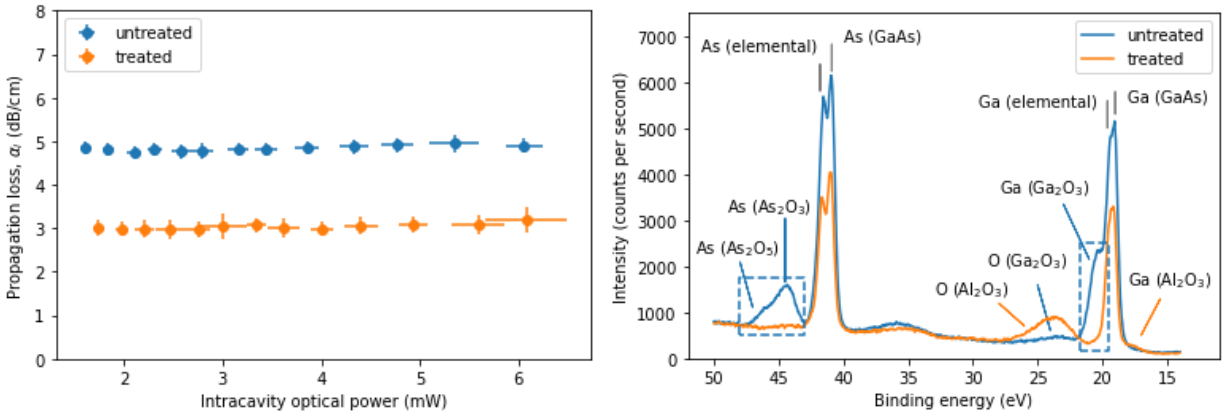
RESULTS/DISCUSSION

Figure 2a shows a typical normalized transmission spectrum recorded for of one of the alumina treated devices from which the Q_i values are extracted. The asymmetry of the resonance is evidence of optical absorption in the MRR cavity which causes it to heat up and induces a thermo-optic shift of the resonant frequency [7]. The Q_i comparison results are presented in the histogram in figure 2b. Taking the median Q_i values, 220k and 160k, to be representative of the treated and untreated sample groups respectively, we estimate that the alumina surface passivation treatment has improved the intrinsic Q of the MRRs by a factor of 1.4



(a) (b)

Fig. 2a. Transmission spectrum (plotted as resonant frequency detuning) measured for one of the ALD treated MRR resonances (black circles), numerically fitted Lorentzian function with thermo-optic 'skew' (red line) and 'cold cavity' Lorentzian fit (blue line) with the skew nullified. b. Histogram of the intrinsic Q values recorded for 10 resonances of both the ALD treated and untreated MRR devices.



(a) (b)

Fig. 3a Propagation loss, α_i, plotted as a function of MRR intracavity optical power for untreated (blue circles) and treated (orange circles). b. XPS surface chemistry analysis for ALD treated (orange lines) and untreated (blue lines) GaAs with native Ga and As oxides highlighted (dashed blue boxes).

In figure 3a the propagation loss, α_i, derived from the intrinsic Q values measured for the median treated and untreated devices, are plotted over a range intracavity optical power (power range over which non-linear absorption effects are not observed) showing that the differential loss remains consistent over a large power range. XPS measurements on treated and untreated GaAs samples, presented in figure 3b, elucidate the nature of the surface passivation. Spectral peaks corresponding to the oxides of Ga and As, observed in the untreated sample data (highlighted by dashed blue boxes,) are not evident in the spectrum of the treated sample, which instead, exhibits features corresponding to Ga bonded to Al_2O_3 and an oxygen signal from Al_2O_3, neither of which appear the spectrum of the untreated sample. This indicates that the alumina coating suppresses the formation of native oxides within the surface reconstruction layer of the GaAs that contribute to surface absorption.

CONCLUSIONS

The intrinsic quality factor and waveguide propagation loss of suspended GaAs MRR devices are improved by a factor of 1.4 through atomic layer deposition of a (8 ± 2) nm layer of alumina. XPS indicates that this is due to the passivation of the surface by suppression of native Ga and As oxides. The improvement in propagation loss afforded by the surface passivation method described here, brings the suspended GaAs photonic platform closer to the performance of Silicon photonics, to the point where the inherent advantages of a III-V material platform can become decisive.

Acknowledgement: This work was supported by EPSRC grant no. EP/V052179/1.

References

[1] J. H. Shin and N. Dagli, "Ultralow Drive Voltage Substrate Removed GaAs/AlGaAs Electro-Optic Modulators at 1550 nm," in IEEE Journal of Selected Topics in Quantum Electronics, vol. 19, no. 6, pp. 150-157, Nov.-Dec. 2013

[2] P. Jiang and K. Balram, "Suspended gallium arsenide platform for building large scale photonic integrated circuits: passive devices," Opt. Express 28, 12262-12271 (2020).

[3] D. Parrain, C. Baker, G. Wang, B. Guha, E. Santos, A. Lemaitre, P. Senellart, G. Leo, S. Ducci, and I. Favero, "Origin of optical losses in gallium arsenide disk whispering gallery resonators," Opt. Express 23, 19656-19672 (2015).

[4] B. Guha, F. Marsault, F. Cadiz, L. Morgenroth, V. Ulin, V. Berkovitz, A. Lemaître, C. Gomez, A. Amo, S. Combrié, B. Gérard, G. Leo, and I. Favero, "Surface-enhanced gallium arsenide photonic resonator with quality factor of 6×10^{-6}," Optica 4, 218-221 (2017).

[5] B. Jacob, F. Camarneiro, J. Borme, O. Bondarchuk, J. B. Nieder and B. Romeira, "Surface Passivation of III–V GaAs Nanopillars by Low-Frequency Plasma Deposition of Silicon Nitride for Active Nanophotonic Devices," ACS Applied Electronic Materials 2022 Vol. 4 Issue 7 Pages 3399-3410.

[6] Bogaerts, W., De Heyn, P., Van Vaerenbergh, T., De Vos, K., Kumar Selvaraja, S., Claes, T., Dumon, P., Bienstman, P., Van Thourhout, D. and Baets, R. (2012), Silicon microring resonators. Laser & Photon. Rev., 6: 47-73.

[7] Gao, M., Yang, QF., Ji, QX. et al. Probing material absorption and optical nonlinearity of integrated photonic materials. Nat Commun 13, 3323 (2022).

Integrated Photonic Processor Enabling Dynamic Mitigation of Turbulence-Induced Scintillation in an Optical Free Space Link

(Student paper)

A. Martinez[1], G. Cavicchioli[1], S. Seyedinnavadeh[1], F. Zanetto[1], C. Mazzucco[2], M. Re[2], M. Mattivi[2], F. Morandi[1], A. D'Acierno[2], U. Spagnolini[1], F. Morichetti[1] and A. Melloni[1]

[1]Dipartimento di Elettronica, Informazione e Bioingegneria, Via Colombo 81, Milan, 20133, Italy
[2] Huawei Technologies Italia srl, Segrate, Italy
corresponding author: andrea.melloni@polimi.it

We present an integrated programmable optical processor implementing an adaptive optical receiver for the mitigation of turbulence-induced scintillation in a Free Space Optical communication link. The effectiveness of the proposed receiver is demonstrated on 5 Gbit/s OOK signals transmitted through an indoor setup emulating hundreds meters long link.
Keywords: *Free space optics, programmable photonics, optical processor, silicon photonics*

INTRODUCTION

Adaptive optics is one of the strategies that can be used to compensate the effects of turbulence-induced scintillation in a Free Space Optics (FSO) [1]. The effects of atmospheric turbulence on optical beams can be described as random phase and amplitude modulation (scintillation), which reduces the coupling efficiency with the receiver and causes strong fading of the signal after the photodetector [2]. Optical beam scintillation can be mitigated with an adaptive optical system (consisting of a multiple aperture receiver), which samples the distorted wavefront at multiple points where the optical signal locally maintains spatial coherence. Since the sampled portion of the beam-front has uncorrelated amplitude and phase (randomly varying on a time scale of several hundred Hz [3]), the adaptive optical receiver has to compensate for these time-varying phenomena in order to recover the spatial coherence of the beam.

In this work, we report on an adaptive optical receiver that consists of a programmable optical processor (POP) that coherently recombines optical beams sampled by a 16-element integrated optical phased array (OPA). The POP is made of a binary-tree mesh of thermally tuneable Mach-Zehnder Interferometers (MZIs), which self-configure and stabilize by using local feedback loops. Adaptive compensation of scintillation of free space optical beams is demonstrated on intensity modulated optical signals at a data rate of 5 Gbit/s, which are intentionally distorted by an indoor atmospheric turbulence emulator.

INTEGRATED PHOTONIC PROCESSOR FOR TURBULENCE MITIGATION

A schematic of the integrated FSO receiver is shown in Fig. 1(a). It consists of a programmable optical processor (POP) composed by 15 integrated MZI arranged in 16x1 binary mesh. Each MZI is individually controlled by means of two thermal phase shifters. The MZI mesh is connected to an integrated OPA made of 16 optical antennas. A top-view photograph of the circuit (3.2 x 1.3 mm size), which was fabricated in a commercial silicon photonic foundry, is shown in Fig. 1(b). The antennas of the OPA are realized by using surface grating couplers (GCs). Each CG is about 48 µm-long and 23 µm-wide, with a 24 µm-long taper. The elevation angle of the radiated field is 3°, the azimuth angle is 0°, and the divergence is 5.6°×9.8° (Fig. 1(c)). The spacing between the GCs is optimized to match the coherence radius r_0 of the turbulent beam at the input of the chip (i.e., after propagating though a collimating optical system positioned in front of the OPA, see Fig. 2(a)). In the considered device, the OPA was designed by assuming a turbulent beam with a scintillation index $\sigma_I^2 = 0.01$ (corresponding to an outdoor link several hundred meters long) and the 16 identical GCs are arranged in two concentric rings with a radius 60 µm (inner ring, 7 GCs) and 180 µm (outer ring, 8 GCs), respectively, and a central GC, as shown in Fig. 1(d). In their native state (thermal actuators off), the balanced MZIs of the POP operate in cross state. In these conditions, the main paths across the MZI mesh are the ones passing through the cross ports of the MZIs, as shown in Fig. 1(e) with the camera view of the light emitted by the OPA. By suitably controlling the phase shift in the MZI arms, the amplitude and the phase of the light emitted by each GC of the OPA can be arbitrarily controlled and hence the shape of the radiated beam. Fig. 1(f) shows the camera view of the OPA emission when the light intensity emitted from the 16 GCs of the OPA is almost the same.

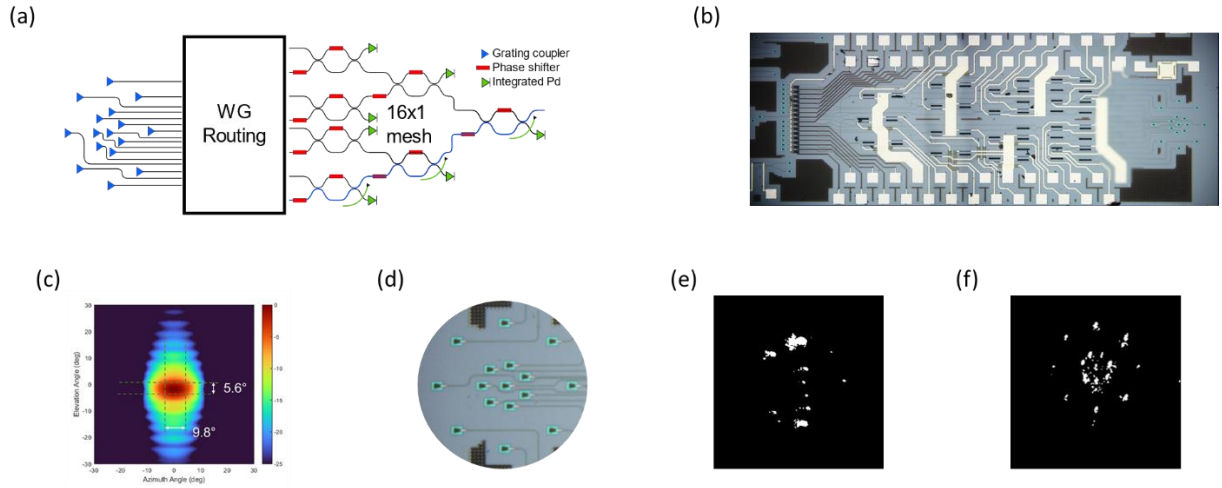


Fig. 1. (a) Scheme of the multi-aperture receiver: Optical Phased Array (OPA), and programmable optical processor (POP). (b) Top-view microphotograph of the silicon photonic PIC with OPA and POP. (c) Simulated far-field radiation pattern of the single grating coupler. (d) Close-up photo of the OPA. Camera picture of the emitted light from the OPA when: (e) native state of the POP with all the MZIs in cross state and (f) the POP is reconfigured to emit the same power from each grating.

To couple a Gaussian-shaped beam with a waist of 42 mm to an OPA with a diameter of 180 μm, an optical system consisting of a 45°-tilted dielectric mirror and a biconcave lens with a focal length of 500 mm was implemented (Fig. 2(a)). The automatic control of the integrated POP is performed by monitoring the state of each MZI by means of an integrated Ge photodiode (PD) coupled at an output port. A feedback control loop is used to minimize the signal read from the PDs in order to coherently recombine the optical signals at the input of each MZI to the opposite output port. To this end, the photonic chip is wire bonded to a custom electronic board that reads the signal from the PDs and changes the operating point of the thermal tuners (Fig. 2(b)). The PDs have a linear response on a dynamic range of around 40 dB, as shown in Fig. 2(c). To mitigate the turbulence effects, the control board reads the voltage of the integrated PDs, then it applies a bias voltage to the thermal actuators located above each MZI to minimize one of the MZI output ports (Fig. 2(d)). The optimization is performed using the dithering technique, which allows the power at a particular port of the mesh to be minimized without calculating its transfer function [3]. The control board performs a lock-in measurement that is frequency and phase selective so that a single dithering frequency can be used for different actuators, allowing a wider control bandwidth (e.g., to control the 30 heaters only 2 dithering frequencies are necessary) [4]. With this technique, each single actuator can be controlled independently and all the MZIs can be tuned in parallel. The coherently recombined signal of the last MZI of the tree is coupled out using a vertically-aligned single-mode fiber.

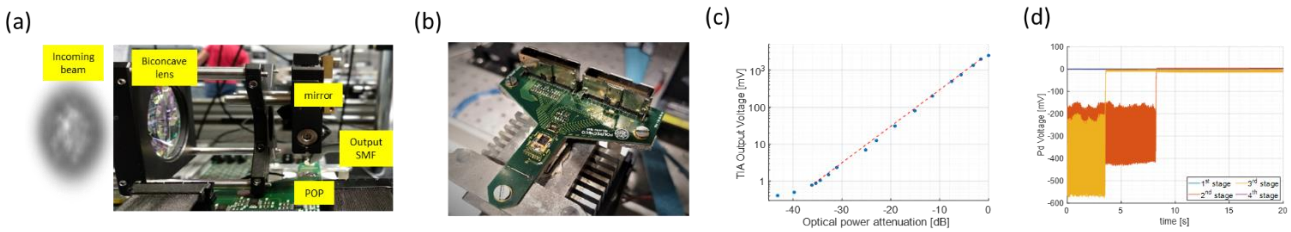


Fig. 2. (a) Photo of the experimental setup. (b) Photo of the PIC bonded to the control PCB. (c) Ge PD responsivity after the TIAs. (d) PDs readout voltage minimization. Each PD corresponds to a different stage of the binary mesh.

EXPERIMENTAL RESULTS

To validate the mitigation of turbulence effects we built an indoor FSO link emulator using a beam expander and a thermal gun. The beam expander generates a beam with a diameter around 5 cm while the thermal gun is used to intentionally introduce turbulence in the 3-m-long link. By changing the gun position, we could vary the turbulence strength from an effective refractive index parameter $C_n^2 = 10^{-14}$ to $10^{-10}[m^{-2/3}]$. In this way, the spectral component associated to the turbulence extends up to a frequency range of about 500 Hz, which is even higher than typical values reported in the literature (300 Hz) [1]. The results shown in this section were obtained by placing the gun to emulate a turbulence strength in the order of $10^{-12}[m^{-2/3}]$. Due to the size of the beam and short length of the link, the wander effect was negligible.

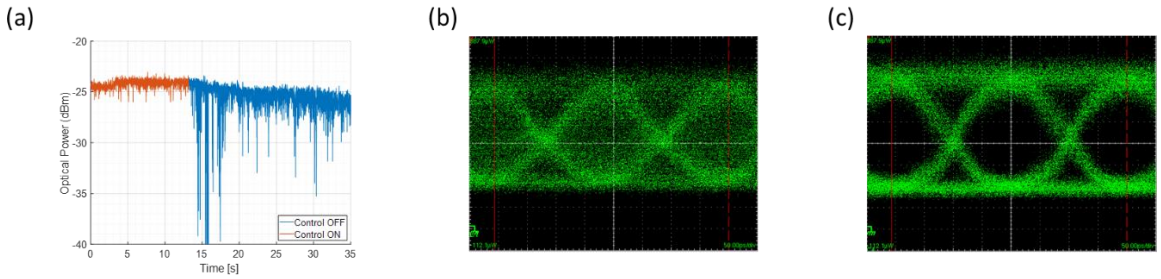


Fig. 3. (a) Optical power of the incoming FSO beam at the output of the integrated adaptive receiver in the presence of induced turbulence when control is on (orange) and off (blue). Eye diagram of the received 5 Gbps OOK in the presence of turbulence when the adaptive control of the POP is (b) deactivated and (c) activated.

Fig. 3(a) shows the signal acquired at the output of the POP with the control off (blue) and with the control on (orange). When the control is not active, the optical fields propagating in the different arms of the MZI mesh interact constructively or destructively depending on the random phase front of the incoming beam affected by scintillation. As a result, an average power level of -25.5 dBm with standard deviation of about 2 dB and power fading as large as 15 dB is observed. When the control is active, the POP dynamically compensates for the relative amplitude and phase differences between the signals by minimizing the power at each integrated PD. In this way, it keeps the POP output power at the maximum level. In this case, the average received power is -24.4 dBm with a standard deviation equal to 0,33 dB and the maximum fading is less than 2 dB. System-level measurements were performed for different conditions of the FSO link using an intensity modulated 5 Gbps signal OOK NRZ. When artificial turbulence is applied to the FSO link and the adaptive control is off (Fig. 3(b)), the eye diagram is evidently affected by the intensity fading induced by scintillation. Instead, when the control loop is activated (Fig. 4(c)), the eye remains open, proving the effective mitigation of scintillation effects.

In conclusion, we demonstrated the effectiveness of a multi-aperture integrated adaptive receiver assisted by a photonic processor to mitigate the scintillation effects in a turbulent FSO link. Scintillation compensation can be improved by increasing the BW of the control loop to reduce high frequency components. And by introducing a proper optic system in front of the OPA such that each antenna can sample a larger portion of the beam e.g., using a beam reducer and an array of micro lenses on top of the OPA.

Acknowledgements: The research has been carried out in the framework of the Huawei-Politecnico di Milano Joint Research Lab. Part of this work was carried out at Polifab, Politecnico di Milano, Milan, Italy.

References

[1] Wang, Y., Xu, H., Li, D. et al. Performance analysis of an adaptive optics system for free-space optics communication through atmospheric turbulence. Sci Rep 8, 1124 (2018). https://doi.org/10.1038/s41598-018-19559-9

[2] X. Zhu and J. M. Kahn, "Free-space optical communication through atmospheric turbulence channels," in IEEE Transactions on Communications, vol. 50, no. 8, pp. 1293-1300, (2002).

[3] M. A. Cox et al, "Structured Light in Turbulence," in IEEE Journal of Selected Topics in Quantum Electronics, vol. 27, no. 2, pp. 1-21, (2021).

[4] F. Zanetto, et. al., "Dithering-based real-time control of cascaded silicon photonic devices by means of non-invasive detectors," IET Optoelectronics, vol. 15, p. 111–120, (2021).

[5] D. A. B. Miller, "Self-configuring universal linear optical component," Photonics Research, 1, 2013.

Miniature and non-contact photoacoustic system using silicon photonics-based Laser Doppler Vibrometer and compact excitation source

(Student paper)

Emiel Dieussaert[1,2,*], Xavier Rottenberg[3], Roel Baets[1,2], Yanlu Li[1,2]

[1]Photonics Research Group, Ghent University-IMEC, Belgium
[2]Center for Nano- and Biophotonics, Ghent University, Belgium
[3]IMEC, Leuven, Belgium
[*] Emiel.Dieussaert@ugent.be

Conventional photoacoustic (PA) systems use bulky high-power excitation laser sources and ultrasonic transducers that need to be in contact with the sample, and hence have many application limitations. In this paper, we present photoacoustic measurements using a small silicon photonics-based Laser Doppler Vibrometer (LDV) and a compact pulsed laser diode. The successful demonstration indicates that a compact and contactless PA system is possible.
Keywords: *Photoacoustics, Laser Doppler Vibrometer, Silicon Photonics*

INTRODUCTION

In recent years, photoacoustic systems have been demonstrated to improve upon existing solutions by combining the benefits of light and sound, particularly in biomedical applications where conventional optical imaging is limited in depth by scattering [1,2,3]. In conventional photoacoustic systems, a pulsed excitation laser is directed toward a sample. There, the excitation light absorbed in the sample is converted into an acoustic wave through the photoacoustic effect. The resulting acoustic waves, which can be detected by using an array of detectors, give information about the light absorption inside the sample. The spatial origin of the acoustic wave can be determined with proper algorithms. Using different excitation wavelengths, the spectral information of the absorption profile can also be obtained [2,3]. One important application where multiple excitation wavelengths are used in the biomedical domain is determining the oxygenation profile inside tissue [4].

Most often, contact-based detectors (such as piezoelectric or optomechanical sensors [5]) are used for detecting ultrasound waves. Here, contact-based methods such as physical contact, a coupling medium, or immersion of the sample are necessary due to a large impedance mismatch between the air and the sample [6]. For many applications, especially in the biomedical domain, these contact methods are impractical or create a risk of contamination of the sample [7]. Optical techniques such as Laser Doppler Vibrometry (LDV) provide a non-contact alternative to detect the vibrations at the surface of the sample caused by the photoacoustic pressure wave [8]. Photoacoustic imaging applications often need detection at multiple locations on the sample. For LDV however, increasing the number of sensing locations increases the number of optical elements and complexity, resulting in an expensive and bulky detector system. Here, we demonstrate a system using a silicon photonic integrated circuit to enable non-contact and compact photoacoustics [9]. Using CMOS-like techniques, most of the passive optical components and interconnecting waveguides can be integrated onto a small silicon chip [10,11]. Hereby enabling relatively low cost (for medium to large-volume production) and very compact (< few mm^2) LDV systems, even for multi-beam LDVs.

A compact and contactless photoacoustic system requires a compact photoacoustic excitation source. In photoacoustic demonstrations, usually a bulky and expensive high-power pulsed laser source is used as the excitation laser (e.g. Nd YAG Lasers, …). These lasers can provide short pulses (<10 ns) with high pulse energy (>1 mJ) and therefore provide a large photoacoustic signal. In recent years, laser diode- and LED-based pulsed sources were suggested as a compact and relatively inexpensive alternative [12].

In this paper, we combine, for the first time, the use of a silicon photonic LDV with a compact pulsed laser diode to demonstrate compact and non-contact photoacoustics. We detect the photoacoustic responses of a target embedded in a silicone sample that mimics the acoustic properties of biological tissue. We show that we can detect photoacoustic signals from absorber concentrations in the physiological range for blood.

METHODS

Figure 1a shows a schematic of the setup used in this paper. In figure 1b, a schematic layout of the on-chip homodyne LDV is depicted. An external 1550 nm laser couples light into the chip through a fiber glued to a grating

coupler. On the chip, the light is split into a measurement and reference beam. The measurement beam goes to a transmitting antenna and is directed toward a target. After reflection upon the target, the measurement light is collected again on the photonic integrated circuit (PIC) and there the light is combined with the reference light in a 90-degree optical hybrid. In the hybrid, the measurement and reference light are combined into multiple light signals with a relative phase shift of 90 degrees between them. Four photodetectors at the output of the hybrid convert the intensity, resulting from interference, into electrical signals. From these photocurrents, in-phase and quadrature signals can be obtained and the phase difference between the reference and measurement beam can be demodulated. Here, we designed the amplifier electronics with a bandwidth of 3 MHz. Assuming a non-moving chip, we can record the movement of the target due to the path length change of the measurement beam. The measurement beam was focused onto the silicone sample and aligned such that specular reflection was collected.

As the source, a pulsed laser diode package at 905 nm (OSRAM SPL S4L90A_3 A01) was mounted on a pulsed driver (LDP-V 240-100) (as can be seen in figure 1d). During experiments, the laser driver provided 500 ns pulses of 160 A at a repetition rate of 1 kHz to the laser diode package, resulting in pulses of 250 µJ with a peak power of around 500 W at a repetition rate of 1 kHz. The diode was placed around 3 mm from the silicone sample and without additional focusing optics.

The silicone sample has an approximate thickness of 1cm ± 1mm. A channel with a diameter of 3 mm lies at a depth of 5 mm ± 1.5 mm. The channel can be filled with different water-based ink solutions to change the absorption. Here, we used black India ink solutions of 0.01%, 0.05%, and 0.10%. From a measured spectrum, it is estimated that this agrees respectively with an absorption coefficient of 1.2 cm^{-1}, 6 cm^{-1}, and 12 cm^{-1}.

For the measurements, we record for 10 seconds with triggered acquisition for each excitation source emission (at 1 kHz) and through averaging of the 10000 segments, we obtain the results shown in figure 2.

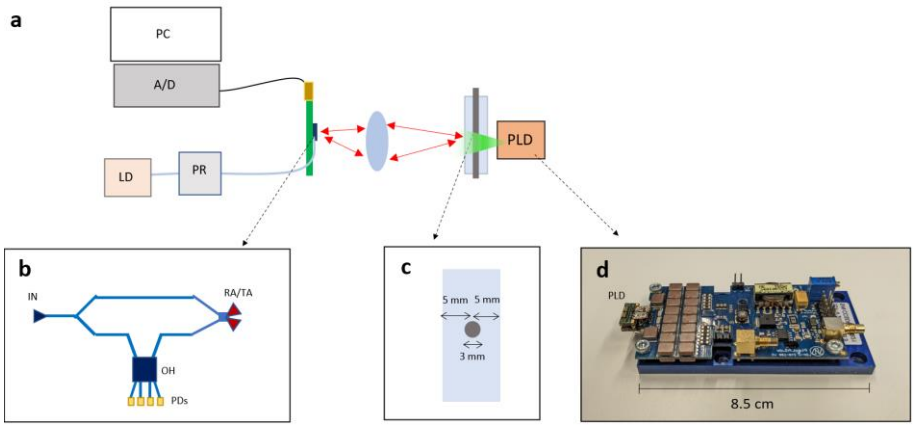


Fig. 1 a) Schematic of photoacoustic setup. A 1550 nm laser diode (LD) is connected to the PIC after going through the polarization rotator (PR). The signals from the LDV system get digitized through an analog-digital converter (A/D) connected to a PC. A pulsed laser diode (PLD) is used as a compact and miniature excitation source. b) Schematic depiction of on-chip homodyne LDV, consisting of: Input grating coupler (IN), receiving and transmission antennas (RA/TA), optical hybrid (OH) and the on-chip photodetectors (PDs) c) Schematic depiction of the silicone sample with dimensions and an embedded ink channel. d) Picture of the compact electrical driver and pulsed laser diode.

RESULTS

Figure 2 shows the velocity signal recorded by the on-chip LDV. Time 0 indicates excitation source emission. As can be seen, the excitation of the laser diode induces a response in the detection system. This is due to electrical and or optical interference from the excitation and detection system. Around 7 to 8 µs after the excitation, a photoacoustic response is detected. From figure 2, it can also be seen, especially for higher concentrations, that another smaller response appears around 7 to 8 µs after the initial photoacoustic response. This is the reflection of the acoustic wave, from the excitation side of the silicone sample, whereby the polarity of the pressure wave has switched, as expected for an acoustic reflection at a solid-air interface. Considering a sound velocity of 1000 µm/µs for silicone [14], and given that the absorption happens mostly on the excitation side of the tube, the time delays match reasonably well with the propagation distances. Small differences can be expected due to the variance in the dimensions of the sample, variance in the speed of sound, and small misalignment of the detection beam.

From figure 2 it can be seen that the lowest concentration where a signal could be measured was for a 0.01% solution. From the absorption spectrum of India ink, it was estimated that the absorption of the solution is around 1.2 cm^{-1}. This is within the physiological absorption range of blood at NIR wavelengths (1-10 cm^{-1}).

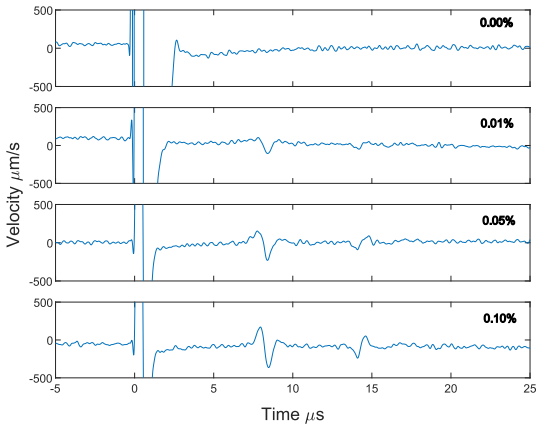


Fig. 2 Photoacoustic response measured by the LDV system from the silicone sample for different black /ndia ink solutions in the channel through the silicon sample inside the sample. Time 0 indicates excitation source emission, and a photoacoustic response is detected around 7 µs after excitation. A second reflection from inside the sample is detected around 14 us.

DISCUSSION

In this paper, we detected photoacoustic signals from a tissue-mimicking sample using a silicon photonics-based LDV and a compact excitation source. The optical chip uses interference to detect the photoacoustic vibrations at the surface of the silicone sample and was able to get a photoacoustic response for a target with an absorption well within the physiological range of blood (as low as 1.2 cm^{-1}) [15]. In the photoacoustic system, a pulsed laser diode was used as a compact excitation source. This paper demonstrates the feasibility of a compact contactless photoacoustic system using silicon photonic LDVs and compact excitation source.

References

[1] L. Wang, B. Thompson, *Photoacoustic Imaging and Spectroscopy*, CRC Press, 2009
[2] P. Beard, *Biomedical Photoacoustic Imaging*, Interface Focus, vol. 1, pp. 602–631, 2011
[3] M. Xu, L. Wang, *Photoacoustic imaging in biomedicine,* Review of Scientific Instruments, vol. 77, 2006
[4] N. Sun, A. Bruce, B. Ning, R. Cao, Y. Wang, F. Zhong, S. M. Peirce, S. Hu, *Photoacoustic microscopy of vascular adaptation and tissue oxygen metabolism during cutaneous wound healing,* Biomedical Optics Express, vol. 13, pp. 2695, 2022
[5] W. Westerveld, W. J. Mahmud-Ulu-Hasan , R. Shnaiderman, V. Ntziachristos, X. Rottenberg, S. Severi, V. Rochus, *Sensitive, small, broadband and scalable optomechanical ultrasound sensor in silicon*, Nature Photonics, vol. 15, pp. 341–345, 2021
[6] R. Manwar, L. Saint-Martin, K. Avanaki, *Couplants in acoustic biosensing systems*, Chemosensors, vol. 10, 2022
[7] T. Sartoretti, E. Sartoretti, et al. *Bacterial contamination of ultrasound probes in different radiological institutions before and after specific hygiene training: do we have a general hygienical problem?*, European Radiology, vol. 27, pp. 4181–4187, 2017
[8] G. Wissmeyer, M. Pleitiz, A. Rosenthal, V. Ntziachristos, *Looking at sound: optoacoustics with all-optical ultrasound detection,* Light: Science and Applications, vol. 7, 2018
[9] S. Y. Siew, B. Li et al., *Review of silicon photonics technology and platform development,* Journal of Lightwave Technology, vol. 39, pp. 4374-4389, 2021
[10] Y. Li, E. Dieussaert, R. Baets, *Miniaturization of laser doppler vibrometers—a review*, Sensors vol. 22, 2022
[11] Y. Li, R. Baets, Homodyne laser doppler vibrometer on silicon-on-insulator with integrated 90 degree optical hybrids, Optics Express, vol. 21, pp. 13342, 2013
[12] M. Singh, W. Xia, Portable and affordable light source-based photoacoustic tomography, Sensors, vol. 20, 2020, pp. 6173, 2020
[13] B. Cox, J. G. Laufer, S. R. Arridge, P. Beard, *Quantitative spectroscopic photoacoustic imaging: a review,* Journal of Biomedical Optics, vol. 17, 2012
[14] D. L. Folds, *Speed of sound and transmission loss in silicone rubbers at ultrasonic frequencies*, Journal of the Acoustical Society of America, vol. 56, pp. 1295-1296, 1974
[15] D. J. Faber, M. Aalders, E. Mik, B. Hooper, M. Van Gemert, T. Van Leeuwen, *Oxygen Saturation-Dependent Absorption and Scattering of Blood,* Physical Review Letters, vol. 92, pp. 028102, 2004

Integrated Microwave Photonic Receiver for Radar Applications

Student paper

Federico Camponeschi[1], Manuel Reza[1], Claudio Porzi[1], Filippo Scotti[2], Luca Di Donato[3], Giovanni Del Greco[3] and Paolo Ghelfi[2]

[1] Scuola Superiore Sant'Anna, Institute of Communication, Information and Perception Technologies, 56124 Pisa, Italy
[2]CNIT, Telecommunications Interuniversity National Consortium, 56124 Pisa, Italy
[3]Leonardo Electronics, RF&Digital Advanced Architectures Engineering, 00131, Roma, Italy
* Federico.camponeschi@santannapisa.it

Two fully integrated and packaged photonic-based RF receivers based on silicon-on-insulator technology have been proposed and experimentally demonstrated. Technological solutions are implemented to enhance the power handling capacity of the PIC. The frequency agility makes these architectures suitable for radar applications.
Keywords: *microwave photonics, photonic integrated circuits, silicon-on-insulator*

INTRODUCTION

The large degree of flexibility and reconfigurability inherent in photonics-based radio frequency (RF) receivers strongly enhances the range of radar applications [1]. Recent advancements in the maturity of the photonic integrated circuits (PIC) technology have enabled the realization of fully integrated microwave photonic receivers [2]. In particular, frequency down-conversion is an important operation that allows the intermediate frequency (IF) signal to be processed after an analog to digital converter (DAC) stage. The operating band of a photonics-based downconverter can be strongly enhanced by making use of an optical frequency comb (OFC). Based on this approach, two down-converter architectures, labelled as "basic" and "advanced", have been designed and implemented in Silicon-On-Insulator (SOI) technology platform. The PIC is designed in order to support large levels of the input power, for mitigating the RF-to-IF convertion loss of the receivers. Both architectures are subsequently fully packaged and experimentally characterized by measuring the convertion loss, spurious-free dynamic range (SFDR) and the RF frequency response.

INTEGRATED PHOTONIC RECEIVER ARCHITECTURE AND DESIGN

The core concept of the proposed architectures relies on the modulation of an OFC by an incoming RF signal. In this way, one of the beatings at a subsequent photodiode will fall within the comb spacing, designed to be less than the typical bandwidth of the ADC. In this work, the optical comb is generated by an integrated Mode-Locked Laser (MLL), which is reported in [3]. In the "basic" architecture, shown in Fig. 1(a), the comb is modulated by the RF signal from the antenna by means of a dual-drive travelling wave electrode Mach-Zehnder modulator (DDMZM) realized using high-speed pn-junction phase shifters. To maximize the modulator extinction ratio (ER), limited by the deviation of the input multi-mode interference (MMI) splitter from the ideal 50/50 splitting ratio, a variable optical splitter (VOS), implemented as a balanced Mach-Zehnder Interferometer (MZI), is used at the modulator input. A large ER is indeed reflected in an improved dynamic range of the receiver. After modulation, several frequency replicas of the input RF signal for each comb line are created in the optical domain. The two out-of-phase modulator outputs are sent to a SiGe balanced photodetector (BPD), where the beating process between the input signal sidebands with the MLL lines generates a down-converted version of the RF input signal at an IF. Using balanced detection maximizes the PIC output RF power while providing large common noise rejection. One of the shortcomings of this basic architecture, while simple and effective, is that the signal bandwidth is limited to half the MLL frequency spacing which in our work is 3.5 GHz. Additionally, in this "basic" scheme an electrical band-pass

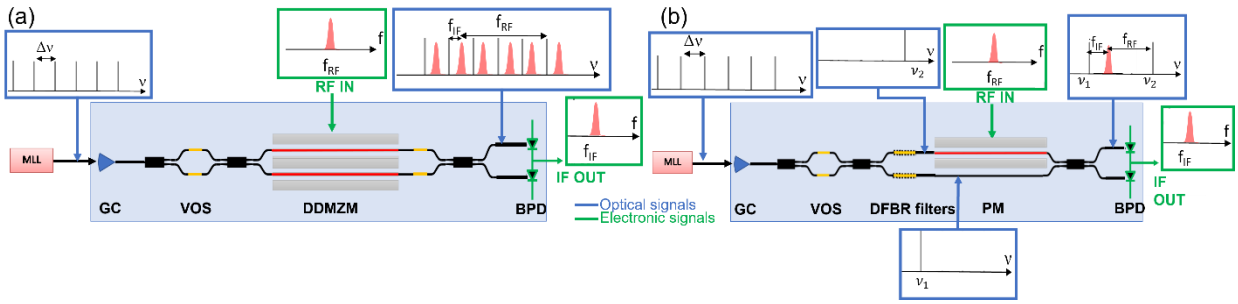


Fig. 1. Schematic layout of the "basic" (a) and "advanced" (b) architectures.

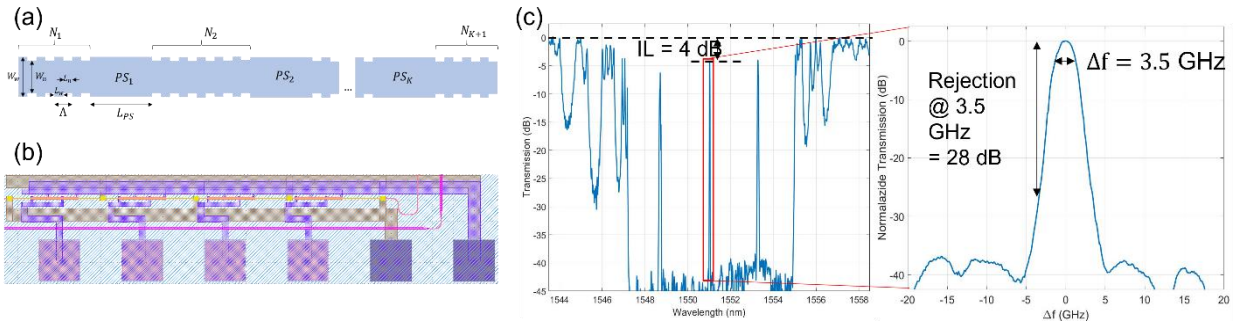


Fig. 2. DFBR optical filter structure (a), mask layout (b) and transfer function (c).

filter (BPF) is required after the BPD to select the desired IF frequency. The "advanced" architecture, illustrated in Fig. 1(b), proposes to overcome such limitations by introducing two optical BPFs which select and separate two different MLL modes. One of the selected tone is subsequently modulated by the RF signal through a phase modulator (PM). At the BPD, the beating between the unmodulated MLL line, that acts as the local oscillator (LO), and the modulated RF signal generates the IF frequency, removing the need of an electrical BPF. Selecting a line within an optical frequency comb with a 3.5 GHz frequency spacing needs filters with very stringent requirements. In this work, 4th-order distributed feedback resonator (DFBR) optical filters are implemented by placing four phase sections (PS) between five sidewall-corrugated waveguide Bragg grating mirrors, as shown in Fig. 2(a). Because of the extremely small fractional bandwidth, active tuning of the PSs through local micro-heaters is required to align the multiple resonances [4]. In addition, the two filters central frequencies need to be centered to an exact frequency difference, so that an additional active tuning mechanism is required, and a top metal heater has been deposited over the whole structures. This type of filters presents a very compact footprint and can achieve very large stopbands (tens of nm) with extremely narrow passband widths. In particular, the filter implemented in this realization has a 3.5 GHz 3-dB bandwidth and a 28 dB rejection measured at 3.5 GHz far from the center of the passband, as shown in Fig. 2(c). For both implementations, the MLL source is coupled to the PIC through a fiber grating coupler. Because increasing optical power is reflected into a decrease of the conversion loss, defined as the ratio between the RF input power and the IF output power, the PIC has been designed to support high optical intensities without triggering the two-photon absorption (TPA) by defining shallow-etch waveguides instead of strip waveguides The VOSs are also placed immediately after the input grating couplers in order to split the optical power before TPA loss accumulate.

EXPERIMENTAL CHARACTERIZATION

The down-converter PIC module of Fig. 3(a) has then been packaged in a lab-sytle evaluation board, including the gluing of the fiber array, the wire-bonding of the PIC on the PCB, the temperature stabilization by means of a Peltier cell, as shown in Fig. 3(b). The receiver demonstrator has then been implemented, interfacing the down-converter module with the external optical and RF components and instruments. The "basic" architecture has been characterized by performing a two-tone analysis for spurious free dynamic range (SFDR) evaluation, i.e. system linearity, as shown in Fig. 4(a). The RF-to-IF conversion loss turns out to be 48 dB with a SFDR of 79.4 dB*Hz$^{2/3}$. The conversion loss value is in line with state-of-the-art values of microwave photonic transceivers in SOI and is lower than the value obtained in the implementation reported in [5]. Moreover, the frequency response of the down-converter has been tested. In Fig. 4(b) the RF signal frequency ranges from ~ 0.75 GHz to ~ 20 GHz with a step which keeps the IF signal frequency fixed. The behavior of the output power mostly depends on frequency response of the wire-bondings which connect the DDMZM electrodes to the PCB: the power is decreased by 10 dB in the frequency range considered. The IF bandwidth is half the MLL repetition rate. In our characterization of the "advanced" architecture, the two optical filters have been centered in correspondence of two comb lines spaced by 10.5 GHz, as illustrated in Fig. 5(a). In this condition, the measured RF-to-IF conversion loss is 84 dB.

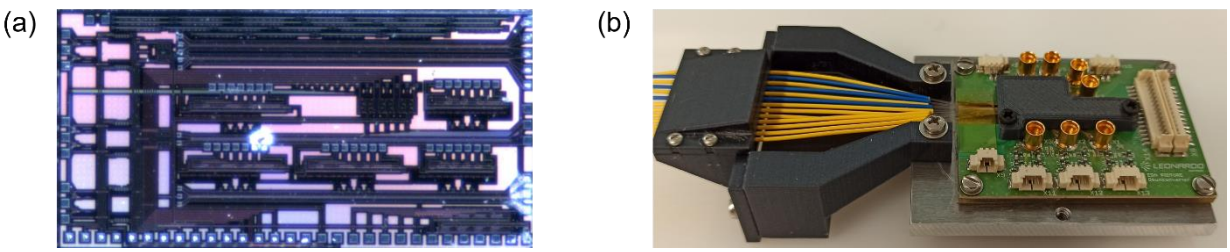


Fig. 3. Down-converter bare PIC picture (a) and packaged PIC (b).

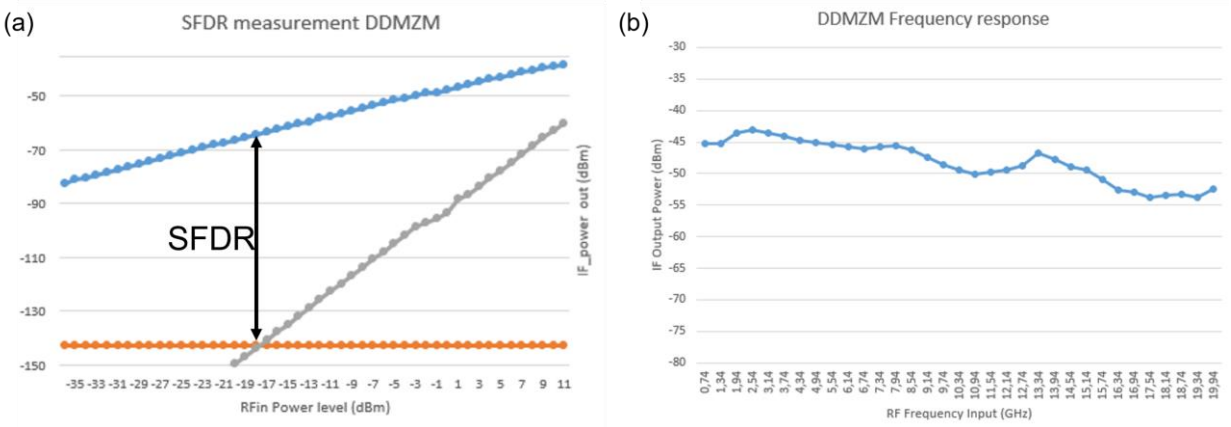


Fig. 4. "Basic" architecture two tone test (a) and RF response (b).

This high loss has been ascribed to the filters which present an insertion loss of ~5 dB and which filter out most of the power coming from the MLL. The RF response, showed in Fig. 5(b), has been observed measuring the conversion loss as the RF frequency varies from 8 to 13 GHz. As the RF signal frequency increases, the conversion loss decreases due to the frequency dependence of the PM. The frequency flexibility demonstrated by both architectures makes them suitable for radar applications. Furthermore, the "advanced" architecture is also suitable for applications where the input signal frequency is unknown, such as defense and multi-protocol communication.

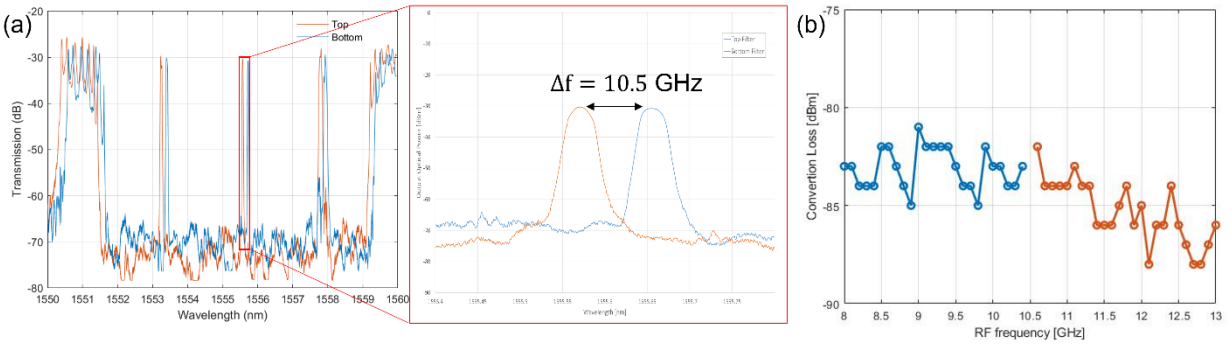


Fig. 5. Transfer function of the two filters (a), "advanced" architecture RF response (b).

DISCUSSION

In this paper, two fully integrated photonic RF receivers have been proposed and experimentally demonstrated. The frequency flexibility exhibited by such architectures makes them suitable for radar applications. The PIC design aims at reducing the RF-to-IF convertion loss exploiting waveguides more resilient to TPA and BPD. The "advanced" architecture is based on two very compact DFBR filters which present a narrow passband of few GHz. In future implementations, III-V/SOI hybrid integrated architectures with semiconductor optical amplifiers (SOAs) on the silicon chip may be considered to minimize the RF-to-IF conversion loss.

Acknowledgement: The authors thank the European Defense Agency (EDA) for the support to this work in the context of the project entitled "Photonic integrated circuits for multiband RF transceiver in arrayed systems (PICTURE)" funded by France and Italy and coordinated by Leonardo S.p.a. in the frame of the Project n° B-1487-IAP1-GP of the European Defense Agency.

References

[1] P. Ghelfi *et al.*, *"A fully photonics-based coherent radar system"*, Nature, vol. 507, pp. 341-345, 2014
[2] D. Marpaung *et al.*, *"Integrated microwave photonics"*, Nature Photonics, vol. 13, pp. 80-90, 2019
[3] Y. Ibrahimi *et al.*, *"Low FSR Mode Locked Laser Based on InP-Si_3N_4 Hybrid Integration"*, Journal of Lightwave Technology, vol. 39, no. 24, pp. 7573-7580, 2021
[4] C. Porzi *et al.*, *"Silicon Photonics High-Order Distributed Feedback Resonator Filters"*, IEEE Journal of Quantum Electronics, vol. 56, no. 1, 2020
[5] F. Falconi *et al.*, *"A Combined Radar & Lidar System Based on Integrated Photonics in Silicon-on-Insulator"*, Journal of Lightwave Technology, vol. 39, no. 1, pp. 17-23, 2021

Automatic mitigation of tilt and phase-front distortions in multichannel chip-to-chip free-space optical links

(Student paper)

SeyedMohammad SeyedinNavadeh[1], Maziyar Milanizadeh[1], Francesco Zanetto[1], Marc Sorel[2,3], Giorgio Ferrari[1], David A.B. Miller[4], Andrea Melloni[1], Francesco Morichetti[1]

[1] Department of Electronics, Information and Bioengineering, Politecnico di Milano, via Ponzio 34/5, 20133, Milano, Italy
[2] School of Engineering University of Glasgow, Glasgow, G12 8QQ, UK
[3] TeCIP Institute, Scuola Superiore Sant'Anna, 56124 Pisa, Italy
[4] Ginzton Laboratory, Stanford University, Spilker Building, Stanford, CA 94305, USA
*corresponding author e-mail: francesco.morichetti@polimi.it

We demonstrate automatic compensation of tilt and phase front distortions in a multichannel chip-to-chip free-space optical (FSO) link. The system exploits a pair of integrated photonic processors made of self-configuring meshes of Mach-Zehnder Interferometers (MZIs) that automatically find the best orthogonal communication channels with more than 30 dB mutual isolation.

Keywords: *Programmable Photonic Circuits, Free-Space Optics, Orthogonal Communication Channels, Silicon Photonics*

INTRODUCTION

Free-space optics (FSO) communication links are subjected to several challenges, including pointing errors and scintillation due to turbulent atmosphere [1]. A solution to mitigate these impairments makes use of adaptive optical systems that can be dynamically controlled to compensate for time-varying conditions of the link [2]. Integrated programmable photonic processors consisting of generic reconfigurable architectures are a promising approach to implement adaptive optics on a chip. Recently, we demonstrated that a silicon photonic mesh of Mach-Zehnder Interferometers (MZIs) controlling an array of optical antennas can be used both as an adaptive transmitter (Tx) to automatically shape and steer FSO beams [3] and as a receiver (Rx) to separate multiple spatially overlapped FSO beams [4]. A pair of self-configuring MZI meshes can automatically establish chip-to-chip FSO links on multiple beams by finding the best orthogonal communication channels [5].

In this work, we report on a chip-to-chip system that can provide automatic compensation of tilt and phase front distortions in multichannel FSO links. Tilt-tolerant and phase-distortion robust communication is demonstrated in a two-mode FSO system with more than 30 dB mutual isolation even in the presence of realistic impairments.

MULTI-CHANNEL CHIP-TO-CHIP FREE SPACE OPTICAL LINK

Figure 1(a) shows a microphotograph of the photonic integrated circuit (PIC) employed in this work. It is realized in a standard Si-Photonics platform (AMF foundry) with 220-nm-wide waveguides and is designed to work around a wavelength of $\lambda = 1.55$ μm. It consists of a waveguide mesh of thermally tuneable MZIs with a 9x2 diagonal architecture [6], implementing a programmable photonic processor. At one end of the photonic processor (left side shown in Fig. 1a), 9 single-mode waveguides are connected to a 9-element optical antenna array, configured in a 3x3 square with spacing of $d = 50$ μm (Fig. 1a$_3$). The elements of the array are realized by surface grating couplers (GCs) with $\approx 9° \times 5°$ beamwidth and $10°$ of tilt of the out-of-plane radiated light. At the other end of the chip (right side), 2 single-mode waveguides, denoted with IO_j , $j = \{1,2\}$, are used for input/output fiber coupling.

A pair of photonic chips are employed as transmitter (Tx) and receiver (Rx), respectively, as shown in Fig. 1(b). For deflecting the vertically emitting beam of the array of GCs, a tilted mirror is placed on top of both chips (not shown in the schematic). The setup includes two biconvex lenses in Fourier configuration for collimation/focusing of the beam from the PICs. A spatial light modulator (SLM) is inserted in the path between the two chips, which is used to introduce arbitrary distortions of the phase front of the FSO beams to dynamically emulate pointing errors and time-varying obstacles in the link. A photograph of the FSO chip-to-chip link implemented in the lab setup is shown in Fig. 1(c), with a zoom of the SLM in the inset of the figure. Each photonic chip is mounted on a printed circuit board and a custom-designed electronic board is used for automatically controlling the working point of each photonic chip through integrated thermal tuners. The self-configuring algorithm is based on the maximization of the optical power at IO_j ports and is implemented by using different dithering frequencies for each MZI [6].

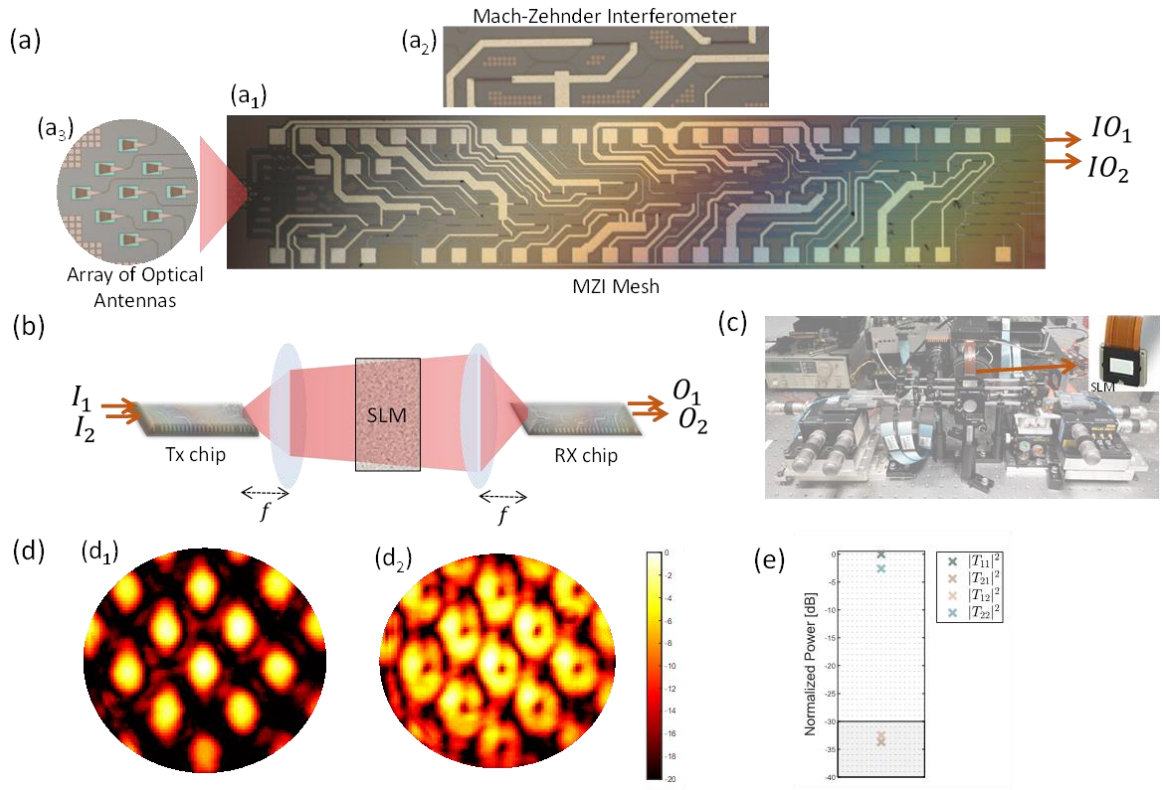


Fig. 1. Photograph of the photonic chip integrating a programmable processor made of a two-diagonal mesh of thermally tuneable MZIs (a_2) connected to an 3x3 array of optical antennas (grating couplers, a_3); (b) Schematic and (c) photograph of the chip-to-chip experimental setup integrating an SLM for arbitrary manipulation of FSO beams; (d) Camera-view measurement of the shape of the 1st and 2nd modes that are automatically obtained by tuning the 1st and 2nd rows of the two processors (SLM off, no intentional phase perturbation). (e) Received power (normalized to the 1st channel) of the 1st and 2nd mode, together with the mutual residual crosstalk.

The photonic processor at the Tx/Rx side can self-configure to find the pair of most strongly-coupled FSO channels. To this aim, the MZIs of each diagonal of the mesh are sequentially tuned to coherently combine the contributions of the beam sampled by the array of GCs [4] in such a way that the Tx and Rx meshes can adapt to the status of the link for finding two orthogonal channels. Figures 1(d_1) and (d_2) shows the shape of the beams that are automatically obtained for the 1st and 2nd modes, when no intentional phase perturbation is introduced in the link (SLM off) [7]. The multiple replicas in the pattern are due to the fact that the spacing between array elements is larger than half wavelength. The diagram in Fig. 1(e) shows the normalized power for the two channels ($|T_{11}|^2, |T_{22}|^2$) as well as the crosstalk between them ($|T_{21}|^2, |T_{12}|^2$) (power levels are normalized to that of the 1st channel). The coupling efficiency of the 2nd channel is slightly lower, but the mutual crosstalk between two channels is less than < -30 dB.

AUTOMATIC MITIGATION OF TILT AND PHASE FRONT DISTORTION

As a first experiment, the SLM is used to intentionally introduce a tilt to the beam propagating between the two chips (Fig. 2a). This effect is achieved by generating a linear phase change across the SLM to induce a maximum horizontal tilt of 10 mrad, which causes focusing error on the aperture of the Rx chip. The reduction of the coupling efficiency versus the tilt angle is shown by the pink curve ($|T_{11}|^2$) in Fig. 2(a_2) for the fundamental FSO mode (1st channel). A large sensitivity to tiny misalignments is observed and up to 25 dB loss are induced by a tilt angle as low as 2.5 mrad if no active compensation is performed (processors control switched off). The oscillating behaviour of the received power versus the tilt angle is due to the presence of grating lobes in the far field of the beams, which can provide coupling between different diffraction orders. The experiment is then repeated when the electronic controller of the two processors is activated to dynamically compensate for the tilt of the beam. As shown by the green curve ($|\bar{T}_{11}|^2$) in Fig. 2(a_2), active compensation can recover more than > 20 dB power loss due to pointing errors. The residual decrease in the coupling efficiency is due to the limited field of view of the beam which is radiated by the GCs and collimated by the lens system. Figures 2(a_3) and 2(a_4) show the camera view of the measured far-field radiated by the Tx chip compensating for the tilt induced by the SLM.

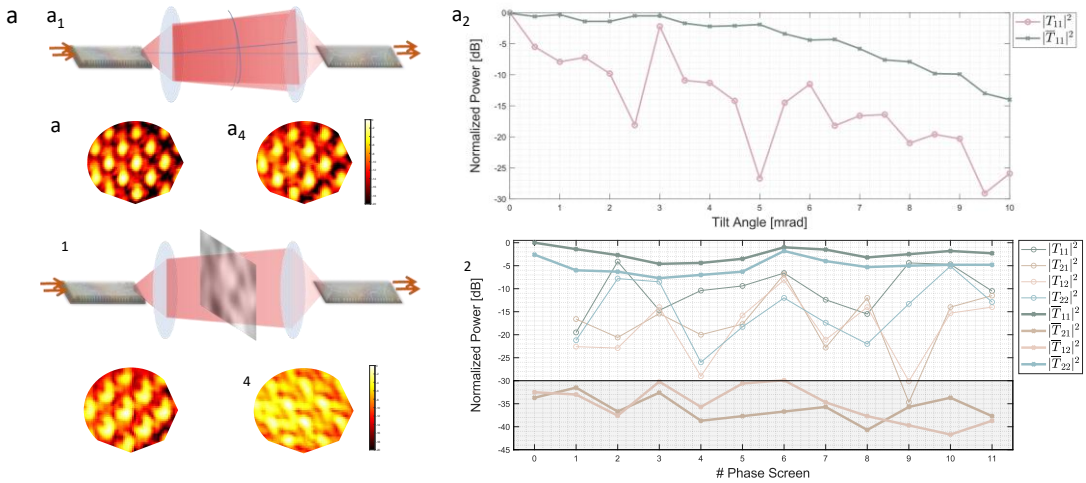


Fig. 2. Automated impairment mitigation in chip-to-chip FSO links. (a_1) Compensation of pointing errors generated by a linear phase profile in the SLM; (a_2) Normalized received power vs. tilt angle when the active control of the photonic processors is OFF (pink curve) and when is activated (green curve); (a_3 - a_4) Measured intensity profiles of the far-field beam radiated by the TX chip compensating for the tilt induced by the SLM; (b_1) Compensation of arbitrary phase front distortions induced by the SLM; (b_2) Normalized received power of the 1st and 2nd mode and mutual crosstalk for eleven different phase front perturbations when active control of the photonic processors is OFF (thin curves) and when is activated (thick curves); (b_3 -b_4) Measured intensity profiles of the far-field (1st mode) radiated by the TX chip compensating for phase distortions induced by the SLM.

Random profiles in the SLM were generated to introduce arbitrary perturbations in the phase front of the FSO beams (Fig. 2b_1). The diagram in Fig. 2(b_2) shows the normalized received power of the 1st and 2nd mode, and the mutual crosstalk between them, for eleven different configurations of the SLM when the photonic processors are off (thin curves, $|T_{ij}|^2, i,j = \{1,2\}$) and when they are activated (thick curves, $|\bar{T}_{ij}|^2, i,j = \{1,2\}$) for compensating phase perturbations. Perturbations in the phase profile of the FSO beams cause both severe losses in the received power of the channels (up to 25 dB) and a strong reduction of the mutual crosstalk. Results show that the dynamic control of the two processors largely recovers the power levels observed in the absence of perturbations [see Fig. 1(e)]. Figures 2(b_3) and 2(b_4) shows some examples of the far field beams radiated by the Tx chip to perform compensation of phase front distortion.

CONCLUSION

We demonstrated automatic compensation of tilt and phase front distortions in a multichannel chip-to-chip communication system emulating realistic conditions of FSO links. The system exploits a pair of programmable processors that self-configure to find the best orthogonal modes and more than 30 dB mutual isolation is achieved on pairs of spatially overlapped channels even in the presence of time-varying impairments. The system can be scaled to a larger number of orthogonal channels by using integrated processors with more MZI rows.

Acknowledgements: This work was supported by the European Commission through the H2020 project SuperPixels (grant 829116), and by the Air Force Office of Scientific Research (AFOSR) under award number FA9550-17-1-0002. Part of this work was carried out at Polifab, Politecnico di Milano, Milan, Italy.

References

[1] A. Trichili, M. A. Cox, B. S. Ooi, and M. Alouini, "Roadmap to free space optics," J. Opt. Soc. Am. B 37, A184-A201 (2020)
[2] M. Li, M. Cvijetic, Y. Takashima, and Z. Yu, "Evaluation of channel capacities of OAM-based FSO link with real-time wavefront correction by adaptive optics," Opt. Express 22, 31337-31346 (2014)
[3] M. Milanizadeh, F. Toso, G. Ferrari, et al. "Coherent self-control of free-space optical beams with integrated silicon photonic meshes," Photon. Res. 9, 2196-2204 (2021)
[4] M. Milanizadeh, S. SeyedinNavadeh, F. Zanetto, et al. Separating arbitrary free-space beams with an integrated photonic processor. Light Sci Appl 11, 197 (2022).
[5] D. A. B. Miller, "Establishing Optimal Wave Communication Channels Automatically," Journal of Lightwave Technology, vol. 31, no. 24, pp. 3987-3994, 2013.
[6] F. Zanetto, V. Grimaldi, F. Toso, et al., "Dithering-based real-time control of cascaded silicon photonic devices by means of non-invasive detectors," IET Optoelectron., 15: 111-120, 2021
[7] S. SeyedinNavadeh, M. Milanizadeh, F. Zanetto, et al., "Multi-channel free-space optical communication between self-configuring silicon photonics meshes", European Conference on Integrated Optics (ECIO) 2022, Paper F.E.2

Third-Order Intermodulation Distortion Suppression Analysis for Dual-Parallel Mach-Zehnder Modulator Using Optical Carrier Band Processing

Cristina Catalá-Lahoz[1], Luis Torrijos-Morán[1], Daniel Pérez-López[2], Li Xu[3], Wang Tianxiang[3] and Diego Pérez-Galacho[1*]

[1]Photonics Research Labs, iTEAM Research Institute, Universitat Politècnica de València, Valencia, 46022, Spain
[2]iPronics Programmable Photonics S.L., Av. de Blasco Ibáñez, 25, Valencia, 46010, Spain
[3]Central Research Institute, Huawei Co. LTD.
[*]diepega@upv.es

Third-order distortion in microwave photonic links using dual-parallel Mach-Zehnder modulators is theoretically studied for linearization. Four-tone test is considered in the mathematical derivation and results show that linearization is feasible under a proper tuning of DC operation voltages of the modulator and processing of the optical spectrum. Simulations are also provided showing a 34 dBm suppression at the third-order intermodulation products.
Keywords: *Electro-optic modulators, Linearization, Microwave Photonics, Optics.*

INTRODUCTION

Microwave photonic links (MPL) offer several advantages compared to conventional electrical schemes such as broadband operation, lightweight, immunity to electromagnetic interference and low loss. This fact makes them an interesting option for different radio frequency (RF) applications as in the case of antenna remoting, radio-over-fiber, or wireless communications, among others [1]. In this context, the main limitation factor of MPL usually comes from the electro-optic modulator that introduces nonlinearity in the rest of the link. Third-order intermodulation distortion (IMD3) is the most challenging nonlinearity produced as it lies close to the fundamental tones and cannot be easily filtered [2]. To improve the linearity of modulators in MPL, the modulated optical spectrum is processed to compensate the distortion terms produced by the beating at the PD [3],[4]. The linearization of more complex modulation schemes based on dual-parallel MZM (DPMZM) was also investigated by adjusting the power of the electrical drive signals, the optical input power splitting ratios, optimizing the operation points in single-drive configurations or shifting the electrical phase of the RF inputs [5]–[8]. To date, all these DPMZM linearization approaches are based either on RF predistortion techniques or using one of the parallel MZM to improve the linearity of the complete structure. An exhaustive mathematical description of the DPMZM linearization is still to be investigated. In this paper, we show a complete analysis of the distortion appearing in DPMZM when two RF signals (each one containing two different tones) are applied in both the upper and lower MZM of the DPMZM, so that a four-tone test is considered. Theoretical results and simulations are provided, describing the cancelation of all the IMD3 components that are produced at the PD.

RESULTS

The proposed MPL is depicted in Fig. 1a. It consists of a DPMZM in push-pull configuration (that is a phase shift of π between driving RF signals at each MZM arm). As it is shown, the optical carrier is therefore modulated by two different RF signals: RF_1 ($\omega_{1,2}$) and RF_2 ($\omega_{3,4}$) for the lower and upper MZM, respectively, so that we consider a four-tone test.

The field after modulation can be expressed as follows

$$E_{out}(t) \propto e^{j\phi_3}\left[e^{j\phi_1}S_1(m) + S_1(-m)\right] + \left[e^{j\phi_2}S_2(m) + S_2(-m)\right]. \quad (1)$$

Where $S_{1,2}(m)$ expressions correspond to each individual MZM and are defined in terms of Bessel functions as

$$S_1(m) = \sum_{n=-\infty}^{+\infty} J_n(m)e^{jn\omega_1 t} \sum_{k=-\infty}^{+\infty} J_k(m)e^{jk\omega_2 t}, \quad (2)$$

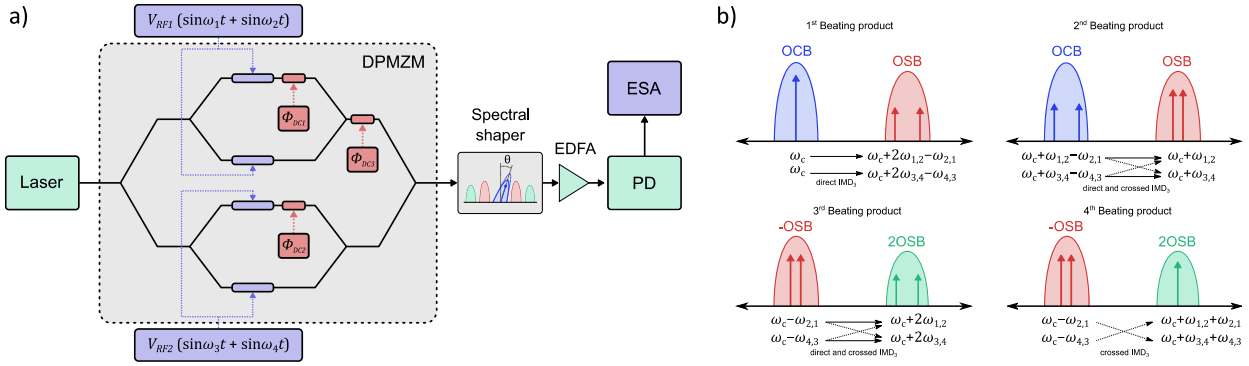


Fig. 1. a) MPL considered including the DPMZM under a four-tone test, the laser, optical processor for the linearization, erbium-doped fiber amplifier (EDFA), photodetector (PD) and electronic spectrum analyzer (ESA). b) Representation of the optical modulated spectrum and the different beating products that produce IMD3.

$$S_2(m) = \sum_{n=-\infty}^{+\infty} J_n(m) e^{jn\omega_3 t} \sum_{k=-\infty}^{+\infty} J_k(m) e^{jk\omega_4 t}. \tag{3}$$

Up to four beating products (BPs) are obtained, producing IMD_3 at the photodiode, see Fig. 1b. The first one produces direct IMD_3 terms (that only depend on one of the RF frequencies, —e.g., $2\omega_1 - \omega_2$). The second BP in turn produces direct IMD_3 terms and crossed IMD_3 terms that depend on both RF_1 ($\omega_{1,2}$) and RF_2 ($\omega_{3,4}$) frequencies —e.g., $\omega_1 - \omega_2 + \omega_3$. The third BP involves both direct and crossed IMD_3 terms —e.g., $2\omega_1 - \omega_2$ and $2\omega_1 - \omega_3$. Finally, the fourth BP produces only crossed terms —e.g., $\omega_1 + \omega_2 - \omega_3$. After PD, we can classify the 8 contributors for IMD_3 terms depending on the BP that produce them as follows

$$\begin{aligned} I_{PD} = R_{PD}|E_p|^2 = {} & I_{3,1}\sin\left((2\omega_{1,2} - \omega_{2,1})t\right) + I_{3,2}\sin\left((2\omega_{3,4} - \omega_{4,3})t\right) + \\ & I_{3,3}\sin\left((2\omega_{1,1,2,2} - \omega_{3,4,3,4})t\right) + I_{3,4}\sin\left((2\omega_{3,3,4,4} - \omega_{1,2,1,2})t\right) + \\ & I_{3,5}\sin\left((\omega_{3,3,4,4} - \omega_{4,4,3,3} + \omega_{1,2,1,2})t\right) + I_{3,6}\sin\left((\omega_{1,1,2,2} - \omega_{2,2,1,1} + \omega_{3,4,3,4})t\right) + \\ & I_{3,7}\sin\left((\omega_{1,1} + \omega_{2,2} - \omega_{3,4})t\right) + I_{3,8}\sin\left((\omega_{3,3} + \omega_{4,4} - \omega_{1,2})t\right), \end{aligned} \tag{4}$$

where R_{PD} is the responsivity of the PD, $I_{3,1}$, $I_{3,2}$ are direct IMD_3, and $I_{3,3}$, $I_{3,4}$, $I_{3,5}$, $I_{3,6}$, $I_{3,7}$ and $I_{3,8}$ are crossed IMD_3 terms, previously explained.

By multiplying Eq. (1) by its conjugate we obtain the current at the PD so that we can relate it to all I_3 terms using Eq. (4). For the first and second direct IMD_3 coefficient $I_{3,1}$ and $I_{3,2}$, these yields

$$I_{3,1} = 4R_{PD}P_i(k - k^2) \cdot \left[\frac{1}{2}\beta\sin\phi_1 + \Phi_1 A J_0^2 J_1 J_2\right] \tag{5}$$

$$I_{3,2} = 4R_{PD}P_i(k - k^2) \cdot \left[\frac{1}{2}\beta\sin\phi_2 - \Phi_2 A J_0^2 J_1 J_2\right] \tag{6}$$

whence β, Φ_1 and Φ_2 are defined as

$$\beta = A J_0^2 J_1 J_2 \cos\theta + A J_0 J_1^3 \cos\theta + J_0^2 J_1 J_2, \tag{7}$$

$$\Phi_1 = \sin(\phi_1 - \phi_2 + \phi_3 - \theta) + \sin(\phi_1 + \phi_3 - \theta) - \sin(-\phi_2 + \phi_3 - \theta) - \sin(\phi_3 - \theta), \tag{8}$$

$$\Phi_2 = \sin(\phi_1 - \phi_2 + \phi_3 - \theta) - \sin(\phi_1 + \phi_3 + \theta) + \sin(-\phi_2 + \phi_3 + \theta) - \sin(\phi_3 + \theta). \tag{9}$$

where A and θ is the amplitude suppression and phase shift imposed to the OCB by the spectral shaper, respectively. On the other hand, assuming $\phi_1 = -\phi_2$ and no OCB processing —i.e., $A = 1$ and $\theta = 0$, all crossed

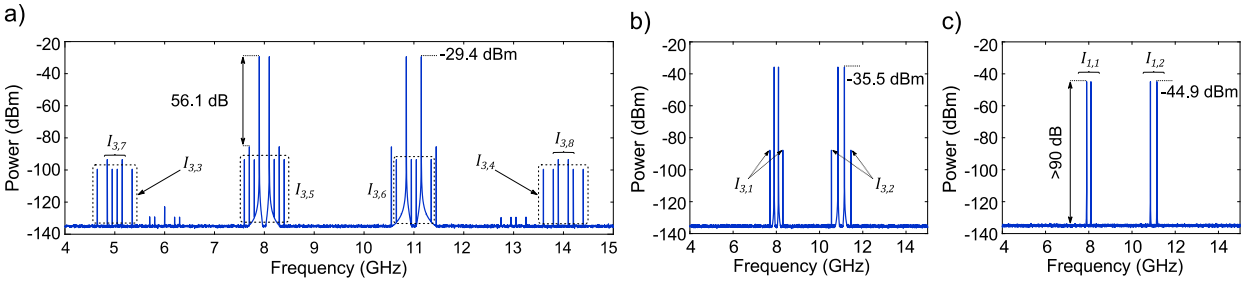


Fig. 2. a) Simulated MPL RF spectrum without linearization tuning. b) RF spectrum with the cancelation of crossed IMD₃ terms . c) RF spectrum of the complete linearization configuration including OCB processing.

IMD₃ terms ($I_{3,3}$, $I_{3,4}$, $I_{3,5}$, $I_{3,6}$, $I_{3,7}$, $I_{3,8}$) are directly proportional to the phase shifts applied by the DC voltages, and can be described by the following expression

$$I_{3,C} \propto \sin(2\phi_1 + \phi_3) - \sin(\phi_3). \tag{10}$$

To cancel crossed IMD₃ terms, we must first equal Eq. (8) to zero. Fixing $\phi_3 = 2\phi_1$ the equation is solved for $\phi_3 = \pi$, thus $\phi_1 = \pi/2$ and $\phi_2 = -\pi/2$. Now, to calculate θ, we introduce these values in Φ_1 and Φ_2 expressions and solve the system of equations, which yields $\theta = \pi$. Finally, to fully cancel direct IMD₃ terms, we solve β in Eq. (7) for this value of θ applying Taylor series expansion to the third order in m (small signal approximation). This condition if fulfilled when an amplitude suppression of $A = 1/3$ is applied to the OCB, so that direct IMD₃ contributors in Eq. (5) and (6) are theoretically canceled. Figure 2a shows the simulated RF spectrum without linearization, —i.e., the bias voltages of the DPMZM $\phi_1 = \phi_2 = \pi/2$, $\phi_3 = 0$ and no OCB processing, $\theta = 0$ and $A = 1$. The resulting RF spectrum contains all the IMD₃ theoretically described including both direct and crossed terms. A fundamental to IMD₃ ratio (FIR) of 56.1 dBm is obtained at this stage. Figure 2b contains the RF spectrum with only the DC bias voltages adjusted to suppress IMD₃ crossed terms in Eq. (8), —i.e., $\phi_1 = \pi/2, \phi_2 = -\pi/2, \phi_3 = \pi$ and no OCB processing. Only direct IMD₃ are obtained in the spectrum. Figure 2c depicts the linearized RF spectrum with the theoretical values obtained before: $\phi_1 = \frac{\pi}{2}, \phi_2 = -\frac{\pi}{2}, \phi_3 = \pi$, an attenuation of $A = 1/3$ and phase of $\theta = \pi$ imposed on the OCB. Simulations show a FIR over 90 dBm, which means an IMD₃ suppression above 33.9 dBm compared to Fig. 2a.

DISCUSSION

In conclusion, OCB processing to linearize a MPL based on a DPMZM is theoretically demonstrated. A four-tone test is considered in the study, which allow us to provide an exhaustive mathematical derivation of all IMD3 terms that are produced in the PD mixing. Simulations show that crossed IMD3 terms can be cancelled out by properly tuning the DC voltages of the modulator, while direct IMD3 terms need from a precise OCB processing to completely linearize the link. Overall, the theoretical description herein presented extends mathematical derivations in previous works to a more complete structure, enabling the modulation of two different RF signals simultaneously, up to 4 frequencies, with complete isolation and no distortion between them. Moreover, the linearization method does not need any extra RF components and other predistortion devices, which allows its integration and development in integrated circuits.

References

[1] J. Capmany and D. Novak, "Microwave photonics combines two worlds," Nat. Photonics **1**, 319–330 (2007).
[2] J. Yao, "Microwave photonics," J. Light. Technol. 27, 314–335 (2009).
[3] Y. Cui, Y. Dai, F. Yin, J. Dai, K. Xu, J. Li and J. Lin, "Intermodulation distortion suppression for intensity-modulated analog fiber-optic link incorporating optical carrier band processing," Opt. Express 21, 23433 (2013).
[4] G. Liu, O. Daulay, Q. Tan, H. Yu and D. Marpaung "Linearized phase modulated microwave photonic link based on integrated ring resonators," Opt. Express 28, 38603 (2020).
[5] Y. Zhou, L. Zhou, M. Wang, Y. Xia, Y. Zhong, X. Li and J. Chen "Linearity characterization of a dual-parallel silicon Mach-Zehnder modulator," IEEE Photonics J. 8, (2016).
[6] S. Kim, W. Liu, Q. Pei, L. R. Dalton and H.R. Fetterman "Nonlinear intermodulation distortion suppression in coherent analog fiber optic link using electro-optic polymeric dual parallel Mach-Zehnder modulator," Opt. Express 19, 7865-7871 (2011).
[7] S. Li, X. Zheng, H. Zhang and B. Zhou "Highly Linear Radio-Over-Fiber System Incorporating a Single-Drive Dual Parallel Mach-Zehnder Modulator," IEEE Photonics Technol. Lett 22, 1775-1777 (2010).
[8] W. Jiang, Q. Tan, W. Qin, D. Liang, X. Li, H. Ma and Z. Zhu "A linearization analog photonic link with high third-order intermodulation distortion suppression based on dual-parallel Mach-Zehnder modulator," IEEE Photonics J. 7, 2015).

Loss engineering of a bimodal waveguide platform for biosensing

Student paper

Samuel M. Hörmann [1, 2, *], Jakob W. Hinum-Wagner [1, 2], Gandolf Feigl [2], Alexander Bergmann [2]

[1] ams-OSRAM AG, Tobelbader Straße 30, 8141 Unterpremstätten, Austria

[2] Institute of Electrical Measurement and Sensor Systems, Graz University of Technology, Inffeldgasse 33/I, 8010 Graz, Austria

[*] samuel.hoermann@ams-osram.com

An advantageous implementation of an integrated photonic biosensor is the bimodal waveguide interferometer. To fully utilize its potential and minimize the limit of detection, it is essential to holistically design its waveguide platform. To this end, we incorporate an ab initio model of the surface-roughness-induced scattering to find a balance between predicted sensitivity and losses for a silicon nitride strip waveguide platform.

Keywords**:** *Bimodal, biosensor, scattering, surface roughness, silicon photonics, silicon nitride*

INTRODUCTION

Point-of-care devices are poised to revolutionize the healthcare sector [1]. Integrated photonic biosensors are seamlessly integrateable into CMOS fabs and thus can be reliably produced at ultra-large scale [2]. Typically, they rely on transducing the refractive index change induced by binding events between the analyte and bioreceptors. To this end, the bioreceptors are immobilized on a waveguide that facilitates the interaction of the guided light and the bioreceptor-analyte-complex in the solution flown around the waveguide. Their limit of detection (LOD) can be in the femto- and attomolar range [1]. Thus, they are ideal to contribute to this revolution in personal medicine and rapid diagnostics, where precision and manufacturability are vital. However, this technology can only fully utilize its potential, if the integrated photonics is holistically designed. Often, only the sensitivity is maximized while the losses are neglected. To minimize the LOD, however, a balance needs to be found between these two parameters. For that purpose, we utilize a recently developed model [3] of the surface-roughness-induced scattering to incorporate the scattering losses into the design of a bimodal waveguide platform (see Fig. 1). This model is based on the volume current method and allows the ab initio calculation of the scattering loss coefficient for a given waveguide's mode and surface roughness autocorrelation.

RESULTS

Using silicon nitride as the waveguide's core material is beneficial in many ways: First and foremost, it is transparent in the visible to near-infrared wavelength range which overlaps with the therapeutic window. Secondly, it has a lower refractive-index contrast leading to lower surface-roughness-induced scattering losses. Finally, it may be deposited monolithically in CMOS fabs [4]. For these reasons, we consider a silicon nitride waveguide platform based on strip waveguides (as in Fig. 1 and Fig. 2).

In a previous analysis, we investigated different forms of the surface roughness' autocorrelation for their descriptive power [5]. We discovered that a kernel of the Matérn class is beneficial over the established exponential kernel. Furthermore, within the scattering model exhibits the degree of anisotropy of the autocorrelation shows a significant impact on the scattering coefficient. Moreover, conflicting evidence regarding the assumption of perfect vertical striations can be found in microscope images of the sidewall roughness [6], [7] and in a previous evaluation of the anisotropy [8]. Hence, we base our calculations on a two-dimensional, anisotropic Matérn 3/2 kernel κ with finite correlation lengths l_y and l_z, which are along the waveguide height and length, resp. (see Fig. 2). This reads

$$\kappa(y,z) = \sigma^2 \left(1 + \frac{\sqrt{3}y}{l_y}\right)\left(1 + \frac{\sqrt{3}y}{l_z}\right) e^{-\sqrt{3}\left(\frac{y}{l_y}+\frac{z}{l_z}\right)} \tag{1}$$

with the surface roughness' standard deviation σ [9]. For the calculations, we also need the spectrum of the z-component, which can be calculated via the Fourier transform [3].

In an integrated, refractometric biosensor each mode's propagation coefficient β has a sensitivity S per waveguide length to a homogeneous change in the relative permittivity ε_p in a subsection A of the waveguide cross-section described by

$$S = \frac{\partial \beta}{\partial \varepsilon_p} = \frac{\varepsilon_0 \omega}{4\,P} \int_A \left\| \vec{E}(x,y) \right\|^2 dx\, dy \tag{2}$$

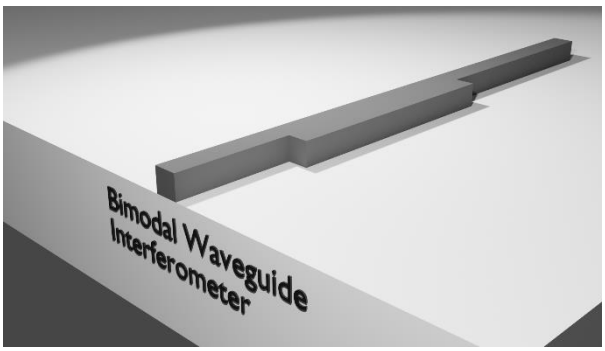


Fig. 1. Sketch of a bimodal waveguide interferometer based on strip waveguides with a vertical step junction.

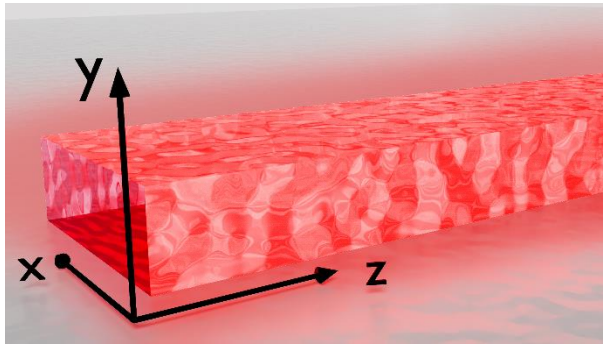


Fig. 2. Stylized image of surface-roughness-induced scattering. Taken from [3].

where $\vec{E}(x,y)$ is the mode's electric field and P is its power [10]. In a bimodal waveguide interferometer, the relevant parameter is the difference of the two modes' sensitivity $S = |S_1 - S_2|$ in the bimodal section. Rather than the sensitivity difference, however, the sensitivity difference over the sum of the loss coefficients is our figure of merit (FOM), since it determines the maximum slope of the spectral interference pattern:

$$FOM = \frac{|S_1 - S_2|}{\alpha_1 + \alpha_2} \tag{3}$$

That is because, lower losses allow for a longer optimal length of the bimodal section, which evaluates to $(\alpha_1 + \alpha_2)^{-1}$, causing higher total sensitivity achievable with the platform. We consider only the sidewall-roughness-induced scattering, since this is the primary loss contributor in silicon photonics.

The sidewall roughness' parameters were evaluated from AFM measurements of the sidewall of a corresponding fabricated integrated photonic system. The deposition and measurement techniques will be discussed in more detail in a following publication. According to the above-stated framework, we used HDP CVD to deposit the silicon oxide layer on top of a silicon substrate. To structure the silicon nitride waveguide core, LPCVD with DUV and reactive ion etching was utilized. The system was not cladded, to enable the interaction of the modes with the sensing medium and to retain access to the sidewalls for the AFM measurements. The surface roughness' parameters are characteristic of the fabrication process and ideally irrespective of the silicon photonic layout. The best fitting parameters of the Matérn kernel for this fabrication process are: $\sigma = 2.2$ nm, $l_z = 82$ nm, $l_y = 68$ nm.

We compute the waveguide's modes in Ansys Lumerical (version: 2022 R1, module: MODE, solver: Finite Difference Eigenmode (FDE)). Using the above formulae, we can calculate the predicted sensitivity, the scattering losses, and FOM for each combination of width and height. By definition, the parameter space of the bimodal system is limited by the necessity to have exactly two modes of the same polarization. Further, we set the wavelength to 850 nm and we used the refractive indices: $n_{SiN} = 1.9$, $n_{silica} = 1.455$, and $n_{water} = 1.325$. As an additional restriction, we consider only transverse-electric-like (TE) modes.

The resulting sensitivity to refractive index changes in the cladding (in our case the water over the waveguide system) per unit length is depicted in Fig. 3. We recognize that there is a maximum at low widths and high heights of the waveguide. Hence, higher waveguides have increased interaction with the vicinity. This is caused by the higher intensity of the TE-like modes at the sides of the waveguide. However, the more impactful FOM shows its maximum at high widths and low heights. This disparity illustrates the importance of the holistic approach. Moreover, we recognize that there is approximately a factor of two between the best and worst platform design, as predicted by the above model.

DISCUSSION

An important circumstance that should be considered for the implementation of the waveguide platform in actual structures is that the FOM from eq. (3) and Fig. 4 is proportional to the slope of the spectral interference at the inflection point, but only if the length of the bimodal section equals the optimal $(\alpha_1 + \alpha_2)^{-1}$. For the configuration with a height of 200 nm and a width of 1200 nm, this evaluates to 111 mm. That is one to two orders of magnitudes higher than typically used interferometric structures [1], [2]. Naturally, the longer the sensing structure, the more area it will occupy on the die and the higher the costs. If another length is fabricated, the actual length needs to be used instead in eq. (3), which reduces the scattering's impact and increases the importance of high sensitivity.

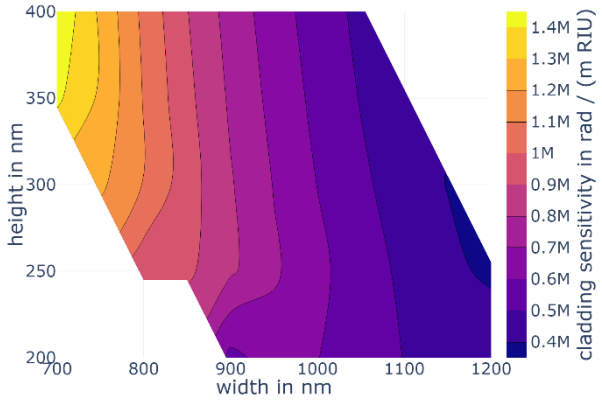


Fig. 3. Sensitivity per unit length of the bimodal waveguide platform operated in the TE-like mode at a wavelength of 850 nm to refractive index changes in its cladding.

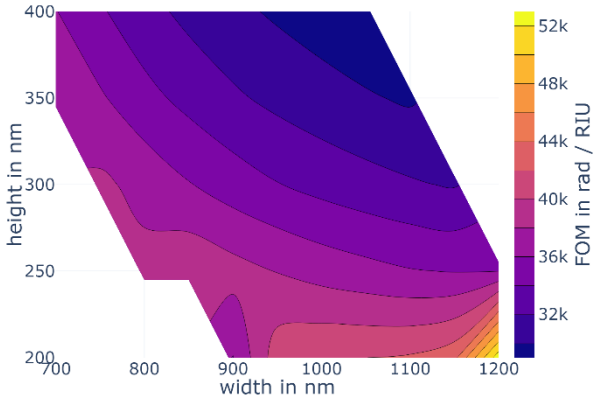


Fig. 4. FOM of the bimodal waveguide platform operated in the TE-like mode at a wavelength of 850 nm for refractive index sensing.

Finally, we want to stress that real fabrication conditions will lead to non-ideal waveguides. Real waveguides will have sloped sidewalls leading to deformed electric field profiles and subsequently to different sensitivity and losses. Hence, the above predictions will only be valid if the process parameters are adjusted well enough such that the simulated modes tolerably represent the real ones.

CONCLUSION

We saw above that a holistic approach, which includes surface-roughness-induced scattering, drastically changes the design choices for the bimodal waveguide platform of a refractometric biosensor. For an optimal sensing performance of a bimodal waveguide interferometer fabricated within the above parameters, a bimodal section with a low height and high width is predicted to be advantageous. Furthermore, we notice the advantage this scattering model has in being able to directly calculate the losses from the surface roughness' parameter and the modes. To the best of our knowledge, the anisotropic Matérn kernel with finite correlation lengths was also applied for the first time in the context of surface-roughness-induced scattering. As mentioned above, this autocorrelation function is expected to better capture the statistical characteristics than the commonly applied exponential kernel, as analyzed in [5]. That is because, the latter leads to non-continuously differentiable sample functions, whereas the former is one time continuously differentiable.

References

[1] M. Soler, M. C. Estev, M. Cardenosa-Rubio, A. Astua, L. M. Lechuga, *How Nanophotonic Label-Free Biosensors Can Contribute to Rapid and Massive Diagnostics of Respiratory Virus Infections: COVID-19 Case*, ACL Sensors, vol. 5, no. 9, 2020

[2] L. Chrostowski, M. Hochberg, *Silicon photonics design*, Cambridge University Press, 2015

[3] S. M. Hörmann, J. W. Hinum-Wagner, A. Bergmann, *An Ab Initio, Fully Coherent, Semi-Analytical Model of Surface-Roughness-Induced Scattering*, Journal of Lightwave Technology, 10.1109/JLT.2022.3224777, 2022

[4] D. J. Blumenthal, R. Heideman, D. Geuzebroek, A. Leinse, C. Roeloffzen, *Silicon Nitride in Silicon Photonics*, in Proceedings of the IEEE 106.12, pp. 2209-2231, 2018

[5] S. Hörmann, J. W. Hinum-Wagner, J. Sattelkow, D. Rist, A. Bergmann, *Comparison of Gaussian Process Kernels for Surface Roughness Modelling,* in Proceedings of the 23rd European Conference on Integrated Optics, pp. 57-59, 2022

[6] C. G. Poulton, C. Koos, M. Fujii, A. Pfrang, T. Schimmel, J. Leuthold, W. Freude, *Radiation modes and roughness loss in high index-contrast waveguides*, IEEE Journal of selected topics in quantum electronics, vol. 12, no. 6, 2006

[7] J. H. Jang, W. Zhao, J. W. Bae, D. Selvanathan, S. L. Rommel, I. Adesida, A. Lepore, M. Kwakernaak, J. H. Abeles, *Direct measurement of nanoscale sidewall roughness of optical waveguides using an atomic force microscope*, Applied physics letters, vol. 83, no. 20, 2003

[8] E. Jaberansary, T. M. Masaud, M. M. Milosevic, M. Nedeljkovi, G. Z. Mashanovich, H. M. Chong, *Scattering loss estimation using 2-D Fourier analysis and modeling of sidewall roughness on optical waveguides*, IEEE Photonics Journal, vol. 8, no. 5, 2013

[9] C. E. Rasmussen, C. K. I. Williams, *Gaussian Processes for Machine Learning*, MIT Press, 2005

[10] J. Milvich, D. Kohler, W. Freude, C. Koos, *Surface sensing with integrated optical waveguides: a design guideline*, Optics express, vol. 26, no. 16, 2018

Two-dimensional layered $PtSe_2$ for High Speed Near-Infrared Electro-Optic Modulation

Yi Wang, Zunyue Zhang, Shuqi Xiao and Hon Ki Tsang*

Department of Electronic Engineering, The Chinese University of Hong Kong, Shatin, New Territories, Hong Kong SAR

**Corresponding author: hktsang@ee.cuhk.edu.hk*

Platinum diselenide can be grown by chemical vapor deposition as a two-dimensional (2D) material and is relatively stable in air. We experimentally demonstrate a 2D $PtSe_2$ electro-optic intensity modulator at 1550nm wavelength. The fabricated $PtSe_2$ modulator has a response speed of 4.8 GHz and a modulation depth of 6 dB.

Keywords**:** *2D materials, $PtSe_2$, Near-infrared, Modulators*

INTRODUCTION

Two-dimensional (2D) layered platinum diselenide ($PtSe_2$) is of interest for optoelectronic applications because of its attractive properties such as high carrier mobility, good air stability and a layer-tunable bandgap ranging from 0 (bulk) to 1.2 eV (monolayer) [1]. Besides, high quality and scalable 2D layered $PtSe_2$ thin films could be prepared by relatively straightforward synthesis methods which could control the number of monolayers with good repeatability [2]. Hence there has been previous publications reporting the use of 2D $PtSe_2$ for high speed infrared photodetectors [3,4], but its use for optical modulators has been relatively unexplored.

Bound states in the continuum (BIC) PICs have been demonstrated to be an exceptional platform for hybrid integration of 2D materials for providing a naturally flat substrate for integrating 2D materials [5]. Photonic layers are formed by an etch-free E-beam lithography process with low-refractive-index polymer while 2D materials are on the flat high-refractive-index dielectric substrate with negligible influence on the properties of materials during fabrication processes. Here, we propose and experimentally demonstrate a waveguide-integrated $PtSe_2$-based electro-optic (EO) intensity modulator. Double-layered CVD-grown $PtSe_2$ thin films are hybrid integrated with BIC optical waveguide on a crystalline dielectric substrate. In our experiments we used a lithium niobate crystal as the passive substrate. The $PtSe_2$ layer could be modulated with a modulation bandwidth of 4.8 GHz bandwidth and direct intensity modulation, with 6 dB modulation depth, was observed over a broad operation wavelength range from 1500 to 1580 nm, under ambient conditions.

DEVICE FABRICATION AND CHARACTERIZATION

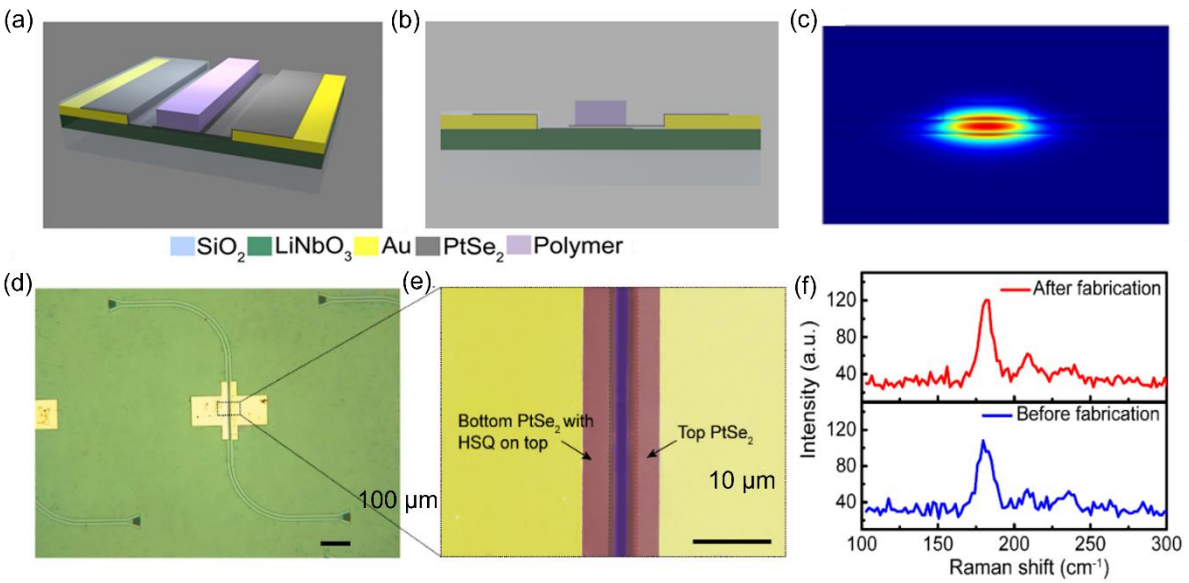


Fig. 1(a) Schematic illustration of the double-layered $PtSe_2$ modulator. (b) Cross section of the device. (c) Mode profile in the cross section of the BIC waveguide. (d) Optical microscope image of the $PtSe_2$ modulator (scale bar: 100 μm). (e) False-color SEM image illustrating the dashed region in Fig.1(d) (scale bar: 10 μm). The waveguide, Ti/Au metallization and $PtSe_2$ thin film

are represented in blue, yellow and red, respectively. The red dashed line represents the boundary of bottom $PtSe_2$ thin film, while the green line represents the boundary of top layer $PtSe_2$. (f) Raman spectroscopy of the $PtSe_2$ thin film before and after the whole fabrication process.

Figure 1(a) displays the schematic illustration of the $PtSe_2$ modulator and Fig. 1(b) depicts the cross section of device design. Two layers of $PtSe_2$ thin film (in grey colour) separated by a thin insulator formed by a layer of 150 nm thick HSQ (blue) was placed on the $LiNbO_3$ substrate (green). The polymer waveguide (purple) has a thickness of 500 nm sits on top of the $PtSe_2$ capacitor. Here we use a commercially available E-beam resist ZEP 520A (with a refractive index of 1.54) to form the waveguide. Two gold electrodes (yellow) are placed on each side of waveguide. The left electrode is contacted with the lower layer of $PtSe_2$, while the right electrode is contacted with the top layer. The mode profile of the BIC waveguide at 1550 nm is shown in Fig. 1(c). Light is mainly confined in the $LiNbO_3$ substrate below the polymer waveguide while keeping strong interaction with the $PtSe_2$ thin film. The $PtSe_2$ modulator was fabricated by the following process sequence: First, the metal electrodes were lithographically patterned, and 5 nm Ti/100 nm Au were deposited by e-beam evaporation. Then the bottom layer of CVD-grown $PtSe_2$ thin film was wet transferred onto the substrate, followed by EBL patterning and Ar plasma etching. The dielectric layer was started from spin coating of ~150 nm HSQ E-beam resist. After EBL exposure, the HSQ thin film was patterned and turned into SiO_2. The top layer of $PtSe_2$ thin film was wet transferred and patterned in the following steps. Finally, the polymer waveguides were fabricated by spin coating followed by EBL patterning. The optical and scanning electron microscope (SEM) images of the device are shown in Fig. 1(d) and Fig. 1(e). The waveguide width is designed to be 2 µm in order to support low-loss BIC mode. The distance between two metal electrodes is 10 µm. The length and width of double layer of $PtSe_2$ capacitor are designed to be 200 µm and 4 µm, respectively. The thickness of the $PtSe_2$ sample is about 4 nm, and was measured by an atom force microscopy (AFM). The quality of the material is confirmed by Raman spectroscopy as illustrated in Fig. 1(f), which shows the measured spectrum before (blue) and after (red) fabrication. No obvious defect peaks or peak position shift were introduced by the whole fabrication process, indicating that there is no structural damage to the $PtSe_2$ thin film.

RESULTS

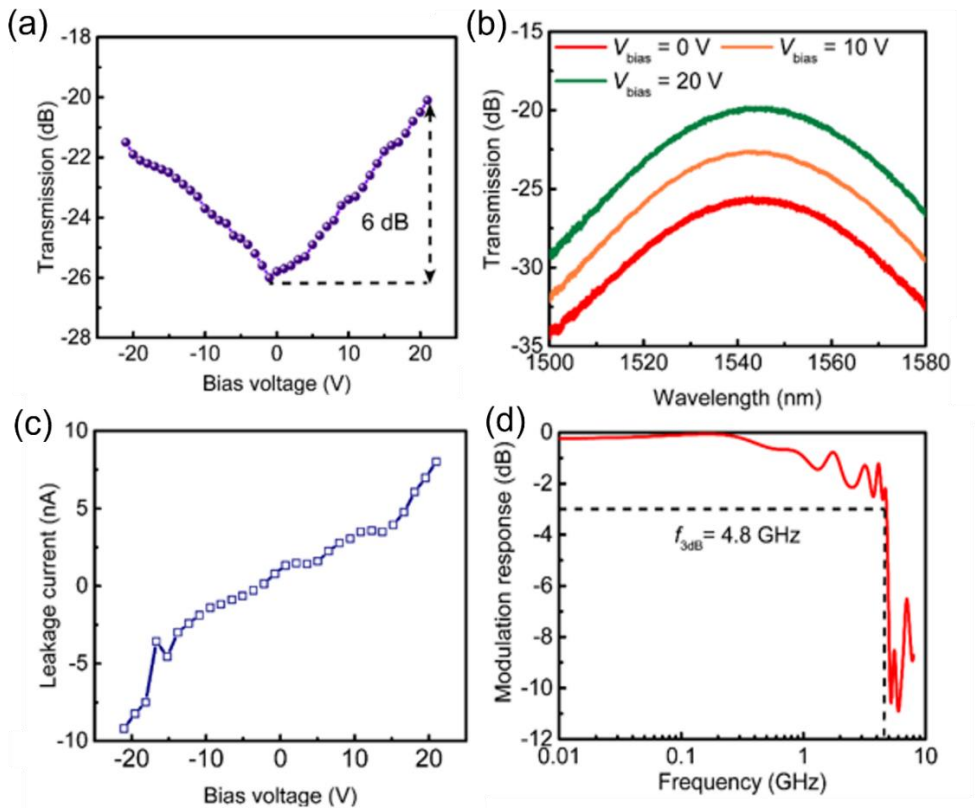


Fig. 2(a) Transmission of light at 1550 nm under different bias voltage V_{bias} from -21 V to 21 V. (b) Broadband optical transmission of the $PtSe_2$ modulator. (c) I-V measurement for the leakage current. (d) Frequency response of the $PtSe_2$ modulator.

The static optical transmission of the $PtSe_2$ modulator was measured with a tunable semiconductor laser, which was coupled to the input waveguide by an optical fiber and a waveguide grating coupler. A mechanical fiber polarization controller was adjusted at the input to couple the TM mode into the waveguide. Fig. 2(a) illustrates the

transmission of the device which had 200 µm length of evanescently coupled $PtSe_2$ thin films. The applied bias voltage was varied from -21 V to 21 V. At 1550 nm, the transmission of light through the single straight waveguide was clearly dependent on the voltage applied across the $PtSe_2$ capacitor. The total optical loss of the input and output grating couplers were about 18 dB in the device and we observed an additional voltage dependent loss of about 6 dB while there was about 2dB excess insertion loss from the $PtSe_2$ thin films. The operation principle of the $PtSe_2$ modulator is based on the change in free carrier density under different applied voltages, similar to previously reported double layer graphene modulators [6]. We observed an asymmetry in the modulation response at negative bias and positive biases, that is possibly caused by the different carrier mobility of electrons and holes. Fig. 2(b) shows the wavelength spectral response of our device measured under different bias voltages. From 1500 nm to 1580 nm, the device had a similar modulation depth of about 6dB, indicting a broad optical bandwidth of operation for the $PtSe_2$ modulator. The *I-V* curve of the device is shown in Fig. 2(c). The leakage current was under 10 nA at 20 V bias. The breakdown voltage of the dielectric layer (150 nm HSQ) was measured to be around 30 V. It should be noted that the switching voltage of the device is determined by the dielectric constant and thickness of the dielectric. The switching voltage of the $PtSe_2$ modulator could be reduced by thinning the thickness of the dielectric layer, but the switching speed will be reduced by the larger capacitance and increase in the resistance-capacitance (RC) time constant.

The response speed of the $PtSe_2$ modulator was characterized by the small signal response. A radio frequency (RF) signal generated from a network analyzer combined with a D.C. voltage through bias tee, was applied to the $PtSe_2$ modulator. Light at a wavelength of 1550 nm was directly coupled into the device from the grating coupler and the out-coupled light was received by a 10 GHz high-speed photodetector. Fig. 2(d) plots the measured frequency response S_{21} (S_{21}: ratio between the optical amplitude modulation and the RF signal) of the modulator. The 3dB cutoff frequency of our device is measured to be 4.8 GHz. As CVD-grown $PtSe_2$ has relatively high carrier mobility under ambient conditions [4], the response speed of the modulator is mainly limited by the RC time constant. By simplifying the $PtSe_2$ modulator as an electric circuit, the RC time limited 3 dB bandwidth f_{3dB} can be calculated by $f_{3dB} = 1/(2\pi RC)$, where R is a sum of the output impedance of network analyzer $R_o = 50\ \Omega$ and the contact resistance at the gold/$PtSe_2$ interface, which is about 150 Ω. Considering the structure of $PtSe_2$ capacitor, with a length of 200 µm, a width of 4 µm and 150 nm SiO_2 dielectric, a capacitance of 174 fF could be estimated. We estimated an RC limited bandwidth of about 4.6 GHz which is in reasonable agreement with the experimentally measured bandwidth. The speed of the $PtSe_2$ modulator could be further improved by optimizing the device structure. For example, the capacitance can be reduced by increasing the thickness of dielectric layer or integrating the $PtSe_2$ capacitor with an optical cavity to minimize the area of planar capacitor while keeping the modulation efficiency in the meantime.

CONCLUSION

In conclusion, we proposed and experimentally verified that $PtSe_2$ may be used for optical intensity modulators. The proof-of-concept device operated at 1550 nm wavelength with a modulation depth of 6 dB and about 4.8GHz modulation bandwidth. The performance of the device could be further improved for higher speed modulation by optimizing the device structure such as integrating with an optical cavity. This work paves the way of $PtSe_2$ based photonic devices, showing that $PtSe_2$ could be potentially utilized for high-speed optoelectronic devices.

Acknowledgements: This work was supported by RGC/NSFC Joint Research Scheme N_CUHK423/21, Yi Wang and Zunyue Zhang thank ITF for financial support from the Talent Hub scheme.

References

[1] Zhao, Y.; Qiao, J.; Yu, Z.; Yu, P.; Xu, K.; Lau, S. P.; Zhou, W.; Liu, Z.; Wang, X.; Ji, W., High electron mobility and air stable 2D layered PtSe2 FETs. *Advanced Materials* 2017, *29* (5), 1604230.

[2] Wang, Y.; Li, L.; Yao, W.; Song, S.; Sun, J. T.; Pan, J.; Ren, X.; Li, C.; Okunishi, E.; Wang, Y.-Q., Monolayer PtSe2, a new semiconducting transition-metal-dichalcogenide, epitaxially grown by direct selenization of Pt. Nano letters 2015, 15 (6), 4013-4018.

[3] Wang, Y.; Yu, Z.; Tong, Y.; Sun, B.; Zhang, Z.; Xu, J.-B.; Sun, X.; Tsang, H. K., High-speed infrared two-dimensional platinum diselenide photodetectors. Applied Physics Letters 2020, 116 (21), 211101.

[4] Wang, Y.; Yu, Z.; Zhang, Z.; Sun, B.; Tong, Y.; Xu, J.; Sun, X.; and Tsang, H.K., Bound-States-in-Continuum Hybrid Integration of 2D Platinum Diselenide on Silicon Nitride for High-Speed Photodetectors. ACS Photonics 7, no. 10 (2020): 2643-2649.

[5] Yu, Z.; Wang, Y.; Sun, B.; Tong, Y.; Xu, J. B.; Tsang, H. K.; Sun, X., Hybrid 2D Material Photonics with Bound States in the Continuum. Advanced Optical Materials 2019, 7 (24), 1901306.

[6] Liu, M.; Yin, X.; Zhang, X., Double-layer graphene optical modulator. Nano letters 2012, 12 (3), 1482-1485.

Generic Platform Integrated Frequency Shifter for Low Bandwidth Heterodyne Detection Systems

P. López-Querol[1*], A. Soria-Gómez[1], A. Quirce[2], I. Equivias[1], J. M. G. Tijero[1] and A. Pérez-Serrano[1]

[1] CEMDATIC-ETSI Telecomunicación, Universidad Politécnica de Madrid (UPM), 28040 Madrid, Spain.
[2] Instituto de Física de Cantabria (IFCA), Universidad de Cantabria-CSIC, 39005, Santander, Spain.
[*]pablo.lquerol@upm.es

An integrated frequency shifter based on an IQ modulator fabricated through an open-access indium phosphide generic integration platform has been designed and characterized. It is intended for low bandwidth heterodyne detection systems. Its performance is demonstrated up to 300 MHz with a SMSRs greater than 15 dB. **© 2023 The Author(s)** ***Keywords***: *Photonic Integrated Circuits, heterodyne detection, IQ modulator, frequency shifter.*

INTRODUCTION

Heterodyne detection systems are based on shifting the signal frequency away from DC, thus minimizing the effects of flicker noise and unambiguously detect beat notes around the carrier signal at both sides of the spectrum [1]. Low bandwidth heterodyne detection is used in systems such as coherent lidars or dual-comb spectrometers, that require frequency shifting ranges from tens to hundreds of MHz. This allows to use low-cost electronic devices in the detection system [1].

Traditionally, Acousto-Optic Modulators (AOMs) have been used to perform the function of frequency shifters in such systems. Nevertheless, these modulators are difficult to integrate. They require hybrid integration and open-access foundries do not offer it as a Building Block (BB) for their generic integration processes. An interesting alternative is using IQ modulators as frequency shifters [2], because they can be easily integrated using the standard BBs offered by a generic integration platform. Frequency shifts up to 10 GHz with a Side Mode Suppression Ratio (SMSR) between 16 and 23 dB have been demonstrated in [3] for a silicon-based Photonic Integrated Circuit (PIC). In the case of Indium Phosphide (InP), there are demonstrations of IQ modulators used as fast digital transmitters in coherent communication systems achieving rates up to 128 Gb/s [4], but its use as frequency shifter has not been reported.

In this contribution, an InP integrated IQ modulator designed through an open access generic integration foundry using its standard BBs is experimentally characterized and demonstrated as a frequency shifter, achieving good operation up to 300 MHz with SMSR greater than 15 dB.

DESIGN AND FABRICATION

The PIC has been fabricated by SMART Photonics in a Multi-Project Wafer (MPW) run. The design has been made using standard BBs of the 1st generation PDK from the foundry. As part of the design process, initial software simulations and theoretical conceptualizations were made. Fig. 1 shows a photograph of the fabricated device highlighting the different integrated devices. It consists of two dual-parallel branches, I and Q, each one composed by a dual-drive Mach-Zehnder Modulator (MZM), followed by an Electro-Optic Phase Modulator (EOPM) which allows to operate both branches in quadrature. Several couplers are used for combining and splitting the signal, and two Semiconductor Optical Amplifiers (SOAs) are used at the input and at the output respectively to boost the signal. It is important to remark that at the output of each MZM there is an integrated photodiode, which allow us to characterize each MZM separately.

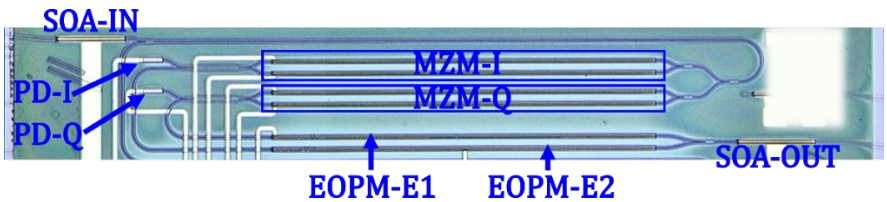


Fig.1. Scheme of the InP integrated frequency shifter.

RESULTS AND DISCUSSION

The 1st generation of the foundry PDK is characterized by having a shared common n-substrate for all the p-n junctions in which the DC BBs are based, i.e. all share the same ground contact. This, combined with the fact that EOPMs are based on electro-optic effects and therefore they can only operate in reverse bias, makes not possible to operate the MZMs in push-pull mode. Therefore, prior to the frequency shifter realization we need to set up an analytical model considering the mentioned features. This model is based on measurable parameters of the system, such as the π voltage of the EOPMs and the phase shift due to the difference in optical paths. These parameters can be measured for each MZM since the current measured in each integrated PD is given by

$$I_{PD} \propto cos^2\left(\frac{\varphi_i - \varphi_j - \varphi_0 + \pi}{2}\right) \qquad (1)$$

where $\varphi_{i,j} = \frac{\pi}{V_{\pi i,j}} V_{i,j}$ being $V_{i,j}$ the voltage applied to the EOPM and being φ_0 the phase difference due to optical paths in each arm.

Fig. 2 shows the response of each MZM (I branch and Q branch) measured the integrated PDs. This is done by injecting CW light into the chip and biasing the MZMs with different voltages. Unlike in the case of modulators based on $LiNbO_3$, this response has been observed to be very stable and repetitive over time.

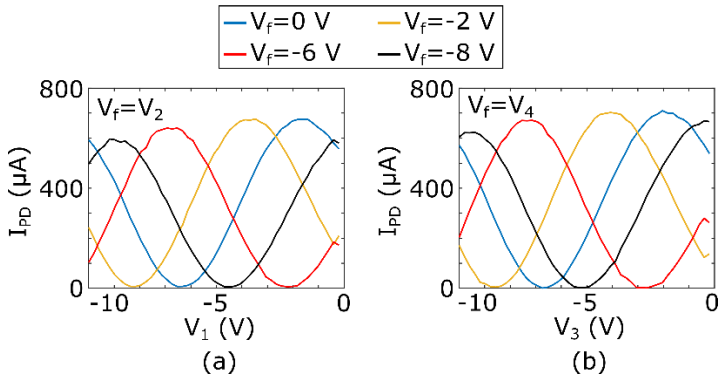


Fig. 2. Measured photocurrent at PD-I (a) and PD-Q (b) for different bias points.

After obtaining the MZM parameters, the voltages of each EOPM are set based on the analytical model to operate the IQ modulator as a frequency shifter. These voltages are as follows

$$V_1 = -V_{\pi 1}\left(1 - \frac{\varphi_0^I}{\pi}\right) - RV_{\pi 1}\sin(\omega_s t), \qquad \text{and} \qquad V_2 = -\frac{V_{\pi 2}}{2} - RV_{\pi 2}\sin(\omega_s t), \qquad (2)$$

for the MZM on the I branch, and

$$V_3 = -V_{\pi 3}\left(1 - \frac{\varphi_0^Q}{\pi}\right) \mp RV_{\pi 3}\cos(\omega_s t), \qquad \text{and} \qquad V_4 = -\frac{V_{\pi 4}}{2} \pm RV_{\pi 4}\cos(\omega_s t), \qquad (3)$$

for the MZM on the Q branch, where $R \ll 1$ to operate in low amplitude modulation regime. Notice that the shift that will be induced to the carrier is the one set by the frequency of the RF modulation signal, i.e, ω_s. Furthermore, the voltages of the EOPMs placed at the output of each MZM should be adjusted to make I and Q branches work in quadrature, i.e. with a phase difference of $\frac{\pi}{2}$. The optical carrier to be shifted is injected into the chip from an external tunable laser which has narrow linewidth (10 kHz). Fig. 2 shows the measured results for two different frequency shifts: 100 MHz (a) (b) and 250 MHz (c), These spectra are measured gathering the output light of the PIC with a lensed fiber and then using a high resolution (10 MHz) Brillouin Optical Spectrum Analyzer. The frequency shift can be controlled to be positive or negative just by adjusting the sign of the harmonic signals in Eq. (3). The SMSR worsens when increasing the frequency shift. This degradation is attributed to the electrical contacts of the EOPMs, which are designed for DC operation. However, up to 300 MHz a SMSR between 15-20 dB is maintained.

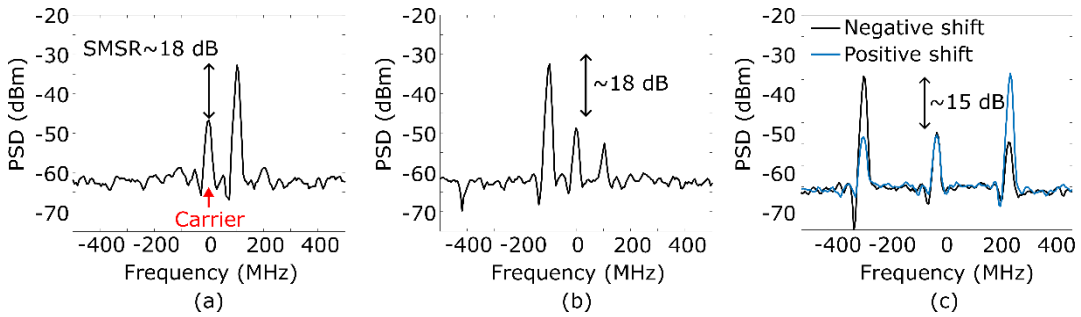


Fig. 2. Measured spectra at the output of the device for frequency shifts of (a) 100 MHz positive (b) 100 MHz negative and (c) 300 MHz positive and negative

4. Conclusions and outlook

We have demonstrated experimentally an integrated frequency shifter using standard BBs from an open access InP foundry. The proposed architecture is capable to induce a frequency shift up to 300 MHz with SMSRs greater than 15 dB, working the system better for low frequency shifts. The obtained performance is good enough for using the proposed design in more complex low-bandwidth heterodyne detection systems such as low-cost coherent lidars and dual-comb spectrometers.

Acknowledgements: Authors acknowledge Galileo Galilei for reviewing the paper.

References

[1] C. Quevedo-Galán, et al., "Dual-comb spectrometer based on gain-switched semiconductor lasers and a low-cost software-defined radio," *IEEE Access* **9**, pp. 92367 – 92373 (2021).
[2] M. Izutsu, et al., "Integrated optical SSB modulator/frequency shifter," *IEEE J. Quantum Electron.* **17**(11), pp. 2225 – 2227 (1981).
[3] M. Lauermann, et al., "Integrated optical frequency shifter in silicon-organic hybrid (SOH) technology," *Opt. Express* **24**(11), p. 11694 (2016).
[4] N. Andriolli, at al., "InP monolithically integrated coherent transmitter", *Opt. Express* **23**(8), pp. 10741-10746 (2015).

Single-mode polymer ring resonator for sensor applications

(Student paper)

Lase Milgrave[1,*], Arturs Bundulis[2], Janis Alnis[1] and Aigars Atvars[3]

[1]Institute of Atomic Physics and Spectroscopy, University of Latvia, Jelgavas iela 3, Riga, 1004, Latvia
[2]Institute of Solid State Physics, University of Latvia, Kengaraga iela 8, Riga, 1063, Latvia
[3]Institue of Astronomy, University of Latvia, Jelgavas iela 3, Riga, 1004, Latvia
[*] lase.milgrave@lu.lv

Integrated optical sensors have the potential to change and develop the sensor market. We have fabricated an integrated SU-8 microring resonator and tested it as a humidity sensor. The sensor showed a very fast response to changes in relative humidity (RH) and an acceptable sensitivity of 7.3 pm/% RH (0–30% RH). This sensor could be used in environmental monitoring and where rapid gas detection is necessary.
Keywords: *ring resonator, polymer photonics, humidity sensor, optical sensor, SU-8*

INTRODUCTION

One of the many applications of integrated optics is sensors. Demand for sensors is constantly increasing. From temperature and gas sensors to numerous biosensors – the research in these fields is highly active as integrated optical sensors offer a small footprint, electromagnetic immunity, the ability to work in hazardous environments, and low cost [1]. There are different approaches to the working principle of such sensors (e.g., Mach-Zehnder interferometer, fiber sensors), one of them being optical resonators. Specifically, whispering gallery mode (WGM) microresonators. WGM resonances are morphology-dependant resonances that travel near the surface of the resonator due to total internal reflection and constructive interference [2]. The resonance condition for spherical resonators is [3]:

$$m\lambda_{res} = 2\pi R n_{eff}, \quad (1)$$

where m – azimuthal mode number (an integer number of wavelengths that fit the optical path), λ_{res} – resonance wavelength, R – radius of the resonator, n_{eff} – effective refractive index. From eq. 1 it is clear that if one chooses a material that changes its radius and/or refractive index due to some environmental change, this resonator can be used as a sensor.

WGM resonators are suitable for sensor applications due to their high quality (Q) factors, which are linked to high sensitivity, as well as wide resonator material and geometry options [4]. For integrated sensors, polymers are a great choice as many are suitable for lithography methods, are sensitive to various environmental changes, and can be biocompatible [5]. Most common geometries are disk and ring resonators, but other shapes are possible as long as it creates a smooth and curved surface so that total internal reflection can occur. SU-8 is a negative photoresist, which is developed using UV photolithography. Once fully cross-linked, SU-8 is mechanically and chemically stable. It is sensitive to temperature changes, relative humidity (RH) changes, and other gasses. To alter its qualities, coatings [6] and dopants [7] can be added.

We propose a SU-8 ring resonator that can be used for gas sensing and has other potential applications. Its simple design and fabrication offer high reputability in the fabrication process. The chosen geometry provides single-mode operation, as well as fast gas sensing.

RESULTS

To fabricate the sensor, we used single-step UV photolithography. SU-8 was spin-coated on a soda-lime glass substrate, creating a 1 µm thick layer. The sample was soft-baked, then direct writing lithography (375 nm) was used to pattern the design (Fig. 1a). Afterwards the sample was post-baked, developed, and hard-baked. Finally, the glass substrate was broken along previously scribed lines. This meant that the polishing of waveguide ends was not necessary. The chip consists of 18 single-mode ring resonators and adjacent waveguides. The resonators partially or fully overlap with the waveguide (Fig. 1b). The width of the resonator and the waveguide match. We fabricated resonators with widths of 3, 4, and 5 µm. The resonator diameters are 600 and 660 µm (Fig. 1c). This diameter corresponds to the free spectral range (FSR) of approximately 100 GHz, which is the standard channel separation in telecommunications. In addition, as we used a scanning 760 nm laser (200 GHz scan range) and an

oscilloscope to observe the resonances, the chosen diameter meant that we could observe two resonances simultaneously.

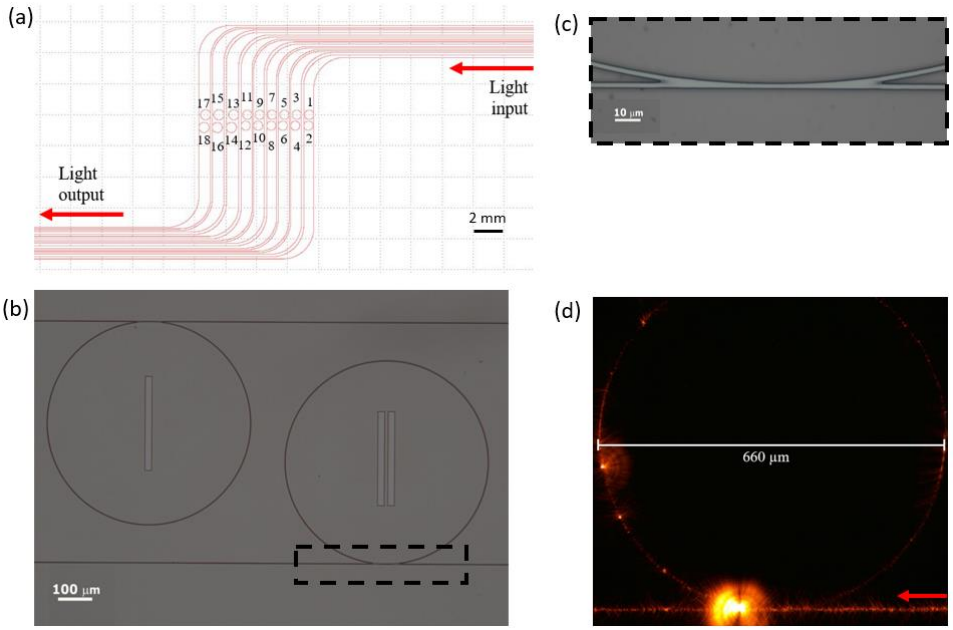


Fig. 1. SU-8 ring resonator: (a) Chip design; (b) Microscope image of resonators; (c) Resonator and waveguide overlap region; (d) Ring resonator as seen in camera when light is coupled into it.

To evaluate the sensor's performance, we created an experimental set-up (Fig. 2), which consists of a pump laser (AVAP 760 nm single-mode VCSEL), air humidifier/dry air flow, humidity chamber made from organic glass, oscilloscope, and *LabVIEW* program for data analysis. Inside the humidity chamber is the optical sensor, optical components, camera, and photodiode that collects the transmission spectra. For reference measurements we used two electronic temperature and humidity sensors. Light was coupled into the waveguide using direct focusing on the end of the waveguide with 20x microscope objective. Optical losses were measured to be 22 dB. While this is not the most efficient coupling method, it was suitable for our experiments as the laser beam can be easily adjusted and switched to other waveguides.

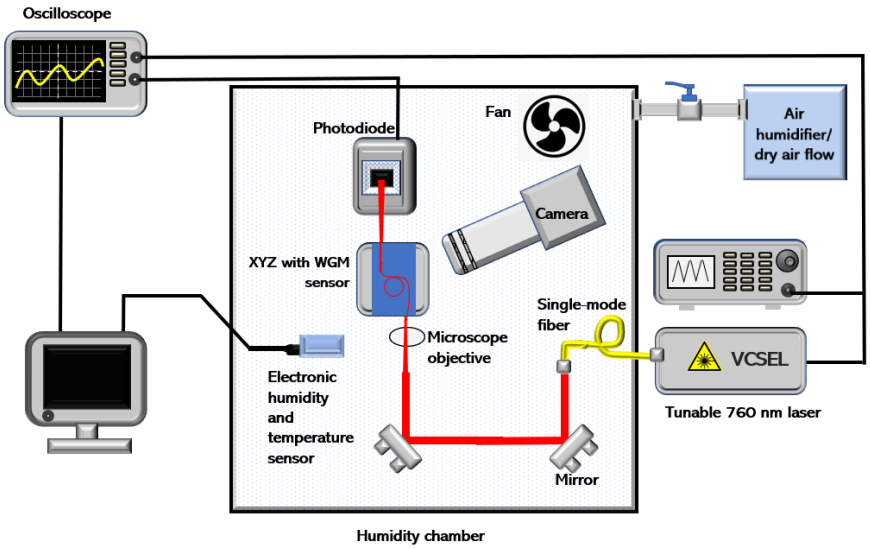


Fig. 2. Experimental set-up: chip is placed inside the humidity chamber to test its performance as humidity sensor.

We performed experiments in the full range of relative humidity (0–100% RH). In Fig. 3a two transmission spectra can be seen at different RH. Redshift was observed as air humidity increased. At 0% RH the *Q* factor was 1.9×10^4. To observe the resonance wavelength shift from 0 to 100% RH, we had to detect several peaks as the shift of one peak in our chosen laser scan region corresponds to a shift of approximately 40% RH. We experimentally measured the hysteresis of the sensor and calculated its sensitivity (Fig. 3b). As expected, the hysteresis is high, on average

16%, which is typical for polymers [8]. The sensor response was non-linear – sensitivity decreased with increasing RH. We calculated the sensitivity *S* as the slope of the linear parts of Δλ(RH) graph. The sensitivity is 7.3 pm/% RH (0–30% RH), 5.5 pm/% RH (30–60% RH), 3.7 pm/% RH (60–90% RH). While these results are average, the response and recovery times of the sensor are very short (2.7 and 4.3 s respectively), which could be attributed to the chosen geometry.

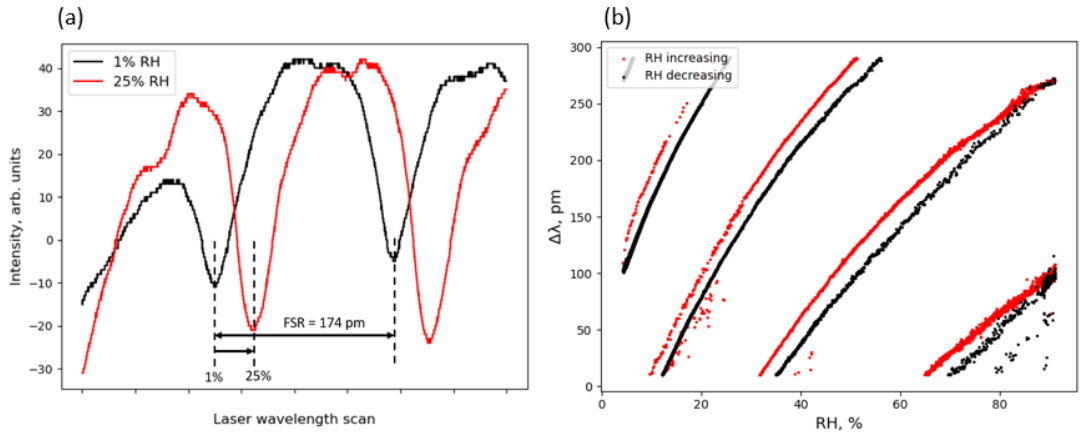


Fig. 3. Experimental results: (a) Transmission spectra at two RH levels. Redshift is observed as RH increases; (b) Resonance wavelength shift due to the change in the RH.

DISCUSSION

We have discussed the fabrication of an integrated SU-8 ring resonator and we have experimentally tested its performance as a humidity sensor. The fabrication process is simple and the costs are low. The results show that SU-8 is suitable for humidity sensing and has potential in sensing other gasses, which could be useful in environmental monitoring and industrial applications. The issue of low selectivity could be solved by using sensor systems on a single chip or by applying selective coatings. The chosen geometry – ring resonator – has great response and recovery times, which might be useful in detecting hazardous gasses. To achieve a higher *Q* factor, light should be coupled into the resonator more efficiently both by using a different coupling method and by changing the design, specifically the gap between the resonator and the waveguide. In the future, the long-term stability and the sensitivity of other gasses should be tested.

Acknowledgments: This work was funded by ERDF project No. 1.1.1.5/19/A/003 “The Development of Quantum Optics and Photonics at the University of Latvia” and ERDF project No. 8.2.2.0/20/I/006.

References

[1] J. Haus, *Optical Sensors: Basics and Applications*. WILEY-VCH, 2010
[2] X. Jiang, A. J. Qavi, S. H. Huang, and L. Yang, *Whispering-Gallery Sensors*, Matter, vol. 3, no. 2, pp. 371–392, 2020
[3] M. R. Foreman, J. D. Swaim, and F. Vollmer, *Whispering gallery mode sensors*, Adv. Opt. Photonics, vol. 7, pp. 168–240, 2015
[4] A. K. Mallik *et al.*, *Whispering gallery mode micro resonators for multi-parameter sensing applications*, Opt. Express, vol. 26, no. 24, 2018
[5] G. C. Hill *et al.*, *SU-8 MEMS Fabry-Perot pressure sensor*, Sensors Actuators, A Phys., vol. 138, no. 1, pp. 52–62, 2007
[6] E. Nitiss, A. Bundulis, A. Tokmakovs, J. Busenbergs, and M. Rutkis, *All-Organic Waveguide Sensor for Volatile Solvent Sensing*, Photonic Sensors, vol. 9, no. 4, pp. 356–366, 2019
[7] A. Airoudj, D. Debarnot, B. Bêche, and F. Poncin-Epaillard, *New sensitive layer based on pulsed plasma-polymerized aniline for integrated optical ammonia sensor*, Anal. Chim. Acta, vol. 626, pp. 44–52, 2008
[8] M. Eryürek *et al.*, *Integrated humidity sensor based on SU-8 polymer microdisk microresonator*, Sensors Actuators, B Chem., vol. 242, pp. 1115–1120, 2017

High Coupling Efficiency Waveguide Grating Couplers for Bound-states-in-the-Continuum waveguide on Lithium Niobate

(Student paper)

Xuetong Zhou[1], Ying Xue[2], Fan Ye[1], Ziyao Feng[1], Yuan Li[1], Xiankai Sun[1], Kei May Lau[1,2] and Hon Ki Tsang[1*]

[1]Department of Electronic Engineering, The Chinese University of Hong Kong, Shatin, Hong Kong, P.R. China
[2]Department of Electronic and Computer Engineering, Hong Kong University of Science and Technology, Clear Water Bay, Kowloon, Hong Kong, P.R. China
[*]Corresponding author: *hktsang@ee.cuhk.edu.hk*

We propose a new approach to increase the coupling efficiency of grating couplers in the low-index-contrast bound-states-in-the-continuum (BIC) waveguides. The design is based on patterning a high refractive index material (polysilicon) on the low-index BIC circuits formed on lithium niobate. Coupling loss for TM as low as 1.33 dB is predicted.
Keywords: *Integrated optics, waveguide gratings, lithium niobate, bound states in the continuum.*

INTRODUCTION

Waveguide grating couplers (GCs) are an attractive approach to couple light between optical fibers and integrated waveguides, offering the advantages of large fabrication tolerance, wafer-scale testing, and arbitrary positioning on the chip, without needing the facet polish or high alignment tolerance associated with edge couplers. GCs can also be integrated with waveguide photodetectors and lasers [1, 2]. Using the optimized shift-pattern overlay method [3, 4], coupling efficiency of silicon grating couplers as high as -0.89 dB was experimentally realized using only photolithography with a standard silicon photonics foundry process [5]. Lithium niobate on insulator (LNOI) has attracted much attention, offering the advantages of high modulation bandwidth and low modulation voltages [6]. One important block of development in LiNbO3 photonics is the high-efficiency grating coupler. However, in the lithium niobate platform, realizing high coupling efficiency grating coupler remains a challenge. This is not only due to the mode mismatch between the fiber and waveguide, but also due to the smaller refractive index contrast. To improve the coupling efficiency of gratings on LNOI platform, the use of a bottom metal reflector to improve the directionality was needed. Using this approach, the best results experimentally obtained for TM coupling was 2.1 dB [7] with very fine structure due to the grating apodization, and 0.89 dB was reported for TE coupling [8], but the fabrication of metal mirrors adds additional fabrication processes of substrate thinning and backside metal deposition. Another challenge is that the etching lithium niobate typically produces some off-vertical etch angle as it is very difficult to consistently achieve vertical etching. To avoid the difficult etching of lithium niobate, silicon on lithium niobate based grating couplers have been proposed. However, the coupling efficiency reported for silicon directly on lithium niobate gratings was only about -18 dB [9]. Silicon nitride gratings on lithium niobate have much better results, with silicon nitride gratings on LNOI attaining 4.02 dB [10] and 5.82 dB [11] coupling losses.

In this paper, we propose a novel approach that can significantly improve the coupling efficiency beyond that attained for the silicon nitride gratings on LNOI. The basic idea is based on taking advantage of the guiding of light using BIC on the LNOI platform [12], and using the high refractive index of a polysilicon overlay layer. The high refractive index overlay has been previously used in silicon waveguide gratings [13]. On the BIC based LNOI platform, the main difference is that the high refractive index overlay forms a slot waveguide in the vertical direction, and the structure moves more of the mode into the etched polysilicon grating region, thus increasing the grating strength. Besides, the vertical slot structure can also be regarded as a cavity in the vertical direction. By carefully designing the thickness of the low index silica and the upper polysilicon layer, we can use the cavity to improve the coupling efficiency of the grating. The 3D FDTD simulation of the proposed structure predicted the coupling losses to be as low as 1.33 dB. The proposed structure in Fig. 1 does not need the etching of the LiNbO3, and the minimum feature size required for the grating is 387 nm. The grating design is therefore compatible with patterning by the deep ultraviolet photolithography tools commonly available in foundries, and the grating is therefore suitable for large-volume production using photolithography, unlike finer nanostructured gratings that require electron beam lithography. The silica deposition on the LNOI and the deposition of the polysilicon layer are standard processes commonly available in silicon processing facilities. Also, this design method does not require substrate thinning for adding bottom metal reflectors (as done in references [7, 8]) to improve the coupling efficiency.

Device Structure and simulation

The 2D and 3D schematic diagram of the proposed waveguide grating coupler on LNOI (X-cut) is shown in Fig. 1. The structure is formed by the deposition of silica on the LNOI wafer, and channel waveguides are formed by etching the silica at an appropriate width (2.0 μm) to create the low-loss BIC channel waveguide. In the BIC waveguide most of the mode is confined in the high index lithium niobate [12]. The waveguide grating is formed by depositing, patterning and etching a polysilicon overlay on the top silica. As the deposited silica has a smaller refractive index than the polysilicon or the lithium niobate, the polysilicon-silica-lithium niobate structure will form a slot waveguide in the vertical direction. The slot waveguide pulls more of the mode into the silica region [14], and there is thus better optical overlap with the polysilicon grating, improving the grating strength. Besides, the high(poly-Si)-low(silica)-high(LiNbO3) refractive index structure can form a cavity in the vertical direction. With careful design of the thickness of the silica layer and polysilicon layer, we can improve the directionality and have most of the light emitted upwards to further improve the coupling efficiency of the grating. In our proposed design, the simulations were for an X-cut LNOI wafer, but the same approach can be applied to Z-cut LNOI wafers. In this paper, the BIC mode is used simply to avoid the practical difficulty of etching the LiNbO3 layer. For the BIC mode, most of the light in the waveguide region is still in lithium niobate, and it is possible to use the LNOI BIC waveguide for acousto-optic modulation [15] and electro-optic modulation [16]. Thus, the method we proposed here works effectively as a grating coupler and can also utilize the excellent electro-optic properties of the LNOI platform. The working principle described in this paper can also be used with designs where the LiNbO3 layer is etched to form conventional channel waveguides. We designed the polysilicon grating to couple the quasi TM mode into the BIC channel waveguide.

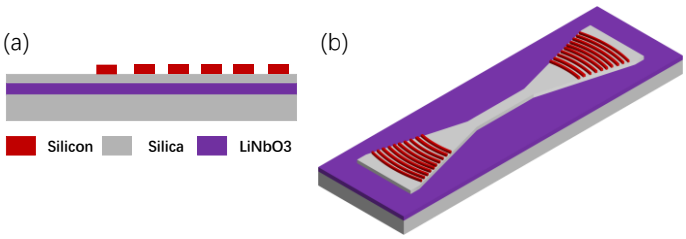


Fig.1 Schematic of the high coupling efficiency grating for lithium niobate on insulator. (a) 2D cross-section view. (b) 3D view.

We carried out design optimization, using the genetic algorithm to optimize the thickness of the silica layer and the polysilicon grating, with each period optimized using a different duty cycle. The optimization algorithm was used for an LNOI wafer with 400 nm thick lithium niobate and silica substrate of 2 μm thickness on a silicon handle wafer. The optimization algorithm is similar to the one we used previously for silicon grating couplers [17], and the final optimized parameters of the proposed grating are shown in Fig.2. There are some discontinuities in the parameters in Fig.2, as is needed to engineer the grating strength for improved matching of the diffracted mode with the optical mode and in reducing the back reflection, and which was also evident in the vertical silicon grating coupler design [17].

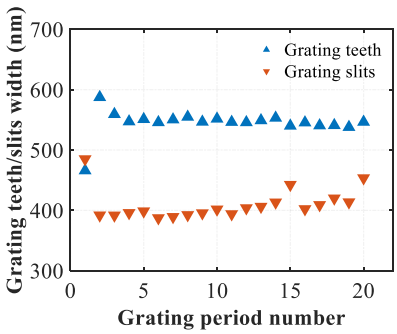


Fig.2. Final structural parameters after optimization for the grating coupler.

The optimized grating has a minimum feature size of 387 nm. The final optimized thickness of the deposited silica layer and polysilicon layer are 300 nm and 300 nm, respectively. The top polysilicon overlay is fully etched, which simplifies the fabrication process. As the BIC waveguide is quite wide (2 μm), the alignment of the polysilicon mask with the waveguide falls well within the overlay accuracy of photolithography, and the design is compatible for fabrication by photolithography. The proposed grating coupler has high coupling efficiency for coupling to standard single-mode fiber with a core diameter of 9 μm and mode field diameter of 10.4 μm at 1550 nm. The optimized grating efficiently couples the TM polarization into the BIC waveguide. The simulated transmission spectra of the optimized waveguide coupler, obtained from the final 3D FDTD simulation, is presented in Fig.3. The final optimized grating coupler has a predicted coupling efficiency of -1.33 dB at 1548.4 nm and 3 dB bandwidth of 46 nm from 1517 nm to 1563 nm.

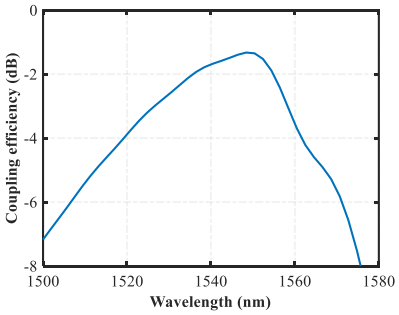


Fig.3. Coupling efficiency spectra of the final optimized grating coupler.

DISCUSSIONS

We proposed a new high coupling efficiency grating coupler in the LiNbO3 platform using a high index polysilicon grating on silica. The vertical slot waveguide and cavity structure enable the grating to provide high coupling efficiency. The proposed grating coupler has a minimum feature size of 387 nm and is compatible for fabrication using photolithography. 3D simulation results predict a coupling efficiency of -1.33 dB at 1548.4 nm with a 3 dB bandwidth of 46 nm from 1517 nm to 1563 nm. The fabrication of the grating coupler is still underway at the time of writing this summary, but we expect to present experimental results at the conference to validate the simulations.

Acknowledgements

This work was funded by Hong Kong Research Grants Council General Research Fund 14207021.

References

[1] X. Chen et al., "The Emergence of Silicon Photonics as a Flexible Technology Platform," Proc. IEEE, vol. 106, no. 12, pp. 2101-2116, 2018.
[2] J. H. Song et al., "Grating Coupler Embedded Silicon Platform for Hybrid Integrated Receivers," IEEE Photonics Technol. Lett., vol. 24, no. 3, pp. 161-163, 2012.
[3] X. Zhou and H. K. Tsang, "High Efficiency Multimode Waveguide Grating Coupler for Few-Mode Fibers," IEEE Photonics J., vol. 14, no. 4, pp. 1-5, Aug. 2022.
[4] X. Zhou and H. K. Tsang, "Optimized shift-pattern overlay for high coupling efficiency waveguide grating couplers," Opt. Lett., vol. 47, no. 15, pp. 3968-3971, Aug. 2022.
[5] X. Zhou and H. K. Tsang, "Photolithography Fabricated Sub-decibel High-efficiency Silicon Waveguide Grating Coupler," IEEE Photonics Technol. Lett., 2022.
[6] C. Wang et al., "Integrated lithium niobate electro-optic modulators operating at CMOS-compatible voltages," Nature, vol. 562, no. 7725, pp. 101-104, Oct 2018.
[7] S. Kang et al., "High-efficiency chirped grating couplers on lithium niobate on insulator," Opt. Lett., vol. 45, no. 24, pp. 6651-6654, Dec 15 2020.
[8] B. Chen et al., "Low-loss fiber grating coupler on thin film lithium niobate platform," APL Photonics, vol. 7, no. 7, 2022.
[9] Z. Chen, Y. Wang, H. Zhang, and H. Hu, "Silicon grating coupler on a lithium niobate thin film waveguide," Opt. Mater. Express, vol. 8, no. 5, 2018.
[10] X. Han et al., "Single-step etched grating couplers for silicon nitride loaded lithium niobate on insulator platform," APL Photonics, vol. 6, no. 8, 2021.
[11] Y. Liu et al., "Efficient grating couplers on a thin film lithium niobate-silicon rich nitride hybrid platform," Opt. Lett., vol. 45, no. 24, pp. 6847-6850, Dec 15 2020.
[12] Z. Yu, X. Xi, J. Ma, H. K. Tsang, C.-L. Zou, and X. Sun, "Photonic integrated circuits with bound states in the continuum," Optica, vol. 6, no. 10, 2019.
[13] G. Roelkens, D. Van Thourhout, and R. Baets, "High efficiency Silicon-on-Insulator grating coupler based on a poly-Silicon overlay," Opt. Express, vol. 14, no. 24, pp. 11622-30, Nov. 2006.
[14] X. Zhou, T. Zhang, L. Chen, W. Hong, and X. Li, "A Graphene-Based Hybrid Plasmonic Waveguide With Ultra-Deep Subwavelength Confinement," J. Lightwave Technol., vol. 32, no. 21, pp. 4199-4203, 2014.
[15] Z. Yu and X. Sun, "Acousto-optic modulation of photonic bound state in the continuum," Light Sci. Appl., vol. 9, p. 1, 2020.
[16] J. Zhang, B. Pan, W. Liu, D. Dai, and Y. Shi, "Ultra-compact electro-optic modulator based on etchless lithium niobate photonic crystal nanobeam cavity," Opt. Express, vol. 30, no. 12, pp. 20839-20846, Jun 6 2022.
[17] Y. Tong, W. Zhou, and H. K. Tsang, "Efficient perfectly vertical grating coupler for multi-core fibers fabricated with 193 nm DUV lithography," Opt. Lett., vol. 43, no. 23, pp. 5709-5712, Dec. 2018.

Experimental demonstration of a low-loss broadband directional coupler based on subwavelength gratings metamaterials

(Student paper)

JAIME VILAS[1,2,*], RAQUEL FERNÁNDEZ DE CABO[2], IRENE OLIVARES[1], DAVID GONZÁLEZ-ANDRADE[3], ANTONIO DIAS-PONTE[1] AND AITOR V. VELASCO[2].

[1]Alcyon Photonics S.L, Génova 11, Madrid, 28004, Spain

[2]Instituto de Óptica Daza de Valdés, Consejo Superior de Investigaciones Científicas (CSIC), Serrano 144, Madrid, 28006, Spain

[3]Centre de Nanosciences et de Nanotechnologies, CNRS, Université Paris-Saclay, Palaiseau, 10 Bd Thomas Gobert, 91120, France

[*]j.vilas@alcyonphotonics.com

Directional couplers are widely used for power distribution in silicon photonic integrated circuits, requiring reduced losses across a broad bandwidth for specific splitting ratios. In this work, we demonstrate a very low-loss, broadband and splitting ratio-agnostic directional coupler based on subwavelength metamaterials. Results show average loss < -0.24 dB for splitting ratios ranging from 0.08 to 1, across a 170 nm bandwidth (1505-1675 nm).

Keywords: *Directional coupler, power splitter, power coupling, subwavelength metamaterials.*

INTRODUCTION

Silicon-on-insulator (SOI) platforms leverage the maturity of microelectronics fabrication technologies to provide compact and efficient photonics integrated circuits (PICs), effectively reducing manufacturing and infrastructure costs [1]. Optical power splitters and combiners are key components in almost any PIC, and are often cascaded to compose optical filters such as wavelength division multiplexers (WDM) [2]. Directional couplers (DC) are ubiquitously used for this purpose, owing to their straightforward and simple design. Furthermore, DCs commonly present low losses and a splitting ratio (k) tailorable through the length of the coupling section. However, conventional DCs suffer from limited bandwidth and fabrication tolerances. Many different approaches have been explored to address these shortcomings [3], including subwavelength gratings (SWG) metamaterials, which have been proven to increase operational bandwidth in DCs [4]. SWG consist of arrayed segments of core and cladding materials, with a period (Λ) significantly smaller than the operational wavelength (λ). Dispersion and refractive index of the resulting metamaterial can be engineered through geometrical design of the segmented waveguide [5]–[7].

In this work, we demonstrate the use of SWG metamaterials to design a compact DC, geometrically engineered to achieve low losses across a broad bandwidth independently of the splitting ratio. Experimental results show average excess losses ($\overline{EL}$) below 0.24 dB and splitting ratio deviations below ±1 dB over a 170 nm bandwidth.

PRINCIPLE OF OPERATION

The architecture of our 2×2 SWG DC is divided in three areas, as depicted in Fig. 1(a). The coupling area is labelled A and comprises two parallel mono-mode waveguides of length L_A separated by a gap of width W_{gap}. In this area input light is progressively coupled to the opposite waveguide. To reduce the spectral dependence of this coupling effect, a geometrically optimized SWG region has been included. The SWG segments span a total width W, with a fixed period (Λ) and duty cycle (DuC). DuC is computed as:

$$DuC = \frac{L_{core}}{L_{core}+L_{cladding}} \quad (1)$$

Where L_{core} and $L_{cladding}$ represent the length of the core and cladding segments, respectively. The number of periods (N_A) determine the length of the coupling region ($L_A = N_A\Lambda$), and can be judiciously selected to define the k value of the device.

The taper areas, labelled B in Fig. 1(a), include input/output SWG tapers, optimized to efficiently transition the optical mode between the input/output S-bends and the coupling area. These tapers are N_B periods long, resulting in a section length of $L_B = N_B\Lambda$, and maintain the period and duty cycle of area A. N_B has been engineered to strike a balance between minimizing the coupling that takes place in the tapers and reducing losses caused by a non-adiabatic transition.

Finally, the input and output areas (labelled C in Fig. 1(a)) feature S-bends that connect the input and output ports

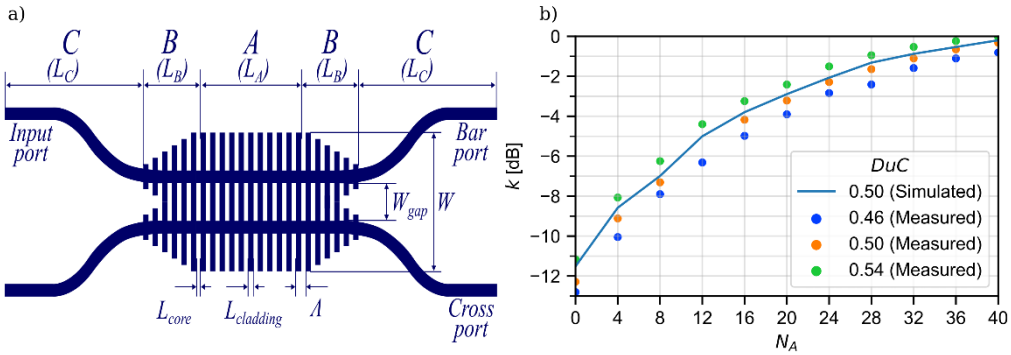


Fig. 1. (a) Schematic of the proposed design and (b) dependence of the splitting ratio on the number of periods in area A for the fabricated and simulated devices with different duty cycles.

with the SWG tapers. The radii of the curves that compose the S-bends are engineered to minimize coupling in the area without inducing curvature losses.

We have defined the following figures of merit to characterize the performance of the SWG DC. The splitting ratio deviation (Δk) is defined as the deviation from the central k value in a target bandwidth. The splitting ratio is defined in Eq. (2), where $|S_{cross}|^2$ and $|S_{bar}|^2$ are the optical power output in the cross and bar ports, respectively. Similarly, the excess losses (EL) are shown in Eq. (3), where $|S_{input}|^2$ is the input power. Other figures of merit include average excess losses ($\overline{EL}$) for all measured devices (-11 dB ≤ k ≤ 0 dB), and EL_3, defining the excess losses of the device closest to k = -3 dB (i.e. even division between the cross and bar ports).

$$k\,[dB] = 10log_{10}\left(\frac{|S_{bar}|^2}{|S_{bar}|^2+|S_{cross}|^2}\right) \quad (2)$$

$$EL[dB] = -10log_{10}\left(\frac{|S_{bar}|^2+|S_{cross}|^2}{|S_{input}|^2}\right) \quad (3)$$

DEVICE DESIGN

The proposed design was optimized for the transverse electric (TE) polarization in a SOI platform with Si thickness of 0.22 µm, SiO_2 cladding and buried oxide with a cladding thickness of 2.2 µm. To ensure mono-mode behaviour, waveguide width was set to 0.45 µm. Design was carried out through full three-dimensional finite-difference time-domain (3D FDTD) simulations, first optimizing the coupling area. As Λ increases, the beat length of the device decreases, which in turn increases the sensitivity of k to variations in L_A. We have balanced this effect by increasing W_{gap}, which reduces coupling intensity and increases the beat length. By fixing W = 2.6 µm, we optimized the bandwidth and EL of the device, resulting in Λ = 0.26 µm and W_{gap} = 0.5 µm. Three DuC values were evaluated (i.e., 0.54, 0.5, 0.46), all of them with a minimum feature size (MFS) higher or equal to 0.12 µm.

Further simulations were carried out to optimize the taper length to 1.56 µm (N_B = 6). Taper impact on k was measured by using a back-to-back configuration of the SWG tapers (N_A = 0), resulting in k = -11 dB. As such, k = -11 dB is the minimum splitting ratio achievable within the first beat length. The first beat length (k = 0 dB) takes place for N_A = 40. Finally, we embedded the S-bends 0.65 µm into the tapers and set their lengths to 5 µm. Separation between ports was set to 2.95 µm.

RESULTS

Fabrication was carried out by Applied Nanotools through their NanoSOI services, using the electron-beam lithography process. The fabricated dies contained three sets of eleven DCs each, with increasing N_A between 0 and 40. The DuC was varied on a per-set basis, with DuC = 0.54 yielding the bests results and thus being featured in the figures of merit from this point on. Fibre-chip coupling is optimized by including high-efficiency broadband SWG edge couplers[8].

In Fig. 1(b) we have presented the measured k at a wavelength of 1550 nm for all devices under test. These results accurately match simulation results and show that k exhibits the expected sinusoidal dependence with the coupler length. The missing device with DuC = 0.5 and N_A = 12 represents an outlier, likely caused by a faulty coupling structure. The spectral response of k is displayed in Fig. 2(a). All devices under test present Δk < ±1 dB across the full wavelength range, conforming to common standards of bandwidth measurements for DCs.

Finally, Fig. 2(b) shows the $\overline{EL}$ of all devices under test as a function of the wavelength, while the shaded area represents the standard deviation. Measurements for the full 170 nm bandwidth show $\overline{EL}$ < 0.24 dB, with further

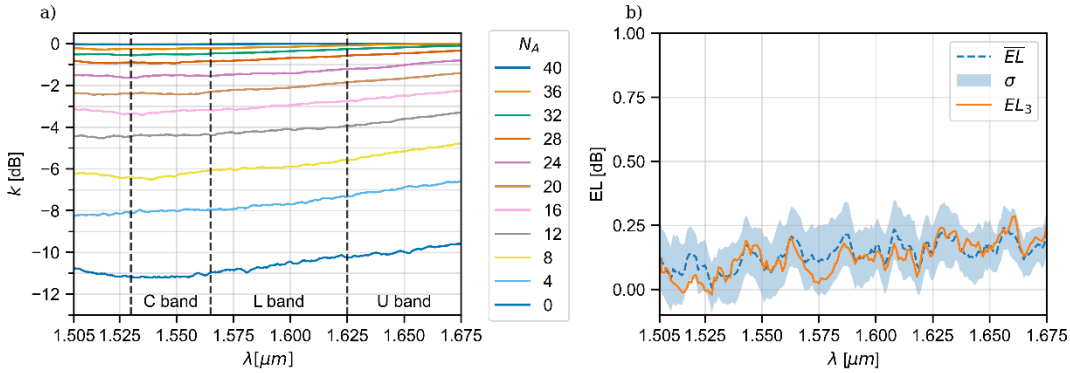


Fig. 2. (a) Spectral response of the splitting ratio for all the devices under test with DuC = 0.54. (b) Average spectral dependence of the excess losses ($\overline{EL}$), standard deviation (σ) and individualized results for the 3 dB splitting ratio (EL_3).

reductions down to < 0.20 dB and < 0.23 dB in the C and L communication bands, respectively. These results further prove that *k* can be straightforwardly tailored during design without impacting device performance in a significant manner. In order to provide a common ground for comparison with other state-of-the-art DCs [3], [4], [9]–[12], we have individualised EL_3 for N_A = 16 (*k* ≈ -3 dB). Compared to these devices, we achieved the best measured losses, with only the device by Ye *et al.* [9] achieving higher experimental bandwidth, albeit at the cost of four times more losses.

DISCUSSION

In conclusion, we have designed and fabricated a low-loss broadband directional coupler using subwavelength gratings metamaterials, obtaining competitive results against estate-of-the-art devices. Measurements of the devices within the first beat length show average losses below 0.24 dB and splitting ratio deviation below ± 1 dB across a broad bandwidth of 170 nm, proving that the splitting ratio can be straightforwardly tailored during design. Coupler length ranges from 3 μm (*k* = -11 dB) to 13.40 μm (*k* = 0 dB), including coupling and input/output taper areas. The performance of our device makes it a strong candidate for general power distribution in SOI PICs, more so for the implementation of multi-stage MZI-based optical filters.

Acknowledgements: This work is a part of grant (DIN2020-011488) and is funded in part by the Spanish Ministry of Science and Innovation (MCIN/AEI/10.13039/501100011033) and the European Union "NextGenerationEU/PRTR". Further funding is provided by the MCIN/AEI/10.13039/501100011033 under grants PTQ2021-011974, RTI2018-097957-B-C33, PID2020-115353RA-I00; European Social Fund Plus grant (PRE2021-096954); Community of Madrid (STARTUP2020\L2550); Community of Madrid – FEDER funds (S2018/NMT-4326, APOYO-JOVENES-KXHJ8C-16-VCKM78).

REFERENCES

[1] M. Hochberg and T. Baehr-Jones, *Towards fabless silicon photonics*, Nat. Photonics, vol. 4, no. 8, pp. 492–494, 2010.
[2] T. H. Yen and Y. J. Hung, *Fabrication-Tolerant CWDM (de)Multiplexer Based on Cascaded Mach-Zehnder Interferometers on Silicon-on-Insulator*, J. of Lightwave Technology, vol. 39, no. 1, pp. 146–153, 2021.
[3] G. F. R. Chen, J. R. Ong, T. Y. L. Ang, S. T. Lim, C. E. Png, and D. T. H. Tan, *Broadband Silicon-On-Insulator directional couplers using a combination of straight and curved waveguide sections*, Sci. Rep., vol. 7, no. 1, p. 7246, 2017.
[4] R. Halir *et al.*, *Colorless directional coupler with dispersion engineered sub-wavelength structure*, Opt. Express, vol. 20, no. 12, pp. 13470-13477, 2012.
[5] R. Fernández de Cabo, J. Vilas, P. Cheben, A. v. Velasco, and D. González-Andrade, *Experimental characterization of an ultra-broadband dual-mode symmetric Y–junction based on metamaterial waveguides*, Opt. Laser Technol., vol. 157, p. 108742, 2023.
[6] D. González-Andrade *et al.*, *Experimental demonstration of a broadband mode converter and multiplexer based on subwavelength grating waveguides*, Opt. Laser Technol., vol. 129, p. 106297, 2020.
[7] P. Cheben, R. Halir, J. H. Schmid, H. A. Atwater, and D. R. Smith, *Subwavelength integrated photonics*, Nature, vol. 560, pp. 565–572, 2018.
[8] P. Cheben *et al.*, *Refractive index engineering with subwavelength gratings for efficient microphotonic couplers and planar waveguide multiplexers*, Opt. Lett., vol. 35, no. 15, pp. 2526–2528, 2010.
[9] C. Ye and D. Dai, *Ultra-Compact Broadband 2 × 2 3 dB Power Splitter Using a Subwavelength-Grating-Assisted Asymmetric Directional Coupler*, J. of Lightwave Technology, vol. 38, no. 8, pp. 2370–2375, 2020.
[10] Y. Wang *et al.*, *Compact Broadband Directional Couplers Using Subwavelength Gratings*, IEEE Photonics J., vol. 8, no. 3, pp. 1-8, 2016.
[11] H. Xu and Y. Shi, *Ultra-compact polarization-independent directional couplers utilizing a subwavelength structure*, Opt. Lett., vol. 42, no. 24, pp. 5202–5205, 2017.
[12] L. Liu, Q. Deng, and Z. Zhou, *Subwavelength-grating-assisted broadband polarization-independent directional coupler*, Opt. Lett., vol. 41, no. 7, pp. 1648–1651, 2016.

Studying Open Scattering Channels in an Analog Physical Simulation

(Student paper)

Reinier van der Meer[1], Michiel J.A. de Goede[2], Ben Kassenberg[2], Pim Venderbosch[2], Henk Snijders[2], Jörn Epping[2], Caterina Taballione[2], Hans van den Vlekkert[2], Jelmer J. Renema[1,2], and Pepijn W.H. Pinkse[1]*

[1]MESA+ Institute, University of Twente, PO Box 217, 7500 AE Enschede, The Netherlands
[2] QuiX Quantum BV, Enschede, The Netherlands
* corresponding author e-mail

We simulate a small multiple-scattering system with an 12x12 programmable integrated photonic processor on which we encode the full scattering matrix of the system, acting as an analog and physical simulation device. We show that we can measure the singular value distribution of transmission efficiencies of a 6-channel scattering system in this way. Already the raw data gets close to the predicted bimodal distribution.
Keywords: *Multiple scattering, Integrated photonic processor, quantum metrology*

INTRODUCTION

Scattering waves are found in many places in nature and technology. Unraveling their physics is important for understanding transport of both electrons, phonons of photons through disordered media. Many of their properties can be described by random matrix theory [Bee1997], alhtough it turns out to be difficult to match some of the more striking predictions of that theory to experiments. For instance, the theory predicts that the transmission through disordered systems is dominated by nontransmiting channels and -counterintuitively- by some near-perfect transmitting channels, also known as 'closed' and 'open channels', respectively [Rot2017]. This bimodal behavior of the transmission eigenvalues [Do1982, Mel1988] underlies many different phenomena, such as electronic conductance fluctuations, suppression of electronic shot noise and increased optical transmission through random disordered systems. Despite the central role of open channels in scattering physics, only indirect evidence for their existence has been reported. Measuring the entire bimodal transmission is impossible in electronics because of the small size of electrons. In free-space optics it is a challenge, since one needs to resolve all the modes of the transmission matrix describing the system [Goe2013].

In random matrix theory, the system-specific details are replaced by a unitary scattering matrix

$$\mathbf{S} = \begin{pmatrix} \mathbf{R} & \mathbf{T} \\ \mathbf{T}' & \mathbf{R}' \end{pmatrix},$$

where the submatrices **T** and **R** are the transmission and reflection matrices, respectively. This scattering matrix contains the appropriate statistical properties of the system, while remaining agnostic to the microscopic details of the scatterer. This allows to study their physics on any system that captures these statistics.

We use the approach of random matrix theory to physically simulate our diffusive system on a state-of-the-art 12-mode one-way integrated photonic processor, shown in the inset of Fig. 1a) and schematically in Fig. 1b). The processor is a commercial SiN integrated photonic system, on which more details can be found in [Tab2021]. On this network, an entire scattering matrix **S** is implemented using the Clements decomposition of an arbitrary unitary into a network of programmable beam splitters [Cle2016]. The first six output modes are treated as 'reflection' modes and output modes 7-12 as transmission modes. Compared to traditional scattering systems in, the advantage of the integrated photonic processor is that the channels are discrete single-mode fiber inputs and outputs, avoiding problems with finite numerical aperture of input and output optics. It also avoids the problem of over or under sampling of the input and output fields [Pai2020].

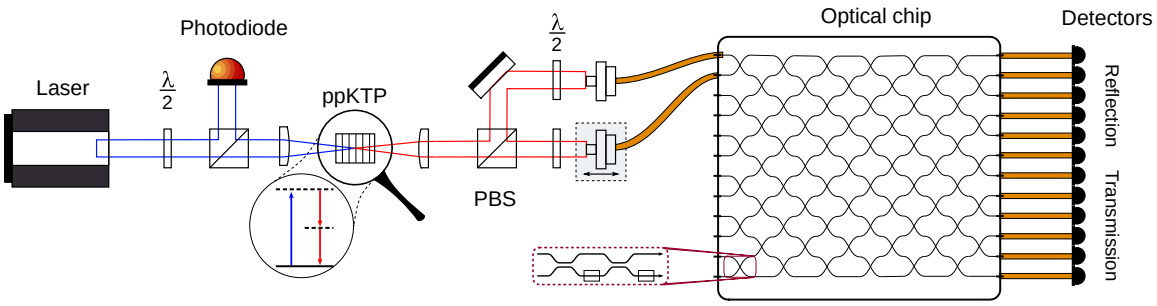


Fig. 1. The setup for characterization of the artificial scattering system: On the left is the Spontaneous Parametric Down-Conversion (SPDC) source injecting pairs of photons into the 12x12 programmable optical processor that acts as the scattering system. Since the chip does not reflect any light, output modes are assigned as reflection or transmission channels, so that a full scattering matrix of a 6-channel scattering system can be simulated.

After programming a scattering matrix in the processor, we characterize this system as if it were an unknown scattering system as described further down. We measure and extract the 6x6 transmission matrix **T**. From this, six singular values can be found by standard singular-value decomposition. By itself, six singular values are not sufficient to build up a smooth singular value distribution to compare meaningfully to theory. A major advantage of this network is, however, that it is fully reconfigurable. It is therefore straightforward to program different matrices. We implemented a total of 200 randomly generated scattering matrices. These scattering matrices are generated by a numerical simulation of a 6-mode scattering system with appropriate settings. The simulation of the 12-mode S-matrices follows the model as proposed by Dorokhov, Mello, Pereira and Kumar [Do1982, Mel1988], which divides the scattering system into short segments. Each segment is shorter than the transport mean free path and longer than the wavelength. Adding a new segment can now be described as a perturbative correction [Rot2017]. We follow the method of Ko and Inkson [Ko1988]. The matrices are computed by simulating a one-dimensional 6-mode waveguide with perfectly reflecting boundaries. The waveguide is divided into 40 equally sized sections over the length of the waveguide. Each section has a probability of 10% to have a scatterer placed at a random coordinate inside this waveguide segment, corresponding to the weak scattering regime. Furthermore, given the transport mean free path, the number of segments N determines the average transmission efficiency. We chose $N = 40$ and $\langle T \rangle = 0.37$, allowing us to observe open channels with 200 random instances of these waveguides. Stronger-scattering waveguides, i.e. with more segments and scatterers, have lower average transmission such that an insufficient number of singular values can be sampled to resolve the open channels.

Matrix characterisation

Characterisation of the matrices on the network is performed by sending pairs of single photons into the network and sampling their output distribution with a battery of superconducting nanowire single-photon detectors (SNSPDs). Although it would in principle be possible to characterise the matrix with classical coherent light in an interferometrically stable setup, performing the readout with single photons has the advantage that we do not need interferometric stability of the fibers connecting the PIC network with the outside world [Lai2012, Dha2016], because of the phase insensitivity of the single-photon quantum state. Hence, our quantum readout is more robust than the equivalent classical method.

The matrix amplitudes are sampled by sequentially injecting single photons into each input mode and measuring the output distribution. The photon flux is corrected for known experimental fluctuations such as the variations of pump power over time, relative detector efficiencies, and fiber-to-chip coupling losses. The phases of the matrix elements are characterized by sequentially measuring two-photon interference in the network for a given set of combinations of two input and two output modes [Lai2012].

To reduce experimental measurement time, we only characterized the phases of six input modes to all 12 output modes. The matrix amplitudes are measured for the entire **S** matrix so that the 1-photon output distribution can be normalised.

RESULTS

First results are shown in Fig. 2, where the singular value distributions of the transmission matrix without any further processing is plotted. Contrary to data with traditional scattering media or multimode fibers, already the raw data show a shoulder indictive of the expected bimodal distribution. The non-physical data points at $\tau^2 > 1$ are caused by measurement noise such as dark counts, imperfect control of the chip, multiphoton states and detector blinding (nonlinear loss).

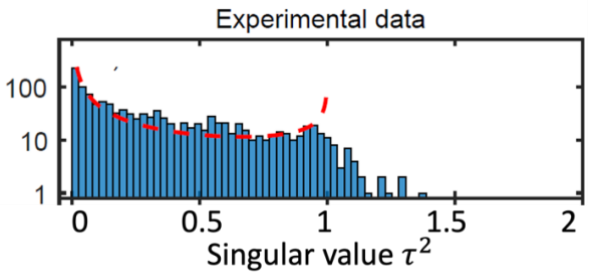


Fig. 2. The singular values distribution of the transmission matrix for a data set of 200 matrices. The red dashed line is the theoretical distribution as predicted by [Goe2013]. The non-physical values higher than 1 result from residual measurement noise.

DISCUSSION

It is slightly unsatisfying that notwithstanding the exquisite control over this system, the raw data does not convincingly show the bimodal distribution. However, we think imposing the reasonable condition that the system does not exhibit gain should be enough to bring forth the bimodal distribution, without imposing the much more stringent unitarity condition. To the best of our knowledge, the bimodal distribution has never been seen without imposing unitarity, which will already lead to a bimodal distribution of the singular value distribution of random Gaussian matrices.

Acknowledgements: We acknowledge funding from the Nederlandse Organisatie voor Wetenschappelijk Onderzoek (NWO) via QuantERA QUOMPLEX (Grant No. 680.91.037), and Veni (grant No. 15872). Furthermore, we would like to thank Allard Mosk for discussions.

References

[Bee1997] C. W. J. Beenakker, *Random-matrix theory of quantum transport*, Rev. Mod. Phys. **69**, 731–808, DOI: 10.1103/RevModPhys.69.731 (1997).

[Cle2016] W. R. Clements, P. C. Humphreys, B. J. Metcalf, W. S. Kolthammer & I. A. Walmsley, *Optimal design for universal multiport interferometers*, Optica **3**, 1460–1465, DOI: 10.1364/OPTICA.3.001460 (2016).

[Do1982] O. Dorokhov, *Transmission coefficient and the localization length of an electron in N bound disordered chains*, JETP Lett. **36** (1982).

[Goe2013] A. Goetschy & A.D. Stone, *Filtering Random Matrices: The Effect of Incomplete Channel Control in Multiple Scattering.* Phys. Rev. Lett. **111**, 063901; DOI: 10.1103/PhysRevLett.111.063901 (2013).

[Ko1988] D. Y. K. Ko & J. C. Inkson, *Matrix method for tunnelling in heterostructures: Resonant tunneling in multilayer systems.* Phys. Rev. B **38**, 9945–9951; DOI: 10.1103/PhysRevB.38.9945 (1988).

[Lai2012] A. Laing, & J.L. O'Brien, *Super-stable tomography of any linear optical device*, arXiv:1208.2868 (2012).

[Mel1988] P. A. Mello, P. Pereyra & N. Kumar, *Macroscopic approach to multichannel disordered conductors*, Annals Phys. **181**, 290–317, DOI: 10.1016/0003-4916(88)90169-8 (1988).

[Pai2020] P. Pai, J. Bosch & A. P. Mosk, *Optical transmission matrix measurement sampled on a dense hexagonal lattice*, OSA Continuum **5**, 637 (2020).

[Rot2017] S. Rotter & S. Gigan, Light fields in complex media: Mesoscopic scattering meets wave control. Rev. Mod. Phys. 89, 015005, DOI: 10.1103/RevModPhys.89.015005 (2017).

[Tab2021] C. Taballione, R. van der Meer, H. J. Snijders, P. Hooijschuur, J. P. Epping, M. de Goede, B. Kassenberg, P. Venderbosch, C. Toebes, H. van den Vlekkert, P. W. H. Pinkse & J. J. Renema, *A universal fully reconfigurable 12-mode quantum photonic processor*, Mater. Quantum. Technol. **1**, 035002; DOI: 10.1088/2633-4356/ac168c (2021).

Integrated On-chip Light Control via Out-coupling Grating Structures for Quantum Applications

(Student paper)

Anastasiia Sorokina[1,2,*], Pascal Gehrmann[1,2], Guochun Du[3], Carl-Frederik Grimpe[3], Steffen Sauer[1,2], Elena Jordan[3], Tanja Mehlstäubler[3,4,5], and Stefanie Kroker[1,2,3]

[1]Institute of Semiconductor Technology, Technische Universität Braunschweig, Hans-Sommer-Str. 66, Braunschweig, 38106, Germany
[2]Laboratory for Emerging Nanometrology, Technische Universität Braunschweig, Langer Kamp 6a/b, Braunschweig, 38106, Germany
[3]Physikalisch-Technische Bundesanstalt, Bundesallee 100, Braunschweig, 38116, Germany
[4]Institut für Quantenoptik, Leibniz Universität Hannover, Welfengarten 1, Hannover, 30167, Germany
[5]Laboratorium für Nano- und Quantenengineering, Leibniz Universität Hannover, Welfengarten 1, Hannover, 30167, Germany
[*] a.sorokina@tu-braunschweig.de

Integrated optics are a vital approach toward scalable trapped-ion quantum computers. We present numerical results for controlling linearly polarized light with various focusing features of a µm-beam via grating structures. Furthermore, we discover a multi-wavelength addressing by optimizing the design of the structure and manipulating the beam's overlap.
Keywords: *Integrated Optics, Grating Coupler, Light Polarization, Quantum Computing*

INTRODUCTION

Integrated optics for quantum experiments on chips are an essential toolbox for the miniaturization of the setup and its robustness, allowing the realization of more complex operations and simultaneously enhancing their precision. The application range of integrated photonic systems is constantly expanding to areas including trapped-ion quantum computers (QCs) [1, 2, 3], quantum sensing with trapped ions [4] and neutral atoms [5, 6], as well as quantum communication [7]. Current approaches to govern and focus laser light for optical addressing typically rely on the use of bulk optics, leading to undesired influences on the fidelity of operations and preventing further scalability [1]. Circumventing the large bulk optics and providing the optical requirements of the atoms, in terms of wavelength and intensity, require an accurate simulation, fabrication, and characterization of the integrated on-chip systems. Especially for QCs with ions as qubits, the preparation and operation of atoms require addressing multiple ion transitions with linearly and circularly polarized light in a broad range of wavelengths, from UV to NIR. This can be accomplished by Si_3N_4- and AlN-based integrated waveguides (WGs) and grating couplers (GCs), providing an efficient solution for flexible on-chip light routing with a small footprint and integration ability with the trap electrodes. In addition, integrated optics for multi-wavelength operation help to enhance the robustness of on-chip light guidance and increase the scalability of quantum chips for a wide range of trapped ion architectures.

Here, we present and numerically demonstrate a WG and focusing GCs for optical ion addressing at the wavelengths of $\lambda_1 = 760\ \mathrm{nm}$ and $\lambda_2 = 935\ \mathrm{nm}$ based on the Si_3N_4/SiO_2 material platform. The structures are designed for linearly polarized light with predefined figures of merit, like focused beam sizes ($\omega_0 = 2 - 30\ \mu\mathrm{m}$) and emission angles ($\vartheta_{\mathrm{em}} = -75°$ to $75°$). Fig. 1 left shows the schematic overview of the GCs integrated within the ion trap, and Fig. 1 right schematically demonstrates the WG and GC system in more detail. The electrodes create a trapping potential above the chip surface, and the optical components allow addressing multiple transitions to prepare and control the ion-qubits.

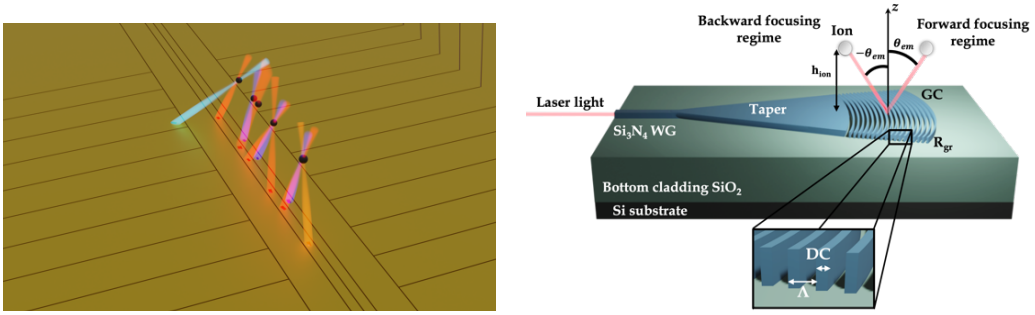


Fig. 1 left: Schematic view on the trapped-ion QC chip with circular- and elliptic beam shapes, right: WG-GC design scheme with forward and backward light focusing regimes.

RESULTS AND DISCUSSION

Single-mode waveguide for NIR

The finite-difference eigenmode (FDE) solver of Lumerical MODE was utilized to evaluate single-mode (SM) and multi-mode (MM) regimes for different Si_3N_4/SiO_2 WG geometries at λ_1 and λ_2. Nested sweeps of the core width w_{core} and the core height h_{core} have been performed to investigate the modal confinement and the modal polarization purity of the fundamental quasi-TE and quasi-TM modes, respectively. Fig. 2 left shows the modal effective refractive index n_{eff} of quasi-TE_{00} mode in the SM regime at $\lambda_1 = 760\ \mathrm{nm}$. SM WG geometries with large $w_{\mathrm{core}}/h_{\mathrm{core}}$ - ratios offer a very high modal polarization purity but suffer from lower mode confinement. To further expand the functionality of the WGs for scalable light routing on-chip and enable a multi-wavelength operation with $\lambda_2 = 935\ \mathrm{nm}$ in the same WG, a reasonable mode confinement factor at the longer wavelength has been considered in the choice of the WG geometry. Therefore, the WG geometry $520 \times 200\ \mathrm{nm}^2$ was chosen to support a moderately high confined quasi-TE_{00} mode with high mode polarization purity and suppression of weakly guided quasi-TM_{00} mode. Although the WG is on the border of the SM regime, the higher order mode is near cut-off and is therefore expected to be extinguished by high bending losses in WG bends.

Additionally, the FDE solver was used to investigate WG bends (see Fig. 2 right). The total mode-mismatch loss of the input and output interfaces L_{MM} and the radiation loss $L_{\mathrm{rad.}}$ have been simulated at different bending radii r_{bend} at both wavelengths for the quasi-TE_{00} mode of the chosen WG geometry. Subsequently, the total bending losses $L_{\mathrm{bend,tot.}}$ were calculated using estimated propagation losses $L_{\mathrm{propag.}}$. Based on experimental data, a propagation loss per unit length $\alpha_{\mathrm{propag.}} = 0.75\ \mathrm{dB/cm}$ was assumed for $\lambda_2 = 935\ \mathrm{nm}$ [8]. Due to the decreased mode confinement, the longer wavelength dictates the limitations of the bending radius. A minimum total loss of $L_{\mathrm{bend,tot.}} = 0.013\ \mathrm{dB}$ can be achieved by a radius of $r_{\mathrm{bend}} = 60\ \mu\mathrm{m}$. For even more compact light routing on-chip, we have implemented WG bending radius of $r_{\mathrm{bend}} = 20\ \mu\mathrm{m}$, where minor losses of $L_{\mathrm{bend,tot}} = 0.09\ \mathrm{dB}$ are expected.

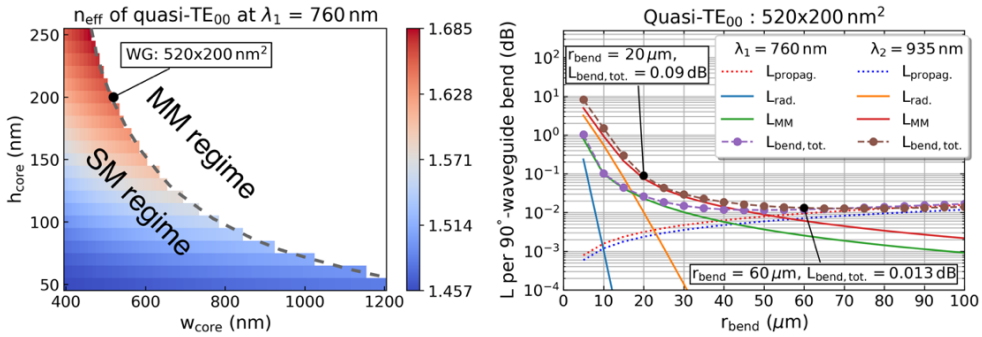


Fig.2 left: Nested parameter sweep results for $n_{\mathrm{eff}} = f(w_{\mathrm{core}}, h_{\mathrm{core}})$ of quasi-TE_{00} at $\lambda_1 = 760\ nm$, right: losses of a 90°-waveguide bend in dB of quasi-TE_{00} at $\lambda_1 = 760\ nm$ and $\lambda_2 = 935\ nm$.

Focusing grating coupler in forward and backward regimes

The in-coupled laser light is guided by the WG and extended by the taper to the area of the GC. Control over emission angle (ϑ_{em}) and grating strength are maintained by nonlinear apodization of grating period (Λ) and duty cycle (DC). Altering the radius of the GC (R_{gr}) leads to a Gaussian beam profile with a well-controlled focused beam size at the position of the trapped ion. The described design concept has been applied, and the produced near- and far-field were studied using a finite-difference time-domain solver (FDTD) of Lumerical FDTD. Forward and backward focusing regimes for light delivery have been considered (see Fig. 3). By choosing relatively large Λ and DC, forward focusing enables the generation of a focused µm-beam while maintaining the manufacturing constraints. However, additional intensity peaks due to higher-order diffraction require further optimization of a full-layer chip to minimize the parasitic influence of scattered light on the ion. In contrast, the backward focusing regime can suppress undesired higher-order diffraction but yields a trade-off concerning fabrication limits. The presented GC designs allow controlling beam parameters independently in the longitudinal (LD) and transversal (TD) directions of the light propagation, bringing the light above the surface in circular- and elliptical shapes. Therefore, GCs can be used for addressing not only a single trapped ion with minimum beam crosstalk but also a chain of the trapped ions by keeping the small beam radius in LD and enlarging it in TD, as shown in Fig. 3A. Additionally, we have optimized the design of the WG and GC system in such a way that by using the same structure, light confinement and a beam overlap can be achieved for λ_1 and λ_2 simultaneously. Thus, we can substantially minimize the number of optical components on the chip by addressing two transitions in the same ion concurrently.

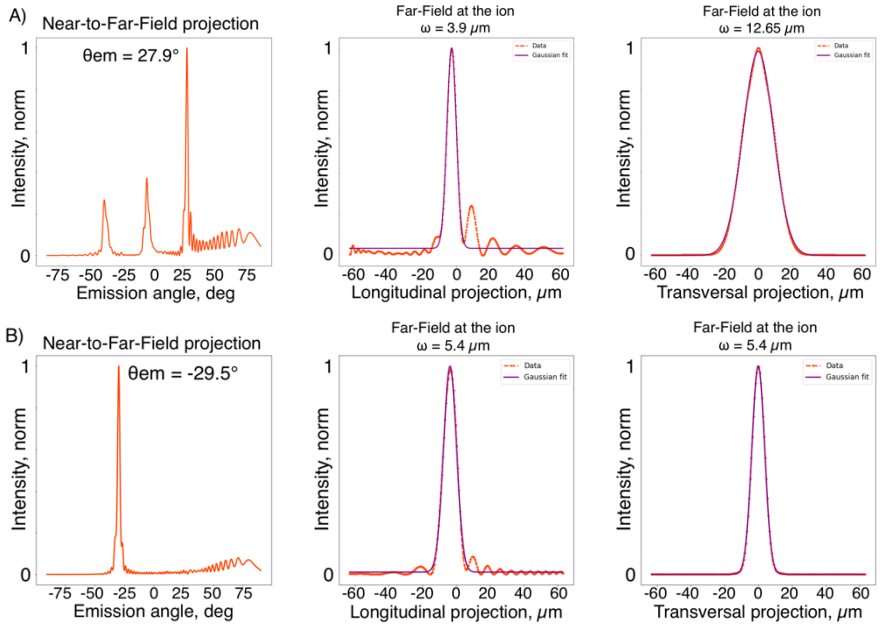


Fig. 3. Optical far-field characteristics of the GC in A) forward regime ($\vartheta_{em} = 27.9°$) with an elliptical beam shaping, where $\omega_{0,LD} = 3.9\ \mu m, \omega_{0,TD} = 12.65\ \mu m$ and B) backward focusing regime ($\vartheta_{em} = -29.5°$) with a spherical beam shaping, where $\omega_{0,LD} = \omega_{0,TD} = 5.4\ \mu m$. The ion position is 100 µm above the chip surface.

Moreover, we have evaluated the designed GCs efficiency and the influence of the layers on the focused beam. Hence, the total percentage of light reaching the ion above the chip surface can be expressed in the following way:

$$T = \frac{\frac{1}{2}\int_{\text{GC area}} Re\{\vec{P}\}\mathrm{d}\vec{S}}{P_{\text{in}}} \cdot 100, \tag{1}$$

where $\vec{P}$ is the Poynting vector, P_{in} is the input power coupled into the WG, and the GC area is an area above the GC in the near-field. Thereby, the simulated light efficiency in the near-field with the presence of SiO_2 layers is almost $T = 50\ \%$, and the efficiency in the near-field with all layers can drop down to $T \approx 30\ \%$. Due to the presence of multiple layers, such as a transparent conductive coating (ITO) and air, a multitude of interference mechanisms as well as reflections and refraction can occur. This substantially affects the overall optical performance of the device. However, in the framework of our trapped-ion chip design, the beam characteristics are rather prevalent. Further optimization of the GC performance can be accomplished by breaking the symmetry of the structure and varying the etching depth.

OUTLOOK

Based on the insights yielded from our design studies, we are extending the optical control to other polarization states, such as left and right circularly polarized light. Transferring the applied concepts towards the UV regime, we aim to utilize the advantages of AlN material to address transitions for photoionization, cooling and detection. The fabricated structures are then characterized by a near-field beam profiling setup to verify the numerical results and to encourage further design iterations toward higher beam-shaping features.

Acknowledgments: The authors gratefully acknowledge support by B-IGSM and the DFG Research Training Group GrK1952/1 “Metrology for Complex Nanosystems”. We thank the Quantum Valley Lower Saxony, ATIQ and the cluster of Excellence Quantum Frontiers (EXC-2123 – 390837967).

References

[1] C. Bruzewicz, *Trapped-ion quantum computing: Progress and challenges*, APR, vol. 6, no. 2, p. 021314, 2019
[2] K. Mehta, *Integrated optical multi-ion quantum logic*, Nature, vol. 586, no. 7830, pp. 533-537, 2020
[3] R. Niffenegger, *Integrated multi-wavelength control of an ion qubit*, Nature, vol. 586, no. 7830, pp. 538-542, 2020
[4] M. Day, *A micro-optical module for multi-wavelength addressing of trapped ions*, QST, vol. 6, no. 2, p. 024007, 2021
[5] A. Isichenko, *Photonic integrated beam delivery in a rubidium 3D magneto-optical trap*, arXiv: 2212.11417, 2022
[6] A. Ferdinand, *A scalable infrastructure for strontium optical clocks*, CLEO: Science and Innovations, pp. STu5O-1, 2022
[7] G. Moody, *2022 Roadmap on integrated quantum photonics*, Journal of Physics: Photonics, vol. 4, no. 1, p. 012501, 2022
[8] A. Subramanian, *Low-loss singlemode PECVD silicon nitride photonic wire waveguides for 532–900 nm wavelength window fabricated within a CMOS pilot line*, IEEE Photonics Journal, vol. 5, no. 6, pp. 2202809-2202809, 2013

Optical isolator element using nano-pixel for photonic integrated circuits

Haisong Jiang, Cangui Tang, and Kiichi Hamamoto

Interdisciplinary Graduate School of Engineering Sciences, Kyushu University,
6-1, Kasuga-koen, Kasuga, Fukuoka 816-8580, Japan
* jiang.haisong.447@m.kyushu-u.ac.jp

On-chip optical isolators are highly required components and have been researched and developed in optical communication system. In this study, we have proposed an integration-available ultra-compact isolator element based on nano-pixel configuration. The footprint of isolator element is designed in 3.0 × 3.0 μm^2. The simulated result exhibited superior an isolation ratio of 16.3 dB with excess loss of 1.2 dB at 1550 nm wavelength.
Keywords: *Nano-pixle, Isolator*

INTRODUCTION

In recent years, low-loss and high-performance photonic integrated circuits (PICs) have been researched widely for optical communication systems [1]. Among on-chip optical components, integrated optical nonreciprocal devices, such as optical isolators and circulators, which block the back-reflected light to protect optical systems, are still missing elements in current PICs. Previously, integrated optical isolators based on magneto-optical effects [2-3], nonlinear photonic effects [4-5] and spatiotemporal modulation [6-7] have been reported, however, they are not well deployed in several reasons including performance, processing difficulty, and others. In this paper, we newly propose an integrated isolator element based on optical nano-pixel waveguide configuration. The nano-pixel structure waveguide attracts attention recently as new optical waveguide device structure [8-10] because of the compact design capability. In addition, nano-pixel structures manage to influence the spatial properties of the optical field, including its amplitude, polarization, and phase distribution and we have proposed and demonstrated asymmetric power coupler [11], higher-order modes compressor [12], spot size convertor [13] based on nano-pixel waveguide configuration. In this work, we newly propose an integration-available isolator element based on nano-pixel waveguide configuration for PICs. The footprint is ultra compact of 3.0 × 3.0 μm^2. By optimizing the number and the position of the nano-pixel arrangement using direct binary search (DBS) [14], an isolation ratio of 16.3 dB with excess loss of 1.2 dB at 1550 nm wavelength has been successfully confirmed using FDTD (finite-difference time-domain) simulation.

CONCEPT

Nano-pixel is consisted of a rectangular waveguide region which is divided into small pixels with around a hundred nano-meter scale. Each pixel is set with single digit binary data. The actual pixel is selected to be “1” or “0”, which means fully occupied with the waveguide material (corresponding to 1) or void (corresponding to 0). And in this work, “air-hole” is introduced for the void case. One of the merits of this nano-pixel structure is the device size. Many of the reported devices [14-25] are in the dimension of several micrometer squares in the footprint. Figure 1 (a) shows the schematic of the proposing isolator element using nano-pixel configuration. Once light is injected into the nano-pixel waveguide region, the designed pixel arrangement with the combination of occupied and void causes

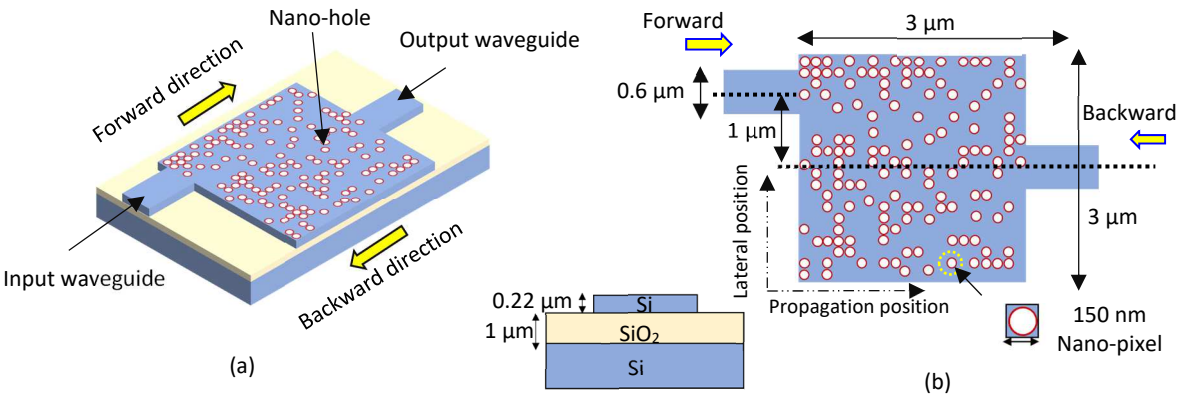


Fig. 1 The structure of isolator element using nano-pixel. (a) The schematic of isolator element, and (b) the configuration of isolator element.

the light scattering, and the scattered light in the optical waveguide interferes with each other. By setting the lateral position of the input waveguide and the output waveguide differently and choosing the number and the position of the air hole arrangement, the light interference in the forward direction and the return direction will be different. Especially the input and output waveguide layout against nano-pixel waveguide region is one of the keys of the isolation characteristics. We are based on the reciprocal propagation property caused in nano-pixel waveguide region. This phenomenon is not common in ordinal optical waveguide. To cause this reciprocal effect, the input for the forward light is located at laterally far side from the center whereas the output is located at the center of the nano-pixel waveguide region (see Fig. 1).

DESIGN AND OPTIMIZATION

The waveguide geometries are indicated in Fig. 1 (b). A single-mode waveguide with a width of 0.6 µm and a length of 1 µm is connected to the left and the right of the nano-pixel waveguide region. The output port is connected to the lateral center of nano-pixel waveguide region, and the input port is connected to 1 µm away from lateral center of nano-pixel waveguide region. The nano-pixel waveguide region has the waveguide width and length of 3 µm each which corresponds to the footprint of 3 × 3 μm^2. The nano-pixel waveguide region is divided into square nano-pixel sections. Each section is designed as square with 150 nm in the side-length. Circular air holes are arranged in void with 130 nm diameter. Totally 400 nano-pixel sections are arranged (which corresponds to 20 × 20 sections) in the nano-pixel waveguide region. Since each hole is cylindrical and filled with air for the void case in the nano-pixel, the refractive index is set to be 1 at the hole-area in simulation. The layer structure was a strip waveguide with Si core layer on top of SiO2 cladding layer. The thickness of the Si core layer was set to be 0.22 µm, and the thickness of the under cladding-layer was set to be 1 µm.

As explained above, the nano-pixel waveguide region is divided into 400 sections, these are too many possible layouts. Since it is not realistic to simulate all of the possible layouts and verify the results, we have designed the nano-pixel waveguide by using dual binary scarch (DBS) [14] algorithm in this work. 2D FDTD method with injected light of 1550 nm (TE-mode) was used in the simulation. The nano-pixel structure pattern is considered as a matrix contributed by 0 and 1, in which 1 corresponds to waveguide material whereas 0 corresponds to void. A randomly chosen pixel is first perturbed so as to switch its state, then device characteristic is calculated. If the characteristic is improved, the pixel state is retained, if not, the perturbation is reversed and the algorithm proceeds to the next pixel. This process is continued until the target characteristic is obtained. The characteristic of the device is defined as the isolation ratio. The isolation ratio τ is defined as:

$$\tau = 10*\log10\,[(Pout1 / Pout2] \qquad (1),$$

where Pout1 and Pout2 are the output power in the forward direction and backward direction, respectively. In this optimization process, CPU of the PC was Intel (R) Core (TM) i9-10940X CPU @ 3.30 GHz and RAM was 128 GB. It took approximately 120 hours to design and optimize the device in this work.

RESULT

After optimization process, we have got the isolator element using nano-pixel configuration. 138 holes are arranged inside optimized isolator element with 3.0 µm × 3.0 µm nano-pixel waveguide. Figure 2 shows the electromagnetic field of light of optimized isolator element in forward direction and backward direction. It is clearly shown that the output in forward direction high whereas output in backward direction is quite low. Figure 3 shows the normalized output power of optimized isolator element in forward direction and backward direction during the FDTD simulations shown in Fig. 2. The horizontal axis shows time and [fs] represents 10-15s. The vertical axis shows the

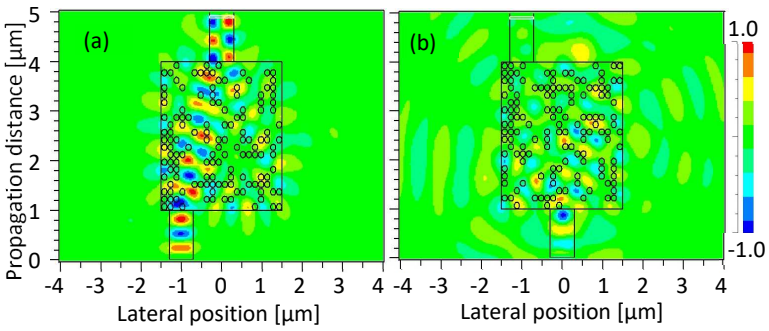


Fig. 2 The electromagnetic field of light of optimized isolator element. (a) In forward direction and (b) in backward direction.

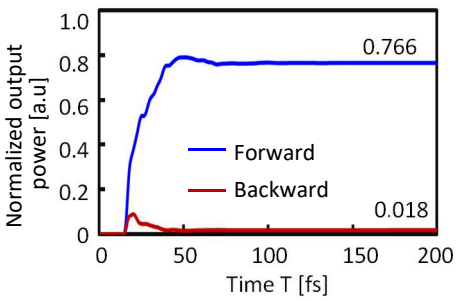


Fig. 3 The normalized output power of optimized isolator element.

output of light, and since it is normalized by the incident light, it takes a value of 0 to 1. The output power of the isolator in the forward direction is 0.766 whereas the one in backward is 0.018, respectively. An isolation ratio of 16.3 dB and with 1.2 dB of excess loss using nano-pixel structure was achieved.

We also investigated the wavelength dependence of isolation ratio for the isolator element. Figure 4 shows the calculated transmission spectra of isolator with TE-mode. As shown in the Fig. 4, more than 15 dB of isolation ratio was confirmed from 1540 nm to 1560 nm of wavelength. The 1 dB bandwidth of this device was 20 nm, and across the entire 1 dB bandwidth, the device excess loss was 1.2~ 1.3 dB.

Fabrication accuracy for nano-hole is another important challenge for isolator element based on nano-pixel configuration. Herein, we also analyzed the isolation ratio of the proposed isolator element based on nano-pixel configuration with the change of the air hole diameter. When we change the diameter of the hole from 120 to 150 nm, therefore, the space of the holes is simultaneously adjusted from 40 to 0 nm. Figure 5 shows the calculated isolation ratio with different diameters. As shown in Fig. 5, there is less effect on the isolation ratio due to the nano-pixel hole fabrication errors. More than 15 dB of isolation ratio was confirmed from 125 nm to 140 nm of nano-hole diameters.

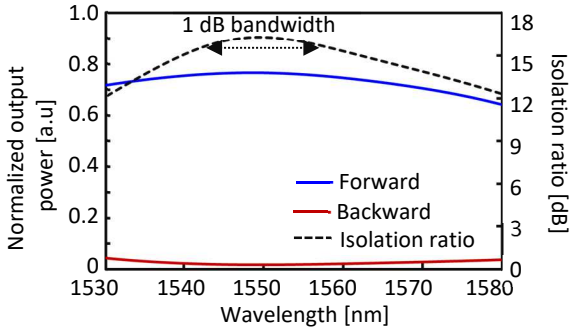


Fig. 4 The calculated transmission spectra of isolator element.

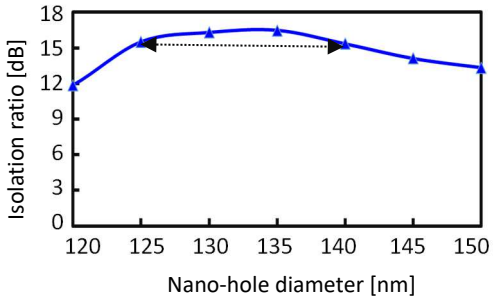


Fig. 5 The calculated isolation ratio with different diameters.

CONCULUTION

We have proposed an integrated isolator element based on nano-pixel waveguide. The isolator element with a small footprint of 3.0 × 3.0 μm^2 has been designed and optimized by DBS algorithm. By optimizing the number and the position of the nano-pixel arrangement, an isolation ratio of 16.3 dB with excess loss of 1.2 dB at 1550 nm wavelength has been confirmed. This paper is intended to report the possibility of isolator using nano-pixel for the first time as to our knowledge, and still there is a number of possibility in achieving higher performance when we change the size, the number of air-holes, as well as the waveguide configuration.

References

[1] D. Marpaung et al., Integrated microwave photonics. Laser Photonics Rev., vol. 7, no. 4, pp. 506-538, 2013
[2] R. Yamaguchi et al., Low-loss waveguide optical isolator with tapered mode converter and magneto-optical phase shifter for TE mode input, Opt. Express vol. 26, no. 16, pp. 21271-21278, 2018
[3] S. Liu et al., TE-mode magneto-optical isolator based on an asymmetric microring resonator under a unidirectional magnetic field, Opt. Express vol. 30, no. 6, pp. 9934-9943, 2022
[4] L. Fan et al., An all-silicon passive optical diode, Science, vol. 335, no. 6067, pp. 447-450,2012
[5] Y. Shi et al, Limitations of nonlinear optical isolators due to dynamic reciprocity, Nat. Photonics vol. 9, pp. 388-392, 2015
[6] J. Wang et al., Non-reciprocal polarization rotation using dynamic refractive index modulation, Opt. Express, vol. 28, no. 8, pp. 11974-11982, 2020
[7] E. A. Kittlaus, et al, Nonreciprocal inter-band brillouin modulation, Nat. Photonics vol.12, pp. 613-619, 2018
[8] B. Shen et al., An integrated-nano photonics polarization beam splitter with 2.4×2.4 μm^2 footprint, Nat. Photonics, vol. 9, pp. 378-382, 2015
[9] J. Huang et al., Digital nanophotonics: the highway to the integration of subwavelength-scale photonics, Nanophotonics vol. 10, no. 3, pp. 1011-1030, 2021
[10] Y., Shimamura et al., First implementation of asymmetric power splitter by using nano-pixel integrated with sensing high-mesa waveguide, in Tech. Digest of 27th Microoptics Conference, Jena, Germany, pp. 41-42, 2022
[11] H. Jiang et al., Demonstration of space-mode “compressor” by using nano-pixel, in Tech. Digest of 27th Microoptics Conference, Jena, Germany, pp. 60-61, 2022
[12] Chen et al., Vertical field enhancement of a spot-size converter using a nanopixel waveguide and window structure. Opt. Express, vol. 29, no. 2, pp. 2757-2768, 2021
[13] W. Chang et al., Ultra-compact mode (de) multiplexer based on subwavelength asymmetric Y-junction, Opt. Express, vol. 26, no. 7, pp. 8162-8170, 2018
[14] K. Nakamura et al., Hybrid algorithm based on the grey wolf optimizer and direct binary search for the efficient design of a mosaic-based device, J. Opt. Soc. Am. , vol. B39, no. 5, pp. 1329-1337, 2022

A Compact Apodized Grating Coupler for Perfectly Vertical Coupling

(Student paper)

Mingxiang Yang[1,2], Yunjie Yan[1], Zhenlin Wu[1], Mingshan Zhao[1] and Geert Morthier[2]

[1]School of Optoelectronic Engineering and Instrumentation Science, Dalian University of Technology, 116024, Dalian, China
[2]Photonics Research Group, INTEC, Ghent University - IMEC, 9052, Ghent, Belgium
* corresponding author e-mail: Geert.Morthier@UGent.be

We present a compact perfectly vertical apodized grating coupler in the C-band on the silicon-on-insulator platform. The optimized and measured coupling losses of apodized GCs are 3.0dB and 5.86dB respectively for the TE mode in the C-band. The apodized grating couplers were fabricated by e-beam with a simple 70 nm shallow etch and a minimum feature of 100 nm, compatible with CMOS technology.

Keywords**:** *Apodized grating couplers (GCs), coupling loss, compact perfectly vertical GCs, inverse design.*

INTRODUCTION

Grating couplers (GCs) are crucial components in integrated photonics circuits based on the silicon-on-insulator (SOI) platform, which has been widely used for coupling light to and from optical fibers, photodetectors, lasers, and so on. In recent years, the application of GCs for free-space optical (FSO) communication has received more attention, because GCs can also be used to convert an optical waveguide mode to a free-space radiation mode establishing the connection between chips and free-space [1]. Due to the three-dimensional (3D) character of FSO, the free-space optical beams are typically collimated and the optical mode field is Gaussian distributed. Especially in the focal plane array (FPA) systems, the direction of the free-space beams is perfectly vertical to the surface of the silicon chip [2]. Therefore, high-performance GCs as the reception elements are extremely important to realize perfectly vertical coupling. An emission GC for perfectly vertical coupling inevitably induces second-order diffraction resulting in low coupling efficiency (CE). For receiving GC, due to the symmetry of the grating geometry for uniform GC, the leftward and the rightward propagating guided modes of the uniform grating will meet the Bragg condition at the same wavelength also leading to low CE. So far, a lot of effort has already been devoted to the design and optimization of GCs. In order to increase the coupling efficiency, the slanted grating [3], polymer wedge [4], multi-layer gratings [5], and front mirror [6] have been constructed to break the symmetry of geometry and reduce second-order diffraction. However, those complex structures require a complex fabrication technique that is not compatible with CMOS processes. Fortunately, the emerging inverse design approach provides a novel method for the design of GCs, allowing more degrees of freedom to design apodized GCs to match the Gaussian beam for better coupling efficiency. HP LABS had reported experimental coupling losses of 2 dB for inverse-designed grating couplers with a partial etch depth of 159 nm and a Si height of 304 nm [7]. Those dimensions are however not compatible with the current mainstream silicon photonics process with a 220 nm thick silicon device layer.

In this work, through using the gradient-based inverse design methods, we optimize apodized GCs resulting in a Gaussian-like distribution that better matches the input Gaussian beam. The apodized GCs are designed and fabricated on 220 nm silicon-on-insulator with a 70 nm shallow etch, which is provided in most silicon platform foundries. We experimentally demonstrate a high-performance perfectly vertical apodized GC working in the C-band with a compact footprint of 27×40 μm^2. The designed and measured coupling losses of apodized GCs are 3 dB and 5.86 dB for TE mode, respectively. This is the best performance of compact perfectly vertical GCs in the C-band with a minimum feature size of 100 nm, compatible with CMOS technology.

DESIGN

The apodized GCs are designed using the gradient-based inverse design methods [8] that are included in the Python suite called LumOpt. Compared to the previous particle swarm optimization (PSO), relying on random perturbations, the gradient-based optimization algorithm enables obtaining the best solution in fewer iterations. Moreover, gradient-based inverse design methods can realize super multi-parameter optimization through the adjoint method in electromagnetic design problems. For the design of GCs, the number of degrees of freedom for optimization depends on the number of periods of the grating. Because of this, we can design the apodized grating with different leakage factors for every period to achieve the Gaussian distribution of the power field of the grating.

The typical silicon-on-insulator (SOI) structure with a 220 nm silicon device layer and a 2 µm buried oxide layer on a silicon substrate is used to design apodized GCs with 70 nm shallow etching. A Gaussian optical beam at 1550 nm wavelength with an effective mode diameter of 10.4 µm (waist diameter) at an angle of 90° is used as the input beam during the design. The optimization purpose is to improve the mode overlap between the fields scattered from the grating and the predefined field profile. In order to overlap a Gaussian input beam, the intensity of the light diffraction from the grating should increase and decrease gradually along the direction of the grating. This means the leakage factor of the grating should also gradually grow and then fall in the direction of the grating. The apodized grating structure can satisfy this non-linear variation. The gradient-based optimization using the adjoint method is employed to rapidly generate electromagnetic structures with many degrees of freedom using 2D-FDTD simulation. Minimum feature size is enforced at the same time to ensure manufacturability.

Table 1. Width of the ribs and grooves of the apodized grating coupler

P	1	2	3	4	5	6	7	8	9	10	11	12	13	14	15
R (nm)		454	489	564	881	476	361	468	551	401	397	361	374	396	405
G (nm)	100	100	100	100	109	145	117	124	157	173	190	186	187	155	168
P	16	17	18	19	20	21	22	23	24	25	26	27	28	29	30
R (nm)	262	233	102	439	395	424	189	417	125	427	378	410	385	138	351
G (nm)	286	100	173	131	159	136	150	104	140	184	144	192	116	220	171

The schematic diagram of the geometry of the optimized apodized GCs is depicted in Fig. 1(a) and includes 30 periods (P) with the rib (R) and groove (G) dimensions as listed in Table I, where R1 and G1 are the width of the nearest rib and groove to the output waveguide respectively. The minimum width and spacing during optimization are limited by the feature size of 100 nm to simplify fabrication. The different widths of rib and groove for every period break the symmetry of the grating geometry. The simulated electric field of the optimized apodized GCs is shown in Fig. 1(b). And visually it is obvious from Fig. 1(b) that the field profile of the apodized grating is strong in the middle. Most of the optical power is vertically coupled to the left output waveguide and the electric fields on the right side are weak, as shown in Fig. 1(d), proving that the apodized GC obtained by inverse design exhibits a high directivity and exceeds 50% (3.0 dB) coupling efficiency. As Fig. 1(e) shows, the normalized intensity of optical diffraction from the apodized grating results in a Gaussian-like distribution, which better matches the input Gaussian beam to achieve higher coupling efficiency.

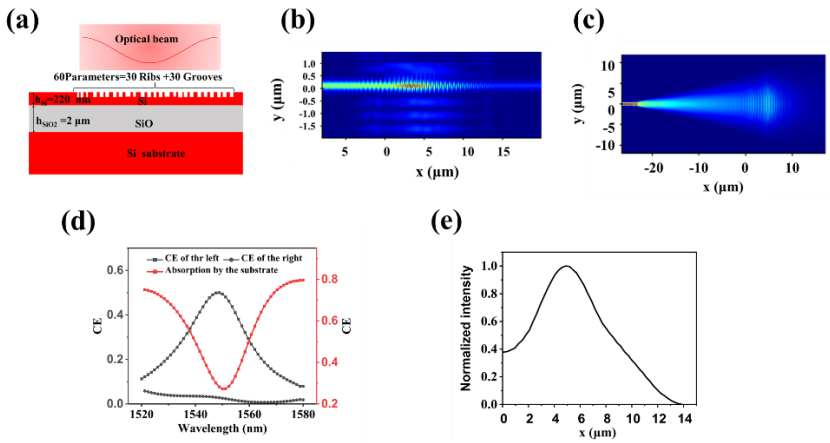


Fig. 1. (a) Schematic diagram of the geometry of the apodized GCs. (b) simulated electric field of the apodized GCs. (c) Electric field amplitude distributions of apodized grating coupling form 3D-FDTD simulation. (d) Coupling efficiency of the apodized GCs. (e) The intensity of the light distribution along the direction of the grating.

To further validate the accuracy of the geometric structure, the apodized grating coupler is then simulated in the 3D-FDTD simulation environment. Moreover, the focusing grating with circular lines is used to decrease the footprint, making the GC more suitable for high-density photonics integrated circuits. The electric field amplitude distributions of the optical field at 1550nm are illustrated in Fig. 1(c). And the light is coupled into the left waveguide by the compact taper.

FABRICATION AND EXPERIMENT

We fabricated apodized GCs on a standard SOI wafer with a silicon layer thickness of 220 nm and BOX layer thickness

of 2 µm. The grating couplers and the connecting waveguide are defined with 70 nm shallow etch using electron beam lithography (EBL) and inductively coupled plasma (ICP) etching. The minimum feature size of 100 nm can be fabricated using these processes to attain the minimum feature of the designed apodized GCs. To enable measurement, two GCs with the same structure are connected to a 500 µm-long straight waveguide. Fig. 2(a) shows an optical microscope image, a zoom-in on one GC, and a scanning electron microscope (SEM) image for apodized GC. The fabricated focusing apodized GCs have a compact footprint of 27×40 µm^2.

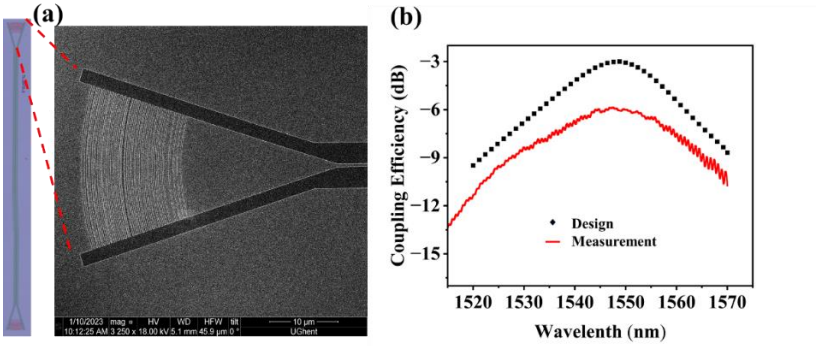


Fig. 2. (a) Microscope image of the fabricated device and the zoom-in SEM image of the apodized GC. (b) Designed and measured coupling loss of the apodized grating coupler.

For the optical characterization, we used the optical measurement setup, including a tunable laser a polarization controller, and an optical power meter. The fundamental mode of standard SMF-28 fibers, which are used as input and output couplers for 0°, can be regarded as a free-space Gaussian optical beam with 10.4 µm diameter (waist diameter). The measured coupling efficiency of the apodized grating coupler over a wavelength range (1520 nm ~ 1570 nm) is shown in Fig.2 (b). The peak of the coupling loss is 5.86 dB/facet for the TE mode at the wavelength of 1547 nm. It can also be seen from Fig.2 (b) that the transmission spectrum of the apodized GC is smooth, which proves that the back reflection of the apodized GC is effectively suppressed. The measurement results are worse than the design results. We suppose that this is due to the fabrication process. As measured by SEM, each period of the fabricated grating is 5-15nm narrower than that of the design. Therefore, we plan to optimize the fabrication process to improve the performance of GCs.

DISCUSSION

In conclusion, we proposed compact apodized GCs using the inverse design on the SOI platform for perfectly vertical coupling. The optical scattering of the optimized apodized GCs exhibits a Gaussian-like distribution that better matches the input Gaussian beam, resulting in higher coupling efficiency. The simulated and measured coupling losses of optimized apodized GCs are -3.0 dB and -5.86 dB for TE mode, respectively. The footprint of the compact focusing apodized GCs is 27×40 µm^2, making it suitable for lager-array integration. To the best of our knowledge, the experimental coupling efficiency is the best realized so far on 220 nm thick Si with just a single 70 nm etch depth and no bottom mirror. In addition, the proposed compact apodized GCs are compatible with CMOS technology.

Acknowledgments: This work was supported by the China Scholarship Council (CSC).

References

[1] Bütow J, Eismann J S, Milanizadeh M, et al. Spatially resolving amplitude and phase of light with a reconfigurable photonic integrated circuit. arXiv preprint arXiv:2204.09284, 2022.
[2] Li C, Cao X, Wu K, et al. Lens-based integrated 2D beam-steering device with defocusing approach and broadband pulse operation for Lidar application. Optics express, 2019, 27(23): 32970-32983.
[3] Wang B, Jiang J, Nordin G P. Embedded slanted grating for vertical coupling between fibers and silicon-on-insulator planar waveguides. IEEE Photonics Technology Letters, 2005, 17(9): 1884-1886.
[4] Schrauwen J, Scheerlinck S, Van Thourhout D, et al. Polymer wedge for perfectly vertical light coupling to silicon//Integrated Optics: Devices, Materials, and Technologies XIII. SPIE, 2009, 7218: 99-106.
[5] Mak J C C, Wilmart Q, Olivier S, et al. Silicon nitride-on-silicon bi-layer grating couplers designed by a global optimization method. Optics express, 2018, 26(10): 13656-13665.
[6] Chen X, Li C, Tsang H K. Fabrication-tolerant waveguide chirped grating coupler for coupling to a perfectly vertical optical fiber. IEEE Photonics Technology Letters, 2008, 20(23): 1914-1916.
[7] Van Vaerenbergh T, Sun P, Hooten S, et al. Wafer-level testing of inverse-designed and adjoint-inspired vertical grating coupler designs compatible with DUV lithography. Optics Express, 2021, 29(23): 37021-37036.
[8] Lalau-Keraly C M, Bhargava S, Miller O D, et al. Adjoint shape optimization applied to electromagnetic design. Optics express, 2013, 21(18): 21693-21701.

Dual phase-amplitude silicon modulator driven by an ENZ transparent conducting oxide

Juan Navarro-Arenas[1,2], Jorge Parra[2], Pablo Sanchis[2,*]

[1]Institute of Materials Science (ICMUV), Universitat de València, Carrer del Catedrátic José Beltrán Martinez, 2, 46980, Valencia, Spain

[2]Nanophotonics Technology Center, Universitat Politècnica de València, Camino de Vera s/n, 46022, Valencia, Spain

[*]pabsanki@ntc.upv.es

An ultracompact electro-optical ENZ/Si modulator with dual phase-amplitude operation is proposed. A 4 µm-long modulator is designed to achieve a π-phase shift modulation or an amplitude modulation with an extinction ratio of 10 dB.

Keywords**:** *ENZ, TCO, electro-optical, modulator*

INTRODUCTION

Nanoelectronics technology has always relied on the continued scaling down of the transistor size to achieve the exponential growth in computing speed seen during the last decades. Today, however, the limits of lithography, the frontier with quantum phenomena—in which transistors may not continue to function as intended—, and the huge costs of fabrication, address the need to start planning for the end of Moore's Law [1]. In this context, silicon photonics (SiPh) has demonstrated many advantages such as ultra-high speed, ultra-low energy consumption and new functionalities. In the case of neuromorphic computing, for example, recently demonstrated optical neural networks offer computation speeds that are orders of magnitude beyond von Neuman electronic computers [2]. Other emerging industries that could benefit from SiPh are LiDAR systems [3] or integrated quantum computing based on photonics [4].

For most of the applications, optical phase shifters and amplitude modulators are required to perform operations with light. Furthermore, simultaneous phase and amplitude modulation would be very valuable in many cases. Optical neural networks require complex-valued modulation to shape the inputs and outputs of the network [5], [6]. This is usually achieved through a concatenation of an asymmetric Mach–Zehnder interferometer (MZI), with one arm being phase-modulated, followed by a phase shifter. Tuning principles are varied in the current literature; e.g. those based on the thermo-optic effect [7], on the free-carrier effect [8], or the micro-electro-mechanical systems (MEMS) [9]. However, trade-offs in terms of speed, power consumption and footprint are usually given.

In this paper, an ultracompact dual phase shifter-amplitude modulator is proposed. The tuning mechanism relies on the epsilon-near-zero (ENZ) effect in transparent conducting oxides (TCOs) of high mobility. The ENZ occurs when the real permittivity becomes close to zero resulting in a large enhancement of modal confinement and extreme optical nonlinear effects [10]. In our device such an effect can be triggered electro-optically with a metal-oxide-semiconductor (MOS) stack structure mounted on top of a Si waveguide. Such a compact implementation eliminates the need to a build two sets of modulators—one for phase, one for amplitude—and, therefore, significantly reduces the device footprint.

Description of device operation

TCO's permittivity in the near-infrared regime can be well described by the interaction of light with free electrons. Following Drude's model, possible switching mechanisms can either manipulate the effective electron mass m_e^* or the electronic concentration *N*—the plasma frequency is proportional to the square root of N/m_e^*—. Usually, effective electron mass is perturbed all-optically by intraband transitions triggered upon the absorption of high-power pulses [10],[11], while concentration can be tuned electro-optically by means of a metal/oxide/TCO capacitor structure [12].

Here an electro-optical modulator is implemented in a silicon waveguide loaded with a metal/oxide/TCO layer stack (see Fig. 1(a)). The TCO acts as a semiconductor in the proposed device. It is modeled as a high-mobility cadmium oxide (the parameters and equations of our model can be found in literature [10-12]). The TCO acts also as the ground electrode of the device. The top metal layer serves as a second

electrode while the insulator (SiO_2) behaves as a charge blocking layer. When a gate voltage is applied (V_G) in the capacitor, electrons accumulate at the interface between the insulator and the TCO. Obtaining the electron density distribution inside the TCO requires solving the biased Poisson's equation to evaluate the band bending. To this end, the Thomas-Fermi approximation (MTFA), developed by Paasch and Übensee [12] was implemented and solved numerically by the finite element method (FEM).

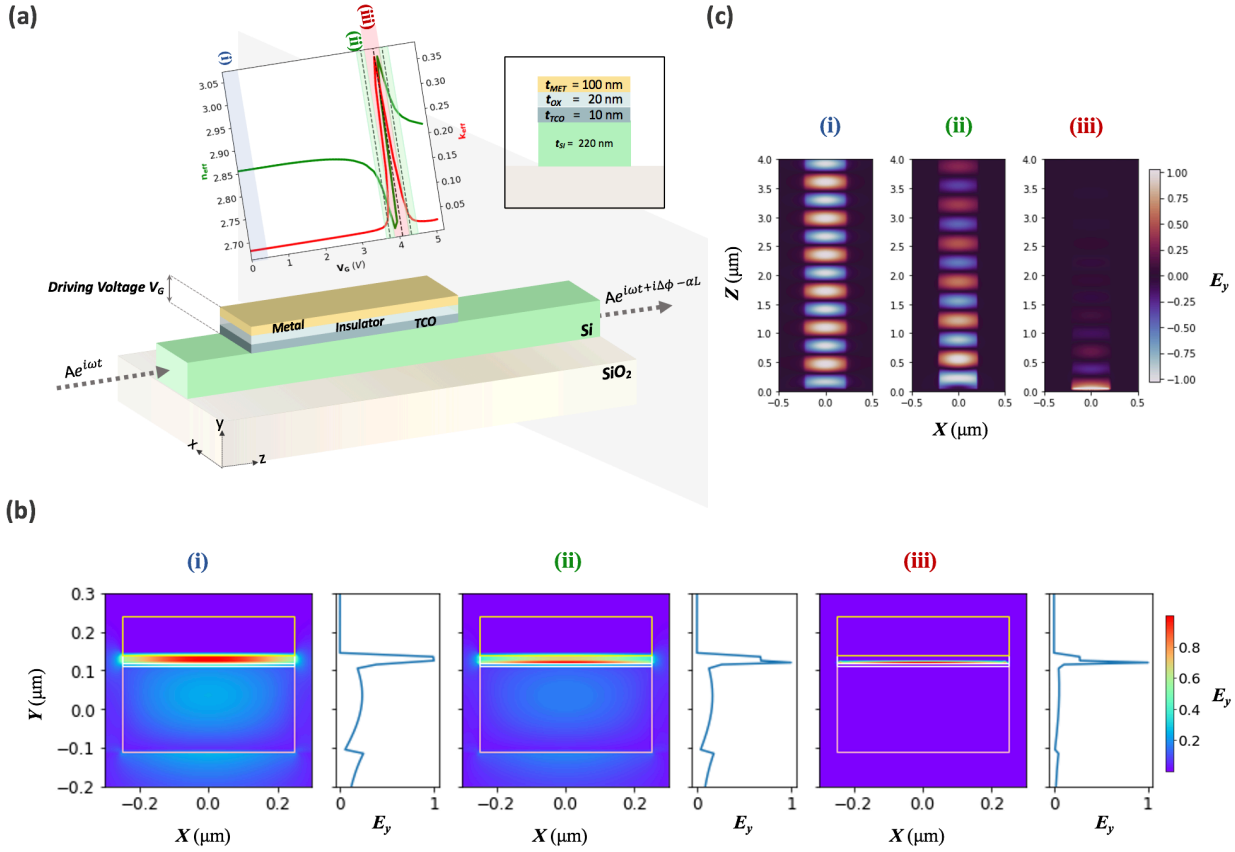


Fig. 1. (a) Sketch of the dual phase-amplitude modulator. The silicon waveguide is loaded by a capacitor stack (Au/SiO_2/TCO) that drives the modulator performance so that the effective index of the propagating optical mode is changed when a gate voltage is applied. E_Y field distribution cross-section in the (b) Z-X (inside the TCO layer) and (c) in the Y-X plane (including a 1D cross-section at x = 0 μm) of the device in the (i) OFF, (ii) phase and (iii) amplitude operation regimes.

The solution gives rise to a relationship between the Drude's permittivity and the applied gate voltage. This relationship is used to calculate the optical mode of the hybrid silicon waveguide loaded by the capacitor structure and its complex effective refractive index (n_{eff} and κ_{eff}). The optical mode was calculated by the FEM method implemented in the RSoft CAD environment from Synopsys. For an optimized device geometry such as the one presented in the cross-section of the device, the resulting effective index variation (see both insets in Fig. 1(a)) defines three regimes in which the device can operate: *(i) OFF* state, in which the modulator has low optical losses and the transmission is maximized (blue region in Fig. 1), (ii) phase modulation, in which the effective refractive index is tuned past or just after the ENZ resonance (green regions) so that a net phase difference is extracted with minimal losses, (iii) amplitude modulation, in which the index is tuned at the midpoint of the ENZ resonance (red region) so that the modal confinement is maximized in the low permittivity region and, thus, optical absorption is maximized.

Guided modes, accompanied by its cross-section at x = 0 μm, for the three operation regimes are shown in Figure 1b. Confinement within the TCO's accumulation layer is enhanced the most in the amplitude operation regime, as can be seen in Figure 1b(iii). In the phase regime, Figure 1b(ii), a large portion of the E_y field exist within oxide film. On the contrary, Figure 1b(i) shows that the modal overlap with the TCO's accumulation layer is minimal.

Dual phase-amplitude modulator performance

The modulator was designed for operation at a wavelength of 1550 nm and TM polarization. The 3D spatial distribution of the mode propagation was computed by the finite-difference time-domain method (3D-FDTD) for the three configurations. In the OFF state, which is shown in Fig. 1c(i), i.e. without applying a voltage to the modulator, the insertion losses are as low as 0.1 dB/µm. In the phase modulation operation regime, which is depicted in Figure 1c(ii), the device is driven by a voltage of 3.7 V, inducing a 0.24π/µm phase shift with optical losses around 0.75 dB/µm. Finally, in the amplitude modulation operation regime shown in Figure 1c(iii), the device requires a voltage of 4V for which an extinction ratio of 2.2 dB/µm is achieved. Therefore, a modulation length of around 4 µm is necessary to obtain a π-phase shift with insertion losses of 3 dB. For such a modulation length, the optical losses at the OFF state are as low as 0.4 dB while an extinction ratio of around 10 dB is achieved when switching to the amplitude modulation regime. Another important aspect is the energy consumption, as it grows quadratically with the gate voltage and scales proportionally with the footprint of the device. In the proposed modulator, a 4-µm long device would require an energy below 500 fJ for modulation.

Conclusions

Phase-amplitude modulation functions are mostly accomplished by means of a concatenation of Mach–Zehnder interferometers or ring resonator structures and individual phase shifter in current photonic integration circuits. These approaches come at expense of a large device footprint that could limit large-scale integration. To the best of our knowledge, the proposed ENZ/Si modulator is the first one of its class to present the possibility of manipulating the phase or the amplitude of the optical field with high performance in a compact (few microns long) device. Therefore, such a device would be highly beneficial for emerging high-impact fields as neural networks or reconfigurable photonics.

Acknowledgements

This work was supported by grants PID2019-111460GB-I00, Margarita Salas fellowship (MS21-037) funded by the European Union Next-Generation EU, funded by MCIN/AEI/10.13039/501100011033, by "ERDF A way of making Europe" and "ESF Investing in your future", PROMETEO/2019/123 by Generalitat Valenciana, and 2-PAID-10-22 by Universitat Politècnica de València.

References

[1] M. Haselman and S. Hauck, *The Future of Integrated Circuits: A Survey of Nanoelectronics*, in Proc. IEEE, vol. 98, no. 1, pp. 11–38, 2010.
[2] Y. Shen et al., *Deep learning with coherent nanophotonic circuits*, Nat. Photonics, vol. 11, no. 7, pp. 441–446, 2017.
[3] X. Zhang, K. Kwon, J. Henriksson, J. Luo, and M. C. Wu, *A large-scale microelectromechanical-systems-based silicon photonics LiDAR*, Nature, vol. 603, no. 7900, pp. 253–258, 2022.
[4] J. W. Silverstone et al., *On-chip quantum interference between silicon photon-pair sources*, Nat. Photonics, vol. 8, no. 2, pp. 104–108, 2014.
[5] R. Wang et al., *Multicore Photonic Complex-Valued Neural Network with Transformation Layer*, Photonics, vol. 9, no. 6, 2022.
[6] H. Zhang et al., *An optical neural chip for implementing complex-valued neural network*, Nat. Commun., vol. 12, no. 1, p. 457, 2021.
[7] J. Parra et al., *Silicon thermo-optic phase shifters: a review of configurations and optimization strategies*, in preparation.
[8] X. Chen et al., *Modeling and Analysis of Optical Modulators Based on Free-Carrier Plasma Dispersion Effect*, IEEE Trans. Comput. Des. Integr. Circuits Syst., vol. 39, no. 5, pp. 977–990, 2020.
[9] C. Errando-Herranz, A. Y. Takabayashi, P. Edinger, H. Sattari, K. B. Gylfason, and N. Quack, *MEMS for Photonic Integrated Circuits*, IEEE J. Sel. Top. Quantum Electron., vol. 26, no. 2, pp. 1–16, 2020.
[10] E. Li and A. X. Wang, *Femto-Joule All-Optical Switching Using Epsilon-Near-Zero High-Mobility Conductive Oxide*, IEEE J. Sel. Top. Quantum Electron., vol. 27, no. 2, pp. 1–9, 2021.
[11] J. Navarro-Arenas, J. Parra, and P. Sanchis, *Ultrafast all-optical phase switching enabled by epsilon-near-zero materials in silicon*, Opt. Express 30, 14518, 2022.
[12] X. Liu et al., Tu*ning of Plasmons in Transparent Conductive Oxides by Carrier Accumulation*, ACS Photonics, vol. 5, no. 4, pp. 1493–1498, Apr. 2018.

Coherency-broken cascaded SiN Bragg filters for attaining ultra-high rejection considering both TE/TM polarization.

(Student paper) / (Invited paper)

David E. Medina-Quiroz[1,*], Sébastien Tanzilli[2], Laurent Vivien[1], Laurent Labonté[2], Éric Cassan[1] and Carlos Alonso-Ramos[1]

[1]Université Paris-Saclay, CNRS, Centre de Nanosciences et de Nanotechnologies, 91120, Palaiseau, France
[2]Universite Cote d'Azur, CNRS, Institut de Physique de Nice (INPHYNI), Parc Valrose, 06108 Nice Cedex 2, France
[*] corresponding author: david.medina@universite-paris-saclay.fr

Emerging applications ranging from Raman spectroscopy to quantum communications are evolving to be on-chip, thus, ultra-high rejection integrated filters have been increasing on demand. Here, we propose and demonstrate a silicon nitride (SiN) Bragg filter with an asymmetric sinusoidal geometry based on a non-coherent cascading multimodal approach. We fabricated and characterized these filters in an 800 nm SiN platform. We measured more than 50 dBs of optical rejection for each polarization in a bandwidth of less than 10 nm. Moreover, with this approach we expect the possibility to manage the TE/TM rejection bandwidths and even an overlap of both stopbands by changing the geometrical parameters of the filter waveguide.

Keywords: *high rejection, polarization, multimodal, cascaded*

INTRODUCTION

The growing demand for more sophisticated photonic circuits in silicon photonics and its applications has led to the improvement of single components on chip. Particularly, integrated optical filters are of interest because they enable a cost effective solution for wavelength division multiplexing and isolation between optical signals. However, most integrated filters face the challenge of performing differently based on the polarization of the optical input mode [1], [2], which limits the waveguide geometrical parameters and thus, hindering the full potential of the photonic circuit. To overcome this issue, polarization independent filters have been introduced in silicon photonics [3]–[6]. Despite being the preferred platform for photonic integration, the silicon on insulator (SOI) platform has the drawback of high TE/TM birefringence due to its high core/cladding index contrast, which requires the use of complex geometries or dual-grating approaches [3], [4], [7] for managing polarization properly.

The silicon nitride (SiN) platform offers a valuable alternative to SOI for photonic integrated circuits (PICs) due to its lower index contrast, which makes it easier to manage polarization. Additionally, the SiN platform has a transparency range that includes visible light, making it useful for applications in the visible light and biosensing fields [8]. It also does not suffer from the two-photon absorption effect, allowing for the use of nonlinear optical processes that tend to require high pumping powers [9]. There have been many efforts to achieve high-level optical rejection, but this has typically been done with single mode waveguides without considering polarization. Researchers have demonstrated ultra-high rejection levels, such as 68 dB with a 3 nm optical narrowband in a non-telecom waveband (700-800 nm) for single TE-like mode waveguides [10]. However, the goal of achieving ultra-high rejection larger than 40 dB for a Telecom band taking into account both TE/TM polarization has yet to be achieved. Such filters in the SiN platform, characterized by low propagation losses [11], would be of great interest for applications such as on-chip quantum communications [12] and Raman spectroscopy [13].

In this purpose, we propose an asymmetric sinusoidal Bragg geometry design based on Ref. [14] and initially implemented with Si waveguides. The design thus takes into consideration the conditions of lower index contrast SiN waveguides, with a focus on controlling polarization-tagged filtering bandwidths. Following the approach adopted in Ref. [15], by taking advantage of the multimodal nature of the filter, it is possible to cascade single sections and thus, maximize the optical rejection. This technique can be extended for both TE/TM polarizations. The design allows for the control of the effective index values for the two polarizations, which helps to match and control the TE/TM filtering resonances and therefore, it should be possible to control the overlap between the two rejection bandwidths.

RESULTS

Accordingly, we carried out mode solver simulations using a commercial software [16] by sweeping the waveguide width (W_{wg}) while considering a fixed waveguide thickness of 800 nm (see Fig.1c). An obvious choice to match the

effective index values of the first TE and TM modes would be to pick a width of 800 nm (square waveguide). However, we also took into account that the cutoff effective index for the second mode of each light polarization is in this case is extremely close to the refractive index of the substrate index material (n_{SiO_2} ~1.44). Hence, the waveguide width chosen for fabrication was fixed to W_{wg} = 1300 and the other parameters to Λ = 470 nm (Bragg period) and W_c = 100 nm (corrugation). The filters were first designed by cascading different numbers of sections, e.g. 1, 3, 5 and 7, each section being 500 µm long, and then fabricated by immersion lithography [17] at CEA-Leti.

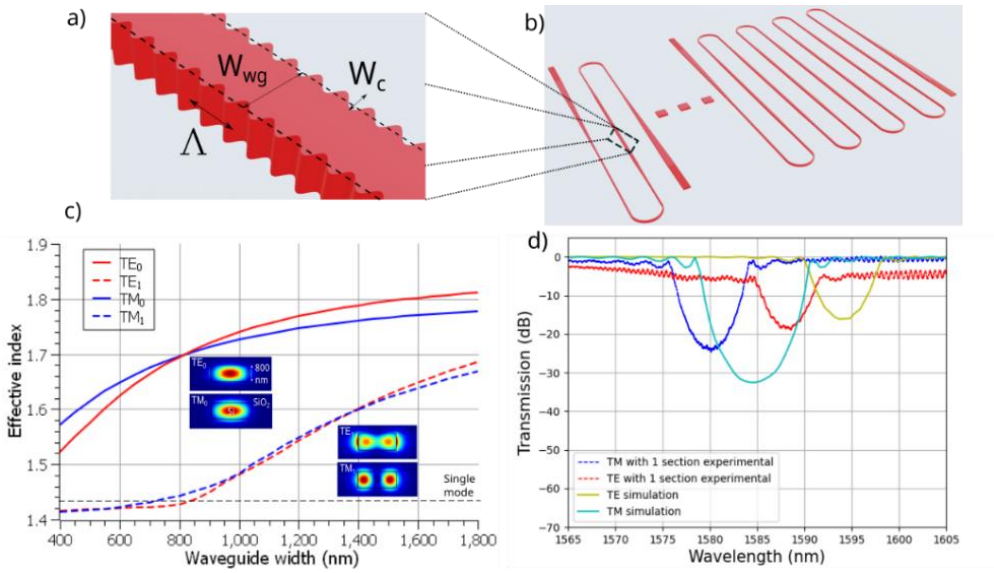


Fig. 1. General characteristics of the chosen sinusoidal Bragg geometry, (a) Geometrical parameters and (b) The cascaded multisection design. Computed (c) Effective index values obtained for the TE/TM mode as a function of the SiN waveguide width (W_{wg}) at λ = 1600 nm and (d) experimental and simulation comparison of a single section filter.

The characterization was carried out at the optics laboratory at C2N using a fiber-to-fiber set-up. The insertion loss of the device was approximately 10 dB per grating and a reference filter was measured and used for normalizing all the measured results. The polarization was first chosen by using a free space polarizer and then optimized with a polarization controller. For the single section filter, we measured the transmission spectra of the one section filter and compared the result with the transmission simulated with variational 2D-FDTD calculation, as depicted in Fig.1d, with a relatively good agreement with yet a slight wavelength shift attributable to a period mismatch.

Obviously, the rejection is limited here to ~20 dB, as it is known due to the fabrication and phase errors [18]. Increasing the number of sections increases steadily the rejection for each polarization and the overlapping area as seen in Fig.2, which reports the measured transmission spectra for (Fig.2a) a cascaded 3-section filter, where 40 dB of optical rejection was measured for the TM and TE light polarization, separately. Subsequently, for the filters with 5 and 7 sections (Figs.2b and 2c respectively), The rejection continues to increase until ~50dB. Higher rejection levels for both light polarizations are thus expected with more filtering sections, bringing experimental evidence on the possibility to filter both polarizations simultaneously by more than 60dB. It is of note that the bandwidth of the stopbands for both polarizations remains stable during the cascading, which only increases the rejection while maintaining the behavior of the filter.

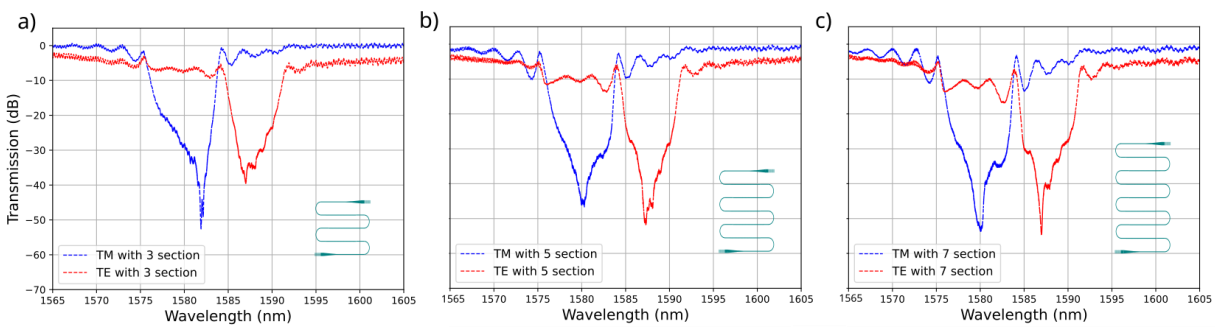


Fig 3. Measured transmission spectra for both fundamental TE/TM modes for the proposed cascaded geometry with number of sections ranging from 3 (Fig. 3a)), 5 (Fig. 3b)), and 7 (Fig. 3c)).

DISCUSSION and CONCLUSION

To conclude, we have started to investigate the behavior of multimode Bragg filters in the SiN platform and experimentally demonstrated that limited rejection of single Bragg filters due to phase errors and fabrication imperfections can be dealt by cascading single sections of multimode filters connected by single mode waveguides. This strategy has the advantage of utilizing only passive devices while dramatically increasing the rejection. Each section adds up to the total rejection as the back reflections are radiated out due the bends connecting them and finally overcoming the initial 20 dBs of a single filter to attain ultra-high rejection ~50dBs for the 5 and 7 section filter. Evidence for even higher rejection is implied as the number of sections is increased.

Following these results, further investigations of the dependence of the filters' wavelength bandwidths have been carried out in view to flexibly control the rejection for both light polarizations simultaneously. The related studies will be presented later on at the conference.

References

[1] G. T. Reed et al., "Issues associated with polarization independence in silicon photonics," IEEE Journal on Selected Topics in Quantum Electronics, vol. 12, pp. 1335–1343, Nov. 2006, doi: 10.1109/JSTQE.2006.883136.
[2] D. Dai, L. Liu, S. Gao, D. X. Xu, and S. He, "Polarization management for silicon photonic integrated circuits," Laser and Photonics Reviews, vol. 7. pp. 303–328, May 2013. doi: 10.1002/lpor.201200023.
[3] D. Liu and D. Dai, "Silicon-based polarization-insensitive optical filter with dual-gratings," Optics Express, vol. 27, p. 20704, Jul. 2019, doi: 10.1364/oe.27.020704.
[4] C. Klitis, G. Cantarella, M. J. Strain, and M. Sorel, "High-extinction-ratio TE/TM selective bragg grating filters on silicon-on-insulator," Optics Letters, vol. 42, p. 3040, Aug. 2017, doi: 10.1364/ol.42.003040.
[5] H. Wang et al., "Polarization-independent tunable optical filter with variable bandwidth based on silicon-on-insulator waveguides," Nanophotonics, vol. 7, pp. 1469–1477, 2018, doi: 10.1515/nanoph-2018-0058.
[6] E. Duran-Valdeiglesias et al., "Dual-polarization silicon nitride bragg filters with low thermal sensitivity," vol. 44, p. 4578, 2019, doi: 10.1364/OL.44.004578ï.
[7] L. Vivien, S. Laval, B. Dumont, S. Lardenois, A. Koster, and E. Cassan, "Polarization-independent single-mode rib waveguides on silicon-on-insulator for telecommunication wavelengths," Optics Communications, vol. 210, no. 1, pp. 43–49, 2002, doi: https://doi.org/10.1016/S0030-4018(02)01681-4.
[8] P. Muellner, E. Melnik, G. Koppitsch, J. Kraft, F. Schrank, and R. Hainberger, "CMOS-compatible Si3N4 waveguides for optical biosensing," in Procedia Engineering, 2015, vol. 120, pp. 578–581. doi: 10.1016/j.proeng.2015.08.728.
[9] D. J. Blumenthal, R. Heideman, D. Geuzebroek, A. Leinse, and C. Roeloffzen, "Silicon nitride in silicon photonics," Proceedings of the IEEE, vol. 106. Institute of Electrical; Electronics Engineers Inc., pp. 2209–2231, Dec. 2018. doi: 10.1109/JPROC.2018.2861576.
[10] X. Nie, N. Turk, Y. Li, Z. Liu, and R. Baets, "High extinction ratio on-chip pump-rejection filter based on cascaded grating-assisted contra-directional couplers in silicon nitride rib waveguides," Optics Letters, vol. 44, p. 2310, May 2019, doi: 10.1364/ol.44.002310.
[11] H. E. Dirani et al., "Ultralow-loss tightly confining si 3 n 4 waveguides and high-q microresonators," Optics Express, vol. 27, p. 30726, Oct. 2019, doi: 10.1364/oe.27.030726.
[12] X. Lu et al., "Chip-integrated visible–telecom entangled photon pair source for quantum communication," Nature Physics, vol. 15, pp. 373–381, Apr. 2019, doi: 10.1038/s41567-018-0394-3.
[13] A. Dhakal, A. Z. Subramanian, P. Wuytens, F. Peyskens, N. L. Thomas, and R. Baets, "Evanescent excitation and collection of spontaneous raman spectra using silicon nitride nanophotonic waveguides," doi: 10.1364/OL.99.09999.
[14] H. Qiu et al., "Silicon band-rejection and band-pass filter based on asymmetric bragg sidewall gratings in a multimode waveguide," Optics letters, vol. 41, no. 11, pp. 2450–2453, 2016.
[15] D. Oser et al., "Coherency-broken bragg filters: Overcoming on-chip rejection limitations," Laser & Photonics Reviews, p. 1800226, 2019.
[16] "FDTD solutions, lumerical solutions, inc., Http://www.lumerical.com."
[17] C. Dupre et al., "Immersion lithography introduction in si photonics platform," in Photonics west, 2020, pp. paper 11284–13.
[18] Lu, Z., Jhoja, J., Klein, J., Wang, X., Liu, A., Flueckiger, J., Pond, J., & Chrostowski, L. (2017). Performance prediction for silicon photonics integrated circuits with layout-dependent correlated manufacturing variability. Optics Express, 25(9), 9712. https://doi.org/10.1364/oe.25.009712

Design of a Broadband Polarization Controller Based on Silicon Nitride-Loaded Thin-Film Lithium Niobate

Jiří Čtyroký[1,2*], Ivan Richter[2] and Jiří Petráček[3,4]

[1] CAS Institute of Photonics and Electronics, Chaberská 57, 18251 Prague, Czech Republic
[2] Faculty of Nuclear Sciences and Physical Engineering, Czech Technical University in Prague, Břehová 7, 11519 Prague 1, Czech Republic
[3] Faculty of Mechanical Engineering, Brno University of Technology, Technická 2896/2, 61669 Brno, Czech Republic
[4] Central European Institute of Technology, Brno University of Technology, Purkyňova 656/123, 61200 Brno, Czech Republic
[*] ctyroky@ufe.cz

Polarization controller is designed on Si_3N_4-loaded thin film $LiNbO_3$. Broadband operation in the wavelength band from 1.45 to 1.65 µm is achieved by using a mode evolution TM/TE splitter/converter, two mode evolution 3-dB couplers and two electro-optic phase shifters. A single TE-mode output can be can be achieved by applying control voltages lower than 5 V for any input polarization state.

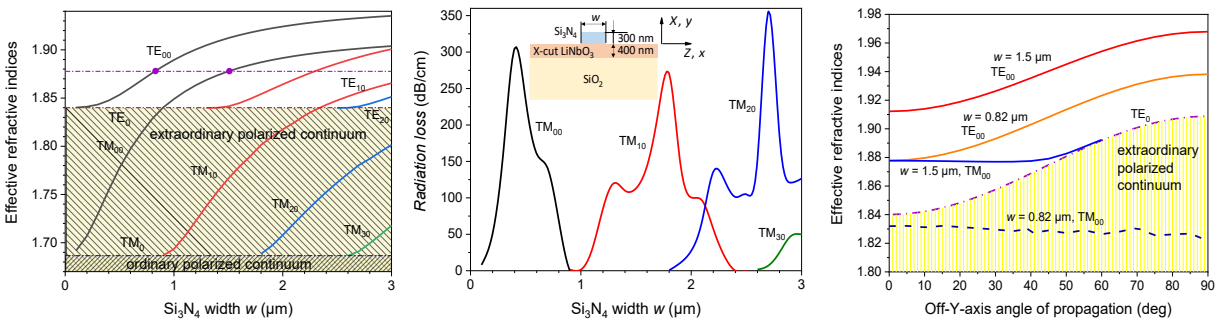
Keywords: *Polarization control, mode evolution splitter, broadband 3-dB couplers*

INTRODUCTION

Polarization controllers are important components of optical communication systems. Integrated-optic polarization controllers in Ti:$LiNbO_3$ waveguides have been described already several decades ago [1]. Recent development of the lithium niobate on insulator (LNOI) technology [2] allows to design more compact electro-optic devices with lower control voltage [3]. Our design, although similar to that described in [3], was proposed independently and differs in several features. Firstly, we choose the silicon nitride-loaded LNOI waveguides [4, 5] as an alternative to $LiNbO_3$ rib waveguides in order to avoid uneasy etching of the $LiNbO_3$ crystal. Secondly, to ensure broadband operation, we implemented an adiabatic mode evolution TM/TE coupler [6] as a polarization splitter/converter, and thirdly, mode evolution 3-dB couplers, somewhat similar to those described in [7] and [8], are designed. An X-cut $LiNbO_3$ slab is chosen for efficient electro-optic phase shifting. Numerical simulations by COMSOL Multiphysics and the proprietary Fourier modal method [9] predicted the total loss in the polarization controller of about 0.5 dB in the range from 1.45 to 1.65 µm. The operation voltage of phase shifters, required to direct the full input power to the single TE_{00} mode of the output port, was found to be lower than 5 V.

PROPERTIES OF Si_3N_4-LOADED LNOI WAVEGUIDES

The thickness of the $LiNbO_3$ slab was chosen as 400 nm, the Si_3N_4 layer is 300 nm thick. Air is used as an upper cladding, since any higher-index overlayer reduces the strength of the required TM/TE coupling. The dispersion and radiation loss curves of the waveguides oriented along the Y-axis of the $LiNbO_3$ crystal are shown in Figs. 1(a) and 1(b), respectively. The waveguide cross-section is shown in the inset of Fig. 1(b). Fig. 1(c) shows the angular dependences of the effective refractive indices for propagation declined from the crystal Y-axis by an angle. Results were calculated for the wavelength of 1550 nm using COMSOL mode solver.



(a) (b) (c)

Fig. 1. Dispersion properties of the Si_3N_4-loaded LNOI waveguides. X, Z are crystal axes of the $LiNbO_3$ slab, x, y are coordinates.

The TE modes propagate without radiation into the $LiNbO_3$ slab since their effective indices are larger than the effective index of the planar TE_0 mode of the $LiNbO_3$ crystal slab. The TM modes–although predominantly ordinary polarized–are free of radiation losses only for wide enough waveguides.

POLARIZATION CONTROLLER

The configuration of the polarization controller is schematically shown in Fig. 2. The TE-polarized input mode propagates through the TM/TE splitter/converter essentially unaffected, while the TM-polarized mode is converted into the TE mode of the bottom waveguide. Two cascaded combinations of the phase shifter and the 3-dB coupler are used to coherently combine the TE-polarized fields from both output ports of the TM/TE splitter/converter into a single output port. It can be easily shown that by proper adjustment of the relative phase of inputs of any (lossless) 3-dB coupler, the amplitudes in both output ports can be equalized. The second phase shifter is used to adjust the relative phase so that both input waves are coherently superposed in one of the output ports of the second 3-dB coupler. The control voltages U_{eq} and U_c of the phase shifters can thus be optimally adjusted by minimizing the output from the other port.

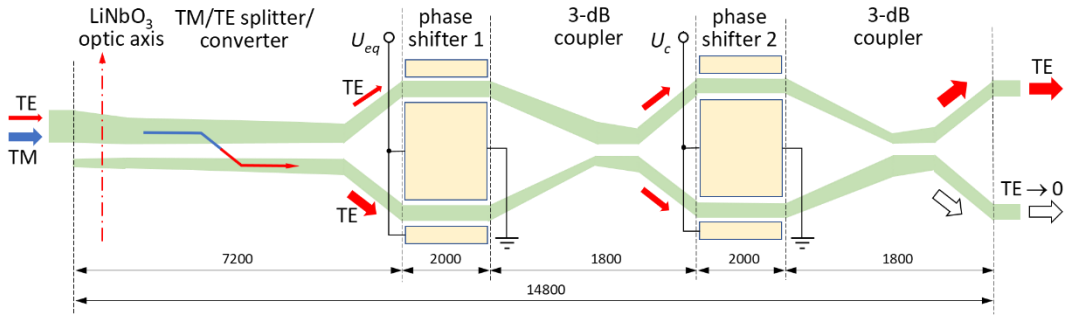


Fig. 2. Configuration of the polarization controller.

ADIABATIC MODE EVOLUTION TM/TE COUPLER

The design of an adiabatic mode evolution TM/TE coupler started with the observation that the effective indices of the TE_{00} mode of the waveguide of the width of 0.8 µm and of the TM_{00} of the waveguide of the width of 1.5 µm are nearly identical (see the violet dots in Fig. 1(a)). If these waveguides come close to each other, the modes get hybridized due to the 3D vector character of their electric fields. This is reflected by the appearance of the avoided crossing of their dispersion curves [6] which corresponds to the polarization conversion during the mode evolution. The spectral position of the avoided crossing depends on the waveguide widths and on their separation. Proper adiabatic shaping of the coupler is required to ensure efficient polarization conversion in the required wavelength band.

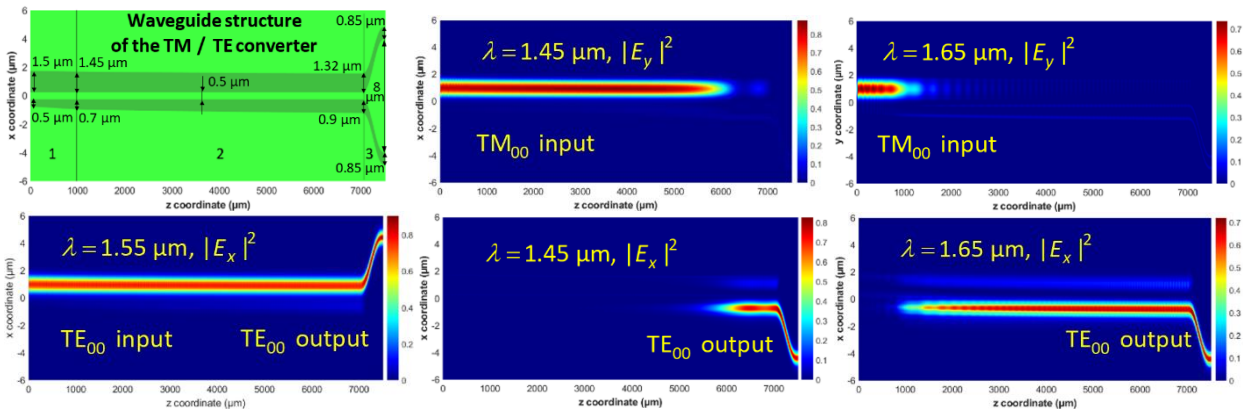


Fig. 3. Broadband adiabatic TM/TE splitter/converter. Waveguide structure and field distributions of the TM mode for the wavelengths 1.45 µm and 1.65 µm and of the TE mode for the wavelength 1.55 µm.

The designed waveguide structure shown in Fig. 3 consists of a 1000 µm linear taper section 1 ensuring sufficient decoupling of the input waveguides, the 6000 µm long adiabatic mode evolution section 2, and the 500 µm long output bends 3 separating the waveguides from the 0.5 µm gap to edge-to-edge distance of 8 µm and simultaneous tapering both waveguides to the output width of 0.85 µm. In section 2, both waveguides are logarithmically tapered; the upper one from 1.45 µm at the input to 1.32 µm at the output while the bottom one from 0.7 µm to 0.9 µm. Fig. 3 also shows the conversion from the input TM_{00} mode of the upper waveguide to the input TE_{00} mode of the bottom one for wavelengths 1.45 µm and 1.65 µm. The TE_{00} input mode propagates essentially unaffected to the upper output branch for any wavelength in this band. The TM/TE coupler loss not exceeding 0.2 dB in the spectral range from 1.45 µm to 1.65 µm was calculated using the full-vector 3D Fourier modal method [9].

BROADBAND 3-dB COUPLERS

To ensure the broadband operation, we implemented adiabatic mode evolution 3-dB couplers consisting of input adiabatic asymmetric waveguide bends followed by a mode evolution pair of waveguides linearly tapered to identical widths, which are then separated by symmetric bends. The design is shown in Fig. 4, together with the demonstration of its broadband operation. Numerical simulation using the Fourier modal method predicted the total loss lower than 0.05 dB and the splitting asymmetry lower than 0.2 dB in the whole spectral range.

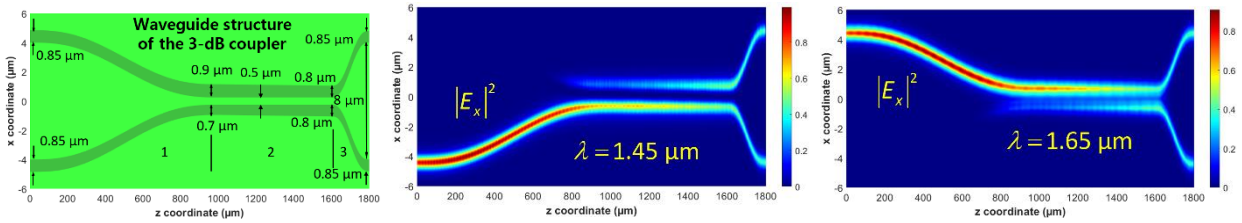


Fig.4. Broadband 3-dB coupler. Waveguide structure and field distributions at the wavelengths of 1.45 µm and 1.65 µm.

ELECTRO-OPTIC PHASE SHIFTERS

Standard push-pull configuration of the electro-optic phase shifters is implemented. The designed electrodes are 6 µm wide, separated by 1 µm from the Si_3N_4 stripe, and are composed of 150 nm SiO_2 buffer covered with 200 nm of gold. Numerical simulations by COMSOL showed that the voltage of 1 V applied to the electrodes excites nearly uniform horizontal electric field intensity of 2×10^5 V/m in the $LiNbO_3$ slab. The distribution of the electric field is shown in Fig. 5. Optical absorption loss due to the presence of electrodes lower than 0.25 dB/cm and the half-wave voltage of the phase shifters lower than 5 V were predicted.

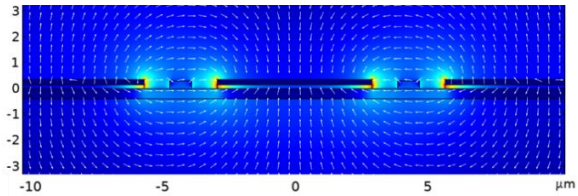


Fig. 5. Distribution of the DC electric field in the phase shifters.

CONCLUSION

A successful proof-of-concept design of the broadband polarization controller based on the "etch-less" Si_3N_4-loaded thin film $LiNbO_3$ was presented. An efficient polarization control was numerically demonstrated in the wavelength band from 1.45 to 1.65 µm with low insertion loss and low operation voltage.

References

[1] R. Noé, H. Heidrich, and D. Hoffmann, *Automatic endless polarization control with integrated-optical Ti:LiNbO3 polarization transformers*, Opt. Lett., vol. 13, pp. 527-529, 1988.

[2] A. Boes, B. Corcoran, L. Chang, J. Bowers, and A. Mitchell, *Status and Potential of Lithium Niobate on Insulator (LNOI) for Photonic Integrated Circuits,* Laser & Photonics Reviews, vol. 12, no. 4, p. 1700256, 2018.

[3] Z. Lin *et al.*, *High-performance polarization management devices based on thin-film lithium niobate,* Light Sci Appl, vol. 11, no. 1, p. 93, 2022.

[4] P. Zhang *et al.*, *High-speed electro-optic modulator based on silicon nitride loaded lithium niobate on an insulator platform,* Opt. Lett., vol. 46, no. 23, pp. 5986-5989, 2021.

[5] X. Han *et al.*, *Mode and Polarization-Division Multiplexing Based on Silicon Nitride Loaded Lithium Niobate on Insulator Platform*, Laser & Photonics Reviews, vol. 16, no. 1, 2021.

[6] R. Gan *et al.*, *Fabrication tolerant and broadband polarization splitter-rotator based on adiabatic mode evolution on thin-film lithium niobate,* Opt. Lett., vol. 47, no. 19, pp. 5200-5203, 2022.

[7] H.-C. Chung, C.-H. Chen, Y. Hung, Jr., and S.-Y. Tseng, *Compact polarization-independent quasi-adiabatic 2×2 3 dB coupler on silicon,* Opt. Express, vol. 30, no. 2, 2022.

[8] D. Guo and T. Chu, *Compact broadband silicon 3 dB coupler based on shortcuts to adiabaticity*, Opt. Lett., vol. 43, no. 19, pp. 4795-4798, 2018.

[9] J. Čtyroký, *3-D Bidirectional Propagation Algorithm Based on Fourier Series*, J. Lightwave Technol., vol. 30, no. 23, pp. 3699-3708, 2012.

Simulation study of propagation losses due to sidewall roughness of GaAs waveguides for single-photon sources in quantum applications

(Student paper)

Miloš Ljubotina[1], Jasper De Witte[2], Dries Van Thourhout[2], Bart Kuyken[2], Leonardo Midolo[3], Marko Topič[1] and Janez Krč[1]

[1]University of Ljubljana, Faculty of Electrical Engineering, Tržaška cesta 25, Ljubljana, 1000, Slovenia
[2]Photonics Research Group, Ghent University - IMEC, Technologiepark-Zwijnaarde 126, Ghent, 9052, Belgium
[3]Center for Hybrid Quantum Networks, Niels Bohr Institute, University of Copenhagen, Blegdamsvej 17, Copenhagen, 2100, Denmark
e-mail: milos.ljubotina@fe.uni-lj.si

Quantum optical technologies impose stringent requirements on device performance that may be overcome through photonic integration. In this work, we investigate light propagation losses incurred by sidewall roughness of GaAs waveguides used in single-photon sources, and the effect of this roughness on adiabatic coupling efficiency between GaAs and SiN.
Keywords: *Gallium arsenide, waveguides, propagation loss, sidewall roughness, coupling efficiency*

INTRODUCTION

Nowadays, quantum technologies present an important field of research and hold promise for many revolutionary applications. One of these technologies is quantum communication, which paves the way for a quantum internet and other applications. A key aspect of quantum communication technologies is their stringent requirements for device performance, such as very low optical loss and high indistinguishability of photons from single-photon sources. In addition to discrete system realizations for quantum communication, integrated solutions are also being explored [1].

Employing photonic integrated circuits, different components used in quantum communications can be integrated into a single chip through heterogeneous integration. In this regard, QuantERA project µTP4Q (A versatile quantum photonic IC platform through micro-transfer printing) aims to explore ways to integrate key components, such as InAs quantum-dot (QD) single-photon sources, $LiNbO_3$ modulators and switches, superconducting nanowire single-photon detectors, and low-loss passive circuitry based on a SiN platform [1], [2]. Heterogeneous integration of the components on a SiN interposer will be investigated by using the micro-transfer-printing (µTP) process [3]. This technique allows us to fabricate the components on their native platforms, select the best-performing devices, and subsequently integrate them into a single chip. It is essential that optical losses of the components and their interconnections are as low as possible. Therefore, highly efficient optical coupling between the interposer and transfer-printed components is required, as well as very low internal loss in components and in connection circuitry. Furthermore, for the actual implementation of such systems, it is important to consider fabrication-related effects, such as µTP-induced misalignment and light propagation loss caused by waveguide (WG) surface roughness.

In this work we study the optical losses in GaAs strip WGs for single-photon sources (including InAs QDs) associated with sidewall surface roughness. We quantify the light propagation losses with respect to randomly generated sidewall variations with different statistical parameters in simulations. The roughness can originate from different fabrication process steps, such as electron beam lithography and etching [4]. Secondly, we also show how such sidewall roughness of WGs affects the efficiency of adiabatic coupling between micro-transfer-printed GaAs WGs and SiN WGs of the interposer.

METHODS AND STRUCTURES

Simulations were performed with the finite-difference time-domain (FDTD) method using Ansys-Lumerical software. With respect to experimental observations, we applied the surface roughness to both sides of the GaAs WGs in the longitudinal direction. In our study we apply a generic randomly generated roughness to get a more general view and understanding of its effects in relation to its statistical parameters. No variations in the topology of the sidewalls were assumed in the vertical direction. Also, no roughness was applied to the top or bottom surface of the WGs either. This anisotropic sidewall roughness was characterised by its root-mean-square (RMS) value, σ_{rms}, and its correlation length, L_{corr}. The roughness was generated by employing the technique described in [5] and adapting existing scripts for random roughness generation available in Ansys-Lumerical software. The roughness functions on both sides of the WGs were uncorrelated. We chose the range of values for σ_{rms} and L_{corr}

based on preliminary measurements of actual samples using scanning electron microscopy [6]. Simulations were performed for a wavelength of 930 nm (central emission of InAs QDs) if not stated differently.

Fig. 1a shows the top view of a segment of a GaAs strip WG used in simulations (note the different scales of the vertical and horizontal axes), while Fig. 1b shows the top view and a cross-sectional view of a GaAs taper for adiabatic coupling to SiN WGs [3]. In the first case, the isolated WG is surrounded by air entirely and has a base cross-section of 300 nm in width and 170 nm in height. In both types of simulations, the fundamental TE mode transmission (T_{TE1}) is the primary parameter of interest. The refractive index of the bonding layer (BCB) was set to 1.54, while for other materials the corresponding refractive indices were taken from the material library of the simulation tool. According to the available values for the extinction coefficient, no material absorption was considered at the given wavelength.

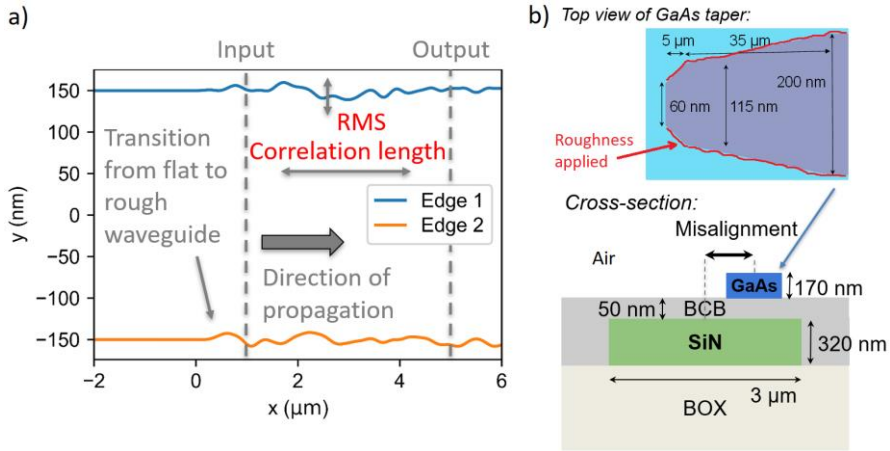


Fig. 1. a) Example of sidewall variations and setup of simulations for an isolated GaAs WG. b) Structure for the GaAs-SiN adiabatic coupler as used in simulations.

RESULTS

The results of simulations of GaAs WGs with sidewall roughness as a function of σ_{rms} and L_{corr} are presented in Figs. 2a and 2b, respectively. A 4 μm long WG section was included in the propagation loss calculations based on these simulations. The symbols in the plots represent simulations with different pseudo-random number generator (PRNG) seeds, while the curves represent the average of 10 simulations with different seeds at a given value of the x-axis parameter. It can be observed that an increase in σ_{rms} or a decrease in L_{corr} leads to a substantial increase in propagation losses. It should be noted that a large spread of the loss values is obtained by varying the PRNG seed. Therefore, in addition to σ_{rms} and L_{corr}, the spatial frequency spectra of the randomly generated roughness were also considered (see insets). In the two cases shown in Fig. 2b, it can be observed that the power spectra of the sidewall variations of the WG with lower loss (right inset) are shifted towards higher spatial frequencies compared to the WG with higher loss (left inset).

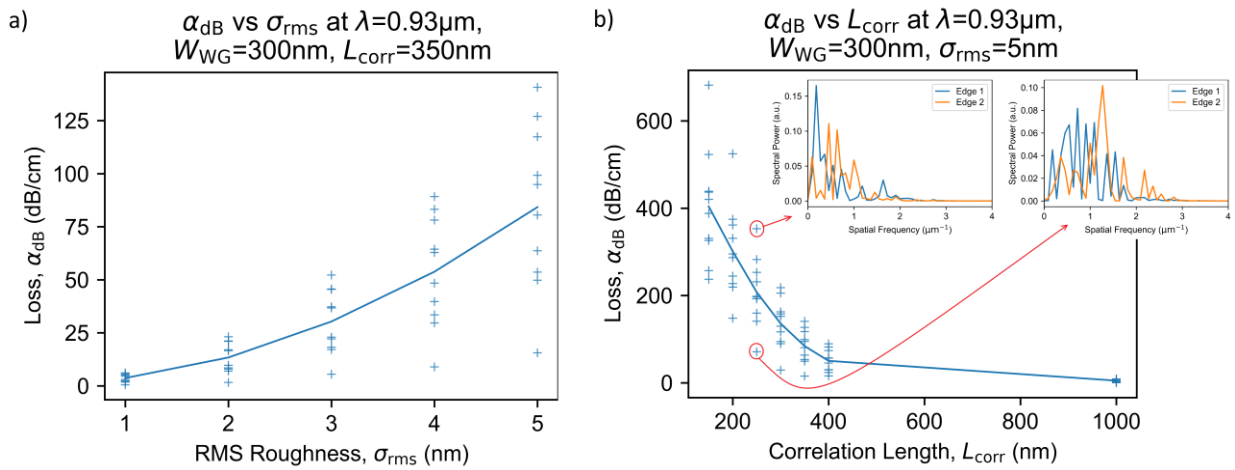


Fig. 2. a) Simulated propagation loss of rough GaAs WGs with respect to RMS roughness for a 350 nm correlation length. b) Simulated propagation loss of rough GaAs WGs with respect to correlation length for a 5 nm RMS roughness. The insets show the power spectra of the sidewall variations for two GaAs WGs used in simulations.

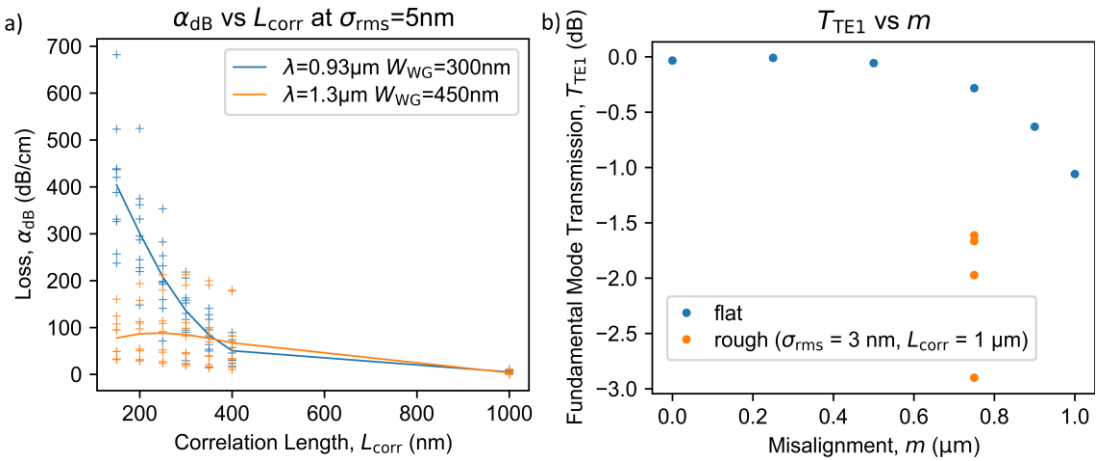


Fig. 3. a) Simulated propagation loss of rough GaAs WGs with respect to correlation length for a 5 nm RMS roughness and two WG types differing in width and target wavelength of operation. b) Simulated fundamental TE mode transmission of the GaAs-SiN adiabatic coupler with respect to misalignment for an ideally flat GaAs WG and additional points for the case of a rough GaAs WG at a misalignment of 0.75 µm and four different PRNG seeds.

From the results presented in Fig. 2, it is clear that sidewall roughness can be the cause of losses in GaAs WGs from below 10 dB/cm to greater than 400 dB/cm. In the parameter range where the simulations were performed, low L_{corr} (below 300 nm) leads to high losses in the hundreds of decibels per centimeter. In our conference presentation we will link these values with experimental observations on fabricated GaAs WGs, reaching values of 50-70 dB/cm.

To indicate the role of wavelength with respect to the losses, in Fig. 3a we also show simulation results for a wavelength of 1300 nm (also using a wider WG – 450 nm, still assuring single-mode operation for this wavelength). In this case, we can observe that the increase in losses associated with a low L_{corr} is much smaller – the average losses remain below 100 dB/cm, whereas they exceed 400 dB/cm for the initial waveguide at a 930 nm wavelength.

In Fig. 3b we show preliminary results of the effect of GaAs WG sidewall roughness on the efficiency of the GaAs-SiN adiabatic coupler shown in Fig. 1b with respect to the misalignment of the two WGs caused by the µTP process (see misalignment definition in Fig. 1b). It is clear that the sidewall imperfections have a significant impact on the performance of such couplers, as the fundamental TE mode transmission of a coupler with flat GaAs WG sidewalls decreases from -0.3 dB to around -2.0 dB on average (with respect to the PRNG seed) for a selected misalignment of 0.75 µm when rough sidewalls are used. Further results will be shown in the conference presentation.

CONCLUSIONS

We performed a simulation study on the propagation losses of GaAs WGs due to sidewall roughness as a function of σ_{rms} and L_{corr}. It was shown that for σ_{rms} of a few nm and for L_{corr} below 300 nm very high losses (above 100 dB/cm) occur. Using a wider WG and longer wavelength can result in substantially lower loss in case of short correlation lengths. Furthermore, we showed preliminary results on the effect of GaAs WG sidewall roughness on the performance of a GaAs-SiN adiabatic coupler.

Acknowledgements: This project was funded within the QuantERA II Programme that has received funding from the European Union's Horizon 2020 research and innovation programme under Grant Agreement No 101017733 and national funding agency (MIZS) contract No.C3330-22-252001. Co-authors from University of Ljubljana also acknowledge the financial support from the Slovenian Research Agency (Research Programme P2-0415, and M.L. for PhD funding).

References

[1] R. Uppu, L. Midolo, X. Zhou, J. Carolan, and P. Lodahl, "Single-photon quantum hardware: towards scalable photonic quantum technology with a quantum advantage," *Nat. Nanotechnol.*, vol. 16, no. 12, pp. 1308–1317, Dec. 2021.

[2] R. Uppu *et al.*, "On-chip deterministic operation of quantum dots in dual-mode waveguides for a plug-and-play single-photon source," *Nat Commun*, vol. 11, no. 1, Art. no. 1, Jul. 2020.

[3] G. Roelkens *et al.*, "Micro-Transfer Printing for Heterogeneous Si Photonic Integrated Circuits," *IEEE Journal of Selected Topics in Quantum Electronics*, vol. 29, no. 3: Photon. Elec. Co-Inte. and Adv. Trans. Print., pp. 1–14, May 2023.

[4] L. Midolo, T. Pregnolato, G. Kiršanskė, and S. Stobbe, "Soft-mask fabrication of gallium arsenide nanomembranes for integrated quantum photonics," *Nanotechnology*, vol. 26, no. 48, p. 484002, Nov. 2015.

[5] E. Jaberansary *et al.*, "Scattering Loss Estimation Using 2-D Fourier Analysis and Modeling of Sidewall Roughness on Optical Waveguides," *IEEE Photonics Journal*, vol. 5, no. 3, pp. 6601010–6601010, Jun. 2013.

[6] Y. Wang *et al.*, "Electroabsorption in gated GaAs nanophotonic waveguides," *Applied Physics Letters*, vol. 118, no. 13, 2021.

Broadband, low-loss O-band Silicon Polarization Splitter-Rotator

(Student paper)

Theoni Prousalidi[1,2], Giannis Poulopoulos[1], Carmelo Scarcella[2], Harry Zervos[1], Stéphane Detraz[2], Milana Lalović[2,3], Lauri Olanterä[2], Awanish Pandey[2], Ulrik Sandven[2], Christophe Sigaud[2], Csaba Soos[2], Jan Troska[2] and Hercules Avramopoulos[1]

[1] School of Electrical and Computer Engineering, National Technical University of Athens, 15780 Zografou, Athens, Greece
[2] CERN, Esplanade des Particules 1, 1211 Geneva, Switzerland
[3] School of Electrical Engineering, University of Belgrade, Belgrade, Serbia
* theoni.prousalidi@cern.ch

A novel O-band polarization splitter-rotator based on mode conversion and coupling is proposed. The device is broadband, tolerant to fabrication imperfections and compatible with DUV lithography MPW processes, requiring single-step etching. Simulations show $TM_0 \rightarrow TE_0$ efficiency greater than 89% across the O-band with peak value of 96.3%, and TE_0-TE_0 efficiency of >99%. The simulated crosstalk is <-85 dB and the polarization dependent loss <0.5 dB in the O-band.
Keywords: *Silicon Photonics, polarization splitter-rotator, O-band*

INTRODUCTION

Silicon Photonics (SiPh) technology has gained attention in recent years, due to its compatibility with CMOS fabrication processes [1] that enable the low-cost development of photonic integrated circuits (PIC) with sub-micron precision, through multi-project wafer (MPW) services [2]. The high index contrast of the material allows the development of ultra-compact devices that can also be low-power and tightly co-integrated with electronics. However, silicon-on-insulator (SOI) waveguides exhibit strong birefringence which makes the SiPh devices highly polarization-sensitive. To overcome this drawback different approaches have been exploited to achieve on-chip polarization diversity [3]. Polarization splitters-rotators (PSR) are key components in polarization diversity circuits, necessary at the interface between fibers and PICs. They are also important in various applications, like coherent optical receivers, data-centre transceivers and quantum photonics [4]. However, it is difficult to realize waveguide-type polarization rotators since it is complicated to rotate the optical axis of a planar waveguide. To achieve that, the symmetry of the waveguide cross-section must be broken [5]. Different types of PSRs have been reported employing cascaded bends, stacked waveguides, bi-level tapers, off-axis dual cores, subwavelength structures and slanted waveguides [6]–[8]. These structures, although they usually show good performance, require complex fabrication processes like multiple etch-depths and special etching and have low fabrication tolerance. Moreover, very few O-band PSRs that meet the requirements for easy fabrication and tolerance have been proposed.

In this work, we propose a broadband O-band PSR based on mode conversion and phase matching that implements the TM_0-TE_1-TE_0 mode conversion in a structure that consists of an adiabatic taper and an asymmetric directional coupler (ADC) with one tapered arm [9]. Air is used as top cladding to break the vertical symmetry, therefore only a single etch depth is necessary, making its fabrication simple and fully compatible with deep-UV lithography MPW processes [10]. The tapered ADC improves its tolerance to fabrication imperfections. The PSR is compatible with the 100G CWDM4 MSA Ethernet standard. In this paper, we describe the detailed simulation and design process of the PSR and report its simulated performance.

SIMULATIONS AND DESIGN

The proposed PSR is designed on a 220 nm SOI wafer and the refractive indices for Si and SiO_2 are n_{Si} = 3.504 and n_{SiO2} = 1.4469 at 1300 nm respectively. As shown in Fig. 1 Left, the device consists of two sections, the taper and the coupler, connected to the input and output waveguides with nominal widths (w_0=w_{out}=380 nm). The principle of operation of the PSR is based on mode conversion ($TM_0 \rightarrow TE_1$) in the taper and mode coupling due to phase matching ($TE_1 \rightarrow TE_{0\text{-cross}}$) in the coupler. The TE_0 at the input propagates unchanged through the PSR to the through port, while TM_0 is rotated to TE_0 at the cross port.

Fig. 1 Right shows the effective indices (n_{eff}) of the eigenmodes of the Si waveguide varying its width, as calculated using the Finite Difference Eigenmode (FDE) solver by Lumerical. Due to the vertical asymmetry introduced by the air top-cladding, for a critical width of around 590 nm, the TM_0-TE_1 modes are hybridized and therefore mode conversion is achieved around this region. The taper widths are selected so that the taper input (w_0) is single mode, while its output (w_3) also supports mode TE_1. As w_0 the nominal waveguide width is selected (w_0=380 nm). w_3 is selected to be larger than the critical width so that the whole hybridization region is included in the taper (w_3=750 nm). To achieve adiabatic mode conversion with high efficiency and short length, a three-segment taper approach is employed. The middle segment (L_{tp2}) is where the mode conversion happens. It should include the

critical width for all operation wavelengths and should have a very small taper angle to be adiabatic. The first and third segments (L_{tp1}, L_{tp3}) can have steeper slopes to ensure a short taper, without compromising the efficiency. We choose w_1=500 nm and w_2=670 nm (w_1<590 nm<w_2).

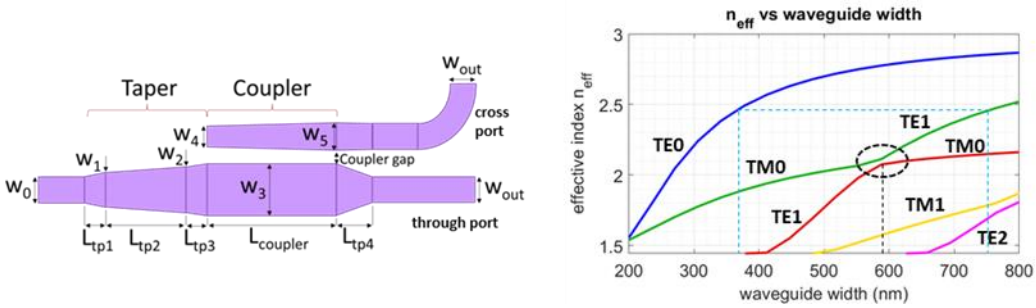


Fig. 1: Left: Top view of the geometry of the proposed PSR. Right: the calculated effective indices of the eigenmodes of a Si waveguide with air top-cladding and Si height of 220 nm vs. the waveguide width.

The lengths of the three segments are optimized with the EigenMode Expansion (EME) propagation solver by Lumerical, to achieve maximum mode conversion efficiency (MCE) at 1300 nm. Fig. 2 (a) shows the TE_0-TE_0 and TM_0-TE_1 efficiency varying the middle segment length. The optimal length is calculated to be L_{tp2}=170 μm, where $MCE_{TM0\text{-}TE1}$ = 97%. We also calculate L_{tp1}=7 μm and L_{tp3}=11 μm. No coupling occurs for TE_0 in this region, therefore TE_0 propagates unchanged through the taper with efficiency of almost 100%.

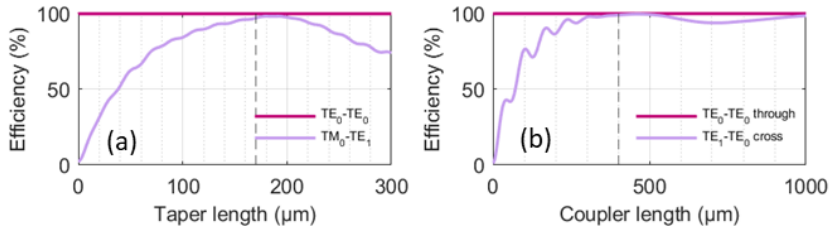


Fig. 2: (a) MCE of TM_0-TE_1 and TE_0-TE_0 propagation vs. length of the taper section L_{tp2}, (b) MCE of TM_0-TE_1 and TE_0-TE_0 propagation vs. coupler length $L_{coupler}$.

After converting TM_0 to TE_1, a narrow, tapered waveguide is placed next to the wide waveguide at the output of the taper section, to form an ADC. With correct choice of the waveguide widths of the ADC, the phase matching condition is satisfied, meaning n_{eff_TE1} at the wide waveguide is equal to n_{eff_TE0} at the narrow one. This way, TE_1 will be efficiently coupled to TE_0 at the cross waveguide. For w_3=750 nm, this is satisfied for a width of around 365 nm for the narrow waveguide (highlighted in Fig. 1 Right with dashed light blue lines). In the case of a cross waveguide with uniform width, the latter would have to be chosen with nanometer accuracy and any deviation induced by fabrication would cause the breaking of the phase matching condition. By making it tapered, the fabrication tolerance of the design is improved, since even if the final dimensions deviate from the specified ones, the phase matching condition will be met at some point along the taper. Also, the bandwidth of the design is enlarged, since the phase matching points are slightly different for the various O-band wavelengths, but they can always be found along the coupling region. Eventually, we choose w_4=340 nm and w_5=390 nm (around the 365 nm phase matching point for 1300 nm). Also, the coupler gap is chosen to be ≥180 nm ensuring low fabrication complexity. Then, the length of the coupler is optimized using the EME solver to maximize the coupling efficiency. The simulation results are shown in Fig. 2 (b). The optimal length is found to be $L_{coupler}$=400 μm wielding a TE_1-$TE_{0\text{-cross}}$ efficiency of 99% at 1300 nm. For the TE_0 at the wide waveguide in the coupling section, no phase matching condition is satisfied, so TE_0 will propagate straight to the through port with very small crosstalk at the cross port and negligible losses.

Fig. 3 shows the simulated light propagation across the whole device, generated using the EME solver. For TE_0 input (Fig. 3(a)) all the power propagates to the through port, while for TM_0 input (Fig. 3(b)), it is rotated to TE_1 and then coupled to TE_0 of the cross output port. The transmission and crosstalk varying the wavelength across the O-band

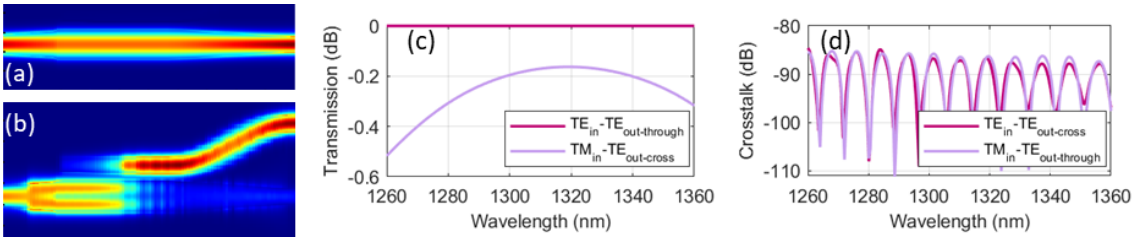


Fig. 3: (a) Top view of the simulated light propagation along the PSR with TE_0 input mode and (b) TM_0 input mode. (c) Simulated wavelength characteristics of the proposed PSR. The TE_0-TE_0 and TM_0-TE_0 transmissions. (d) The crosstalk.

are shown in Fig. 3 (c) and (d) respectively. The TE_{in}-$TE_{out\text{-}through}$ insertion loss is almost 0 dB across the O-band, while the TM_{in}-$TE_{out\text{-}cross}$ conversion loss is <0.5 dB, making the design highly efficient and broadband. The crosstalk for both TE and TM input is <-85 dB across the O-band. The polarization dependent loss (PDL) is <0.5 dB in the O-band.

Since this is an on-chip PSR that will be connected at its input and output with standard waveguides with SiO_2 top-cladding, the EME solver was used to simulate the interface. It was thus verified that no losses are introduced because of the different cladding, and coupling efficiency is almost 100% for both propagation directions.

A tolerance study was carried out to investigate the effect of the variation of two parameters on the PSR performance: the waveguide width (Δw), induced by variations of the lithography process, and of the SOI wafer height (Δh). Typically, Δw is limited to ±5 nm for DUV lithography and Δh to ±2 nm, however we varied them in a wider range for certainty [11]. The results are reported in Fig. 4 (a) and (b) respectively. Polarization conversion loss for TM_0 input remains below 0.5 dB for Δw = ±10 nm and below 1.5 dB for Δh = ±5 nm. This showcases a very good tolerance to fabrication imperfections and full compatibility with MPW services. This is very important for real applications that require reliable, efficient and broadband PSRs, without having access to more advanced and expensive fabrication techniques. In this regard, the design has been included in an MPW chip submission (under fabrication), targeting the development of SiPh coarse wavelength division multiplexing (CWDM) transceivers for High Energy Physics (HEP) experiments at CERN [12], that require on-chip polarization diversity.

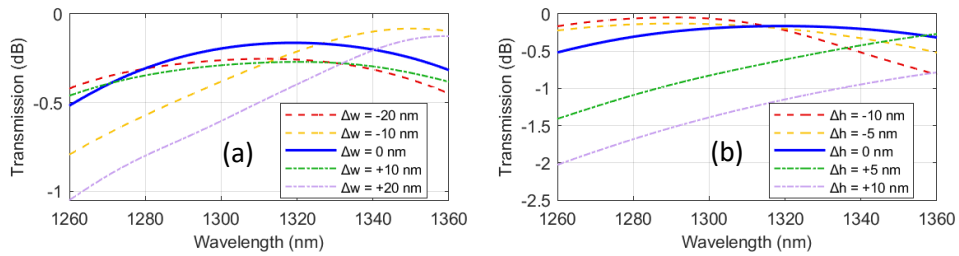


Fig. 4: TM_{0in}-$TE_{0cross\text{-}out}$ transmission varying (a) the width of the PSR and (b) the height of the SOI wafer.

CONCLUSIONS

We presented a novel broadband PSR element designed for the 220-nm top SOI integration platform. The design has a length of 610 μm. Simulations show a TE-TE efficiency of >99% across the O-band, and TM-TE MCE of 96% at 1310 nm and >89% across the O-band. The simulated PDL is <0.5 dB across the O-band and <0.4 dB in the 100G CWDM grid. The crosstalk is <-85 dB in the O-band. The novelty of the design is built upon a mode hybridization taper and tapered ADC for the mode coupling, resulting in low complexity fabrication, low loss and broadband O-band operation, while showcasing increased tolerance to fabrication imperfections. It employs a single etch depth and is fully compatible with deep UV lithography MPW processes. It has been included in an MPW chip submission as part of a SiPh test chip for HEP experiments at CERN.

References

[1] W. Bogaerts and L. Chrostowski, "*Silicon photonics circuit design: methods, tools and challenges*," Laser & Photonics Rev., vol. 12, no. 4, p. 1700237, 2018.
[2] M. Pantouvaki *et al.*, "*50Gb/s silicon photonics platform for short-reach optical interconnects*," in Optical Fiber Communication Conference, pp. Th4H--4, 2016.
[3] D. Dai, L. Liu, S. Gao, D. X. Xu, and S. He, "*Polarization management for silicon photonic integrated circuits*," Laser Photonics Rev., vol. 7, no. 3, pp. 303–328, 2013.
[4] L.-T. Feng *et al.*, "*On-chip coherent conversion of photonic quantum entanglement between different degrees of freedom*," Nat. Commun., vol. 7, no. 1, p. 11985, 2016.
[5] Y. Yin, Z. Li, and D. Dai, "*Ultra-broadband polarization splitter-rotator based on the mode evolution in a dual-core adiabatic taper*," J. Light. Technol., vol. 35, no. 11, pp. 2227–2233, 2017.
[6] K. Tan, Y. Huang, G.-Q. Lo, C. Yu, and C. Lee, "*Experimental realization of an O-band compact polarization splitter and rotator*," Opt. Express, vol. 25, no. 4, pp. 3234–3241, 2017.
[7] G. B. de Farias et al, "*Demonstration of a low-loss and broadband Polarization Splitter-Rotator with a Polysilicon waveguide in SOI platform*," in 2019 SBFoton International Optics and Photonics Conference (SBFoton IOPC), pp. 1–5, 2019,.
[8] Y. Ma *et al.*, "*Symmetrical polarization splitter/rotator design and application in a polarization insensitive WDM receiver.*," Opt. Express, vol. 23, no. 12, pp. 16052–16062, Jun. 2015.
[9] Y. Shen, Z. Ruan, K. Chen, L. Liu, B. Chen, and Y. Rao, "*Broadband polarization splitter-rotator on a thin-film lithium niobate with conversion-enhanced adiabatic tapers,*" Opt. Express, vol. 31, no. 2, pp. 1354–1366, 2023.
[10] D. Dai and J. E. Bowers, "*Novel concept for ultracompact polarization splitter-rotator based on silicon nanowires,*" *Opt. Express*, vol. 19, no. 11, pp. 10940–10949, 2011.
[11] Y. Xing et al, "*Capturing the Effects of Spatial Process Variations in Silicon Photonic Circuits,*" ACS Photonics, Nov. 2022.
[12] T. Prousalidi *et al.*, "*Towards optical data transmission for high energy physics using silicon photonics,*" J. Instrum., vol. 17, no. 05, p. C05004, 2022.

Towards Photonic Integrated Ion Traps for high-performance Quantum Computing and Atomic Clocks

(Student paper)

Carl-Frederik Grimpe[1,*], Guochun Du[1], Elena Jordan[1], Anastasiia Sorokina[2,3], Pascal Gehrmann[2,3],Steffen Sauer[2,3], Stefanie Kroker[1,2,3] and Tanja E. Mehlstäubler[1,4,5]

[1]Physikalisch-Technische Bundesanstalt, Bundesallee 100, Braunschweig, 38116, Deutschland
[2]Institut für Halbleitertechnik, Technische Universität Braunschweig, Hans-Sommer-Str. 66, Braunschweig, 38106, Deutschland
[3]Laboratory for Emerging Nanometrology, Langer Kamp 6 a/b, Braunschweig, 38106, Deutschland
[4]Institut für Quantenoptik, Leibniz Universität Hannover, Welfengarten 1, Hannover, 30167, Deutschland
[5]Laboratorium für Nano- und Quantenengineering, Leibniz Universität Hannover, Schneiderberg 39, Hannover, 30167, Deutschland
[*]carl.grimpe@ptb.de

Ion traps are a promising platform for the realization of high-fidelity quantum information processors and high-accuracy optical clocks. Integrated photonic components are essential for scaling ion trap systems to large numbers of qubits. We will present our work on ion traps with integrated light guidance and manipulation. **Keywords:** *Ion traps, Quantum computing, Photonic integrated circuits, Microfabricated outcoupling gratings, Waveguides, Atomic clocks*

INTRODUCTION

Trapped ion quantum computers are one of the most promising platforms for efficiently solving classically intractable problems, such as combinatory optimization problems, material design, and drug delivery, just to name a few [1,2,3]. Currently, the world leading trapped ion quantum computers operate with around 20 qubits, offering high fidelities of >99% for single and two-qubit gate operations [4,5,6]. The number of qubits is not sufficient to solve classically intractable problems. Integrated photonics in ion traps will allow making the decisive step to scale up to higher numbers of qubits [1]. Photonic integrated circuits (PICs) enable laser light delivery with high pointing stability and customized spot size to each ion qubit at wavelengths ranging from ultraviolet (UV) to near-infrared (NIR) range.

Trapped-ion-based optical clocks serve as highly stable frequency standards that can be applied for timing information in navigation, very long baseline telescopes, tests of fundamental physics, and geodesy [7,8,9]. The physics package that provides the reference frequency will greatly benefit from integrated optics. The systems will consume less energy, get more compact, portable, easier to maintain, and more affordable.

In our research projects, we work on the development of photonically integrated ion traps for quantum computing and optical clocks. We design ion traps with passive optical devices such as waveguides, focusing grating outcouplers and tapers for incoupling from optical fibers. We characterize the fabricated PICs based on the outcoupled light using beam tomography. The integrated traps will be characterized in a dedicated test setup.

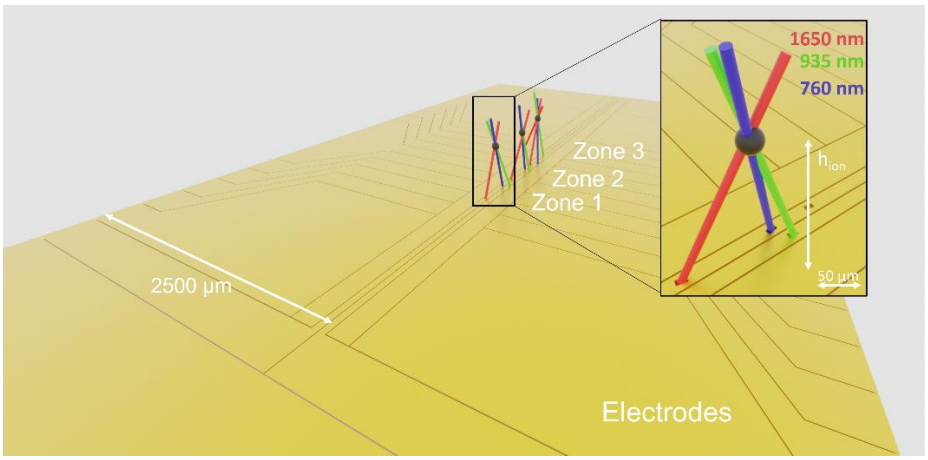


Fig. 1. Surface Ion trap with integrated photonics to control outcoupled beams for addressing the ions (black spheres) in different trap zones. The colored beams display the different wavelengths implemented (Blue: 760 nm, Green: 935 nm, Red: 1650 nm).

Beam geometry and ion trap requirements

We use $^{172}Yb^+$ ions to design and characterize our prototype ion trap with integrated optics. The $^{172}Yb^+$ level scheme (Figure 2 a)) shows all the relevant transitions and their corresponding wavelengths which cover the range from UV to NIR. Specific angles, beam waists, power, and light polarization are required to drive the transitions. Moreover, crosstalk between the different zones and scattering must be avoided. Figure 2 b) shows a basic design of our linear surface ion trap. With the same working principle as a typical Paul trap, the surface trap uses DC electrodes (blue) and RF electrodes (red) to generate a dynamic potential to trap ions in space. In our configuration, the ion height h_{ion} is designed to be 100 µm above the surface. With $\Omega_{RF} = 2\pi \cdot 20$ MHz and $U_{RF} = 200$ V, we obtain a radial secular frequency of $2\pi \cdot 3.03$ MHz and a trap depth of 264.78 mV. Three of the trapping zones are provided with different beam geometries for the NIR transitions (see Fig. 1). To enter a specific zone the ion will be shuttled. The integrated trap design is inspired by *Karan Mehta et al.* [11]. Furthermore, opening windows in the gold electrodes are necessary for beams to not get backreflected from the gold layer. Their influence on the trapping potentials and the possibilities to coat them with ITO are under investigation.

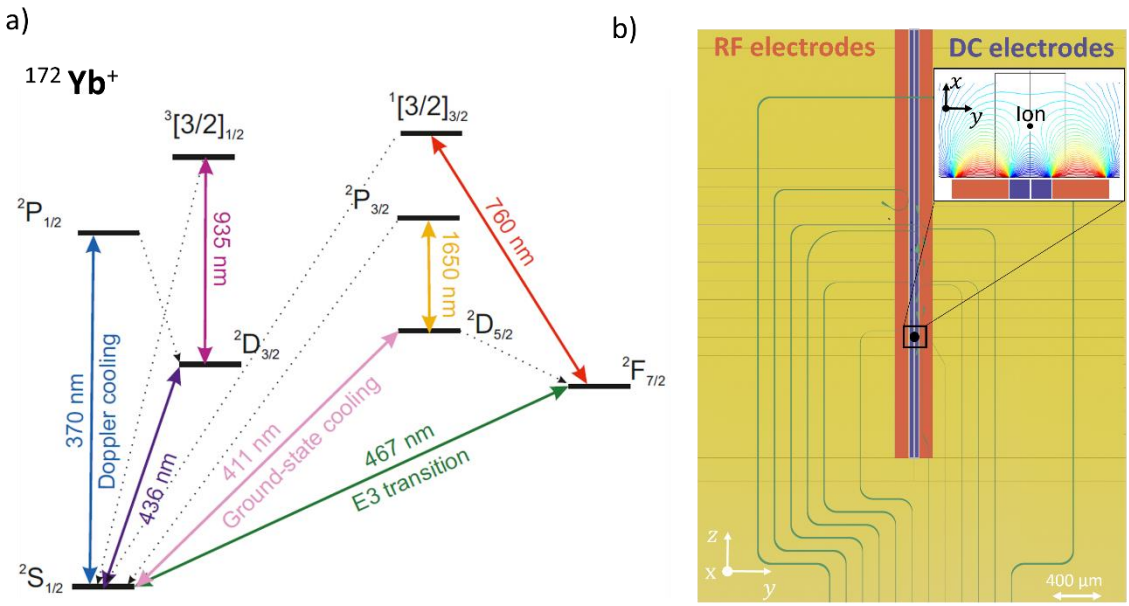


Fig. 2. a) $^{172}Yb^+$ level scheme (based on [12]) b) Sketch of a surface ion trap, the electric potential trapping the ion, and the PIC (green).

Light delivery

To guide the laser light on the chip, different passive optical elements are utilized. The light is coupled in from a fiber array using a two-layer butt coupling scheme. It is sent to the ion for optical control via tailored waveguides and focusing grating outcouplers. The waveguides are designed to provide single-mode operation and high confinement of the fundamental quasi-TE mode. The grating coupler design aims for a Gaussian beam with µm-beam waist by changing the duty cycle, the period, and the grating curvature. Besides that, other passive optical components like MMI splitters and mode converters are utilized. The material of choice for the NIR wavelengths is Si_3N_4. To further address the UV wavelengths, AlN- and Al_2O_3-based PICs are under investigation. The cladding material is SiO_2 and the substrate is Si. Our simulations are carried out with Lumerical FDTD, Lumerical MODE, and COMSOL Multiphysics.

Optical characterization setup

A characterization setup is used to evaluate the performance of the designed integrated optical components. Our setup is designed to target the needed wavelengths ranging from UV to NIR. It consists of three major parts:

1. A *laser system* able to address the wavelengths required to work with $^{172}Yb^+$-ions. The seven lasers are selected to secure a narrow bandwidth operation that avoids dispersive influences of the grating outcouplers (see Tab. 1). This leads to entirely fiber-coupled setups for the IR lasers and free-space setups for the UV wavelengths.
2. A *hexapod* with an attached nanopositioner that aligns the fiber arrays to the chip. Six degrees of freedom and the smallest step size of 2.5 nm serve to maximize the incoupling efficiency.

3. A *microscope* for monitoring the grating coupler emission. The hexapod holding the fiber array and the sample holder is hereby mounted on the microscopes x-y-stage. To reconstruct the beam, emission at different heights above the chip is measured with the help of an automated focusing unit. Four different objectives and a dual-camera port with a CMOS and an InGaAs camera enable measurements from 350 to 1700 nm.

Wavelength [nm]	Power [mW]	Linewidth [MHz]	Range [nm]
370	13	0.15	1
399	>50	1	4
411	23	0.1	5
467	~15	0.1	3
760	9	1	2
935	13	8	2
1650	20	0.1	2

Tab. 2. Different laser types are used to cover the required wavelengths for $^{172}Yb^{+}$. The power values correspond to the specified output powers of the laser sources.

DISCUSSION

The integration of photonics in surface electrode ion traps for scalable quantum computers and optical clocks faces some major challenges. To address the relevant ion transitions photonics from UV to NIR are required which results in different material platforms to integrate into a chip. Furthermore, the beam must be delivered with certain characteristics to interact with the ion effectively, so the focussing grating couplers have to be designed in a way that avoids stray light and provides single-ion addressing. Moreover, standard grating couplers are limited to the emission of linear polarization, however, circular polarization is desired for state preparation in trapped ions. Finally, we have implemented a characterization setup for PICs capable to work from UV to NIR

Acknowledgments: The authors gratefully acknowledge support from the Braunschweig International Graduate School of Metrology B-IGSM and the DFG Research Training Group GrK1952/1 “Metrology for Complex Nanosystems”. Furthermore, we thank the Quantum Valley Lower Saxony, ATIQ (FKZ 13N16126) and cluster of Excellence QuantumFrontiers (EXC-2123–390837967). Moreover, we thank Karan Mehta for his help, support and discussions.

References

[1] C. D. Bruzewicz et al., Trapped-Ion Quantum Computing: Progress and Challenges, Appl. Phys. Rev. vol. 6, no.2, pp. 021314 (2019)
[2] J. Benhelm, G. Kirchmair, C. Roos, et al. Towards fault-tolerant quantum computing with trapped ions. Nature Phys 4, 463–466 (2008)
[3] B. Bauer et al. Quantum Algorithms for Quantum Chemistry and Quantum Material Science, Chemical Reviews , vol 120, no.22, pp. 12685-12717, (2020)
[4] IonQ, IonQ Aria: Practical Performance (Part One), https://ionq.com/posts/july-25-2022-ionq-aria-part-one-practical-performance (accesssed 16.01.2023)
[5] Quantinuum, Major Upgrade for System Model H1-1, Powered by Honeywell, https://www.quantinuum.com/hardware/n20 (accessed 17.01.2023)
[6] Access 20 fully-connected qubits using a 19” rack., AQT, https://www.aqt.eu/pine-system-20-qubit-control/ (accessed 17.01.2023)
[7] A. D. Ludlow, et al., Optical atomic clocks, Rev. Mod. Phys., vol. 87, pp. 637 (2015)
[8] J. Stuhler, et al., Opticlock: Transportable and easy-to-operate optical single-ion clock, Measurement: Sensors, vol. 18, pp. 100264 (2021)
[9] T. E. Mehlstäubler, et al., Atomic clocks for geodesy, Rep. Prog. Phys., vol. 81, no. 6, pp. 064401 (2018)
[10] D. Allock, Surface-Electrode Ion Traps for´ Scalable Quantum Computing, PhD thesis, Oxford University, UK (2011)
[11] K. Mehta, C. Bruzewicz, R. McConnell, et al. Integrated optical addressing of an ion qubit. Nature Nanotech 11, 1066–1070 (2016)
[12] T. Burgermeister, Development and characterization of a linear ion trap for an improved optical clock performance. Hannover: Gottfried Wilhelm Leibniz Universität, PhD thesis (2019)

Fabrication Tolerant Directional Coupler

(Student paper)

Yichen Liu[1,2], Umar Khan[1,2], and Wim Bogaerts[1,2]

[1] Photonics Research Group, Ghent University-IMEC, Ghent, Belgium
[2] Center of Nano and Biophotonics, Ghent, Belgium
[*] Yichen.liu@ugent.be

We present the design of a fabrication-tolerant directional coupler in a passive photonic integrated chip fabricated on Imec's iSiPP50G silicon photonics platform. Based on Finite Difference Eigenmode, Finite-Difference Time-Domain simulations, and experimental measurements. We demonstrate that such a design is tolerant to waveguide width fabrication errors. The experimental results are in good agreement with the simulations.
Keywords: *fabrication tolerant, directional coupler, photonic intergrated circuit*

INTRODUCTION

Components on a photonic integrated chip (PIC) control the propagation of light on the chip. With the maturity of manufacturing technology, people's needs for chip functions are becoming more and more diverse, the circuits are becoming more complex. The high refractive index contrast between the waveguide core and cladding ensures high integration in chip fabrication, but also makes the performance of on-chip optics more sensitive to fabrication errors [1][2]. For example, a directional coupler (DC) is an essential component of almost all chips, and the manufacturing error of its waveguide width will cause a large error between the actual coupling ratio and the design value, which will affect all components that contain DC. Therefore, designing and manufacturing on-chip components that are insensitive to manufacturing errors at a low cost is of great significance for improving product yield and reducing manufacturing costs.

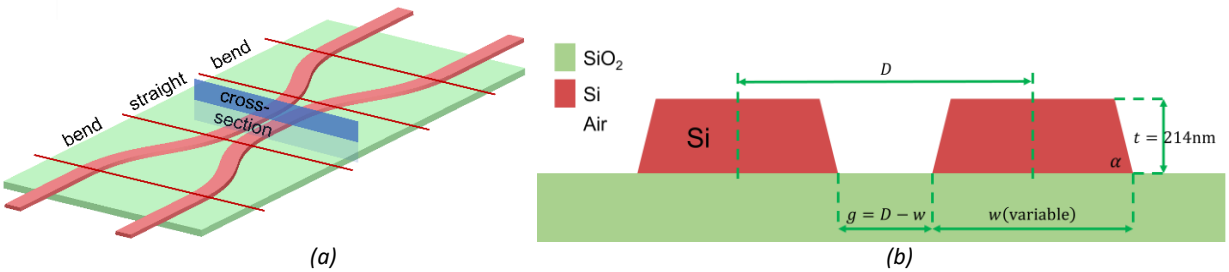
STRUCTURE MODEL OF THE DIRECTIONAL COUPLER

A DC usually consists of two waveguides in close proximity, so that the evanescent field of electromagnetic waves can couple the energy of light from one mode to the other. The math model [3] that describes the cross-transmission characteristics of the coupler is shown in Equ.(1):

$$P = \sin^2(\kappa' L + \kappa_0) \tag{1}$$

Where P is the overall power coupling, κ' is the coupling per unit length of the straight coupler section, L is the length of the straight section of the DC, and κ_0 is the coupling from the bend section.

The corresponding schematic diagram is as figure 1(a). Figure 1(b) shows the cross-section through the straight section of a directional coupler with SiO_2 base and air cladding.



(a) (b)

Figure 1: (a) Schematic diagram of a directional coupler showing the straight and the curved sections. (b) Diagram showing the cross-section through the straight section of the directional coupler.

In IMEC's iSiPP50G silicon photonics platform, the base angle $\alpha > 85°$; the thickness t is 214nm; the default value of centre line distance D is 700nm; the default value of waveguides base width w is 450nm, g demonstrates the base gap of the waveguides. The waveguides are made of Si and the DC can be SiO_2 cladding or air cladding.

Based on the current manufacturing process, we use the following approximations when the width changes due to a fabrication variation:

- both waveguides are symmetrical trapezoids
- the absolute change is same for both waveguides and it occurs symmetrically on the left and right sides of the waveguide. That means that we assume that D is invariant under fabrication variations.

Now we consider the result of the manufacturing error of the waveguide width. As the waveguide becomes wider, the waveguide confines the modes more strongly, which leads to a decrease in the coupling strength. But on the other hand, a wider waveguide will make the gap between the two waveguides smaller (if we consider D as constant), which will lead to a larger coupling strength. Therefore, over the range of waveguide widths we can fabricate, if these two factors affecting coupling can be balanced, then we will obtain the waveguide insensitive to fabrication errors.

TOLERANT COUPLER SIMULATION RESULTS

We perform a set of simulations to validate the idea of this tolerant design. For a given D of a symmetric directional coupler, we scan the width of the waveguides and calculate how the transmission changed with the width of the waveguides.

We first use Ansys Lumerical finite difference eigenmode (FDE) to calculate the coupling per micrometre (κ') in the straight section of the DC (figure 1 (b)). Because FDE is an algorithm applied to two-dimensional structures, it is relatively faster than three-dimensional structures. In the sweep, the waveguide width changes from 478nm to 548nm, while keep D=700nm. As shown in figure 2(a), we can find that the tolerance region for the DCs we simulate is $520\text{nm} < w < 530\text{nm}$. Through the quick simulation of FDE, we can know that our design ideas are generally correct. This makes it meaningful that we use FDTD to calculate the coupling ratio across DC.

Then we use Ansys Lumerical Finite-Difference Time-Domain (FDTD) method to simulate the complete coupler with the bend sections shown in Figure 1(a). We simulate different lengths of the DC to see whether the length of straight sections have large influence on the tolerant region.

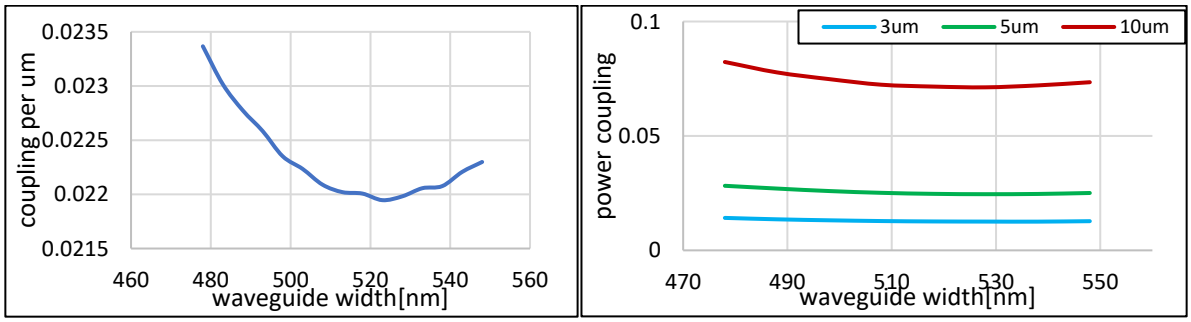


Figure 2 (a) Calculated κ' using FDE solver for different waveguide widths, with D=700nm. (b) Calculated cross port power coupling using FDTD solver for different waveguide widths and lengths of the tolerant design, with D=700nm

From the simulations results in figure 2(b), we can see that with a width variation of $\pm 35\text{nm}$ around 513nm, the relative differences $\left(\frac{\max-\min}{\max+\min}\right)$ of these DCs are 6.1%, 7.0%, and 7.2% for $L = 3, 5 \text{ and } 10\mu\text{m}$ respectively. The tolerance region for the DCs we simulate is $520\text{nm} < w < 530\text{nm}$. The tolerance region of these DCs with different lengths calculated by FDTD are very close, we think this is because the coupling strength of DC is mainly provided by the straight section if this DC is not particularly short. The tolerance intervals calculated by FDTD and FDE algorithms are also close. This means that, based on our idea, we don't necessarily need to use the time-consuming FDTD for the calculation.

TOLERANT COUPLER MEASUREMENT RESULTS

In this chapter, we present the preliminary design and experimental measurement results of the tolerant couplers. We did not measure the couplers directly, because the transmission $T_c(\lambda)$ of the coupler is close to that of the grating $T_g(\lambda)$, and we do not have a very accurate method to calculate the influence of the grating from the measurement results.

So, we use Mach–Zehnder interferometers (MZIs) for measurement. The two DCs in each MZI are designed to be identical. It should be mentioned that in our experiments all elements are purely passive elements with air cladding.

To calculate the coupling strength, we use the following lossless MZI mathematical model:

$$F = \begin{bmatrix} \sqrt{1-P(\lambda)} & i\sqrt{P(\lambda)} \\ i\sqrt{P(\lambda)} & \sqrt{1-P(\lambda)} \end{bmatrix} \begin{bmatrix} e^{-i\frac{2\pi n_{eff}(\lambda)\Delta L}{\lambda}} & 0 \\ 0 & 1 \end{bmatrix} \begin{bmatrix} \sqrt{1-P(\lambda)} & i\sqrt{P(\lambda)} \\ i\sqrt{P(\lambda)} & \sqrt{1-P(\lambda)} \end{bmatrix} \begin{bmatrix} 0 \\ 1 \end{bmatrix} \quad (2)$$

In the equation above, $\begin{bmatrix} 0 \\ 1 \end{bmatrix}$ is the normalized input field and TE polarized; $P(\lambda)$ is the cross-port power coupling of DCs; ΔL is MZI arm length difference; λ is the wavelength; $n_{eff}(\lambda)$ is the effective index of the waveguide; F is the output complex Rayleigh coefficient of each port. The cross/bar port power coupling is the square of the absolute value of each element.

One of our measurements with $w = 548\text{nm}$ is shown in figure 3. We show this measurement result since the bar port has a maximal extinction ratio which means the 50% power coupling at the corresponding wavelength. So, the bar/cross ports power is comparable and makes the picture look nice.

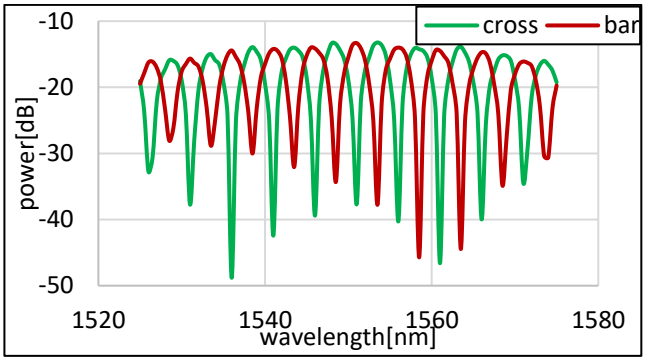


Figure 3 Measurement results of two MZI ports with waveguide width 548nm.

After data processing steps and fit the power coupling $P(\lambda)$ with equation (2), we obtain the cross-port power coupling of these DCs with different waveguide widths.

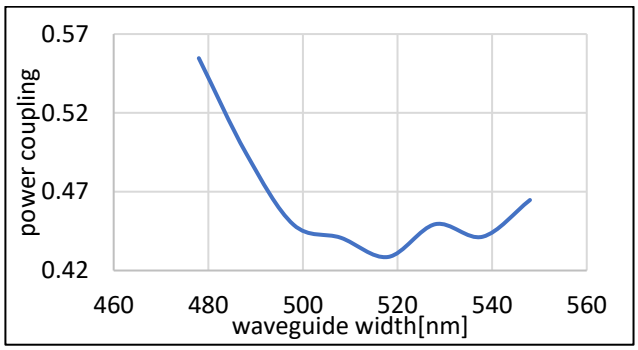


Figure 4 Cross-port power coupling of DCs with different waveguide width, 9.98um straight section length

From the results shown in figure 4, we find that the tolerance region of these DCs is around 520nm. There could be a deviation of several nanometres compared with the simulation results. This may be due to two main reasons: the thickness of the manufactured waveguide is different from the design value (214nm); the side wall angle of the waveguide is not $85°$. But generally, we can find the waveguide width tolerant region of DCs. In this region, the DCs transmission characteristics are insensitive to changes in waveguide width.

CONCLUSIONS

To conclude, the design of the tolerant directional coupler is presented and validated by FDE simulation, FDTD simulation and measurements. Our experimental measurements are in good agreement with the FDTD simulation results. Since this was a preliminary experiment to evaluate the idea, we didn't scan the waveguide width over a wide range. In the following experiments and measurements, we will apply a wider range of scanning and more sweep steps of the waveguide width. In the future, we will combine the ideas of tolerance DC and broadband DC to design and manufacture tolerance and broadband DC.

References

[1] Bogaerts, W., Pérez, D., Capmany, J. et al. *Programmable photonic circuits.* Nature 586, 207–216 (2020).
[2] Xing Y, Dong J, Khan U, et al. *Capturing the effects of spatial process variations in silicon photonic circuits*. ACS Photonics, 2022.
[3] Y. Xing, U. Khan, A. Riberio, and W. Bogaerts, *Behavior model for directional coupler*, Proc. Symp. IEEE Photon. Soc. Benelux, pp. 128-131, 2017

Design of Mid-Infrared Supercontinuum Generation in a strip-loaded LNOI Waveguide through lateral leakage engineering

(Student paper)

Kokou Firmin Fiaboe[1,2], Alberto Della Torre[1], Arnan Mitchell[2], Christelle Monat[1], Christian Grillet[1], Thach Nguyen[2]

[1]Université de Lyon, Institut des Nanotechnologies de Lyon(INL), UMR CNRS 5270, Ecully, France

[2]School of Engineering, RMIT University, Melbourne, Australia

* kokou-firmin.fiaboe@ec-lyon.fr

We study the lateral leakage of a silicon nitride loaded lithium niobate waveguide in the mid-infrared regime. We then combine lateral leakage and dispersion engineering to numerically demonstrate mid-infrared supercontinuum generation extending from 1200nm to 5000nm.

Keywords**:** *Mid infrared, Nonlinear Optics, Lithium Niobate, Lateral Leakage, Supercontinuum Generation*

INTRODUCTION

Mid-infrared (mid-IR, 2-20µm) broadband sources are of great interest in many different fields such as environmental monitoring, bio-imaging and security[1]. Since many molecules have strong vibrational absorption in the mid-IR spectrum regime, mid-IR broadband sources can enable the parallel detection of multiple gas species[2]. Despite the great potential that mid-IR technologies offer, its range of applications is still limited, mostly because of the size and cost of mid-IR sensing devices. Therefore, there is a great need to develop compact and cost effective integrated mid-IR platforms to access these applications. On-chip mid-IR supercontinuum generation (SCG) has been demonstrated in several group-IV platforms [3-5]. Great efforts have been devoted by our group to achieve SCG in silicon-germanium on silicon[3] and germanium on silicon waveguides [4].

Lithium niobate (LN), with its large optical transparency window (400nm-5000 nm) and strong electro-optic effect, has been historically widely used in optoelectronics and more recently, for photonic integrated circuits [5][6] . Also, LN is a promising nonlinear material for realizing SCG in the mid-IR regime and second harmonic generation (SHG) in near infrared regime, as it possesses strong second order nonlinearity and moderate third order nonlinearity [7]. Although LN waveguides with strong field confinement can be achieved by directly etching LN thin films [8],the etching of LN has been notoriously difficult [6]. Instead, we use a LN on insulator (LNOI) thin film optically loaded with a strip of silicon nitride (SiN) and we already demonstrated several integrated photonic components in this platform.

In this work, we design a SiN loaded LN waveguide through the engineering of lateral leakage in the mid-IR regime. We analyse numerically the generation of mid-IR supercontinuum extending from 1200 to 5000nm and show that the simultaneous presence of second and third order nonlinearities in PPLN can achieve octave spanning supercontinuum and efficient SHG which this creates a pathway for stabilization of our mid-IR sources through the f-2f self-referencing technique within a compact single-waveguide system

DESIGN AND SIMULATIONS

Lateral leakage describes an effect that occurs in a photonic waveguide which was first seen in silicon on insulator rib or ridge waveguide [9] , where the effective refractive index of the optical waveguide mode is a lower than the orthogonally polarized slab mode. Since LN is birefringence material, we found that in LNOI waveguide the effective index of the TE waveguide mode can be lower than the one of the TM slab mode, which will lead to the leakage of the TE waveguide mode. Thus, our first step when designing the waveguide is to achieve low lateral leakage of the waveguide mode in the mid-IR regime.

We calculated the effective refractive index difference between the TE waveguide mode and the TM slab mode for SiN loaded LNOI ridge waveguides (Fig. 1a) as function of the LN film thickness and the wavelength. We chose a SiN thickness dimensions in [10] which is 400nm and SiN waveguide width of 3000nm. We have used an x-cut LNOI substrate where the TE waveguide mode experiences the extraordinary refractive index of LN and TM slab mode experiences the LN ordinary index. Figure 1(b) shows the resulting effective refractive index difference between the

TE waveguide and TM slab mode $\Delta n_{eff} = \Delta n_{eff,TE} - \Delta n_{eff,TM}$. The black line in the map indicates where the effective refractive index difference Δn_{eff} is zero.

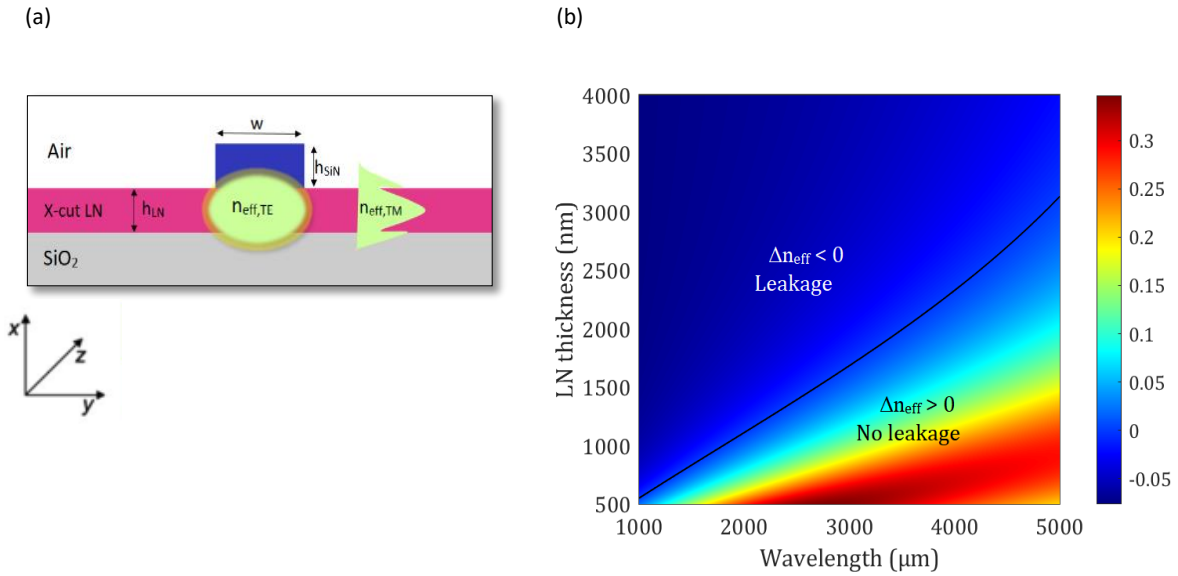


Fig. 1. (a) Illustration of SiN loaded LN waveguide and the modes (b) Calculated effective index difference between TE waveguide mode and the TM slab mode. Waveguide with Δn_{eff} <0 can suffer from lateral leakage

The graph indicates that waveguides with certain LN thickness and operated at wavelengths above the zero line of the effective refractive index difference might lead to a leaky waveguide mode. On the contrary, below the zero line, where the effective refractive index difference is greater than zero, there should not be any leakage of the TE waveguide mode. We observed that by making the LN thickness thinner and thinner, it pushes the leakage wavelength lower and lower. Therefore, for a given LN thickness, some lower wavelengths will suffer from lateral leakage.

Considering these trade-offs, we choose a LN thickness of 600nm which should support modes without leakage down to 1100nm. We now investigate the dispersion required for SCG. The main objective of our dispersion engineering is to achieve low anomalous dispersion to maximize the bandwidth of the SC. We numerically calculate the dispersion of the waveguide using 600nm LN thickness and 400nm SiN thickness. Fig 2(a) shows the simulated results of the dispersion for the TE waveguide mode of three different waveguide widths of 3000nm, 3500nm and 4000nm. Fig. 2(b) shows the integrated dispersion[11] for these different widths for a pump at 2070nm. For each waveguide width, the zero crossing of the integrated dispersion give some prediction of the spectral position of the dispersive wave (DW), hence the dashed black line cross the respective curve between 1200nm-1400nm and 4500-5000nm wavelength.

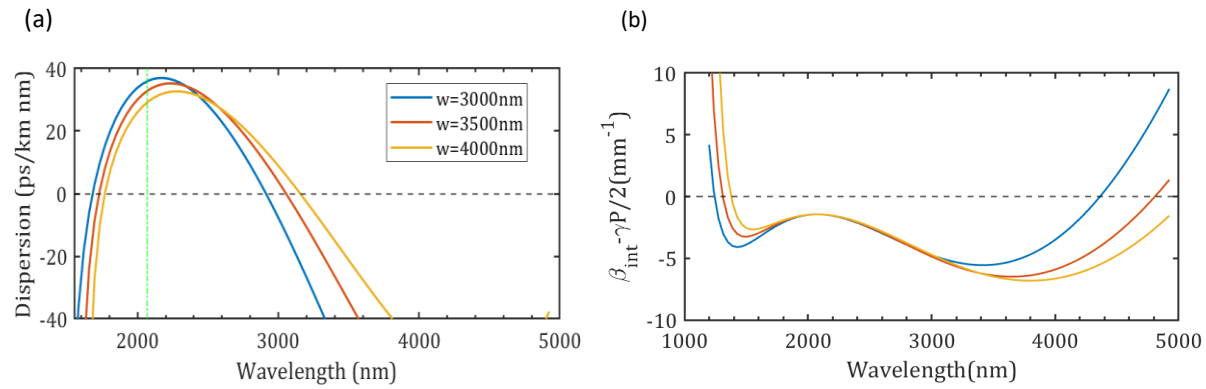


Fig. 2. (a) Simulated Dispersion for selected waveguide widths. (b) Corresponding dispersion operator for a 2070nm pump wavelength

We simulate SCG in a 1 cm long SiN loaded PPLN waveguide with 3000nm width, 600nm LN thickness and 400nm SiN thickness by numerically solving the nonlinear Schrodinger equation using the split step Fourier method. Our

model includes second and third order nonlinearity, higher order dispersion, self-steepening and losses. The simulated supercontinuum shows in Fig. 3 is obtained using a pump with an off-the-shelf femtosecond thulium-doped fiber laser (Brevity +, NOVAE) which outputs 90fs pulses at a 20MHz repetition rate[2]. We use 1kW peak power to pump the waveguide at 2070nm in the anomalous dispersion regime. The generated SC extend from 1200nm to 5000nm wavelength. Also, there is a second and third harmonic that appears giving some light all down to 800nm, however the power is -20dB lower than the primary SC light.

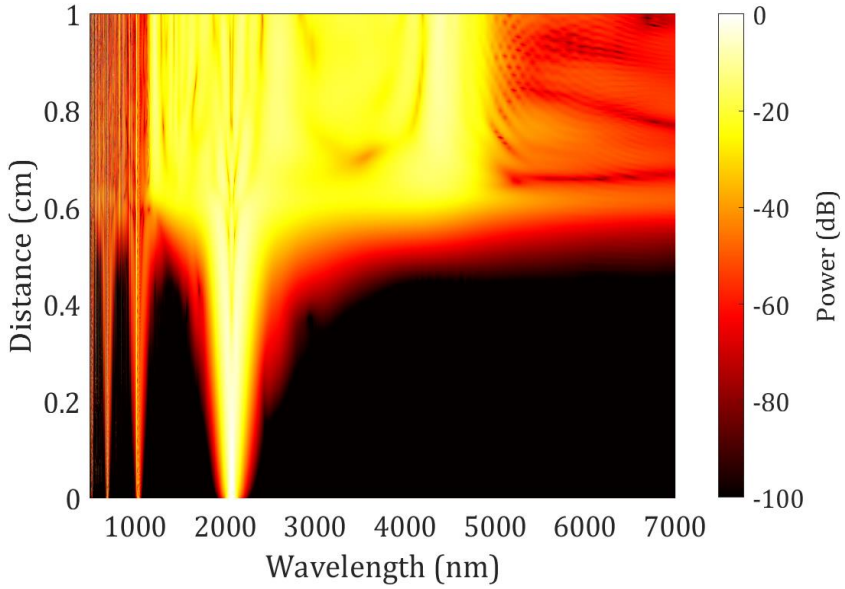


Fig. 3. Simulated spectral pulse evolution along the waveguide length for a peak power of 1kW.

CONCLUSION

In conclusion, we numerically demonstrated mid-IR SC generation in a strip-loaded LNOI waveguide. We designed the waveguide to support mode without leakage and to generate a broadband spectrum for spectroscopy applications. Finally, the generated SHG can enable the stabilization of our mid-IR sources through the f-2f self-referencing technique.

Acknowledgements: The I3E ECLAUSion project between France and Australia, H2020 EU framework, Marie Skłodowska-Curie grant (No 801512), Agence Nationale de la Recherche (ANR) MIRSiCOMB (ANR-17-CE24-0028), International Associated Laboratory in Photonics between France and Australia (LIA ALPhFA).

References

[1] R. Soref, *Mid-infrared photonics in silicon and germanium*, Nat. Photonics, vol. 4, no. 8, pp. 495–497, 2010
[2] E. Tagkoudi, D. Grassani, F. Yang, C. Herkommer, T. Kippenberg, and C.-S. Brès, *Parallel gas spectroscopy using mid-infrared supercontinuum from a single Si 3 N 4 waveguide* , Opt. Lett., vol. 45, no. 8, pp. 2195, Apr. 2020
[3] M. Sinobad *et al.*, *Mid-infrared octave spanning supercontinuum generation to 85 μm in silicon-germanium waveguides*, Optica, vol. 5, no. 4, p. 360, 2018
[4] A. Della Torre *et al.*, *Mid-infrared supercontinuum generation in a low-loss germanium-on-silicon waveguide,* APL Photonics, vol. 6, no. 1, 2021
[5] A. Boes *et al.*, *Lithium niobate photonics: Unlocking the electromagnetic spectrum*, Science, vol. 379, no. 6627, pp. 1-12, 2023
[6] D. I. Zhu *et al.*, *Integrated photonics on thin-film lithium niobate*, Adv. Opt. Photonics, vol. 13, no2, 2021
[7] M. Garcia-lechuga, J. Siegel, J. Hernandez-rueda, and J. Solis, *Imaging the ultrafast Kerr effect , free carrier generation , relaxation and ablation dynamics of Lithium Niobate irradiated with femtosecond laser pulses*, J. Appl. Phys. vol. 116, pp. 113502, 2014
[8] A. Boes, B. Corcoran, L. Chang, J. Bowers, and A. Mitchell, *Status and Potential of Lithium Niobate on Insulator (LNOI) for Photonic Integrated Circuits*, Laser Photonics Rev. vol. 12, no. 4, pp. 1700256, 2018
[9] M. A. Webster, R. M. Pafchek, A. Mitchell, and T. L. Koch, *Width dependence of inherent TM-mode lateral leakage loss in silicon-on-insulator ridge waveguides*, IEEE Photonics Technol. Lett., vol. 19, no. 6, pp. 429–431, 2007
[10] A. Boes *et al.*, *Improved second harmonic performance in periodically poled LNOI waveguides through engineering of lateral leakage*, Opt. Express, vol. 27, no. 17, p. 23919, 2019
[11] A. Della Torre *et al.*, *Mid-infrared supercontinuum generation in a varying dispersion waveguide for multi-species gas spectroscopy*, IEEE J. Sel. Top. Quantum Electron., vol. , pp. 1–10, 2022

Integration of superconducting nanowire single-photon detectors in subwavelength-grating-structured waveguides

Regular paper

Alejandro Sánchez-Postigo[1,*], Connor Graham-Scott[1] and Carsten Schuck[1]

[1] Institute of Physics, University of Münster, Heisenbergstraße 11, 48149 Münster, Germany
[*] alejandro.sanchezpostigo@uni-muenster.de

Superconducting nanowire single-photon detectors (SNSPDs) offer leading measurement capabilities for quantum technology applications. Ultra-short waveguide-integrated SNSPDs embedded in optical cavities hold promise for simultaneously achieving high absorption efficiency and timing performance, but scattering loss dramatically reduce the detection efficiency. In this work, we explore the use of subwavelength grating metamaterials to mitigate such scattering loss.

Keywords: *SNSPD, waveguide, subwavelength grating metamaterial, SWG*

INTRODUCTION

Advances in key areas of photonic quantum technology such as quantum sensing, quantum key distribution and quantum information processing depend on the development of scalable, fast, and efficient methods to detect single photons [1]. Superconducting nanowire single-photon detectors (SNSPDs) have emerged as one of the most attractive single-photon detector technologies for quantum photonics [2]. SNSPDs comprise an electrically and optically accessible, ultra-thin (~5 nm), narrow (~100 nm) superconducting wire strip that is supplied with a bias current via two electrodes. When photons impinge on the SNSPD, they are absorbed and the superconducting state is supressed, which results in a voltage pulse that can be measured, thereby enabling photon counting. In conventional, standalone SNSPDs, the nanowire is arranged in a meander-like pattern, often embedded in a resonant structure that optimizes absorption of photons impinging under normal incidence from an optical fiber. SNSPDs have four important figures of merit: the detection efficiency, the dark count rate, the recovery time (τ_r), and the timing uncertainty or jitter (τ_{jitter}). Except for the dark count rate, which is mainly related to electrical noise and background radiation, the other performance metrics strongly depend on the geometry of the nanowire: The detection efficiency is limited by the area over which photons are allowed to interact with the nanowire. The detector speed is affected by the kinetic inductance of the nanowire, which increases with nanowire length, resulting in long recovery times. Finally, the jitter increases if the nanowire has bends where current crowding can occur and to a lesser extent with nanowire length.

For quantum optics experiments, photonic integrated circuits provide low loss and interferometric stability for single-photon manipulation. As illustrated in Fig. 1(a), in waveguide-integrated SNSPDs the superconducting nanowire is deposited on top of a dielectric waveguide, in the evanescent field of the guided mode, allowing for absorption along the direction of light propagation. By engineering the interaction length, conventional, U-shaped waveguide-integrated SNSPDs can provide absorption efficiencies higher than 90%, yet at the expense of reduced timing performance [2]. To enhance the latter, ultra-short, transversally oriented SNSPDs in optical cavities were realized, as depicted in Fig. 1(b) [3]. The dramatic reduction of the nanowire length yielded remarkable speed, τ_r ~ 500 ps, and low jitter, τ_{jitter} = 32 ps. Here, the light interacts with the nanowire in each of multiple round trips in the cavity, theoretically achieving a near-unity absorption efficiency despite short nanowire length. However, in practice, the absorption is strongly reduced due to scattering losses at the crossing between the waveguide and the slabs that support the nanowire, resulting in relatively low on-chip detection efficiencies near 30%.

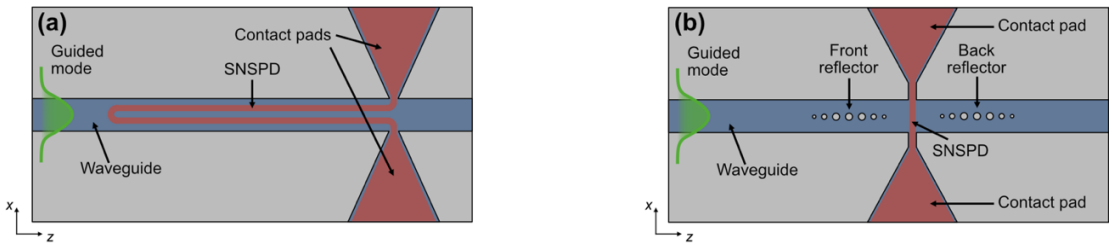


Fig. 1. (a) Conventional U-shaped waveguide-integrated SNSPD (top view). (b) Cavity-enhanced waveguide-integrated SNSPD proposed by Vetter et al. to increase speed and reduce jitter while keeping high absorption efficiency (top view) [3].

In this work, we show our preliminary work toward the goal of enhancing the on-chip detection efficiency of cavity-enhanced SNSPDs, integrated on silicon nitride waveguides for 1550-nm wavelength. This objective will be achieved by cladding the waveguide with a subwavelength grating metamaterial that suppresses scattering losses.

WAVEGUIDE-INTEGRATED SNSPD ENHANCED BY SUBWAVELENGTH GRATING METAMATERIALS

Subwavelength grating (SWG) metamaterial waveguides are periodic structures with a period or pitch,

$$\Lambda < \frac{\lambda}{2n_B}, \tag{1}$$

that frustrates all diffraction orders, where λ is the operating wavelength and n_B is the effective index of the supported mode. Then, as schematized in Fig. 2, the structure behaves as a homogeneous metamaterial. As a first approximation, an SWG structure formed by alternating materials with refractive indices n_1 and n_2 and a duty cycle DC = a/Λ (see Fig. 2) can be modelled, for the in-plane polarization, as an isotropic metamaterial with refractive index

$$n_{\parallel} = [\mathrm{DC} \cdot n_1^2 + (1 - \mathrm{DC}) \cdot n_2^2]^{\frac{1}{2}} \tag{2}$$

when the structure is periodic in the propagation direction (z), as in Fig. 2, and

$$n_{\perp} = [\mathrm{DC} \cdot n_1^{-2} + (1 - \mathrm{DC}) \cdot n_2^{-2}]^{-\frac{1}{2}} \tag{3}$$

when the structure is periodic in the transverse direction (x). Anisotropic models and more accurate, wavelength-dependent approximations for the equivalent refractive indices $n_{\parallel}$ and $n_{\perp}$ can be found in [4]. By judiciously choosing the pitch and duty cycle (DC = a/Λ), the refractive index, dispersion, and birefringence of the metamaterial can be tailored. This index-engineering property has led to photonic integrated devices with unprecedented performance, including fiber-chip couplers, optical antennas, Bragg filters, and polarization management structures [4].

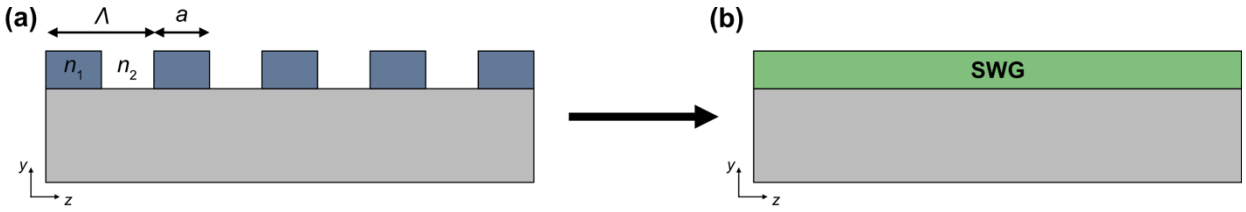


Fig. 2. (a) A periodic waveguide operating in the subwavelength regime, i.e., Λ satisfies Eq. (1). (b) The periodic waveguide behaves as an equivalent homogeneous metamaterial waveguide.

Here, we leverage the diffractionless nature of SWG waveguides to mitigate the scattering loss at the nanowire supports (slabs) in cavity-enhanced SNSPDs. A schematic representation of the proposed geometry is shown in Fig. 3(a). A waveguide core is assisted by a periodic lateral cladding with a pitch that meets Eq. (1). Consequently, light travels through the SWG-cladding waveguide as in a conventional waveguide with a metamaterial cladding [see Fig. 3(b)]. In this scenario, unlike in conventional SNSPDs [3], the crossings due to the nanowire supports are virtually invisible. Furthermore, the SWG-enhanced SNSPD can be smoothly embedded within an optical cavity just by increasing the pitch of the periodic waveguide to meet the Bragg condition (i.e., $\Lambda = 0.5\lambda/n_B$) at the front and back parts of the structure. In addition, the absorption efficiency could be increased by placing more nanowires in parallel on the cladding strips, thereby forming a superconducting nanowire avalanche photodiode (SNAP).

To analyze the absorption efficiency of the proposed structure, we calculate the imaginary part of the effective index of the fundamental mode that is supported by the Si_3N_4 waveguide perturbed by the nanowire. Figure 4(a) illustrates the simulated structure, in which the lateral SWG cladding is replaced by a homogeneous isotropic metamaterial with an equivalent refractive index of 1.72, which corresponds to an SWG cladding with $n_1 = 2$ (Si_3N_4 strips), $n_2 = 1$ (air gaps), $\Lambda = 400$ nm, and DC = 50% [4]. For simulation purposes, the width of the lateral cladding is considered infinite. An NbTiN thin film is deposited on top of the structure, with complex refractive index 4.83 + j5.11 [5]. The nanowire is covered with an HSQ protective layer. The effective index of the mode, estimated using an FEM simulation [6], is 1.58 + j0.07, which corresponds with an absorption rate of 2.4 dB/µm. Assuming a nanowire width of 100 nm, this yields an absorption of 0.24 dB per nanowire, consistent with previous results [3].

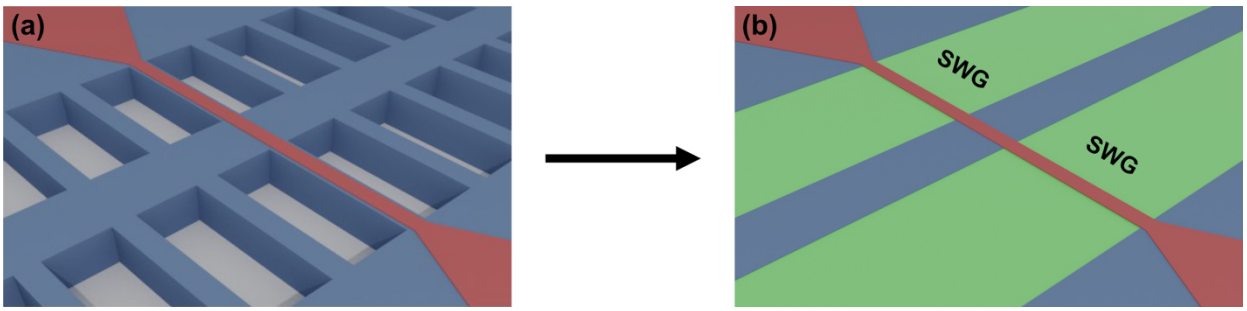


Fig. 3. (a) Proposed SWG-cladding-enhanced waveguide-integrated SNSPD. (b) Equivalent homogeneous metamaterial model for the proposed SWG-cladding-enhanced waveguide-integrated SNSPD.

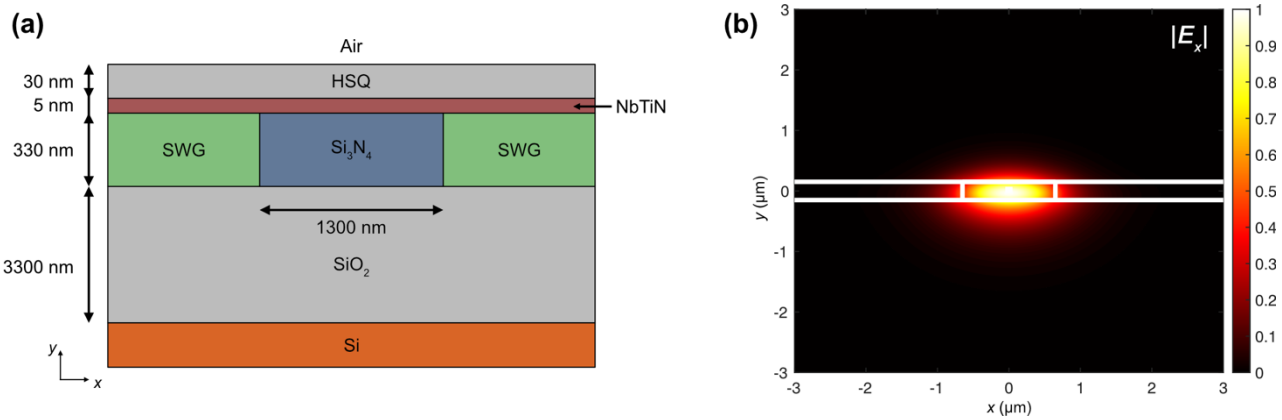


Fig. 4. (a) Schematic representation, not to scale, of the waveguide-integrated superconducting nanowire substituting the SWG lateral cladding with an equivalent metamaterial (front view). (b) Amplitude profile of the TE-polarized fundamental mode supported by the structure in (a) at a wavelength of 1550 nm.

CONCLUSION

In this work, we present our first attempts toward the implementation of a new waveguide-integrated SNSPD concept that has the potential to optimize the absorption efficiency while exhibiting outstanding timing performance. By taking benefit from the non-diffractive and non-reflective nature of subwavelength gratings, minimum scattering losses are expected, in contrast to reported cavity-enhanced SNSPDs that are not based on subwavelength metamaterials. First simulations show an absorption per nanowire of 0.2–0.3 dB, which is comparable to other state-of-the-art devices and provides good insight for the implementation of the proposed SWG-enhanced SNSPDs.

Acknowledgements: Marie Skłodowska-Curie Actions Postdoctoral Fellowship (ESSENS, 101064466). Funded by the European Union. We acknowledge support from the Horizon 2020 Framework Programme (SURQUID, 899824); Views and opinions expressed are however those of the author(s) only and do not necessarily reflect those of the European Union. The European Union cannot be held responsible for them.

References

[1] J. O'Brien et al., *Photonic quantum technologies*, Nature Photonics, vol. 3, pp. 687-695, 2009.
[2] S. Ferrari et al., *Waveguide-integrated superconducting nanowire single-photon detectors*, Nanophotonics, vol. 7, no. 11, pp. 1725-1758, 2018.
[3] A. Vetter et al., *Cavity-enhanced and ultrafast superconducting single-photon detectors*, Nano Letters, vol. 16, no. 11, pp. 7085–7092, 2017.
[4] J. M. Luque-González et al., *A review of silicon subwavelength gratings: building break-through devices with anisotropic metamaterials*, Nanophotonics, vol. 10, no. 11, pp. 2765-2797 (2021).
[5] Supplementary material of M. A. Wolff et al., *Broadband waveguide-integrated superconducting single-photon detectors with high system detection efficiency*, Applied Physics Letters, vol. 118, no. 15, p. 154004, 2021.
[6] FemSIM – https://www.synopsys.com/photonic-solutions/rsoft-photonic-device-tools/passive-device-femsim.html

Polarization beam splitter in the silicon nitride platform for the 1 µm wavelength band

(Student paper)

Zindine Mokeddem[1,*], Laurent Vivien[1], Delphine Marris-Morini[1], Eric Cassan[1], Pavel Cheben[2], Jens H. Schmid[2], Dan-Xia Xu[2], Yuri Grinberg[2], Maziyar Milanizadeh[2], Carlos-Alonso Ramos[1], Daniele Melati[1]

[1]Centre de Nanosciences et de Nanotechnologies, CNRS, Université Paris-Saclay, 91120 Palaiseau, France
[2]Advanced Photonics and Electronics Research, National Research Council Canada, K1A 0R6 Ottawa, Canada
[*]zindine.mokeddem@universite-paris-saclay.fr

Efficient and broadband devices able to control the polarizations state are an essential building block of any photonic integration platform. Here, we present the design and the experimental demonstration of an integrated polarization beam splitter realized in silicon nitride platform for the 1 µm optical wavelength band. The device has an experimental insertion loss smaller than 1 dB and a polarization extinction ratio of about 24 dB and 11 dB for TE and TM polarization, respectively.
Keywords: *integrated photonics, SiN platform, polarization*

INTRODUCTION

Silicon Nitride (SiN) photonic integrated circuits have attracted a strong interest in the last few years. The platform is especially interesting for quantum applications because it can offer ultra-low propagation losses, low non-linear losses, reduced birefringence, and a broadband transparency window from the visible to the upper part of the near infrared. Despite being less pronounced compared to the silicon-on-insulator platform, the dependence of the optical response of photonic devices to the polarization state of the light remains an issue also in the silicon nitride platform. For example, polarization control is critical in quantum key distribution to ensure the indistinguishability of the two transmitters [1]. Devices capable of controlling the polarization state (e.g., splitters or rotators) hence still play a key role [2,3]. So far, only a few devices have been demonstrated in silicon nitride, mostly using Mach-Zehnder interferometers or multi-mode interference couplers, but they tend to have relatively large insertion loss and footprint [4,5,6]. The need for high performance devices is particularly relevant at wavelengths shorter than the typical optical communication bands in the near infrared. This wavelength range has great interest for many applications such as free-space quantum communications in satellite networks [7] and single photon sources where single InAsP quantum dots has been demonstrated in the 1 µm wavelength band, achieving a very-pure single photon emission [8].

Here, we propose and experimentally demonstrate a SiN polarization beam splitter (PBS) realized by cascading two tapered asymmetric directional couplers. Our fabricated device shows high efficiency, a compact footprint and a broadband operation range in the 920 nm - 970 nm wavelength range.

RESULTS

The PBS is realized by cascading two tapered asymmetric directional couplers, as schematically represented in Fig. 1(a). The directional couplers are designed to ensure phase matching condition at a wavelength of 950 nm between the fundamental transverse-magnetic mode (TM0) of the waveguide WG1 (or WG3 for the second coupler) and the first-order transverse-magnetic mode (TM1) of the waveguide WG2. As a result, the TM0 mode in the input waveguide WG1 is efficiently couples to the TM1 mode in the central waveguide WG2. The TM1 in WG2 then couples back to TM0 in the output waveguide WG3 (cross port). At the same time, the device is ensured to be asynchronous for the transverse-electric (TE) modes in order to minimize coupling of the fundamental TE0 mode in WG1 to TE modes of WG2. The TE0 mode of the input waveguide WG1 hence remains in the waveguide WG1 and propagate to the through port. In addition, a linear tapered structure is introduced in the two directional couplers to increase the robustness of the device to wavelength variations and fabrication imperfections. The variation of the width in WG1 (WG3) and WG2 have opposite sign and the gap of the directional couplers is hence maintained constant. In the two coupling regions, the phase matching condition is fulfilled at the center of the two tapers. In the first coupler the width of the taper waveguide WG1 is decreased while the one of WG2 is increased, while the opposite occurs in the second coupler. With this structure, we can ensure that the phase matching condition will be respected in one point in the tapered region even with the presence of fabrication imperfection.

The fabricated device (as show Fig. 1(c)) has a SiN core with a thickness h = 400 nm, a 3-µm-thick SiO2 upper cladding and 4.5-µm-thick SiO2 buried oxide. A finite-difference eigenmode solver was used to choose the two widths w_1 and w_2 (as show Fig. 1(b)) that satisfy the phase matching condition. An eigenmode expansion solver was used to simulate the TM mode transmission to optimize the coupling length (Lc) and the width variation (Δw) (as show Fig. 1(a)). The gap (w_{gap}) between the two waveguides is fixed at w_{gap} = 0.35 µm. The phase matching condition is fulfilled for w_1 = 0.51 µm and w_2 = 1.28 µm. The maximum power conversion from TM0 to TM1 with was achieved with L_c = 111 µm and Δw = 0.03 µm. An S-bend of 100 µm radius is used to gently approach and separate WG1 from WG2 (and WG3 from WG2) to avoid back reflections that can occur by the abrupt introduction of the central waveguide WG2.

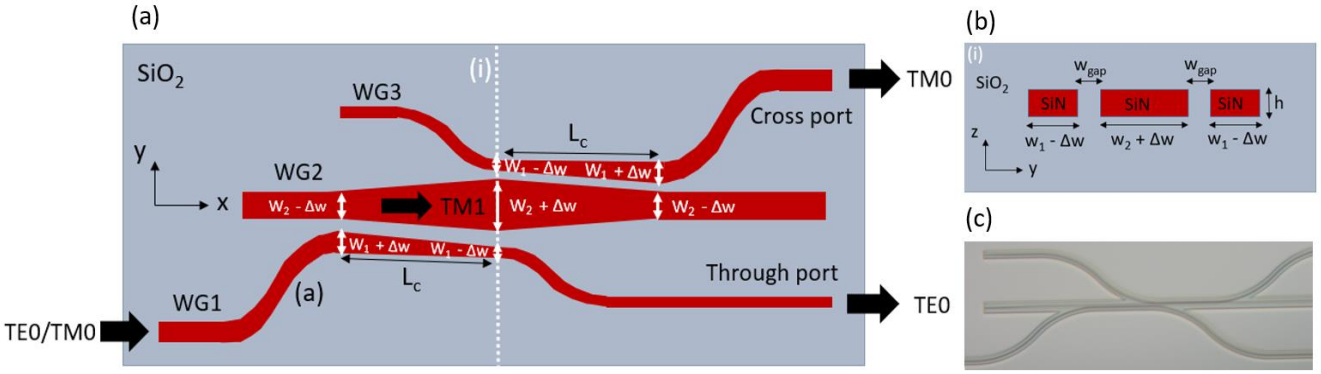


Fig. 1. (a) Schematic of the SiN polarization beam splitter. (b) Cross-sectional view of the directional coupler at the position (i) maked with the white dashed line in (a). (c) Microscopic image of the fabricated PBS.

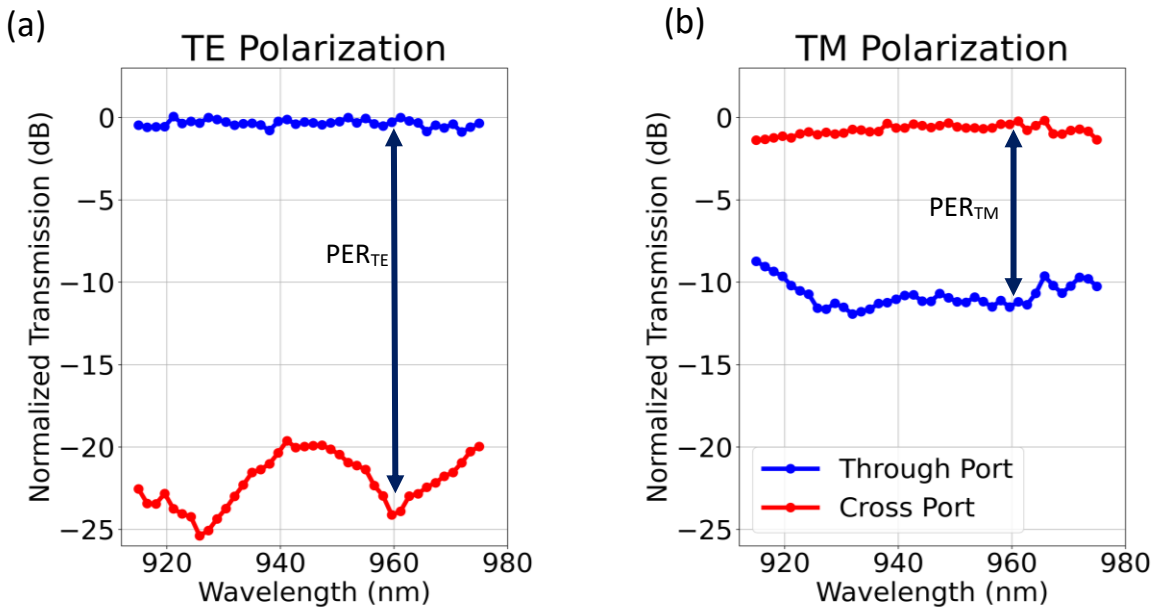


Fig. 2. Measured transmisions at the through and cross ports for (a) TE mode input and (b) TM mode input.

The PBS performance was measured by characterizing the polarization extinction ratio (PER) and insertion loss (IL), respectively defined as:

$$PER_{TE} = 10 \cdot \log_{10}\left(\frac{T_{through}}{T_{cross}}\right)$$

$$PER_{TM} = 10 \cdot \log_{10}\left(\frac{T_{cross}}{T_{through}}\right)$$

$$Il_{TE} = -10 \cdot \log_{10}(T_{through})$$

$$Il_{TM} = -10 \cdot \log_{10}(T_{crosss})$$

Here $T_{through}$ and T_{cross} are the normalized transmission from the input waveguide WG1 to the through and cross output port, respectively (see Fig. 1) The normalization is made with respect to the transmission of a reference waveguide without the PBS. The experimental transmission for the two polarizations over a wavelength range between 920 nm and 970 nm is reported in Fig. 2. When we excite the TE0 mode at the input port, negligible coupling occurs and as expected light ends up at the through port with an insertion loss IL_{TE} = 0.27 dB at λ = 950 nm. On the contrary, when the TM0 mode is excited at the input, the phase matching condition is fulfilled and the light couples efficiently in the two directional couplers and propagates to the cross port. Also in this case the PBS operates with low insertion losses of IL_{TM} = 0.53 dB at λ = 950 nm. In both cases, insertion losses remain smaller than 1 dB on the entire wavelength range between 920 nm and 970 nm. In the same range, PER_{TE} and PER_{TM} are higher than 19 dB and 10 dB, respectively. At the central wavelength λ = 950 nm, PER_{TE} = 20 dB and PER_{TM} = 11 dB.

DISCUSSION

In summary, a highly performing PBS in the silicon nitride platform was successfully demonstrated in the wavelength range around 950 nm using a cascade of two tapered asymmetrical directional couplers. The device has a compact footprint of about 222 µm with low insertion losses below than 1 dB and PER above 10 dB in the 920 nm – 970 nm band. Larger PER, especially for the TM polarizations, could be obtained either cascading multiple PBS or exploiting polarization filters.

Acknowledgements: This work has been supported by an Ideation Fund-Small Teams Initiative by the National Research Council Canada

References

[1] H.Semenenko, P.Sibson, A.Hart, M.Thompson, J.Rarity, C.Erven, "Chip-based measurement-device-independent quantum key distribution," Optica, vol. 7, No. 3, March 2020

[2] K. Gallacher, P. Griffin and E. Riis," Silicon nitride waveguide polarization rotator and polarization beam splitter for chip-scale atomics systems," APL Photonics 7, 046101, April 2022

[3] D. Wang, Y. Hu, W. Yue, Y. Zeng, Z. Tu, Y. Cai, W. Wang, Q. Fang, M. Yu, "Broaband and compact polarization beam splitter based on asymetrical directional coupler with extra optimizing designs," Applied Optics Vol. 58, No. 30, October 2019

[4] B. Bhandari, C. Chul-Soom Im, O. Raj Sapkota and S. Lee, "Highly efficient broadband silicon nitride polarization beam splitter incorporating serially cascaded asymmetric directional couplers," Optics Letters, vol. 45, no. 21, November 2020

[5] S. Guerber, C. Ramos, D. Benedikovic, E. Duràn-Valdeiglesias, X. Le Roux, N. Vulliet, E. Cassan, D. Marris-Morini, "Broadband Polarization Beam Splitter on a Silicon Nitride Platform for O-Band Operation," IEEE Photonics Technology Letters, vol. 30, No. 19, October 2018

[6] J. Zhan, J. Brock, S. Veilleux, M. Dagenais, « Silicon nitride polarization beam splitter based on polarization-independant MMIs and apodized Bragg gratings", vol. 29, No. 10, May 2021

[7] J. Rarity, P. Tapster, P. Gorman, P. Knight, "Ground to satellite secure key exchange using quantum cryptography," New J. Phys 4, 82 October 2002

[8] D. Dalacu, K. Mnaymneh , J. Lapointe, X. Wu, P. Poole, G. Bulgarini, V. Zwiller, M. Reimer, "Ultraclean Emission from InAsP Quantum Dots in Defect-Free Wurzite InP Nanowires," Nano Lett. 2012, 12, 11, 5919-5923, October 2012

Multiphysics simulation approach for polymer waveguide microring resonator based ultrasonic detectors

Jan-Jonas Schumacher[1], Paul Muellner[1], Moritz Eggeling[1], Rainer Hainberger[1]

[1]AIT Austrian Institute of Technology GmbH, Giefinggasse 4, Vienna, 1210, Austria
* rainer.hainberger@ait.ac.at

We report a 2D FEM simulation approach to analyse the dynamic structural and optical response of polymer waveguides to ultrasonic waves in dependence of material parameters, acoustic frequency, and angle of incidence. This simulation approach provides better physical insight and facilitates the optimization of microring resonator based ultrasonic detectors.
Keywords: *polymer mircoring resonator, multiphysics simulation, ultrasonic detection*

INTRODUCTION

Polymer microring resonators (MRR) have proven to be very attractive ultrasonic detectors due to their high sensitivity, large frequency range, and compactness [1,2]. Despite successful experimental use for photoacoustic imaging over many years, thorough multiphysics simulations of the ultrasonic detection mechanisms considering the frequency and angle dependent response of the waveguide structure have not yet been reported. In this study, we take a major step in this direction by introducing a suitable simulation approach.

Figure 1a) illustrates the operation principle of an MRR-based ultrasonic detector. Here, we assume a spherical ultrasound wave being generated by an acoustic point source in water with amplitude A and frequency f, where the pressure at a distance R can be expressed as $u(R,t) = A/R\, e^{i2\pi f(t-R/c_s)}$ with c_s being the speed of sound in water. Without incident ultrasonic wave the condition for the m-th order resonance in an MRR with radius r is given by

$$m\lambda_m = n_{\mathrm{eff},0}\, 2\pi r, \tag{1}$$

where λ the wavelength and $n_{\mathrm{eff},0}$ the unperturbed effective refractive index of the guided optical mode. The ultrasonic wave induces changes of the local effective refractive index along the MRR. The change of the local effective refractive index at a specific position on the MRR at the point of time t, depends on the local pressure $u(R,t)$, the direction of incidence $\vec{R}/|\vec{R}|$, and the frequency of the ultrasonic wave. Therefore, the time dependent resonance condition of an MRR perturbed by the incident ultrasonic spherical wave can be written as

$$m\lambda_m(t) = \int_0^{2\pi} n_{\mathrm{eff}}\big(\varphi, f, \Phi(t)\big) r d\varphi, \tag{2}$$

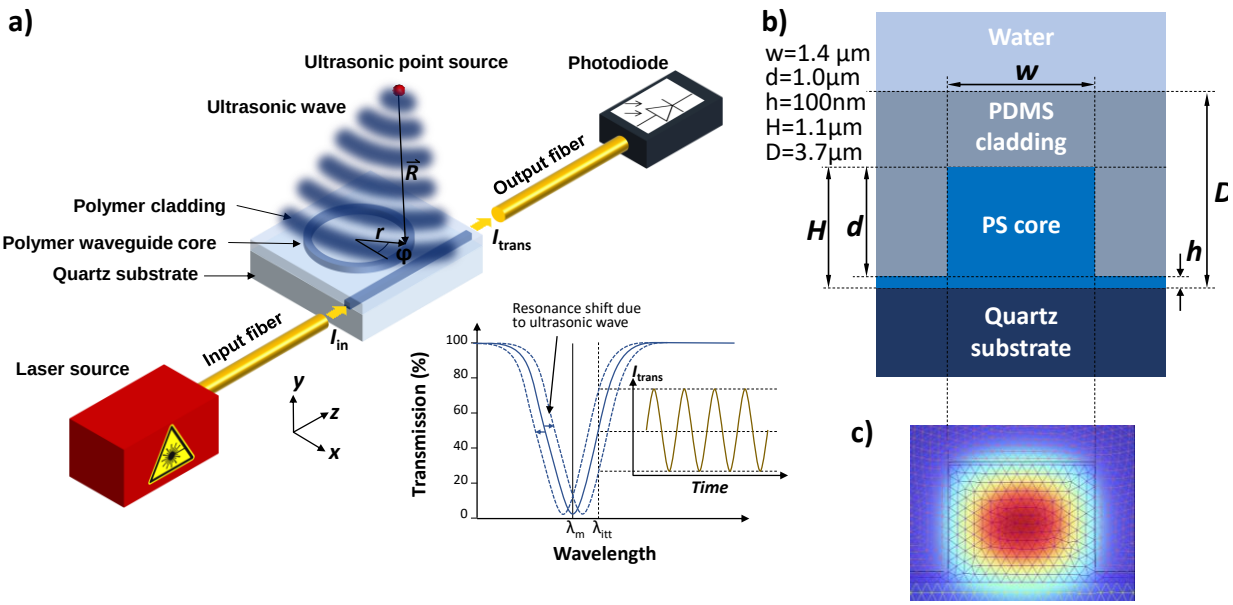


Fig. 1. a) Operation principle of an MRR used as ultrasonic detector, where the shift of the optical resonance interrogated at λ_{itt} results in a modulation of the transmitted optical power I_{trans}, b) waveguide cross-section, c) FEM eigenmode analysis of deformed waveguide structure.

where the polar angle φ is used to parametrize the position on the MRR and $\Phi(t) = t - R/c_s$ is the local phase value of the acoustic wave. The ultrasound wave exerts pressure on the waveguide structure, leading to deformation and stress in the structure. The deformation of the waveguide core cross section modifies the effective refractive index. In addition, the stress σ in the core and cladding material directly changes the local refractive index due to the elasto-optic effect, which can be defined as [3]:

$$n_x \approx n_0 - C_1\sigma_x - C_2(\sigma_y + \sigma_z) \quad (3a)$$

$$n_y \approx n_0 - C_1\sigma_y - C_2(\sigma_x + \sigma_z) \quad (3b)$$

$$n_z \approx n_0 - C_1\sigma_z - C_2(\sigma_x + \sigma_y) \quad (3c)$$

In the equations above (3a-c), n_x, n_y, and n_z are the refractive indices for light polarized in the *x*-, *y*-, and *z*-direction. n_0 is the refractive index of the material without stress and C_1 and C_2 are the elasto-optic constants. The stress components are denoted by σ, where the subscript defines the stress direction.

We employed COMSOL for a 2D Finite Element Method (FEM) based multiphysics study of the structural and optical response of the polymer waveguide shown in Figure 1b) to an incident ultrasonic wave in water. We assumed that the acoustic wavefront can locally be represented as plane wave. Table 1 summarizes the physical parameters used in the simulations. In a first step, the deformation of the waveguide structure in response to the acoustic wave was calculated. The bottom of the glass substrate was positioned by a fixed constraint, assuming negligible displacements of the glass. Since we consider fabrication by nanoimprint lithography, we include a residual layer next to the waveguide core of 100 nm thickness. We added an isotropic loss factor damping value η=0.01 for the PDMS cladding, which is a typical value for rubber-like materials [4]. In a second step, an optical eigenmode analysis for the deformed structure was performed (see Figure 1c)) considering the deformation and the elasto-optic effect due to strain. The optical wavelength λ in our simulations was set to 780 nm. We could not find experimental data for C_1 and C_2 of PDMS in literature. However, birefringence measurements for transparent rubbers suggest a relative elasto-optic constant $C_0 = C_2 - C_1$ beyond 1000 TPa^{-1} [5,6]. Therefore, we exemplarily investigated two combinations of C_1 and C_2 with a fixed relative elasto-optic constant C_0= 2000 TPa^{-1}. The deformation of the coupling region is neglected [1]. A change in the ring radius is also considered to be insignificant due to the assumption of a stiff substrate and strong adhesion of the polymer core material to the glass.

Material	Young's modulus (MPa)	Poisson's ratio	Density (kg/m^3)	n_0	C_1 (TPa^{-1})	C_2 (TPa^{-1})
Polystyrene (PS)	300	0.33	965	1.5775	48*	29*
Polydimethylsiloxane (PDMS)	0.75 / 1.5 / 3.0	0.49	1000	1.4050	0 1000	2000 3000
Glass	7250	0.17	2210	1.4540		

*Table 1: Physical constants used in simulation (*elasto-optic constants from [7] at 632.8 nm).*

RESULTS AND DISCUSSION

Figures 2a)-c) show the change of the effective refractive index n_{eff} of the TM-like guided mode in the waveguide under the influence of an ultrasonic wave with the local pressure amplitude on the surface of the cladding of 0.1 MPa as a function of the phase of the acoustic wave for three different frequencies (1 MHz, 10 MHz, 100 MHz) and two angles of incidence (0° and 20° with respect to the surface normal). The blue curves show the change purely caused by the geometric deformation of the waveguide core, *i.e.*, without considering the elasto-optic effect. Positive strain values compress the waveguide core, resulting in a reduced n_{eff}. On the other hand, the elasto-optic effect increases the refractive material index for positive strain values [1]. Therefore, these two phenomena have a counteracting effect on n_{eff} as can be seen in the orange curves in Fig. 2, which include the elasto-optic effect. For 100 MHz, the PDMS cladding material (Young's modulus E_{PDMS}=0.75 MPa) cannot follow the ultrasonic wave any more instantaneously and there is a phase lag between the structural oscillation of the waveguide and the sound wave. Next, we investigated the influence of the pressure on the effective refractive index change Δn_{eff} over a full period of the acoustic wave (Fig. 3a). Figure 3b summarizes the slope values $d\Delta n_{\mathrm{eff}}/dP$ for the different PDMS elasto-optic constants and angles of incidence using E_{PDMS}=0.75 MPa. The sensitivity of the refractive index change to the pressure clearly reduces with increasing frequency. In Fig 3c), also different values for E_{PDMS} are investigated. Higher values of E_{PDMS} result stronger optical response assuming that the elasto-optic constants of PDMS do not change.

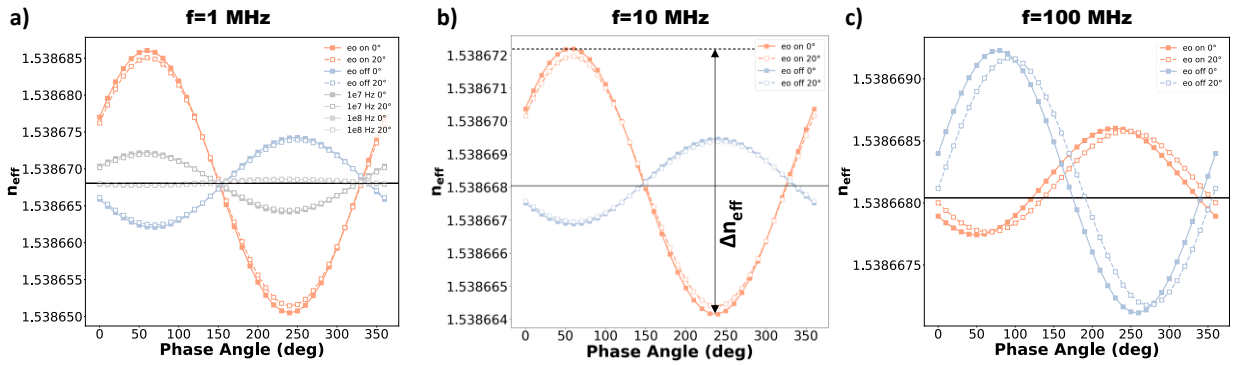


Fig. 2. Change of the effective refreactive index n_{eff} for different phase angles of the incident acoustic wave (0.1 MPa) without (eo off, blue lines), i.e. only geometric deformation, and with taking into account the elasto-optic effect (eo on, orange lines) for incident angles of 0° and 20°. The black line indicates the mode index of the non-deformed waveguide. For PDMS, a Young's modulus of 0.75 MPa and elasto-optic constants C_1=1000 TPa^{-1} and C_2=3000 TPa^{-1} were assumed. a) Ultrasound frequency 1 MHz with added 10 MHz and 100 MHz(both only with elasto-optic effect) to display the amplitude scaling, b) 10 MHz, c) 100 MHz.

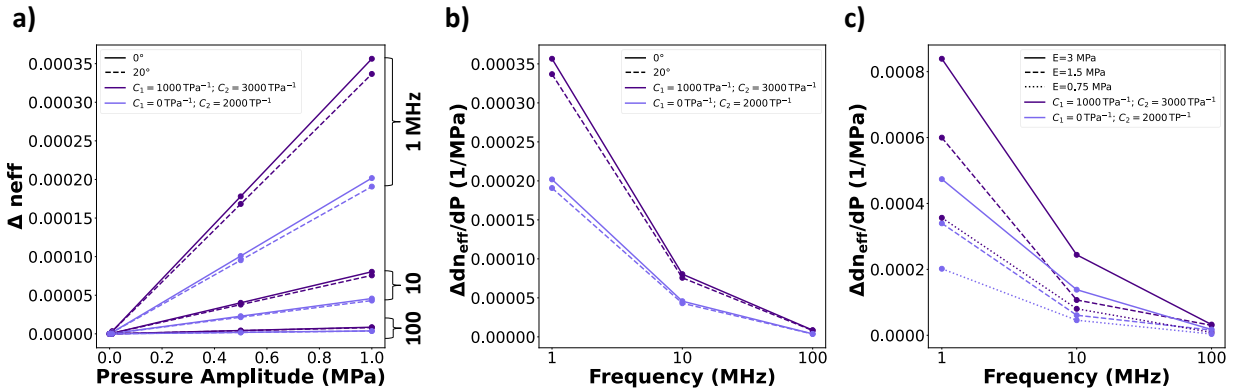


Fig. 3. a) Effective refractive index change Δn_{eff} over a full period of the acoutic wave as a function of the pressure amplitude (E_{PDMS} = 0.75 MPa, b) Slope $d\Delta n_{eff}/dP$ (MPa^{-1}) as function of frequency for two different elasto-optic constant settings for PDMS and two angles of incidence using E_{PDMS} = 0.75 MPa, c) Slope $\Delta n_{eff}/\Delta P$ (MPa^{-1}) as funtion of frequency for three different values of E_{PDMS} and an angle of incidence 0°.

CONCLUSION AND OUTLOOK

In this work, we have proposed a 2D FEM simulation model to analyse the dynamic structural and optical response of polymer waveguides to ultrasonic waves in dependence of material parameters, acoustic frequency, and angle of incidence. As a next step, we will use the model to generate data for calculating the wavelength shift of the MRR according to equation (2), which allows for a 3D approximation in a generalized form of the approach reported in [8].

Acknowledgements: This work was supported by the REAP project, which received funding from the European Union's Horizon 2020 research and innovation programme under grant agreement No 101016964 under the Photonics Public Private Partnership (PPP) call H2020-ICT-2020-2 with the topic ICT-36-2020 - Disruptive photonics technologies.

References

[1] C.-Y. Chao et al., *High-frequency ultrasound sensors using polymer microring resonators*, IEEE Transactions on Ultrasonics, Ferroelectrics, and Frequency Control, vol. 54, no. 5, pp. 957–965, 2007

[2] S. Ashkenazi et al., *Ultrasound detection using polymer microring optical resonator*, Applied Physics Letter, vol. 85, no. 22, pp. 5418–5420, 2004

[3] D. L. MacAdam et al., *Matrix Theory of Photoelasticity*, Springer, Berlin Heidelberg, 1979

[4] COMSOL Multiohysics, *Damping in Structural Dynamics: Theory and Sources*, https://www.comsol.de/blogs/damping-in-structural-dynamics-theory-and-sources/ (accessed: Jan. 31 2023), Stockholm

[5] A. Angioletti et al., *Rubber Birefringence and Photoelasticity*, Rubber Chemistry and Technology, vol. 38, no. 5, pp. 1115–1163, 1965

[6] Y. Hazan et al., *Silicon-photonics acoustic detector for optoacoustic micro-tomography*, Nature Communications, vol. 13, no. 1, p. 1488, 2022

[7] F. Ay et al., *Prism coupling technique investigation of elasto-optical properties of thin polymer films*, Journal of Applied Physics, vol. 96, no. 12, pp. 7147–7153, 2004

[8] Z. Zhang et al., *Theoretical and experimental studies of distance dependent response of micro-ring resonator-based ultrasonic detectors for photoacoustic microscopy*, Journal of Applied Physics 116 (14), p. 144501, 2014

High performance integrated silicon polarization beam splitter based on all-dielectric metamaterial cladding

Andraž Debevc, Marko Topič and Janez Krč

University of Ljubljana, Faculty of electrical engineering, Tržaška cesta 25, 1000 Ljubljana, Slovenia

A polarization beam splitter is an essential building block in integrated silicon photonics. We propose a polarization beam splitter design based on all-dielectric metamaterial cladding structures. Exceptionally high extinction ratio and low insertion loss were achieved in an ultra-wide bandwidth for both polarizations.

Keywords: *Silicon photonics, polarization beam splitter, all-dielectric metamaterials*

INTRODUCTION

In photonic integrated circuits (PICs) based on silicon (Si) material platform polarization handling components are crucial due to a strong waveguide (WG) birefringence. The high refractive index contrast between Si and SiO_2 combined with asymmetry in WG width and height result in a large difference in effective refractive index of the transversal electric (TE) and magnetic (TM) mode in single mode WGs. This means that the performance of silicon photonics devices is typically polarization dependent. To tackle this, a so called polarization diversity approach can be employed requiring polarization management components [1]. A polarization beam splitter (PBS) splits a signal at the input, which can include both, TE and TM mode, into TE mode at one output and TM mode at another output. A PBS is an essential building block in polarization diversity circuits. Low insertion loss (IL), high extinction ratio (ER) and wide bandwidth (BW) for both polarizations as well as small footprint are required in the design of a PBS in PICs. Meeting all these requirements at the same time is a challenge. Various approaches have been used to achieve polarization splitting, including devices based on directional couplers (DCs), multimode interferometers (MMIs), Bragg gratings and many more [2]. Over the last few years all-dielectric metamaterials have been researched to achieve high performance polarization splitting [3]. An all-dielectric metamaterial consists of two or more periodically exchanging materials with the period well below the wavelength of light. Such a structure acts as an anisotropic material exhibiting different refractive indexes in the direction parallel to the layers and perpendicular to the layers. By etching subwavelength Si ridges parallel to a strip Si WG core, a so called WG with metamaterial cladding can be formed. Due to the anisotropic nature of the cladding structure, the evanescent field is modified, altering the coupling between adjacent WGs. All-dielectric metamaterial cladding can, if properly designed, drastically suppress the coupling of TE modes, whereas the coupling of TM modes is increased [4]. This can be utilized in the design of a PBS based on a DC with metamaterial cladding. [5]. Such devices can achieve exceptionally large extinction ratios (ER), however, their bandwidth (BW) is limited due to inherent properties of the DC. In this contribution we present a novel PBS design based on two compact MZIs with metamaterial cladding along with a metamaterial TE polarizer to simultaneously achieve wide BW, high ER and low insertion loss (IL).

DESIGN AND METHODS

Our proposed design (Fig. 1a and 1b) is based on two WGs with metamaterial cladding structure in between the two WG cores. By changing the geometry of the metamaterial structure the coupling length (defined as the length at which all the light couples to the adjacent WG) for the TE and TM mode is affected. In the first step we design the geometry of the metamaterial cladding to achieve exceptionally long coupling length for TE mode (> 1 cm) and short coupling length for TM mode (12.6 µm). To achieve broadband coupling of the TM mode to the adjacent WG, leading to a high transmission of the TM mode at the Cross port of the device, we propose a structure including two metamaterial compact MZIs. By cascading two MZIs in a point symmetrical configuration, we can achieve broadband coupling of the TM mode, which could not be achieved by a single DC structure [6]. The structure consists of three straight sections of two WGs with metamaterial cladding, acting as DCs and two bends where the WGs remain in parallel. This leads to a small difference in path length between the two WGs in the bends, since the there is a slight difference in bend radii of the two WGs. This way we can achieve the required phase delay in MZI operation. Due to relatively short bent sections the coupling that occurs there is very small. The structure can be therefore described discretely by interchanging DCs and phase delays as is schematically shown in Fig. 1b. Our proposed concept results in a significantly more compact device, compared to conventional cascaded MZI configuration. The metamaterial cladding structure is employed in between WG cores along the whole structure to suppress the coupling of TE mode, ensuring high transmission of the TE mode at the $Thru_{int}$ port. To reduce the remaining TM polarization at the Thru port of the device and further increase the ER, we employ a bend TE polarizer with metamaterial cladding. The design concept was adopted from [7]. The metamaterial cladding with variable fill

factor (ratio between the rib width and the period) ensures that the TM mode is diffracted into free space without significantly affecting the transmission of the TE mode which passes thru the polarizer with low loss. The designed PBS has a footprint of 82 µm and a minimal feature size of 70 nm.

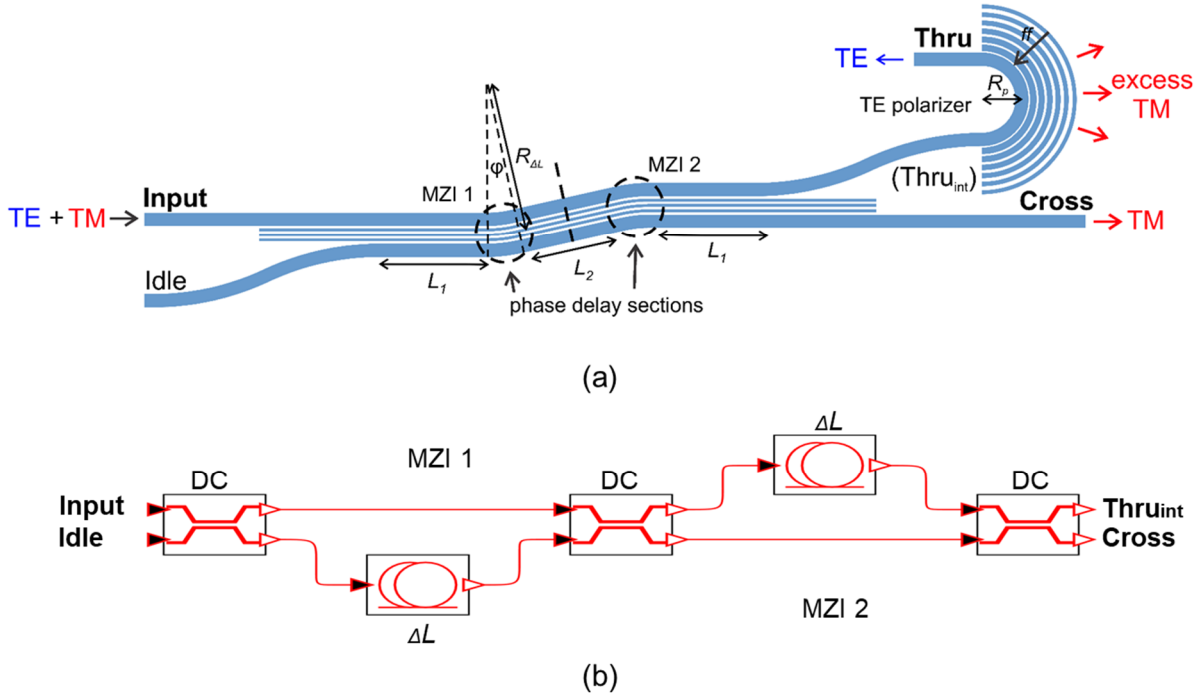


Figure 1: (a) The geometry of our proposed PBS device. Main geometrical parameters as well as input and output ports are depicted in the figure. (b) A network level schematic of the metamaterial compact dual MZI part of the device (without the TE polarizer).

To design and optimize the geometry of the PBS we employed different simulation methods. To design the metamaterial cladding structure FEM mode analysis using COMSOL program package was used. The coupling length was calculated using coupled mode theory from the symmetric and antisymmetric modes of WG systems. To define selected geometry parameters of the dual MZI structure (L_1, L_2, φ) we employed transfer matrix method (TMM) coupled with a simulated annealing optimization algorithm with the purpose of maximizing the bandwidth of the device. In these calculations we assumed the circuit topology shown in Fig. 1b. The TE polarizer was designed following the concepts described in [7]. Its performance was numerically evaluated by FDTD simulations using Lumerical program package. For final designs we also employed full 3-D FDTD simulations of the entire device as shown in Fig. 1a, to accurately evaluate and predict its performance.

The device was fabricated using 100 keV electron beam lithography (EBL) at Applied Nanotools, Inc. [8] with a silicon on insulator (SOI) wafer (2 µm thick buried oxide, 220nm thick Si layer) was used as the substrate. The fabrication process allows for fabrication of devices with minimal feature sizes down to 70 nm. Characterization of fabricated devices was performed using a tunable laser source and a power meter. We used a fiber polarization controller to tune the input polarization. Grating couplers were employed to couple the light from the optical fiber to the chip.

RESULTS

3-D FDTD results for the optimized PBS structure (including the TE polarizer) are shown in Fig. 2. The results for TE mode show a high transmission at the Cross port (above -0.2 dB) of the device in the whole simulated wavelength range from 1300 nm to 1700 nm. The simulated TE mode transmission at the Cross port of the device is below -32 dB in the whole simulated wavelength range. The simulated TM transmission at the Cross port is above -1 dB in a wide wavelength range of 300 nm. At the Thru port the simulated TM transmission remains below -33 dB in the wavelength range of over 300 nm. The simulation results indicate noticeable polarization splitting performance of the device with *ER* > 33 dB, *IL* < 1 dB in the *BW* of 273 nm.

Measurement results for the fabricated device are shown in Fig.2. Measurements were performed in a wavelength range from 1450 nm to 1590 nm due to a limited tuning range of the laser. We fabricated two sets of devices: one was connected to TE mode grating couplers and the other to TM mode grating couplers. This enabled us to separately measure the TE and TM mode transmission at all ports of the device. It can be observed that the measurement results follows predictions from simulations. Note that in certain cases transmission exceeds 0 dB.

This is a measurement artefact that occurred due to the variability of grating couplers. For that reason, the *IL* cannot be accurately determined, however, we can make a conservative assessment that it remains below 2 dB in a *BW* of at least 140 nm. The measured *ER* of the device is above 30 dB in a *BW* of at least 140 nm. As it was indicated by simulations, the bandwidth of the device is possibly significantly wider.

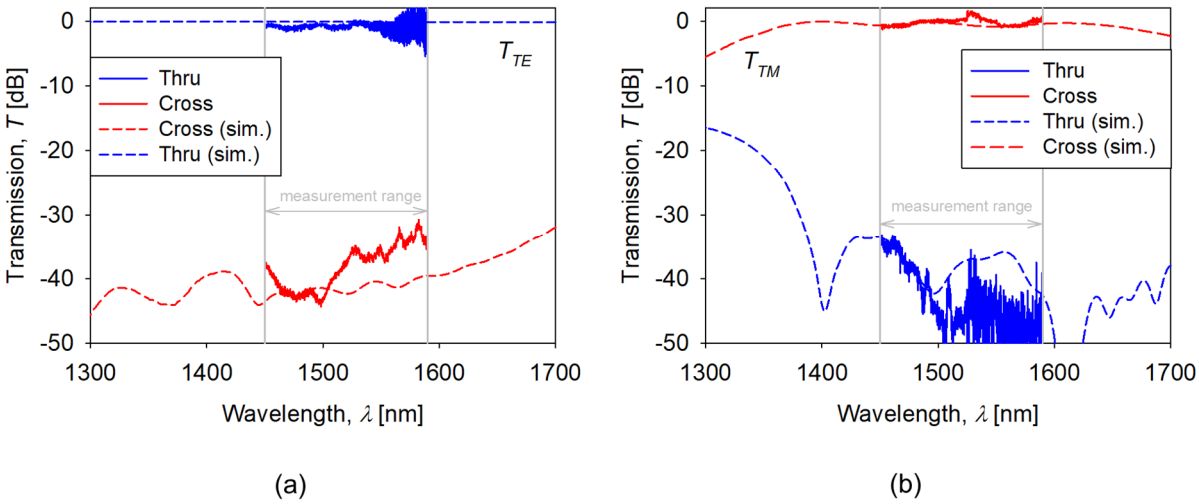


Figure 2: FDTD simulation results and experimental results for TE mode (a) and TM mode (b) transmission at the Thru and Cross ports of the PBS device.

CONCLUSION

We theoretically and experimentally demonstrated a novel polarization beam splitter device in integrated silicon photonics utilizing all-dielectric metamaterial structures. Exceptionally high *ER*, low *IL* and ultra-wide *BW* were predicted by simulations. Measurements of fabricated device confirmed high performance polarization splitting of the proposed PBS.

Acknowledgements: The authors acknowledge the financial support from the Slovenian Research Agency (Research Programme P2-0415 and A.D. for PhD funding). Applied Nanotools, Inc. is acknowledged for fabrication of the devices using the NanoSOI Fabrication Service. B. Batagelj and co-coworkers from Radiation and Optics Lab at the University of Ljubljana are acknowledged to kindly offer the use of their optical measurement equipment.

References

[1] D. Dai, L. Liu, S. Gao, D.-X. Xu, and S. He, "Polarization management for silicon photonic integrated circuits," *Laser Photonics Rev.*, vol. 7, no. 3, pp. 303–328, 2013, doi: 10.1002/lpor.201200023.

[2] Y. Zhang *et al.*, "On-chip silicon polarization and mode handling devices," *Front. Optoelectron.*, vol. 11, no. 1, pp. 77–91, Mar. 2018, doi: 10.1007/s12200-018-0772-6.

[3] Z. Yu, H. Xu, D. Liu, H. Li, Y. Shi, and D. Dai, "Subwavelength-Structure-Assisted Ultracompact Polarization-Handling Components on Silicon," *J. Light. Technol.*, vol. 40, no. 6, pp. 1784–1801, Mar. 2022, doi: 10.1109/JLT.2021.3134469.

[4] S. Jahani *et al.*, "Controlling evanescent waves using silicon photonic all-dielectric metamaterials for dense integration," *Nat. Commun.*, vol. 9, p. 1893, May 2018, doi: 10.1038/s41467-018-04276-8.

[5] S. Z. Ahmed *et al.*, "Ultra-high extinction ratio polarization beam splitter with extreme skin-depth waveguide," *Opt. Lett.*, vol. 46, no. 9, pp. 2164–2167, May 2021, doi: 10.1364/OL.420824.

[6] A. Debevc, M. Topič, and J. Krč, "High extinction ratio and an ultra-broadband polarization beam splitter in silicon integrated photonics by employing an all-dielectric metamaterial cladding," *Opt. Express*, vol. 30, no. 26, pp. 46693–46709, Dec. 2022, doi: 10.1364/OE.476333.

[7] H. Xu, D. Dai, and Y. Shi, "Anisotropic metamaterial-assisted all-silicon polarizer with 415-nm bandwidth," *Photonics Res.*, vol. 7, no. 12, p. 1432, Dec. 2019, doi: 10.1364/PRJ.7.001432.

[8] "Applied Nanotools Inc.," Jan. 04, 2018. https://www.appliednt.com/ (accessed Jan. 20, 2023).

Towards bimodal photonic sensing with coherent readout in silicon nitride

Student paper

Antonia Torres-Cubillo[1,*], J. Manuel Luque-González[1], Alejandro Sánchez-Postigo[1,3], J. Gonzalo Wangüemert-Pérez[1,2], Íñigo Molina-Fernández[1,2] and Robert Halir[1,2]

[1]Telecommunication Research Institute (TELMA), Universidad de Málaga, Louis Pasteur 35, 29010 Málaga, Spain
[2]IBIMA-BIONAND, Parque Tecnológico de Andalucía, 29590 Málaga, Spain
[3]Currently at Institute of Physics, University of Münster, Heisenbergstraße 11, 48149 Münster, Germany
[*] atc@ic.uma.es

Photonic integrated sensors have emerged as an attractive tool for medical diagnosis and environmental monitoring, offering quantitative results in real time. In this work, we develop and experimentally validate a novel silicon nitride bimodal interferometric sensor with a coherent phase retrieval. This approach has potential to combine the compactness and relaxed temperature sensitivity of bimodal sensors with the linear and unambiguous phase readout of coherent detection.

Keywords: *Integrated photonics, bimodal waveguide, refractive index sensor, coherent readout*

INTRODUCTION

Photonic integrated sensors have attracted a lot of research interest over the past decade [1], as they can be used to perform label-free chemical analysis and deliver quantitative results in real time. In fact, several sensing configurations have been proposed to detect analytes such as pathogens [2] and hazardous gasses [3], which is critical in medical diagnosis and environmental monitoring. Furthermore, silicon-based sensors are compatible with standard CMOS fabrication processes and can potentially be mass-produced, encouraging the development of new concepts like lab-on-a-chip devices and distributed sensor networks.

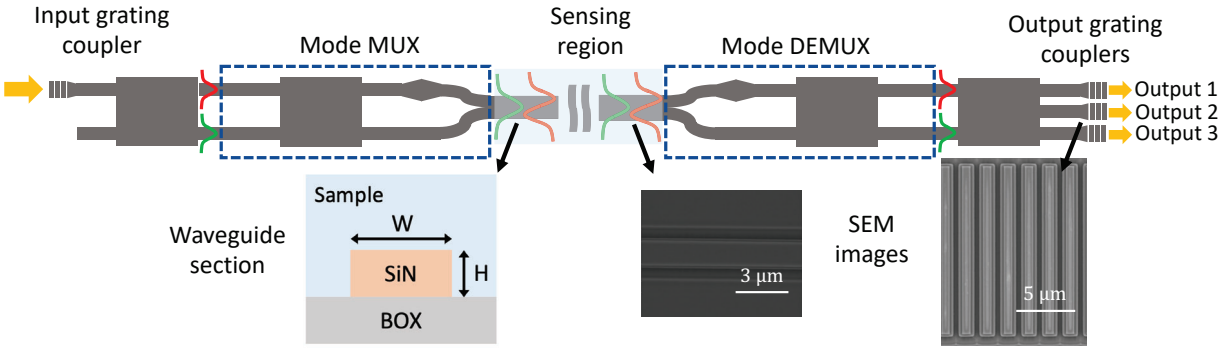


Fig. 1. Schematic representation of the bimodal refractive index sensor. Input light is split by a 2×2 MMI and used to excite the first two TE modes of the bimodal sensing waveguide. A sensing window is etched to enable sample-light interaction. After propagating through the waveguide, the two modes are demultiplexed and enter a 2×3 MMI, which provides three 120° outputs, ready for the coherent phase readout.

Among the different sensing configurations, interferometric sensors offer fixed-wavelength operation and can be extremely sensitive: Mach Zehnder interferometers combined with a 120° 2×3 hybrid enable coherent phase detection [4], overcoming limitations like directional ambiguity and sensitivity fading, and yielding remarkable detection limits [5]. However, this configuration requires both a sensing and a reference arm and is sensitive to temperature fluctuations. Bimodal sensors emerge as an interesting alternative [6, 7]: two different modes propagate through the same waveguide, but with different sensitivities to the surroundings, thus creating an interference pattern at the output when the refractive index of the sample changes. This differential interferometry not only reduces the footprint of the sensor, but also increases its robustness, as both modes will be affected by the same temperature changes in the waveguide.

In this work, we present a silicon nitride interferometric sensor, which combines a bimodal sensing waveguide with a coherent phase readout and the use of calibration algorithms [see Fig. 1], validated with preliminary sensing experiments.

WORKING PRINCIPLE

A schematic representation of the proposed refractive index sensor is shown in Fig. 1. The sample circulates through a microfluidic channel which will be placed on top of the sensing region. A sensing window is opened over this area to enable an overlap between the sample and the evanescent field of the guided modes. A change in the concentration of the analyte in the sample induces a proportional change of its refractive index (Δn_c), which is translated by the waveguide into a change in the effective index of each mode ($\Delta n_{\mathrm{eff},1}, \Delta n_{\mathrm{eff},2}$). In a bimodal waveguide, the fundamental mode is more confined than the second-order mode and its effective index will change at a smaller rate. We define the differential sensitivity of the waveguide as

$$S_d = \frac{\partial n_{\mathrm{eff},2}}{\partial n_c} - \frac{\partial n_{\mathrm{eff},1}}{\partial n_c}. \quad (1)$$

Our interferometric sensing architecture transforms the index change in the cladding into three readily detectable output signals. For that purpose, fixed-wavelength laser light is split into the two single-mode inputs of a mode multiplexer [8] used to excite the first-order and second-order modes of the sensing bimodal waveguide. Due to the interaction with the sample, after propagating through the waveguide, the two modes have accumulated a relative phase shift $\Phi = S_a S_d \Delta n_c$, where

$$S_a = \frac{2\pi}{\lambda_0} L \quad (2)$$

is the sensitivity of the architecture, λ_0 is the vacuum wavelength and L is the length of the sensing waveguide. The two modes are demultiplexed into two fundamental modes, which enter the 120° hybrid**.** This device delivers three interferometric output signals, with a phase shift of 120° between them. These signals can be detected with photodetectors and combined to generate an IQ signal with phase Φ. Deterministic hardware errors can be corrected with different calibration algorithms [4, 9]. Once the phase is read, the change in analyte concentration can be immediately inferred.

SENSOR DESIGN

Our sensors have been designed for the Cornerstone silicon nitride platform [10]. This platform offers a 300 nm device layer and a 3 μm BOX thickness. The 2 μm silicon dioxide cladding is removed over the sensing region to enable light-matter interaction. The operation wavelength is 1520 nm and the employed polarization is TE. The three main components of our sensors are the bimodal sensing waveguide, the mode multiplexer and the 120° hybrid.

Simulations using FIMMWAVE mode solver software [11] were carried out to design the sensing waveguide, which is 1.8 μm wide and supports the two first TE modes. To evaluate its differential sensitivity, the change in the effective index of the guided modes was calculated as a function of a change in the refractive index of the cladding around a value of 1.32 RIU, which corresponds to pure water at the operating wavelength. The second TE mode is significantly more sensitive to changes in the cladding than the fundamental one, yielding a differential sensitivity of $S_d = 0.08\ \mathrm{RIU/RIU}$, from which we get a system sensitivity of $S_a \cdot S_d = 1.72 \cdot 10^3\ \mathrm{rad/RIU}$, for a waveguide length of $L = 5.2\ \mathrm{mm}$. The mode converter and multiplexer comprises a 2×2 MMI, a 90° phase-shifter and a sinusoidal profile Y-branch, as shown in Fig. 1. The operational principles of this architecture are explained in detail in [12]. The 2×2 MMI has a width of 7.4 μm and a length of 127 μm, the phase shifter is 25.5 μm in length with a maximum width of 1.1 μm and the Y-branch is 30 μm long. The 2×3 MMI section of the 120° hybrid is 13.3 μm wide and 264 μm long. Light input and output is carried out by grating couplers, which are positioned with a pitch of 127 μm to enable the use of a fiber array polished at 26° as a cost-effective way to detect several simultaneous outputs.

EXPERIMENTAL RESULTS

A simple experimental setup consisting of a laser source operating at a fixed wavelength, an angled-polished fiber array, three photodetectors, alignment stations and a data acquisition module was arranged to validate our sensors. An isopropanol droplet, with a refractive index of 1.35 RIU, was carefully deposited on top of the sensing window. The evaporation of the sample caused a monotonic change of the refractive index of the cladding, thus inducing a proportional phase shift between the fundamental and the second TE modes of the bimodal waveguide. This phase shift was retrieved from the three output signals of the sensor, from which a fragment is shown in Fig. 2(a). We were able to correct the effect of hardware errors such as the observed power imbalances between the outputs by means of a simple ellipse-to-circle blind calibration algorithm [4], delivering a precise phase readout, represented in Fig. 2(b).

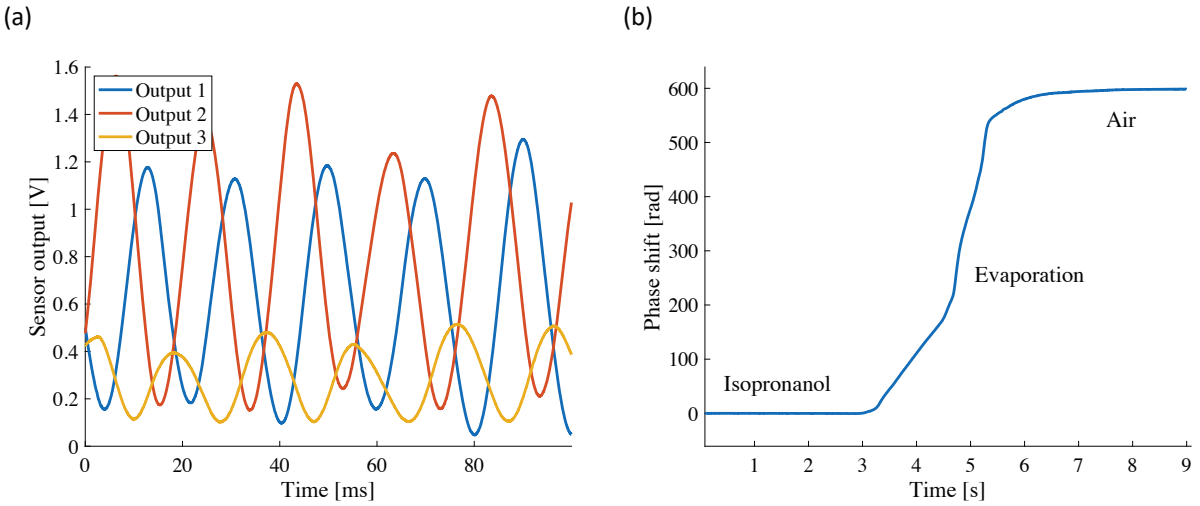


Fig. 2. (a) Sensor output signals. The evaporation of an isopropanol droplet causes a monotonic change in the refractive index of the cladding, resulting in three 120° shifted interferometric signals. (b) Phase readout. The retrieved phase enables the calculation of the sensitivity of the system.

We observed a phase shift of 600 rad from the deposition of the isopropanol droplet ($\mathrm{RI} = 1.35\ \mathrm{RIU}$) to its complete evaporation, leaving only air ($\mathrm{RI} = 1\ \mathrm{RIU}$) on the waveguide. The calculated systemic sensitivity is $S_a \cdot S_d = 600/(1.35 - 1) = 1.71 \cdot 10^3\ \mathrm{rad/RIU}$, which matches the theoretical value. These results are promising and encourage further experiments towards the detection of clinically relevant analytes.

CONCLUSIONS

We have developed a sensing configuration combining a bimodal interferometer with a coherent phase readout, facilitated by a simple architecture to perform the modal MUX/DEMUX. Our sensors have been fabricated on a silicon nitride platform and have been experimentally validated by simple sensing experiments, yielding promising results. Further work will involve a sophisticated microfluidics system to enable a controlled interaction with the sample for a precise sensor characterization and the detection of complex chemical substances. We consider that this is a significant step towards a robust, compact and cost-effective label-free sensing device.

Acknowledgements: This work has received funding from the Ministerio de Universidades, Ciencia e Innovación (FPU19/03330) and the Junta de Andalucía (Agencia Andaluza del Conocimiento PY18-793). We would also like to acknowledge the Universidad de Málaga.

References

[1] N. L. Kazanskly et at., *Advancement in silicon integrated photonics technologies for sensing applications in near-infrared and mid-infrared region: A review*, MDPI Photonics, vol. 9, no. 5, 2022.
[2] J. Maldonado et al., *Label-free detection of nasocomial bacteria using a nanophotonic interferometric biosensor*, Analyst, vol. 145, 2020.
[3] M. Vlk et al., *Extraordinary evanescent field confinement waveguide sensor for mid-infrared trace gas spectroscopy*, Light: Science and Applications, vol. 10, no. 26, 2021.
[4] R. Halir et al., *Direct and sensitive phase readout for integrated waveguide sensors*, IEEE Photonics Journal, vol. 5, no. 4, 2013.
[5] J. Leuermann et al., *Coherent silicon photonics interferometric sensor with an inexpensive laser source for sensitive label-free immunoassays*, Optics Letters, vol. 45, no. 24, 2020.
[6] L. Torrijos-Morán et al., *Integrated optical bimodal waveguide biosensors: Principles and applications*, Results in Optics, vol. 9, 2022.
[7] O. Calvo-Lozano et al., *One-step and real-time detection of microRNA-21 in human samples for lung cancer biosensing diagnosis*, Analytical Chemistry, vol. 94, no. 42, pp. 14659-14665, 2022.
[8] D. González-Andrade et al., *Experimental demonstration of a broadband mode converter and multiplexer based on subwavelength grating waveguides*, Optics and Laser Technology, vol. 129, 2020.
[9] P. Reyes-Iglesias et al., *High-performance monolithically integrated 120° with relaxed hardware constraints*, Optics Express, vol. 20, no. 5, 2012.
[10] https://www.cornerstone.sotonfab.co.uk
[11] https://www.photond.com
[12] D. González-Andrade et al., *Ultra-broadband mode converter and multiplexer based on sub-wavelength structures*, IEEE Photonics Journal, vol. 10, no. 2, pp. 2201010, 2018.

Development of SiON-based photonic integrated circuits for the blue/near-UV wavelength range

Ronan Kervazo[1], Loïc Bodiou[1*], Jean-Claude Simon[1], Monique Thual[1], Christophe Levallois[2], Julie Le Pouliquen[2], Stéphane Trebaol[1] and Joël Charrier[1]

[1] Univ. Rennes, CNRS, Institut FOTON - UMR 6082, F-22305 Lannion, France
[2]Univ. Rennes, INSA, CNRS, Institut FOTON - UMR 6082, F-35000 Rennes, France
[*] loic.bodiou@univ-rennes1.fr

In this paper, the design of integrated photonics components for blue/near-ultraviolet wavelength range is presented. Optical properties of the silicon oxynitride (SiON) in this spectral range are exploited to develop a complete library of photonic integrated components for operation in blue/near-UV spectral range.
Keywords**:** *Integrated Optics, Near Ultraviolet, Waveguide, multimode interferometer (MMI)*

INTRODUCTION

NUV (near ultraviolet) photonic devices, like coherent sources and optical functions, may address, in a near future, large domains of applications as for the next generation of biomedical diagnosis tools in particular through Raman spectroscopy as a noninvasive chemical and biological analysis technique of pollutants, medicine, cells...[1,2] They can also address new paradigm in optical frequency metrology, optical functions and sensors in this uncovered wavelength domain [3]. Coherent sources as narrow lasers and optical frequency combs are important tools in fundamental and applied physics [4]. The need of coherent sources in the NUV is also driven by the rich variety of molecular and atomic spectral features to probe [5].

Leveraging from mature microelectronics technologies, Silicon On Insulator (SOI) has emerged, over the past two decades as the preferred technology for photonic integration. However, silicon is not a good candidate for short wavelength operation due to its low bandgap energy preventing efficient transmission for wavelengths shorter than 1.1 µm. Development of new UV-transparent materials platforms is therefore needed. Amongst the possible blue-UV transparent materials candidates, recent years have witnessed the demonstration of different integrated components based on aluminium nitride [6], silicon nitride [7], alumina [8] and silicon oxynitride [9]. These materials have been identified thanks to their transparency and their low propagation loss in blue and violet range that are summarized in Table 1.

Material	AlN (Bulk Single Crystal)	AlN (Film Polycrystalline)	Si_3N_4	Al_2O_3 (Atomic Layer Deposition)	SiON
Propagation loss	350 nm: 43 dB/cm 420 nm: 42 dB/cm	350 nm: 3 dB/cm 420 nm: 1 dB/cm	410 nm: 20 dB/cm 420 nm: 15 dB/cm	370 nm: 4 dB/cm 430 nm: 3 dB/cm	300 nm: 1 dB/cm 400 nm: 0.8 dB/cm
Transmission in near-UV and visible ranges	No transmission	300 to 700 nm	450 to 700 nm	250 to 700 nm	200 to 700 nm

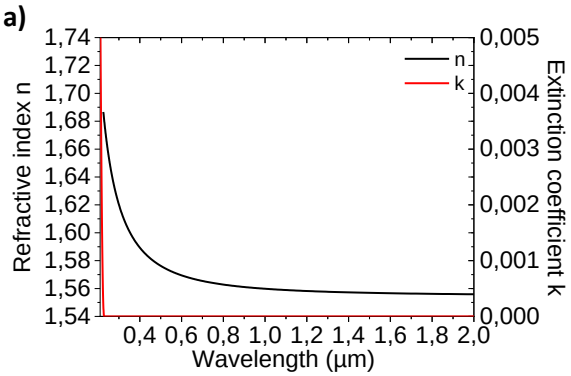
Table. 1. Propagation loss in the near-UV and visible wavelength range for different materials [9,10]

Silicon oxynitride (SiON) can be used for infrared integrated photonics and toroid, microdisks resonators [11] and microring resonators [12] have been demonstrated. Applications in the visible (780 nm) have also been developed taking benefit from the material optical nonlinearities [13]. If the use of SiON has yet been restricted to infrared and red wavelength ranges, SiON platform could also be promising for UV-blue sensing applications. Low propagation losses down to 1 dB/cm in multimode waveguides were demonstrated at 400 nm [9].

This paper presents the simulation and development of photonic integrated components operating at short wavelengths based on silicon oxynitride layers. First, the deposition technique and optical properties of SiON layers are described. Then the optical design of SiON waveguides and multimode interferometers (MMI) are presented.

RESULTS

Thin film deposition was performed by Plasma Enhanced Physical Vapor Deposition (PECVD) on thermally oxidized (2-µm thick SiO_2) 3" silicon wafer, placed in the vacuum chamber on a holder set at 280°C. The gas mixture was composed of SiH_4, NH_3, N_2O, Ar, and N_2 with flow rates of 400 sccm, 50 sccm, 200 sccm, 620 sccm and 250 sccm, respectively. Based on preliminary calibrations, the deposition time was adjusted to obtain 300-500 nm thick films. Refractive indices of the SiON thin films were deduced from ellipsometry spectra and show a low material absorption in the blue/near-UV wavelength range (Figure 2).



c)

Wavelength (nm)	405	420	450
SiO_2	1.479	1.474	1.471
SiON	1.588	1.579	1.575

Fig. 2. (a) Refractive index and extinction coefficient of the SiON developed by Foton Institute, (b) Cross-section of the ridge waveguide, (c) Refractive index used for the simulation [14]

To design a SiON/SiO_2 ridge waveguide that would support single-mode propagation, we have to calculate its geometrical dimensions (width and height). Simulations based on the finite difference method were carried out for 3 different wavelengths: 405, 420 and 450 nm. The curves presented in Figures 3 represent the dimensions for which the effective index of a given mode is larger than the silica cladding refractive index. To obtain single mode propagation, geometrical dimensions (width and height) must therefore lie out of the grayed areas.

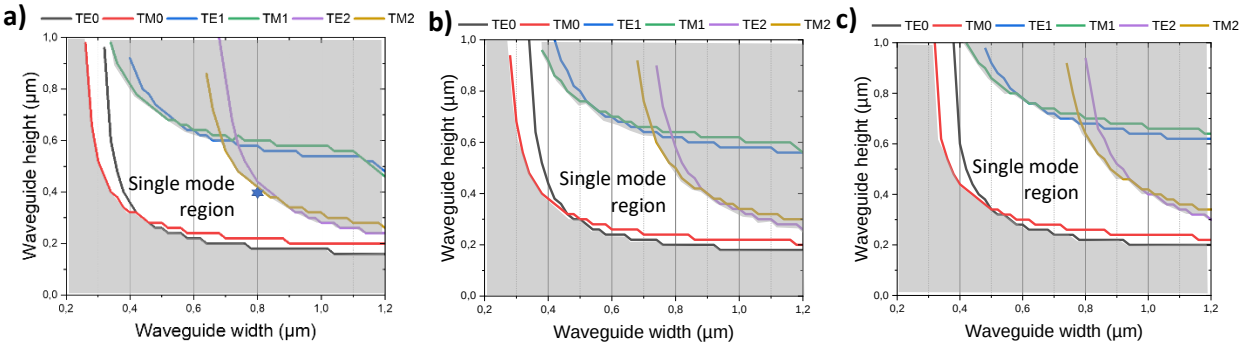


Fig. 3. Modal behavior of the SiON waveguide for different propagation wavelengths: (a) 405 nm, (b) 420 nm, (c) 450 nm.

According to these results and for experimental reasons, a thickness of 0.4 µm was selected for all wavelengths. The width of the waveguide was chosen equal to 0.8 µm for wavelength of 405 nm (see the blue stars in Figures 3). These dimensions can then be used to design more complex passive optical integrated devices such as multimode interferometer (MMI), Bragg resonators, µ-ring resonators.

The FDE solver also calculate the losses associated to the curvature of the waveguide. The mode conversion losses and the radiative losses have been calculated for a 0.8*0.4 µm waveguide at 405 nm. The bend losses become negligeable for radii larger than 1500 µm.

As an example of the various integrated passive building blocks that can be implemented for short wavelength operation, multimode interferometer (MMI) based on SiON design is presented. As a first step, a 1×2 MMI used as a 50-50 splitter was simulated by using an eigenmode expansion solver. To find the optimal MMI dimensions (MMI width, MMI length, separation between output waveguides, width and length of tapers between the input/output waveguides and the multimode section), a circular iterative process is performed to converge towards optimal MMI parameters with respect to the device transmission. Fig. 4a displays the field propagating in the MMI structure optimized for a wavelength of 405 nm and whose dimensions are labelled in Fig. 4b.

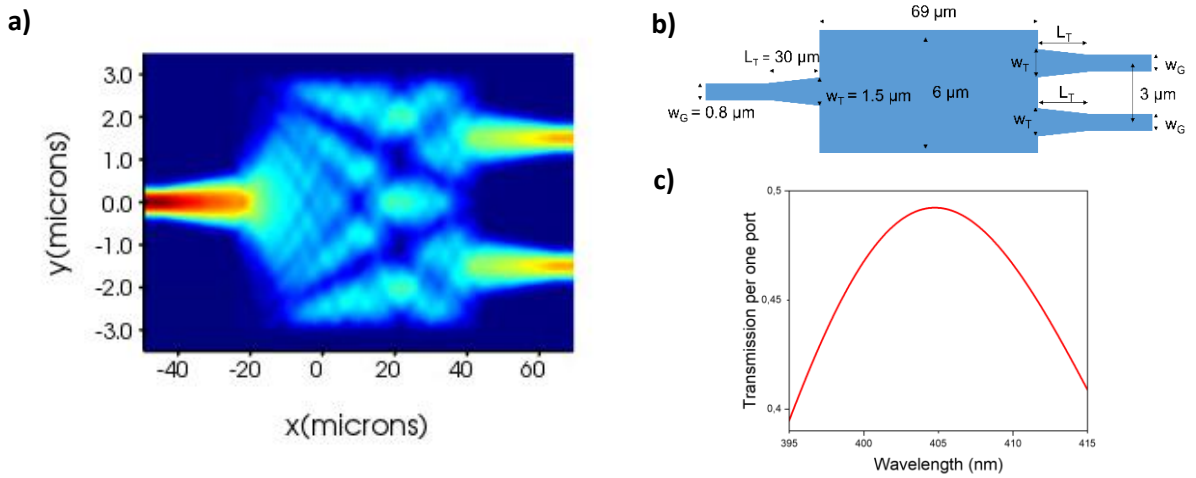


Fig. 4. (a) Simulated E field profile for MMI at 405 nm, (b) Dimensions of the simulated MMI (w_G is the waveguide width, w_T is the taper width and L_T is the taper length), (c) Transmission as a function of the wavelength of the SiON-based multimode interferometer designed for a 405-nm-wavelength propagation

A maximal transmission equal to 49.2% at 405 nm, corresponding to 0.03 dB loss per port, was determined for the component neglecting propagation losses. The same work has been done for the wavelengths of 420 and 450 nm. These components show transmission rates of 49.9% % and 49.8% corresponding to 0.004 and 0.01 dB loss per port at 420 and 450 nm respectively.

In conclusion, waveguides and multimode interferometer were designed by simulation. Optimal dimensions were determined to first fabricate single mode waveguides and more complex passive components. An example of MMI design was presented and demonstrated numerically. Very high transmissions for the two ports could be obtained for three different wavelengths. Additional simulations towards the design of efficient MMI-based multiplexers and demultiplexers with applications in molecular physics [3] are under way to further demonstrate the potential of SiON platform for blue/near-UV integrated photonics.

References

[1] E. Segev, et al., *Patterned photostimulation via visible-wavelength photonic probes for deep brain optogenetics*, Neurophoton.
vol. 4, no. 1, 011002,2016
[2] R. Gillibert, et al., *Raman Tweezers for Small Microplastics and Nanoplastics Identification in Seawater*, Environmental Science & Technology, vol. 53, no. 15, pp 9003-9013, 2019
[3] M. Corato-Zanarella, *et al., Widely tunable and narrow-linewidth chip-scale lasers from near-ultraviolet to near-infrared wavelengths*, Nat. Photon., 2022
[4] R. M. Godun, et al., *Frequency ratio of two optical clock transitions in $^{171}Yb^{+}$ and constraints on the time-variation of fundamental constants*, Physical Review Letters, vol. 113, no.21, 210801, 2014
[5] K. Enomoto, *et al., Comparison of resonance frequencies of major atomic lines in 398–423 nm*, Appl. Phys. B., vol.122, no. 126, 2016
[6] T.-J. Lu, et al., *Aluminum nitride integrated photonics platform for the ultraviolet to visible spectrum*, Opt. Express vol.26, pp. 11147-11160, 2018
[7] A. Siddharth, et al., *Near ultraviolet photonic integrated lasers based on silicon nitride,* APL Photonics, vol. 7, 046108, 2022
[8] G. N. West, et al., *Low-loss integrated photonics for the blue and ultraviolet regime*, APL Photonics, vol.4, 026101, 2019
[9] K. B. Mogensen, et al., *Ultraviolet transparent silicon oxynitride waveguides for biochemical microsystems*, Opt. Lett. 26, 716-718, 2001
[10] D. J. Blumenthal, *Photonic integration for UV to IR applications*, APL Photonics, vol. 5, 020903, 2020
[11] D. Chen, et al., *On-Chip Ultra-High-Q Silicon Oxynitride Optical Resonators*, ACS Photonics 2017 4 (9), 2376-2381, 2017
[12] A. Samusenko *et al., A SiON Microring Resonator-Based Platform for Biosensing at 850 nm*, Journal of Lightwave Technology, vol. 34, no. 3, pp. 969-977, 2016
[13] G. Piccoli, et al., *Silicon oxynitride platform for linear and nonlinear photonics at NIR wavelengths,* Opt. Mater. Express 12, 3551-3562, 2022
[14] L. Bodiou, et al., *Development of a SiON-based integrated platform for the blue/near-UV range wavelength*, in Proceedings of the Conference SPIE Photonics Europe 2022, Integrated Photonics Platforms II, 1214807, 2022

Parallel Sensing with Multiple Microrings on a Single Bus Waveguide

(Student paper)

Z. Zheng[1,3], W.A.P.M. Hendriks[1], Y. Wang[2], S.M. García-Blanco[1], and L. Chang[1]*

[1]Integrated Optical Systems, MESA+ Institute for Nanotechnology, University of Twente, P.O. Box 217, 7500 AE Enschede, The Netherlands

[2]Biomedical Signals and Systems, University of Twente, P.O. Box 217, 7500 AE Enschede, The Netherlands

[3]Nonlinear Nanophotonics, MESA+ Institute for Nanotechnology, University of Twente, P.O. Box 217, 7500 AE Enschede, The Netherlands

* l.chang@utwente.nl

We developed a signal processing method that enables parallel sensing with multiple microrings on the same bus waveguide. The basic idea is to utilize fast Fourier Transform (FFT) and inverse fast Fourier Transform (IFFT) to identify signals originating from rings with different free spectra ranges (FSR). We demonstrate this algorithm with a refractive index sensing measurement. Compared with the conventional single-ring-single-resonance method, it shows improvements in multi-channel capability and higher time resolution with the same experiment hardware.

Keywords**:** *Integrated Optics, Ring Resonators, Parallel Sensing, Fourier Transform*

INTRODUCTION

Integrated optical microring sensors have been widely researched for applications such as biosensing, and chemical analysis [1-3]. High quality (Q) factor ring resonator sensors with Q > 10^5 and the detection limitation of 10^{-6} refractive index units (RIU) have been demonstrated [2]. In these studies, one of the many resonances from a single ring is tracked. In order to multiplex this type of sensor, N times rings need to connect to N times individual bus waveguides in parallel. This means splitting input laser power by N. Furthermore, it required N times photodetectors and N times corresponding data acquisition system. This not only leads to a much more complex system but also more noise per channel due to the N times less optical power in every channel (unless N time more powerful laser is used).

Positioning M rings in serial on the same bus waveguide, eliminates the power splitting and only requires one detector for all M channels (rings). However, resonances from all M rings are mixed on the same detector. Therefore, clear separation and identification is key. This involves both the physical level signal separation and the software level identification. In this work, we will discuss in detail how to achieve this in-serial multiplexing. The advantage of this in-serial multiplexing is that it is completely compatible with the N time in-parallel multiplexing mentioned above. Therefore much larger degree of multiplexing of M×N channels is achievable by combing both in-serial and in-parallel multiplexing.

In this work, we discuss in detail the system design, simulation, and signal processing steps with measured data. Then the algorithm is further verified by experimentally demonstrating NaCl solution concentration sensing with a 4-ring system.

SYSTEM DESIGN AND SIMULATION

An example of optical chip design is shown in Fig. 1 (a). Four high Q rings with different radii are evanescently coupled to one bus waveguide. A tunable laser is butt-coupled from the left, and the transmitted intensity as a function of wavelength (i.e., optical frequency) is measured from the right. The simulated transmission spectra (i.e., near the wavelength of 1030 nm) of the individual rings and their combined transmission are shown in Fig. 1 (b). One could not identify which resonances originated from which ring from the combined transmission spectrum directly. This becomes possible by analyzing the data in the Fourier domain if we take care of the following three aspects of the system design. First, rings on the same waveguide need to have different radii. This leads to different FSR, therefore, different resonance periodicities that could be identified with FFT. Second, a higher Q factor is preferred in order to multiplex more rings on the same bus waveguide. This is due to the fact that a higher Q means smaller full width at half maximum (FWHM). Therefore, more resonances (from other rings) fit in one FSR. Third, by decreasing the ring size, thus increasing the FSR could also increase the multiplex ability. However, in order to clearly distinguish different FSR in the Fourier domain, the laser should scan over multiple FSR. Therefore, there is a limitation to the maximum FSR for a given tunable laser source.

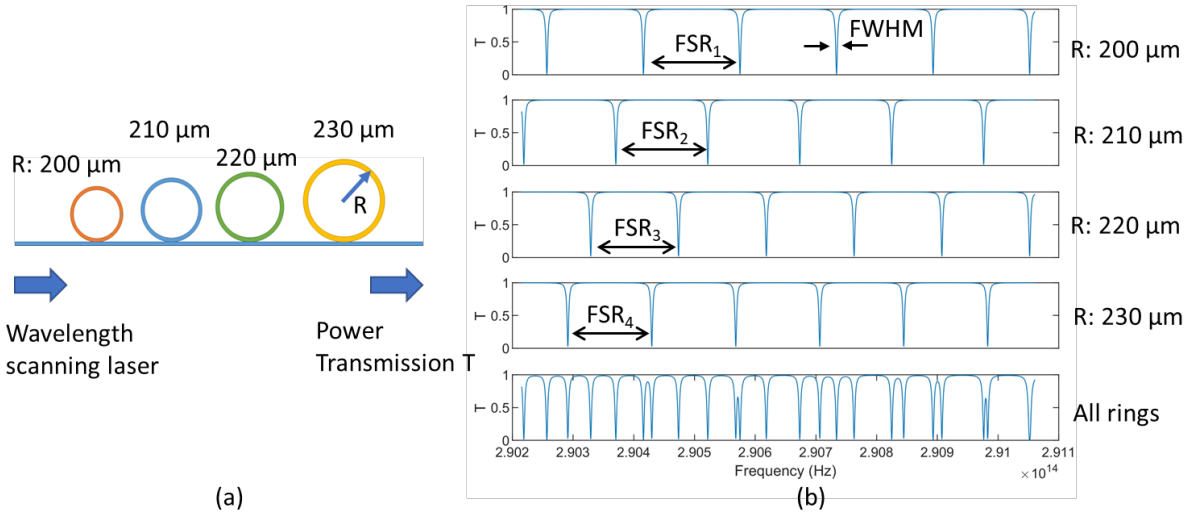


Fig. 1. (a) Example an optical chip layout with 4 rings on one bus waveguide. (b) Simulated transmission spectra (near a wavelength of 1030 nm) of the individual rings and their combined (multiplication of the individual transmission) transmission.

EXPERIMENT RESULTS AND ANALYZE

In our ring resonator sensing experiments, a tunable laser Toptica CTL1050 is used, which could scan from 1020 nm (2.9391×10^{14} Hz) to 1070 nm (2.8018×10^{14} Hz). A small section of a measured spectrum of a 4-ring chip is shown in Fig. 2 (a). The FFT of the measured spectrum is shown in Fig. 2 (b), where the x-axis has been scaled to show the radius of the rings. Peaks at 200 µm, 210 µm, 220 µm, and 230 µm are corresponding to the ring size we fabricated on the chip. Higher order peaks (at integer times of these radii) are clearly visible in these high Q rings. In order to obtain all the resonances of ring 1 (R: 200 µm), data near the peaks of 200 µm, 400 µm, 600 µm … (up to 5000 µm) are selected (set other data to 0), and then IFFT. This process is repeated for every ring and the result is shown in Fig. 2 (c). All resonances of every ring are able to be identified. It also becomes clear that the higher peaks in the regional data are caused by resonance overlap from different rings.

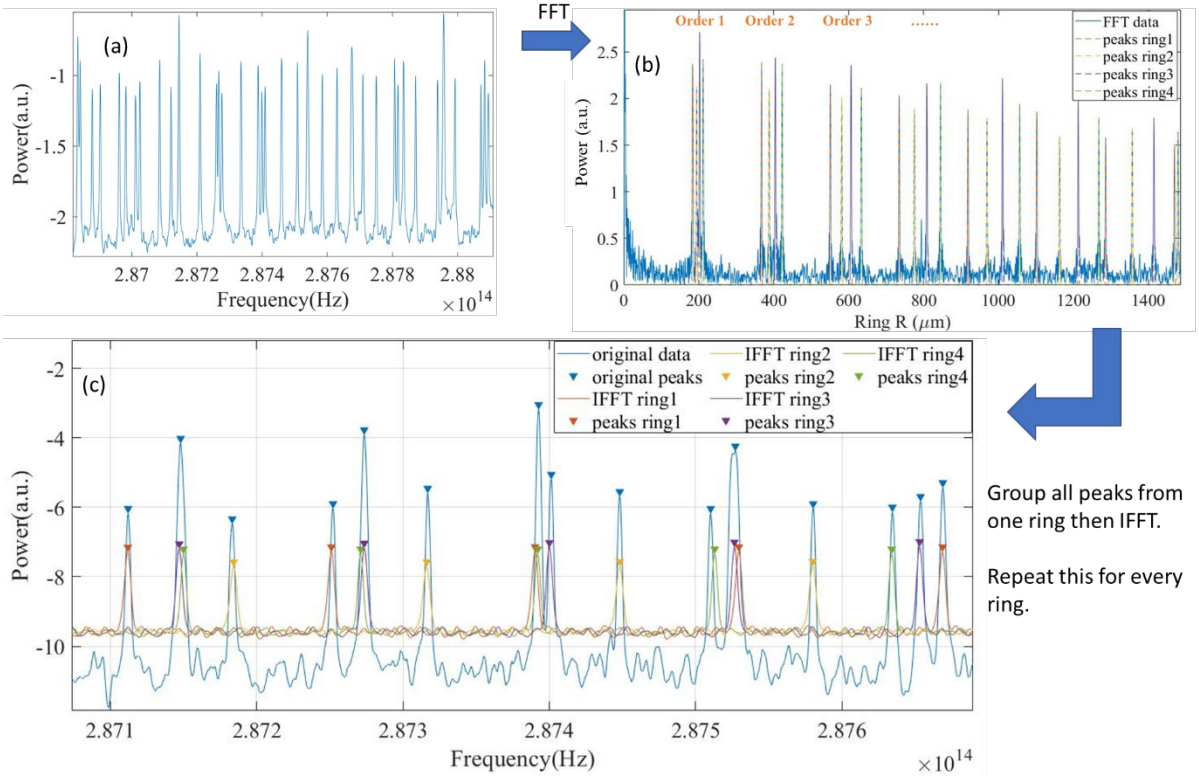


Fig. 2. (a) A small section of a measured spectrum of a 4-ring chip. In our data acquisition system, lower optical power has a higher output number, therefore, resonance drops become peaks in this plot. It has no influence on further data processing. (b) FFT of, (a), the measured spectrum. (c) Four times (1 time per ring) IFFT of the selected peaks in (b) overlay with the measured spectrum. Every IFFT includes all peaks from the same ring from order 1 to order 25.

In this study, by following all resonances instead one, we also improve the time resolution. Every resonance in the IFFT data is measured at a different moment in time. The scanning speed (2 nm/s) of the laser is known. Therefore, by tracking every peak in the IFFT data instead of only one peak, we largely increase The sensing time resolution from 1 point/scan to over 100 points/scan.

NaCl water solution concentration sensing is used to demonstrate this algorithm for identifying moving resonances in a sensing application. An image of the chip with PDMS microfluidic channel is shown in Fig. 3 (a). NaCl solution with different concentration flow over ring 2. As shown in Fig. 3 (b), resonances of ring 2 shift with different NaCl concentrations, and resonances from other rings stay the same. Therefore, this algorithm works for real sensing applications. Due to the improved time resolution, fast changes at the moment of switching concentration are tracked. Since we only record data during the forward wavelength scan, there are gaps, in time, after every scan (time for the laser to move back to its starting wavelength). These gaps are noticeable if they happened at the moment of fast resonance shift as seen in Fig. 3(b) where the refractive index changes fast.

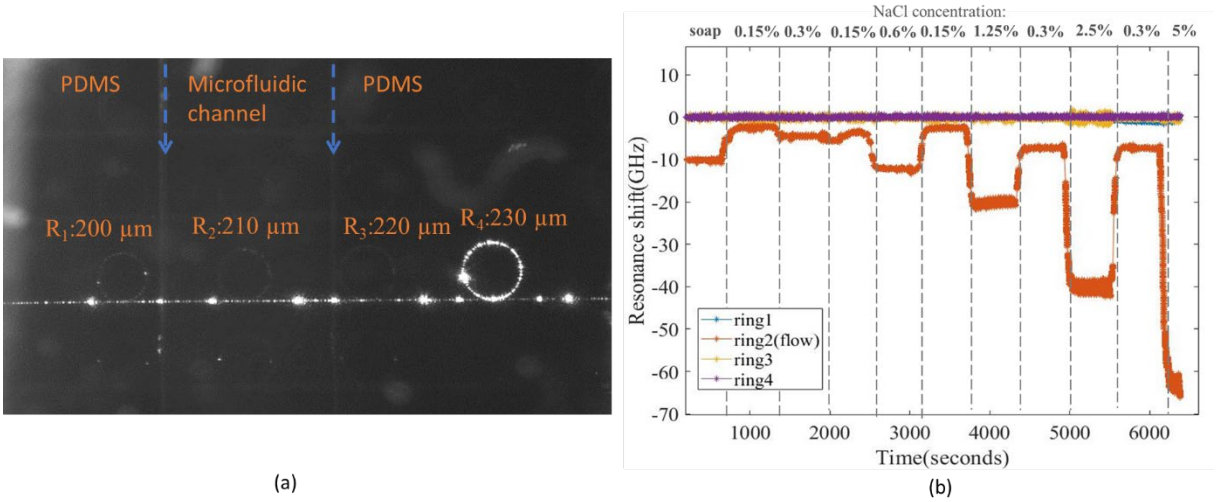


Fig.3. (a) An image the chip with 4 rings on one bus waveguide, and PDMS microfluidic channel over ring 2. (b) Resonance shift of all 4 rings over time. Only ring 2 changes due to various NaCl concentration.

CONCLUSIONS AND OUTLOOKS

This work demonstrates in-serial parallel sensing on one bus waveguide. The developed analysis algorithm is not only able to identify signals from different rings but also improves the time resolution. We believe this is a promising technique and several aspects can be further studied. For example, we would like to investigate the maximal number of rings that could be measured on one bus waveguide. We notice that the noise of this algorithm seems smaller than directly following one resonance in the measured spectrum even in the case of only one ring on the bus waveguide. We will carefully verify this finding and explain it in future.

References

[1] X. D. Fan, I. M. White, S. I. Shopova, H. Y. Zhu, J. D. Suter, and Y. Z. Sun, "*Sensitive optical biosensors for unlabeled targets: A review*," (in English), Anal. Chim. Acta, vol. 620, no. 1-2, pp. 8-26, Jul 14 2008.

[2] M. de Goede et al., "*Al2O3 microring resonators for the detection of a cancer biomarker in undiluted urine*," Opt. Express, vol. 27, no. 13, pp. 18508-18521, 2019/06/24 2019.

[3] P. Steglich, M. Hülsemann, B. Dietzel, and A. Mai, "*Optical biosensors based on silicon-on-insulator ring resonators: A review*," (in English), Molecules, vol. 24, no. 3, p. 519, Feb 1 2019.

Taiji Resonators for Self-Referenced Exceptional Point Sensing

(Student paper)

Bjorn Jongebloed[1*], Ward A.P.M. Hendriks[1], Sonia M. García-Blanco[1]

[1]Integrated Optical Systems, University of Twente, P.O Box 217, 7500 AE Enschede, the Netherlands
[*]b.jongebloed@utwente.nl

Integrated photonics can be used to create biosensors. By integrating a microring resonator with a Bragg grating, a self-referenced sensor can be created. The self-referenced sensor is a robust sensor, since it is sensitive to the presence of biomarkers, while being insensitive to temperature and bulk refractive index variations. To improve the sensitivity of the sensor, the microring resonator can be replaced by a Taiji resonator. This paper discusses the theoretical potential of this device for exceptional point sensitivity.
Keywords**:** *Biosensing, Self-referenced sensors, Taiji resonator, Exceptional points*

INTRODUCTION

Integrated photonics is a promising technology to create devices that scale-up non-invasive diagnostics. For example, photonic integrated circuits (PICs) can be fabricated that contain microring resonators, that are well-suited to be used as biosensors. The microring resonator (MRR) can sense changes in the environment of the device by measuring changes in the resonance spectrum. In biosensing applications, the resonator is typically covered with acceptor molecules that selectively bind to a particular biomarker. If a bodily fluid is studied, such as blood or urine, the biomarkers in the sample can attach to the acceptor molecules. As a result, the effective refractive index of the waveguide changes locally, resulting in a changed optical path length. The change in optical path length causes the resonances to shift, which can be measured.

In a standard MRR sensor, shifts in resonance frequency can be caused by a variety of factors, including changes in temperature and variations in the bulk refractive index. As a result, simply observing a shift in resonance does not necessarily mean that biomarkers have bound to the acceptor molecules. To ascribe changes in the resonance spectrum to the presence of biomarker molecules, a reference is required. The reference is used to distinguish between different signal sources. Typically two transducers, or rather MRRs, are used. One of the MRRs is sensitive to biomarker adhesion, the other is not. However, using multiple transducers can introduce uncorrelated noise. To compensate for the uncorrelated noise contributions, a self-referenced MRR can be designed.

The self-referencing behaviour of the sensor is obtained by including a waveguide Bragg grating (WBG) in the path of the cavity. The WBG acts as a reflector, lifting the degeneracy between the clockwise and counterclockwise resonator mode. As a result, the single resonances split into resonance doublets. The frequency separation of the resonances in the doublet is directly related to the WBG reflectivity. By measuring the frequency separation, instead of the absolute position of the resonances, any signal that changes the grating reflectivity can be measured [1]. By filling the trenches of the WBG with acceptor molecules, the reflectivity changes upon biomarker adhesion. Since the reflectivity is primarily affected by the biomarker adhesion, rather than the temperature and bulk refractive index variations, the MRR with WBG is said to be self-referenced. As a result, the sensor readout becomes insensitive to these temperature and bulk refractive index variations.

Self-referencing of MRRs has been demonstrated in Al_2O_3 PICs, in which the resonator cavity is equiped with a PMMA WBG [1, 2]. These devices are highly sensitive to changes in the grating reflecitivity, which is sensitive to changes in the index contrast. The index contrast changes strongly upon biomarker-acceptor binding, but it is less sensitive to temperature and bulk refractive index changes. It is believed that the sensitvity to changes in index contrast can be improved by moving to so-called exceptional point sensors [3]. In this paper, a design for an exceptional point sensor, that still exhibits self-referenced behaviour, is presented.

TAIJI RESONATORS

Exceptional points may show up in non-Hermitian systems. One of the structures that exhibits the loss-gain mechanism needed to find exceptional points is the so-called Taiji resonator. The non-Hermicity of the system can be exploited to show phenomena such as unidirectional reflection, that is an important aspect in unidirectional lasers [4]. However, the use of Taiji resonators may also pave the way for sensors with exceptional point sensitivity. At an exceptional point, the sensor read out varies with the nth square root of a specific parameter, instead of linearly. The use of a Taiji resonator as a self-referenced exceptional point sensing is studied in this paper.

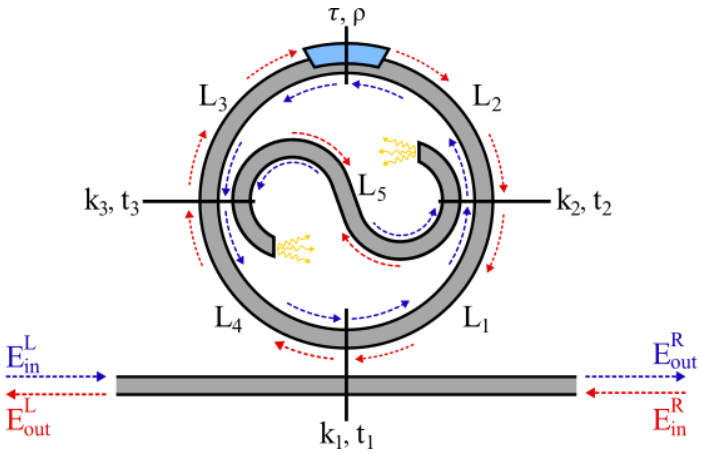


Fig. 1. Geometry of a self-referenced Taiji resonator.

To show the promising behavior of the Taiji resonator as an exceptional point sensor, as depicted in figure 1, time-dependent coupled mode theory is applied. Using coupled mode theory, the frequency splitting of a passive Taiji resonator, equipped with a Bragg grating as shown in Figure 1, can be determined by solving [3]

$$\frac{d}{dt}\begin{bmatrix} A_{cw} \\ A_{ccw} \end{bmatrix} = \begin{bmatrix} j\omega_0 - \alpha & \kappa_{12} \\ \kappa_{21} & j\omega_0 - \alpha \end{bmatrix}\begin{bmatrix} A_{cw} \\ A_{ccw} \end{bmatrix}, \tag{1}$$

In this eigenvalue problem, A_{cw} and A_{ccw} correspond to the amplitudes of the modes propagating in the clockwise and counterclockwise direction. The resonance frequency of the modes is given by ω_0, and κ_{12} and κ_{21} represent the coupling from counterclockwise (CCW) to clockwise (CW) mode and vice versa. Finally, α represents the losses experiences by the modes, including propagation losses, as well as losses due to coupling to the counterpropagating mode.

The coupling coefficient κ represents the amount of energy transferred from one mode to another per unit time. In a Taiji resonator, this coupling is not symmetric. In the S-shaped branch within the ring cavity, energy is only coupled from the CW to the CCW mode, while there is no coupling from the CCW to the CW mode through this branch. In this way, there is a loss-gain mechanism that is responsible for the exceptional point sensitivity.

The coupling per roundtrip from the CW to the CCW mode κ_{21}, and the coupling from the CCW to the CW mode κ_{12} are given by

$$\kappa_{12} = \rho\frac{v_g}{L}; \qquad \kappa_{21} = \rho\frac{v_g}{L} + \eta k_2 k_3 \frac{v_g}{L}. \tag{2}$$

In equation (2), v_g is the group velocity and L is the circumference of the outer ring structure of the Taiji resonator. The parameters ρ, k_2 and k_3 represent the grating reflection coefficient and the coupling coefficients between the outer ring and S-shaped branch, respectively. The parameter η represents the phase acquired by propagating through the S-shaped branch. Assuming that the fields in the CW and CCW mode can be described by

$$a_{cw}(t) = A_{cw}\exp(j\omega_0 t); \qquad a_{ccw}(t) = A_{ccw}\exp(j\omega_0 t) \tag{3}$$

and substituting these fields in equation (1) results in

$$j\omega_0\begin{bmatrix} A_{cw} \\ A_{ccw} \end{bmatrix} = \begin{bmatrix} j\omega_0 - \alpha & \rho\frac{v_g}{L} \\ \rho\frac{v_g}{L} + \eta k_2 k_3 \frac{v_g}{L} & j\omega_0 - \alpha \end{bmatrix}\begin{bmatrix} A_{cw} \\ A_{ccw} \end{bmatrix}. \tag{4}$$

To find the resonance splitting, one can find the eigenvalues of the two-by-two matrix described by equation 4. The eigenvalues are given by

$$\omega_{\pm} = j\omega_0 - \alpha \pm \frac{v_g}{L}\sqrt{\rho^2 + \eta k_2 k_3 \rho}, \tag{5}$$

such that the resonance splitting becomes $\Delta\omega = |\omega_+ - \omega_-|$,

$$\Delta\omega = \frac{v_g}{L}\sqrt{\rho^2 + \eta k_2 k_3 \rho}. \tag{6}$$

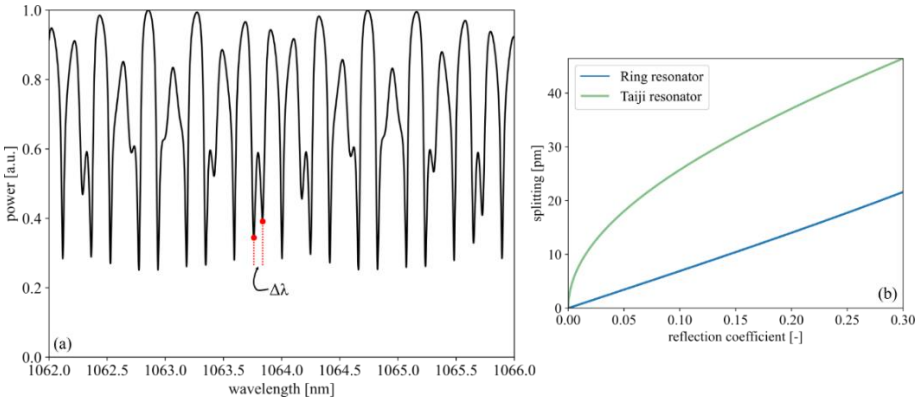


Fig. 2. Transmission spectrum of a Taiji resonator (a), evaluated for $\boldsymbol{L = 3484\ \mu m}$, $\boldsymbol{k_2 = k_3 = 0.7}$, $\boldsymbol{n_{eff} = 1.55}$, $\boldsymbol{\alpha = 0.98}$ *and* $\boldsymbol{\rho = 0.63}$. *The resonance splitting for the Taiji resonator is compared (b) with that of an MRR, where* $\boldsymbol{k_2 = k_3 = 0}$.

The frequency splitting is maximized if $\eta = 1$. In case $\rho \ll k_2 k_3$, then $\rho^2 \ll k_2 k_3 \rho$, and equation 5 reduces to

$$\Delta\omega = \frac{v_g}{L}\sqrt{k_2 k_3 \rho} \propto \sqrt{\rho}. \tag{7}$$

In this limit, the resonance splitting grows with the square root of ρ meaning that the sensor operates at an exceptional point. If the S-shaped branch would not have been there, so $k_2 = k_3 = 0$, or if the aforementioned limit does not hold, the frequency splitting would be proportional to $\Delta\omega \propto \rho$.

To support the claim that the Taiji resonator allows for exceptional point sensitivity, the full transmission function of the device is derived. The transmission function follows from applying the scattering matrix method to the waveguide structure shown in figure 1. The transmission function is given by

$$T = \left| t_1 - \frac{\left(\alpha^4 L_1 L_2 L_3 L_4 e^{j\beta L}\right)^2 \det S\, t_1 t_2^2 t_3^2 k_1^2 - \left(\alpha^5 L_1 L_2^2 L_4 L_5 e^{j\beta(L_1+2L_2+L_4)} e^{j\beta L_5}\right)\rho t_2 k_1^2 k_2 k_3 + \left(\alpha^4 L_1 L_2 L_3 L_4 e^{j\beta L}\right)\tau k_1^2 t_2 t_3}{1 + 2(\alpha^5 L_1 L_2^2 L_4 L_5 e^{j\beta(L_1+2L_2+L_4)} e^{j\beta L_5})\rho t_1 t_2 k_2 k_3 - 2(\alpha^4 L_1 L_2 L_3 L_4 e^{j\beta L})\tau t_1 t_2 t_3 - (\alpha^4 L_1 L_2 L_3 L_4 e^{j\beta L})^2 \det S\, t_1^2 t_2^2 t_3^2} \right|^2 \tag{8}$$

and a section of the spectrum is shown in figure 2a. In equation 8, α represents the propagation losses and β refers to the propagation constant of the waveguide mode. The parameter L_i, t_i and k_i correspond to the arc lengths, coupling coefficients and transmission coefficients as shown in figure 1. Finally, ρ and τ give the reflection and transmission coefficient of the WBG, while S describes the scattering matrix of the WBG. To show the improved sensitivity, the resonance splitting is monitored as the reflection coefficient changes. The resulting resonance splitting for a regular self-referenced MRR sensor and the Taiji resonator is shown in figure 2b. From this figure, it is evident that the Taiji resonator allows for a higher sensitivity with respect to changes in grating reflectivity.

CONCLUSION AND OUTLOOK

Under specific conditions, the Taiji resonator allows for exceptional point sensitivity while maintaining self-referenced behavior. Comparing the resonance splitting in a regular self-referenced MRR with the resonance splitting in the Taiji resonator, it is clear that the resonance splitting varies with the square root of the reflection coefficient. This square root dependence is an indication of exceptional point sensitivity.

The following step is to fabricate the Taiji resonators that are equipped with a WBG. After fabrication, it is important to demonstrate that resonance splitting can be observed in the Taiji resonators in practice. Afterwards, the sensitivity of the device is to be determined, such that a comparison can be made with the self-referenced MRR sensors. To continue the study of the self-referenced Taiji resonators, the devices are fabricated from Al_2O_3 and those devices are provided with a Bragg grating made from PMMA. From these first experiments, resonance splitting has been observed. Future work involves the determination of the sensitivity of the devices.

References

[1] M. de Goede et al., *Al_2O_3 microring resonators for detection of cancer biomarker in undiluted urine*, Optics Express, vol. 27, no. 13, pp. 18508, 2019
[2] B. Jongebloed et al., *Grating engineering for self-referenced Al_2O_3 microring resonator sensors*, in proceeding of the IEEE Photonics Benelux Annual Symposium, 2022
[3] Q. Zhong et al., *Sensing with exceptional surfaces in order to combine sensitivity with robustness*, Physics Review Letters, vol. 122, no. 15, pp. 153902, 2019
[4] A. Calabrese, *Unidirection reflection from an integrated 'taiji' microresonator,* Phot. Research, vol. 8, no. 8, pp. 1333, 2020.
[5] H. A. Haus, *Waves and fields in optoelectronics TT*, Prentice-Hall, Englewood Cliffs, pp. 197-234, 1984.

High-frequency Scalable Modelling of 100 GHz Class Uni-Travelling Carrier Photodiodes

Student paper

Risab Gnanamani[1,2], Chhandak Mukherjee[1], Christophe Caillaud[2], Marina Deng[1], Herve Bertin[2], Nicolas Vaissière[2], Cristell Maneux[1]

[1] IMS Laboratory, University of Bordeaux, UMR CNRS 5218, 33405 Talence, France
[2] III-V Lab, A Joint Lab between Nokia Bell Labs, Thales Research & Technology and CEA-LETI, 91767 Palaiseau, France
* risab.gnanamani@3-5lab.fr

In this paper, we demonstrate a scalable compact model to predict the performances of high speed UTC-PDs up to 110 GHz. Excellent agreement between the model and measurements has been achieved, allowing to find the optimal diode dimension for bandwidth up to 70 GHz.
Keywords: *UTC-PD, Predictive modelling, Optimization*

INTRODUCTION

With the continuous increase in data traffic, the need for high bandwidth optical receiver is growing. Uni-travelling carrier photodiodes (UTC-PD) are remarkable candidates as their operation relies only on electron transport [1]. We have recently reported high speed and high responsivity photodiodes of bandwidth above 70 GHz with 0.6 A/W responsivity [2]. In this paper, we focus on the development of a scalable model for these components capable to predict bandwidth up to above 70 GHz, which allows us to optimize PD geometry and determine the main limitation of photodiode structure for further optimization.

SCALABLE MODEL DEVELOPMENT AND RESULTS

S-parameter (S11) measurements up to 110 GHz under three bias points (-0.5V, -1V, -2V) were performed on our photodiodes of various dimensions and on their corresponding test structures following SOLT calibration. The parasitic effects of pads and transmission lines were removed using a de-embedding method described by Eq. (1) [3], where the inputs are the measured S-parameters of the diode (S_{meas}) and the related open (S_{OC}) and short circuit (S_{SC}) test structures.

$$S_{de-emb} = \frac{S_{OC} + S_{SC} - 2S_{meas} - S_{meas}(S_{OC} - S_{SC})}{2S_{OC}S_{SC} + S_{SC} - S_{OC} - S_{meas}(S_{OC} + S_{SC})} \quad (1)$$

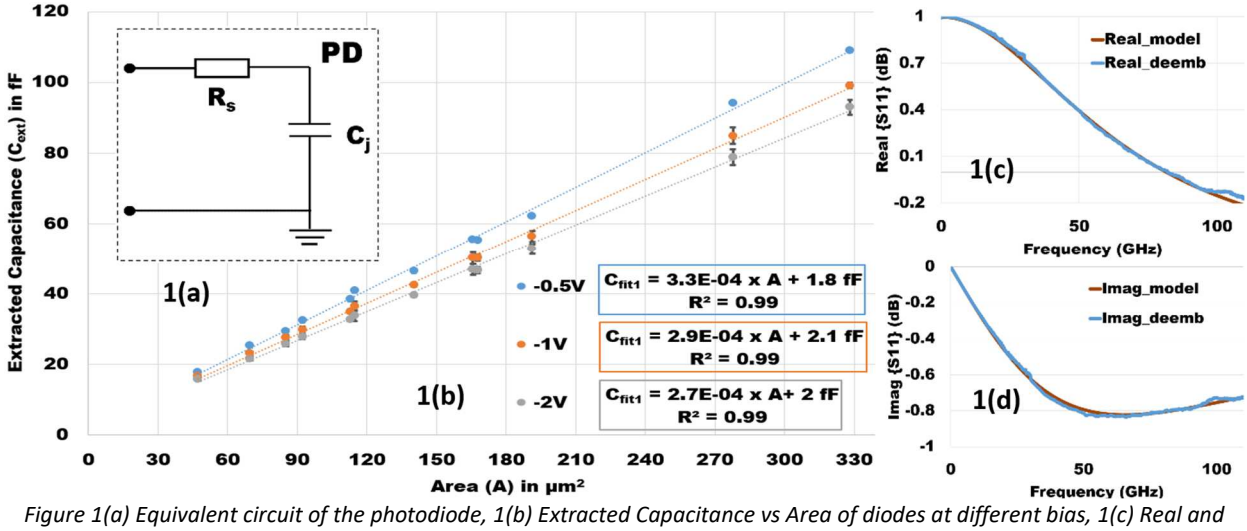


Figure 1(a) Equivalent circuit of the photodiode, 1(b) Extracted Capacitance vs Area of diodes at different bias, 1(c) Real and 1(d) Imaginary parts of S11 showing equivalent model fit with the De-embedded measurements for a 5x25µm² diode

Next we extract the parameters of the equivalent circuit (Fig. 1(a)) for each diode geometry in comparison with the de-embedded S-parameters. We plot the extracted values of the junction capacitance (C_{ext}) over surface from the model fitting (Fig. 1(b)), with standard deviation reported for the -1V and -2V curves, depicting linear area-dependence of the capacitance. A very good agreement between de-embedded measurements and the model is observed, as shown in In Fig. 1(c) and (d), for a 5x25µm² PD. The error bars in Fig.1(b) show the standard deviation

ranging between 0.3-2.1 fF. From the linear regressions, we can formulate Eq. (2) (reported for -2V), to model the scaling behavior of the junction capacitance (C_{fit1}).

$$C_{fit1}(-2V) = (2.74 \times 10^{-4} \times A\,) + (2 \times 10^{-15}\,) \quad (2)$$

From Eq. (2), we observe that there is a 2 fF parasitic capacitance independent of the surface area which roughly remains constant for all biases. To elaborate a geometry-dependence of the capacitance, we refer to the parameter scaling methodology associated with HICUM model [4] and write the extracted capacitance as shown in Eq. (3) in terms of the area (A) and perimeter (P), which is then transformed into Eq. (4)

$$C_{ext} = C_A.A + C_P.P \quad (3)$$

$$\frac{C_{ext}}{A} = C_A + C_P.\frac{P}{A} \quad (4)$$

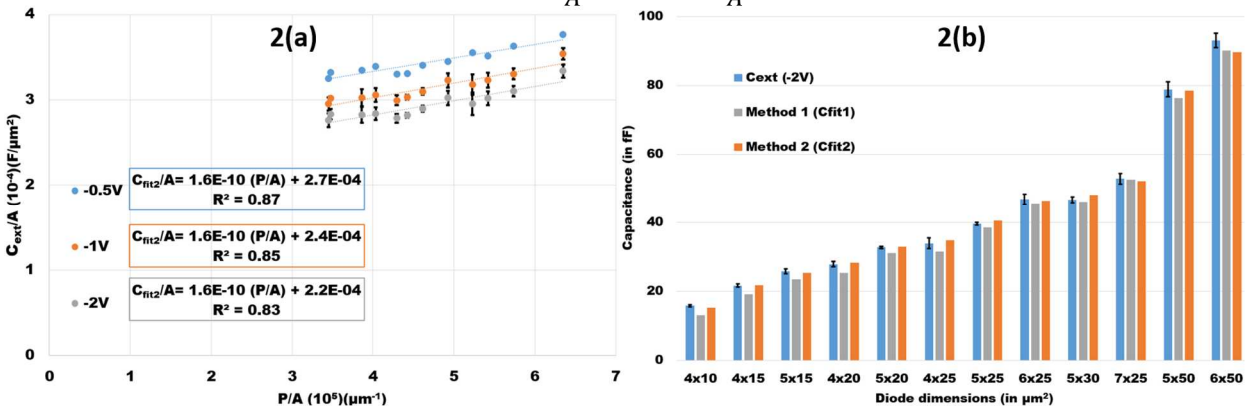


Figure 2(a) Dimensional capacitance contribution extraction plot, 2(b) Extracted and simulated capacitances at -2V

The normalized capacitance in Eq. (4) is plotted in Fig. 2 (a) as a function of the quantity P/A from which intrinsic capacitance C_A and perimeter-dependent component C_P can be extracted from the intercept and the slope, respectively, for different bias voltages as shown in inserts of Fig. 2 (a). We can observe that the perimetric contribution C_P is practically independent of the bias, hence it's not depend on PD junction, but on the surrounding (passivation, …). C_P plays a smaller contribution in bigger PDs and a larger part of capacitance in smaller PDs, with maximum of 20.5% for 4x10µm^2 PD. Fig. 2 (b) shows that method 2 gives better accuracy than method 1 for the capacitance, with error less than 1 fF. We can then estimate the depletion thickness, *d*, for each bias voltage from the C_A using the standard capacitance formula (eq. (5)) as listed in Table 1(a) that would be used, in turn, to calculate the transit times.

$$d_{@2V} = \frac{\varepsilon_0 \times \varepsilon_r}{C_{A@2V}} \quad (5)$$

d at each bias	Thickness in nm
-0.5V	437
-1V	504
-2V	549

Bias	f_{RC}_4x10	f_{RC}_4x15	f_{tr}	V_s_4x15
-1V	124 GHz	99.7 GHz	100 GHz	1.2x10^5
-2V	135 GHz	108 GHz	80 GHz	1x10^5

Table 1(a) Depletion layer thickness at each bias, 1(b) RC & transit cut-off frequency, electron velocity of diodes at different bias

In our photodiodes, we have a 440 nm collector (including undoped absorber and transition layer) followed by a 180 nm absorber gradually doped to boost photodiode transit time [1]. The strong bias dependence of the depletion width can be explained by the low doping of the absorber-collector interface.

The same scaling methodology is followed for the diode series resistance (R_{ext}). To have a linear model we convert extracted resistance into conductance (G_{ext}) for the analysis. In a similar manner as before, Eq. (6) can be obtained from the conductance vs P/A plot (Fig. 3(a)), where the slope and intercept give the perimeter-dependent component (G_P) and the intrinsic conductance (G_A), respectively. Using the scaling equation, we can recalculate the resistance, as shown in Fig. 3(b) along with the extracted resistance, depicting very good agreement.

$$G_{fit}(-2V) = (3.4 \times 10^8 \times A\,) + (8 \times 10^2 \times P\,) \quad (6)$$

Once the scaling rules for the diode R-C elements are accurately extracted, we can model the full frequency response (Fig. 4(a)), by calculating the transit time using the standard UTC-PD photocurrent equation [1] together with the equivalent circuit shown in Fig. 4(b). With the known the values, we readjusted the electron velocity in the collector (V_{s1}=1.2x10^5 and V_{s2}=1x10^5 for -1V and -2V, respectively) to obtain a better fit the measured bandwidth.

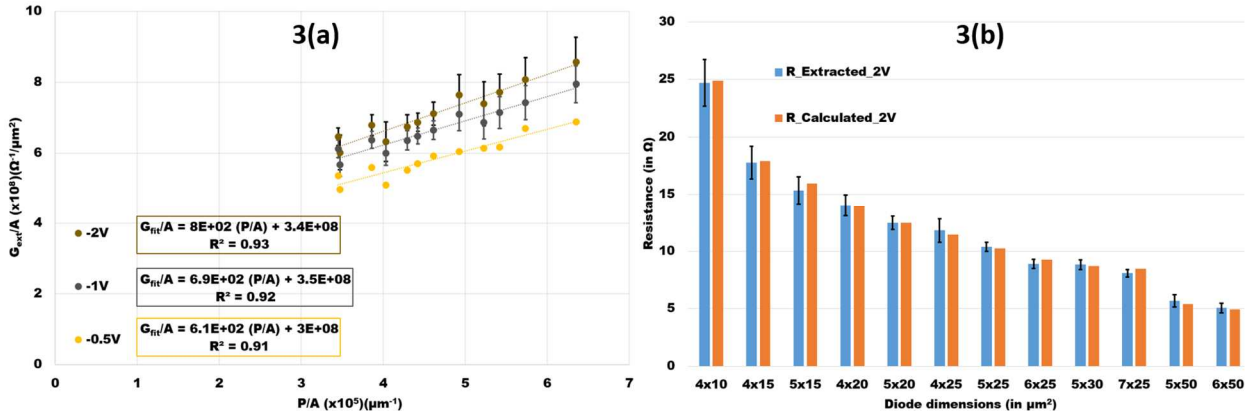


Figure 3(a) Dimensional conductance contribution extraction plot, 3(b) Extracted and simulated resistances at -2V

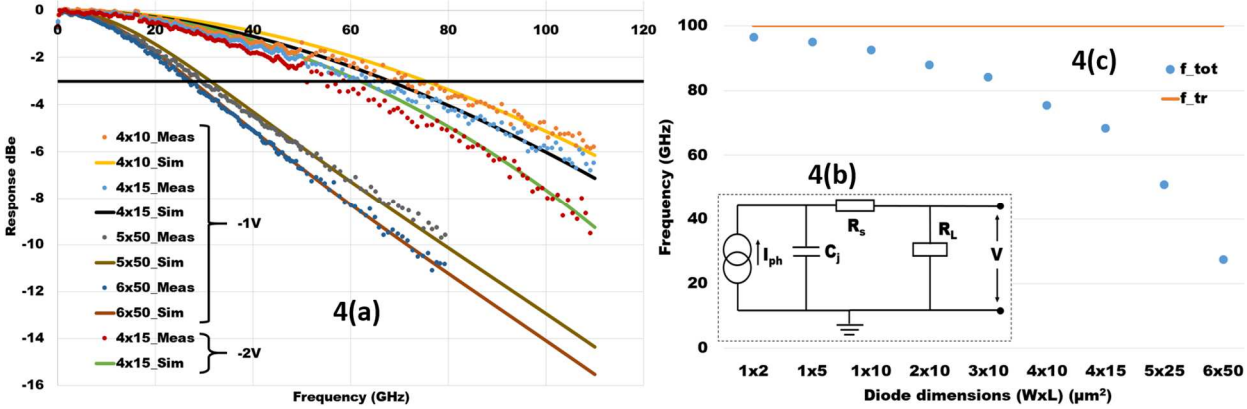


Figure 4(a) Frequency response of PDs of different dimension (in µm²) at different bias 4(b) Equivalent circuit for RC response 4(c) Response of extrapolated dimensions using our predictive model

With the same electron velocity at -1V, we simulate responses of various diodes under 1mA photocurrent (I_{ph}) in Fig. 4(a), showing good agreement between simulated data and the measured response. We also compare measured and simulated frequency responses of a 4x15µm^2 photodiode at -1V and -2V. From the measured response, we see that the 3dB bandwidth is around 62 GHz at -1V, and around 57 GHz at -2V for 4×15 µm² PD and 71 GHz at -1V for 4×10 µm² PD. Transit times of the diodes are listed in Tab. 1(b). Note that the variation of electron velocity is the dominant factor for transit time limited response; hence higher bandwidth can be obtained by reducing the collector thickness. From our model, Fig. 4(c) shows that maximum bandwidth is 100 GHz and that below 2x10µm^2 (88 GHz) bandwidth improvement is negligible. To improve further, reducing the collector thickness is the only way.

CONCLUSION

We have demonstrated a scalable modeling approach for the R-C parameters in UTC-PDs, which can accurately capture the high-frequency behavior of the device and can be used for predicting its physical characteristics through geometrical extrapolation of parameter values. The model has been validated for a wide range of dimensions and bias voltages. The benefit of our proposed scalable model lies in its use in future designs especially to accurately and reliably predict the high-frequency performance of scaled devices. From our predictive model, we have shown that our structure can reach up to 88 GHz bandwidth. In future iterations of this work, we plan on further exploring the scalable model for predictive simulation in the context of optoelectronic integrated circuits.

References

[1] T. Ishibashi, N. Shimizu, S. Kodama, H. Ito, T. Nagatsuma, and T. Furuta, "*Uni-Traveling-Carrier Photodiodes*" in Ultrafast Electronics and Optoelectronics, 1997, p. UC3.

[2] C. Caillaud *et al.*, "*Ultra Compact High responsivity Photodiodes for >100 Gbaud Applications*" *2021 European Conference on Optical Communication (ECOC)*, 2021, pp. 1-4, doi: 10.1109/ECOC52684.2021.9606076.

[3] D. Konstantinou, C. Caillaud, S. Rommel, U. Johannsen, and I. Tafur Monroy, "*Investigation of de-embedding techniques applied on uni-traveling carrier photodiodes*" Int. J. Microw. Wirel. Technol., pp. 1–13, 2021

[4] B. Ardouin et al., "*Modeling and parameter extraction of SiGe: C HBT's with HICUM for the emerging terahertz era*," The 5th European Microwave Integrated Circuits Conference, Paris, France, 2010, pp. 25-28.

Ultra-High-Extinction-Ratio Electro-Optic Switch Element

(Student paper)

Peng Bao[1], Chunhui Yao[1], Jinlong Wei[2], Giuseppe Talli[2], Maxim Kuschnerov[2], Qixiang Cheng[1,*] and Richard Penty[1]

1. Centre for Photonic Systems, Electrical Engineering Division, Department of Engineering, University of Cambridge, 9 JJ Thomson Avenue, Cambridge, CB3 0FA, U.K.
2. Huawei Technologies Duesseldolf GmbH, European Research Center, Riesstraße 25, 80992 Munich, Duesseldolf, Gemany

[*] qc223@cam.ac.uk

We present a novel approach for designing 2×2 electro-optic switch elements with ultra-high extinction ratio that offsets the impact of modulating-indueced free-carrier absorption. A curved directional coupler with tunable coupling efficiency and a differential electro-optic phase shifter pair are employed to correct any loss and phase imbalance in a Mach-Zehnder interferometer structure. Simulations show that the proposed device can completely suppress the crosstalk at the designed wavelength of 1550 nm and maintain <-30 dB crosstalk over a bandwidth from 1530 nm to 1570 nm, ideally for constructing a large-scale electro-optic switch fabric.

Keywords: *Optical switches, photonic integrated circuits, high-extinction-ratio, electro-optic.*

Introduction

The exploding demands for cloud services have promoted the need for massive data traffic within data centres. To meet this rapid growth in data volume, switching technologies with high speed, large bandwidth, and low crosstalk are desired. Leveraging mature CMOS technologies, the silicon-on-insulator (SOI) platform features low cost, compact footprint, and low power consumption, and hence is regarded as a promising platform for developing high-performance optical switching technologies for data centre applications. Mach-Zehnder interferometers (MZIs) are widely used on the SOI platform for broadband optical switching, permiting nanosecond-scale switching speed by using electro-optic (E-O) phase shifters. However, current E-O switch elements usually have a limited extinction ratio, restricting them from being implemented for switches with large port counts. Due to the fabrication imperfections, the non-uniform power splitting ratio (i.e., deviating from the ideal 50:50) of the 3-dB couplers in the MZI increases the crosstalk. In addition, E-O phase shifters typically rely on p-i-n junctions that operate in carrier injection mode. The injected carriers not only modify the refractive index of the waveguide to realize the phase shift, but also induce undesired inherent insertion loss due to free-carrier absorption (FCA). This is problematic for an MZI-based switch operating in the bar state, where only one of the phase shifters is turned on. The FCA-induced loss causes a power imbalance inside the interferometer, leading to power leakage into the cross port (i.e., crosstalk). Efforts have been made to improve the crosstalk performance. For example, Ref[1] uses an additional MZI as a variable splitter to compensate for the splitting ratio mismatch between the front and rear splitters [1], whereas nested MZI phase shifters are applied to balance the loss in the two arms [2, 3]. However, these methods require extra active components, which increases the device footprint and complicates the control scheme.

In this paper, we propose a novel design approach of ultra-high-extinction-ratio E-O switch elements. Our design can, in theory, completely suppress the crosstalk and thus achieve an infinite extinction ratio at the designed wavelength by simultaneously balancing the losses in the two MZI arms using a differential E-O phase shifter pair and compensating the fabrication imperfection via a tunable curved directional coupler (DC). Further simulation results indicate a broad bandwidth of at least 40 nm with a crosstalk value below -30 dB.

Device schematic and principle

Figure 1(a) illustrates the schematic of the proposed 2×2 high-extinction-ratio E-O switch element, which consists of a curved tunable DC and a curved DC as the power-splitting elements and a pair of differential E-O phase shifters. As shown by Fig. 1(b), the two metal heaters are allocated asymmetrically on the tunable DC to vary the transverse temperature gradient between the two waveguide cores, such that its power splitting ratio can be tuned larger or smaller to compensate for the potential deviation in the splitting ratio of the other DC due to fabrication imperfections. A pair of differential E-O phase shifters are designed to operate simultaneously to keep the losses of the two MZI arms the same, as shown by Fig. 1(c). Specifically, the differential E-O phase shifter pair counts on the impact of Joule heating which opposes the index modification brought about by carrier injection. When the switch is set in the bar state (i.e., with a π phase difference), the two phase shifters are turned on at different voltage levels, so that one is minimally affected by the Joule heating whereas the other is severely affected that the change

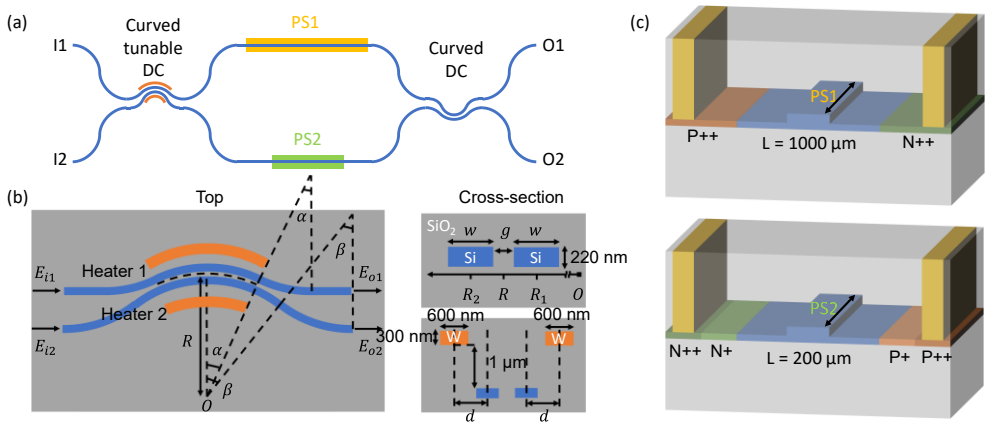


Fig. 1. (a) Schematic of the switch element. (b) Schematic of the curved tunable DC. (c) Cross-section schematic of the differential E-O phase shifters.

in effective refractive index caused by the Joule heating effectively cancels out the change caused by the carrier injection. In this manner, the two phase shifters are able to achieve a π phase difference and maintain the same insertion loss. In the following, the detailed design processes of the differential E-O phase shifter and the tunable DC are discussed successively.

Parameter design and simulations

The tunable DC employs a curved waveguide design, which enables a broad bandwidth as well as a high fabrication variation tolerance compared to conventional ones with straight waveguides. Its asymmetric nature is also suitable to work as a tunable DC. Figure 1(b) shows the schematic structure of the curved tunable DC, where w is the waveguide width, g is the waveguide separation in the coupling region, R and α are the bending radius and bending angle of the coupling region, respectively. The bottom waveguide is bent at a larger angle β to increase the separation from the top waveguide. Two tungsten (W) heaters, with a width of 600 nm and a height of 300 nm, are placed 1 μm above the silicon layer with a lateral distance d to the centre of the coupled waveguides. The structural parameters of the tunable DC are optimized using the particle swarm optimization (PSO) method [4]. The waveguide separation g was set as 300 nm to ensure a sufficient coupling length for thermal tuning and β was set to twice the value of α. The optimized design parameters are $w = 395\ nm, R = 60, \alpha = 9.4°$. The optimal position for the heater is found to be $d = 1\ \mu m$. 3D FDTD simulations were performed to calculate its coupling ratio at different heater power levels. Figure 2(a) illustrates the relationship between the power dissipated by the curved tunable DC and its cross-coupling ratio. As can be seen, it consumes only about 10 mW of power (0.55 V) to tune the coupling ratio from 0.5 to either 0.45 or 0.55. At this power level, the simulated temperature of the heater is about 169 °C. Figure 2(b) shows the wavelength dependence of the coupling ratio at different power levels. A broad bandwidth can be observed that the coupling ratio of the curved tunable DC decreases by less than 0.05 with the wavelength deviating from 1550 nm within ±20 nm.

To optimize the design of differential E-O phase shifters, we swept the structural parameters, including the doping profile of the p-i-n junction, the width of the intrinsic region, and the length of the phase shifter, and observed the relationship between the insertion loss and the phase shift at different parameters. Our simulation results illustrate that the E-O phase shifter's loss and phase shift characteristics are significantly influenced by its length. Longer phase shifters can provide the same phase shift at a lower insertion loss compared to shorter ones. Besides, phase shifters with a wider intrinsic region and a higher level of doping can also reduce the loss when providing the same amount of phase shift. Accordingly, we designed a differential EO phase shifter pair with different lengths, as detailed in Fig. 1(c). Figures 2(c) and 2(e) depict the curves of the insertion loss versus the phase shift and the I-V characteristics for the differential phase shifters, respectively. To obtain a π phase shift, the pair of phase shifters are designed to be driven by different levels of voltages (the longer phase shifter with 1.7 V while the shorter one with 0.89 V). In this case, their insertion losses keep the same at about 2 dB, while the total power consumption is around 70 mW (0.89 V × 6.6 mA + 1.7 V × 38.1 mA).

To evaluate the crosstalk performance of the proposed high-extinction-ratio E-O MZI, we perform the transfer matrix analysis. The transfer matrices between the input and output electric fields can be expressed as

$$\begin{bmatrix} E_{o1} \\ E_{o2} \end{bmatrix} = C_{curved} \cdot P_{EO} \cdot C_{curved} \cdot \begin{bmatrix} E_{i1} \\ E_{i2} \end{bmatrix} \quad (1)$$

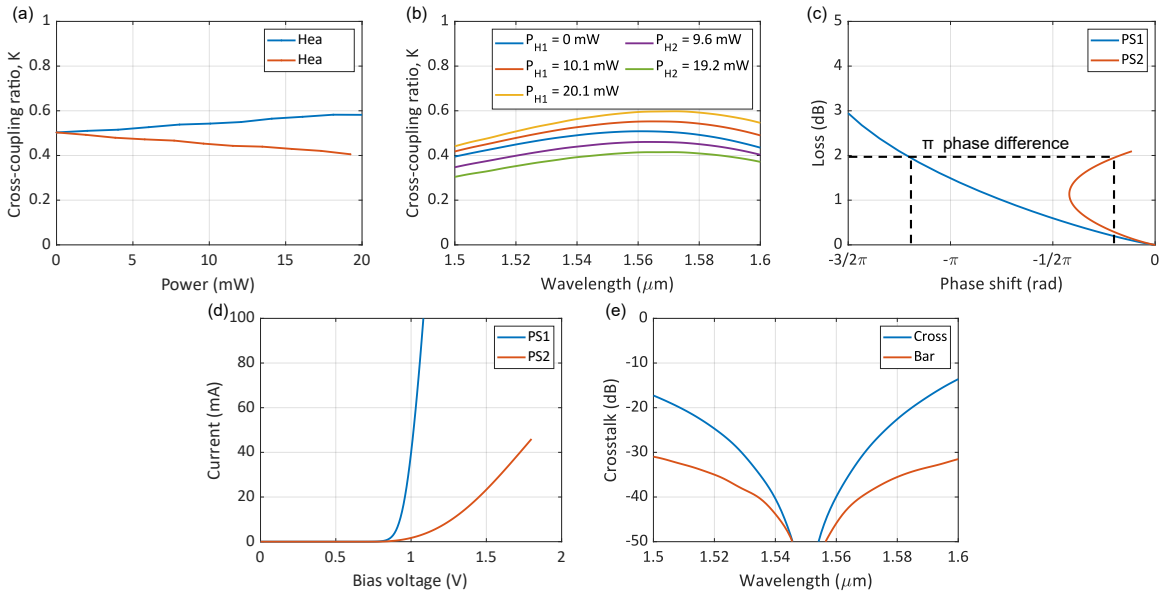


Fig. 2. (a) Cross-coupling ratio versus the power dissipated for the tunable DC. (b) Wavelength dependence of the tunable DC. (c) Insertion loss versus phase shift for the phase shifters. (d) Current versus bias voltage for the phase shifters. (e) Crosstalk versus wavelength for the proposed high-extinction-ratio switch element.

where C_{curved} is the transfer matrix of the curved coupler, and P_{EO} is the transfer matrix of the E-O phase shifter. C_{curved} is given by:

$$C_{curved} = \begin{bmatrix} te^{-j\left(\frac{\pi}{2}+\Delta\varphi'\right)} & ke^{-j\frac{\pi}{2}} \\ ke^{-j\frac{\pi}{2}} & te^{j\left(\frac{\pi}{2}+\Delta\varphi'\right)} \end{bmatrix} \quad (2)$$

where t is the straight-through coefficient, k is the cross-coupling coefficient, and $\Delta\varphi'$ is the phase difference between the two output ports of the curved DC. The transfer matrix of the EO phase shifter P_{EO} is:

$$P_{EO} = \begin{bmatrix} \alpha_1 & 0 \\ 0 & \alpha_2 e^{j\Delta\varphi} \end{bmatrix} \quad (3)$$

where α_1 and α_2 are the optical field transmission factor of the EO phase shifters. Figure 2(e) shows the crosstalk of our high-extinction-ratio E-O switch element in both cross and bar states. The crosstalk was calculated by substituting simulation data into Eq. 1. The simulated crosstalk becomes infinitesimal at 1550 nm for both states. The design good wavelength tolerance with the crosstalke below -30 dB in the range 1530 nm to 1570 nm for the cross state, whilst is it is even smaller in the bar state.

Conclusion

In this paper, we present a novel design approach of a 2×2 E-O switch element with ultra-high extinction ratio and ultra-low crosstalk. A curved tunable DC and a differential E-O phase shifter pair are employed to compensate for any fabrication imperfection and balance electro-absorption losses in the two interferometer arms. The device can completely suppress the crosstalk at 1550 nm, while keeping the crosstalk below -30 dB from 1530 nm to 1570 nm. The compact footprint and feature of high-extinction-ratio make our proposed switch element highly suitable for various switch architectures, such as the double-layer network (DLN) which is sensitive to first-order crosstalk in its middle stage. We foresee the proposed switch element to find wide applications in building high-radix silicon photonic switches with ultra-low crosstalk.

References

[1] K. Suzuki *et al.*, "Ultra-high-extinction-ratio 2 × 2 silicon optical switch with variable splitter," *Optics Express, Vol. 23, Issue 7, pp. 9086-9092*, vol. 23, no. 7, pp. 9086–9092, Apr. 2015

[2] A. v. Rylyakov *et al.*, "Ultralow crosstalk nanosecond-scale nested 2 × 2 Mach–Zehnder silicon photonic switch," *Optics Letters, Vol. 41, Issue 13, pp. 3002-3005*, vol. 41, no. 13, pp. 3002–3005, Jul. 2016

[3] Z. Lu, D. Celo, H. Mehrvar, E. Bernier, and L. Chrostowski, "High-performance silicon photonic tri-state switch based on balanced nested Mach-Zehnder interferometer," *Scientific Reports 2017 7:1*, vol. 7, no. 1, pp. 1–7, Sep. 2017

[4] R. Eberhart and J. Kennedy, "New optimizer using particle swarm theory," *Proceedings of the International Symposium on Micro Machine and Human Science*, pp. 39–43, 1995

Narrow bandwidth tunable optical filter using apodized sampled gratings in InP-based generic integration platform

(Student paper)

Xiao Li[1,2], Kevin Williams[1], Yuqing Jiao[1]

[1]Eindhoven Hendrik Casimir Institute (EHCI), Eindhoven University of Technology, Eindhoven, 5600MB, the Netherlands
[2]Center for Optical and Electromagnetic Research, College of Optical Science and Engineering, State Key Laboratory of Modern Optical Instrumentation, Zhejiang University, Hangzhou 310058, China
* x.li4@tue.nl

We demonstrate a narrow bandwidth tunable optical filter based on cascaded multi-mode interference (MMI) and apodized sampled grating (ASG) on generic InP integration platform. The transmission mode bandpass filter on an active-plus-passive platform can achieve narrow 3 dB bandwidth (BW <0.3 nm) with low non-adjacent/adjacent channel crosstalk (ER > 45.8, SER > 80 dB), low insertion loss (IL < 5 dB), and wide tuning range (FSR = ~20 nm), making it potentially be applied to future densely integrated optical THz heterodyne system.
Keywords: *InP, Foundry, 3-dB Bandwidth, Filter, Apodized Sampled Grating*

INTRODUCTION

Integrated tunable filter is a very important building block for optical data communications and signal processing applications, such as wavelength division multiplexing (WDM), THz heterodyne system, microwave signal generation system, etc. The filter is always required to have narrow bandwidth (BW < 0.5 nm) for THz heterodyne system to select single wavelength for optical injection locking. Many works have been done on the narrow BW filter in recent years, using different structures, like Bragg gratings (BGs), Mach–Zehnder interferometers (MZI), ring resonators, arrayed-waveguide grating (AWG), sampled grating (SG), etc. The reflection from BG needs external device like an optical circulator to extract the filtered light, and the tuning range is restricted by the limited effective index change[1]; the MZI-based filter needs several different elements to achieve narrow BW wavelength selection, which causes high optical loss, and the tuning mechanism can be complicated[2]; The ring resonator with low crosstalk and low insertion loss (IL) is always used in high-index contrast platform. It utilizes the vernier effect to enlarge the free spectral range (FSR)[3]; the AWG-based filter is combined with semiconductor optical amplifiers (SOAs). The circuit requires a large number of SOA gates to control the wavelength selection, bringing challenges in cost and flexibility[4]. In the meanwhile, The sampled gratings (SGs) with comb-like reflection spectrum, always be studied as wide FSR filter using vernier effect, and the BW can be largely reduced using low coupling coefficient of SGs[5,6], which is a promising device to achieve narrow BW tunable optical filter.

The InP-based Photonic Integrated platform is based on butt joint active-passive epitaxy, which provides more flexibility to achieve optical system on one chip[7]. So far narrow BW optical tunable filters are not available on this platform. However, the low-index contrast layer stack in this platform is suitable to achieve such device with SGs.

In this paper, we aim to achieve a narrow bandwidth optical wavelength-tuning filter with low adjacent/non-adjacent channel crosstalk (high extinction ratio/side-lobe extinction ratio, ER/SER), low insertion loss (IL), wide FSR on InP-based generic integration platform. The filter is composed of multiple cascaded multi-mode interferences (MMIs) and ASGs. The transfer matrix method has been used in this work, in order to simulate the reflection spectrum of the filter. The ASG using Gaussian type apodization to modulate the duty ratio of SG periodically can largely increase the SER of the reflection spectrum. Following are the detailed introduction and simulation results of our designed transmission mode bandpass filter.

RESULTS

The layers of the shallow-etched grating (on top of the substrate and below the top cladding) in InP-based generic integration platform is depicted in Fig. 1(a). The gratings are buried in the shallow etched waveguide layer, which have optical properties fixed by the platform, including the coupling coefficient κ as 50 cm^{-1} and effective index n_{eff} as 3.266. The grating layer thickness T and the n-InP layer thickness D in the waveguide core are both 30 nm, and the width of shallow waveguide w is 2 μm[7]. Λ denotes the period of the grating. When selecting the Bragg wavelength λ_{Bragg} as 1550 nm, the Λ can be calculated as 237.3 nm through the Bragg equation $\lambda_{Bragg} = 2n_{eff}\Lambda$. Meanwhile, the duty ratio of grating dr_{BG} = a/ Λ is set to 0.5 for low IL and symmetrical reflection spectrum output.



Fig. 1. (a): Schematic diagram of uniform DBRs in SMART Photonics platform. The layer stack has been simplified, without showing doping differences in p-InP and n-InP layers. (b): Schematic diagram of the top view of tunable filter.

Fig. 1(b) shows a schematic diagram of the tunable filter based on cascaded MMIs and ASGs. The device consists of two 2*2 MMIs with two sets of ASGs. The two ASGs in each set are nominally identical. When light is injected into the 3-dB MMI coupler, the light will be equally divided into two output ports with a π/2 phase difference. Then the light reflected from the ASG1 groups will be constructively imaged into the waveguide other than the input port. In this way, the device can guide the reflected and filtered light without the need of a circulator. By cascading such structures with slightly detuned ASGs, the Vernier effect can be achieved. It could enlarge the FSR for the filter to cover the C band. At the same time, by putting electrodes on different sets of ASGs, we could use current injection or reverse voltage bias to change the refractive index of the grating layer. Under this mechanism, the filter can be tuned with a wide range.

The sampled grating is composed of several gratings with straight waveguides in between. The period, the gratings length in each periodic section, the total number, and the total length of SGs are defined as L_2, L_1, N_{SG}, and L ($L = N_{SG}*L_2$). To easily characterize the sampled grating, we set dr_{SG} ($= L_1/L_2$) as the duty ratio of the sampled grating. The spacing between the peaks FSR_{SG} in the comb-like reflection spectrum can be calculated as follows,

$$FSR_{SG} = \frac{\lambda_{Bragg}^2}{2n_{eff}L_2} \tag{1}$$

It is known that the reflection spectrum from sampled grating always has a high side-lobe level around each peak, which leads to high crosstalk when it is used as a filter. In this case, the apodization method provides an efficient method to suppress the side-lobe extinction ratio, by modulating the refractive index difference in periodic structure, which has been widely used in Bragg grating structures[8]. In InP-based generic integration platform, since the κ constant and the duty ratio of the basic grating is fixed, we choose to modulate L_1 for the SG to achieve an effective apodization. Fig. 2(a) and (b) show n_{eq} and κ profiles of an ASG through modulating $L_1(i)$, where the L_1 in the center of the SG has a maximum L_{1m}. In this paper, Gaussian function is used to apodize the SG as follow,

$$dr_{SG}(i) = dr_{SGm} * \exp\left(-\left(\frac{2.24\left(i-\frac{N_{SG}}{2}\right)}{N_{SG}}\right)^2\right) \qquad i = [1, N_{SG}] \tag{2}$$

where dr_{SGm} is the maximum duty ratio in the center of the SG, which equals L_{1m}/L_2. The i is the section number for the SG. Fig. 2(c) shows the dr_{SG} curves under Uniform (non-apodization) and Gaussian apodization function modulation with N_{SG} = 20 and dr_{SGm} = 0.2. The Uniform function has a constant dr_{SG} of 0.2, while the Gaussian function modulated dr_{SG} curve changes symmetrically, from around 0.07 at edges to 0.2 at the center of the SG.

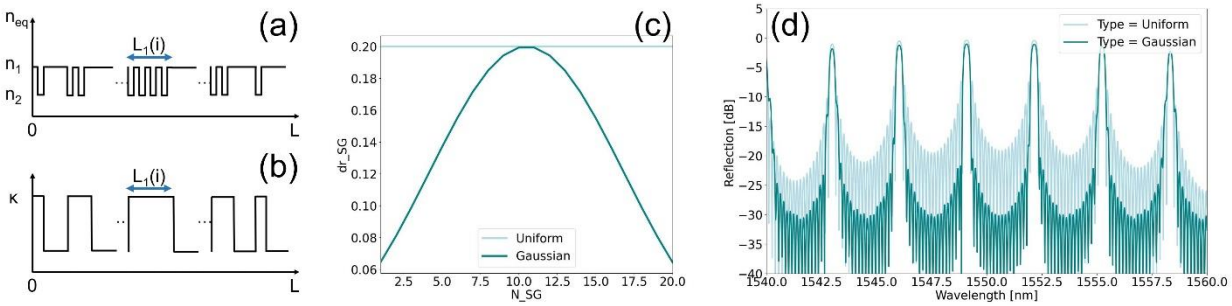


Fig. 2. Schematic diagrams of (a): refractive index profile and (b): the coupling coefficient profile of an apodized sampled grating by modulating the grating length L1. (c): The dr_{SG} curves of sampled grating under Uniform and Gaussian function apodization (N_{SG} = 20, dr_{SGm} = 0.2). (d) The reflection spectrums of Uniform SG and Gaussian-type ASG with same fundamental parameters (N_{SG} = 20, L_2 = 100 μm, dr_{SGm} = 0.2).

Fig. 2(d) shows the calculated reflection spectrum through Transfer Matrix Method under Uniform and Gaussian type apodization, with N_{SG} = 20, L_2 = 100 µm, dr_{SG} = 0.2, and FSR_{SG} = 3.68 nm. The SER and IL of the reflected spectrum for Uniform-type sampled grating are around 6.90 dB and 0.42 dB, respectively, but the SER for Gaussian-type ASG has been significantly increased to around 19.46 dB, which clearly shows that the Gaussian apodization method is more promising. However, the ~1.03 dB IL is a bit higher for Gaussian-type than the Uniform-type, which can be compensated by increasing the number of N_{SG}. Due to the low coupling efficiency of the grating, the 3 dB bandwidth is quite small, which is less than 0.3 nm. The distorted modes far away from the central wavelength are mainly because of the phase mismatch caused by the effective index changing along the sampled grating.

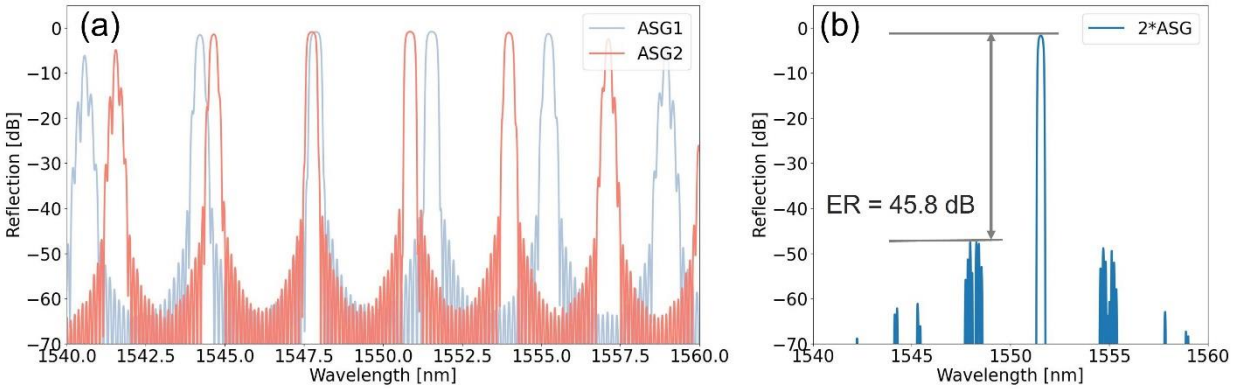


Fig. 3. (a): The reflection spectrums of two Gaussian-type apodized sampled gratings, separately. (b): The reflection spectrum of two cascaded Gaussian-type apodized sampled gratings.

When choosing the parameters for two cascaded ASGs for Vernier effect, the FSR of filter should be considered, which is defined as,

$$FSR = \frac{FSR_{SG1} * FSR_{SG2}}{FSR_{SG2} - FSR_{SG1}} \quad (3)$$

where FSR_{SG1} and FSR_{SG2} are the peak spacing in the reflection spectrum of ASG1 and ASG2 ($FSR_{SG1} < FSR_{SG2}$), respectively. When choosing the L_1 of ASG1 and ASG2 as 100 µm and 118 µm respectively, we can achieve an FSR larger than 20 nm. The final optimized parameters for ASG1 and ASG2 are $N_{SG1} = N_{SG2}$ = 25, dr_{SGm1} = 0.325, dr_{SGm2} = 0.3. Fig. 3(a) shows the reflection spectrum of two Gaussian-type ASGs, in which the SER are both higher than 40 dB, and the IL less than 1 dB. The reflection spectrum of the cascaded two Gaussian-type ASGs, shown in Fig. 3(b), shows a narrow BW = 0.3 nm with high ER > 45 dB, SER > 80 dB, and low IL < 1.75 dB. When considering the loss of MMI (IL_{MMI} = 0.75 dB), we predict the IL for the filter to be less than 5 dB.

DISCUSSION

In this paper, we propose a narrow bandwidth tunable optical filter using cascaded ASGs. Through Gaussian-type apodization on the duty ratio of the SG periodically, the side-lobe extinction ratio can be highly reduced. The filter can achieve a high extinction ratio > 45 dB, low insertion loss < 5 dB, narrow 3 dB bandwidth < 0.3 nm, and wide FSR > 20 nm, which is a promising device on optical integration circuits for THz heterodyne system.

References

[1] P. Prabhathan, et al., "Compact resonant Bragg-grating filters using submicron silicon-on-insulator (SOI) waveguide for optical communication network," In Optoelectronic Devices and Integration III, Vol. 7847, pp. 123-132, 2010.
[2] Y. Ding, et al., "Bandwidth and wavelength-tunable optical bandpass filter based on silicon microring-MZI structure," Opt. Express, vol 19, no. 7, pp. 6462-6470, 2011.
[3] S. Radosavljevic, et al., "Mid-infrared Vernier racetrack resonator tunable filter implemented on a germanium on SOI waveguide platform," Opt. Materials Express, vol 8, no. 4, pp. 824-835, 2018.
[4] N. Kikuchi, et al., "Monolithically integrated 64-channel WDM channel selector with novel configuration," Electron. Lett., vol. 38, no. 7, pp. 331–332, 2002.
[5] X. H. Zou, et al., "Periodically chirped sampled fiber Bragg gratings for multichannel comb filters," IEEE Photon. Technol. Lett., vol 18, no. 12, pp. 1371-1373, 2006.
[6] T. Segawa, et al., "High-speed wavelength-tunable optical filter using cascaded Mach–Zehnder interferometers with apodized sampled gratings," IEEE J. Quantum Electron., vol 44, no. 10, pp. 922-930, 2008.
[7] L. M. Augustin, et al., "InP-based generic foundry platform for photonic integrated circuits," IEEE J. Sel. Top. Quantum Electron., vol 24, no. 1, pp. 1-10, 2017.
[8] A. D. Simard, et al., "Apodized silicon-on-insulator Bragg gratings," IEEE Photon. Technol. Lett., vol 24, no. 12, pp. 1033-1035, 2012.

Design and optimization of graphene-on-silicon nitride integrated waveguide mode filters

(Student paper)

Fernando Martín-Romero*, Francisco J. Díaz-Fernández and Víctor J. Gómez

[1]Nanophotonics Technology Center, Universitat Politècnica de València, Valencia, Spain
* fmarrom@ntc.upv.es

In this work, we report on the design and optimization of graphene-on-silicon nitride integrated waveguide mode filters for suppressing the spurious propagation of either TE_0 or TE_1 modes. The integrated waveguide consists of a silicon nitride waveguide partially covered by single layer graphene films. We then compare the efficiency and fabrication tolerance of the devices to those of similar graphene-on-silicon integrated waveguide mode filters.
Keywords: *Mode filter, Graphene, Silicon nitride, Waveguide*

INTRODUCTION

Given the increase in demands regarding Internet traffic, new multiplexing techniques have been explored. Mode Division Multiplexing (MDM) is a technology that has attracted attention, because it can extend the capacity of a single wavelength channel by taking advantage of higher-order modes. In a traditional MDM system, the fundamental modes generated by the signal sources are individually modulated by separate electro-optic (EO) modulators. Then, they are converted to higher-order modes, and multiplexed into a few-mode fiber. This method suffers from high insertion losses, large device footprint and high costs.

Waveguide mode filters are promising devices in order to overcome those limitations, since they can selectively modulate a certain guided mode [1]. An interesting case are graphene covered waveguide filters [2]–[5], where patterned graphene films are integrated coplanar to the waveguide core. Graphene is a material with a large absorption coefficient and a broad absorption bandwidth [6]. These optical properties allow to make filters with high extinction and selection ratios in a broad bandwidth. In this work, we simulate the efficiency and optimize the design of TE_0 and TE_1 mode filters based on graphene-on-silicon nitride (SiN) integrated waveguides. Then, we compare our results to the simulated performance of graphene-on-silicon integrated waveguide filters [2].

RESULTS

The design of the filter is depicted in Fig. 1(a) for the TE_0 case. The waveguide consists of a SiN core embedded in a silicon dioxide (SiO_2) cladding, and the core of the waveguide is partially covered by a graphene film. Fig. 1(b) shows the profile of the TE_0 mode consisting of a single lobe centered on the waveguide core, while Fig. 1(c) shows the TE_1 mode having two lobes at both sides of the core, with the peak electric-field intensities displaced from the center. Therefore, if the graphene film is designed to cover only the central area around where the field intensity of the TE_0 mode reaches its maximum, then the fundamental mode will be absorbed, while the TE_1 mode will be transmitted. Analogously, if two graphene strips are placed over the core, at the sides where the TE_1 mode shows the maximum intensity, the fundamental mode will be transmitted and the TE_1 mode will be absorbed. Since the graphene film is one-atom thick, it induces a negligible change in the real part of the effective index of the modes, while strongly affecting the imaginary part. Therefore, the mode profiles are not modified by graphene.

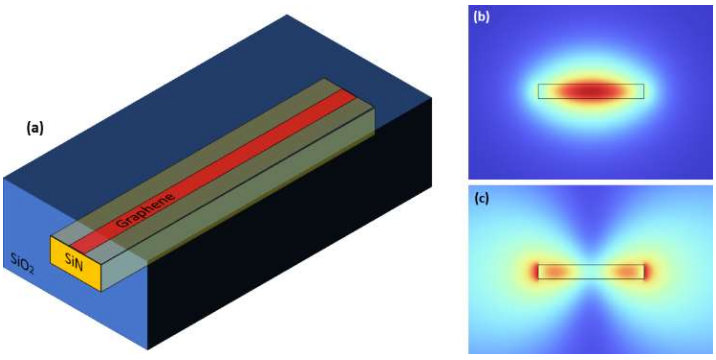


Fig. 1. (a) Scheme of the TE_0 graphene-on-silicon nitride integrated waveguide mode filter. (b) TE_0 mode profile. (c) TE_1 mode profile.

In order to assess the efficiency of the mode filter, we use the parameters defined in [2]. The first one is the extinction ratio $ER = \alpha_{stop} - \alpha_{pass}$, and it corresponds to the difference between the absorption coefficient of the stop-mode and the pass-mode. The second one is the selection ratio $SR = ER/\alpha_{pass}$, defined as the extinction ratio divided by the absorption coefficient of the pass-mode.

The length required to obtain a certain contrast C between modes is $L = C/ER$, while the insertion losses of the device are given by $IL = \alpha_{pass} \times L = C/SR$. The goal is to obtain a device with the lowest $L \times IL$ product possible:

$$IL \times L = \frac{C^2}{ER \times SR} \tag{3}$$

Therefore, the figure of merit that needs to be maximized in order to optimize the device is the $ER \times SR$ product.

For each mode, the absorption coefficient can be computed by dividing the power absorbed by the graphene film of width (w_g) and the input power (P_{in}) as

$$\alpha = 4.34 \times \frac{Re(\sigma_g)/2}{P_{in}} \int_{w_g} |E_{\parallel}|^2 dx \tag{4}$$

where a conversion factor to dB units is introduced [6]. The real part of the conductivity of graphene (σ_g) can be extracted from the Kubo formula, which describes the surface conductivity of graphene [7]:

$$\sigma = i\frac{e^2 k_B T}{\pi\hbar^2(\omega + i2\Gamma)}\left(\frac{\mu_c}{k_B T} + 2\ln\left(e^{-\mu_c/k_B T} + 1\right)\right) + \frac{ie^2(\omega + i2\Gamma)}{\pi\hbar^2}\int_0^{\infty} \frac{f_d(-\varepsilon) - f_d(\varepsilon)}{(\omega + i2\Gamma)^2 - 4\left(\frac{\varepsilon}{\hbar}\right)^2} d\varepsilon \tag{5}$$

where $f_d(\varepsilon) = 1/(\exp[(\varepsilon - \mu_c)/(k_B T)] + 1)$ is the Fermi-Dirac distribution function.

In order to optimize the device, we have studied the performance of a TE_0 filter and a TE_1 filter for a silicon nitride core with dimensions $W = 1500$ nm and $H = 200$ nm, embedded in silicon dioxide. In the case of the TE_0 filter (Fig. 2), we have computed the ER, SR and $ER \times SR$ parameters for different values of the graphene film width (w_g) and the separation between the graphene film and the surface of the core (h), while in the case of the TE_1 filter (Fig. 3), we varied the width of each film (w_g) and the lateral distance between them (l). Then, we have compared the results to those presented in [2] for a simulated graphene-on-silicon integrated waveguide mode filter of the exact same core dimensions.

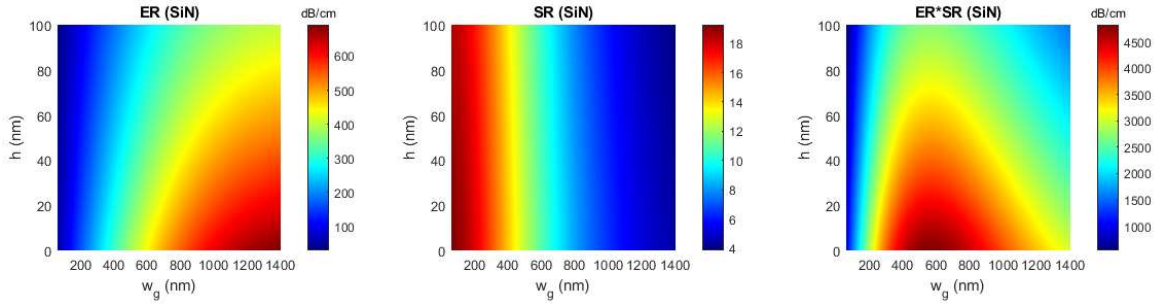


Fig. 2. ER, SR and ER×SR parameters for a TE_0 graphene-SiN filter with respect to graphene film width and vertical separation.

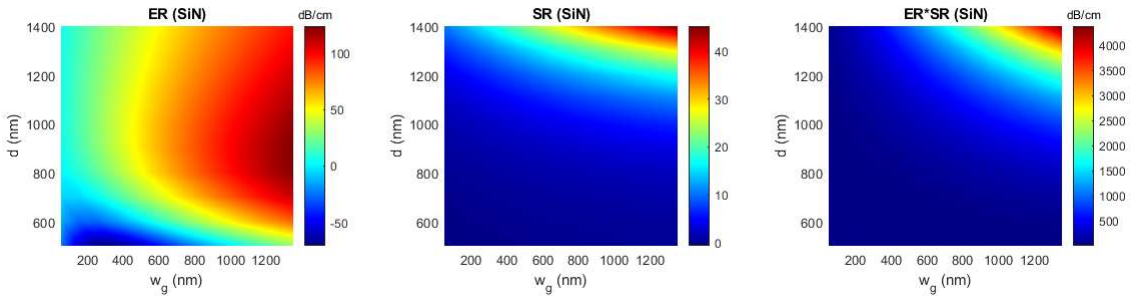


Fig. 3. ER, SR and ER×SR parameters for a TE_1 graphene-SiN filter with respect to graphene film width and lateral separation between films.

DISCUSSION

Fig. 2 shows that it is most effective to deposit graphene on the surface of the core ($h = 0$), due to a stronger interaction between graphene and the evanescent field, which can be assumed to be true for both filters. Compared to the work done by Xing *et al* on graphene-on-silicon mode filters [2], silicon nitride shows a higher extinction and selection ratios for the TE_0 filter, as well as a higher figure of merit. In the case of a graphene-on-silicon mode filter, the optimal design consists of a center graphene film of $w_g = 260$ nm with $ER \times SR = 680\ \mathrm{dB/cm}$. Whereas, for the graphene-on-SiN integrated waveguides, the optimal design shows $w_g = 580$ nm with $ER \times SR = 4840\ \mathrm{dB/cm}$. This improvement could be explained by the fact that the TE_0 and TE_1 modes in the SiN waveguide show less overlapping than those of silicon (Fig. 4). For the TE_1 graphene-on-SiN filter, the ER, SR and figure of merit increase with the graphene width (w_g). This can be explained when taking into account the intensity profiles for the TE_0 and TE_1 modes (Fig. 4). In silicon (Fig. 4a) the TE_1 mode shows a higher localization than in SiN (Fig. 4b), and therefore enough power can be absorbed with a narrower graphene film. For SiN, ER shows a maximum of 120 dB/cm for a separation between both films of l =900 nm. If the films are separated a longer distance, the fundamental mode losses can be strongly reduced. For this reason, the figure of merit can be optimized for larger l values where graphene is placed away from the surface of the core. However, it must be considered that at a separation of 900 nm, the figure of merit is $ER \times SR = 280$ dB/cm, which is already comparable to the case of silicon.

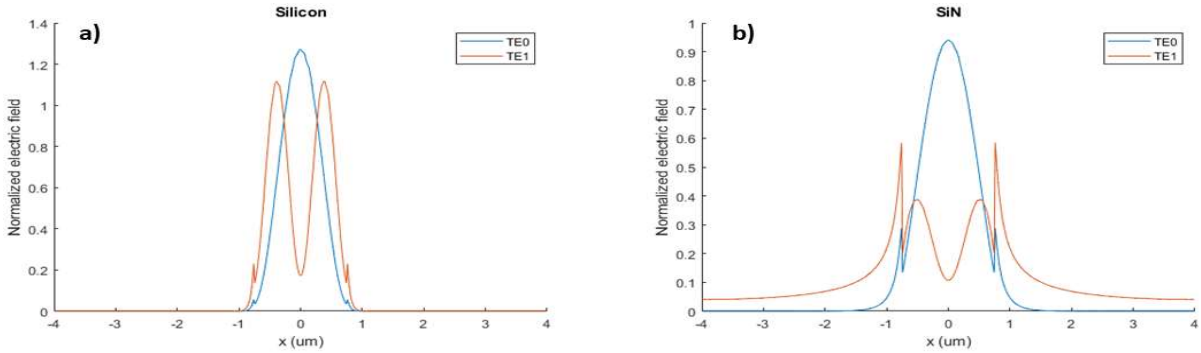


Fig. 4 Intensity profile for TE_0 and TE_1 modes in the silicon waveguide and the silicon nitride waveguide.

The proposed graphene-on-SiN integrated devices would allow to selectively filter the fundamental mode of a waveguide with a figure of merit more than 7 times larger than that of a graphene-on-silicon mode filter. In addition, if we define the fabrication tolerance of the TE_0 filter as the range of w_g values in which the $ER \times SR$ product is above 90% of its maximum value, it can be observed that the tolerance for graphene-silicon filters is ±80 nm, while for graphene-SiN it is +180 nm -200 nm. The graphene-on-SiN TE_1 filter shows a lower ER than the silicon filter, but it allows a further reduction in the losses suffered by the fundamental mode.

References

[1] T. Lian *et al.*, *Mode-selective modulator and switch based on graphene-polymer hybrid waveguides*, Opt. Express, OE, vol. 30, n.º 13, pp. 23746-23755, 2022

[2] P. Xing, K. J. A. Ooi, y D. T. H. Tan, *Ultra-broadband and compact graphene-on-silicon integrated waveguide mode filters*, Sci Rep, vol. 8, n.º 1, Art. n.º 1, 2018

[3] Z. Xing *et al.*, *Waveguide-integrated graphene spatial mode filters for on-chip mode-division multiplexing*, Opt. Express, OE, vol. 27, n.º 14, pp. 19188-19195, 2019

[4] Z. Chang y K. S. Chiang, *Ultra-broadband mode filters based on graphene-embedded waveguides*, Opt. Lett., OL, vol. 42, n.º 19, pp. 3868-3871, 2017

[5] J. Wang, X. Zhang, Y. Chen, Y. Geng, Y. Du, y X. Li, *Design of a graphene-based silicon nitride multimode waveguide-integrated electro-optic modulator*, Optics Communications, vol. 481, p. 126531, 2021

[6] S. J. Koester y M. Li, *Waveguide-Coupled Graphene Optoelectronics*, IEEE Journal of Selected Topics in Quantum Electronics, vol. 20, n.º 1, pp. 84-94, 2014

[7] T. Ando, Y. Zheng, y H. Suzuura, *Dynamical Conductivity and Zero-Mode Anomaly in Honeycomb Lattices*, J. Phys. Soc. Jpn., vol. 71, n.º 5, pp. 1318-1324, 2002

Free Spectral Range Sensing as a Novel Measurement Technique

Student paper

Gandolf Feigl[1,*], Jakob Hinum-Wagner[2], Samuel Hörmann[2] and Alexander Bergmann[1]

[1] Graz University of Technology, Institute of Electrical Measurement and Sensor Systems, Inffeldgasse 33/I, Graz, 8010, Austria
[2]ams OSRAM AG, Tobelbader Str. 30, Graz, 8141, Austria
[*]gandolf.feigl@tugraz.at

A novel method for direct measurement of label-free analyte concentration for refractometric sensors using integrated photonic Mach-Zehnder interferometers is proposed. The protocol for simulation and modeling of the concentration-dependent shift of the free spectral range is presented for an isopropanol-ethanol binary mixture bulk sensing example and the model is compared to experiments.

Keywords: *Photonic integrated circuit, biosensor, label-free, integrated photonics, MZI, PIC, FSR*

INTRODUCTION

Photonic integrated circuits (PIC) represent a promising approach for biosensors that can be used for rapid medical testing in point-of-care (PoC) diagnostics [1]. The main advantages of using PICs, as compared to traditional biosensing approaches, are their high sensitivity, robustness, high levels of design freedom, and capabilities towards miniaturization, integration, and multiplexing [2]. The most commonly used platform for biosensing is silicon nitride (SiN) which can be produced in a CMOS process in a foundry, paving the way for cost-effective mass production [3]. PIC biosensors are often realized as Mach-Zehnder interferometers (MZI). The area of the MZIs sensing arm is not cladded, enabling interaction between the evanescent field of the waveguide and the environment. A change in the refractive index (RI) of the environment of the sensing area changes the effective RI of the light in the waveguide. This leads to a phase shift of the light in the sensing arm and the detected interferometric signal provides information about the presence and concentration of an analyte on the sensor surface. A schematic of an MZI-based PIC biosensor is illustrated in fig.1. Albeit MZIs being well-studied devices, reliable measurement of label-free analytes in PoC environments still remains a challenge [4]. In this work, a simple approach for direct concentration measurement of a liquid bulk sample via the concentration-dependent free spectral range (FSR) of an MZI is presented. The RI of a liquid bulk sample $n(\lambda, c, T)$ depends on the laser wavelength λ, the analyte concentration c, as well as the bulk sample temperature T. The propagation of the laser mode through the waveguide is determined by the effective RI of the waveguide n_{eff} which depends on the RI of the waveguide's environment and can be computed from numerical simulations for a given waveguide geometry and cross-section for both the reference and the sensing arm and their environment. The FSR depends on the MZI's design including the length of the reference and sensing arm L_{ref} and L_{sens}, respectively, and the effective group indices of reference and sensing arm, $n_{g,ref}(\lambda)$ and $n_{g,sens}(\lambda, c, T)$, respectively.

$$\mathrm{FSR}\,(\lambda, c, T) = \frac{\lambda^2}{L_{ref} * n_{g,ref}(\lambda) - L_{sens} * n_{g,sens}(\lambda, c, T)} \tag{1}$$

with

$$n_g = n_{eff} - \lambda \frac{\partial n_{eff}}{\partial \lambda} \tag{2}$$

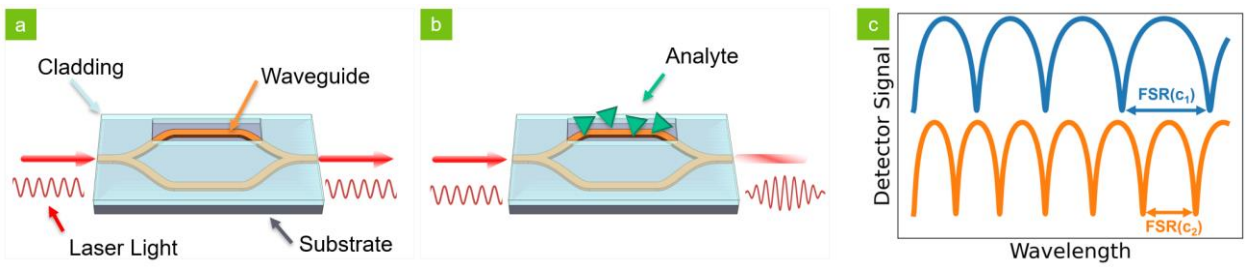


Fig. 1: Sensor concept of an MZI. (a) Laser light can be coupled in and out of the sensor. The area of the sensing arm is not cladded, enabling interaction with surrounding media in the sensing window. (b) When the RI of the sensing area changes, the output signal is altered. (c) Detector signal and FSR for a bulk sample with different analyte concentrations.

The FSR of an MZI can be measured by tuning the wavelength of the laser light over a wavelength range covering several intensity minima and maxima of the interferometer, see fig. 1c. Knowing the model data of the effective refractive index, the concentration of the analyte can be extracted.

MODEL

Establishing a reliable model for predicting the FSR of an MZI requires precise knowledge of the bulk RI and the dependence on the respective parameters. For a detailed determination of the RI of a isopropanol – ethanol (EOH) binary mixture, the chromatic dispersion, as well as the EOH concentration and solution temperature were considered. Since the FSR is very sensitive to small RI changes in the environment, also the change of the dependency on c and T was taken into account. Empirical data from Fontao et al. [5] and Sani et al. [6] were evaluated to obtain a function for the RI of the form

$$n(\lambda, c, T) = n_0 + \frac{\partial n}{\partial \lambda} * \lambda + \frac{\partial n}{\partial c} * c + \frac{\partial n}{\partial T} * T + \frac{\partial^2 n}{\partial c \partial T} * T * c \tag{3}$$

Refractive indices calculated from eq. (3) and the given geometry of our MZIs were used to simulate the mode propagation in the waveguide using Ansys LUMERICAL MODE solver. The simulation yields the effective refractive indices $n_{eff,ref}$ and $n_{eff,sens}$ for the specified wavelength and bulk sample RI range. Together with the bulk RI results from eq. (3), the wavelength, concentration, and temperature dependence of $n_{eff,sens}$ can be obtained. The simulation results for $n_{eff,sens}$ are shown in fig. 2.

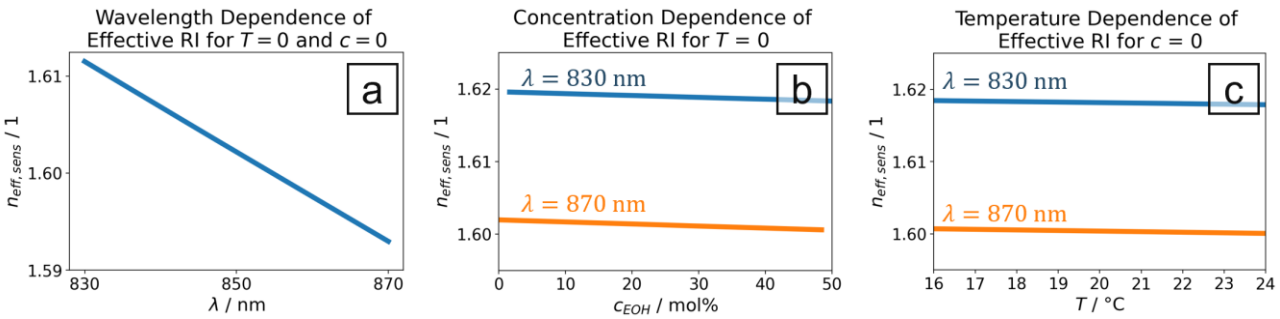


Fig. 2: Simulation results for the effective RI of the sensing arm of the MZI. The wavelength (a), concentration (b), and temperature (c) dependence were simulated. For (b) and (c), different wavelengths were used for the simulation to calculate the non-zero interdependencies of the changes in λ and c, and λ and T, respectively.

For a model containing linear interdependencies of the changes in λ and c, and λ and T, respectively, the function for the effective RI of the sensing arm $n_{eff,sens}(\lambda, c, T)$ reads

$$n_{eff,\,sens}(\lambda, c, T) = n_0 + \frac{\partial n}{\partial \lambda} * \lambda + \left(\frac{\partial n}{\partial c} + \frac{\partial^2 n}{\partial \lambda \partial c} * \lambda\right) * c + \left(\frac{\partial n}{\partial T} + \frac{\partial^2 n}{\partial \lambda \partial T} * \lambda\right) * T \tag{4}$$

For reasons of readability, the subscript of $n_{eff,sens}$ on the right-hand side of the equation has been dropped. With eq. (4), the FSR can be calculated using eq. (1-2). For FSR measured from experiments, the model can be used to extract the NaCl concentration from the solution:

$$c = \frac{\frac{-\lambda^2}{FSR\ * L_{sens}} + \frac{L_r * n_{g,ref}}{L_{sens}} - n_0 - \frac{\partial n}{\partial T} * T}{\frac{\partial n}{\partial c}} \tag{5}$$

EXPERIMENTAL AND RESULTS

A microfluidic channel was directly printed onto a chip containing MZI sensing structures to transport liquids over the sensor surface. A tunable laser with a central wavelength of 850 nm was used to tune the wavelength between 830 nm and 870 nm. The sensor surface was flushed with isopropanol and with isopropanol-ethanol mixtures of three different EOH concentrations $c_{EOH,mix}$, see tab. 1. The experimental setup is shown in fig. 3. From the sensor signal, the FSR was calculated using a peak finding algorithm and the FSR vs. wavelength is shown in fig. 4. As a baseline correction for the

model, a linear calibration function $f_{cal}(\lambda) = A\lambda + B$ was applied to the pure isopropanol measurement. The calibrated model is able to correctly predict the concentration-dependent shift of the FSR and infer the EOH concentration $c_{EOH,model}$ from the measurement points using eq. (5). The results for the concentration and the corresponding standard deviations σ are shown in tab. 1.

Tab. 1: The EOH concentration from the calibrated model $c_{EOH,model}$ and the corresponding standard deviation σ is compared to the concentration of the mixture $c_{EOH,mix}$.

Mixture 1			Mixture 2			Mixture 3		
$c_{EOH,mix}$ / mol%	$c_{EOH,model}$ / mol%	σ / mol%	$c_{EOH,mix}$ / mol%	$c_{EOH,model}$ / mol%	σ / mol%	$c_{EOH,mix}$ / mol%	$c_{EOH,model}$ / mol%	σ / mol%
18.4	21.5	13.1	36.3	44.6	10.2	41.4	45.1	12.1

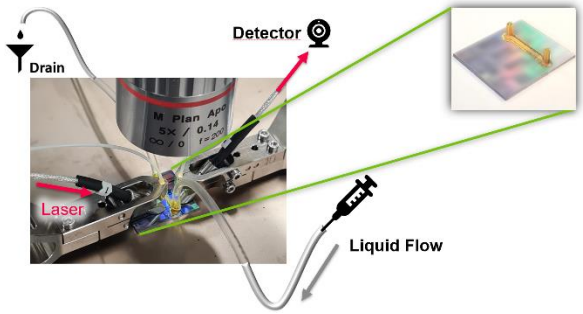


Fig. 3: Experimental setup. The chip with the sensing structures is mounted on a wafer prober platform and laser light is coupled in and out using grating couplers. Tubes are connected to the printed microfluidic channel to transport the liquids over the sensor.

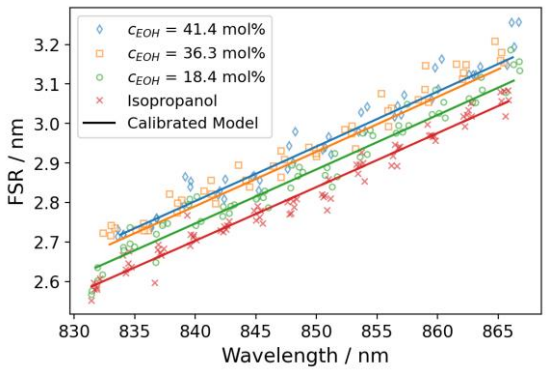


Fig. 4: Measured FSR for isopropanol and three different isopropanol-ethanol mixtures. The calibrated model (solid lines) is able to predict the concentration-dependent shift of the FSR.

DISCUSSION

The presented model for direct measurement of analyte concentration in bulk solution through the concentration-dependent shift of the FSR of the interferometric signal of an MZI is able to correctly estimate the EOH concentration from a bulk isopropanol-ethanol binary mixture. The calculated EOH concentrations are higher than the molar concentrations from the mixing ratios, indicating an underestimation of the model parameter $\frac{\partial n}{\partial c}$. Modelling the FSR requires precise knowledge of the sample's RI, including dependencies regarding λ, c and T. The empirical data found in literature does not allow for a reliable estimation of the interdependencies of the changes in λ and c, and was therefore omitted. It is expected that a more precise knowledge of the chromatic dispersion and concentration dependence on the bulk RI of the sample under test, especially in the wavelength and concentration intervals of the experiment would greatly improve the model. The concentration results calculated from the model exhibit a comparably high standard deviation, which can be attributed to disregarded effects like RI fluctuations due to temperature and concentration changes or discrepancies in the data processing, including data clipping and peak-finding algorithm. More work is needed to validate of the model, however, the presented approach poses a simple concentration measurement technique that is easily implementable for biosensors in PoC applications, eliminating the need for peak tracking algorithms or complex read-out schemes.

References

[1] E. Luan, H. Shoman, DM. Ratner, KC. Cheung and L. Chrostowski, *Silicon Photonic Biosensors Using Label-Free Detection*, Sensors, vol. 18 no. 10 2018

[2] J. Milvich, *Waveguide-Based Photonic Sensors: From Devices to Robust Systems*, KIT Scientific Publishing, Karlsruhe, 2020

[3] L. Chrostowski et al., *Silicon Photonic Circuit Design Using Rapid Prototyping Foundry Process Design Kits*, IEEE Journal of Selected Topics in Quantum Electronics, vol. 25, no. 5, pp. 1-26 2019

[4] M. Soler and LM. Lechuga, *Biochemistry strategies for label-free optical sensor biofunctionalization: advances towards real applicability*, in Analytical and Bioanalytical Chemistry 2021

[5] M. Fontao, M. Iglesias, *Effect of Temperature on the Refractive Index of Aliphatic Hydroxilic Mixtures (C2–C3)*, International Journal of Thermophysics, vol. 23, pp. 513–527, 2002

[6] E. Sani, A. Dell'Oro, *Spectral optical constants of ethanol and isopropanol from ultraviolet to far infrared*, Optical Materials, vol. 60, pp. 137-141, 2016

Tilted MMI based (de)multiplexer for monolithically integrated multichannel transmitters on InP platform

(Student paper)

Shirley Prado de la Cruz[1,2*], Vladyslav Vakarin[1], Giancarlo Cerulo[1], Christophe Caillaud[1], Nicolas Vaissiere[1], Alessandro Aimone[1], Jean Decobert[1], Frédéric Grillot[2,3] and Frédéric Pommereau[1]

[1]III-V Lab, a joint lab of Nokia Bell Labs, Thales Research and Technology and CEA LETI, Palaiseau, 91120, France
[2] LTCI, Télécom Paris, Institut Polytechnique de Paris, 19 place Marguerite Perey, Palaiseau, 91120, France
[3] Center for High Technology Materials, University of New Mexico, Albuquerque, New Mexico, USA
[*] shirley.prado@3-5lab.fr

We present a wavelength (de)multiplexer based on a tilted multimode interferometer structure on the InP platform in O band. The device shows an average cross-talk of 13 dB and insertion loss below 9 dB. It presents a footprint of 0.09 mm^2 and a remarkable fabrication tolerance with a sensitivity to dimensional errors of < 110 pm/nm. The fabrication process is compatible with the integration of active components such as electrically modulated lasers.
Keywords: *(de)multiplexer, InP, integrated photonics*

INTRODUCTION

Wavelength division multiplexers (WDM) and (de)multiplexers are key building blocks for the monolithic integration of high-speed telecommunication photonic integrated circuits (PIC). They allow to achieve higher transmission capacity, by supporting the transmission of different wavelengths at the same time. The most common structure used for this component are the arrayed waveguide gratings (AWG) [1], where broad coarse wavelength multiplexing has been demonstrated [2]. Other structures have also been explored such as waveguide grating routers (WGR) [3]. These structures allow to have low crosstalk, low insertion loss and have been demonstrated on different material platforms such as SOI, Si_3N_4, etc [4]. However, their combination with high performance III-V lasers is challenging. On the other hand, the inclusion of passive components on InP platforms, offers the possibility to realize complex PICs, leveraging mature technologies available for high-performance active components (such as laser, modulators and amplifiers) [5]. Nonetheless, InP passive components, such as AWGs, have a considerable footprint and require high fabrication precision. In this work, we study a 5-channel (de)multiplexer based on angled multimode interferometer (AMMI) made on InP platform. The experimental results show a more fabrication tolerant component with a sensitivity to dimensional errors up to 110 pm/nm and gives the device with a compact footprint.

FABRICATION AND CHARACTERIZATION

The device was fabricated on a n-doped InP substrate, where the epitaxial layers were grown by metalorganic vapour phase epitaxy (MOVPE). The waveguide shown on Fig. 1 (a) consists of an optical guide layer of GaInAsP surrounded by two InP claddings. The fabrication starts with the deposition of a Si_3N_4 layer by plasma enhanced chemical vapor deposition (PECVD). The devices were defined by electron beam lithography, in order to guarantee high-accuracy on the definition of the waveguides. However, it is important to point out that the fabrication is fully compatible with a state of the art contact lithography. The pattern is transferred to the Si_3N_4 mask by reactive ion etching (RIE). The waveguides are deeply etched (3.3µm) using the Si_3N_4 mask on inductively coupled plasma (ICP) etching, with a $Cl_2/H_2/Ar$ gas. Finally, a passivation was made with Si_3N_4 to protect the surface of the structure.

Fig. 1 (b) shows the structure of the wavelength division (de)multiplexer studied on this work. It is based on a tilted multimode interferometer, with a multimode waveguide section width W_{MDW} varying from 19.5 µm to 20.5 µm, according to the wavelength desired to be extracted. The input and output 2-µm wide waveguides are tilted with respect to the main multimode waveguide's horizontal axis. For this study, it was chosen an angle of 7° for compatibility with the active components.

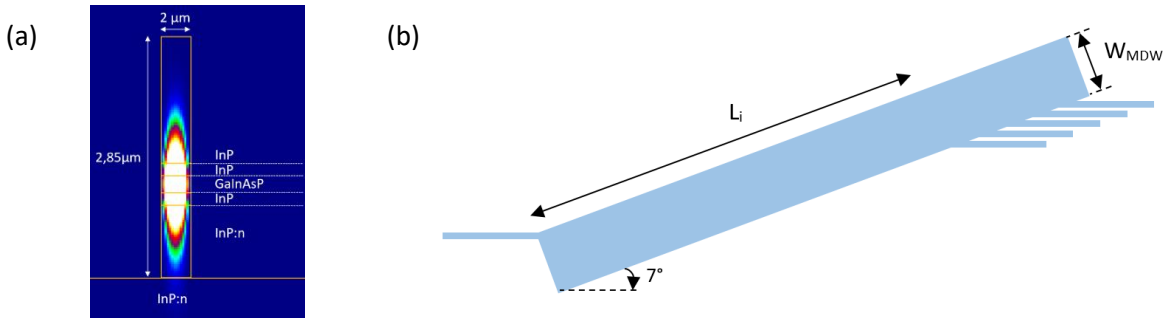


Fig. 1. (a) Waveguide cross-section. (b) Schematics of the angled MMI (de)multiplexer with five output channels.

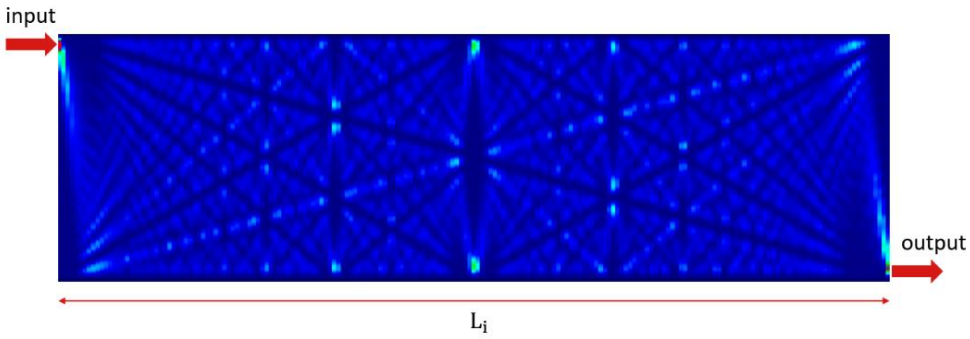


Fig. 2. Simulation of the multimode waveguide to determine the position of the channel for the wavelength desired to be extracted, TE polarization.

The output channels have a spacing of 20 nm. Their position L_i was calculated using the self-imaging condition of a MMI described at [4]. Then, it was precisely determined by simulation with FIMMPROP [6] as shown in Fig.2.

A SOA-based broadband source operating in the O-Band wavelength range (1260 nm – 1360 nm) was used to characterize the device in TE polarization. Then, both input and output facets of the device were coupled with lensed polarization maintaining fibers to keep control of the polarization state. Finally, the device transmission was recorded on an optical spectrum analyzer.

RESULTS AND DISCUSSION

A photograph of the fabricated device is shown in Fig. 3. The obtained device's footprint is as low as 0.09 mm^2. The bends used for access waveguides are implemented with high curvature radius (>1mm) to avoid radiation loss.

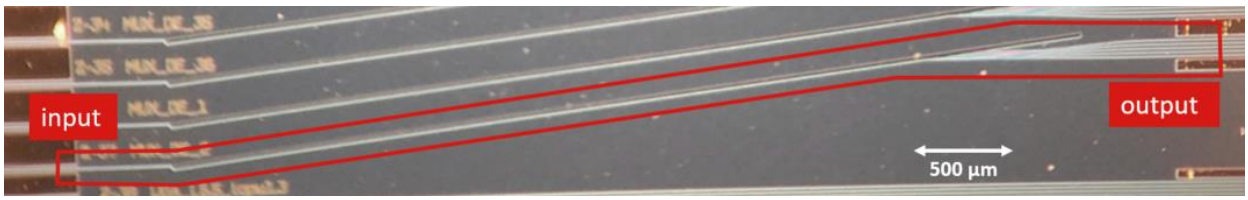


Fig. 3. Microscope photo of the angled MMI (de)multiplexer with five channels.

Different device configurations, based on different geometries, were studied. For each configuration, the width of the multimode waveguide (W_{MDW}) and the position L_i of the output channels are varied and optimized, based on simulation results. For all devices, an output channel spacing of 20nm was chosen. We present a configuration that allows having channels with output wavelength of 1290 nm, 1310 nm, 1330 nm and 1350 nm as shown on Fig. 4(a). The position of the transmission spectra for the design is in a good agreement with the simulation shown on Fig.4(b) and can be adjusted at will. An average cross-talk of 13dB and IL below 9 dB were obtained. IL can be further reduced by lowering waveguide propagation loss. In this particular case, the used deep etch waveguide technology was the limiting factor, with propagation losses >4 dB/cm.

The fabrication sensitivity ($\Delta\lambda/\Delta W_{MDW}$) of the device is around 110 pm/nm as evaluated experimentally by width variation implementation on the chip, as shown on Fig. 4(c) and makes it compatible with state of the art lithography. The tolerance to dimensional errors measured on this device is comparable to the tolerance measured on the SOI platform [7].

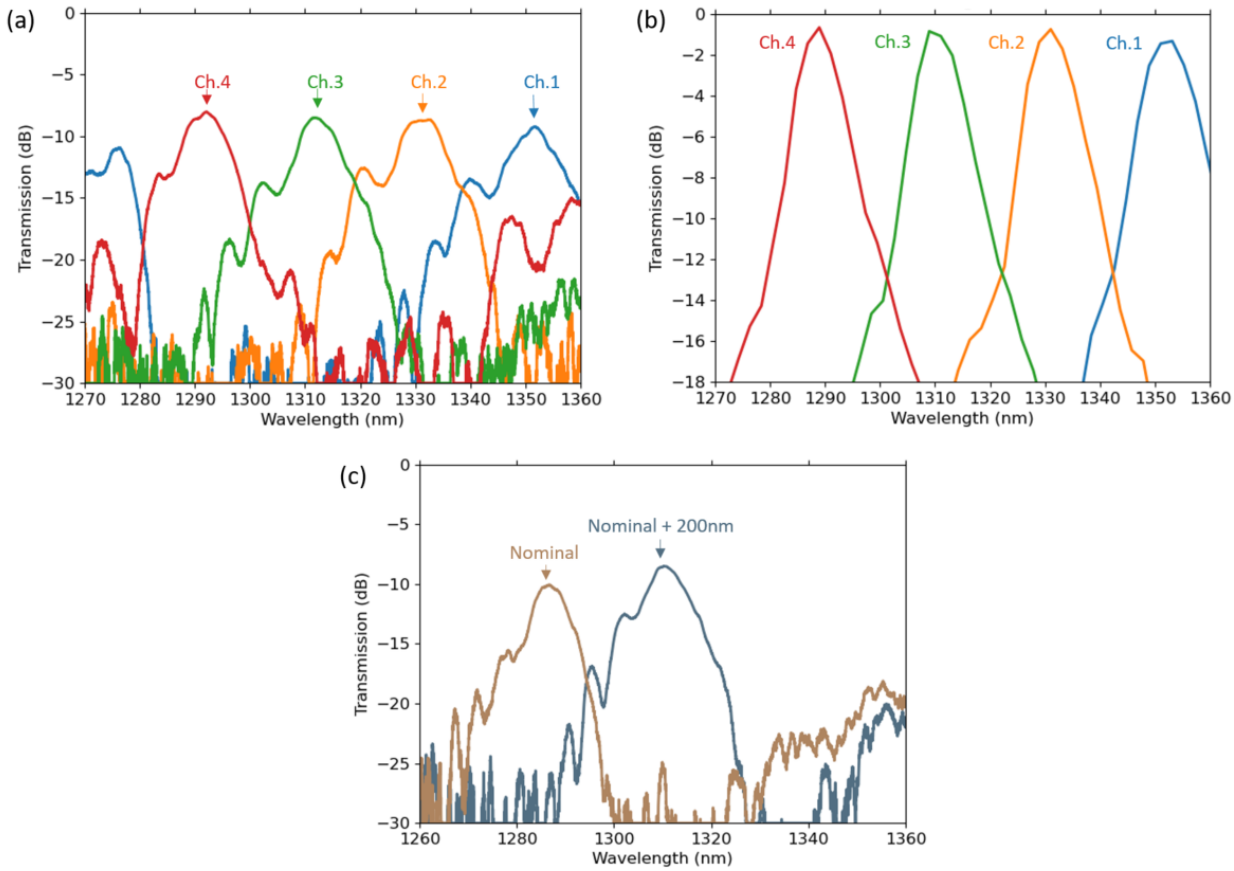


Fig. 4. Transmission spectra (a) measured and (b) simulated. (c) Transmission spectra measured showing the fabrication sensitivity.

CONCLUSION

In summary, we have designed and experimentally demonstrated an angled MMI (de)multiplexer in the O band on InP platform with IL below 9 dB, average crosstalk lower than 13 dB, high fabrication tolerance with a sensitivity to dimensional errors of <110 pm/nm and a footprint as low as 0.09 mm^2. This first result paves the way for the implementation of high performance multi-wavelength III-V transmitters.

References

[1] Y. Yoshikuni et al., *Semiconductor arrayed waveguide gratings for photonic integrated devices*, IEEE Journal of Selected Topics in Quantum Electronics, vol. 8, no. 6, pp. 1102-1114, Nov.-Dec. 2002

[2] Nasuhi Yurt, *Design and fabrication of a broadband polarization and temperature insensitive arrayed waveguide grating on InP*, Optics Express vol. 13, no. 14, pp. 5535-5541 ,2005

[3] Z. Fan, et al., *8×8 Cyclic Arrayed Waveguide Grating Router Based on InP Platform in O-Band*, in Proceedings of 2019 Asia Communications and Photonics Conference (ACP), Chengdu, China, pp. 1-3, 2019

[4] Y.Hu et al., *Mid-infrared wavelength division (de)multiplexer using an interleaved angle multimode interferometer on the silicon-on-insulator platform*, Optics Letters, vol. 39, no 6, pp. 1406-1409 ,2014

[5] G. Cerulo et al., *1.3µm SI-BH Electro-Absorption Modulated Laser Operating at 56Gbauds/s with 8.4dB Dynamic Extinction Ratio*, in Proceedings of 2018 European Conference on Optical Communication (ECOC), Rome, Italy, pp. 1-3, 2018

[6] FIMMPROP by Photon Design

[7] T.Domínguez Bucio et al., *Athermal silicon nitride angled MMI wavelength division (de)multiplexers for the near-infrared*, Optics Express, vol. 25, no. 22, pp 27310-27320, 2017

EUROPEAN CONFERENCE ON INTEGRATED OPTICS

Automated Model for Characterization of VCSEL Circuit-level Parameters Using Machine Learning

Andrea Marchisio[1], Ihtesham Khan[1], Lorenzo Tunesi[1], Muhammad Umar Masood[1], Enrico Ghillino[2], Vittorio Curri[1], Andrea Carena[1], and Paolo Bardella[1]

[1] Politecnico di Torino, Corso Duca degli Abruzzi, 24, 10129, Torino, Italy
[2] Synopsys, Inc., 400 Executive Blvd Ste 101, Ossining, NY 10562, United States
paolo.bardella@polito.it

We propose a machine learning-based model to extract physical parameters characterizing stationary-and-dynamic behavior of a VCSEL. The model is trained with circuit-level simulations of light-current and S21 characteristics. Excellent results are achieved as a relative prediction error.

Keywords: *machine learning, VCSEL, physical model, parameters extraction*

INTRODUCTION

In the last decades, a significant number of physical models have been proposed in the literature to describe the complex behavior of edge-emitting or vertical-cavity laser diodes, either with a phenomenological or an empirical approach. With an accurate description of advanced physical effects, these tools allow a better understanding of the laser behavior and the optimization of device properties according to designers' needs. As a drawback, the number of involved physical parameters (geometrical properties, material characteristics, electrical and thermal effects) is generally so large that it may be challenging to find a correct set of parameters fitting experimental laser measurements, starting from the fundamental light-current (L-I) characteristics and the small signal modulation responses (S21). The extraction of these physical parameters from experimental curves can be time-consuming, since it often relies on brute-force minimization routines, trial-and-error approaches, or regression analysis. We propose a Machine Learning (ML) approach to the problem, based on Deep Learning (DP), which can extract from experimental measurements the parameters required by a circuit-level model of a Vertical-Cavity Surface-Emitting Laser (VCSEL) [1], implemented in Synopsys OptSim™ [2]. With respect to other works, which focused on edge emitting devices [3] or required two separate simulations to take into account temperature-dependent effects [4], we propose a single DL-based agent that can deal with all the electrical, optical, and thermal effects considered in OptSim™.

VERTICAL-CAVITY SURFACE-EMITTING LASER MODEL

For the description of the optical and electrical properties of the VCSEL, we rely on the model available in Synopsys OptSim™ [2], which implements and expands the circuit-level model originally proposed in [1]. There, the explicit spatial dependence of the number of carriers $N(r,t)$ in the transverse plane is eliminated by assuming cylindrical symmetry and by introducing a two-term Bessel series expansion:

$$N(r,t) = N_0(t) - N_1(t) J_0(\sigma_1 r/R)$$

with J_0 and J_1 Bessel functions of the first kind, σ_1 first nonzero root of J_1, and R effective radius of the active layer. The temporal evolution of the expansion coefficients $N_0(t)$ and $N_1(t)$ is given by the following spatially independent rate equations:

$$\frac{\mathrm{d}N_0}{\mathrm{d}t} = \frac{\eta_\mathrm{i} I}{q} - \frac{N_0}{\tau_\mathrm{n}} - \frac{G\left[\gamma_{00}(N_0 - N_\mathrm{tr}) - \gamma_{01} N_1\right]}{1+\varepsilon S} S - \frac{I_\mathrm{l}}{q}; \quad \frac{\mathrm{d}N_1}{\mathrm{d}t} = -\frac{N_1}{\tau_\mathrm{n}}(1+h_\mathrm{diff}) + \frac{G\left[\phi_{100}(N_0 - N_\mathrm{tr}) - \phi_{101} N_1\right]}{1+\varepsilon S} S$$

with η_i injection efficiency, τ_n carrier lifetime, G gain coefficient, N_tr transparency carrier number, I_l leakage term, ε gain compression factor, h_diff diffusion coefficient. The four coefficients γ_{00}, γ_{01}, ϕ_{100}, ϕ_{101} quantify the interaction with the fundamental transverse mode profile, assumed to have a Gaussian profile [1].

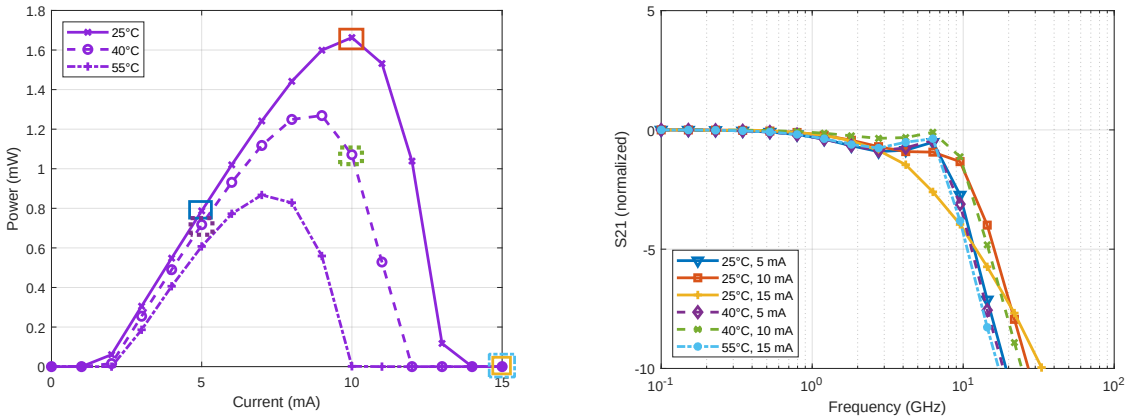
The temporal evolution of the photon number S in the cavity and its associated phase ϕ [5] are described by the following rate equations:

$$\frac{\mathrm{d}S}{\mathrm{d}t} = -\frac{S}{\tau_\mathrm{p}} + \frac{\beta_\mathrm{sp} N_0}{\tau_\mathrm{n}} + \frac{G\left[\gamma_{00}(N_0 - N_\mathrm{tr}) - \gamma_{01} N_1\right]}{1+\varepsilon S}; \qquad \frac{\mathrm{d}\phi}{\mathrm{d}t} = \frac{\alpha}{2} \frac{G\left[\gamma_{00}(N_0 - N_\mathrm{tr}) - \gamma_{01} N_1\right]}{1+\varepsilon S}$$

with τ_p photon lifetime, β_sp spontaneous emission coefficient, α linewidth enhancement factor. The output power P_out is obtained from S through a proper multiplication coefficient k_f.

The device temperature is dynamically calculated as [6]

$$T = T_\mathrm{amb} + (IV - P_\mathrm{out}) R_\mathrm{th} - \tau_\mathrm{th} \frac{\mathrm{d}T}{\mathrm{d}t}$$



(a) (b)

Fig. 1: Example of a VCSEL dataset entry. Markers indicate the samples stored in the recordset. (a) L-I curves at 25 °C, 40 °C, and 55 °C; (b) S21 curves evaluated in the conditions indicated by rectangles in (a).

with V applied voltage, T_{amb} ambient temperature, R_{th} thermal impedance and τ_{th} thermal time constant. The parameters G, N_{t}, I_{l} depend on the device temperature T through empirical laws:

$$G(T) = G_0 \frac{a_{\text{g0}} + a_{\text{g1}}T + a_{\text{g2}}T^2}{b_{\text{g0}} + b_{\text{g1}}T + b_{\text{g2}}T^2}$$

$$N_{\text{tr}}(T) = N_{\text{tr0}}\left(c_{\text{n0}} + c_{\text{n1}}T + c_{\text{n2}}T^2\right)$$

$$I_{\text{l}}(N_0, T) = I_{\text{l0}} \exp\left[\frac{-a_0 + a_1 N_0 + a_2 N_0 T - a_3/N_0}{T}\right]$$

DATASET GENERATION & MACHINE LEARNING ENGINE

The dataset is obtained by changing the 22 VCSEL parameters listed in Table 1; for each parameter, a value is randomly generated with uniform distribution in the reported range. During the generation of the random set of values, nonphysical combinations of parameters can be generated, leading, for instance, to thresholds far outside the investigated current ranges. These combinations are discarded and only 14 000 valid records are used in the final data set.

The following values are calculated for each set of random parameters:

- 16 samples from each L-I characteristic, for T_{amb} 25 °C, 40 °C, and 55 °C, respectively.
- 16 samples of the S21 responses calculated at 5 mA, 10 mA, and 15 mA at 25 °C
- 16 samples of the S21 responses calculated at 5 mA and 10 mA at 40 °C
- 16 samples of the S21 responses calculated at 15 mA at 55 °C

The L-I points are calculated with 16 currents uniformly distributed in the range 0 to 15 mA, while the S21 characteristics are obtained from 16 frequencies logarithmically spaced in the 100 mHz-50 GHz interval. As a result, each record is formed by 192 samples. An example of L-I curves at different temperatures and the corresponding S21 responses are shown in Fig. 1. After the generation of the dataset, the ML-based framework to extract the VCSEL model parameters is finally developed. The proposed ML agent is constructed with a parallel Deep Neural Network (DNN) architecture, meaning that each individual VCSEL parameter is extracted by its own dedicated DNN. Thus, we are able to increase the prediction accuracy by independently optimizing the DNN hyperparameters for each VCSEL parameter under test. In particular, we scanned different combinations of hidden layers number ([2, 3, 4, 5, 6, 7]), of neurons per layer ([20, 30, 50, 100]) and batch size ([100, 200, 500, 1000, 2000]), with fixed learning rate of 0.001. In the proposed DNN model, the Mean Squared Error (MSE) is used as loss function, while *ReLU* is the activation function of each hidden layer. Of the entire dataset, 70% is dedicated to training, while 30% is for testing. The parallel DNN architecture is developed using TensorFlow™ with the Keras API.

RESULTS AND CONCLUSIONS

The accuracy of the predictions made by a DNN unit is evaluated using the relative prediction error $\left(\Delta = \frac{\text{Predicted Value} - \text{Actual Value}}{\text{Actual Value}}\right)$ of each considered parameter. The findings of the DL agent are shown in Fig. 2 as a histogram of the relative error of the parameters that are considered, together with the standard deviation (σ) of the relative prediction error. The most critical parameters are related to the leakage current (a_2 and I_{l0}); for all the considered parameters the error is less than $\approx$ 20%. The proposed approach can find a reasonably accurate set of VCSEL parameters in a short time using a fully automated and model-agnostic mechanism. In order to generate the

Table 1: Parameters investigated and corresponding variation ranges for generating dataset.

Parameters	Range	Parameters	Range
Injection efficiency η_i	0.7 to 1	Transparency carrier N_{tr}	2×10^6 to 1×10^7
Photons to power k_f	1×10^{-8} W to 6×10^{-8} W	Gain saturation factor ε	1×10^{-6} to 5×10^{-6}
Carrier lifetime τ_n	0.5 ns to 5 ns	Leakage current factor I_{l0}	1 A to 2 A
Photon lifetime τ_p	1.5 ps to 3.5 ps	Transp. number param. C_{n0}	1 to 10
Gain coeff. g_0	1×10^4 s^{-1} to 2×10^5 s^{-1}	Transp. number param. C_{n1}	-0.1 K^{-1} to -0.01 K^{-1}
Gain coeff. a_{g0}	-1×10^4 to -4×10^3	Transp. number param. C_{n2}	0 K^{-2} to 1×10^{-4} K^{-2}
Gain coeff. a_{g1}	5 K^{-1} to 20 K^{-1}	Leakage current param. a_0	2000 K to 10 000 K
Gain coeff. a_{g2}	0.02 K^{-2} to 0.2 K^{-2}	Leakage current param. a_1	0 K to 3×10^{-4} K
Gain coeff. b_{g0}	1×10^3 to 1×10^4	Leakage current param. a_2	1×10^{-9} to 4×10^{-8}
Gain coeff. b_{g1}	-100 K^{-1} to 0 K^{-1}	Diffusion parameter h_{diff}	1 to 20
Gain coeff. b_{g2}	0 K^{-2} to 1 K^{-2}	Thermal impedance R_{th}	500 K W^{-1} to 8000 K W^{-1}

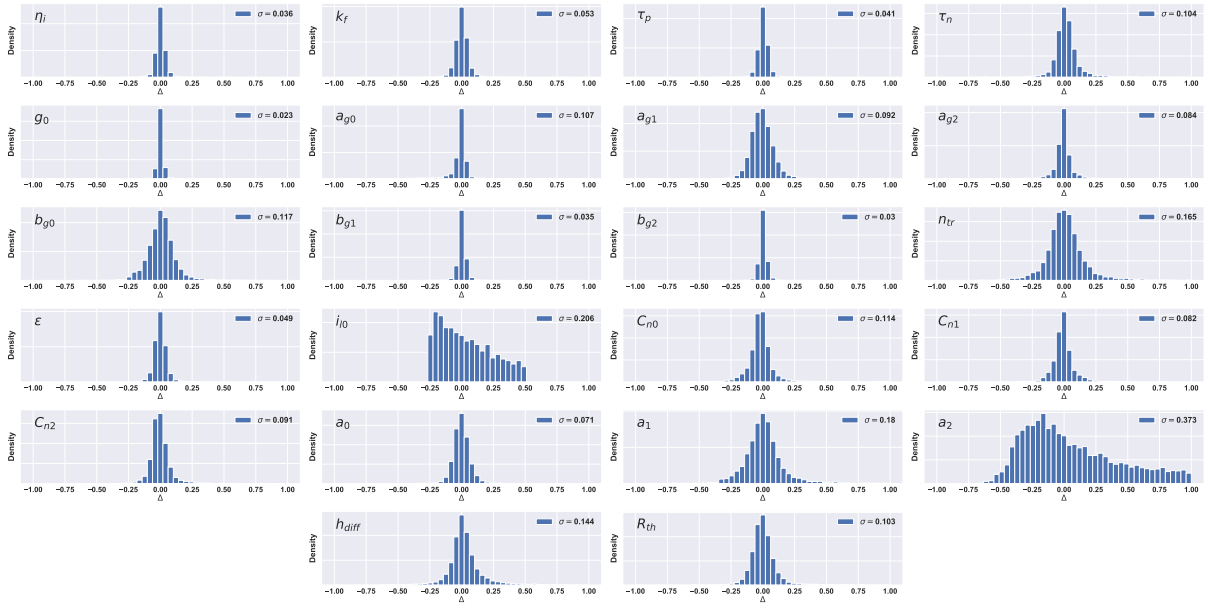


Fig. 2: Relative predicting error of the DL agent for the 22 parameters listed in Table I. In each histogram, the relative error standard deviation is also numerically reported.

dataset and to train the DL agent, the simulation is executed for a few hours on the latest workstations. In addition, the proposed model can easily be scaled up with a high level of accuracy for a larger number of parameters (compared to the 22 parameters that are analyzed in this work) due to its parallel architecture, which has the capability to be rapidly expanded without compromising accuracy. This enables the proposed architecture to be advantageously adapted to study other laser classes.

We present a method that uses DL to extract the essential physical parameters that characterize the stationary and dynamic behavior of the VCSEL source. Circuit-level simulations of the L-I and S21 characteristics of VCSELs, including temperature-related effects, are used to generate the data sets. The proposed technique is fully automated and can be operated for fast and accurate extraction of VCSEL parameters. Furthermore, the suggested scheme is easily scalable to a more vast set of parameters in more complicated models, rather than being restricted to the given set-up.

References

[1] P. Mena *et al.*, "A comprehensive circuit-level model of vertical-cavity surface-emitting lasers," J. Light. Technol. **17**, 2612–2632 (1999).

[2] https://www.synopsys.com/photonic-solutions/pic-design-suite.html.

[3] Z. Ma and Y. Li, "Parameter extraction and inverse design of semiconductor lasers based on the deep learning and particle swarm optimization method," Opt. Express **28**, 21971–21981 (2020).

[4] I. Khan *et al.*, "Two-step machine learning assisted extraction of VCSEL parameters," in *2023 SPIE Physics and Simulation of Optoelectronic Devices XXXI,* (SPIE, 2023), pp. 12415–49.

[5] M. X. Jungo *et al.*, "VISTAS: a comprehensive system-oriented spatiotemporal VCSEL model," IEEE J. Sel. Top. Quantum Electron. **9**, 939–948 (2003).

[6] N. Bewtra *et al.*, "Modeling of quantum-well lasers with electro-opto-thermal interaction," IEEE J. Sel. Top. Quantum Electron. **1**, 331–340 (1995).

Investigation of periodic poling in LNOI

(Student paper)

Laura Bollmers[1], Peter Mackwitz[2], Marcello Massaro[1], Boris Koppitz[3], Michael Rüsing[3], Lukas M. Eng[3,4], Gerhard Berth[2], Artur Zrenner[2], Christof Eigner[1], Laura Padberg[1], Christine Silberhorn[1]

[1] Paderborn University, Integrated Quantum Optics, Institute for Photonic Quantum Systems (PhoQS), Warburger Str. 100, 33098 Paderborn, Germany
[2] Paderborn University, Nanostructure Optoelectronics, Warburger Str. 100, 33098 Paderborn, Germany
[3] TU Dresden, Institute of Applied Physics, Nöthnitzer Strasse 61, 01187 Dresden, Germany
[4]ct.qmat: Dresden-Würzburg Cluster of Excellence—EXC 2147, TU Dresden, 01062 Dresden, Germany
[*] laura.bollmers@uni-paderborn.de

Lithium niobate on insulator (LNOI) is a material platform of growing interests due to its outstanding properties. We investigate periodic poling in LNOI to quasi-phase match our nonlinear optical processes. For this purpose, we use finger electrodes and show their fabrication. We also show our periodic poling results and demonstrate finally a second harmonic generation process in a periodically-poled waveguide.
Keywords: *LNOI, periodic poling, second harmonic generation, domain inversion*

INTRODUCTION

Quantum optics is a field of research that explores the behavior of light and matter at the quantum level. The study of quantum optics is motivated by the desire to understand the fundamental nature of light and its interactions with matter and the potential for developing new technologies based on these interactions. Explicitly integrated quantum optics focuses on integrating multiple quantum optical elements, such as lasers, detectors, and nonlinear crystals, into a single system. This approach allows for the manipulation and control of light at the quantum level, leading to new possibilities for quantum computing, communication, and metrology. Additionally, this approach allows for exploring new phenomena such as quantum entanglement and quantum teleportation.

Overall, the field of quantum optics and explicitly integrated quantum optics are motivated by the desire to understand and control the behavior of light at the quantum level, which has the potential to lead to new technologies and a deeper understanding of the natural world. Typically, quantum optical setups are bulky setups that occupy whole tables and require very tightly controlled environments to achieve the required stability. More advanced applications require an increasing number of components and stability. However, integrated photonic systems are inherently more stable and scalable, allowing for more complex applications to be developed in a fraction of the footprint. One material of choice for integrated photonic application is lithium niobate, due to its outstanding properties which enable e.g., low propagation losses [1] and high optical nonlinearities [2].

Although significant improvements have been made in integrated optical devices in lithium niobate, the miniaturization progress has reached the realms of integrated optics and quantum photonics. One of the most promising opportunity to overcome this limitation is the so-called silicon on insulator (SOI) platform. Due to its special design, the refractive index change between the waveguide and the substrate is immense [3] and offers great possibilities for miniaturization. Nevertheless, due to its inversion symmetry, silicon offers no second order nonlinearity [4]. Consequently, only third order nonlinear processes can be used in SOI. The corresponding nonlinear optical coefficient $\chi^{(3)}$, which is a measure of the strength of nonlinear optical interactions, is up to 12 orders of magnitude smaller than the one of the second order nonlinearity [5] of lithium niobate. Therefore, lithium niobate on insulator (LNOI) which combines the excellent properties of lithium niobate, including a second order nonlinearity, and the advantages of SOI platform is the best choice for quantum devices.

The key components for integrated photonics and quantum optics in LNOI are waveguides, modulators and nonlinear interactions achieved via periodic poling. Periodic poling is utilized for quasi-phase matching processes, which are needed for efficient frequency conversions, which is the critical component in LNOI. In recent years, significant progress has been made in periodic poling in LNOI. However, structured analyses of the poling behavior and efficient poling over several millimeters lengths, are still lacking. We want to take this step and present our current results on structural periodic poling in LNOI.

RESULTS

Quasi-phase matching is essential for efficient frequency conversion, requiring periodically-poled structures in LNOI. For our experiments, we use commercially available x-cut LNOI (NANOLN). The domain inversion happens along the z-axis of the crystal. We use so-called finger electrodes where domain inversion is realized by applying high-voltage pulses. Therefore, high-quality electrodes are a crucial component for periodic poling. We characterize the final results via second harmonic (SH) microscopy and finally measure in a frequency conversion process in a waveguide. The propagation direction is perpendicular to the poling. Consequently, we fabricate our waveguides along the y-axis.

FINGER ELECTRODES

For finger electrode fabrication, we spin coat resist onto an LNOI sample in the first step. The resist is structured subsequently via laser lithography or electron-beam lithography. After developing, chromium and gold is deposited as finger electrodes. As a last step, a lift-off process is done.

Laser lithography provides the possibility of efficient production due to the high writing speed of the system. To the best of our knowledge, we are the first group to use laser lithography to fabricate finger electrodes. Typically, electron-beam lithography is chosen for this purpose since it offers a higher resolution. The higher resolution of the electron-beam lithography compared with laser lithography can be seen in figure 1, which shows the resulting finger electrodes for a laser lithography (left) and for electron-beam lithography (right) based process.

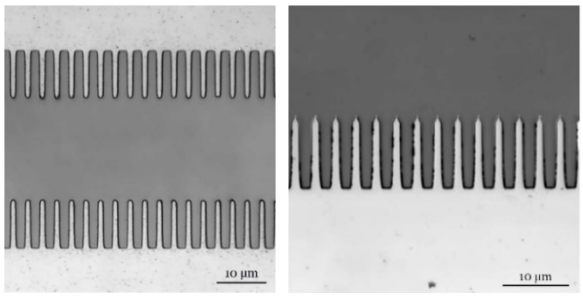


Fig. 1. Finger electrodes after fabrication. On the left the fabrication process is done by using a laser lithography system and on the right the process is done via an electron-beam lithography.

Irrespectively from which lithography system is used, it is essential for high-quality poling that the finger electrodes are stable, adhesive and homogenous along the entire length. Since the efficiency of quasi-phase-matched processes increases within the length of the periodically-poled area, long periodically-poled areas are desirable, which clearly require long electrodes.

PERIODIC POLING

For periodic poling, we invert the domains periodically in the crystal by applying a high-voltage pulse to the finger electrodes. A deep understanding of the complex interaction between the poling parameters is essential to achieve high-quality periodic poling. This includes a structured analysis of the crucial parameters like the poling pulse, especially the voltage and the time, the electrodes' geometry, the metal used for the finger electrodes and the lithium niobate thin-film layer itself.

We investigated the shape of the poling pulse and focused on the interaction between the applied voltage and the time. For this purpose, we tested different parameter combinations and visualize the domains via SH microscopy. One example of such an SH microscope image is shown in figure 2 (left), in which the domain walls (yellow) between the inverted and non-inverted domains can be seen.

DISCUSSION

The quality of fabricated poling structures can be inferred from their SH microscope images, as discussed above. Thus, the shape of the domain walls provides a deeper insight into the switching behavior of lithium niobate upon poling. Utilizing the findings from those measurements allows us to optimize and tailor the poling process to such a degree that homogeneous and reproducible fabrication of periodically poled structures becomes feasible. Yet, those images can also be used for exhibiting the limits of our current fabrication methods, and thus allows a profound comparison to the work of different research groups. Here, the poled structure becomes a key issue, as

well as maximum length at which those structures can be fabricated reproducibly. Maximizing the poled length is crucial for increasing conversion efficiencies for both classical photonics and quantum conversion processes.

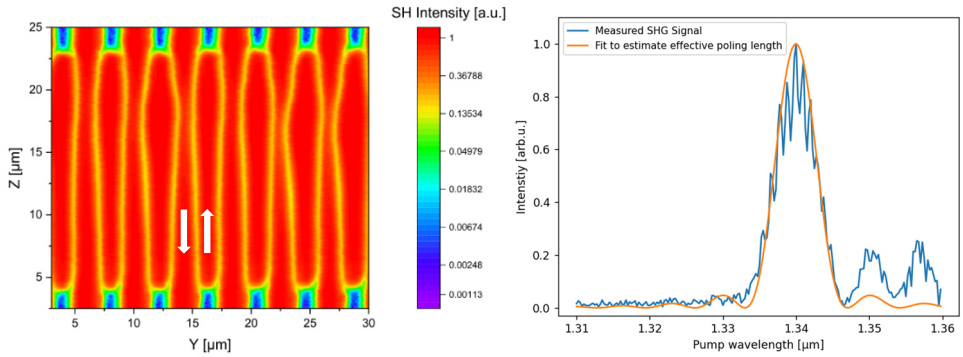


Fig. 2. Example for an SH microscope image of a periodically-poled LNOI sample with a poling period of 3 µm in which the domain walls (yellow) are visualized (left). The arrows indicate the direction of the spontaneous polarization. Measured SHG signal for our 7.5 mm long periodically-poled sample (blue) with a poling period of 2.8 µm and a fit function (orange) to estimate the effective poling length (right).

Therefore, we poled LNOI with a poling period of 3 µm along 5 mm periodically, which is also the maximum poling length that is shown by other research groups [6]. Furthermore, we investigate our inverted domains via SH microscopy to check whether the domains looked uniform over the whole length or not. We saw a few discrepancies between the domains at the middle of the electrode and the ones at the edges of the electrode, which indicates once again the special challenge of poling a long area periodically. Despite that, our results are promising since we managed periodic poling. Thus, we also tested periodic poling over 7.5 mm with different poling periods (2.9 µm, 2.8 µm and 2.7 µm).

To analyze our periodic poling result for 7.5 mm, we do SH microscopy. Moreover, we do an optical study by investigating the nonlinear properties via a second harmonic generation (SHG) process. Our measured SHG signal for a poling period of 2.8 µm is shown in figure 2 (right). We use a sinc-function to identify the effective poling length of our sample, which measures the quality of the poling.

Whenever poling was perfect, the effective length should equal to the length of the electrode. Our sample's calculated effective poling length is 567 µm which is lower than the finger electrodes' physical length. The discrepancy between the physical and effective poling lengths shows that using the same poling pulse for short and long poling areas does not result in the same quality of periodic poling.

By gaining a deeper understanding of the interaction of the parameters relevant to periodic poling, adaptive poling is feasible. This knowledge can be used to estimate the poling parameters better. Furthermore, this knowledge is beneficial to adapt the poling parameter to pole an extended area periodically. A homogenous and reproducible domain inversion is one of the most significant challenges for periodic poling along several millimeters.

Overall, we show our fabrication process for finger electrodes, which includes the use of a laser lithography system and an electron-beam one. Furthermore, we show the latest results of our periodic poling investigation of different poling lengths. Additionally, we demonstrate that poling lengths up to 7.5 mm are possible and show our nonlinear optical conversion analysis.

Acknowledgements: Funded by the Deutsche Forschungsgemeinschaft (DFG, German Research Foundation) – SFB-Geschäftszeichen TRR142/3-2022 – Projektnummer 231447078 and FOR5044 – Projektnummer 426703838.

References

[1] M. Stefszky, R. Ricken, C. Eigner, V. Quiring, H. Herrmann, C. Silberhorn, *Waveguide cavity resonator as a source of optical squeezing*, Physical Review Applied, vol. 7, no. 4, pp. 044026, 2017

[2] L. Arizmendi, *Photonic applications of lithium niobate crystals*, physica status soldi (a), vol. 201, no. 2, pp. 253-283, 2004

[3] P. Prabhathan, V. M. Murukeshan, Z. Jing, P. V. Ramana, *Compact SOI nanowire refractive index sensor using phase shifted Bragg grating*, Optics Express, vol. 17, no. 17, pp. 15330-15341, 2009

[4] Q. Lin, J. O. Painter, G. P. Agrawal, *Nonlinear optical phenomena in silicon waveguides: modelling and applications*, Optics Express, vol. 15, no. 25, pp. 16604-16644, 2007

[5] R. W. Boyd, *Nonlinear optics*, Elsevier, Amsterdam, 3. ed. 2008

[6] I. Krasnokutska, J. L. J. Tambasco, A. Peruzzo, *Submicron domain enginerring in periodically poled lithium niobate on insulator*, arXiv preprint arXiv, 2108: pp. 10839, 2021

Observation and enhancement of stimulated Brillouin scattering in tellurite covered silicon nitride waveguides.

(Student paper)

Roel Botter[1,*], Bruno Segat Frare[2], Batoul Hashemi[2], Kaixuan Ye[1], Yvan Klaver[1], Jonathan Bradley[2] and David Marpaung[1]

[1]Nonlinear Nanophotonics, MESA+ Institute of Nanotechnology, Department for Science and Technology, Applied Nanophotonics, University of Twente, Drienerlolaan 5, 7522 NB, Enschede, the Netherlands
[2]Bradley Research Group, Department of Engineering Physics, McMaster University, 1280 Main Street West, Hamilton, Ontario, L8S 4L7, Canada
* r.a.botter@utwente.nl

We show, for the first time, stimulated Brillouin scattering in tellurite covered silicon nitride waveguides. In the standard geometry the measured peak gain coefficient is 4.5 $m^{-1}W^{-1}$. We further enhance the Brillouin gain by applying cladding engineering, reaching a peak gain coefficient of 8.5 $m^{-1}W^{-1}$.

Keywords: *stimulated Brillouin scattering, non-linear optics, tellurite, silicon nitride*

INTRODUCTION

Stimulated Brillouin scattering (SBS) is a third order non-linear optical effect, based on the interaction of optical and acoustic waves [1]. In SBS, the interference between two counterpropagating light waves, a probe and a higher frequency pump, create an acoustic wave through electrostriction. This acoustic wave then creates a moving grating through the photoelastic effect. The pump light is reflected by the grating, undergoing a Doppler shift in the process. As a result, the reflected light is downshifted to the frequency of the probe, resulting in a narrowband amplification. SBS on chip is an emerging field, and has shown promising results in applications including sensing and communications [2].

Traditionally, silicon nitride waveguides have low Brillouin gain coefficients, of 0.1 $m^{-1}W^{-1}$ or lower, [3, 4]. This is because silicon oxide cladded silicon nitride does not guide acoustic waves. We have previously shown that a multilayer waveguide can guide the acoustic waves, leading to a gain coefficient of 0.4 $m^{-1}W^{-1}$ [5]. Another option is to use hybrid integration of novel materials.

A promising material for on-chip SBS is tellurite, or tellurium oxide (TeO_2), which has shown to be a good opto-acoustic material [6]. Low loss circuits can be made with tellurite covered silicon nitride waveguides, showing losses down to 0.25 dB/cm [7]. These waveguides can be used for supercontinuum generation [7], and can also be doped

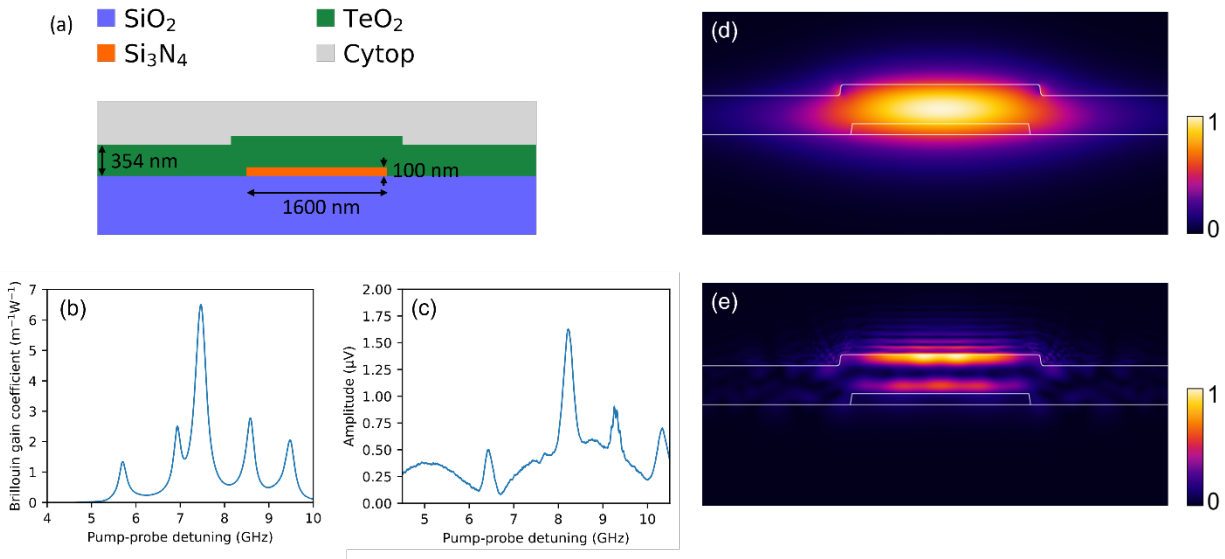


Figure 1: The tellurite covered silicon nitride waveguide. (a) the geometry of the waveguide. The Brillouin response of the waveguide (b) as simulated using COMSOL, and (c) as measured in the experiment. (d) the optical mode of the waveguide, and (e) the displacement field of the acoustic response of the highest Brillouin gain peak.

for use as on-chip amplifiers [8]. However, no investigation of SBS in these waveguides has been carried out thus far.

RESULTS

The first waveguide geometry for SBS considered here is shown in Figure 1 (a). The waveguide is patterned in a 100 nm thick silicon nitride layer. This layer is then coated with a 354 nm thick tellurite layer via sputtering, and cladded with Cytop, a fluoropolymer. The silicon nitride core of this waveguide is 1.6 µm wide. We used COMSOL to simulate the Brillouin response of our waveguide. The resulting gain spectrum can be seen in Figure 1(b), the highest Brillouin peak is 6.5 $m^{-1}W^{-1}$ at a frequency shift of 7.47 GHz. Figure 1 (d) shows the optical mode of the waveguide, and Figure 1(e) shows the displacement field of the acoustic response of the highest gain peak. The simulation tells us that there are multiple acoustic modes leading to a Brillouin interaction, resulting in multiple peaks.

The displacement field in Figure 1 (e) shows how the tellurite layer, as a softer material, is able to guide the acoustics, as expected. It also shows the acoustic waves leaking into the even softer polymer on top.

Figure 1 (c) shows the measured Brillouin response. We can use this to calculate the gain coefficient based on the pump power and waveguide length. The highest measured peak corresponds to a gain coefficient of 4.5 $m^{-1}W^{-1}$ at 8.22 GHz. Overall there is good agreement between spectra, and the peaks identified in the simulation are also visible in the measurement.

ENHANCING THE SBS GAIN THROUGH CLADDING ENGINEERING

As discussed before, the acoustic wave is leaking into the polymer cladding. This results in a reduction of the Brillouin gain, as the acoustic waves in the cladding cannot interact with the optics, preventing optimal opto-acoustic interaction. The polymer is also acoustically lossy, resulting in a further inhibition of the Brillouin process. In an effort to reduce the acoustic leakage, we introduce a thin layer of silicon oxide, a harder material, with a speed of sound of 5960 m/s, between the tellurite and polymer layers, thereby providing improved acoustic confinement. Figure 2 (a) shows the geometry of this new waveguide. Here a 200 nm layer of silicon nitride is covered by 299 nm of tellurite, which is then cladded by a 46 nm layer of silicon oxide, before adding the polymer layer.

Our simulations, depicted in Figure 2 (b) show that the addition of this layer has varying effects on the different acoustic modes. Some are suppressed, but one in particular is strongly enhanced, resulting in a doubling of the peak Brillouin gain. The new peak gain is 11 $m^{-1}W^{-1}$, with a frequency shift of 8.57 GHz. The acoustic response in Figure 2 (e) shows how the acoustic field in the polymer cladding has been reduced, as expected.

Figure 2 (c) shows the measured Brillouin response. Here we see 2 peaks which correspond to a Brillouin gain coefficient of 8.5 $m^{-1}W^{-1}$, at 7.11 and 8.91 GHz. This confirms the higher Brillouin gain achieved by the silicon oxide layer.

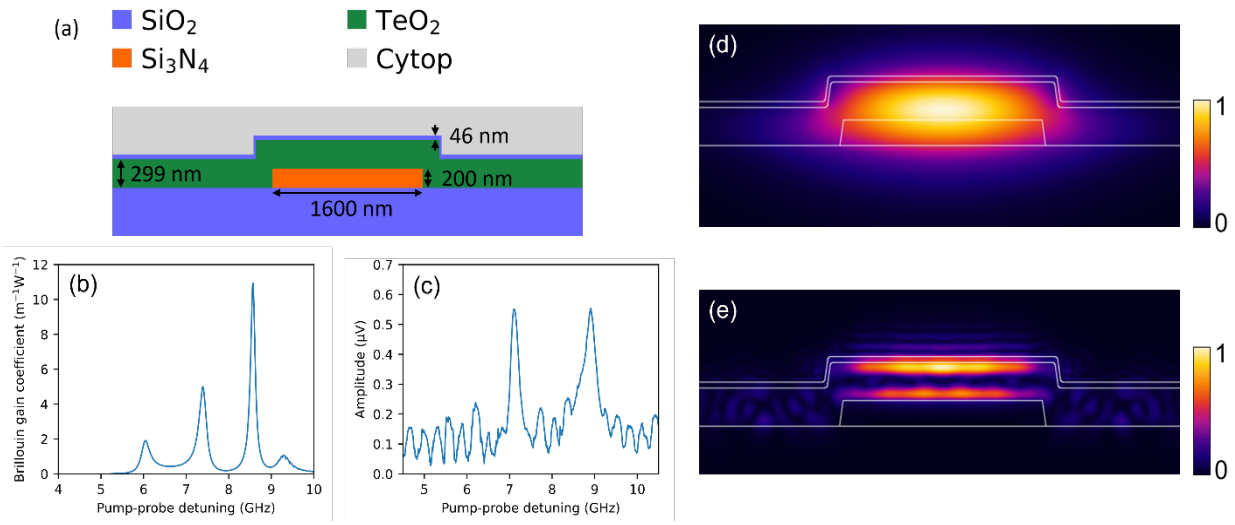


Figure 2: The tellurite covered waveguide with additional silicon oxide layer. (a) the geometry of the waveguide. The Brillouin response of the waveguide (b) as simulated using COMSOL, and (c) as measured in the experiment. (d) the optical mode of the waveguide, and (e) the displacement field of the acoustic response of the highest Brillouin gain peak.

DISCUSSION

We have shown the first stimulated Brillouin scattering in tellurite covered silicon nitride waveguides. The Brillouin response of these waveguides match the predictions of our simulations. We have also shown the enhancement of the Brillouin gain through cladding engineering, where we used a thin layer of silicon oxide to prevent acoustic leakage into the polymer cladding.

The simulations and experimental results of the enhanced Brillouin gain device do not match as well as those of the original device. This is likely due to uncertainty in the exact acoustic losses of the materials, which are unknown.

The thin silicon oxide layer reduced the acoustic field in the polymer, but it does not completely prevent it from leaking into the cladding. We can improve on this by fully cladding the waveguide in silicon oxide, which according to our simulations leads to a peak gain of 35 $m^{-1}W^{-1}$, with a frequency shift of 6.44 GHz. The next step is to develop this cladding to unlock this order of magnitude gain enhancement.

These results open the possibility for creating Brillouin devices on chip, such as narrowband lasers and signal processing components.

References

[1] R. W. Boyd, *Nonlinear Optics*. Elsevier Science Publishing Co Inc, 2008.

[2] B. J. Eggleton, C. G. Poulton, P. T. Rakich, M. J. Steel, and G. Bahl, "Brillouin integrated photonics," *Nat. Photonics*, vol. 13, pp. 664–677, 2019.

[3] S. Gundavarapu *et al.*, "Sub-hertz fundamental linewidth photonic integrated Brillouin laser," *Nat. Photonics*, vol. 13, no. January, 2019.

[4] F. Gyger *et al.*, "Observation of Stimulated Brillouin Scattering in Silicon Nitride Integrated Waveguides," *Phys. Rev. Lett.*, vol. 124, no. 1, 2020.

[5] R. Botter *et al.*, "Guided-acoustic stimulated Brillouin scattering in silicon nitride photonic circuits," *Sci. Adv.*, vol. 8, no. 40, p. eabq2196, 2022.

[6] T. Yano, A. Fukumoto, and A. Watanabe, "Tellurite glass: A new acousto-optic material," *J. Appl. Phys.*, vol. 42, no. 10, pp. 3674–3676, 1971.

[7] N. Singh, H. M. Mbonde, H. C. Frankis, E. Ippen, J. D. B. Bradley, and F. X. Kärtner, "Nonlinear silicon photonics on CMOS-compatible tellurium oxide," *Photonics Res.*, vol. 8, no. 12, pp. 1904–1909, 2020.

[8] H. C. Frankis *et al.*, "Erbium-doped TeO2-coated Si3N4 waveguide amplifiers with 5 dB net gain," *Photonics Res.*, vol. 8, no. 2, p. 4, 2020.

Lithium Niobate near IR waveguides for astrophotonic and spectrometry applications

(Student paper)

Guillermo Martin[1,*], Noémie Mestre[1], Myriam Bonduelle[1], Roland Salut[2], Nadège Courjal[2] and Alain Morand[3]

[1]Univ. Grenoble Alpes, CNRS, IPAG, F-38400, Grenoble, France
[2]Université de Bourgogne, FEMTO-ST, F-25030, Besançon, France
[3]Univ. Grenoble Alpes, CNRS, Grenoble INP, IMEP-LAHC, F-38000, Grenoble, France
[*] guillermo.martin@univ-grenoble-alpes.fr

In order to develop new photonic chips for astronomy and spectroscopy, optimized near infrared waveguides and functions in lithium niobate have been conceived and fabricated. The characterization results on these electro-optic samples, in particular a multiplexed integrated spectrometer and a high contrast beam combiner, will be presented.
Keywords**:** *Electro-optics, lithium-niobate, IR waveguides, spectrometry, astrophotonics*

INTRODUCTION

Integrated optics devices are increasingly being used for astronomical applications, due to the robustness of the systems, which is of special interest in the field of interferometry, where a high number of beam are to be collected, guided and combined, while keeping the relative phase stable, or temporally controlled by means of active scan. In parallel, aside recovering the flux from the source, an interesting application is to obtain directly on-chip the spectrum of the source, without having to disperse light through bulk optics. In this case, the advantage of compact systems, in particular through guided optics, is to avoid difficult alignment of the beam, and in particular, in applications where stability is compulsory, such as drone, nanosat or other air-borne applications.

A diversity of astronomical instruments have been using the performances of passive waveguides (PIONEER, GRAVITY in SiO2/Si [1], FIRST using fibers [2], DRAGONFLY with photonics lanterns [3]). In future instruments, active control of the phase inside the waveguide allows for implementing interesting functions on-chip: Photometry balancing, to increase fringe contrast; fringe locking or fringe scanning [4]; wavelength multiplexing…Therefore, developing dedicated functions for improving the performances of future instruments is a very interesting field of research.

In this presentation, we will show some updated results on novel applications developed using near IR electro-optic Ti:diff waveguides in Lithium Niobate. Mainly, the results that will be presented concern a spatial and temporal multiplexed Fourier transform integrated spectrometer [5], and a high contrast active beam combiner, with corresponding photometries, in order to develop new generation nullers in the field of exoplanet research (LIFE, [6], Asgard/Hi5 [7]).

RESULTS

Near IR multiplexed spectrometers using lithium niobate:

The first device we will present is an integrated optics Fourier transform spectrometer (SWIFTS) that has been fabricated in lithium niobate. It can be shown that the spectral resolution is related to $R = 2nL / \lambda$, where n is the effective refractive index of the guided mode and L is the length of the sampling region. Besides, the spectral etendue (before aliasing) is related to $\lambda^2/4n\Delta z$. Therefore, for typical pixel pitchs of $\Delta z = 10$ μm, the spectral etendue at $\lambda = 1.5$ μm is limited to 37nm. In order to increase the effective spectral etendue, electro-optic modulation of the fringes, by using a Mach-Zehnder modulator at the input of the waveguide (see Fig. 1), allows to temporally scan the fringes under the pixel and reduce the effective sampling distance between two consecutive data. However, as the EO scan is not strong enough to scan a large number of fringes, spatial multiplexing is proposed. In this case, as a proof of concept, 4 parallel waveguides are fabricated, with periodically placed antenna, but slightly shifted between consecutive waveguides. Therefore, we multiply by 4 the number of data (spatial multiplexing) in a first stage, and in a second stage temporal scan allows to fill the gap between consecutive antenna. By stitching the temporal and spatial data, we are able to increase the spectral etendue. Of course, the drawback of this approach is that flux is divided between the number of parallel waveguides, and temporal scanning limits the

exposure time, so this method is reduced to relatively powerful optical sources, in particular, it is very well adapted to laser and SLED spectral characterization.

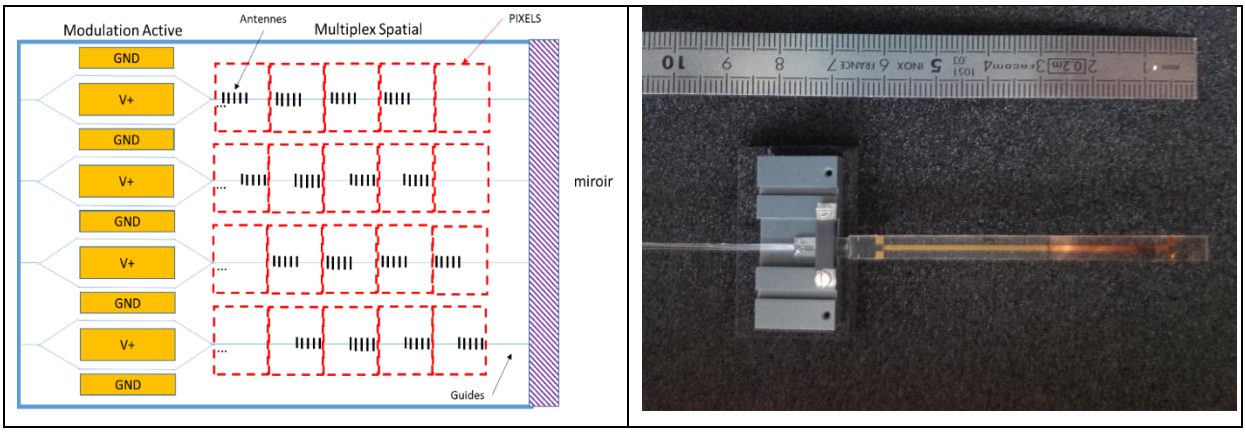


Fig. 1. Left: Schematics of the multiplexed SWIFTS interferometer, with the Mach-Zehnder modulators allowing for temporal fringe scanning. Right: Picture of the assembled device, showing the 5cm long electrodes and the input fibers.

Near IR beam combiners for high contrast interferometry :

A second typical building block is a high contrast interferometer, with parallel control of photometry (see Fig. 2). This is a basic photonic function for nulling interferometry applications. In the system presented here, a first stage of directional couplers allows for photometric control (V2 and V3). Then, the central beam combiner allows for high contrast interferometry, as the fringes are scan through the last EO modulator (V1).

We will present the results on characterization in terms of contrast performances, monochromatic and wideband in the near IR, and polarization behavior.

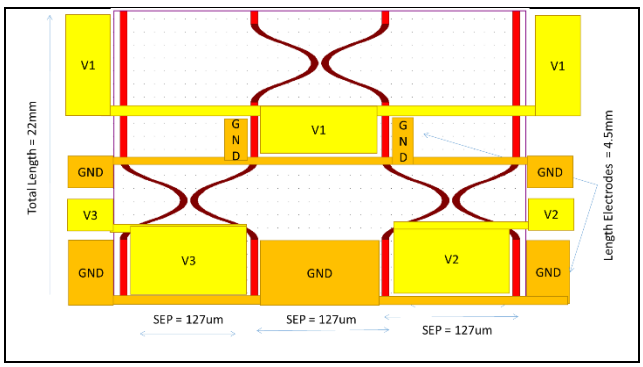


Fig. 2. Schematics of the dual stage nulling interferometer, with a first stage of photometry control and a second stage for fringe scanning. The two central outputs allow for interferometry studies, whereas the external channels allow for photometry control.

DISCUSSION

Preliminary results show that spatial multiplexing (stitching the signal obtained from shifted antenna as shown in figure 1), allows for spectral recovery of an unknown wavelength by comparison to a calibrated dataset, with a resolution of 20pm. This shows that the SWIFTS interferometer works well as a lambdameter, and has now to be validated using wideband sources.

Acknowledgements: Authors acknowledge funding from Labex FOCUS (ANR-11-LABX-0013).

References

[1] Abuter et al., *First light for GRAVITY: Phase referencing optical interferometry for the Very Large Telescope Interferometer*, Astron. Astrophys. 602, 94, 2017
[2] G. Martin et al., *Hybrid electro-optic visible multi-telescope beam combiner for next generation FIRST/SUBARU instruments*, Proc SPIE 12188, 2022
[3] N. Jovanovic et al., *Starlight demonstration of the Dragonfly instrument: an integrated photonic pupil-remapping interferometer for high-contrast imaging*, Mon. Not. R. Astron. Soc. 427: 806-815, 2012
[4] G. Martin; S. Heidmann; J-Y Rauch; L. Jocou and N. Courjal. "Electro-optic fringe locking and photometric tuning using a two-stage Mach-Zehnder lithium niobate waveguide for high-contrast mid-infrared interferometry". Opt. Eng. 53 (3), 034101, 2014
[5] E. le Coarer et al., *Wavelength-scale stationary-wave integrated Fourier-transform spectrometry*, Nat. Phot. 1, 473 (2007)
[6] J. T. Hansen, M. J. Ireland and the LIFE Collaboration, *Large Interferometer For Exoplanets (LIFE) - IV. Ideal kernel-nulling array architectures for a space-based mid-infrared nulling interferometer* A&A, 664, A52, 2022.
[7] Denis Defrère et al., *L-band nulling interferometry at the VLTI with Asgard/Hi-5: status and plans*, Proc. SPIE 12183, Optical and Infrared Interferometry and Imaging VIII, 121830H, 2022

Multiport interferometer from a multimode waveguide

Mikhail Saygin[1], Suren Fldzhyan[1,2], Ivan Dyakonov[1], Sergei Kulik[1,3] and Stanislav Straupe[1,2]

[1]Quantum Technology Centre & Faculty of Physics, M.V. Lomonosov Moscow State University, Moscow, 119991, Russia
[2]Russian Quantum Center, Skolkovo, Moscow 143025, Russia
[3]Laboratory of quantum engineering of light, South Ural State University (SUSU), Chelyabinsk 454080, Russia
* saygin@physics.msu.ru

The introduction of bends into multimode waveguides is known to have undesirable effects on the transmitted information due to mode mixing. Here, we leverage the mode mixing to construct multimode interferometers with a predefined transfer matrix. Using the inverse-design method, we have investigated the capabilities of such type of interferometers to perform useful tasks.

Keywords**:** *Multimode waveguides, waveguide bends, photonic information processing*

INTRODUCTION

Multiport interferometers find wide applications in photonic technologies. The interferometers should be capable to transforming the orthogonal field modes according to a predefined matrix U, such that the output vector of field amplitudes $\boldsymbol{b}$ is related to the input vector $\boldsymbol{a}$ by multiplication on the matrix**:** $\boldsymbol{b} = U\boldsymbol{a}$. In particular, performing matrix-vector and matrix-matrix multiplication, the subroutine intensively used in neural networks, using proper multimode photonic elements, can be more energy efficient than the traditional electronic approaches [1]. Multiport interferometers also play an essential role in quantum simulators, which use the unique properties of photon interference to perform quantum operations [2].

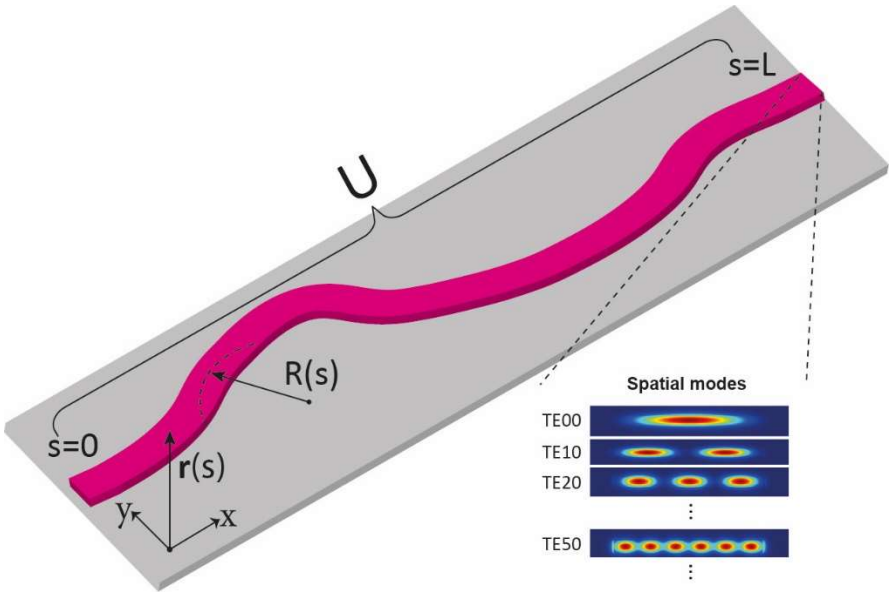


Fig. 1. Illustration of the proposed multiport interferometer: the multimode waveguide implementing a mixing transformation over the spatial modes propagating through it.

Many applications of multiport interferometers require the transfer matrix U to be programmable to perform a specific transformation. For this purpose, several design methods exist that enable one to construct universal schemes that can be reprogrammed to any given transfer matrix by setting proper values of the constituent phase shifters (see, for example, [3]). However, in some applications, one needs only to multiply by a static matrix throughout the whole lifespan of the device. Therefore, considering the need for scaling the multiport devices, using the programmable designs for static interferometers can be overly complex. It is of interest to develop new approaches for designing such static interferometers.

In integrated photonics, the spatial degree of freedom is often exploited, either solely or combined with another degree of freedom. In particular, the multiport interferometers constructed from single-mode waveguide elements are widely used in classical and quantum photonics due to the simplicity of circuit design. In contrast, we investigate the capability of the multimode waveguide to perform linear transformations over the propagating spatial modes.

Using multimode waveguides in integrated photonics can be beneficial, as the devices can be more compact than their single-mode counterparts. In addition, the multimode waveguides can be more easily coupled with photon sources and detectors, especially with quantum emitters.

The proposed multiport interferometer is illustrated in Figure 1. The main element is a planar multiport waveguide with a rectangular cross-section and variable guiding direction, as defined by the dependence of the vector $\boldsymbol{r}(s) = (x(s), y(s))$ pointing to the waveguide centre, where s is the coordinate along the waveguide path with L being the length of the path ($0 \leq s \leq L$). This section is where the controlled inter-mode mixing is implemented to obtain the target transfer matrix between modes of interest. The encoding of the input and output amplitudes $\boldsymbol{a}$ and $\boldsymbol{b}$ is in a set of orthogonal spatial modes of straight waveguides connected to the input and output of the curved MMW. The waveguide path $\boldsymbol{r}(s)$ is completely defined by the local curvature dependence $\kappa(s) = 1/R(s)$, which can take a positive or a negative value, depending on the side where the curvature centre is located with respect to the waveguide section center $\boldsymbol{r}(s)$ and $\kappa(s) = 0$ for a straight section. The inverse-design methods, which have attracted appreciable interest in the recent years, can tackle such tasks [4].

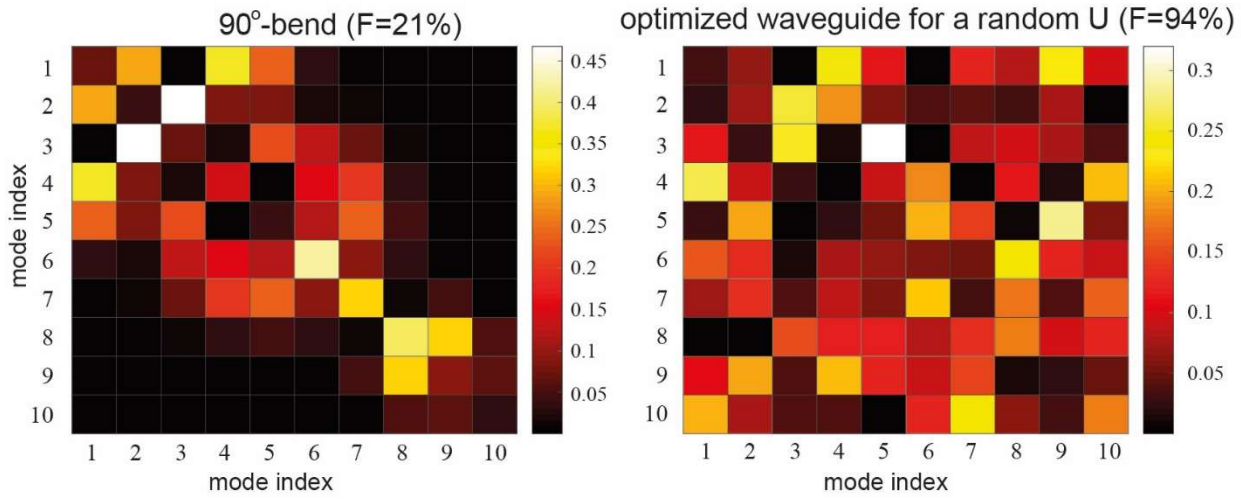


Fig. 2. Histogram of power transfer matrices, corresponding to the 90°-bend of silicon waveguide of $\boldsymbol{R} = \mathbf{10}$ mkm radius (left) and a waveguide with optimized path to implement a randomly generated transfer matrix (right). The following waveguide parameters were used in simulation: (height) $\boldsymbol{h} = \mathbf{0.2}$ mkm, (width) $\boldsymbol{w} = 3$ mkm, (wavelength) $\boldsymbol{\lambda} = \mathbf{1.55}$ mkm.

RESULTS

To find the optimal waveguide path $\boldsymbol{r}(s)$ implementing a desired unitary matrix as close as possible, numerical optimization has been exploited, which were searching for a global maximum of the fidelity measure: $F = |Tr(UU_0^+)|^2/M^2$, where U_0 and U are the target and the actual transfer matrices, M is the matrix size (number of supporting modes). Direct calculation of the transfer matrices requires calculation of field dynamics through the waveguide, which in turn necessitates numerical solution of equations on a 3D grid. To alleviate the burden of computing time, we reduced the full 3D equations for field to equations of propagation of the spatial modes that depends on one spatial variable s and some functional parameter that can be pre-calculated numerically once the waveguide cross-section and materials are given.

Fig. 2 illustrates one example of the approach. Here, the target transformation was to perform mode mixing with a transfer matrix U_0 generated at random from a uniform distribution. The choice of random matrices is motivated by the architecture of programmable interferometers, which we proposed earlier [5]. The figure shows two cases. The left histogram corresponds to an unoptimized multiport bent, supporting $M = 10$ TE modes. Even though the mode mixing is clearly present, it does not provide full mode mixing, thus, the low fidelity $F = 21$ %. The histogram on the right is obtained for the waveguide of the same cross-section, however, its path $\boldsymbol{r}(s)$ has been optimized with respect to the fidelity measure: $F \sim |Tr(UU_0^+)|^2$, where U is the actual transfer matrix, obtained in the course of optimization. In this example, the archived fidelity $F = 94$ %. We have investigated the proposed approach considering several useful transfer matrices, very often required in photonic information processing, including the discrete Fourier transform and Hadamard matrices.

DISCUSSION

In our work we have investigated a new approach to create static multiport interferometers operating on spatial modes of multimode waveguides. The interferometers can perform some useful multiport transformations and

they can be utilized either as stand-alone elements performing specific transfer matrices, or as parts of programmable interferometers, such as those proposed in [5].

Acknowledgements: M.S., S.F., I.D. and S.S. acknowledge support by Rosatom in the framework of the Roadmap for Quantum computing (Contract No. 868-1.3-15/15-2021 dated October 5, 2021 and Contract No. P2154 dated November 24, 2021). Authors acknowledge partial support by the Interdisciplinary Scientific and Educational School of Moscow University ”Photonic and Quantum Technologies. Digital Medicine”. M.S. and S.F. are grateful to the Foundation for the Advancement of Theoretical Physics and Mathematics (BASIS) (Projects No. 20-1-3-31-1 and 22-2-1-89-1). S.K. is supported by the Ministry of Science and Higher Education of the Russian Federation on the basis of the FSAEIHE SUSU (NRU) (Agreement No. 075-15-2022-1116).

References

[1] Y. Shen et al., *Deep learning with coherent nanophotonic circuits*, Nature Photonics, vol. 11, pp. 441-446, 2017
[2] A. Crespi et al., Integrated multimode interferometers with arbitrary designs for photonic boson sampling, Nature Photonics, vol. 7, pp. 545-549 (2013)
[3] W.R. Clements et al., *Optimal design for universal multiport interferometers*, Optica, vol. 3, no. 12, pp. 1460-1465, 2016
[4] S. Molesky et al., Inverse design in nanophotonics, Nature photonics, v.12, pp. 659-670, 2018
[5] M.Yu. Saygin et al., *Robust architecture for programmable universal unitaries,* Physical Review Letters, vol. 124, 010501, 2020

Modelling Brillouin activated microcombs in multi-layered silicon nitride waveguides

(Student paper)

Yvan Klaver[1*], Kaixuan Ye[1], Roel Botter[1] and David Marpaung[1]

[1]Nonlinear Nanophotonics, MESA+ Institute of Nanotechnology, Department for Science and Technology, Applied Nanophotonics, University of Twente, 7522 NB Enschede, The Netherlands

[*] y.klaver@utwente.nl

We investigate a numerical model to simulate the optical frequency comb generation in Kerr and Brillouin active resonators with gain parameters in the same order of magnitude. We show that either a backward or forward comb can be generated directly on a Brillouin laser or a cascaded Brillouin lasing mode respectively for a multi-layered silicon nitride waveguide structure.

Keywords: *Microring resonators, Stimulated Brillouin scattering, Kerr nonlinearity, Optical frequency comb*

INTRODUCTION

Optical frequency combs are a widely studied optical source in which a repetition of the optical signal is coupled to the frequency domain and are used in spectroscopy, metrology, and communications [1]. Particularly for high repetition rate applications such as communication, microcombs also known as Kerr frequency combs have been extensively studied [2]. In this field a high-Q microcavity is pumped with a continuous wave laser to obtain a pulsed output due to the Kerr effect in the microcavity. One of the interests in these microcombs is to have them highly coherent in both RF and optical domain, where the latter is given by the optical linewidth of the comb lines. When stabilised the well-defined frequencies could reduce errors when the comb is used as a grid of data carriers.

A way to achieve high spectral purity in microcombs has been shown in earlier research where they activate microcombs via a Brillouin laser in the same cavity acting as a photonic flywheel [3,4]. A Brillouin laser narrows the linewidth of the pump laser [5] and transfers this high coherence as a starting point to the microcomb. A following step for these Brillouin activated microcombs is to perform this in planar technologies. However, in planar technologies the mode volumes are generally much smaller than in the given examples, this means the Kerr effect is significant and we cannot assume Brillouin scattering dominates until enough power mixes in the Kerr process.

In this paper we will theoretically investigate this region where the Brillouin and Kerr strength are relatively close by use of waveguide properties known for different platforms. Particularly we will investigate multilayer silicon nitride waveguides which exhibit Brillouin scattering with high confinement [6]. For this we will show that microcomb generation via Brillouin lasing is still possible in highly confined waveguides under the conditions that selective inhibition of microcombs followed by inhibition of cascaded Brillouin lasing. Additionally, we show the cascaded Brillouin lasing can activate combs in the forward direction.

METHODS

For the model we have a set of two Lugiato-Lefever equations for the microcombs with cross-phase modulation for the counter propagating waves [7], however we transform this in modal components and couple these via acoustic waves [8]. This results in a large set of coupled mode equations for the forward and backward direction in the resonator described for each longitudinal mode as:

$$\frac{dE_\mu^F}{dt} = -\left(\frac{\Delta\omega_L}{2} + i\delta\omega_P\right)E_\mu^F + iD_{int}(\mu)E_\mu^F - i\gamma v_g\mathcal{F}[E_\tau^F(|E_\tau^F|^2 + 2\langle|E_\tau^B|^2\rangle)]_{\tau\to\mu} - ig^*E_{\mu+m}^B B_\mu^{B^*} - igE_{\mu-m}^B B_{\mu-m}^F + \delta_{\mu,0}\sqrt{FSR_0\Delta\omega_{ext}}E_{in} + \eta_\mu \quad (1)$$

$$\frac{dE_\mu^B}{dt} = -\left(\frac{\Delta\omega_L}{2} + i\delta\omega_P\right)E_\mu^B + iD_{int}(\mu)E_\mu^B - i\gamma v_g\mathcal{F}[E_\tau^B(|E_\tau^B|^2 + 2\langle|E_\tau^F|^2\rangle)]_{\tau\to\mu} - ig^*E_{\mu+m}^F B_\mu^{F^*} - igE_{\mu-m}^F B_{\mu-m}^B + \eta_\mu \quad (2)$$

$$\frac{dB_\mu^F}{dt} = -\left(\frac{\Gamma}{2} + i\delta\omega_B\right)B_\mu^F - i\frac{g^*}{FSR_0\hbar\omega_\mu}E_{\mu+m}^F E_\mu^{B^*} + \xi_\mu \quad (3)$$

$$\frac{dB_\mu^B}{dt} = -\left(\frac{\Gamma}{2} + i\delta\omega_B\right)B_\mu^B - i\frac{g^*}{FSR_0\hbar\omega_\mu}E_{\mu+m}^B E_\mu^{F^*} + \xi_\mu \quad (4)$$

For this we have the optical field E_μ^F and E_μ^B for mode μ in the forward and backward direction respectively. Further we have for the optical equations we have: the optical decay rate $\Delta\omega_L$, pump detuning $\delta\omega_P$, integrated cavity dispersion $D_{int}(\mu)$, nonlinear parameter γ, group velocity v_g, opto-acoustic coupling g, the free spectral range FSR_0, coupling rate $\Delta\omega_{ext}$ and Langevin noise term η_μ. For the acoustic equations we have B_μ^F the photon number amplitude for mode μ in the forward and backward direction respectively and: the acoustic decay rate Γ, acoustic detuning $\delta\omega_B = 2\pi FSR_0 - \Omega_{\mathrm{SBS}}$, frequency of the photons ω_μ and the Langevin noise for the acoustic mode ξ_μ.

The optical modes in this simulation uses a discrete Fourier transform $\mathcal{F}[\dots]_{\tau\to\mu}$to express the Kerr nonlinearity, which is characterised in time domain. Additionally, the cross-phase modulation is given by the term $2\langle|E_\tau^x|^2\rangle$ where the brackets express averaging.

Brillouin gain	g_b	0.58	$m^{-1}W^{-1}$
Nonlinear parameter (Kerr gain)	γ	0.18	$m^{-1}W^{-1}$
Stimulated Brillouin scattering frequency shift	Ω_{SBS}	13.18	GHz
Acoustic decay rate	Γ	92	MHz
Group velocity dispersion	β_2	571	ps^2km^{-1}

Table. 1. Parameters used for simulations of 4 µm wide multi-layered silicon nitride waveguides

We simulate this for the case of multilayer silicon nitride given by [6] and use the simulated values for a waveguide with a width of 4 µm as given in Table 1. In the simulations we vary the pump powers and the acoustic detuning ($\delta\omega_B$) and assume a loss of 5 dB/m with critical coupling ($\eta = \frac{\Delta\omega_{ext}}{\Delta\omega_L} = 0.5$). The simulations are performed by slowly tuning the pump frequency over the resonance whilst running an ODE solver (MATLAB ODE45).

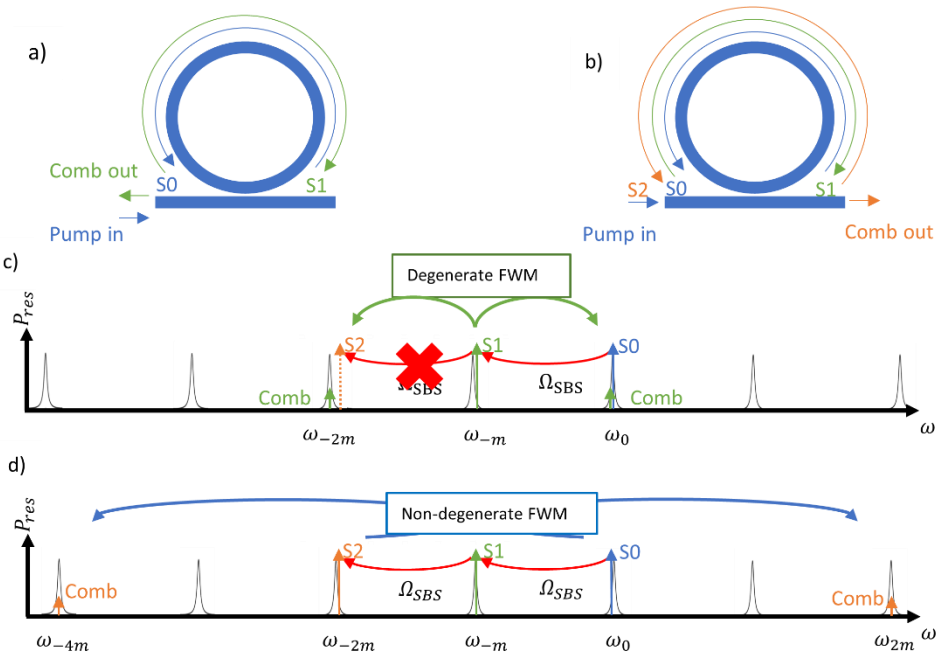


Fig. 1. Development of a a) backward comb or b) forward comb. With the spectral components given in figure c) and d) respectively matched to the propagation directions of a) and b). In c) the S1 lasing mode starts from the pump (S0) but cannot cascade before mixing into a comb via degenerate four-wave mixing (FWM). Whereas in d) the S1 lasing mode cascades into the S2 lasing modes which via non-degenerate FWM can develop a forward comb that is stable.

RESULTS

In the results we find two main comb operations in the resonator: a comb in the backwards direction or a comb in the forwards direction. The formation of these categories is illustrated in Figure 1. Here the comb, either forms in the backwards direction as cascaded lasing does not happen due to the larger detuning or forms in the forwards direction as cascaded lasing can take place. Note also that the forward comb generation will have a linespacing twice the Brillouin shift instead of just one FSR as is the case for the backward comb.

The different operating regimes are shown in Figure 2, where only the acoustic detuning $\delta\omega_B = 2\pi FSR_0 - \Omega_{SBS}$ is changed to switch from backward comb generation to forward comb generation. In these figures we also have the comb line spacing in the backwards direction as one FSR whereas the forwards direction has two FSR spacing as the Brillouin shift is nearly matched to the FSR. For different acoustic detuning and pump powers it was observed that forward combs with one FSR existed, but these were not stable and disappeared quickly.

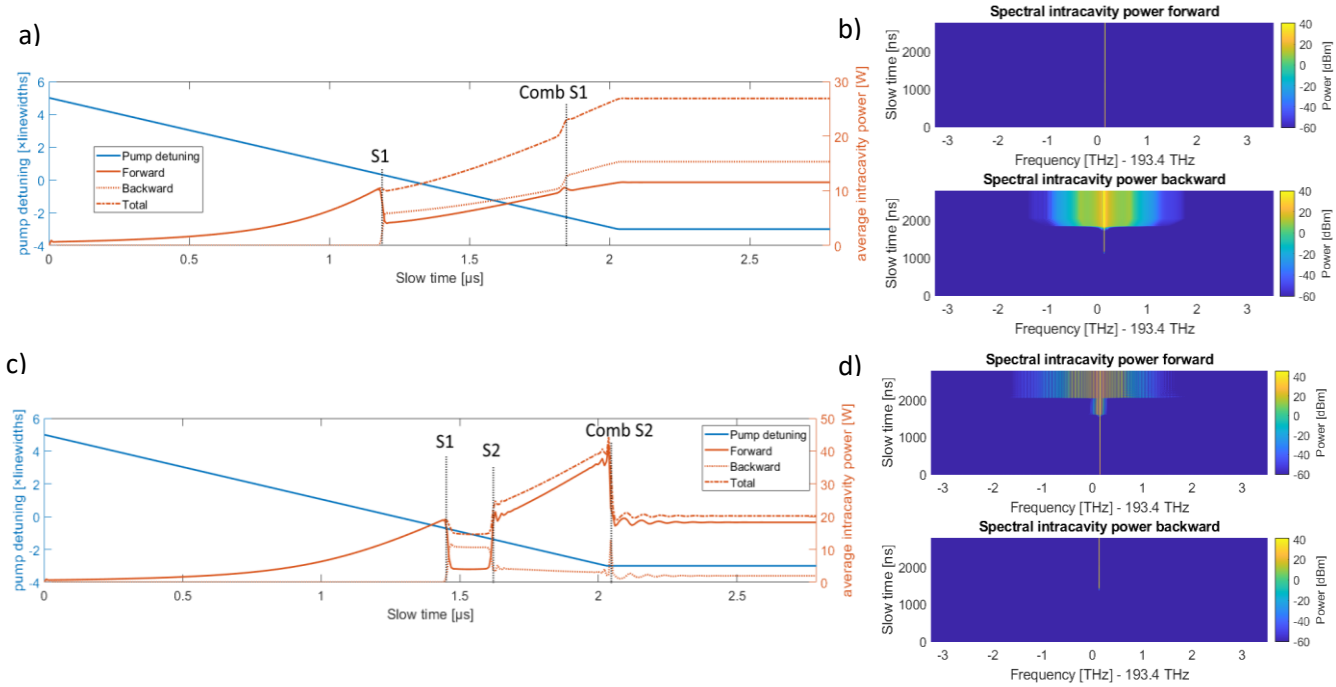


Fig. 2. Example operation of a b) backward comb via Brillouin lasing and d) forward comb via cascaded Brillouin lasing. Where we have corresponding figures showing the pump sweep and intracavity power in the different directions for a) the backward comb and c) the forward comb. In b) and d) the power per mode is given over the same time axis for the forward (top) and backward (bottom) direction. Between these results only the acoustic detuning is changed between b) $\delta\omega_B = 2\pi\times$(100 MHz) and d) $\delta\omega_B = 2\pi\times$(25 MHz)

The transition between forward and backward comb generation is found to be in a small region around 50 MHz depending on the pump power. A narrower waveguide (1.2 µm) which exhibits a relatively larger Kerr but smaller Brillouin nonlinearity had a similar transition but with a narrower region of backward comb generation as microcomb generation starts with less power whilst the cascaded Brillouin lasing threshold increased.

DISCUSSION

Currently we have simulated the Kerr and Brillouin interactions in high-Q resonators and shown that comb generation via Brillouin lasing is possible both in forward and backward direction. For the next step, expansion of the parameter space by including more platforms that observe Brillouin scattering would give more insight in changing the ratio of Brillouin to Kerr nonlinear strength. Additionally, noise dynamics would be an important aspect to simulate to see if the Brillouin lasing in this context still filters high frequency noise of the pump and transfers this to the comb lines.

References

[1] L. Chang, S. Liu, and J. E. Bowers, "*Integrated optical frequency comb technologies*," Nat. Photonics, vol. 16, no. 2, pp. 95–108, 2022.
[2] A. Pasquazi et al., "*Micro-combs: A novel generation of optical sources*," Phys. Rep., vol. 729, pp. 1–81, Jan. 2018.
[3] K. Jia et al., "*Photonic Flywheel in a Monolithic Fiber Resonator*," Phys. Rev. Lett., vol. 125, no. 14, p. 143902, 2020.
[4] Y. Bai et al., "*Brillouin-Kerr Soliton Frequency Combs in an Optical Microresonator*," Phys. Rev. Lett., vol. 126, no. 6, p. 063901, Feb. 2021.
[5] S. Gundavarapu et al., "Sub-hertz fundamental linewidth photonic integrated Brillouin laser," Nat. Photonics, vol. 13, no. 1, pp. 60–67, Jan. 2019.
[6] R. Botter et al., "Stimulated Brillouin Scattering in Multilayer Silicon Nitride Waveguides," pp. 5–8.
[7] Z. Fan and D. V. Skryabin, "*Controlling microresonator solitons with the counter-propagating pump*," Photonics, vol. 8, no. 7, 2021.
[8] R. O. Behunin, N. T. Otterstrom, P. T. Rakich, S. Gundavarapu, and D. J. Blumenthal, "Fundamental noise dynamics in cascaded-order Brillouin lasers," Phys. Rev. A, vol. 98, no. 2, pp. 1–17, 2018.

Multi-Mode Interference for Wavelength Demultiplexing

(Student paper)

Pedro Medeiros[1,2], Francisco Rodrigues[3], Margarida Facão[1], Mário Lima[1,2], António Teixeira[1,2,3]

[1]Universidade de Aveiro, Aveiro, Portugal
[2]Instituto de Telecomunicações, Aveiro, Portugal
[3]PICadvanced, Aveiro, Portugal
*pedrotbmedeiros@ua.pt

This paper presents a two-channel wavelength division demultiplexer based on Multimode Interferometer with two multimode regions to separate 1532.68 and 1596.34 nm wavelengths into distinct ports with a loss of approximately 3 dB. The device was simulated and analysed using industry software with built-in solvers. Designed for a Silicon on Insulator Photonic Platform, this design boasts a simple geometry and compact size.
Keywords: *Photonic Integrated Circuits, Wavelength Demultiplexing, Multimode Interferometer, NG-PON2*

INTRODUCTION

The telecommunications industry is one of the sectors that has made significant investments in the application of Photonic Integrated Circuits technology. Since the utilization of fiber and lasers, Photonics has been an integral part of the infrastructure, allowing the unprecedented quantity of information exchanged today. PIC technology is used as a cost-effective solution that combines increased transmission capacity with advantages as a smaller weight, volume, and power consumption [1]. PIC technologies use is widely spread in Passive Optical Networks (PONs). There are several PON standards in use in today's world, working with different wavelength bands, which adds a degree of complexity to the integration of the standards that operate inside the same legacy infrastructure. The telecom industry uses wavelength multiplexing and demultiplexing so that several wavelength channels are transmitted through the same optical link without the need to change or lay a new connection. Demultiplexing can be achieved in PICs using different components, such as ring resonators, arrayed waveguide gratings (AWGs), Bragg gratings, or multimode interference waveguides, among others. Due to the small size and simple design of multimode interferometers (MMIs), PICadvanced explored the possibility of a demultiplexing component made by a MMI to separate the wavelengths used in Next Generation PON2 (NG-PON2) (narrow band option for upstream). This standard is currently in deployment and is part of technology portfolio worked at PICadvanced [2]. To exclude the necessity of adding bends (the case of side ported MMIs [3]), the design was constrained to have outputs along the same axis. The additional bends were going to have an unwanted impact on the footprint needed for the component and on the circuit design complexity.
A 1532.68/1596.34 nm wavelength demultiplexer was created using a multimode waveguide with two multimode regions and inputs and outputs along x- axis. The purpose of this design was to investigate the possibility of simultaneously recovering single and multiple images of the input field for different wavelengths or different wavelengths.

Multimode Interferometer

MMI takes advantage of the phenomenon of interference occurring among the modes propagating inside the wider area of the component. Inside the multimode region, the input field is replicated at a specific length, being this repetition called a single image. Between single image and input field there is an interference pattern where the input field is replicated in N-folded images, as can be seen in Fig. 1.

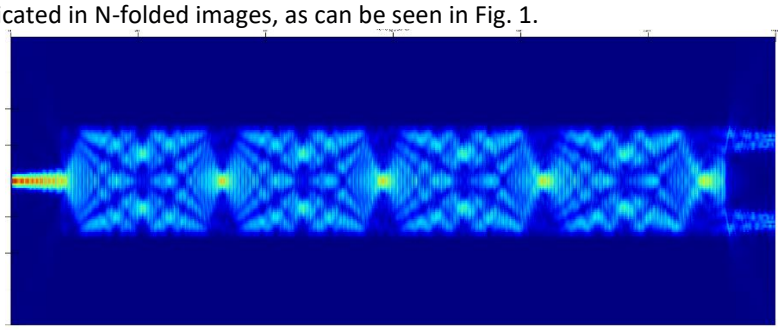


Fig. 1. Propagation Pattern in an MMI, obtained using FDTD solver.

In Fig. 1. it is possible to see the propagating pattern where the repetition of the input field is formed at a length that can be estimated by the following equation [4]:

$$L = \frac{3}{4} L_\pi = \frac{3}{4} \frac{4 n_f W_{e0}^2}{3 \lambda_0} \quad (1)$$

In equation (1), λ_o is the wavelength of propagation, W_{e0} is the width of the mode, and n_f is the strip effective index calculated using effective index method [4] [5]. C band single images are going to appear at a higher length than the one from L band. Typically, the offset between wavelengths is explored by changing the input field y-axis position, creating a pattern where consecutive single images are going to occur at mirrored position by the y-axis. If the multimode region is long enough this offset is going to accumulate, allowing for the occurrence of single images for different wavelengths, at the same length but at different y-axis position, ultimately enabling the separation of the wavelengths into different waveguides. The length at which this happens can be calculated by:

$$L_{DEMUX} = p\left(3L_\pi^{\lambda_b}\right) = (p+q)\left(3L_\pi^{\lambda_a}\right) \quad (2)$$

where *p* is an integer and *q* are an odd integer [6]. The values are dependent on the beat length ratio, which is dependent on wavelength. If the wavelengths are far apart in the electromagnetic spectrum the values are going to be much smaller than when the wavelengths relatively close.
While this approach allows for the recollection of the full single image it also requires a great multimode region length, so that the offset accumulates till there is an x-axis superposition and at the same time y-axis mirroring. In the design of photonic chips, component size is an important limitation/constrain as bigger components mean a lower level of integration, driving up the cost by component of the circuit. Being a technology in development the cost is still elevated when compared with electronics.
To reduce the size of MMIs used for demultiplexing and taking advantage of the offset between single images, the MMI we developed in this paper recovers part of the single image in one of the output waveguides and uses a second multimode region (slot) where multiple images are recovered. The light going through the second multi-mode region suffers a second mode interference, and an image is recovered in a different output waveguide.

RESULTS

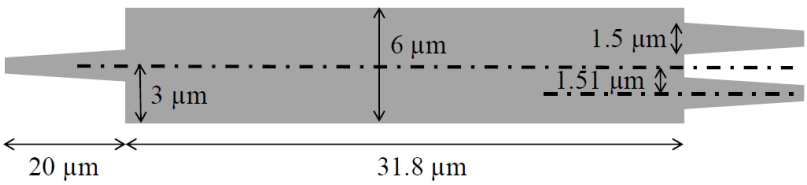


Fig. 2. 3 dB splitter original design **[7]**.

The starting design was based on a 3 dB splitter made in Si/SiO_2 Strip waveguide system from Cornerstone Photonics [7]. The position of the input was changed to the edge and the second multimode region was added as can be seen in Fig. 3.

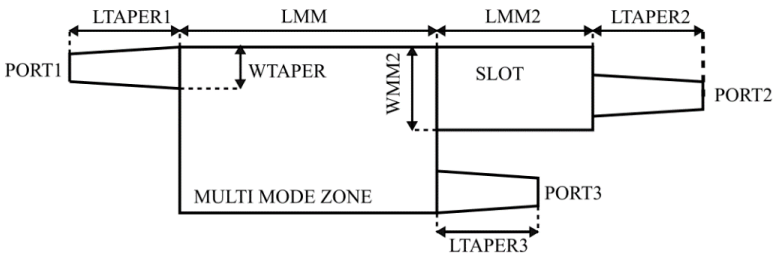


Fig. 3. Slot MMI schematic design.

Using EME sweep tool it was possible to determine a length at which Port3 (bottom output in Fig. 3.) recovers part of the L band single image and the slot recovers part of the C band multiple images. The length of the slot is also swept to determine the ideal length in which it recovers the light into Port2 (upper output in Fig. 3.). The simulation results are presented in Table 1.

Wavelength (nm)	S_{21} (a.u)	S_{31} (a.u)	ER (dB)	IL (dB)
1532.69	0.06119	0.4923	9.055	3.078
1596.32	0.6021	0.001035	27.65	2.203

Table 1. Transmission results and parameters for the two wavelengths at the beginning of the C and L band, in a Slot MMI with a 6 µm multimode region width.

As the footprint of the component is an important constraint, a second slot MMI was designed with a multimode region width of 5 µm. In accordance with expression (1), reducing the width, the length at which the single image appears is going to be smaller, enabling the modelling of a smaller component. The results for this smaller width component are presented in Table 2:

Wavelength (nm)	S_{21} (a.u)	S_{31} (a.u)	ER (dB)	IL (dB)
1532.69	0.01839	0.5009	14.35	3.002
1596.32	0.5657	0.1168	6.853	2.474

Table 2. Transmission results and parameters for the two wavelengths at the beginning of the C and L band, in a Slot MMI with a 5 µm multimode region width.

DISCUSSION

Width (µm)	Multimode Region Length (µm)	Slot Length (µm)
5	193	55.8
6	273.1	103

Table 3. Dimensions of the Slot MMIs with 5 and 6 µm of width.

A 1532.68/1596.34 nm wavelength demultiplexer based on a multimode waveguide with two multimode regions and x-axis inputs and outputs was demonstrated for application in NG-PON2. The component was designed for Si/SiO_2 platform made by Cornerstone Photonics and is being produced using multi-project wafer for testing and validation of simulation results (both designs present on Table 3). The simulations show losses bellow 3 dB and smaller lengths compared to the traditional application method, proving the feasibility of reducing the footprint of MMIS for demultiplexing. This work is supported by the European Regional Development Fund (FEDER), through the Competitiveness and Internationalization Operational Programme (COMPETE 2020) of the Portugal 2020 framework [Project POWER with Nr. 070365 (POCI-01-0247-FEDER-070365)].

References

[1] C. Pinho et al, *Photonic Integrated Circuits for NGPON2 ONU*, Applied Sciences, vol. 10, no. 11, pp. 4024-127, 2020.
[2] ITU, *G.989.2 : 40-Gigabit-capable passive optical networks 2 (NG-PON2): Physical media dependent (PMD) layer specification- Amendment 1*, 2020.
[3] Q. Tang et al, *A side-ported MMI based InP polarization beam splitter*, Optics Communications, vol. 475, no. 11, pp. 4024-127, 2020.
[4] L. Soldano and E. Pennings, *Optical Multi-mode Interference Devices Based on Self-Imaging: Principles and Applications*, Journal of Lightwave Technology, vol. 12, no. 4, pp. 615-627, 1995.
[5] M. Hammer, *1-D mode solver for dielectric multilayer slab waveguide* (Online). Available: computational-photonics.eu/oms.html (Accessed 31 January 2023)
[6] M. Paiam, *Compact Planar 980/1550-nm Wavelength Multi/Demultiplexer Based on Multimode Interference*, IEEE Photonics Technology Letters, vol. 7, no.10, pp. 1180-1182, 1995.
[7] Cornerstone Photonics, *CORNERSTONE STANDARD COMPONENTS LIBRARY (on SOI Platforms)*, February 2022 (Online). Available: cornerstone.sotonfab.co.uk/mpw-design-rules/process-design-kit-pdk (Accessed 31 January 2023).
[8] R. Hunsperger, *Integrated Optics*, Springer Science & Business Media, 2009.
[9] K. Okamoto, *Fundamentals of Optical Waveguides,* Elsevier, 2006.

Towards on-chip wavelength modulation spectroscopy at 1.5 µm via InP integrated photonics and low-cost driving hardware

(Conference paper)

Stefano Tondini[1], Jun Zhang[2], Joel Hazan[1], Martijn Heck[1] and Jia Chen[2]

[1]Eindhoven Hendrik Casimir Institute, Eindhoven University of Technology, Eindhoven, 5612 AE, Netherlands
[2]Environmental Sensing and Modeling, Technische Universität München, Munich, 80333, Germany
* s.tondini@tue.nl

Photonics allows for unprecedented miniaturization and speeding-up of many technological concepts. The case here presented consists of a compact gas-sensing system based on a single photonic integrated circuit with a tunable laser and a photodetector realized on InP and wavelength modulation spectroscopy. Looking out towards the exploitation of such a concept in the field, the feasibility of implementing all the driving and signal processing tasks on a low-cost microcomputer is verified.

Keywords: *Integrated tunable laser, indium phosphide photonic integration, pollution sensing, absorption spectroscopy, digital lock-in amplifier.*

INTRODUCTION

This work aims at prompting the gas sensing performances that can be achieved on a photonic chip by means of a wavelength modulation spectroscopy (WMS) scheme implemented through low-cost hardware. On the one hand, a photonic integrated circuit encompassing a tunable laser with a 50 nm range centered at 1.5 µm and a high-responsivity photodetector can be conveniently realized in the mature InP technology [1] to be coupled with a hollow-core fibre serving as a gas interaction cell [2,3]. On the other hand, advanced absorption spectroscopy techniques can be synthesized on a single microcontroller unit (e.g. Raspberry Pi), which acts as both a laser driver and a digital lock-in amplifier [4] for the signal-to-noise ratio (SNR) improvement of the gas detection. This preliminary study carries the high-level description of a compact system with multi-species pollutant sensing capabilities, detailed for the example of ammonia (1512 nm). The capacity of the system to potentially target different pollutant gases, i.e. N_2O and CH_4, at the same time is ensured by the wide laser tunability range.

SYSTEM/EXPERIMENT DESIGN

The sensing system architecture is depicted in Fig. 1., where three main building blocks can be identified, namely the driving control unit (green rectangle on the left), the photonic integrated circuit (grey square in the middle), and the gas interaction cell that is represented on the right by a coiled hollow-core fibre. It is worth mentioning that, due to the limited sampling and processing frequency required by the WMS (generally, about a few kHz), a digital lock-in amplifier to serve the spectroscopy purpose can be achieved on a low-cost microcomputer. Two main tasks have to be implemented on that. The first is a particular laser driving scheme, which is going to be detailed in the next section. The second is the digital signal processing, described in the Outlook section, to decrease the 1/f noise and increase the SNR.

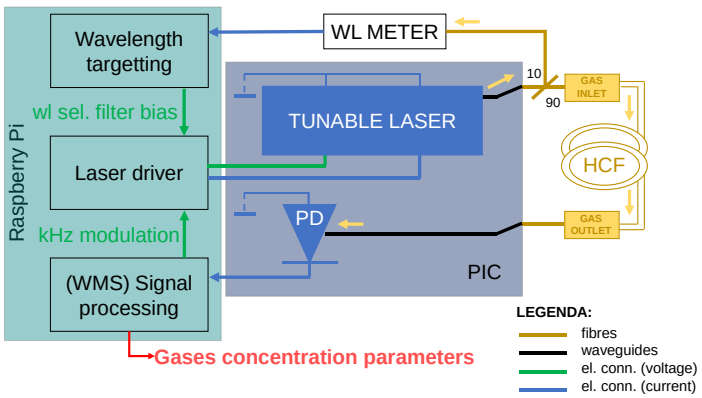


Fig. 1. Schematics of the sensing system where a single microcontroller unit is managing the wavelength targeting, the laser driving and the digital lock-in amplifier tasks on the left, a photonic integrated chip embeds both the light source and the photodetector in the middle, and a hollow-core fibre serves as gas interaction cell on the rightmost part.

Another fundamental task to accomplish is the optical feedback on the laser output, to perform periodical checks/calibrations against drifting and therefore to maintain a box-shaped laser emission all along with the tuning range. This can be achieved by means of a Fiber Bragg Grating metrology system [5] through splitting the laser output.

WMS DRIVING SCHEME

When performing gas spectroscopy in a noisy environment, which is a common condition for air pollution measurements, the wavelength modulation technique allows for extracting only the signal component at the desired frequency and phase, filtering out the other noise contributions [6]. In this section, the driving scheme to apply to the tunable laser is described, based on previous experiments carried out with a commercial laser source [4]. Fig. 2. (a) shows the wavelength modulation as the summation of a slow saw-tooth function and a fast but with smaller amplitude sinusoidal function. With our special laser design (Fig. 2 (c)), we can address the saw-tooth scanning and the sinusoidal oscillation through two separate laser sections. Indeed, inside the Fabry-Perot cavity (Fig. 2 (d)), besides a semiconductor optical amplifier (SOA) we find a 8-arms folded Mach-Zehnder Interferometer (MZI) with linearly increasing imbalances as an intra-cavity wavelength selection filter and an in-line Electro-Optical Phase Modulator (EOPM) for adjusting the cavity modes. Even though the effect of tuning the intra-cavity filter and the in-line EOPM mutually affect each other, we can assume they are independent by involving a compensation term in the filter driving. Therefore, for the low scanning component, we can slide the filter pass-band back and forth on a target wavelength range, and we can fast modulate the wavelength by trimming on the cavity modes (Fig. 2. (b)). The modulation frequency is accomplished by reversely biasing the EOPMs deployed on the MZI arms, capable of up to GHz bandwidth. Some relevant design figures are: 4mm FP cavity length, 800 µm SOA length, 1MHz laser expected linewidth, and a 0.16 nm FP cavity mode spacing. Output optical power in the range of mWs on-chip and 0.85 A/W responsivity photodetectors performances are expected out of the mature InP fabrication platform. Worth to notice is that the 3nm scanning window of Fig. 2. (a) has been selected to match the ammonia absorption peak that is going to be taken as an example in the following section. However, this range can be extended more than 10 times, to target, at the same time, other gas species, which have marked absorption peaks around 1.5 µm.

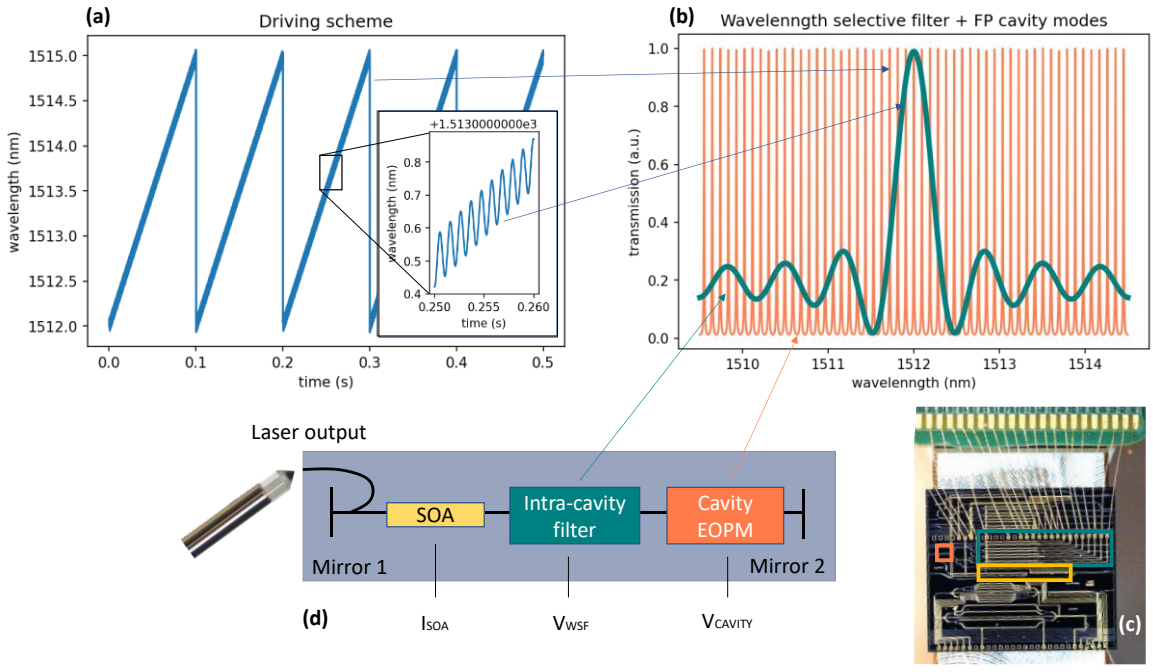


Fig. 2. (a) Ideal driving scheme to be applied to the laser source to achieve WMS, where a slow linear scan over 3 nm is performed at 10 Hz and a faster and smaller sinusoidal modulation at 6 kHz is superimposed to decrease the 1/f noise and to increase the SNR. (b) Simulation of the intra-cavity wavelength selective filter, in green, and the longitudinal modes of the laser cavity, in orange. By the laser design (c-d), these figures can be independently tuned and then the slow and the fast components of the driving scheme can be decoupled, leading to easier laser management during the WMS.

PRELIMINARY FIGURES

As a preliminary result, we show the laser output range in a contour plot, Fig. 3 (a). The map has been built sequentially, by collecting the output spectrum with an optical spectrum analyzer for 1000 target wavelength steps

from the bottom value of 1510 nm to the top value of 1560 nm. It is notorious that the main optical signal lies on the diagonal. This confirms the tuning algorithm applied is well-suited to predict the laser behaviour. The laser output map can be scrubbed from the spurious wavelengths of the multi-mode configurations by means of a dedicated fine-tuning algorithm. However, this is a challenging operation as such noise is mainly due to temperature and humidity variation at the photonic chip level. Alongside the laser figures, Fig. 3. (b) carries a simulation of the NH_3, CO_2, and H_2O absorption lines around 1512 nm at atmospheric conditions (P = 0.96 atm, T = 296 K) for a 30 m optical path length. The plot is based on HITRAN data [7]. While H_2O and CO_2 concentrations are set to realistic average outdoor values, NH_3 is encompassed in the simulation with a 10 ppm concentration. The reason is to show that we can get to a 2% absorbance in such conditions, being not hindered by water vapour and carbon dioxide interferences [8]. Considering a typical absorbance resolution of a WMS system to be 10^{-5}, a detection limit of 5 ppb for NH3 can be achieved [9,10].

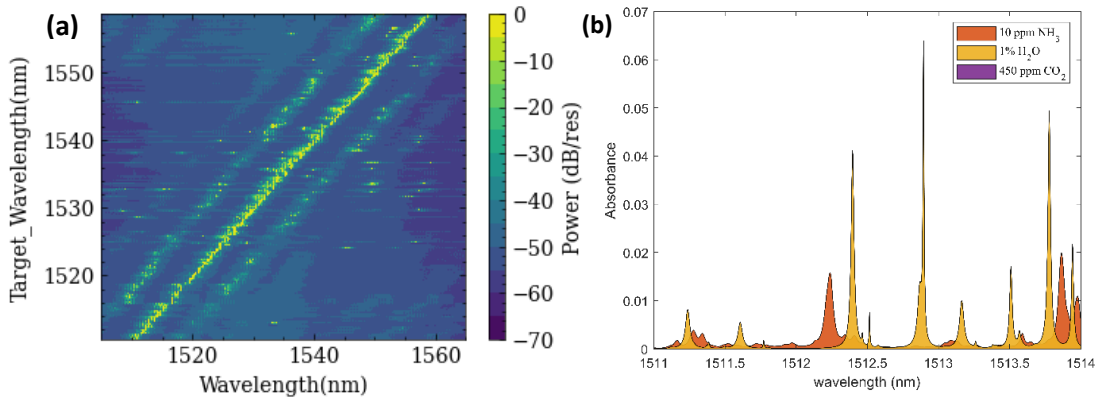


Fig. 3. (a) Tunable laser emission range where the single output wavelengths are emitted sequentially as a deterministic control strategy can be applied to target a specific emission condition. The side modes, which are visible from the contour can be further suppressed by operating the fine-tuning stage of the intra-cavity filter. (b) HITRAN Simulations of the H_2O, CO_2, and NH_3 absorption lines around 1512 nm under atmospheric conditions (P = 0.96 atm, T = 296 K) with a 30 m interaction path length.

OUTLOOK

Advanced WMS techniques can be applied to go beyond the limits of detection recently estimated for 1.5 µm photonics integrated circuits in levels of 100 ppb for NH_3 and at ppm for NO_2 (when considering common noise figures of multi project wafers) [6]. Multi-harmonic based WMS will further allow for improving sensor sensitivity, detection precision and SNR, especially in a harsh environment [3] (real-operation condition). This concept will be experimentally proven in upcoming works.

Acknowledgements: this project has received funding from European Union's Horizon 2020 programme under GA no. 899987.

References

[1] L. M. Agustin, et al., *InP-Based Generic Foundry Platform for Photonic Integrated Circuits*, IEEE Journal of Selected Topics in quantum electronics, vol.24, no. 1 2018
[2] A. Hänsel, M. Heck, *Opportunities for photonic integrated circuits in optical gas sensors*, J. Phys.: Photonics, vol. 2, 2020
[3] J. Chen, et. al., *Low-level and ultralow-volume hollow waveguide based carbon monoxide sensor*, Optics Letters, vol. 45, no. 21, pp. 3577-3579, 2010
[4] Lan, L. et al., *Self-Calibrated Multiharmonic CO2 Sensor Using VCSEL for Urban In Situ Measurement*, IEEE Transactions on Instrumentation and Measurement, vol. 68, 2019
[5] M. Muneeb, et al., Silicon-on-insulator shortwave infrared wavelength meter with integrated photodiodes for on-chip laser monitoring, Optics Express, vol. 22, no. 22, pp 27300-27308, 2014
[6] A. Hänsel, M. Heck, *Feasibility of Telecom-Wavelength Photonic Integrated Circuits for Gas Sensors*, Sensors vol. 18, no. 9, 2018
[7] https://hitran.org/
[8] Ligang Shao, et al., *Simultaneous detection of atmospheric CO and CH4 based on TDLAS using a single 2.3 µm DFB laser*, Spectrochimica Acta Part A: Molecular and Biomolecular Spectroscopy, vol. 222, no. 5, 2019
[9] J. Chen, et. al., *VCSEL-based calibration-free carbon monoxide sensor at 2.3 µm with in-line reference cell*, Applied Physics B, no. 102, pp 381–389, 2011
[10] J. Chen, et. al., *Laser spectroscopic oxygen sensor using diffuse reflector based optical cell and advanced signal processing*, Applied Physics B, no. 100, pp 417–425, 2010

Scalable Free-standing 3D Optical Circuit Design using Direct Laser Writing

(Student paper)

Evangelos Marakis[1,2], Ben Kassenberg[1,3], Ravitej Uppu[1,4], Pepijn W. H. Pinkse[1*]

[1]. *MESA+ Institute for Nanotechnology, University of Twente, The Netherlands*

[2]. *Present address: Institute of Electronic Structure and Laser, Foundation for Research and Technology, Crete, Greece*

[3]. *Present address: QuiX Quantum BV, Enschede, The Netherlands*

[4]. *Present address: Department of Physics & Astronomy, University of Iowa, Iowa City, USA*

[*]p.w.h.pinkse@utwente.nl

We present a design for 3D optical circuits using a DLW (direct laser writing) technique. The design uses polymer stand-offs to create air-clad waveguides to enhance modal confinement to enhance waveguide properties. The 3D geometry offers a compact design with a lot of flexibility for functionalisation, making it attractive for scientific and commercial use. The design is also manufacturable by UV lithography making it more scalable.

Keywords**:** *Direct laser writing, 3D optical circuits, polimer photonics, refractive index contrast, waveguide properties, waveguide interference, UV lithography.*

INTRODUCTION

The field of photonics has undergone a significant transformation with the advent of Direct Laser Writing (DLW) technology[1,2]. This technique offers the ability to create three-dimensional (3D) polymer structures with complex geometries, thereby enhancing the potential for photonic applications. However, the current state of the art for integrated optical circuit nanofabrication relies heavily on ultraviolet (UV) lithography[3,4], which is capable of scaling to industrial standards but restricts the platform to two-dimensional patterning mostly. We here present a simple and very flexible design for 3D optical circuits with high refractive-index contrast. Although the project is currently limited to a conceptual stage, it demonstrates the potential of the platform.

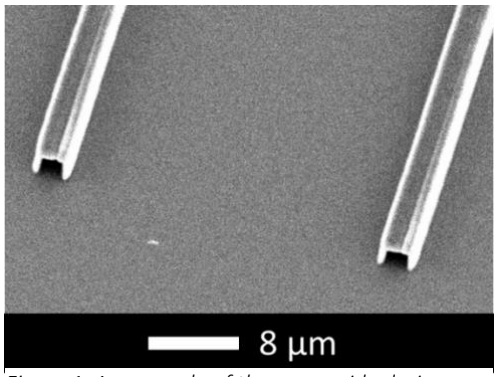


Figure 1: An example of the waveguide design fabricated with DLW. The image was recorded with the use of a scanning electron microscope. The waveguide core width is 2µm.

The proposed waveguide design is based on photonic fiber cores that use supporting stand offs ("leg" structures), as depicted **in Figure 1,** to keep the substrate at a distance. As a consequence, the full index of refraction contrast from the polymer to air is available, allowing small bending radii of the optical waveguide**.** This air-clad waveguide design offers the potential for increasing the density of optical waveguiding structures not only in 2D but also in 3D by adjusting the height of the polymer stand-off, thereby creating platforms of scientific and commercial value.

Furthermore, the design enables higher refractive-index contrast connectivity, enabling the creation of ring resonators on a micrometer scale, thereby increasing the compactness of optical circuits and reducing the required printing surface. This, in turn, increases the chances of commercial application, even in the context of fast prototyping fabrication. The design's simplicity also makes it manufacturable by UV lithography, potentially expanding its reach and impact.

RESULTS

Supported optical modes: We utilized the electromagnetic modal vector-wave equation and a finite-element method (COMSOL Multiphysics) to determine the optical modes that the waveguide designs can support. An example of the calculation can be seen in **Figure 2**. The first three modes of the waveguide design are displayed. The wavelength being considered is 800 nm, the core's width is 1 µm, and its height is 820 nm. The fundamental and second modes have a similar overlap with the waveguide's core, but the fundamental mode is more confined within the core compared to the second mode. The third mode shows a nodal line in the light distribution, with some field extending onto the support structure. This mode is therefore expected to experience higher losses, as most of its profile is attached to the interface of the structure, where fabrication roughness will have a significant impact. The stand offs have no effect on the mode profile of the fundamental and first-order modes and they

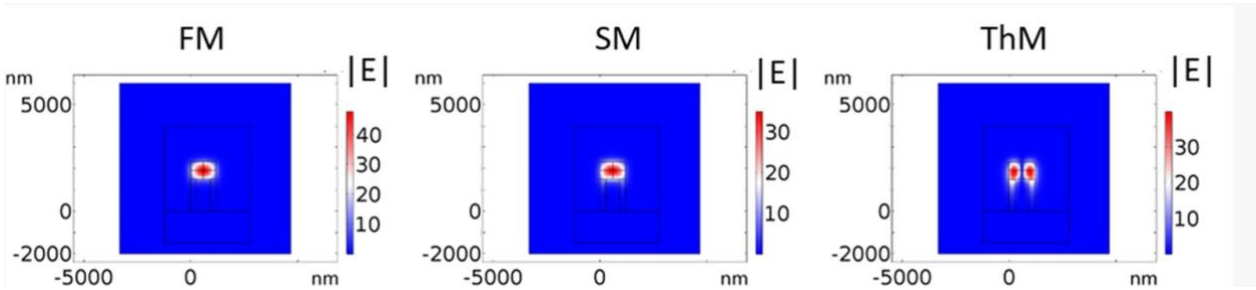


Figure 2: First three modes of the legged waveguide design. The wavelength is 800 nm and the core's width and height are 1 µm and 820 nm, respectively. The fundamental mode (FM) and the second mode (SM) have orthogonal polarisation, but similar field profiles, with the FM being slightly better confined within the core. The third mode (TM) demonstrates is the first mode with a nodal line and is expected to have higher losses due to its attachment to the support structure interface where fabrication roughness is pronounced.

behave similar to an air-clad waveguide. Higher-order modes are affected by the presence of stand-offs. Furthermore, the effective refractive indices of the fundamental and second modes must differ from that of the third mode to prevent coupling to the more lossy mode. By plotting the effective refractive index values for each wavelength against the waveguide's geometrical cross-section, the design can be optimized for specific values and requirements. It is observed that longer wavelengths have reduced effective refractive indices due to decreased confinement within the core. However, this fabrication parameter can be optimized based on the refractive index of the resist used to fabricate the structure. **Figure 3** provides a deeper insight into the waveguide geometry. We compare the effective refractive index values of the first three supported modes with COMSOL. There are configurations where the first and second modes, which both travel mainly within the core, have the same effective

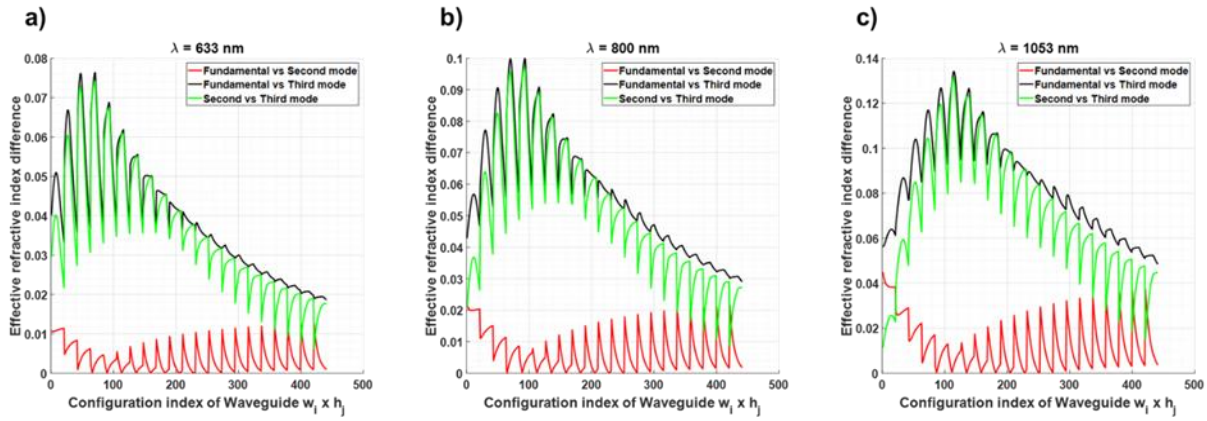


Figure 3: Difference of effective refractive index values between pairs of the three modes of the waveguide geometry computed with COMSOL for three wavelengths. The first and second modes are matched for certain configurations, both traveling within the core at the same effective index. However, there is no match between the third and the fundamental or second modes, indicating independent mode operation.

index. However, there is no effective index overlap for any configuration between the third and the fundamental or second modes.

Experimental validation: Although the fabrication is still in an early stage, the pilot tests on our waveguide designs showed that the optical circuits functioned as waveguides and showed light transmission despite the fabrication errors. The goal was to measure waveguide losses per µm, but couplers that help couple light into the waveguide result in additional losses. We used a 3D curved input-output coupler for the measurements, as it was expected to align with the focus spot, but the coupler and final geometry were not optimized. As shown in Fig. 4, two geometries were created to optimize the optical transmission. The "hippodrome" geometry **(Fig.4 a,c)** measures the combined losses of the waveguide and coupler, including curvature losses. The "staircase" geometry (**Fig.4 b and d**) measures waveguide losses per length, including losses between the waveguide and coupler. Preliminary data show propagation losses of not more than 5 dB/cm.

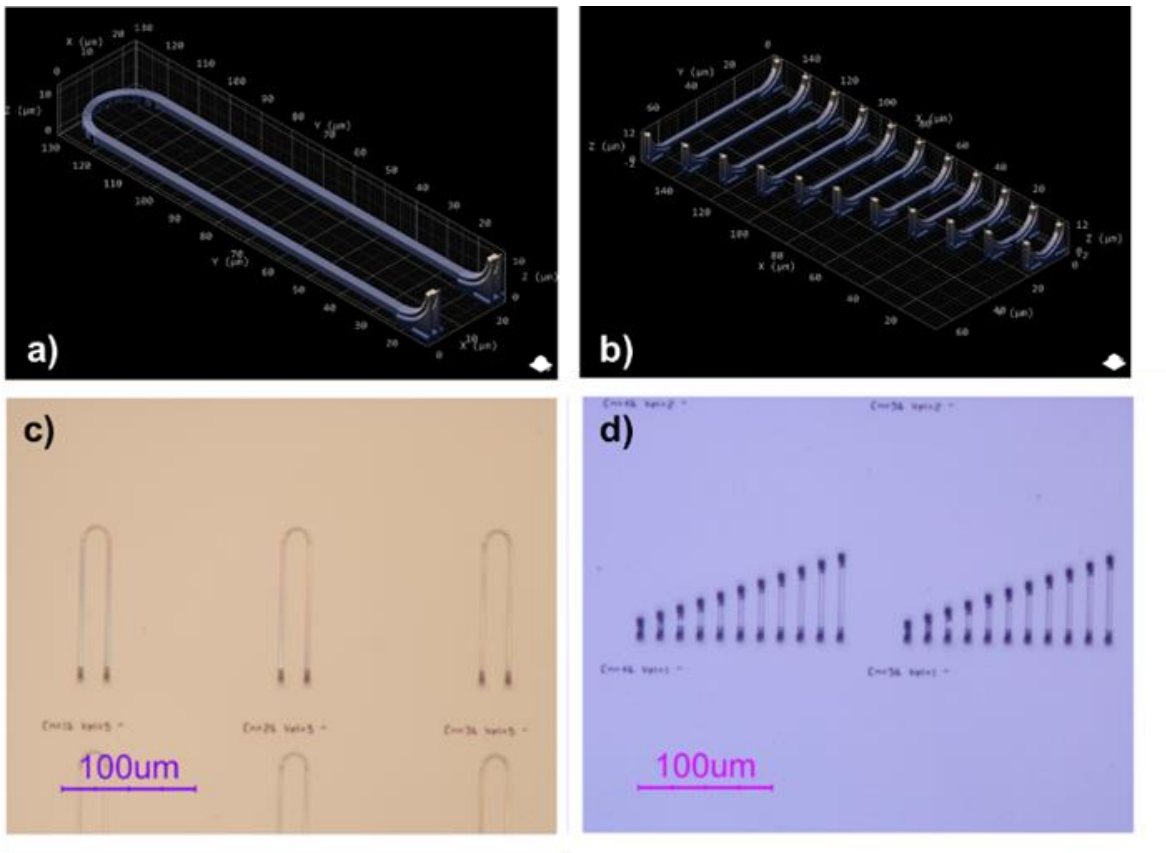


Figure 4: Comparison of waveguide loss measurements using different geometries. (a) and (c) show the "hippodrome" geometry, measuring combined losses of the waveguide and curved coupler. (b) and (d) show the "staircase" geometry, measuring waveguide losses per length, including losses between the waveguide and coupler. The pilot tests on our waveguide designs display functionality and transmission despite the fabrication errors, however, the coupler and final geometry have not been optimized.

DISCUSSION

In conclusion, the proposed design for 3D optical circuits using DLW technology offers a promising solution for advancing photonic applications. With its 3D geometry and high refractive-index contrast, the design has the potential to make circuits with a high density of waveguide components in a compact footprint, making it attractive for both scientific and commercial applications. The pilot test results demonstrate the optical circuits' functionality and optical transmission of the waveguides. The design's simplicity could be leveraged to fabricate similar structures using industrial UV lithography, thereby making it a valuable addition to the field of photonics. In the future further optimization and improvement in the design are needed to fully realize its potential for rapid prototyping and ad-hock polymer waveguiding structures on surfaces.

References

[1] J. Fischer and M. Wegener, Laser Photon. Rev. **7**, 22 (2013).

[2] E. Marakis, R. Uppu, M.L. Meretska, K.J. Gorter, W.L. Vos, and P.W.H. Pinkse, Adv Opt Mater **8**, 1 (2020).

[3] W. Bogaerts, P. de Heyn, T. van Vaerenbergh, K. de Vos, S. Kumar Selvaraja, T. Claes, P. Dumon, P. Bienstman, D. van Thourhout, and R. Baets, Laser Photon. Rev. **6**, 47 (2012).

[4] M. de Goede, M. Dijkstra, R. Obregón, J. Ramón-Azcón, E. Martínez, L. Padilla, F. Mitjans, and S.M. Garcia-Blanco, Opt. Express **27**, 18508 (2019).

Variable photonic integrated delay lines, a review

A. Melloni, M. Petrini, S. Seyedinnavadeh, F. Morichetti

Dipartimento di Elettronica, Informazione e Bioingegneria, P.za Leonardo da Vinci, 32, Milano, 20131, Italy
corresponding author: andrea.melloni@polimi.it

We present a comparison between various continuously variable true-time optical delay lines integrated on chip. Ring resonators and Mach-Zehnder based architecture are reviewed showing the superior properties of MZI structures. A topology that breaks the delay-bandwidth product limit is proposed, achieving a continuously tuneable delay from 0 to 100 ps across a bandwidth of 21 GHz with no signal distortion.
Keywords: *Variable delay lines, Beam forming networks, silicon photonics*

INTRODUCTION

Continuously variable true-time delay lines allow to arbitrary control the propagation delay of an optical signal and can be exploited for a variety of applications. Typical examples include synchronization and buffering of optical signals, optical signal processing and microwave photonic systems, optical coherence tomography, optical beam forming networks for phased-array antennas and more [1-5]. The control of a variable delay with a compact and non-moving device is very difficult to achieve in every field, (analog) electronic, microwave, photonics, acoustic, etc, especially if a large variation of delay, good dynamic, large bandwidth, and operation over a broad wavelength range is required.

Whatever it is the architecture of the device, the delay T is given by

$$T = \frac{n_g L_{eff}}{c}$$

where n_g is the group index of the material or the structure used to induce the delay, L_{eff} is effective length of the optical path and c is the speed of light. The delay T must be no- or weakly frequency dependent to realize a real true-time delay. The approaches can be clustered into two categories, resonant and non-resonant structures. The first one includes photonic crystals, microring resonators (MRRs) and material resonances (especially in gases), whereas the non-resonant approach exploit arrangements of Mach-Zehnder Interferometers (MZI). In case of interferometric structures, the spectral response is periodic.

It is worth to mention that a longer delay is achieved always at the expense of narrower operating bandwidth, as a result of an intrinsic limitation of the bandwidth-delay product. Further, whatever it is the architecture, the insertion loss of a delay line is given by

$$IL = \alpha L_{eff} = \alpha \frac{c\,T}{n_g}$$

where α is the attenuation of the material or waveguide per unit length. In conclusion, the most important parameter for the realization of a variable delay line is the ratio α/n_g, the architecture must guarantee a small frequency dependence behaviour and the device must be reconfigured according to the desired delay.

This review focuses on delay lines implemented as photonic integrated circuits, basically with MRRs and MZI. The former has the advantage of a reduced footprint but has narrow bandwidth, large chromatic dispersion, is affected by nonlinear effects due to intra-cavity field enhancement and require a complex control strategy. The MZI based one has a larger operational bandwidth, a simpler and more accurate control strategy, more resiliency to nonlinearities and a lower group delay dispersion, yet with a larger footprint.

TUNABLE MACH-ZEHNDER AND RING RESONATOR AS BUILDING BLOCK OF DELAY LINES

The MZI and the MRR shown in Fig. 1(a,b) are the two classical building blocks to induce a controllable delay. The tunable directional coupler allows to control the spectral response and hence the group delay. The MRR is typically used around the resonance frequency where the group delay can be very large, being equal to the roundrip time multiplied by the finesse. Large delays can be obtained with small rings and weak coupling coefficients but with a very large spectral dependence inducing severe detrimental effects on the delayed signal. The MZI instead, in the configuration of fig. 1 a), provides a controllable delay with a much larger bandwidth-delay product.

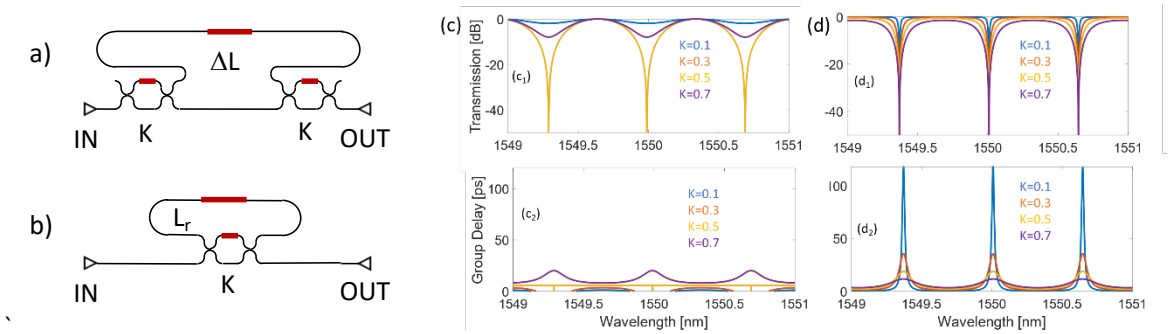


Fig. 1. Scheme of (a) MZI tunable delay line, (b) MRR delay line. (c, d) Spectral characteristics of the MZI and ring resonator.

The dependence of the normalized group delay on the coupling coefficient *K* at the operative frequency of the delay lines is shown in Fig. 2(a). For the ring, two different operative frequencies can be considered, in resonance and in antiresonance. Obviously, a resonating ring induces a delay much higher than off-resonance but the bandwidth-delay product is exactly the same, fig. 2b). The off resonance case has a much broader operating bandwidth, is more convenient but has never been considered a valid option to realize a delay line. For the Mach-Zehnder, the minimum normalized bandwidth (defined on the group delay) is about 0.31, reached for *K* equal to 0.25 and 0.75. For the ring resonator used off-resonance a minimum normalized bandwidth of 0.23 is reached at K ≃ 0.9. On resonance, the ring has an almost null normalized bandwidth with K ≃ 0.

The delay line based on a Mach-Zehnder interferometer has a bandwidth-delay product that is always larger than that of the ring and grows with *K*. The product goes to infinite for *K* = 0; 0.5 and 1 because for these values the bandwidth (defined on the group delay) is infinite. For a given value of the group delay, the bandwidth of the Mach-Zehnder delay line is hence always larger than the bandwidth of a ring-resonator-based delay line, even when used out of resonance.

Fig. 2(c) shows the value of the normalized group delay dispersion $\partial T/\partial\omega$. For the three cases, the dispersion is zero at the operative frequency of the delay lines. As expected, the ring resonator used on resonance exhibits a highly dispersive behaviour. On the contrary, the Mach-Zehnder and the off-resonance ring have a much smoother and similar dependence of the dispersion on frequency. The ring has a maximum dispersion that is almost twice that of the Mach-Zehnder at the same frequency. Lastly, the effect of propagation losses on the intensity transmission is strongly detrimental on the ring in resonance and almost negligible for the off-resonance ring and the MZI.

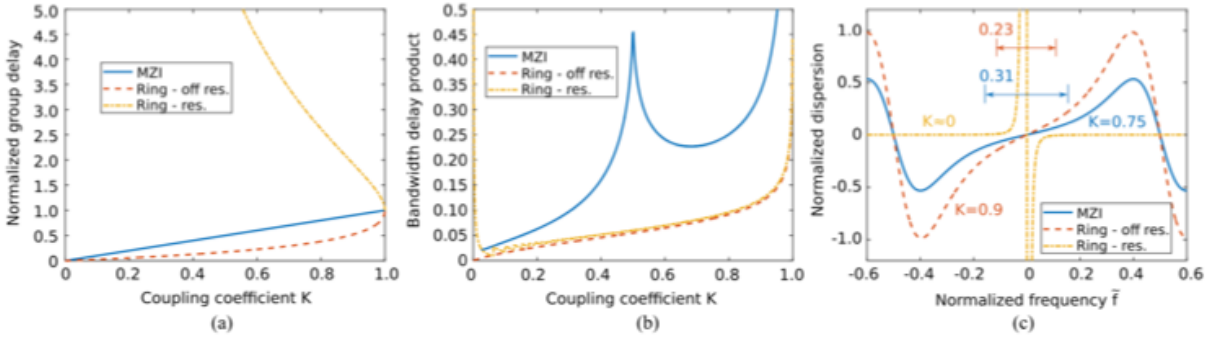


Fig. 2. (a) Normalized group delay and (b) bandwidth-delay product as function of the coupling coefficient K. (c) Group delay dispersion as function of the normalized frequency for the value of K that generates the minimum bandwidth. From [3].

BREAKING THE BANDWIDTH-DELAY CONSTRAINTS

By combining elementary building blocks, a larger delay range or a larger bandwidth can be achieved. A pioneer study comparing photonic crystals and directly coupled ring resonators (CROW) is reported in ref. [2]. With CROW (or SCISSORS, with a more complex control) the delay can be arbitrary increased while keeping the bandwidth constant at the expenses of a higher *IL* and a larger dependence of the delay on the frequency. Excellent results were achieved in [1, 2] but sophisticated control and stabilization schemes must be adopted. MZIs can be combined and cascaded as in [6,7,8] achieving a larger bandwidth-delay product with a reasonably simple control scheme.

An advantageous architecture based on a set of parallel stacked MZI is shown in Fig. 3 [9]. This structure overcomes the typical limitations of the previous circuits, in particular breaking the bandwidth-delay product constraint. The

circuit is composed by four unbalanced MZIs (but the number can be arbitrary), configured in such a way that the (n+1)-th stage is the unbalance of the n-th stage. Each MZI is equipped with two tuneable couplers (TCs, labeled in the picture as K_{Ai} and K_{Bi}, where i=1,2,3,4), in order to continuously modify the group delay, and with a thermo-optic phase shifter (heater) in the upper arm, to adjust the operational central frequency. The tuneable couplers are implemented by means of balanced MZIs, with thermo-optic actuators placed in one of the arms.
When both TCs are in cross condition (K_{Ai}=K_{Bi}=1), each stage provides the maximum delay ΔT_{max} = 1/FSR= 25 ps, the FSR being 340 pm (40 GHz) for a MZI arm unbalance of 1.8 mm. Given a desired group delay ΔT_1, the first *M* (where *M* = ΔT_1/25 ps) pairs of TCs need to be set in cross condition (K_{Ai}=K_{Bi}=1, i=1,.., M), and the (M+1)-th pair is tuned to get the residual delay, as described in [3]. The (M+2)-th pair (if present) has to be set in bar condition. This means that, for every chosen group delay, only the (M+1)-th MZI is effectively working as an interferometer, while all the other TCs are acting just as switches. Hence, the achieved delay-bandwidth product is 2 (while in a single-MZI is 0.5). The delay has been experimentally measured using a 10 Gb/s OOK NRZ modulated signal. The measurement has been performed for a delay of 0, 50 and 100 ps, fig. 3(c-e).
The bandwidth-delay product $B_{3dB}T_D$ of a delay line with M stages against the coupling coefficient K=K_A=K_B is given in fig. 3(f). Defining the bandwidth as the wavelength interval where the group delay changes less than 5% with respect to the central wavelength value [11], the bandwidth-group delay product ($B_{5\%}T_D$) dependence against coupling ratio is reported in fig. 3(g). The benefit of MZI-based delay lines (with respect to all pass ring resonators, shown in red) is evident and becomes more and more evident as the number of stages increases.

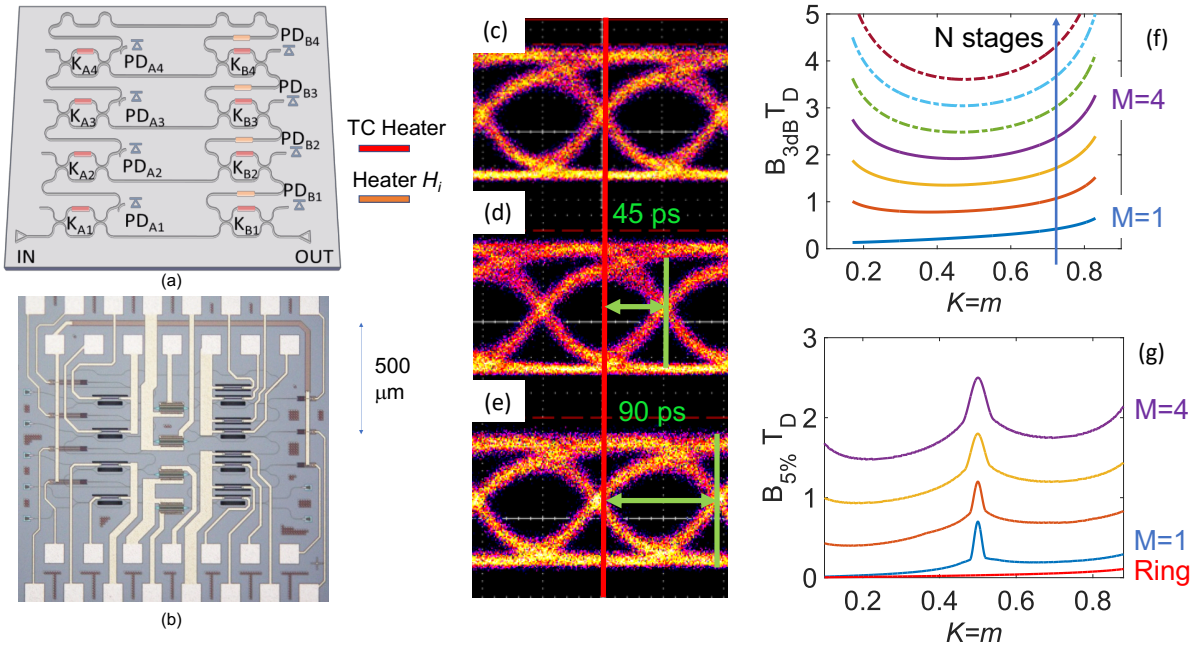


Fig. 3. (a) Schematic of parallel MZI delay line; (b) photograph of the device on a silicon photonics platform; (c-e) Eye diagrams of a 10Gbit/s signal propagating through the shortest path, when it is tuned for the condition M = 3 (45 ps delay) and when it propagates through the longest path. (f) Delay-bandwidth product as a function of K for different number of stages. (g) Same as (f), defining the bandwidth on the group delay flatness. The all-pass ring behavior is reported in red. From [9].

Acknowledgements: The research has been carried out in the framework of the EnTER project, Invitalia n. 0139934. Part of this work was carried out at Polifab, Politecnico di Milano, Milan, Italy.

References

[1] A. Melloni, et al., "Continuously tunable 1 byte delay in coupled-resonator optical waveguides," Optics Letters, 33, October 2008
[2] A. Melloni, A. Canciamilla, C. Ferrari, F. Morichetti, L. O'Faolain, T. F. Krauss, R. D. L. Rue, A. Samarelli and M. Sorel, "Tunable Delay Lines in Silicon Photonics: Coupled Resonators and Photonic Crystals, a Comparison," IEEE Photonics Journal, vol. 2, April 2010.
[3] D. Melati, A. Waqas, Z. Mushtaq and A. Melloni, "Wideband Integrated Optical Delay Line Based on a Continuously Tunable Mach–Zehnder Interferometer," IEEE Journal of Selected Topics in Quantum Electronics, vol. 24, p. 1–8, January 2018.
[4] J. F. Diehl, J. M. Singley, C. E. Sunderman and V. J. Urick, "Microwave photonic delay line signal processing," Applied Optics, July 2015
[5] C. Tsokos, et al., "True Time Delay Optical Beamforming Network Based on Hybrid Inp-Silicon Nitride Integration," JLT 39, 2021.
[6] A. Waqas, D. Melati and A. Melloni, "Cascaded Mach–Zehnder Architectures for Photonic Integrated Delay Lines," IEEE PTL 30, 2018
[7] Z. Mushtaq et al, "Multi-Stage Mach–Zehnder Based Continuously Tunable Photonic Delay Line," Wireless Personal Com. 121, 2021
[8] A. Melloni, D. Melati "Optical delay method and system", US Patent 10,890,717
[9] M. Petrini et al., Variable optical true-time delay line breaking bandwidth-delay constraints, Optics Letters, 48, 2, 2023

Towards Automatic Control of Two ORR-based TTD PIC Optical Beamforming using a Neural Network

Bin Shi[1], Ripalta Stabile[1,2], and Eduward Tangdiongga[1]

[1] Eindhoven Hendrik Casimir Institute, Eindhoven University of Technology, 5600 MB Eindhoven, The Netherlands

[2] Eindhoven AI system Institute, Eindhoven University of Technology, 5600 MB Eindhoven, The Netherlands

[*] b.shi1@tue.nl

In this work, we characterised a 2-ORR-based true time delay on InP photonic integrated circuit, with thermo-optical phase shifters and semiconductor optical amplifiers. The primary results show that the 2 ORRs can provide programable delay bandwidth up to 7.5GHz. We are developing a smart control of the phase shifters and SOA to enable stable optical delay and amplitude.

Keywords: *True Time Delay, Optical Ring Resonator, Photonic Integration, InP platform.*

INTRODUCTION

Optical beamforming networks (OBFN) technology provide advance phase control for modern radar and point-to-point wireless communication systems [1]. The optical ring resonator (ORR) is a promising solution to outperform the electric delay to enhance the bandwidth and avoid signal distortion due to the electromagnetic interference [2]. The development of the photonic integration technology profoundly changes the implementations of the optical components in terms of size, weight, and cost. The photonic integrated ORR-based delay line can provide continues tuning of true time delay (TTD) of the signal with on- and off-resonate operation. The photonic integrated ORR can achieve on- and off- resonate delay in ns [3] and 100's ps [4], respectively. TTD will be applied to the signal path feeding to the elements of a phased-array antenna (PAA), resulting in RF beams pointed to a single or multiple users. If users move, then the beam pointing should track them such that they are kept connected.

The loss of the optical delay line on chip is proportional to loss on the delay path, therefore for antenna array with different paths delay it will result in different signal amplitudes, which cause further loss after equalization [2, 5]. The on-chip gain is one of the solution to this problem. The InP platform is nowadays a matured platform that offers monolithic integration of active and passive photonic components [6]. In our work, we exploit semiconductor optical amplifier to compensate the loss due to the resonance of ORR and enable equalized amplitude at the output. And a 2-ORR structure is employed to tune the pass bandwidth as well as the true time delay of the delay path. We characterised the performance of the fabricated ORR-TTD circuits with tuning the phase shifter on the MZI and on the ring. We are developing the control of the heaters and SOA to mitigate the thermal cross-talk and to provide stable optical delay and signal amplitude for given light source wavelengths.

Experiments

Fig. 1 depicts the schematic of the experimental setup for characterisation of the ORR-TTD integrated chip. A tunable laser is exploited to measure the response of the race-track ORR. The dash box shows the scheme of on-chip optical delay line components on the fabricated chip, including 2 ORRs with individual Mach-Zehnder interferometers (MZIs) for controlling the coupling coefficient, and there is a SOA at the output to control the signal amplitude. The phase shifter 1 and 2 are for the control of phase in the optical ring while phase shifter 3 and 4 are for the control of optical delay by tuning the coupling coefficient, with thermal tuning by heater 1 to 4 as indicated as H1, H2, H3 and H4, in Fig. 1. For the recording the transmission spectrum of the ORRs, the tunable laser is tuned from 1549.7 to 1550.2 nm with 0.01 nm steps, with fixed power of 3.5 dBm. Since we have a SOA on the chip, this SOA can be operated as a photodetector, connecting to an ampere-meter, after calibration with input and output optical power.

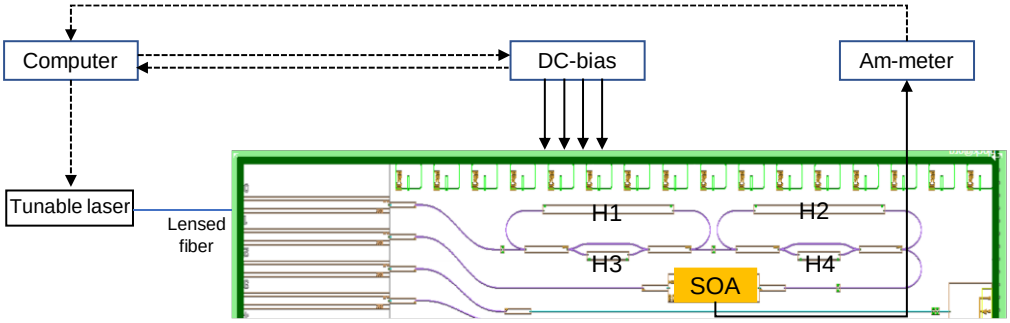


Fig. 1 Schematic of the characterisation experimental setup of ORR-TTD integrated circuit. The InP TTD chip is designed to work in K-band (17-22 GHz).

RESULTS

The response of the 2-ORR structure is shown in Fig. 2. Fig. 2(a-d) show the response transmission spectrum of the 2-ORR TTD, individually tuning voltage on heater H1, H2, H3, and H4, from 0 to 4V with 0.1V per step, with all other heaters off, with the tunable laser scanning in 0.01 nm steps. For increasing the voltage of the heaters, the resonates of the ORRs are shift to the longer wavelength. In Fig. 2(a,b), the extinction ratio of the ORR is 6.7dB and the resonates shift with increasing voltage. And these two figures show that there are two groups of power dip (indicated with blue) shift when tuning the heater voltages. The darker tracks are from the ORR on the effective ring under tuning, while the lighter tracks of dip shift are from the other ORR, which is influenced by a fraction of heat from the other heater. The change of the spectrum from H2 is slightly different to H1 as shown in Fig. 2a due to the resistance of H2 is different to H1. Fig. 2(c,d) show that the extinction ratio increases to maximum when voltage of H3 and H4 are rising up to 2.5V, i.e. increasing the couple coefficient of the ORR, reaching to 14dB. Then it decreases attributing to the further increase of the coupling coefficient with the coupling MZI. However, the resonate wavelength also shifts, due to the thermal cross-talk from H3 and H4, to the race track waveguide of the ORRs, which suggests that the cross-talk demands an accurate control. Fig. 2(e,f) shows the response spectrum variation when tuning the voltage on H3 and H4 when setting bias voltages on the other heater. For tuning H3, the other heaters, H1, H2, and H4, are biased at 2.5, 1, and 0 V, respectively. For tuning H4, the other heaters, H1, H2, and H3, are biased at 2.5, 1, and 2.5 V, respectively. Fig 2(e,f) show that the wavelength resonance can still be controlled by the phase shifters in the rings albeit the patterns become complicated. Nonetheless, the 2-ORR is capable to tune bandwidth and time delay of the delay line. Fig. 2g shows the spectrum of 2-ORR TTD with different pass bandwidth of 3, 4, 6.5, and 7.5 GHz, which are realized by setting different voltages on the heaters to detune the two resonance patterns on the two ORRs.

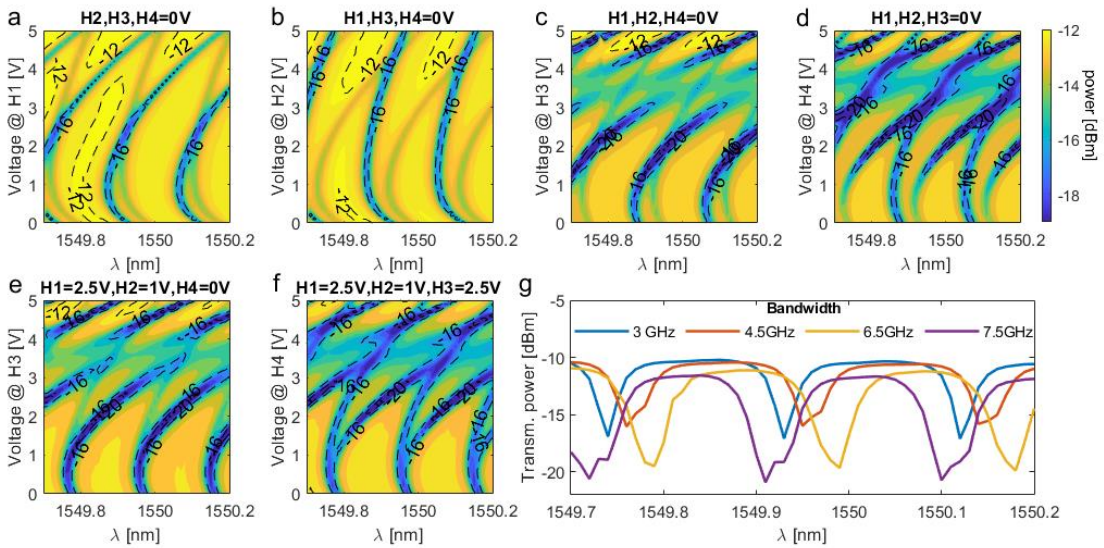


Fig. 2 The response of the 2-ORR TTD on InP photonic integrated circuit, with tuning 4 different heaters.

DISCUSSION

The optical beamforming network comprises cascaded ORR time delays, with 2-ORR TTD components, and connected by MZI or couplers, with equalized output optical power. The loss induced by the on-resonate delay of ORR and the equalized output can be compensated by the gain of the SOA on-chip. So far, the beam pointing control is done by adjusting the voltage level of individual heaters according to a look-up table. For a static and semi-mobile or nomadic user, this way of controlling the beam pointing may be sufficient since once the correct value of voltages is reached, the control will keep the same value and possibly with some adjustments due to the inevitable thermal cross-talk between the heaters. However, if users move, then the look-up table must be updated with new values according to their speeds and direction. Therefore, an automatic, accurate, and fast beam tracking and pointing control is needed to provide seamless connectivity to mobile users. In this context, we are developing the control of thermal crosstalk on the heaters, to have a fast automatic tuning according to the target beam steering angle. The control makes use of a combination of electrical and optical signal processing employing a neural network concept with an optimized cost function regarding latency, complexity and update speeds to serve users moving at walking speeds, i.e. 1-5 m/s. The schematic of the control part is shown in Fig. 3.

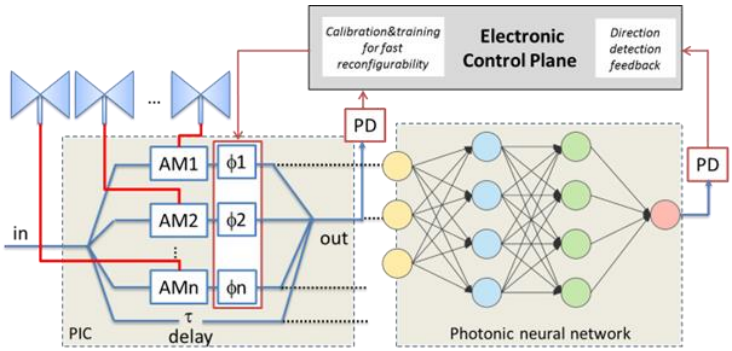


Fig. 3 Schematic of a hybrid electro-optical neural network RF beam pointing controller.

Acknowledgements: This research work is financially supported by the Netherlands Organization of Scientific Research (NWO) under the Zwaartekracht programma, 'Research Centre for Integrated Nanophotonics'. Authors thank Ailee Trinidad and Johan van Zantvoort for the helps on the photonic design and experimental setup.

References

[1] N. M. Tessema et al., "A Tunable Si3N4 Integrated True Time Delay Circuit for Optically-Controlled K-Band Radio Beamformer in Satellite Communication," in Journal of Lightwave Technology, vol. 34, no. 20, pp. 4736-4743, 15 Oct.15, 2016, doi: 10.1109/JLT.2016.2585299.

[2] Liu, Y., Wichman, A., Isaac, B., Kalkavage, J., Adles, E. J., Clark, T. R., & Klamkin, J. (2017). Tuning Optimization of Ring Resonator Delays for Integrated Optical Beam Forming Networks. Journal of Lightwave Technology, 35(22), 4954–4960. https://doi.org/10.1109/JLT.2017.2762641

[3] Xiang, C., Davenport, M. L., Khurgin, J. B., Morton, P. A., & Bowers, J. E. (2018). Low-Loss Continuously Tunable Optical True Time Delay Based on Si3N4 Ring Resonators. IEEE Journal of Selected Topics in Quantum Electronics, 24(4). https://doi.org/10.1109/JSTQE.2017.2785962

[4] Shan, W., Lu, L., Wang, X., Zhou, G., Liu, Y., Chen, J., & Zhou, L. (2021). Broadband continuously tunable microwave photonic delay line based on cascaded silicon microrings. Optics Express, 29(3), 3375. https://doi.org/10.1364/oe.416000

[5] Choo, G., Madsen, C. K., Palermo, S., & Entesari, K. (2018). Automatic monitor-based tuning of an RF silicon photonic 1X4 asymmetric binary tree true-time-delay beamforming network. Journal of Lightwave Technology, 36(22), 5263–5275. https://doi.org/10.1109/JLT.2018.2873199

[6] Smit, M., Leijtens, X., Ambrosius, H., Bente, E., van der Tol, J., Smalbrugge, B., de Vries, T., Geluk, E.-J., Bolk, J., van Veldhoven, R., Augustin, L., Thijs, P., D'Agostino, D., Rabbani, H., Lawniczuk, K., Stopinski, S., Tahvili, S., Corradi, A., Kleijn, E., … Robbins, D. (2014). An introduction to InP-based generic integration technology. Semiconductor Science and Technology, 29(8), 083001. https://doi.org/10.1088/0268-1242/29/8/083001